GFZ

Helmholtz Centre
POTSDAM

HELMHOLTZ CENTRE POTSDAM
GFZ GERMAN RESEARCH CENTRE
FOR GEOSCIENCES

Susanne Lunz

Enhancing the alignment between the celestial reference frames from very long baseline interferometry and Gaia

Scientific Technical Report STR23/02

www.gfz-potsdam.de

Recommended citation of the publication

Lunz, S. (2023): Enhancing the alignment between the celestial reference frames from very long baseline interferometry and Gaia, PhD Thesis, (Scientific Technical Report STR; 23/02) Potsdam: GFZ German Research Centre for Geosciences. https://doi.org/10.48440/gfz.b103-23027

Originally published as

Lunz, S. (2023). Enhancing the alignment between the celestial reference frames from very long baseline interferometry and Gaia, PhD Thesis, Berlin: Technische Universität.
https://depositonce.tu-berlin.de/handle/11303/19717

Imprint

Helmholtz Centre Potsdam
GFZ German Research Centre for Geosciences
Telegrafenberg
D-14473 Potsdam

Published in Potsdam, Germany
2023

DOI: https://doi.org/10.48440/gfz.b103-23027
URN: urn:nbn:de:kobv:b103-23027

This work is published in the GFZ series Scientific Technical Report STR and electronically available via our repository GFZpublic: https://tinyurl.com/GFZ-ST-Reports

Enhancing the alignment between the celestial reference frames from very long baseline interferometry and Gaia

vorgelegt von
M. Sc.
Susanne Lunz
ORCID: 0000-0002-0349-2747

an der Fakultät VI - Planen Bauen Umwelt
der Technischen Universität Berlin
zur Erlangung des akademischen Grades

Doktorin der Ingenieurwissenschaften
- Dr.-Ing. -

genehmigte Dissertation

Promotionsausschuss:

Vorsitzender: Prof. Dr. Jürgen Oberst
Gutachter: Prof. Dr. Dr. h.c. Harald Schuh
Gutachter: Prof. Dr. Lennart Lindegren
Gutachter: Prof. Dr. habil. Sergei A. Klioner

Tag der wissenschaftlichen Aussprache: 23. Mai 2023

Berlin 2023

Acknowledgements

This work is only a snapshot of what is possible to do in this field. First of all, I would like to thank Professor Harald Schuh very much for giving me the opportunity, trust, and freedom to conduct the studies that led to this work. To my colleagues James Anderson, Minghui Xu, and Oleg Titov, I thank you very much for fruitful discussions about my work. In particular, I would like to thank James for his patience in explaining to me in detail the theoretical aspects of processing the phase-referenced data and Minghui for the discussions about the impact of source structure on VLBI observations. I also thank Megan Johnson and the team at USNO for providing me with observation time at the VLBA. I am grateful for the kind colleagues in the VLBI group at GFZ and the helpful IT staff and secretaries. Last but not least, I would like to thank the thesis reviewers, Professor Lennart Lindegren and Professor Sergei Klioner for their time and effort in evaluating my work. I would like to thank Professor Lindegren for his inspiring work on using radio stars to test the alignment for the Gaia bright frame, and I would like to thank Professor Klioner for his great supervision during my undergraduate thesis, introducing me to the topics of Galactocentric acceleration and VLBI.

This work is supported by the DFG grants No. HE 5937/2-2 and No. SCHU 1103/26-1. I acknowledge use of the Very Long Baseline Array under the US Naval Observatory's time allocation. This work supports USNO's ongoing research into the celestial reference frame and geodesy. I also thank the Socorro correlator for reliably and quickly providing the correlated data. The National Radio Astronomy Observatory is a facility of the National Science Foundation operated under cooperative agreement by Associated Universities, Inc.

I acknowledge the use of two large radio telescopes: Tianma65 and Parkes. The Parkes radio telescope is part of the Australia Telescope National Facility which is funded by the Australian Government for operation as a National Facility managed by CSIRO. Some of the observations of radio stars were coordinated within the framework of the Asia-Oceania VLBI Group for Geodesy and Astrometry (AOV). The scheduling and data correlation were supported by three AOV member institutes which include Shanghai Astronomical Observatory of Chinese Academy of Sciences, University of Tasmania in Australia and Geospatial Information Authority of Japan. Experiments V515C and AUA020 were done with participation of the Scientific Equipment Sharing Center of the Quasar VLBI Net-

work of the Institute of Applied Astronomy of the Russian Academy of Sciences (IAA RAS).

This work has made use of the data from the European Space Agency (ESA) mission *Gaia* processed by the *Gaia* Data Processing and Analysis Consortium as well as from the mission HIPPARCOS. Funding for the DPAC has been provided by national institutions, in particular the institutions participating in the *Gaia* Multilateral Agreement.

Calibrators were selected using the helpful NRAO VLBA calibrator search tool, the RFC calibrator search tool and the Astrogeo VLBI FITS image database. This research has made use of the VizieR catalog access tool and the SIMBAD database (Wenger et al. 2000), operated at CDS, Strasbourg, France. Calculations were made in MATLAB by The MathWorks, Inc.

Abstract

The International Celestial Reference System (ICRS) is the reference system used for astrometry and geodesy in space. Its realizations are the International Celestial Reference Frames (ICRFs). The latest realizations are ICRF3 S/X, ICRF3 K, and ICRF3 X/Ka at radio frequencies observed by geodetic very long baseline interferometry (VLBI), and Gaia-CRF3 from observations by the Gaia spacecraft at optical frequencies. The ICRFs are independently derived catalogs of mean positions (and proper motions as well as parallaxes in case of Gaia) of distant compact extragalactic sources with approximately comparable precision. Within the error bounds, the different observation setups should ideally produce identical source positions. However, previous research discovered variances related to the variable nature of the sources as a function of frequency and time. A deeper understanding of the individual source position differences as well as the alignment of the ICRFs in terms of global systematic source position differences benefits the large ICRF and Gaia user community, such as geodetic VLBI for connecting VLBI products across frequencies.

This work adds several case studies to the existing research on the comparison and the alignment of the ICRFs. At optical frequencies, the set of ICRF3 counterparts in the Gaia spacecraft's Early Data Release 3 (Gaia EDR3, including Gaia-CRF3) and in Gaia DR2, the predecessor of Gaia EDR3, are investigated. The position differences of the individual counterparts at the various frequencies are re-evaluated, focusing on the correlation of the normalized distances, offset directions, and global systematic differences with the number of VLBI observations or the extent of radio source structure. The individual VLBI and Gaia position offsets tend to be in the same direction, especially in case of significant offsets. It is shown that large normalized position offsets are related to sources with large radio structure. The global systematic differences, which are an order of magnitude smaller than the individual differences, can be accurately determined, especially if the set of counterparts has been defined. A Celestial Reference Frame (CRF) determined from S/X observations from the same time interval as Gaia DR2 does not indicate any improvements in the alignment of Gaia DR2 compared to ICRF3 S/X.

Since the alignment of Gaia DR2 and Gaia EDR3 depends on the visual magnitude G and the radio sources in ICRF3 are optically faint, the alignment of the bright fraction ($G \leq 13\,\mathrm{mag}$) of the Gaia data releases to ICRF3 requires additional verification. The approach and data of Lindegren (2020a) are adopted, who used optically bright radio stars to test the alignment. Since the resolution of VLBI and Gaia is small enough to detect their proper motions, they must be included in the alignment test and a time variability of the alignment (spin) must also be estimated. However, these results are not yet accurate

enough compared to the expected uncertainties of the individual sources astrometry in the final Gaia data release for this G magnitude range.

In this work, these VLBI data of radio stars are homogenized, and a more realistic error budget for the VLBI positions is established. New, dedicated VLBI observations of bright radio stars were carried out to obtain more urgently needed VLBI positions for the determination of the alignment. The positions are included in two ways: once as absolute one-epoch positions and once as relative positions in order to derive new precise models of stellar motion whenever possible. A significant spin around the Y axis was determined for both Gaia DR2 and Gaia EDR3, albeit the rotations in this direction are still the least well determined. Among other aspects, the accuracy of the results, the effect of nonlinear proper motion, and a G magnitude dependence within the bright fraction are investigated. The effect of possible future VLBI observations of radio stars on the alignment is tested.

In summary, this work evaluates the accuracy of the alignment of the current ICRFs. It furthermore highlights the need to accurately assess VLBI observations of radio stars in the context of the alignment of the Gaia bright frame with ICRF3 and demonstrates how this can be accomplished.

Kurzzusammenfassung

Das International Celestial Reference System (ICRS) ist das Himmelsreferenzsystem, das in der Astrometrie und Geodäsie verwendet wird. Seine Realisierungen sind die International Celestial Reference Frames (ICRFs). Die jüngsten Realisierungen sind im Radiofrequenzbereich der ICRF3 S/X, der ICRF3 K und der ICRF3 X/Ka, welche mit Hilfe von geodätischer very long baseline interferometry (VLBI) beobachtet werden. Außerdem ist es im optischen Frequenzbereich der Gaia-CRF3, welcher aus Beobachtungen des Gaia Weltraumteleskops stammt. Die ICRFs sind unabhängig voneinander abgeleitete Kataloge mittlerer Positionen (und Eigenbewegungen als auch Parallaxen im Falle von Gaia) entfernter kompakter extragalaktischer Quellen mit annähernd vergleichbarer Genauigkeit. Innerhalb der Fehlergrenzen sollten die verschiedenen Beobachtungsmethodiken idealerweise zu identischen Quellenpositionen führen. In früheren Untersuchungen wurden jedoch Abweichungen festgestellt, die mit der frequenz- und zeitvariablen Quellenstruktur zusammenhängen. Ein tieferes Verständnis der individuellen Positionsunterscheide der Quellen als auch der Unterschiede in der Orientierung der ICRFs mittels globaler systematischer Positionsunterschiede der Quellen kommt der großen Nutzergruppe von ICRF und Gaia zugute, wie z. B. der geodätischen VLBI für die Zusammenführung von VLBI-Produkten über Frequenzen hinweg.

Diese Arbeit ergänzt die bestehenden Forschungsarbeiten über den Vergleich und die Orientierung der ICRFs um mehrere Fallstudien. Im optischen Frequenzbereich werden die ICRF3-Gegenstücke im Early Data Release 3 (Gaia EDR3, einschließlich Gaia-CRF3) der Gaia Raumsonde und im Gaia DR2, dem Vorgänger von Gaia EDR3, untersucht. Die Positionsunterschiede der einzelnen Gegenstücke für die verschiedenen Frequenzen werden neu bewertet, wobei der Schwerpunkt auf der Korrelation der normalisierten Entfernungen, der Richtungen der Positionsdifferenzen und der globalen systematischen Unterschiede mit der Anzahl der VLBI-Beobachtungen sowie dem Ausmaß der Radioquellenstruktur liegt. Die individuellen VLBI- und Gaia-Positionsunterschiede bevorzugen die selbe Richtung, insbesondere im Falle signifikanter Differenzen. Es wird gezeigt, dass große normalisierte Positionsunterschiede auf Quellen mit großer Radioquellenstruktur zurückzuführen sind. Die globalen systematischen Abweichungen, die um eine Größenordnung geringer sind als die individuellen Differenzen, können genau bestimmt werden. Dies gilt insbesondere wenn die Teilmenge der verwendeten Gegenstücke vorher definiert wurde. Ein Celestial Reference Frame (CRF), der aus S/X-Beobachtungen des selben Zeitintervalls wie Gaia DR2 ermittelt wurde, zeigt keine Verbesserungen in der Ausrichtung von Gaia DR2 im Vergleich zu ICRF3 S/X.

Da die Orientierung von Gaia DR2 und Gaia EDR3 von der scheinbaren Helligkeit G ab-

hängt und die Radioquellen des ICRF3 eine geringe scheinbare Helligkeit aufweisen, muss die Ausrichtung des hellen Anteils ($G \leq 13\,\mathrm{mag}$) der Gaia-Daten auf den ICRF3 zusätzlich überprüft werden. In dieser Arbeit werden der Ansatz und die Daten von Lindegren (2020a) übernommen, der zur Überprüfung der Orientierung scheinbar helle Radiosterne verwendete. Da die Auflösung von VLBI und Gaia klein genug ist, um Eigenbewegungen von Sternen zu erkennen, müssen diese in den Orientierungstest einbezogen und auch eine zeitliche Variabilität der Orientierung geschätzt werden. Allerdings sind diese Ergebnisse bisher nicht genau genug im Vergleich zu den erwarteten Genauigkeiten der Astrometrie der einzelnen Quellen des hellen Anteils in der endgültigen Gaia-Datenveröffentlichung.

In dieser Arbeit werden die vorhandenen VLBI-Daten der Radiosterne homogenisiert und es wird ein realistischeres Fehlerbudget für die VLBI-Positionen aufgestellt. Es wurden neue, gezielte VLBI-Beob-achtungen von hellen Radiosternen durchgeführt, um mehr dringend benötigte VLBI-Positionen für eine bessere Bestimmung der Orientierung zu erhalten. Die Positionen wurden auf zwei verschiedene Arten integriert: einmal als absolute Positionen aus einer Beobachtungsepoche und einmal als relative Positionen, um wann immer möglich neue präzise Modelle der Sternbewegung abzuleiten. Sowohl für Gaia DR2 als auch für Gaia EDR3 wurde eine signifikante zeitabhängige lineare Rotation um die Y-Achse ermittelt, wenngleich die Rotationen in dieser Richtung noch die geringste Genauigkeit aufweisen. Unter anderem werden die Genauigkeit der Ergebnisse, die Auswirkung der nichtlinearen Eigenbewegung und die Abhängigkeit von der scheinbaren Helligkeit innerhalb des hellen Anteils untersucht. Der Einfluss möglicher zukünftiger VLBI-Beobachtungen von Radiosternen auf die Orientierungsbestimmung wird getestet.

Zusammenfassend evaluiert diese Arbeit die Genauigkeit der Orientierung der aktuellen ICRFs. Sie unterstreicht darüber hinaus die Notwendigkeit, VLBI-Beobachtungen von Radiosternen im Zusammenhang mit der Orientierung des hellen Gaia-Referenzrahmens zu ICRF3 genau zu prüfen, und zeigt, wie dies erreicht werden kann.

Statement of authorship

I hereby certify that I have authored this document entitled "Enhancing the alignment between the celestial reference frames from very long baseline interferometry and Gaia" independently and without undue assistance from third parties. No other than the resources and referenced indicated in this document have been used. I have marked both literal and accordingly adopted quotations as such. There were no additional persons involved in the intellectual preparation of the present document. I am aware that violations of this declaration may lead to subsequent withdrawal of the academic degree.

Potsdam, 04 November 2022

Susanne Lunz

Contents

List of Figures

List of Tables

Acronyms

AF astrometric field.

AGIS Astrometric Global Iterative Solution.

AGN active galactic nuclei.

CARMS Closure amplitude root mean square.

CCD charge-coupled device.

CRF Celestial Reference Frame.

CRS Celestial Reference System.

DPAC Gaia Data Processing and Analysis Consortium.

DR data release.

DSN Deep Space Network.

EOP Earth Orientation Parameter.

ESA European Space Agency.

EVN European VLBI Network.

FK5 Fifth Fundamental Catalogue.

FWHM full width at half maximum.

GFZ German Research Centre for Geosciences.

GNSS global navigation satellite systems.

IAU International Astronomical Union.

ICRF International Celestial Reference Frame.

ICRF1 first realization of the International Celestial Reference Frame.

ICRF2 second realization of the International Celestial Reference Frame.

ICRF3 third realization of the International Celestial Reference Frame.

ICRS International Celestial Reference System.

IERS International Earth Rotation and Reference Systems Service.

ITRF International Terrestrial Reference Frame.

IVS International VLBI Service for Geodesy and Astrometry.

LST Local Sidereal Time.

ME mean formal error.

MS mean standard deviation.

NNR no-net rotation.

NNT no-net translation.

PFA probability of false association.

RMS root mean square.

RUWE re-normalized unit weight error.

SNR signal-to-noise ratio.

TDI Time-Delayed Integration.

TEC total electron content.

TRF terrestrial reference frame.

VGOS VLBI Global Observing System.

VLBA Very Long Baseline Array.

VLBI very long baseline interferometry.

VSH vector spherical harmonics.

WC window class.

WM weighted mean.

WRMS weighted root mean square.

1 Introduction

1.1 Overview

Astrometry is the science of determining exact positions, proper motions, and trigonometric parallaxes for sources in the sky. The positions of the sources must be published in a defined reference system to make datasets from different studies comparable for the various users in geodesy, astrometry, astrophysics, and other fields. For most of the more than two thousand years that astrometry was practiced, stars served as a reference. However, with increasing accuracy and precision of the measurements, the proper motion and parallax signals became visible for many of the stars leading to problems using them as a reference (Perryman 2012).

Nowadays, distant compact extragalactic sources, mostly active galactic nuclei (AGN), are used as reference points. They are far enough away from the observer located in the Solar System to presume that they are sufficiently compact despite the high resolution, that they have no detectable proper motion and no trigonometric parallax signal, and that they are not affected by any complex motions in our Galaxy. AGN were first detected in the 1960s and already in 1998 the first International Celestial Reference Frame (ICRF) in the form of a catalog of AGN positions was approved (Ma et al. 1998). The AGN positions were derived from geodetic very long baseline interferometry (VLBI) observations using radio antennas on Earth. This catalog is the realization of the new quasi-inertial reference system, the International Celestial Reference System (ICRS). It defines an orthogonal triad of axes X, Y, and Z at any epoch. The positions of the sources are then given as angles of right ascension and declination on the celestial sphere with respect to the orthogonal planes defined by the axes.

The latest realization of the ICRS by VLBI as of January 2019 is the third realization of the International Celestial Reference Frame (ICRF3). It contains precise positions of 4 588 AGN, 303 of which realize the orientation of the ICRS axes (Charlot et al. 2020). The ICRF3 provides three realizations of the ICRS, one at each of the three different radio bands, S/X, K, and X/Ka. The predecessors of ICRF3 only included the S/X frequency setup. The common orientation of the celestial reference frames (CRFs) from the three frequency setups, and therefore the same origin for right ascension and declination, is essential to make the positions from different frequencies comparable for the scientific

and operational user. The precise ICRF at S/X bands is for example used by geodetic VLBI to determine the Earth Orientation Parameter (EOP) and the positions of the antennas on Earth.

An independent realization of the celestial reference frame at optical frequencies is the Gaia-CRF3 from January 2022 (Gaia Collaboration et al. 2022). It is determined from observations of the Gaia spacecraft, which is operated by ESA and which was launched in 2014. One advantage of Gaia compared to VLBI is that the Earth's atmosphere does not impact the observations. Not only are the positions at optical wavelengths of interest to the scientific community, but so is the much larger dataset of 1.8 billion sources of the Local Group and our Galaxy contained in the latest Gaia data release (Gaia EDR3, of which Gaia-CRF3 is the reference frame), as opposed to only a few thousand sources in the VLBI-based datasets. Already, the Gaia data releases surpass any other astronomical catalog including those from VLBI, among others, in terms of number of objects and precision of the astrometric parameters such as position, linear proper motion, and parallax. However, Gaia essentially measures only relative positions and proper motions between sources, which means that the Gaia-CRF has six degrees of freedom, one each for the unknown small rotation in the direction of the three ICRS axes in the form of the instantaneous global rigid rotation (orientation offset) and its linear time derivative (spin). Thus, the Gaia-CRF was oriented to ICRS with the help of ICRF3. In addition, the zero spin was defined using the zero proper motions of ICRF3 and proper motions from observations of another spacecraft in the infrared. The final Gaia catalog, which is planned to be released in a few years, will most likely be the most precise source of optical coordinates for several decades. Thus, confirming the Gaia-CRF's global rotation towards the three ICRS axes is critical for high-precision navigation and orientation in space as well as the comparison to observations from ground-based optical telescopes. Considering error propagation, this is especially true after mission completion when the systematic spin and the individual proper motion errors outweigh the individual position errors.

Special care has to be taken to confirm the rotation for the optically bright sources, because they are still commonly employed for attitude control and they are being studied for use in deep space navigation outside of the Medium Earth Orbit when signals of the global navigation satellite systems (GNSS) cannot be reached anymore (Optical Navigation Experiment[1] Martin-Mur et al. 2017). Because of their proximity to Earth, these sources (mostly stars) are not included in either ICRF3 or Gaia-CRF3.

The alignment of the Gaia and VLBI-based CRFs like ICRF3 has been studied by scientists already. Alignment in this context means the determination of the orientation offset in form of a rotation A about the three axes of one of the two respective CRFs from position differences of counterparts between the two CRFs. Additionally a global dipole pattern

[1] mars.nasa.gov/mro/mission/timeline/mtapproach/approachopticalnav/, accessed 12 June 2021.

(glide D) for each of the three axes and higher order systematics using vector spherical harmonics (VSH) parameterization are determined when possible. Mostly, the VSH terms a up to the quadrupole are used, so that a total of 16 transformation parameters between the two frames are determined. A collection of parameters from literature is shown in Fig. 1.1. In the literature, the spin between Gaia and ICRF3 or any other VLBI-based CRFs is assumed to be zero due to the counterparts being AGN. Otherwise, the spin can be determined from proper motion differences or position differences divided by their epoch difference.

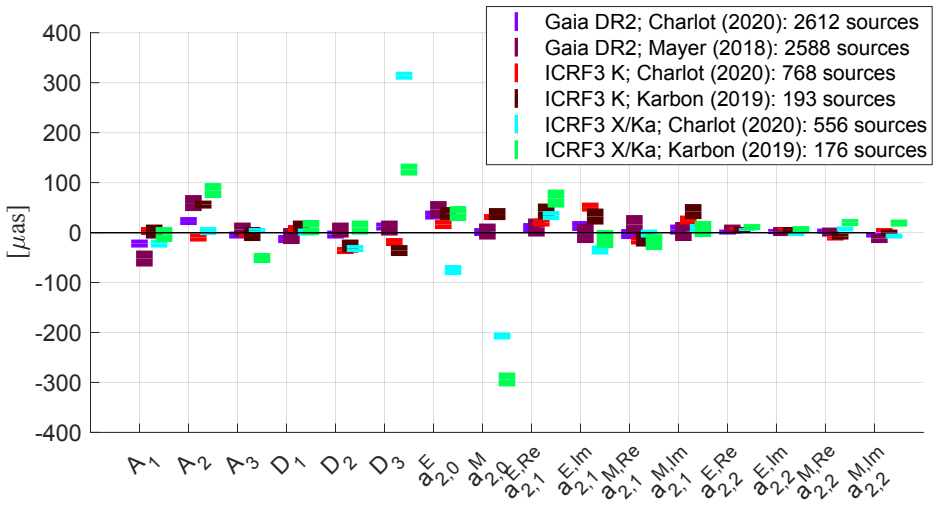

Figure 1.1 Transformation parameters between different CRFs and ICRF3 S/X from the literature review. Two publications each were found listing estimates between Gaia DR2, ICRF3 K and ICRF3 X/Ka.

Karbon and Nothnagel (2019) compared the ICRF3 catalogs and found no statistically significant position differences between the positions at different radio frequencies. This is because the differences between various versions of CRFs with similar data input based on S/X bands have larger position variations than the position differences between the three ICRF3 catalogs. As a result, the researchers created a multi-frequency CRF by combining the normal equations from the three ICRF3 catalogs.

The Gaia and VLBI positions and reference frames have previously been extensively compared by many scientists. While Bourda, G. et al. (2008) and Makarov et al. (2019) identified a set of probably most suitable counterparts between radio and optical CRFs, usually all available counterparts except empirically determined outliers are used. Most studies define the outliers by a specific threshold of normalized arc lengths and possibly also arc lengths (differences between the two positions of a counterpart). Other studies, such as Mayer (2018) and Karbon and Nothnagel (2019) iteratively, instead removed all sources which impact the VSH parameters by more than three times their standard

deviation. When ICRF3 was published, a first comparison to Gaia DR2 was conducted by Charlot et al. (2020) already. There were 2983 counterparts identified (163 counterparts more than in Gaia-CRF2) and the outlier elimination process left 2612 counterparts for the alignment test. The differences in the rotation parameters do not exceed $\pm 25\,\mu$as and the VSH parameters are not significant except the higher order zonal term $a^{E}_{2,0} = 35 \pm 9\,\mu$as. It is hypothesized that this deformation is due to the heterogeneity of the VLBI networks in the north-south direction. It is concluded that the two frames are consistent at the 30 µas level, which is the same as the noise floor of ICRF3 S/X (Charlot et al. 2020). The systematics between the ICRF3, its predecessors, and Gaia DR2 and their dependence on G magnitude were documented by Liu et al. (2020) using also VSH. Similarly, Mayer (2018) studied the alignment between his own CRF based on S/X observations, ICRF3 and Gaia DR2. He tested the impact of various changes in the estimation of his VLBI-based CRF and found among others, that mostly the $a^{E}_{2,0}$ and D_3 parameters are impacted by using Ray tracing. Furthermore, absolute constraints on gradients impact the D_3 parameter. Although the selection of counterparts is slightly different, both studies obtain similar results to Charlot et al. (2020).

In Gaia Collaboration et al. (2022) it is shown that there are no highly significant systematic global differences between ICRF3 S/X and Gaia-CRF3 in terms of VSH. After expanding the exponents of VSH, the largest differences were found in the less populated areas of the sky, which are below a declination of $-30°$ and around the Galactic plane. Gaia Collaboration et al. (2022) found that the orientation of the Gaia-CRF3 towards ICRF3 S/X is sensitive to the selection of counterparts at the level of several µas and for the spin of a few $\mu\mathrm{as\,yr}^{-1}$.

When the two datasets are properly aligned or the systematic differences have been determined to be negligible, radio-optical position offsets can be studied in order to learn more about the astrophysical properties of the objects. Naturally, the statistically significant position offsets were preferred in this case. They arise for example because the AGN are not compact, as assumed by geodetic VLBI but have structure or even multiple components. After an initial crossmatch in Petrov and Kovalev (2017), Kovalev et al. (2017) investigated the radio-optical position offset direction versus radio jet angles from VLBI images for Gaia DR1, and found that the radio-optical offsets are mostly along (0 to tens of milliarcseconds (mas)) or opposite to the jet direction (up to 3 mas). They explain these offsets by extended parsec-scale source structure in the optical domain. Petrov and Kovalev (2017) explain the cause of the differences in the different observing method: while Gaia sees the photocenter of the detected emission on charge-coupled devices (CCDs) (centroid of optical emission), VLBI sees the most compact radio emission at the jet base (opaque radio core). Small offsets up to 1 mas opposite the jet directions were expected to be due to source structure in the radio domain or core shift (Kovalev et al. 2017). Petrov

et al. (2018) showed the improved determination of the findings of Kovalev et al. (2017) using Gaia DR2. Plavin et al. (2019) further categorized the AGN according to these offsets. Gaia EDR3 optical positions and ICRF3 radio positions at various frequencies of individual sources have been previously compared by Xu et al. (2021); Lambert et al. (2021); Liu et al. (2021). Significant position offsets could be explained by consulting VLBI images, such as from the MOJAVE database (Lister et al. 2018). Xu et al. (2021) showed evidence of the ICRF3 S/X and Gaia EDR3 position offsets depending on radio source structure with the help of ICRF3 S/X-based Closure amplitude root mean square (CARMS).

In examining the orientation offset and spin of Gaia DR2, it was found that there is a dependence of the alignment on the apparent brightness (G magnitude) due to a deficiency in the calibration model of the astrometric instrument (Lindegren et al. 2018; Lindegren 2020a). Since the counterparts in the radio CRFs used for the alignment are optically faint, another method had to be found to test the alignment of the bright ($G \leq 13$ mag) fraction of the Gaia catalog to ICRF. Lindegren (2020a) proposed the use of optically bright radio stars observed with VLBI. Geodetic VLBI as employed for the creation of the ICRF is not sensitive enough to provide accurate star positions for radio faint objects. Instead, the stars have to be observed relative to a radio-bright calibrator by phase-referencing VLBI. With this observing method, the orientation offset and the spin between the VLBI-based ICRF and Gaia can be verified, as the stars astrometry is then provided in ICRF. This approach has already been used for the alignment of the HIPPARCOS catalog (Lindegren and Kovalevsky 1995; Lestrade et al. 1999). Using Lindegren's method, the star positions are used for the determination of the orientation offset, and the positions and the proper motions are used for the determination of the spin.

Malkin (2016b) published simulations on using geodetic VLBI observations of radio stars from global VLBI networks to determine the orientation offset between VLBI and Gaia. At that time the possible spin between the two frames and the magnitude dependence of the Gaia calibration were not known. He tested various VLBI and Gaia position uncertainties and number of counterparts. However, the study does not consider any systematic errors such as orbital motion of the stars.

Cantat-Gaudin and Brandt (2021) suggested a Gaia-only solution, in which the proper motion of optically bright and optically faint sources in wide binaries and open clusters were compared with very high precision. Due to the large sample of counterparts, they could also find spin differences between various G magnitude subsets of the bright Gaia dataset. However, with their method only the spin can be determined.

An alignment to the (historic) HIPPARCOS reference frame instead of ICRF3, as it was done for the Gaia EDR3 (Lindegren et al. 2021b), sounds tempting because of the many more counterparts for optically bright sources compared to VLBI data. However,

the accuracy of the alignment is limited to 600 µas in each axis (Kovalevsky et al. 1997) due to the uncertainty of the orientation offset between the HIPPARCOS positions and the ICRS at epoch 1991.25. Accounting for the difference to the Gaia epochs, this leads to a systematic uncertainty of 24 $\mu as\,yr^{-1}$ in the spin determination using HIPPARCOS for comparison.

Thus, the radio star method is the only one that seems to be suitable to achieve formal errors for both orientation offset and spin smaller than the expected position uncertainties of 6 µas and proper motion uncertainties of 2 $\mu as\,yr^{-1}$ for bright sources ($G \leq 13$ mag) in the final Gaia data release[2]. Lindegren (2020,a,b) found a significant orientation offset between ICRF3 and Gaia DR2 using 41 bright radio stars from a literature review. The spin was not significantly determined, however the estimates aligned to those of past work from a comparison to HIPPARCOS. However, the uncertainty of the orientation offset and spin from this method and dataset are not yet sufficiently small as required by the uncertainties of the individual positions and proper motions of the bright sources.

1.2 Objectives

The objectives of this thesis are the evaluation and improvement of the alignment between various celestial reference frames. In particular, the focus lies on:

- the evaluation of the alignment between the ICRF3 realizations at various radio frequencies and between ICRF3 and the Gaia data releases DR2 and EDR3 for optically faint objects. Due to the large number of counterparts this includes the test of additional suitable alignment parameters in addition to the rotations only and a test of the impact of using different subsets for the alignment,
- the quantification of the impact of radio source structure of extragalactic objects on this alignment by providing a CRF product whose observations cover the same time span as the Gaia data release DR2 and by comparing the position offsets to an external radio source structure classification called CARMS,
- the evaluation and enhancement of the alignment of the optically bright fraction of the Gaia data releases DR2 and EDR3 to ICRF3 S/X. Due to the small number of counterparts, only the rotations are investigated.

This is the first time that the determination of the alignment by iteratively rejecting the most discrepant source as introduced in Lindegren (2020a) for the optically bright sources is also tested for the optically faint reference frame. Statistics for quantifying the stability of the iterative parameter analysis are newly derived.

[2] https://www.cosmos.esa.int/web/gaia/science-performance#astrometric performance, accessed 24 October 2021. For bright sources these predictions are uncertain.

This thesis primarily focuses on the improvement of the bright Gaia reference frame alignment. This is achieved by homogenization of existing suitable VLBI data of stars from literature and by quantification of a realistic error budget of absolute VLBI positions in ICRF3 from phase-referencing observations. Thereby two cases are distinguished; on the one hand, absolute star positions from models of stellar motion and, on the other hand, absolute star positions from a single observation epoch. In addition, new dedicated VLBI observations of radio stars were proposed, planned, processed and evaluated. New models of stellar motion were determined for stars whenever possible. Special attention is given to handling the effect of the Galactocentric acceleration on positions and proper motions from VLBI consistent to Gaia. These aspects are novel to this field of research. The goal is to enhance the analysis for Gaia DR2 in Lindegren (2020a) from VLBI side and also to find out the presence of residual spin in Gaia EDR3.

1.3 Thesis outline

This work is subsequently organized as follows:

- Chapter 2 introduces the two astrometric observation techniques compared in this work, VLBI and Gaia, and the concept of ICRS from literature review. The differences between geodetic VLBI used for observations of AGN and the phase-referencing VLBI used for observations of radio stars are pointed out. The origin of the G magnitude dependence is described as well.
- Chapter 3 gives a background on the mathematical models used for the comparison of positions from various CRFs. The emphasis is on identifying radio-optical counterparts, determining the position offsets of individual sources, and estimating the alignment of two CRFs in terms of systematic global differences. The reader is provided with all necessary information required for comprehending the contents of the subsequent chapters.
- Chapter 4 presents the comparison between ICRF3, Gaia DR2, Gaia EDR3, and two dedicated own CRFs based on S/X observations. First, the radio CRFs are contrasted with the ICRF3 S/X, then all radio CRFs are contrasted with the optical CRFs. The impact of number of VLBI observations and the radio source structure on the position differences are discussed. On the evaluation of the systematic global differences, the effect of different subsets of counterparts, as well as alternative transformation methods that do not employ the complete set of rotation, glide, and quadrupole parameters, are examined.
- Chapter 5 focuses on the alignment of the optically bright fraction of the Gaia DRs to ICRF3 in terms of orientation offset and spin. Existing literature data

is homogenized, and the effect of Galactocentric acceleration on the alignment is addressed. New observations of radio stars are proposed and the results of new dedicated observations are presented. The error budget for absolute star positions using phase-referencing is established, and new estimates for stellar motion models for all feasible stars are given. Finally, the influence of the different changes on the alignment is given step by step, and the impact of different subsets and potential future enhancements is examined.

- Chapter 6 provides a general conclusion to the reader as well as future prospects and recommendations.

2 Determination of celestial reference frames

This chapter provides the basis knowledge to understand the subsequent work. The concept of the Celestial Reference System (CRS) and it's realization, the CRF, are explained. An introduction to VLBI is given, with emphasis on explaining the difference between the absolute geodetic VLBI used to create the ICRF and the phase-referencing VLBI used for observations of radio stars relative to a radio source in the ICRF. As a second technique that can be utilized to build a CRF, the observation strategy of the Gaia spacecraft is described. For both techniques, the recent official products used in this thesis are presented.

2.1 International Celestial Reference System and Frame

A reference system is a complete collection of conventions, prescriptions, and models to define a triad of axes at any epoch (Feissel and Mignard 1998). Approved by the 23rd General Assembly of the International Astronomical Union (IAU), the ICRS is the successor of the Fifth Fundamental Catalogue (FK5) (Andersen 1999) and thereby the reference system to be used in astronomy, geodesy, and navigation in space. The ICRS follows the requirements of the second recommendation in the IAU Resolution A4 (Kozai 1991) for a celestial reference system whose origin is in the barycenter of the Solar System and whose axes must not be rotating with respect to sources at cosmological distances. In addition, the ICRS follows the seventh recommendation of Resolution A4, which states that the principal plane of the new conventional reference system should meet the mean equator at epoch J2000.0 and the zero point on that plane as near as possible to the dynamical equinox at epoch J2000.0. The list of suitable extragalactic sources for such a reference frame should preferably be observable by VLBI. However, it was also already considered that a large portion of the selected radio sources should have a well-defined optical counterpart. Furthermore, the average rotation of a large number of extragalactic sources is assumed to be invariant with respect to the rotation of the Universe, which is presumed to be zero. The ICRS is defined by the International Earth Rotation and Reference Systems Service (IERS) in Arias et al. (1995) (therein the abbreviation ICRS stands

for IERS Celestial Reference System) and considers VLBI as the observing technique. The barycentric origin is ensured by modeling the VLBI observations in the framework of General Relativity. An axis stability of 20 µas is given.

The major advantage of moving over to the new reference system is that the FK5 system is based on a dynamical approach, where the mean equator and the mean equinox are moving according to the Earth's axis in space. The FK5 is realized by a catalog of star positions and proper motions at epoch J2000.0 from observations in the optical domain (Fricke et al. 1988). The ICRS is consistent with the FK5 system at J2000.0 (more details can be found in Arias et al. 1995).

The ICRF was decided to be the corresponding fundamental reference frame realizing the ICRS based on VLBI estimates of equatorial coordinates of the selected extragalactic sources (Andersen 1999). Details are given in the IERS Technical Note 23 (Ma and Feissel 1997). Among other standards, models, and constants for the ICRS are contained in the IERS Conventions, the latest approved version of which is provided in Petit and Luzum (2010). The latest official realization is the Third International Celestial Reference Frame (ICRF3; Charlot et al. 2020), adopted by the IAU in January 2019. The ICRS Center of the IERS is responsible for maintaining both the ICRS and ICRF, and the alignment to reference frames at other wavelengths. The International VLBI Service for Geodesy and Astrometry (IVS) (Nothnagel et al. 2017) is a technique center cooperating with the IERS on the VLBI observation technique. It is an international collaboration of organizations dealing with various components of VLBI (Schuh and Behrend 2012).

The first primary realization of the ICRS at optical wavelength was the Hipparcos Catalog, whose frame is aligned to the ICRF within 0.6 mas in orientation offset at epoch J1991.25 and 0.25 mas yr^{-1} in spin (Andersen 1999). According to the IAU Resolution B3 approved by the 26th General Assembly, the reference frame of the 3rd data release from observations of extragalactic sources made by the European Space Agency (ESA) spacecraft Gaia is the new fundamental realization of the ICRS at optical wavelengths starting from 01 January 2022. It is denoted Gaia-CRF3. The Gaia-CRF3 is aligned to the ICRF3 by a set of common extragalactic sources.

An ideal extragalactic source observed for the determination of fundamental reference frames would be emitting radiation in a compact, point-like shape with sufficient signal-to-noise ratio. In order to meet the different user needs, the emission would additionally cover a wide frequency range and emanate from the same location within the extragalactic source. Thus, the positions of an object determined at various frequencies could be easily compared. AGN are usually observed for the determination of the ICRF. The sketch in Fig. 2.1 shows the standard model of AGNs (Antonucci 1993). A jet is originating perpendicular on both sides of the accretion disc surrounding the black hole. The emission is chromatic due to synchrotron self-absorption, with higher frequencies thereby being

emitted closer to the black hole (Marcaide and Shapiro 1984). This spatial dependence of the emission on frequency leads to a dependence of the observed core position on the respective observation frequency. Figure 2.2 shows the dependence of this observed 'core shift' on the observer's angle of view towards the AGN. The locations of the core at a specific frequency can change with time. For example, Plavin et al. (2019) determined a typical core shift between 2 GHz and 8 GHz of about 0.5 mas with a variability of the individual core positions of 0.3 mas. Furthermore, the structure of the emission can be different at the various observing frequencies, and it can also be time dependent (Xu et al. 2020, 2021). The frequency-dependent and observation setup-dependent resolution difference and diffraction limit must also be taken into account. A further complication in comparing VLBI and Gaia reference frames could arise from the fact that most bright radio sources are generally weak at optical frequencies and optically bright sources are typically weak at radio frequencies (Lunz et al. 2020a).

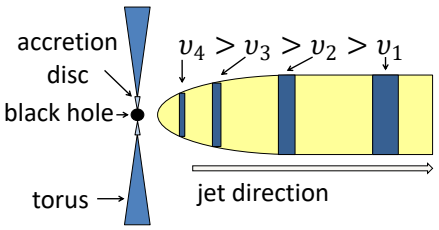

Figure 2.1 Sketch of an AGN and its chromatic jet. The accretion disc (and obscuring torus) is forming around the central black hole. For simplicity, the jet emission is shown on only one side of the black hole. The blue bars in the jet depict the location of the centroids of the (radio) cores at the different frequencies ν_1 to ν_4. The figure is modified from Hada et al. (2011). The sketch is not to scale.

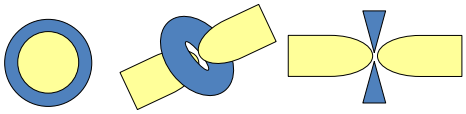

Figure 2.2 Sketch in Fig. 2.1 in dependence on the observer's angle of view. Due to relativistic beaming, one side of the jet is typically much brighter than the other (Sparks et al. 1992). The sketch is not to scale.

2.2 Very long baseline interferometry

In this section, the concept of VLBI and its application to geodesy in terms of absolute astrometry and the determination of CRFs are described in more detail. In the case of faint objects, the signal-to-noise ratio (SNR) of observations is limited, so their positions cannot be determined directly with absolute astrometric VLBI. The relative observation scheme of phase referencing is applied to determine the positions of faint objects in the respective CRF. Furthermore, typically the SNR based on group delays is smaller than the SNR based on phase delays. Therefore, this application of relative astrometric VLBI is explained as well. Finally, the latest official product, namely ICRF3, is introduced. Only

observations of sources with continuum emission are considered, since these are normally used in astrometry.

2.2.1 Concept

Radio wavelengths are orders of magnitude longer than those of the optical emission. Therefore, much larger radio telescopes than optical telescopes are required to obtain similar sharp images at radio frequencies as at optical frequencies. Since it is not possible to build such large radio telescopes, scientists create a synthesized telescope by using interferometry to connect radio signals detected by small antennas (ranging from a few meters to a few hundred meters in diameter). These antennas are distributed over a larger area (e.g., the powerful large regional network Very Long Baseline Array (VLBA) which are ten antennas spanning from Hawaii over the continental USA to U. S. Virgin Islands) or even the whole the Earth (e.g., the IVS network with more than 35 cooperating antennas covering every continent[1])[2]. The development of VLBI began in the 1960s, and the geodetic VLBI observations commonly used today for the determination of CRFs date from 1979. As shown in Sect. 2.2.4, the observations for ICRFs are carried out in frequency bands between 2.3 and 32 GHz. VLBI typically detects only non-thermal emission. As a result, mainly AGN can be detected with geodetic VLBI (Sovers et al. 1998).

[1]https://ivscc.gsfc.nasa.gov/stations/ns-map.html, accessed 12 December 2021.
[2]There have also been projects with VLBI space antennas (e.g., RadioAstron (Kardashev et al. 2013)), however this special case is not discussed here.

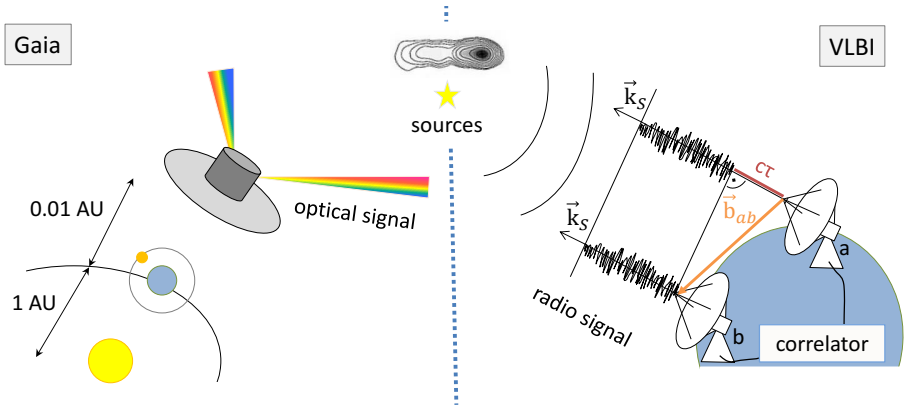

Figure 2.3 Sketch of the Gaia spacecraft (left) and the Earth-based VLBI antennas (right) observing various sources in the sky. The Gaia spacecraft operates at the vicinity of the Lagrange point L2, approximately 0.1 AU from Earth in the line of the Sun and the Earth, and observes in the optical frequency domain. In VLBI, antennas detect the radio signal, which is recorded and sent to a correlator for combination. The $\vec{b}_{ab}$ is the baseline between the two antennas a and b, $\boldsymbol{k}_S$ is the unit vector in the direction of the source reference point S_0, and $c\tau$ is the speed of light times the time delay between the arrival times of the signal at the antennas.

The right side in Fig. 2.3 shows the interferometric principle of VLBI. Two antennas detect the wavefront of the radio signal from a distant source. These observations are scheduled in successive scans, with the antenna network pointed at a different common source for each scan. The interferometer between the antennas a and b forms the baseline vector $\boldsymbol{b}_{ab}$, and $\boldsymbol{k}_S$ is the unit vector from the Earth's center to the radio source. Due to the distance of the radio source, the wavefront is flat when it arrives at the antennas. Furthermore, the signal reaches the two antennas at different times, with a delay τ, mainly due to the geometry of the antennas in the direction of the source.

The received signal is amplified and recorded at each antenna site in a digital format along with a timestamp from a maser clock. This signal pre-processing includes filters to select the requested frequency band, with bandwidth $\Delta\nu$ and with center frequency ν. Almost always, there are many of these subbands (Level 0 Data). The noise is then cross-correlated, which includes time averaging. The correlation produces the main observable, the visibility V (Level 1 Data), which is the radio brightness integrated over the sky as a Fourier transform of the front wave of the signal (e.g., Charlot 1990), as

$$V_{\boldsymbol{b}_{ab},f,t} = \iint\limits_{\Omega_S} I\left(\boldsymbol{S}, f, t\right) \exp\left(-2\pi \mathrm{i} \frac{\boldsymbol{b}_{ab} \cdot \boldsymbol{k}_S}{\lambda}\right) d\Omega, \tag{2.1}$$

where $I\left(\boldsymbol{S}, f, t\right)$ is the intensity of the source's brightness distribution pointing in direction $\boldsymbol{S}$, t is the time of observation, and $d\Omega$ is the differential solid angle, which is used to integrate over the source's extended structure of solid angle Ω_S. The $f = 2\pi c/\lambda$ is the angular frequency. It depends upon on the speed of light c and the wavelength of the observations λ.

If the radio source is spatially extended, a reference point S_0 must be selected, and $\boldsymbol{k}_S$ is then

$$\boldsymbol{k}_S = \boldsymbol{k}_{S_0} + \boldsymbol{S}_0\boldsymbol{S}, \tag{2.2}$$

where $\boldsymbol{S}_0\boldsymbol{S}$ forms the vector orthogonal to $\boldsymbol{k}_{S_0}$ (Charlot 1990). Then, the visibility function can be expressed as

$$V = A \exp[\mathrm{i}(\phi_\mathrm{g} + \phi_\mathrm{str})], \tag{2.3}$$

where

$$\phi_\mathrm{g} = -(2\pi/\lambda)\boldsymbol{b}_{ab} \cdot \boldsymbol{k}_{S_0} \tag{2.4}$$

represents the geometric visibility phase determined for the reference position $\boldsymbol{S}_0$. Furthermore, ϕ_str represents the additional visibility phase due to source structure according

to the brightness distribution $I(\boldsymbol{S}, f, t)$ and A is the visibility amplitude observed by the interferometer. The ϕ_{str} and A depend among others on $\boldsymbol{b}_{ab}$ and $\boldsymbol{S_0 S}$. For the exact formulas, see Charlot (1990).

Thus, $\phi_{\mathrm{t}} = \phi_{\mathrm{g}} + \phi_{\mathrm{str}}$ is the total visibility phase of the observation. The total time delay τ between the times of arrival of the signal at the two antennas as depicted in Fig. 2.3 is then given by (e.g., Charlot 1990)

$$\tau = \frac{\partial \phi_{\mathrm{t}}}{\partial f} = \frac{\partial \phi_{\mathrm{g}}}{\partial f} + \frac{\partial \phi_{\mathrm{str}}}{\partial f} = -(1/c)\boldsymbol{b}_{ab} \cdot \boldsymbol{k}_{S_0} + \tau_{\mathrm{str}} = \tau_{\mathrm{g}} + \tau_{\mathrm{str}}. \tag{2.5}$$

Thereby, the principle of bandwidth synthesis is used. It enables the determination of precise group delay observables by combining the observations of multiple channels distributed over a spanned bandwidth of hundreds of megahertz (to many gigahertz for VLBI Global Observing System (VGOS)) and thus increases the effective bandwidth in terms of delay resolution, but not in terms of SNR (Rogers 1970; Ryan and Ma 1998). In geodetic VLBI the structure delay τ_{str} is typically ignored and only the geometric delay τ_{g} is considered. In reality, the above equation is only valid in case the source has a compact core or in case the source structure is corrected in the processing (e.g., with the help of source structure models, Anderson and Xu 2018). Especially in the new VGOS type observations, this effect is larger than the thermal noise (Xu et al. 2020). Thus, preferably compact sources are chosen as targets for the reference frame determination.

The total time delay τ is furthermore disrupted by other error sources, as given in Schuh and Behrend (e.g. 2012); Reid and Honma (e.g. 2014) as

$$\tau = \tau_{\mathrm{g}} + \tau_{\mathrm{da}} + \tau_{\mathrm{rel}} + \tau_{\mathrm{inst}} + \tau_{\mathrm{clk}} + \tau_{\mathrm{trop}} + \tau_{\mathrm{iono}} + \tau_{\mathrm{ant}} + \tau_{\mathrm{therm}}(+\tau_{\mathrm{str}}), \tag{2.6}$$

where τ_{da} represents the delay due to diurnal aberration and τ_{rel} the delay due to the impact of special and general relativity on τ_{g}. These two delays are rectified using known physics. The instrumental delay τ_{inst} is calibrated using meta information. The frequencies used for CRFs are affected by ionospheric delay τ_{iono}. In the case of dual-frequency observations, τ_{iono} is removed from the higher frequency via linear combination. In case only one frequency band was recorded, the dispersive delays can be modeled using maps of total electron content (TEC) based on GNSS data. The delay due to the missynchronization of the maser clocks τ_{clk} and the tropospheric delay τ_{trop} are typically determined by least-squares estimation in case of absolute geodetic VLBI (Sect. 2.2.2). The τ_{therm} is the delay due to thermal noise. Furthermore, τ_{ant} is the delay due to inaccurate antenna position. The error terms and their magnitudes are further discussed for example in Beasley and Conway (1995); Reid and Honma (2014).

For an ideal radio source where the core shift depends on ν^{-1}, the group delays observed

in any frequency band provide the position of the AGN jet base. In other cases, the radio source position from group delays deviates from the jet base. Moreover, for dual-frequency observations, the delay difference due to core shift in the ionospheric correction must be taken into account. In contrast, the phase delays typically provide the average position of the core within the observing band. For S/X positions, the typical offset between the two position types was estimated to be on the order of 170 µas for an ideal radio source (Porcas 2009).

2.2.2 Absolute astrometry – geodetic VLBI

In case absolute geodetic VLBI should be performed, the VLBI sessions are scheduled automatically using the antenna network of interest and a list of suitable AGN. The radio sources and the sequence of scans is selected depending on the session goal (e.g., determine precise antenna coordinates, source coordinates or EOPs) (Schartner 2019). Geodetic VLBI sessions are typically 24 hours long. For ionosphere corrections, dual-frequency observations are usually recorded[3]. After calibrating the raw phases of the Level 1 Data to ensure consistency across all channels, they are fringe-fitted to produce the group delay observables (Level 2 Data). The difference between this observed delay and the computed delay following the consensus model (Eubanks et al. 1991) is used in geodetic VLBI software to estimate the parameters of interest, such as antenna positions or radio source positions (Level 3 Data).

The data processing of these single sessions includes a variety of aspects, such as correction for clock breaks or outlier rejection (e.g., Schuh and Böhm 2013; Nothnagel 2020). Most geodetic VLBI software uses the Gauß-Markov-Model least squares estimation (Sect. 3.3.1) for the adjustment of the parameters of interest (e.g., Schuh et al. 2021). For the single session analysis, these are for example the clock model parameters, the antenna positions, or the parameters of the wet troposphere. The solution of each session has a rank defect due to missing information of the absolute orientation of the relative observation technique. Thus, additional conditions are applied to the solution. It is aligned to the International Terrestrial Reference Frame (ITRF) via no-net translation (NNT) and no-net rotation (NNR) conditions on suitable antenna positions in the ITRF. Furthermore, it is aligned to the ICRF via NNR conditions on the radio source positions in the ICRF, in case the radio source positions are estimated.

The global solution is the solution of the stacked datum-free normal equations from the single session analysis. The main parameters to be estimated in the global solution are the antenna positions at a reference epoch, antenna velocities, the (daily) EOPs, or the radio source positions at a reference epoch. The nuisance parameters, such as the atmospheric

[3]This is true for the S/X and X/Ka observations, but not for the K band observations or for VOGS.

parameters, were reduced beforehand by the method of Helmert blocking to keep the system of equations small (see Sect. 3.3.1). In the global solution, new consistent datum conditions in terms of NNT and NNR are applied to the stacked normal equation system to remove the rank deficiency, similar to the single session analysis. The session-wise time series of the estimated parameters are also usually derived from the global solution, since the time series then have a consistent datum applied, which is not the case for the single session analysis. More details on the geodetic VLBI processing can be found in, for example, Nothnagel (2022).

The individual radio source positions represent a mean value over all sessions, and their uncertainties are usually unrealistically small. Hence, they can be inflated by applying a scale factor and some noise. The noise can be determined by dividing the list of sessions into two random samples and determining the average position difference for well-determined radio sources in these datasets (Charlot et al. 2020).

2.2.3 Relative astrometry – phase-referencing

In case relative astrometry should be performed, a bright compact calibrator within about 3° to the target of interest and a sufficiently accurate position uncertainty (maximum of 10 mas) has to be selected. This primary calibrator is later used for the calibration of the phases of the target, which is usually too faint to have its phases calibrated by a fringe-fit from its own observations (Beasley et al. 1994; Beasley and Conway 1995). One or multiple secondary calibrators in advantageous geometries with respect to the primary calibrator and the target can be chosen, whenever available, to perform additional calibrations of residual errors to obtain the highest precision of relative target positions (Fomalont and Kogan 2005; Rioja et al. 2017). The calibrators and the target are observed alternately. The switching time between the scans of the calibrator and the target must be shorter than the temporal change of the systematic errors in the phase observable (typically the troposphere in this work, Ulvestad 1999; Ulvestad and Schmitt 2001; Wrobel et al. 2000). The length of the VLBI sessions for dedicated phase-referencing projects and the order of the scans are usually defined by the number and brightness of the sources to be observed, by the required time to obtain a sufficient sampling of the sources, by the amount of calibration scans, and by the slew time of the antennas in the network (Wrobel et al. 2000).

The visibilities (Level 1 Data) are processed in astronomical VLBI software. Various calibrations are performed on the data. External values are used for the correction of antenna positions and EOPs. The dispersive delay is usually corrected with the help of TEC maps (Ulvestad and Schmitt 2001), as usually only one radio frequency band is recorded. The zenith wet delay is corrected using the multi-band delays from dedicated

observations to compact bright AGNs, so called geodetic blocks, which are scheduled every few hours (Mioduszewski 2009; Brunthaler et al. 2005). The secondary calibrators are then used to calculate the remaining atmospheric gradients, which can then be applied to the separation between the primary calibrator and the target. More information on the processing of data relevant to this work is provided in Appendix A.

After these overall calibrations, the visibilities of the primary calibrators are fringe-fitted to their respective a priori position in ICRF, which is a self-calibration. The corrections from the fringe-fit are then applied to the respective target. With this step, the difference of the delay observable between the target and the primary calibrator is

$$\tau_{\text{target}} - \tilde{\tau}_{\text{calibr.}} = \tau_{\text{str}}^{\text{target}} - \tilde{\tau}_{\text{str}}^{\text{calibr.}} + \left(\tau_{\text{pos}}^{\text{target}} - \tilde{\tau}_{\text{pos}}^{\text{calibr.}}\right) + \text{interpolation errors}, \tag{2.7}$$

where the tilde depicts the interpolated delay of the primary calibrator at time t_2 from its scans at times t_1 and t_3 surrounding the scan of the target at time t_2 (Beasley and Conway 1995; Reid and Honma 2014). Thus, the antenna based error terms, which are similar for both sources, are removed (compare to Eq. 2.6). If the target and primary calibrator are compact, the source structure $\tau_{\text{str}}^{\text{target}}$ and $\tau_{\text{str}}^{\text{calibr.}}$ equal zero, respectively. Furthermore, the structure of the primary calibrator can be modeled by self-calibration. This model can than be applied during the fringe-fit of the primary calibrator to remove $\tau_{\text{str}}^{\text{calibr.}}$ from this equation. Thus, only information about the target structure $\tau_{\text{str}}^{\text{target}}$ and the position difference between the target and the primary calibrator $\left(\tau_{\text{pos}}^{\text{target}} - \tilde{\tau}_{\text{pos}}^{\text{calibr.}}\right)$ remain. In this work, the structure of the target is ignored. Since $\phi = 2\pi\nu\tau$, the same principle for the delay holds for the phase observables.

From these calibrated data, the positions of the respective targets can be determined, either by fitting a model directly to their visibility data (Shepherd 1997) or by fitting a model to the image of the corresponding source (Alef 1989; Lestrade 1991). More information on the fringe-fitting and the determination of the star positions from the data relevant to this work is provided in Sect. 5.4.2.

With these processing steps, the target positions are obtained in the ICRF in case the a priori position of the primary calibrator is in ICRF. A relative target position towards the calibrator in one session can be achieved at the level of a few tens of microas when using many scans and small separations between the calibrator and the target (e.g. Reid and Honma 2014). This is about two orders of magnitude smaller than the position uncertainty from a geodetic session and about one order of magnitude smaller than the position uncertainty of the sources in the current ICRF, which is a mean of many sessions, based on group delays. To obtain the uncertainty of the absolute position of the target in ICRF, various error sources, such as the source structure of the primary calibrator, the difference between the positions from group delays and phase delays of the primary

calibrator, or residual errors in the delay model, have to be considered. They are identified in Sect. 5.4.5. Thus, the uncertainties of the absolute target positions in one session from phase-referencing are larger than the CRF position uncertainty of the calibrator alone.

Any errors in the calibrator position to first order directly impact the position of the target (Reid and Honma 2014). The calibrator position must not be known for relative positions and products thereof as long as the calibrator position remains the same for all epochs. However, in case different calibrator positions were used for a set of targets or a series of target positions, such as in Sect. 5.1, this information is obligatory to register the target positions to a common CRF.

Reduction of parallax effect for single-epoch positions

From the VLBI measurements at a single epoch, the topocentric vector $\boldsymbol{k}_S(t)$ between the observer and the source in the barycentric frame at the time of observation t is determined. To obtain the barycentric vector of the source similar to the positions given in ICRF, $\boldsymbol{s}_S(t_\mathrm{B})$ (where B is for 'barycentric'), $\boldsymbol{k}_S(t)$ is corrected by the parallactic displacement of the trigonometric parallax ϖ which depends on the location of the observer $\boldsymbol{o}(t)$ in the barycentric frame,

$$\boldsymbol{k}_S(t) = \langle \boldsymbol{s}_S(t_\mathrm{B}) - \varpi \boldsymbol{o}(t) \rangle, \tag{2.8}$$

following the explanations in Lindegren (2020a). Thereby, the barycentric position of the observer $\boldsymbol{o}(t)$ can be approximated by the position of the Earth's center of mass $(X_E(t), Y_E(t), Z_E(t))$ as given by standard ephemerides, and $\langle\rangle$ denote vector normalization. As a practical implementation to derive the barycentric source positions, the formulas for estimation of the annual parallax projected along α and δ directions, as given in Kovalevsky and Seidelmann (2004, p. 134), were used,

$$\begin{aligned}
\alpha_s(t_\mathrm{B}) &= \alpha_k(t) + (-X_E(t)\sin\alpha_s(t) + Y_E(t)\cos\alpha_s(t))/\cos\delta_s(t)\varpi, \\
\delta_s(t_\mathrm{B}) &= \delta_k(t) + (-X_E(t)\cos\alpha_s(t)\sin\delta_s(t) - Y_E(t)\sin\alpha_s(t)\sin\delta_s(t) \\
&\quad + Z_E(t)\cos\delta_s(t))\varpi,
\end{aligned} \tag{2.9}$$

where the subscript s denotes the position vectors pointing from the barycenter to the source, the subscript k denotes the position vectors pointing from the observer to the source. The equation has to be iteratively solved, however the second order effects are smaller than 0.01 µas in this work and can therefore be neglected. The epoch of observation also needs to get transferred to the barycentric time, which is done by adding the

Römer delay t_{Roe} at a sufficient accuracy to t by

$$t_{\mathrm{B}} = t + \boldsymbol{u}_S(t)'\boldsymbol{o}(t)/c = t + t_{\mathrm{Roe}}, \tag{2.10}$$

where $\boldsymbol{u}_S(t)$ is the unit vector of $\boldsymbol{s}_S(t)$, which can be approximated by its time-independent value, and c is the speed of light (Lindegren 2020a). According to Lindegren (2020a), ignoring the delay in the analysis leads to an error corresponding to the proper motion of the source in this time interval.

Determination of models of stellar motion from position time series

From a series of VLBI measurements at a single epoch (topocentric vector), the standard model of stellar motion (barycentric position, linear proper motion, and trigonometric parallax) at model epoch $t_0 = t_{\mathrm{B}}$ can be determined. Furthermore, some of the targets observed with phase-referencing in this work requite the modeling of linear accelerations.

The formulas are, for example, described in Loinard et al. (2007):

$$\alpha(t) = \alpha_0 + \mu_{\alpha*}t + \varpi f_\alpha(t), \tag{2.11}$$
$$\delta(t) = \delta_0 + \mu_\delta t + \varpi f_\delta(t). \tag{2.12}$$

Thereby, α_0 and δ_0 are positions at a reference epoch t_0, which is usually chosen to be the mean epoch between the first and the last epoch t in order to reduce correlations between the estimates. Furthermore, ϖ is the stellar parallax, and $\mu_{\alpha*}$ and μ_δ are the linear proper motion terms. The aterisk depicts the application of the metric scale factor $\cos(\delta)$. The diurnal parallax was not considered. Following for example Seidelmann (1992); Kovalevsky and Seidelmann (2004), the terms $f_\alpha(t)$ and $f_\delta(t)$ are the projections of the parallactic ellipse in directions of α and δ, calculated as

$$f_\alpha(t) = [X_E(t)\sin\alpha_s(t) - Y_E(t)\cos\alpha_s(t)]/\cos\delta_s(t), \tag{2.13}$$
$$f_\delta(t) = X_E(t)\cos\alpha_s(t)\sin\delta_s(t) + Y_E(t)\sin\alpha_s(t)\sin\delta_s(t) - Z_E(t)\cos\delta_s(t), \tag{2.14}$$

where $\alpha_s(t) = \alpha(t) - \varpi f_\alpha(t)$, $\delta_s(t) = \delta(t) - \varpi f_\delta(t)$, and $(X_E(t), Y_E(t), Z_E(t))$ is the vector between the solar system barycenter and the Earth's center of mass in units of AU. Because the equations depend on a prior knowledge of ϖ, they need to be solved iteratively. The significance of linear acceleration terms $a_{\alpha*}$ and a_δ is tested by fitting the position time series to

$$\alpha(t) = \alpha_0 + \mu_{\alpha*0}t + \varpi f_\alpha(t) + 0.5(a_{\alpha*})t^2, \tag{2.15}$$
$$\delta(t) = \delta_0 + \mu_{\delta 0}t + \varpi f_\delta(t) + 0.5(a_\delta)t^2. \tag{2.16}$$

If the acceleration parameters are introduced, the proper motion parameters become time-dependent, and using the Eq. 2.15 they are referred to the same epoch t_0 as the model position. In this case, their notation changes to $\mu_{\alpha*0}$ and $\mu_{\delta 0}$. Non-linear accelerations such as orbital parameters are neglected in this study.

2.2.4 Recent official products

The latest VLBI-based ICRF is the ICRF3. The ICRF3 is a global solution from absolute geodetic VLBI observations as described in Sect. 2.2.2. Most of the observations were organized and processed by IVS, VLBA, or the Deep Space Network (DSN) institutions. Details of the data setup and processing can be found in Charlot et al. (2020). The ICRF3 is the successor of second realization of the International Celestial Reference Frame (ICRF2) and, for the first time, a multi-frequency radio CRF. One catalog for each of the frequency setups S/X, K, and X/Ka is supplied. The K and X/Ka observations were only started later in time compared to the S/X observations (Fig. 2.4).

The catalogs were determined separately and then aligned to the ICRF3 S/X by a rotation about each of the three ICRF3 S/X axes, respectively, using only the respective common ICRF3 defining sources. The Venn diagram in Fig. 2.5 depicts the number of common sources and defining sources in the three catalogs. The 303 ICRF3 defining sources were selected to have compact source structure, to have stable source position time series, and to be evenly distributed across the sky. Six of the defining sources in ICRF3 K and two of those in ICRF3 X/Ka were not used in the alignment to ICRF3 S/X due to few observations in these CRFs or because they were identified as likely outliers. The ICRF3 S/X itself was aligned to ICRF2 using the 295 ICRF2 defining sources for the NNR condition applied during the analysis(Charlot et al. 2020). No spin was considered.

Also for the first time, the ICRF3 has an epoch (2015.0) because the effect of the Galactocentric acceleration of the barycenter of the solar system with respect to the distant background (secular aberration Kopeikin and Makarov 2006), is modeled as well. It shows up as a global dipole pattern of apparent proper motions towards the Galactic Center (located at α =266.4°, δ=−29.0°). The acceleration vector therefore is pointing towards the Galactic center with a magnitude of $5.8\,\mu\mathrm{as\,yr}^{-1}$ as determined from S/X VLBI observations (Charlot et al. 2020).

As the number of observations in VLBI scales with the square of the number of antennas in the observing network, the square root of the number of observations is inversely correlated with the uncertainties of the least-squares adjustment, and networks with more antennas provide less independent observations, there is a high likelihood that the formal uncertainties from the fit are unrealistically small. Thus, the uncertainties from the least-squares adjustment were inflated as $\sigma_{\alpha*} = \sqrt{(s\sigma_{\alpha*,\mathrm{formal}})^2 + \sigma_{n0}^2}$ and $\sigma_\delta = \sqrt{(s\sigma_{\delta,\mathrm{formal}})^2 + \sigma_{n0}^2}$,

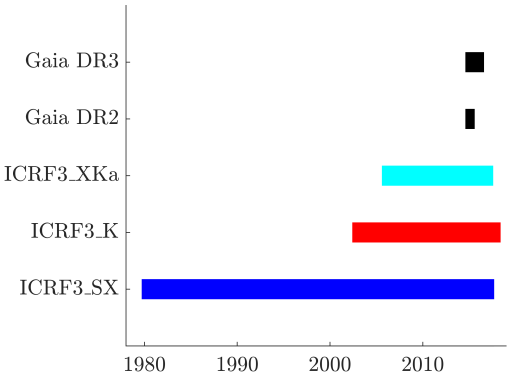

Figure 2.4 Data time spans of ICRF3 at different frequencies, of Gaia DR2, and of Gaia EDR3.

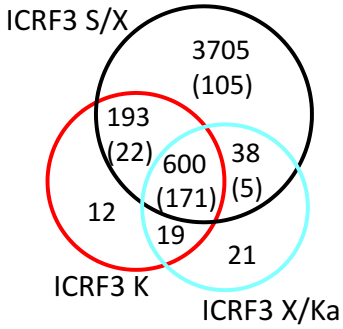

Figure 2.5 Venn-diagram of the crossmatch of the number of sources in the three ICRF3 catalogs. The respective number of defining sources is given in parentheses (according to Charlot et al. 2020).

where s is the scaling factor and σ_{n0} is the noise floor. For ICRF3 S/X and ICRF3 K the scaling factor of 1.5 was used, similar to studies on previous ICRFs (Ma et al. 1998; Fey et al. 2015). A noise floor of 30 µas was applied for each coordinate direction for the three catalogs after investigating the position offset between CRFs based on various subsets. The δ component of ICRF3 K needed a higher noise floor of 50 µas. This results in median uncertainties of 127 µas in $\alpha*$ and 218 µas in δ for ICRF3 S/X, of 74 µas in $\alpha*$ and 136 µas in δ for ICRF3 K, and of 76 µas in $\alpha*$ and 104 µas in δ for ICRF3 X/Ka. The median correlation coefficient is only 0.13 for ICRF3 S/X, but 0.30 for ICRF3 K and 0.43 for ICRF3 X/Ka. It is assumed that the stronger correlations stem from the limited observing geometry for the latter two catalogs. For the 600 sources common to the three catalogs, the ICRF3 S/X uncertainties are only about one third of those for ICRF3 K and ICRF3 X/Ka, whereas for the other two catalogs, the uncertainties are similar (Charlot et al. 2020). This can be explained by the more heterogeneous observations in ICRF3 S/X in terms of total number of observations and position uncertainty. The median difference of the position between ICRF3 K and ICRF3 S/X is 0.20 mas and the median difference of the position between ICRF3 X/Ka and ICRF3 S/X is 0.36 mas.

Charlot et al. (2020) determined the global systematic deformation in terms of the 16 VSH parameters between ICRF2 and ICRF3 at S/X frequencies. For both CRFs, the Galactocentric acceleration was modeled to keep the results comparable. All VSH parameters between the two frames are below a magnitude of 20 µas with uncertainties of less than 5 µas, except D_3 (39 ± 4 µas) and $a^E_{2,0}$ (-39 ± 4 µas). Similarly, as shown in the introduction already, the 16 VSH parameters between ICRF3 S/X and ICRF3 K are below a magnitude of about 50 µas with uncertainties of less than 10 µas. Furthermore, those

between ICRF3 S/X and ICRF3 X/Ka are below a magnitude of 75 µas with uncertainties of less than 10 µas except for D_3 (-314 ± 8 µas) and $a^{M}_{2,0}$ (207 ± 7 µas). Charlot et al. (2020) expects the large deformations to be caused by the limited observing geometry (limited radio source distribution in the South for ICRF3 K and limited antenna network for ICRF3 X/Ka). These small systematic differences and the about one magnitude larger individual source position differences are further evaluated in Sect. 4.3.2.

It is expected that in the future also an ICRF from the new VGOS (Petrachenko et al. 2012), which uses a broadband signal from currently 3 to 10 GHz, is calculated and approved.

Phase referencing data can be obtained from the online archives of the various radio antenna networks regularly used for astrometry, such as VLBA or European VLBI Network (EVN). Already calibrated data, like source images or published positions, can also be found in online archives and in the literature. If these data are used directly, it is necessary to carefully check which primary calibrator positions were used for the calibration and which calibration steps were performed. Without this information, meaningful absolute positions cannot be derived from phase-referenced observations.

Xu et al. (2019a) analyzed the data of 3417 radio sources using about the same observations as used for the determination of ICRF3 S/X. They determined the effect of source structure in the closure phase and closure amplitude signals (for details on how the closure loops where formed, see the publication). The effect is quantified by the closure amplitude root mean square (RMS), CARMS. It represents a lower bound on the detected structural effects in the data. For astrometric studies, the CARMS based on basic noise weighting is recommended:

- CARMS < 0.2 indicates minimum source structure,
- CARMS > 0.3 indicates significant source structure,
- CARMS > 0.4 indicates very extended source structure.

2.3 Gaia

In this section, the Gaia spacecraft and its astrometric product, published in data releases (DRs), are described in more detail.

2.3.1 Concept

The Gaia spacecraft, launched on 19 December 2013 by ESA, is a follow-up mission to the Hipparcos mission with the objective to derive precise astrometry and photometry

for a large group of sources in the Milky Way. One of Gaia's key milestones is to obtain accurate astrometry (three dimensional positions and velocities) for as many sources in the sky as possible. For example, trigonometric parallax measurements have their limitations when taken from ground due to the Earth's atmosphere and systematic errors. The HIPPARCOS mission made significant advances in this topic. It detected 117 955 sources with milliarcsecond accuracy in absolute parallax (ESA 1997). Its successor, Gaia, listed already 2 057 050 sources with a full 5-parameter astrometric solution (angular position, mean proper motion, parallax) in its first data release DR1 based on 14 months of observations. Of these, 93 635 are identical to the stars detected by HIPPARCOS and the parallax precision is already well below one milliarcsecond for this subset, with an additional systematic error of ± 0.3 mas (Brown 2017). It was possible to publish radial velocities as a sixth astrometric parameter already in Gaia DR2.

Initial studies and proposals in the 1990s incorporated an interferometric spacecraft (Lindegren and Perryman 1994, 1996; Høg 2014); however the observation principle of the approved Gaia mission is based on direct imaging on CCD by telescopes onboard the spacecraft and detection by Time-Delayed Integration (TDI) (Perryman et al. 2001). Thus, Gaia detects the photocenter of the sources in the sky. The optical resolution is about $0\farcs1$.

Gaia continuously scans the sky by rotating around its own axis and by orbiting around the Sun at the L2 Lagrangian point (which orbits the Sun at the same rate as the Earth). A sketch is given in Fig. 2.3. In doing so, it accurately measures the angular separation of sources along great circles. The sources can either be located in the two simultaneous fields of view from the two identical telescopes onboard the satellite, which are separated by a known angle, or in one field of view of one of the two telescopes. To achieve this, the two images of the telescopes are mapped on a common focal plane. Various groups of CCD sensors are installed on the focal plane, such as sensors for the sprectroscopic instrument and the photometric instrument. For the focus of this work, the sky mappers and the astrometric instrument are of interest. When a source passes the field of view of one of the telescopes, its emission first gets recorded in the sky mapper CCDs of the respective telescope. Detected sources are classified into different window classes (WCs), mainly based on their G magnitude. The WCs define the pixel binning and TDI blocking gate used on the astrometric field (AF) CCDs for the particular observations. WC0 for $G \leq 13$ mag has no binning, and thus a two-dimensional image and thus two-dimensional coordinates (along- and across-scan) can be derived. For fainter sources, WC1 for $13\,\text{mag} \leq G \leq 16$ mag and WC2 for $G \geq 16$ mag, the pixels in the across-scan direction are binned, and thus only one-dimensional coordinates (along-scan) can be determined. The limiting optical magnitudes for Gaia are $3\,\text{mag} \leq G \leq 21$ mag. On the AF CCDs, the fields of view of both telescopes are combined. This method allows Gaia to determine

absolute parallaxes from the difference in parallax factors of the stars in the two images (Gaia Collaboration et al. 2016).

By repeatedly measuring the sources positions, the change in the source positions through space can be determined. Each of the sources was planned to be observed about 70 times over a period of five years. However, the mission has already been extended until the end of 2022, with a further possible extension until 2025[4].

The raw data are processed by the Gaia Data Processing and Analysis Consortium (DPAC). Details can be found in (Gaia Collaboration et al. 2016). The astrometric catalog is derived by simultaneously fitting various nuisance parameters (instrument attitude and geometric calibration) and the astrometric parameters for well-behaved detected sources (angular position, mean proper motion, parallax) in a combined iterative adjustment, the so called Astrometric Global Iterative Solution (AGIS). All steps in the whole processing chain (such as point spread function model, wavelength calibrations) are iteratively updated with improved results from AGIS and vice versa (Lindegren et al. 2012, 2016). Because of this self-calibration and the measurement principle of deriving angle differences, a rank deficiency of six parameters is present. These are the orientation offset at a reference epoch about the three rotation axes (three constant angles) and the spin about the three rotation axes (three constant angular velocities). To solve for these parameters, external data are required. In AGIS, a so called frame rotator ensures the global zero orientation offset between the preliminary Gaia frame and the VLBI-based ICRF, as well as the zero global spin of distant AGNs. This is realized by applying a NNR condition on selected subsets of the Gaia dataset used in this processing step. The zero orientation offset condition is based on a suitable subset of AGN sources derived from cross-matching the preliminary Gaia dataset with the VLBI-based ICRF and applying some filters. The spin condition is based on the same ICRF subset and a similarly derived AGN subset from a comparison to other AGN catalogs. For Gaia DR2, the ICRF3 S/X prototype (2017-06-30, solution from GSFC, IAU Working Group *Third Realization of International Celestial Reference Frame*) was used for the former, and the AllWISE AGN catalog (Secrest et al. 2015, 2016) was used for the latter. For Gaia EDR3, the sources from Gaia-CRF2 (see next subsection) were selected from the preliminary version of Gaia EDR3 and filtered again, using more stringent astrometric criteria. In addition, the code of the frame rotator was revised in Gaia EDR3, including outlier elimination (Gaia Collaboration et al. 2022). Further details are given in Lindegren et al. (2018); Gaia Collaboration et al. (2022). It is worth noting that the counterparts used for this alignment of the Gaia frame are not identical to those of the respective Gaia-CRF selected from the final Gaia dataset.

These counterparts used for the alignment to ICRF are optically faint, most with $G > 16$ mag. This would not be an issue if the calibration of the astrometric instrument was not

[4]https://sci.esa.int/s/8OJDymW, accessed 23 May 2022.

G magnitude dependent. However, each WC and each type of TDI blocking gate have to be calibrated separately. Because some sources were classified in different WCs at different epochs in time, and because their estimated source parameters should be consistent, there should be some overlap between the various classifications and thus there should be no discontinuity in spin for the whole Gaia dataset. However, in Gaia DR2 the overlap of sources in WC0 and WC1 apparently was not sufficient, as shown by a spin offset of various G magnitude bins in Lindegren et al. (2018). The instrumental calibration for WC0 is more difficult to calibrate due to the two-dimensional data acquisition compared to WC1 and WC2. Lindegren (2020a) concludes that the sources classified in both WC0 and WC1 might not be consistently modeled in terms of astrometry due to this imperfect WC0 calibration, which likely was the immediate reason of the detected spin offset across G magnitudes. Improved calibration models for WC0 and additional constraints should ensure to remove this issue in the upcoming DRs (Lindegren 2020a).

In Gaia EDR3 this WC0 calibration problem was solved by an ad hoc correction of $[-0.016\,6,\ -0.095\,0,\ +0.0283]\,\mathrm{mas\,yr^{-1}}$ per rotation axis to the WC0 calibration parameters in one of the AGIS iterations (Lindegren et al. 2021b). The numbers were derived from comparing the proper motion of that iteration to the position differences between Gaia and Hipparcos divided by their epoch difference. Due to lack of suitable information, the orientation offset between the different WC reference frames was assumed to be zero. Because the Hipparcos reference frame is aligned to ICRS with $\pm 0.6\,\mathrm{mas}$ uncertainty per axis at epoch J1991.25 (Lindegren and Kovalevsky 1995; Kovalevsky et al. 1997), the spin correction is accurate to about $0.024\,\mathrm{mas\,yr^{-1}}$. As this manual correction is unsatisfactory, the DPAC is continuously working on further improving the calibration schemes (for Gaia EDR3 already three times as many calibration parameters were used as for Gaia DR2) so that in future Gaia DRs, this correction is obsolete (Lindegren et al. 2021b).

2.3.2 Recent official products

For this work, two Gaia data releases are investigated, Gaia DR2 and its successor, which is based on a longer time span, Gaia EDR3. The data are available from the Gaia archive[5]. As can be seen from Table 2.2, the 55 % increase in covered time span resulted in an increase of 7 % of the detected sources. For each source, the Gaia astrometry is either given as 2-parameter solution (position only), 5-parameter solution (angular position, mean proper motion, parallax using the standard model of stellar motion as defined in Eq. 2.11), or a 6-parameter solution (a so called pseudo-color was fitted as an additional parameter to the astrometry).The number of sources with a full 5-parameter (and 6-parameter for

[5]https://gea.esac.esa.int/archive/, accessed 12 January 2021.

Table 2.1 Comparison of the median uncertainties of the astrometric parameters of Gaia DR2 and Gaia EDR3 for various subsets of the Gaia datasets.

	unit	Gaia DR2	Gaia EDR3	% increase
$\sigma_{\rm pos,max}$ (G <15)	μas	20–30	10–20	−33
$\sigma_{\rm pos,max}$ (G=17)	μas	80	50	−38
$\sigma_{\rm pos,max}$ (G =20)	μas	550	400	−27
$\sigma_{\rm pos,max}$ (G =21)	μas	1600	1000	−38
σ_{μ} (G <15)	μas yr^{-1}	50–70	20–30	−57
σ_{μ} (G=17)	μas yr^{-1}	160	70	−56
σ_{μ} (G=20)	μas yr^{-1}	1160	500	−57
σ_{μ} (G=21)	μas yr^{-1}	3370	1400	−58
G (Gaia-CRF)	mag	19.5	20.06	3
$\sigma_{\rm pos,max}$ (Gaia-CRF)	μas	400	447	12
G (ICRF3 S/X counterparts)	mag	18.8	18.9	1
$\sigma_{\rm pos,max}$ (ICRF3 S/X counterparts)	μas	290	194	−33

Notes. The information was retrieved from Lindegren et al. (2018); Gaia Collaboration et al. (2018) for Gaia DR2 and from Gaia Collaboration et al. (2022), the Gaia website (https://www.cosmos.esa.int/web/gaia/earlydr3), and this work for Gaia EDR3.

Table 2.2 Comparison of some relevant parameters of Gaia DR2 and Gaia EDR3.

	Gaia DR2	Gaia EDR3	% increase
Epoch (Julian Year)	2015.5	2016.0	
Number of sources (total)	1 692 919 135	1 811 709 771	7
Number of sources (5-parameter+6-parameter)	1 331 909 727	585 416 709+882 328 109	10
Number of sources (6-parameter)	0	882 328 109	
Number of sources (2-parameter)	361 009 408	343 964 953	−5
Number of Gaia-CRF sources	556 869	1 614 173	190
Number of ICRF3 S/X[1]sources	2 820	3 142	11

Notes. The Gaia data time span starts on 25 July 2014 (10:30 UTC) and lasts until 23 May 2016 (11:35 UTC) for Gaia DR2 and until 28 May 2017 (08:44 UTC) for Gaia EDR3. For details see Gaia Collaboration et al. (2018, 2022). [(1)] ICRF3 S/X prototype for Gaia DR2.

Gaia EDR3) astrometric solution increased by 10 %, while the number of sources with a 2-parameter solution decreased by 5 %. This again reflects the positive impact of the additional observations. Mean radial velocities were published for 7 224 631 sources in Gaia DR2 for the first time. They were not changed for Gaia EDR3.

The provisional set of extragalactic AGN counterparts used for rotating the frame was renewed after the processing of the respective Gaia DR. This is the Gaia-CRF. The large increase in identified sources for the Gaia-CRF from Gaia DR2 to Gaia EDR3 is due to slightly different strategies in cross-matching and filtering, as described below, but mainly due to the use of 13 different AGN catalogs in addition to ICRF3 S/X for comparison for Gaia-CRF3, while only the AllWISE catalog in addition to ICRF3 S/X prototype was

used for Gaia-CRF2. The increase in counterparts to ICRF3 S/X is on the level of the increase in detected sources, 11 %.

The selection criteria for Gaia-CRF2 are the following (Lindegren et al. 2018):

- Positional matching with a radius of 100 mas (ICRF3 prototype) or 1 arcsec (AllWISE catalog), then choosing the nearest positional match,
- astrometric_matched_observations ≥ 8,
- astrometric_params_solved $= 31$,
- $|(\varpi + 0.029 \text{ mas})/\sigma_\varpi| < 5$,
- $(\mu_{\alpha*}/\sigma_{\mu_{\alpha*}})^2 + (\mu_\delta/\sigma_{\mu_\delta})^2 < 25$,
- $|\sin b| > 0.1$,
- $\Delta < (2 \text{ arcsec}) \times |\sin b|$,

where b is the Galactic latitude according to Lindegren et al. (2018). The latter two items were not used for crossmatching the ICRF3 S/X prototype. They prevent the subset of crossmatches with the less accurate non-VLBI catalogs from containing non-AGN sources in the area of the sky with a high probability of confusion sources, the Galactic plane. Thereby Δ is the reduced matching distance for sources close to the Galactic plane. It depends on the Galactic latitude b. Using the filters in items 4 and 5 described above, counterparts with significant parallax and proper motions from the Gaia data are excluded already.

For Gaia-CRF3, various AGN catalogs were crossmatched to identify AGN in Gaia EDR3 (see Gaia Collaboration et al. 2022). The selection criteria are the following (Gaia Collaboration et al. 2022):

- The VLBI-based catalogs, such as ICRF3, were crossmatched with a radius of 100 mas, whereas for other catalogs a radius of 2 arcseconds was used. Always the nearest match was selected,
- astrometric_params_solved $= 31$ (5-parameter solution) or astrometric_params_solved $= 95$ (6-parameter solution),
- $|(\varpi + 0.017 \text{ mas})/\sigma_\varpi| < 5$,
- $[\mu_{\alpha*}\mu_\delta]\,\mathrm{Cov}\,(\mu)^{-1} \begin{bmatrix} \mu_{\alpha*} \\ \mu_\delta \end{bmatrix} < 25$,
- $|\sin b| > 0.1$,
- $\Delta < (2 \text{ arcsec}) \times |\sin b|$,

where $\mathrm{Cov}\,(\mu)$ is the covariance of the proper motions. Thus, in contrast to Gaia-CRF2, for the selection of Gaia-CRF3 also the correlations of the proper motions were taken into

account. Again, the last two items were only applied to the non-VLBI catalogs due to their reduced accuracy compared to the VLBI-based catalogs and the larger radius used for crossmatching.

The astrometric uncertainties of the sources (5-parameter and 6-parameter, where 6-parameter solutions are slightly worse) in Gaia DRs are mainly depending on the G magnitude. Table 2.1 lists the mean uncertainties for some subsets of Gaia DR2 and Gaia EDR3 for comparison and the percentage improvement from one DR to the other. The longer data time span mainly improved the proper motions. The ICRF3 S/X counterparts have smaller uncertainties than the other Gaia-CRF sources. This is because the ICRF3 S/X counterparts are optically brighter than the other Gaia-CRF sources and therefore have a smaller standard deviation (Gaia Collaboration et al. 2022). Since the sources of Gaia-CRF3 are fainter than those of Gaia-CRF2, the median uncertainties for Gaia-CRF2 are smaller than for Gaia-CRF3.

In contrast to ICRF3, the Galactocentric acceleration is not corrected in Gaia DR2 or Gaia EDR3. It was however detected in Gaia EDR3 when the internal systematics became small enough (Gaia Collaboration et al. 2021b). A more detailed comparison is given in Sect. 5.2.

Secondary parameters were also derived from the Gaia dataset. The re-normalized unit weight error (RUWE) is a goodness-of-fit statistic describing how well the Gaia observations of a source fit the 5-parameter model of stellar motion. Values larger than 1.4 depict that the model does not fit the data well, that the source is not point-like (given the optical resolution of Gaia), or that it has a time-variable structure (Lindegren et al. 2018; Lindegren 2018).

The alignment could be confirmed to within $\pm 20\,\mu\text{as}$ for orientation and $\pm 20\,\mu\text{as}\,\text{yr}^{-1}$ for spin per axis (Lindegren et al. 2018) for the optically faint part of DR2 with a magnitude range of $G \gtrsim 15$ and a median magnitude of $G \simeq 18.8$. The celestial reference frame of *Gaia* EDR3 was aligned towards ICRF3 with a root mean square (RMS) of $\pm 10\,\mu\text{as}$ at epoch $T = 2016.0$ and a spin of less than $\pm 10\,\mu\text{as}\,\text{yr}^{-1}$, both values at magnitude $G = 19$ (Gaia Collaboration et al. 2021a).

3 Methods for catalog comparison

In this chapter the background on mathematical methods for the catalog comparisons is described. First, the identification of counterparts in two catalogs is outlined. Then, various parameters for the comparison of positions and proper motions are explained. In the last section, the calculation of global systematics between two catalogs is introduced.

3.1 Identification of radio-optical counterparts

It is not known whether the observed emission from VLBI and Gaia stems from the same object. Thus, the catalogs have to be compared using spatial crossmatches and appropriate filters. For the identification of counterparts between ICRF3 and Gaia DR2, the same method as for selecting sources for the Gaia-CRF2 in Sect. 2.3.2 is used. To take care of any additional probability of misidentification in crowded areas, the approach of Petrov and Kovalev (2017) is additionally applied. In this approach, the probability of false association (PFA) is determined from the Gaia DR2 source density in the area around the source depending on the arc length between the VLBI and Gaia positions and the Gaia and VLBI error ellipse. The criterion PFA$< 2 \cdot 10^{-4}$ is used as in Petrov and Kovalev (2017) to filter any crossmatches with high probability of misidentification.

For the identification of stars in the Gaia database, the ability of the Gaia archive to search by name in conjunction with retrieval of data from other astrometric databases is employed. The results are checked against a spatial crossmatching of the VLBI and Gaia positions.

Source names according to the naming convention are used to identify counterparts between the different radio catalogs.

3.2 Position offsets

Position offsets $\Delta\alpha$ and $\Delta\delta$ between counterparts of two catalogs $\tilde{C}$ and C are derived in the local tangent plane, provided that the two catalogs are close to each other, as

$$\Delta\alpha* = (\alpha_i^C - \alpha_i^{\tilde{C}}) \cos\delta_i^{\tilde{C}} \tag{3.1}$$

$$\Delta\delta = \delta_i^C - \delta_i^{\tilde{C}}, \tag{3.2}$$

where $\alpha_i^{\tilde{C}}, \delta_i^{\tilde{C}}$ are the coordinates of the ith source in the first catalog, and α_i^C, δ_i^C are the coordinates of the same source in the second catalog (see for example Mignard et al. 2016). In order to make the offsets in α direction comparable over all declinations, they are multiplied by $\cos\delta$ (and depicted with '*').

The arc length (angular separation) is

$$\rho = \sqrt{(\Delta\alpha*)^2 + (\Delta\delta)^2}, \tag{3.3}$$

assuming the validity of the small angle approximation with position offsets smaller $\sim$150 mas. Considering the possibility of strong correlations between the coordinate directions, the normalized arc length X_ρ is derived from

$$X_\rho^2 = [X_\alpha X_\delta] \begin{bmatrix} 1 & U \\ U & 1 \end{bmatrix}^{-1} \begin{bmatrix} X_\alpha \\ X_\delta \end{bmatrix}, \tag{3.4}$$

where the correlation coefficient of the combined errors is

$$U = \frac{\sigma_{\alpha*,C}\sigma_{\delta,C}r_C + \sigma_{\alpha*,\tilde{C}}\sigma_{\delta,\tilde{C}}r_{\tilde{C}}}{\sqrt{\left(\sigma_{\alpha*,C}^2 + \sigma_{\alpha*,\tilde{C}}^2\right)\left(\sigma_{\delta,C}^2 + \sigma_{\delta,\tilde{C}}^2\right)}}, \tag{3.5}$$

the correlation coefficients of the two CRFs are r_C and $r_{\tilde{C}}$, and the normalized coordinate differences are

$$X_\alpha = \frac{\Delta\alpha*}{\sqrt{\sigma_{\alpha*,\tilde{C}}^2 + \sigma_{\alpha*,C}^2}}, \qquad X_\delta = \frac{\Delta\delta}{\sqrt{\sigma_{\delta,\tilde{C}}^2 + \sigma_{\delta,C}^2}}. \tag{3.6}$$

The normalized separations $X_{\rho,i}$ with $i = 1...n$ between two astrometric catalogs with n counterparts should follow the standard Rayleigh distribution ($\sigma = 1$) in case their uncertainties are normally distributed. The cutoff criterion x for outliers from this distribution are determined from the probability density function Pr as

$$Pr(X_i > x) = exp((-x^2)/2) * n, \tag{3.7}$$

and $Pr(X_i > x) = 0.5$.

The position angle ψ from the direction to the positive declination axis towards the position of interest in direction of the positive right ascension axis, as pictured in Fig. 3.1, is determined as

$$\psi = \text{atan2}(\Delta\alpha*, \Delta\delta). \tag{3.8}$$

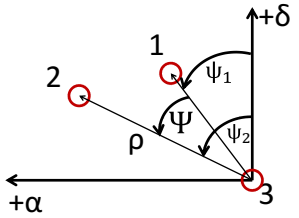

Figure 3.1 The position angle difference Ψ between the arcs with length ρ of two positions towards a third position.

For example, in the case of Fig. 3.1, for ψ_1 for position 1 with reference position 3 $\Delta\alpha*_1 = (\alpha 1 - \alpha_3) * cos(\delta_1)$ and $\Delta\delta_1 = \delta_1 - \delta_3$. The position angle difference Ψ between two positions towards a third position, as pictured in Fig. 3.1, is then determined as

$$\Psi = \psi_2 - \psi_1. \tag{3.9}$$

3.3 Alignment of two celestial reference frames

The alignment of two catalogs is in general validated by the determination of a residual global rigid rotation A between the two reference frames of interest. The rotation thereby is defined by an instantaneous orientation offset ϵ of the three coordinate axes $[\tilde{X}, \tilde{Y}, \tilde{Z}]$ of an arbitrary reference frame $\tilde{C}$ with respect to a reference frame $C = [X, Y, Z]$, and its time derivative, the angular velocity called spin ω. For illustration, sketch of the orientation about the Z axis relative to the coordinate direction of a source S is shown in Fig. 3.2. Ideally, the reference frames are non-rotating with time in order to fulfill the requirement of the ICRS, therefore the spin should be zero and only orientation offset parameters require determination. All following approaches of testing the alignment between two catalogs are implemented using the least-squares algorithm of the Gauß-Markov-Model as described in Sect. 3.3.1. Thereby, the rotation parameters and other parameters of interest are estimated from position or proper motion offsets $\Delta\alpha*$ and $\Delta\delta$, com-

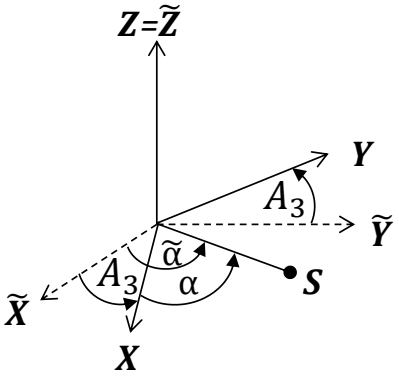

Figure 3.2 The orientation of a reference frame $\tilde{C} = [\tilde{X}, \tilde{Y}, \tilde{Z}]$ with respect to a reference frame $C = [X, Y, Z]$ when the Z axes of the two frames point in the same direction and only a positive orientation offset labelled A_3 in Z is present. Consequently, the right ascension of source S is α in frame C and $\tilde{\alpha} = \alpha + A_3$ in frame $\tilde{C}$. The example is based on Fig. 1 in Lindegren (2020a).

puted similar to Eq. 3.2, of the individual counterparts of the two catalogs. In order for this algorithm to work, the system of equations must be over-determined, which means that information for more counterparts needs to be available than the number of desired parameters.

In the simplest approach, the orientation offset between two catalogs is calculated from position offsets at a common epoch in time or, in a separate analysis, the spin is determined from proper motion offsets at a common epoch in time. The offsets describe a vector field on the celestial sphere and the rotation is the common global feature described mathematically in a functional model as

$$\Delta\alpha* = +\ A_1 \cos\alpha \sin\delta + A_2 \sin\alpha \sin\delta - A_3 \cos\delta, \tag{3.10}$$

$$\Delta\delta = -A_1 \sin\alpha + A_2 \cos\alpha, \tag{3.11}$$

where A_1, A_2, and A_3 are the rotation angles around the three axes of a reference frame and $\Delta\alpha*$ and $\Delta\delta$ are the respective position offsets.

Historically, for example for the orientation of the first realization of the International Celestial Reference Frame (ICRF1) (Ma et al. 1998), additional parameters were included in the functional model:

$$\Delta\alpha* = \ A_1 \cos\alpha \sin\delta + A_2 \sin\alpha \sin\delta - A_3 \cos\delta + D_\alpha(\delta - \delta_0)\cos\delta, \tag{3.12}$$

$$\Delta\delta = -A_1 \sin\alpha + A_2 \cos\alpha + D_\delta(\delta - \delta_0) + B_\delta, \tag{3.13}$$

where the linear trends D_α and D_δ in direction of α and δ are a function of declination with an arbitrary origin δ_0. The bias B_δ is describing a global translation in direction of δ. According to Feissel-Vernier et al. (2006) this parameter is significant in case of systematic declination differences such as "inaccuracy of the tropospheric propagation correction for sources observed at low elevations. This is often the case for sources in the equatorial region, as a result of the terrestrial network geometry." Since then, the tropospheric modeling in VLBI analysis has been evolved and now, this parameter is expected to be negligible. Still, it can be employed as a quality check of the reference frames. The parameters D_α and D_δ however, were already not used for investigation of the orientation of ICRF2 to its predecessor anymore because they were found negligible (Fey et al. 2015).

In the recent years this approach has been refined in two ways. First, Lindegren (2020a) combined the determination of orientation offset and spin between two catalogs. In his method, both position differences and proper motion differences may be used as input parameters to the least-squares adjustment. The position differences also impact the determination of the spin in case the position epochs between the two catalogs differ. In

case multiple differences are inserted for the same object, they also get adjusted. This method is described in detail in Sect.3.3.2. Second, in Sect.3.3.3 the fit of vector spherical harmonics to position or proper motion offsets is introduced. This method is reported for example by Mignard and Klioner (2012) and describes the fit to orthogonal functions, which also allow the determination of higher-order terms in case a sufficient number of counterparts is available.

3.3.1 Least squares adjustment

The Gauß-Markov-Model is the commonly used algorithm in geodesy for the estimation of the parameters of linearized functional models based on the method of least squares. The parametric adjustment is based on simple equations which are introduced here for clarity and can be found for example in Niemeier (2008) and DIN Deutsches Institut für Normung e.V. (2010). The method of least squares can only be applied if the number of observations n is larger than the number of unknown parameters to be determined u.

The functional model f_k, where $k = 1...n$, is a linear model of the true values of parameters $\tilde{X}_j$, where $j = 1...u$. For true values of the observations $\tilde{L}_k$, the relation

$$\tilde{L}_k = f_k(\tilde{X}_1, \tilde{X}_2, \tilde{X}_3, ..., \tilde{X}_u) \tag{3.14}$$

applies. The results of the adjustment $\hat{L_k}$ and $\hat{X}_j$ need to fulfill this functional model as well:

$$\hat{L_k} = L_k + v_k \equiv f_k(\hat{X}_1, \hat{X}_2, \hat{X}_3, ..., \hat{X}_u). \tag{3.15}$$

Thereby v_k are the residuals and L_k are the observed values.

The adjustment algorithm only works, if the adjusted parameters are small. Therefore, usually reduced observations $\boldsymbol{l}$ are used for the calculations instead of observations $\boldsymbol{L}$, where $\boldsymbol{l} = \boldsymbol{L} - \boldsymbol{L_0}$. Thereby, approximate values of observations $\boldsymbol{L_0}$ are obtained by inserting approximate parameters $\boldsymbol{X_0}$ for the parameters $\hat{\boldsymbol{X}}$ in the functional model f. Then, the reduced parameters $\hat{\boldsymbol{x}}$ are estimated, and the desired parameters $\hat{\boldsymbol{X}}$ are determined as $\hat{\boldsymbol{X}} = \boldsymbol{X_0} + \hat{\boldsymbol{x}}$. If the approximate values are unknown, they are usually set to zero. The linearized functional model in matrix notation is expressed as

$$\underset{(n,1)}{\boldsymbol{l}} + \underset{(n,1)}{\boldsymbol{v}} = \underset{(n,u)}{\boldsymbol{A}} \underset{(u,1)}{\hat{\boldsymbol{x}}}, \tag{3.16}$$

where $\boldsymbol{A}$ is the model matrix consisting of n lines and u columns which are created from the in total u coefficients of the n observation equations. The coefficients are determined from the partial derivatives of the linearized functional model with respect to the respective

parameter $\hat{\boldsymbol{x}}_{\boldsymbol{j}}$ at $\boldsymbol{X_0}$. If the functional model is not linear, it is usually linearized by a Taylor expansion. Then, the adjustment is iteratively solved, where the linearization is conducted at $\hat{\boldsymbol{X}}$ of the previous iteration.

The second component for the adjustment model is the stochastic model $\boldsymbol{\Sigma_{ll}}$. It provides information about the uncertainty relation between the observations l_k. The cofactor matrix $\boldsymbol{Q_{ll}} = \frac{1}{\sigma_0^2}\boldsymbol{\Sigma_{ll}}$ of the observations is a squared matrix of size n, where the variances of the observations σ_k^2 are the main diagonal elements. If correlations between observations were present, they would be located at the respective off-diagonal elements of the two correlated parameters. Otherwise, these matrix elements are equal to zero, which simplifies the calculations of the weight matrix $\boldsymbol{P}$ to

$$\underset{(n,n)}{\boldsymbol{P}} = \underset{(n,n)}{\boldsymbol{Q_{ll}}^{-1}} = \begin{bmatrix} \sigma_0^2/\sigma_1^2 & & 0 \\ & \ddots & \\ 0 & & \sigma_0^2/\sigma_n^2 \end{bmatrix}, \tag{3.17}$$

where σ_0^2 is the unknown variance of weight unit. Its absolute value is unknown and not relevant for this adjustment algorithm, which is why it is usually set equal to one, as it is in this work.

From the functional model and the stochastic model, the normal equation system is derived as

$$\hat{\boldsymbol{x}} = \boldsymbol{N}^{-1}\boldsymbol{b}, \qquad \underset{(u,u)}{\boldsymbol{N}} = \underset{(u,n)(n,n)(n,u)}{\boldsymbol{A}'\boldsymbol{P}\boldsymbol{A}}, \qquad \underset{(u,1)}{\boldsymbol{b}} = \underset{(u,n)(n,n)(n,1)}{\boldsymbol{A}'\boldsymbol{P}\boldsymbol{l}}, \tag{3.18}$$

where $\boldsymbol{N}$ is the normal equation matrix. The cofactor matrix $\boldsymbol{Q_{xx}}$ of the estimated parameters $\hat{\boldsymbol{x}}$ is determined as $\boldsymbol{Q_{xx}} = \boldsymbol{N}^{-1}$. It contains information about the uncertainty relations of $\hat{\boldsymbol{x}}$. The residuals of the observations finally are derived from

$$\boldsymbol{v} = \boldsymbol{A}\hat{\boldsymbol{x}} - \boldsymbol{l}. \tag{3.19}$$

The square sum of residuals Q, which can be used as a first quality check using Eq. 3.21, is needed for calculation of the empirical variance of weight unit s_0^2 (also called χ^2).

$$Q = \boldsymbol{v}'\boldsymbol{P}\boldsymbol{v}, \tag{3.20}$$

$$Q \equiv \boldsymbol{l}'\boldsymbol{P}\boldsymbol{l} - (\boldsymbol{A}'\boldsymbol{P}\boldsymbol{l})'\hat{\boldsymbol{x}}, \tag{3.21}$$

$$s_0^2 = \frac{Q}{n-u}. \tag{3.22}$$

Thereby, the principle of adjustment following the method of least squares is the loss function $\boldsymbol{v'Pv} \Rightarrow min.$

The covariance matrix $\boldsymbol{\Sigma_{xx}}$ of the estimated parameters is calculated from

$$\boldsymbol{\Sigma_{xx}} = s_0^2 \boldsymbol{Q_{xx}}. \tag{3.23}$$

The standard deviation of the estimated parameters s_j is equal to the square root of the respective diagonal element of $\boldsymbol{\Sigma_{xx}}$. Correlations of the parameters $\hat{\boldsymbol{x}}_j$ and $\hat{\boldsymbol{x}}_i$, where $j \neq i$, can be derived from the respective off-diagonal elements, the covariances s_{ij}. The correlation coefficient r_{ij} is determined as

$$r_{ij} = \frac{s_{ij}}{s_i s_j}, \tag{3.24}$$

where zero values indicate no linear correlation and values of magnitude 1 indicate full linear correlation. It is only meaningful if a causal linear relationship between the two parameters is present and if the population follows a normal distribution. A general rule of thumb, that is also used for the evaluation in this work, is that correlations larger zero but smaller 0.3 indicate minor linear correlation, values between 0.3 and 0.5 indicate medium linear correlation, values between 0.5 and 0.7 indicate strong linear correlation, and values larger 0.7 indicate very strong linear correlation in case of a sufficiently large sample. Corresponding negative values indicate negative correlations of the same category. A more detailed categorization can be carried out using the Fisher-transformation and t-test. For example, from covariances of astrometric positions $\alpha*$ and δ, the semi-major error axis of the error ellipse in position $\sigma_{\mathrm{pos,max}}$ can be derived. It is determined as (Lindegren et al. 2016)

$$\sigma_{\mathrm{pos,max}} = \sqrt{\frac{1}{2}\left(\sigma_{\alpha*}^2 + \sigma_\delta^2\right) + \frac{1}{2}\sqrt{\left(\sigma_\delta^2 - \sigma_{\alpha*}^2\right)^2 + 4(\sigma_{\alpha*}\sigma_\delta r\left(\alpha*, \delta\right))^2}}. \tag{3.25}$$

It is possible to set up the normal equation system in Eq. 3.18 individually for each observation. Then they are stacked only before inversion of $\boldsymbol{N}$. This results in reduced computational power, for example, when adding new observations to an existing solution to obtain updated estimates. Another possible application is to test the scatter of estimates from different subsets of observations $\boldsymbol{l}$ without re-computing the normal equation matrix for each $\boldsymbol{l}$. This procedure does not lose information, but it is only possible in case

the observations are not correlated. The vectors and matrices get stacked according to

$$(\boldsymbol{N}_1 + \boldsymbol{N}_2 + ... + \boldsymbol{N}_i)\,\boldsymbol{x} = \boldsymbol{b}_1 + \boldsymbol{b}_2 + ... + \boldsymbol{b}_i \tag{3.26}$$

and

$$\boldsymbol{l'Pl} = (\boldsymbol{l'Pl})_1 + (\boldsymbol{l'Pl})_2 + ... + (\boldsymbol{l'Pl})_i\,. \tag{3.27}$$

In the case of application examples with constraints, it should be emphasized that any constraints must be removed from the normal equation system before stacking. Otherwise they would get stacked as well. The constraints are then attached to the stacked product, for example in case of datum information.

For the stacking process it is important that the columns and rows in the individual normal equation matrix only contain common parameters to all observations and are sorted in the same manner. Therefore, in case the desired parameters do not occur in the individual normal equation matrix, zeros are filled in the respective rows and columns of the missing parameter in the matrix. In case other parameters are present, they have either to be fixed or reduced. The reduction of unwanted parameters is done by the method of Helmert blocking (Wolf 1978; Niemeier 2008), which decomposes the normal equation system into desired parameters, denoted by 1, and undesired parameters, denoted by 2:

$$\begin{pmatrix}\boldsymbol{N}_{11}\boldsymbol{N}_{12}\\ \boldsymbol{N}_{21}\boldsymbol{N}_{22}\end{pmatrix} \cdot \begin{pmatrix}\boldsymbol{x}_1\\ \boldsymbol{x}_2\end{pmatrix} = \begin{pmatrix}\boldsymbol{b}_1\\ \boldsymbol{b}_2\end{pmatrix}, \tag{3.28}$$

which can also be written as

$$\boldsymbol{N}_{11}\boldsymbol{x}_1 + \boldsymbol{N}_{12}\boldsymbol{x}_2 = \boldsymbol{b}_1, \quad \boldsymbol{N}_{21}\boldsymbol{x}_1 + \boldsymbol{N}_{22}\boldsymbol{x}_2 = \boldsymbol{b}_2. \tag{3.29}$$

Solving the second last equation for $\boldsymbol{x}_2$ and inserting it into the last equation results in

$$\left(\boldsymbol{N}_{11} - \boldsymbol{N}_{12}\boldsymbol{N}_{22}^{-1}\boldsymbol{N}_{21}\right) \cdot \boldsymbol{x}_1 = \boldsymbol{b}_1 - \boldsymbol{N}_{12}\boldsymbol{N}_{22}^{-1}\boldsymbol{b}_2, \tag{3.30}$$

which equals to

$$\boldsymbol{N}_{\text{reduced}} \cdot \boldsymbol{x}_1 = \boldsymbol{b}_{\text{reduced}}. \tag{3.31}$$

Lastly, also the observation vector product needs adaption,

$$(\boldsymbol{l'Pl})_{\text{reduced}} = \boldsymbol{l'Pl} - \boldsymbol{b}_2'\boldsymbol{N}_{22}^{-1}\boldsymbol{b}_2. \tag{3.32}$$

In this reduction method, the desired parameters $\boldsymbol{x}_1$ are not changed. Therefore, they

can be determined computationally efficient in case orders of magnitude more undesired parameters are present in a normal equation system.

3.3.2 Simultaneous least squares adjustment of orientation and spin

A combined estimation of orientation ϵ and spin ω is possible when positions and proper motions or multiple positions for a source are available in the reference frames under study. This section is following the corresponding algorithms published in Lindegren (2020a).

To compute the differences between the positions and proper motions of a source in the two catalogs, the position and proper motions at epoch T of the reference frame $\tilde{C}$ under investigation must be available at the same epoch t of the target reference frame C. If this is not the case, they can in general be propagated from the original epoch T to the desired epoch t by making use of the parallax ϖ and radial velocities v_r and

$$\boldsymbol{s}(t) = \boldsymbol{u} + (t - T)\boldsymbol{m}, \tag{3.33}$$

where on the unit sphere

$$\boldsymbol{u} = \begin{pmatrix} \cos\alpha\cos\delta \\ \sin\alpha\cos\delta \\ \sin\delta \end{pmatrix} = \begin{pmatrix} u_X \\ u_Y \\ u_Z \end{pmatrix} \tag{3.34}$$

is the barycentric unit vector towards the source, and

$$\boldsymbol{e}_\alpha = \frac{1}{\cos\delta}\frac{\partial}{\partial\alpha}\boldsymbol{u} = \begin{pmatrix} -\sin\alpha \\ \cos\alpha \\ 0 \end{pmatrix}, \quad \boldsymbol{e}_\delta = \boldsymbol{u} \times \boldsymbol{e}_\alpha = \frac{\partial}{\partial\delta}\boldsymbol{u} = \begin{pmatrix} -\cos\alpha\sin\delta \\ -\sin\alpha\sin\delta \\ \cos\delta \end{pmatrix}, \tag{3.35}$$

are its projections of unit length towards increasing α and δ directions. The time-dependent fraction $\boldsymbol{m}$ is calculated with

$$A = \frac{149\,597\,870.7\,\mathrm{km}}{365.25 \times 86\,400\,\mathrm{s\,yr^{-1}}} \tag{3.36}$$

and

$$\boldsymbol{m} = \mu_{\alpha*}\boldsymbol{e}_\alpha + \mu_\delta\boldsymbol{e}_\delta + (v_r\varpi/A)\,\boldsymbol{u}. \tag{3.37}$$

From Eq. 3.33, the new parameters at epoch t are then determined by calculation of the propagated unit vector $\boldsymbol{u}(t) = |\boldsymbol{s}(t)|^{-1}\boldsymbol{s}(t)$, $\boldsymbol{m}(t) = |\boldsymbol{s}(t)|^{-1}\boldsymbol{m}$,

$$\alpha(t) = atan2\left(u_Y(t), u_X(t)\right), \quad \delta(t) = atan2\left(u_Z(t), \sqrt{u_X(t)^2 + u_Y(t)^2}\right), \tag{3.38}$$

$$\boldsymbol{e}_\alpha(t) = \begin{pmatrix} -\sin\alpha(t) \\ \cos\alpha(t) \\ 0 \end{pmatrix}, \quad \boldsymbol{e}_\delta(t) = \begin{pmatrix} -\cos\alpha(t)\sin\delta(t) \\ -\sin\alpha(t)\sin\delta(t) \\ \cos\delta(t) \end{pmatrix}, \tag{3.39}$$

$$\mu_{\alpha*}(t) = \boldsymbol{e}_\alpha(t)'\boldsymbol{m}(t), \quad \mu_\delta(t) = \boldsymbol{e}_\delta(t)'\boldsymbol{m}(t), \tag{3.40}$$

$$\boldsymbol{\varpi}(t) = |\boldsymbol{s}(t)|^{-1}\boldsymbol{\varpi}, \tag{3.41}$$

$$\boldsymbol{v}_r(t) = \boldsymbol{u}(t)'\boldsymbol{m}(t)A/\boldsymbol{\varpi}(t). \tag{3.42}$$

Because the proper motions are modeled as constant angular velocities in the standard model of stellar motion, only uniform rotations apply, which results in an offset $\boldsymbol{\epsilon}(t)$ at epoch t of

$$\boldsymbol{C} = \tilde{\boldsymbol{C}} + \boldsymbol{\epsilon}(t) \times \tilde{\boldsymbol{C}} + \mathcal{O}(\boldsymbol{\epsilon}^2), \tag{3.43}$$

with

$$\epsilon(t) = \epsilon(T) + (t - T)\omega, \tag{3.44}$$

where the rotation A (see Eqs. 3.10 and 3.11) is separated in an orientation offset $\epsilon(T)$ at epoch T and a linear spin ω as the first order time derivative of the orientation offset. Similar to Lindegren (2020a) Eqs. 3.10 and 3.11 are applied for both types of rotation as the functional model.

Two observation equations for source i are important for solving the mathematical problem:

$$\mathbf{0} = \boldsymbol{y}_i - \boldsymbol{K}_i\boldsymbol{x} + \boldsymbol{\gamma}_i, \tag{3.45}$$

and

$$\mathbf{0} = \boldsymbol{\Delta f}_i - \boldsymbol{M}_i\boldsymbol{y}_i - \boldsymbol{\nu}_i, \tag{3.46}$$

with $\boldsymbol{\gamma}_i$ and $\boldsymbol{\nu}_i$ being noise. From Eq. 3.45, the combined design matrix for a common

global rotation in the positions and proper motion of the unknown corrections $\boldsymbol{y}_i$ is

$$\boldsymbol{K}_i = \begin{bmatrix} \cos\alpha_i \sin\delta_i & \sin\alpha_i \sin\delta_i & -\cos\delta_i & 0 & 0 & 0 \\ -sin\alpha_i & cos\alpha_i & 0 & 0 & 0 & 0 \\ 0 & 0 & 0 & 0 & 0 & 0 \\ 0 & 0 & 0 & \cos\alpha_i \sin\delta_i & \sin\alpha_i \sin\delta_i & -\cos\delta_i \\ 0 & 0 & 0 & -\sin\alpha_i & \cos\alpha_i & 0 \end{bmatrix}, \quad (3.47)$$

where the columns correspond to the unknown rotation parameters $\boldsymbol{x}$,

$$\boldsymbol{x} = [\epsilon_X(T), \epsilon_Y(T), \epsilon_Z(T), \omega_X, \omega_Y, \omega_Z], \quad (3.48)$$

and the rows to the unknown corrections $\boldsymbol{y}_i$ for source i, which are to be added to its parameters of frame $\tilde{C}$,

$$\boldsymbol{y}_i = \begin{bmatrix} \Delta\alpha*_i, & \Delta\delta_i, & \Delta\varpi_i, & \Delta\mu_{\alpha*i}, & \Delta\mu_{\delta i} \end{bmatrix}. \quad (3.49)$$

Thus, the total number of unknown parameters of the adjustment is $6 + 5k$, where k is the number of involved counterparts i. The matrix elements for ϖ are zero because the parallax is not affected by the frame rotation. The stochastic model $\boldsymbol{C}_i$ is the 5×5 covariance of the parameters from frame $\tilde{C}$.

From Eq. 3.46, the design matrix for the differences between the parameters of the reference frames $\tilde{C}$ and C at epoch t labeled $\boldsymbol{\Delta f}_i$ is

$$\boldsymbol{M}_i = \begin{bmatrix} 1 & 0 & 0 & t_i - T & 0 \\ 0 & 1 & 0 & 0 & t_i - T \\ 0 & 0 & 1 & 0 & 0 \\ 0 & 0 & 0 & 1 & 0 \\ 0 & 0 & 0 & 0 & 1 \end{bmatrix}, \quad (3.50)$$

where the columns correspond to the corrections $\boldsymbol{y}_i$ and the rows correspond to the parameter differences $\boldsymbol{\Delta f}_i$. If only position differences are available for a source i, $\boldsymbol{M}_i$ consists of the first two rows, whereas likewise if only proper motion differences are available for a source i, $\boldsymbol{M}_i$ consists of the last two rows. The stochastic model V_i is created from the uncertainties and correlations of the data of frame C.

The two observation equations are combined to the loss function

$$\boldsymbol{Q}(\boldsymbol{x}, \{\boldsymbol{y_i}\}_S) = \sum_{i \in S} \left[(\boldsymbol{y}_i - \boldsymbol{K}_i\boldsymbol{x})' \boldsymbol{C}_i^{-1} (\boldsymbol{y}_i - \boldsymbol{K}_i\boldsymbol{x}) + (\boldsymbol{\Delta f}_i - \boldsymbol{M}_i\boldsymbol{y}_i)' \boldsymbol{V}_i^{-1} (\boldsymbol{\Delta f}_i - \boldsymbol{M}_i\boldsymbol{y}_i) \right], \quad (3.51)$$

and they are resulting in solvable normal equations as

$$\left(\sum_{i\in S} \boldsymbol{K}_i' \boldsymbol{C}_i^{-1} \boldsymbol{K}_i\right) \boldsymbol{x} - \sum_{i\in S} \boldsymbol{K}_i' \boldsymbol{C}_i^{-1} \boldsymbol{y}_i = 0, \tag{3.52}$$

$$-\boldsymbol{C}_i^{-1} \boldsymbol{K}_i \boldsymbol{x} + \left(\boldsymbol{C}_i^{-1} + \boldsymbol{M}_i' \boldsymbol{V}_i^{-1} \boldsymbol{M}_i\right) \boldsymbol{y}_i = \boldsymbol{M}_i' \boldsymbol{V}_i^{-1} \Delta \boldsymbol{f}_i \tag{3.53}$$

where i is an element of the set of common sources S. Thereby matrices and vectors for each source i are stacked as described in Sect. 3.3.1.

As an alternative, the system of normal equations is reduced to only include the common rotation parameters $\boldsymbol{x}$ by inserting Eq. 3.53 in Eq. 3.52 and employing the method of Helmert blocking as described in Eqs. 3.28 to 3.32,

$$\left(\sum_{i\in S} \boldsymbol{N}_i\right) \boldsymbol{x} = \sum_{i\in S} \boldsymbol{b}_i, \tag{3.54}$$

with the matrices and vector

$$\boldsymbol{N}_i = \boldsymbol{K}_i' \boldsymbol{M}_i' \boldsymbol{D}_i^{-1} \boldsymbol{M}_i \boldsymbol{K}_i, \quad \boldsymbol{b}_i = \boldsymbol{K}_i' \boldsymbol{M}_i' \boldsymbol{D}_i^{-1} \Delta \boldsymbol{f}_i, \quad \boldsymbol{D}_i = \boldsymbol{V}_i + \boldsymbol{M}_i \boldsymbol{C}_i \boldsymbol{M}_i', \tag{3.55}$$

which is the covariance of $\Delta \boldsymbol{f}_i$. From Eq. 3.54, $\hat{\boldsymbol{x}}$ is retrieved, and by inserting it in Eq. 3.53, the $\hat{\boldsymbol{y}}_i$ are obtained.

Likewise, Eq. 3.51 is reduced to

$$Q(x) = \sum_{i\in S} Q_i(x), \tag{3.56}$$

and

$$Q_i(x) = \left(\Delta \boldsymbol{f}_i - \boldsymbol{M}_i \boldsymbol{K}_i \boldsymbol{x}\right)' \boldsymbol{D}_i^{-1} \left(\Delta \boldsymbol{f}_i - \boldsymbol{M}_i \boldsymbol{K}_i \boldsymbol{x}\right), \tag{3.57}$$

where the residual of the VLBI data with respect to the Gaia data, which was propagated to the VLBI epoch and corrected for the estimated rotation parameters, is $\Delta \boldsymbol{f}_i - \boldsymbol{M}_i \boldsymbol{K}_i \boldsymbol{x}$. The uncertainty of the residuals is determined as $\boldsymbol{D}_i - \boldsymbol{M}_i \boldsymbol{K}_i \boldsymbol{N}_i^{-1} \left(\boldsymbol{M}_i \boldsymbol{K}_i\right)'$.

Furthermore,

$$Q/n = Q(\hat{\boldsymbol{x}})/n \tag{3.58}$$

is similar to the s_0^2 of the solution, where n is the number of VLBI data points.

The amount of information of source i contributed to the solution of $\boldsymbol{x}$ is quantified by

the Fisher information derived from

$$E_i = \underset{\epsilon}{\text{trace}}\,(\boldsymbol{N}_i)\,, \qquad \Omega_i = \underset{\omega}{\text{trace}}\,(\boldsymbol{N}_i)\,, \tag{3.59}$$

where the first three elements of $\boldsymbol{N}_i$ are used for E_i and the latter three for Ω_i. Therefore, if for example a source does not have any information on position but only on proper motion, $\underset{\epsilon}{\text{trace}}\,(\boldsymbol{N}_i)$ equals zero.

3.3.3 Vector spherical harmonics

The methodology of using VSH (e.g., Mathews 1981) for investigating celestial catalogs is described in Mignard and Klioner (2012), while it is claimed by the authors that the idea was initiated in Mignard and Morando (1990). It has been widely used in astronomy and geodesy in the context of celestial reference frames, such as for the determination of large-scale systematics of a single celestial catalog from VLBI or astrometric spacecraft (e.g., Gwinn et al. 1997; Makarov and Murphy 2007; Titov and Malkin 2009; Titov et al. 2011; Titov and Lambert 2013; Gaia Collaboration et al. 2021b) or for testing the alignment and large-scale systematics between reference frames as in Arias et al. (2000); Liu et al. (2018); Karbon and Nothnagel (2019); Liu et al. (2020); Charlot et al. (2020).

VSH are an orthogonal set of toroidal (magnetic) and spheroidal (electric) basis functions $\boldsymbol{T}_{lm}$ and $\boldsymbol{S}_{lm}$ of degree l and order m ($|m| \leq l$) for a vector field $\boldsymbol{V}(\alpha, \delta)$ on a sphere. Thereby $\boldsymbol{S}_{lm} = \boldsymbol{u} \times \boldsymbol{T}_{lm}$ and $\boldsymbol{T}_{lm} = -\boldsymbol{u} \times \boldsymbol{S}_{lm}$. For each point on the sphere as well as for each l and m the rules $\boldsymbol{u} \cdot \boldsymbol{S}_{lm} = 0$, $\boldsymbol{u} \cdot \boldsymbol{T}_{lm} = 0$, and $\boldsymbol{T}_{lm} \cdot \boldsymbol{S}_{lm} = 0$ apply Mignard and Klioner (2012).

According to Mignard and Klioner (2012) "any (square-integrable) complex-valued vector field $\boldsymbol{V}(\alpha, \delta)$ defined on the surface of a sphere and orthogonal to $\boldsymbol{u}$ (radial direction),

$$\boldsymbol{V}(\alpha, \delta) = V^{\alpha}(\alpha, \delta)\boldsymbol{e}_{\alpha} + V^{\delta}(\alpha, \delta)\boldsymbol{e}_{\delta}, \tag{3.60}$$

can be expanded in a unique linear combination of the VSH,

$$\boldsymbol{V}(\alpha, \delta) = \sum_{l=1}^{\infty} \sum_{m=-l}^{l} \left(t_{lm}\boldsymbol{T}_{lm} + s_{lm}\boldsymbol{S}_{lm}\right), \tag{3.61}$$

where the coefficients t_{lm} and s_{lm} can again be computed by projecting the field on the base functions [...]" and $\boldsymbol{e}_{\alpha}$ and $\boldsymbol{e}_{\delta}$ are determined from Eqs. 3.34 and 3.35. Further details on the mathematical principles and the derivation of the harmonic expansions are given in Gwinn et al. (1997); Mignard and Klioner (2012) and are not repeated here.

The global effects of first degree VSH can be interpreted as an infinitesimal rotation

around the three axis of the frame and a dipole displacement called glide. Smaller details of the vector field can be modeled with increasing degree l. The rotation vector $\boldsymbol{A}$ with components $\boldsymbol{A} = [A_1, A_2, A_3] = [a^M_{1,1}, a^M_{1,-1}, a^M_{1,0}]$ of magnetic type M creates a vector field $\boldsymbol{V}^A = \boldsymbol{A} \times \boldsymbol{u}$, which corresponds to

$$\begin{aligned} V^A_\alpha =& \boldsymbol{V}^R \cdot \boldsymbol{e}_\alpha = +A_1 \sin\delta\cos\alpha + A_2 \sin\delta\sin\alpha - A_3\cos\delta, \\ V^A_\delta =& \boldsymbol{V}^A \cdot \boldsymbol{e}_\delta = -A_1 \sin\alpha + A_2\cos\delta, \end{aligned} \tag{3.62}$$

when projected on the local tangent plane (Mignard and Klioner 2012).

Likewise, the glide vector $\boldsymbol{D}$ with components $\boldsymbol{D} = [D_1, D_2, D_3] = [a^E_{1,1}, a^E_{1,-1}, a^E_{1,0}]$ of electric type E represents the glide displacement, which is exactly orthogonal to the rotation pattern at each point on the sphere and thereby creates a vector field $\boldsymbol{V}^D = \boldsymbol{u} \times (\boldsymbol{D} \times \boldsymbol{u}) = \boldsymbol{D} - (\boldsymbol{D} \cdot \boldsymbol{u})\,\boldsymbol{u}$ of a dipole shape pointing from one pole of the axis to the other pole and projected on the sphere.

$$\begin{aligned} V^D_\alpha =& \boldsymbol{V}^D \cdot \boldsymbol{e}_\alpha = -D_1 \sin\alpha + D_2\cos\alpha, \\ V^D_\delta =& \boldsymbol{V}^D \cdot \boldsymbol{e}_\delta = -D_1 \sin\delta\cos\alpha - D_2\sin\delta\sin\alpha + D_3\cos\delta, \end{aligned} \tag{3.63}$$

when projected on the local tangent plane (Mignard and Klioner 2012). The amplitude and direction of the glide vector are calculated as

$$|D| = \sqrt{D_1^2 + D_2^2 + D_3^2}, \qquad \alpha_D = \mathrm{atan2}\frac{D_2}{D_1}, \qquad \delta_D = \mathrm{asin}\frac{D_3}{|D|}, \tag{3.64}$$

which also apply accordingly to the rotations. The physical interpretation of the glide is the effect of the accelerated motion of the observer towards an apex, where the observed sources show the dipole effect as apparent proper motions in the direction of the observer's acceleration. This is the case for the effect of Galactocentric acceleration of the solar system barycenter in space that is seen in the proper motions of extragalactic objects by an observer located in the solar system (Gwinn et al. 1997; Titov et al. 2011). It could however also just be a systematic error.

The two patterns, rotation and glide, should always be simultaneously determined. Otherwise, the determined vector will always be biased in case the condition of discrete orthogonality between the VSHs are not satisfied, which can be the case if the spherical vector fields on the sphere are not evenly distributed (e.g., Gaia Collaboration et al. 2018).

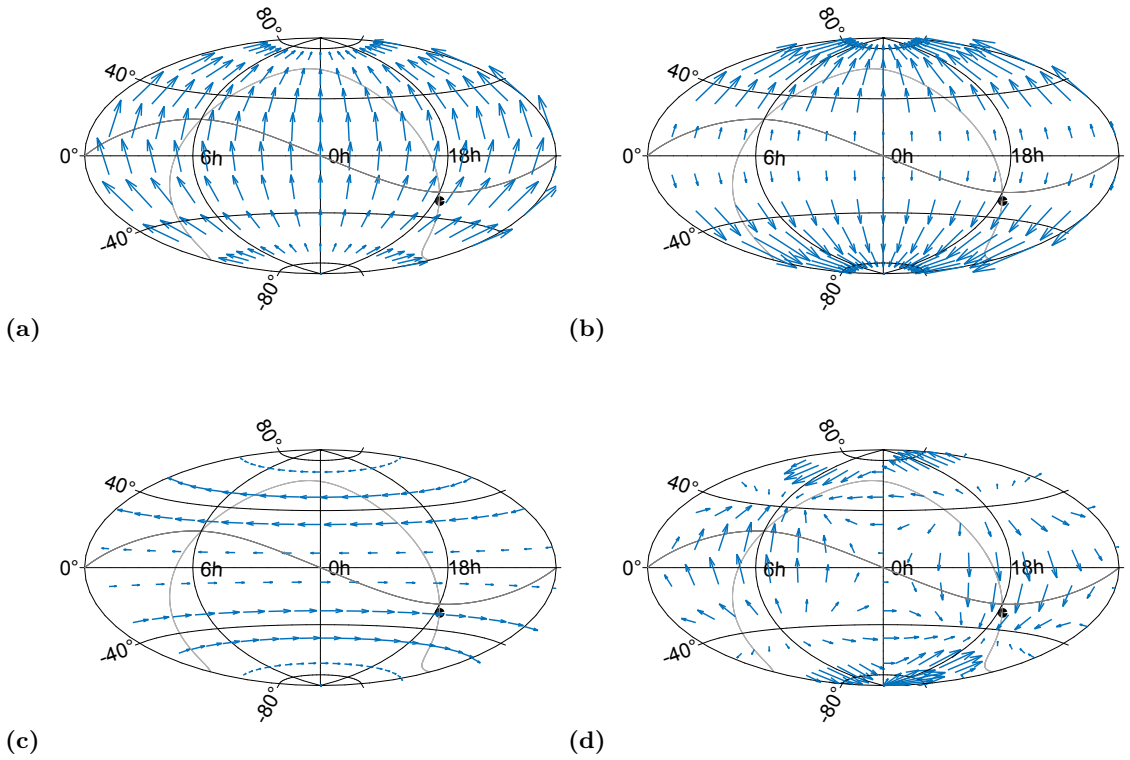

Figure 3.3 Global deformation pattern of the vector field for selected VSH parameters. (a) D_3, (b) $\mathrm{a}^{\mathrm{E}}_{2,0}$, and (c) $a^{\mathrm{M}}_{2,0}$, (d) $\mathrm{a}^{\mathrm{E,Im}}_{2,1}$. The black dot depicts the Galactic center, the dark grey line is the ecliptic, and the light grey line is the galactic plane.

The VSH of degree $l = 2$ describe a quadrupole, and the terms are written as

$$\begin{aligned} V^Q_\alpha = {} & a^M_{2,0} \sin 2\delta \\ & + \sin\delta \left(a^{E,\mathrm{Re}}_{2,1} \sin\alpha + a^{E,\mathrm{Im}}_{2,1} \cos\alpha \right) \\ & - \cos 2\delta \left(a^{M,\mathrm{Re}}_{2,1} \cos\alpha - a^{M,\mathrm{Im}}_{2,1} \sin\alpha \right) \\ & - 2\cos\delta \left(a^{E,\mathrm{Re}}_{2,2} \sin 2\alpha + a^{E,\mathrm{Im}}_{2,2} \cos 2\alpha \right) \\ & - \sin 2\delta \left(a^{M,\mathrm{Re}}_{2,2} \cos 2\alpha - a^{M,\mathrm{Im}}_{2,2} \sin 2\alpha \right), \end{aligned} \tag{3.65}$$

$$\begin{aligned} V^Q_\delta = {} & a^E_{2,0} \sin 2\delta \\ & - \cos 2\delta \left(a^{E,\mathrm{Re}}_{2,1} \cos\alpha - a^{E,\mathrm{Im}}_{2,1} \sin\alpha \right) \\ & - \sin\delta \left(a^{M,\mathrm{Re}}_{2,1} \sin\alpha + a^{M,\mathrm{Im}}_{2,1} \cos\alpha \right) \\ & - \sin 2\delta \left(a^{E,\mathrm{Re}}_{2,2} \cos 2\alpha - a^{E,\mathrm{Im}}_{2,2} \sin 2\alpha \right) \\ & + 2\cos\delta \left(a^{M,\mathrm{Re}}_{2,2} \sin 2\alpha + a^{M,\mathrm{Im}}_{2,2} \cos 2\alpha \right), \end{aligned} \tag{3.66}$$

where Re and Im denote the real and imaginary part. Figures 3.3a to 3.3d show the corresponding spherical vector fields of G_3, $\mathrm{a}^{\mathrm{M}}_{2,0}$, $\mathrm{a}^{E}_{2,0}$, and $\mathrm{a}^{\mathrm{E,Im}}_{2,1}$ as examples. The harmonics of degree $l = 2$ model the pattern of apparent proper motions of distant sources produced by low-frequency gravitational waves (Gwinn et al. 1997).

The 16 parameters from equations 3.62 to 3.66 can be combined at will to provide the functional model for the analysis of celestial catalogs with the help of least squares adjustment as described in Sect. 3.3.1. Thereby the vector field created from both the position offsets $\Delta\alpha*$ and $\Delta\delta$ are used as observations in the design matrix, which results in twice as many observations than sources used for the investigation. The stochastic model consists of the position offset uncertainties, which are derived by variance propagation of the catalog position uncertainties. The celestial reference frames usually provide correlations between the right ascension and declination values of their objects, which is why they can also be inserted in the relevant matrix elements. The same principle holds in case a vector field from proper motion offsets is investigated instead of from position offsets. The axes 1, 2, 3 depicting the rotation and glide components are equivalent to the respective CRF axes X, Y, Z in this work.

3.3.4 Iterations

It is possible to perform least squares adjustment described in Sects. 3.3.1 and 3.3.2 iteratively, i.e., after an initial solution with the entire sample of sources S, the most deviating source is rejected according to the maximum normalized loss function for source i of a given solution $\hat{\boldsymbol{x}}$, $max\,(Q_i/n_i)$, and a subsequent solution with the new sample of sources $S - k$, is computed, and so on. Thereby, k is the number of rejected sources,

$$Q_i/n_i = Q_i(\hat{\boldsymbol{x}})/n_i \tag{3.67}$$

is the normalized loss function, and n_i is the number of data points for source i. The loss function is a measure of the discrepancy of the data from the astrometric model for the source and of the suitability of the uncertainties of its data points. Ideally it should be around unity. Any number of iterations can be performed as long as the normal equation system is still overdetermined.

Statistics are generated for each rotation parameter from $m = 1...p$ iterations in scenario s to evaluate the steadiness of the p iterative solutions (Lunz et al. 2020a). The weighted mean (WM) of a rotation parameter j is determined as

$$\mathrm{WM}_s = \frac{\sum_{m=1}^{p} \left(\hat{\boldsymbol{x}}^m(j)/\boldsymbol{Q}^m_{xx}\,(j,j)\right)}{\sum_{m=1}^{p} \left(1/\boldsymbol{Q}^m_{xx}\,(j,j)\right)}, \tag{3.68}$$

where exemplary $\boldsymbol{Q}^m_{xx}$ is the mth iterate of $\boldsymbol{Q}_{xx}$, the weighted root mean square (WRMS)

describing the scatter of the estimates around the WM is determined as

$$\mathrm{WRMS}_s = \sqrt{\frac{\sum_{m=1}^{p}\left(\left(\hat{\boldsymbol{x}}^m(j) - \mathrm{WM}_s\right)^2 / \boldsymbol{Q}_{xx}^m(j,j)\right)}{\frac{p-1}{p}\sum_{m=1}^{p}\left(1/\boldsymbol{Q}_{xx}^m(j,j)\right)}}, \tag{3.69}$$

and the mean formal error (ME) of the rotation parameter estimates is determined as

$$\mathrm{ME}_s = \frac{\sum_{m=1}^{p}\sqrt{\boldsymbol{Q}_{xx}^m(j,j)}}{p}. \tag{3.70}$$

According to Lunz et al. (2020a), if the WRMS_s is larger than two times the ME_s, the rotation parameter offsets within the iterative parameter series are considered statistically unstable within a scenario.

The mean standard deviation (MS) is calculated as the mean of each iteration series' formal errors renormalized with $\sqrt{Q/n}$ (similar to the calculation of the ME but with multiplication of $\sqrt{Q/n}$):

$$\mathrm{MS}_s = \frac{\sum_{m=1}^{p}\left(\sqrt{\boldsymbol{Q}_{xx}^m(j,j)}\sqrt{Q_m/n_m}\right)}{p}. \tag{3.71}$$

These statistics are furthermore used, for example, to compare different scenarios with different underlying data sets. The significance of the differences in statistics between two scenarios $s1$ and $s2$ is tested by a two-sample t-test of a selected interval of the iteration solutions where the results seem to be stable. This interval can be of different length for both scenarios. This means the first few iterations are deselected in case outliers were included in the sample, and the last few iterations were deselected because of the sparse dataset and probable geometrical impacts of the sky distribution of the counterparts on the results. The significance level was 5% and the null hypothesis was that the means were equal. According to the given Behrens-Fisher problem, it is assumed that the rotation parameters follow a normal distribution with unknown and unequal variances. Furthermore, it is ignored that different stars or a different order of stars is rejected in the given iteration intervals of the two scenarios. "If the test cannot be accepted and the probability value (p-value) is smaller than the significance level, the parameter difference between two scenarios is significant" (Lunz et al. 2020a).

4 Optically faint radio sources

In this chapter the distant and optically faint part of the Gaia data set (the AGN in the Gaia-CRF) and various VLBI-based celestial reference frames are examined in terms of alignment and position differences. Besides the three ICRF3 catalogs, two additional CRFs based on S/X observations are investigated. The first CRF (CRF7918) is set up similar to ICRF3 S/X to check any differences due to different analysis software or setups. For the second CRF (CRFGT), the observation time interval then is restricted to the same time interval as the Gaia data release under investigation, Gaia DR2. The aim is to test whether source structure effects that are variable over time can be mitigated in the comparison between VLBI and Gaia positions. First, the data analysis for deriving own CRFs from VLBI data is described. Then, the counterparts of all the catalogs under review are determined. Finally, individual differences and global systematics are identified between the various radio CRFs themselves and between the radio and optical CRFs. Comparisons to closure-based indicators of detected source structure are conducted.

4.1 Own celestial reference frames at S/X frequencies

For investigating the time-dependency of position offsets between VLBI and Gaia CRFs, two additional CRFs based on S/X VLBI observations are created. In the following, the analysis data and setup are briefly explained. The VieVS@GFZ VLBI software developed by the GFZ in Potsdam, Germany, was used for all processing steps.

4.1.1 Single session analysis

For the single session analysis of this work the VLBI sessions used for ICRF3 S/X were adopted. The data were provided in the NGS file format. The analysis of the group delays was performed with standard modeling and parameter setup used in geodetic VLBI analysis as given in the IERS Conventions (Petit and Luzum 2010) and listed in the following. For the calculation of the geometric delay the ITRF2014 (Altamimi et al. 2016) was used as the a priori terrestrial reference frame (TRF). The a priori CRF was ICRF3 S/X. The reference epoch of the Galactocentric acceleration was set to 2015.0 (same epoch

as for ICRF3). As the dynamical realization of the ICRS, the DE 421 ephemeris (Folkner et al. 2009) were employed.

UT1 and polar motion were retrieved from the IERS 'C04 14' predictions (Bizouard et al. 2019) (For ICRF3, the IERS 'finals.data' predictions (Dick and Thaller 2018) were used) in conjunction with short-period tidal variations (Petit and Luzum 2010). The IAU 2000A nutation (Mathews et al. 2002) and IAU2006 precession (Capitaine et al. 2003; Hilton et al. 2006) models were used for modeling the Earth's spin axis.

The station displacements due to solid Earth tides (Petit and Luzum 2010) and ocean tides (Lyard et al. 2006, FES2004) were applied (For ICRF3 the FES99 TOPEX 7.2 model (Egbert and Erofeeva 2002) and FES99 model (Lefèvre et al. 2002) were used for the latter). The centrifugal effect of the polar motion on the solid Earth (pole tide) was modeled according to Petit and Luzum (2010) and the ocean pole tide according to Desai (2002).

For the tidal atmosphere loading the implementation of Ray and Ponte (2003) by vanDam was used. Non-tidal atmosphere pressure loading was not included in the modeling following the IERS conventions. It would show up as a vertical crust displacement of maximum 2.5 cm for antennas at mid-latitudes. Contributions to the IVS request non-tidal atmosphere pressure loading, thus they were used for ICRF3. (For ICRF3 the APLO model (Petrov and Boy 2004) was used for both atmospheric corrections). The displacement of the reference point in the VLBI antennas due to changing temperature and thus, thermal expansion, was considered (Nothnagel 2009). Temperature and pressure values were taken from GPT2 (Lagler et al. 2013).

The estimated tropospheric zenith delays were based on the VMF1 mapping function (Boehm et al. 2006), and the total gradients were taken from the APG model (Böhm et al. 2013). The ionospheric contribution was removed using the dual S/X frequency data. Furthermore, instrumental calibrations, such as cable delays and clock parameters were corrected.

The estimates were parameterized as follows:

- The zenith wet delays were set up as piece-wise linear functions with 30 minutes intervals and relative constraints of 1.5 cm between the offsets.
- The gradients (east-west and north-south) were estimated every 6 hours with relative constraints of 0.05 cm and absolute constraints of 5 cm between the offsets.
- Instrumental calibrations, such as cable delays and clock parameters, were considered jointly by a 60 min piece-wise linear function, with an offset, a rate and a quadratic term per clock and relative constraints between the offsets of 1.3 cm.
- The EOP parameters were set up every 48 hours (session-wise) with loose absolute

constraints of 10 mas and additional tight relative constraints of 0.1 µas for the nutation components.

- The antenna coordinates were set up as one offset per session.
- The source coordinates were set up as one offset per session. Sources with three or less observations were constrained to their a priori values using a loose value of 1 000 mas.

The first three items describe nuisance parameters, which are not of interest to the present analysis, but cannot be modeled precisely enough to dispense with them.

The resulting normal equations for each session were then stacked for the global solutions described in the following subsections. The first four items were reduced (not solved) in the global solutions. The antenna coordinates were parameterized as one position and one linear velocity per antenna except for the known discontinuities due to, e.g. earthquakes. The source coordinates were parameterized as one position for each source. A total of 56 sources were excluded in the single-session analysis, such as sources with large structure, lensed objects, or stars.

4.1.2 CRF 1979-2018 (CRF7918)

The global solution was derived from single-session data spanning over the same time interval as those used for ICRF3 S/X (03 August 1979 - 27 March 2018). The aim was to obtain a CRF similar to ICRF3 S/X, which can then be compared with a CRF covering only the Gaia observation period (Sect. 4.1.3), using the same analysis software, models and parameterisations.

Combining the data of 6 204 sessions, 122 antennas and 4 537 sources are included in the global solution labelled CRF7918 (ICRF3 S/X has 6 206 sessions, 159 antennas, and 4 536 sources). The number of observations is 16 795 147 (13 190 274 for ICRF3 S/X) and the number of estimates is 3 150 447 In contrast to ICRF3, some antennas were parameterized as session-wise positions, as they were observed too few times for a reliable position and linear velocity estimate. Velocity ties were applied for some antenna pairs, and for antennas with a limited observation time span, the velocities were fixed. Furthermore, no elevation cutoff was applied, whereas it is 5° for ICRF3 S/X.

NNT and NNR constraints were applied for the positions and velocities of a set of 40 datum stations which do not show any discontinuities in ITRF2014 (for ICRF3 S/X 38 datum stations were used). Furthermore, NNR constraints were applied for the positions of the 303 ICRF3 S/X defining sources. The global solution therefore mitigates the lack of defining sources in the sessions before 1990, where sessions with less than three ICRF3 defining sources appear regularly as can be seen in Fig. 4.1.

For ICRF3 S/X, a scaling factor of 1.5 and a noise floor of 30 µas was applied to inflate the formal errors of both coordinate directions (Charlot et al. 2020). The source position uncertainties for CRF7918 were not inflated. A small comparison of the differences in the error budget when inflating or not inflating the error budget is provided in Table 4.1 for the counterparts between CRF7918 and ICRF3 S/X. If the position uncertainties were inflated in CRF7918, the median of the semi-major axis of the formal error ellipse, $\sigma_{\mathrm{pos,max}}$, would be 60 % larger than the one of ICRF3 S/X, whereas it is 6 % smaller without inflation. This has to be considered when evaluating CRF7918 in the following.

4.1.3 CRF Gaia DR2 time (CRFGT)

Another VLBI global solution was determined, in which the observation time interval was restricted to the time interval of Gaia DR2. The research question was whether this would reduce the positional differences between VLBI and Gaia DR2 or whether the VLBI global solution would deteriorate to a large extent. This global solution is labelled CRFGT.

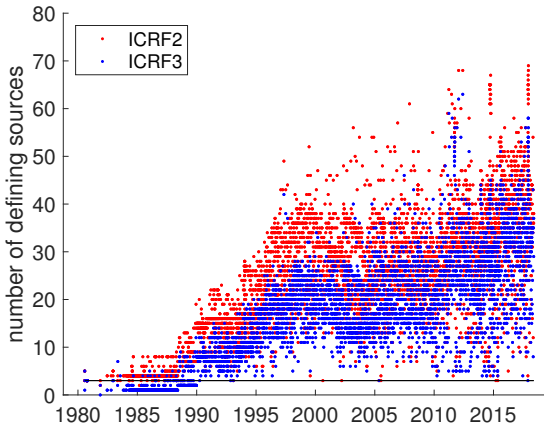

Figure 4.1 Number of defining sources for ICRF2 or ICRF3 in the sessions used in the analysis in Sect. 4.1.1. Sessions with antenna networks spanning a volume less than 10^{18} km^3 and sessions with less than four antennas are excluded from the plot.

Only the 406 sessions observed in the same time period as Gaia DR2 were selected for this global solution (7 % of CRF7918). The number of observations reduced to 1 960 665 (12 % of CRF7918) and the number of estimates to 273 666 (9 % of CRF7918). The number of participating antennas is 49 (40 % of CRF7918) and the number of observed sources is 2 359 (52 % of CRF7918). Similar to CRF7918, some antennas were parameterized as session-wise positions, as they were observed too few times for a reliable position and linear velocity estimate. Velocity ties were applied for some antenna pairs, and for antennas with a limited observation time span, the velocities were fixed.

NNT and NNR constraints were applied for the positions and velocities of a set of 28 datum stations which do not show any discontinuities in ITRF2014. Surely, in future work, the station positions and velocities could be fixed to those of CRF7918. Furthermore, NNR constraints were applied for the positions of 259 of the the 303 ICRF3 S/X defining sources. Four of the 303 defining sources were not observed often enough during the Gaia

DR2 observation time interval, while the other 40 were not observed at all.

Compared to ICRF3, the uncertainties of the source positions were not inflated because there is less risk that they are unrealistically small due to the smaller number of observations because of the shorter observation time. This has to be considered when evaluating CRFGT in the following. Similar to CRF1879, the error budget when inflating or not inflating the error budget similar to ICRF3 S/X was compared in Table 4.1 for the counterparts between CRFGT and ICRF3 S/X. If the position uncertainties were inflated in CRFGT, the median of the semi-major axis of the formal error ellipse, $\sigma_{\mathrm{pos,max}}$, would be 150 % larger than the one of ICRF3 S/X, whereas it is 70 % larger without inflation.

4.2 Counterparts

For VLBI, the crossmatch between the various CRFs is straightforward. Every AGN has a dedicated source name that is used by the VLBI community across all frequencies. The basic comparison in terms of common counterparts and position uncertainties is given for ICRF3 in Sect. 2.2.4. In Table 4.1, ICRF3 S/X, CRF7918, and CRFGT are compared. The ICRF3 S/X and CRF7918 are very similar in terms of number of sources. One source is in ICRF3 S/X but not in CRF7918 (0704+819 with 135 observations), and two sources are in CRF7918 but not in ICRF3 S/X (1030-590 and 2235-556 with three observations, respectively). The sources were observed in two sessions only. Thus, the impact on the following analysis is considered negligible. One source has different names in the two catalogs (0548+37A or 0548+377) and was thus not identified as a counterpart here.

Table 4.1 Counterparts between own CRFs and ICRF3 S/X.

	CRF7918	CRF7918 (>70 obs)	CRF7918 inflated	CRFGT	CRFGT (>70 obs)	CRFGT inflated	CRFGT inflated (>70 obs)
Number of counterparts	4534	4132	4534	2359	1567	2359	1567
Mean ρ	0.48	0.15	0.48	1.20	0.31	1.20	0.31
Median ρ	0.10	0.09	0.10	0.31	0.22	0.31	0.22
Maximum ρ	526.08	22.97	526.08	268.60	22.88	268.60	22.88
Median $\sigma_{\mathrm{pos,max}}$, ICRF3 S/X	0.22	0.20	0.22	0.18	0.15	0.18	0.15
Median $\sigma_{\mathrm{pos,max}}$, own CRF	0.16	0.15	0.25	0.30	0.24	0.45	0.36
Median $\sigma_{\alpha*}$, own CRF	0.11	0.10	0.17	0.20	0.16	0.31	0.24
Median σ_{δ}, own CRF	0.16	0.15	0.24	0.29	0.22	0.43	0.33

Notes. The arc lengths ρ, the semi-major axis of the formal error ellipse $\sigma_{\mathrm{pos,max}}$, and the uncertainties in both coordinate directions $\sigma_{\alpha*}$, σ_{δ} of the counterparts are investigated. The source with the maximum ρ was only observed in one session with six observations. For an explanation of "CRF7918 inflated" (and "CRFGT inflated" as it was derived with the same formulas) see the description of Fig. 4.2. The units are in milliarcseconds.

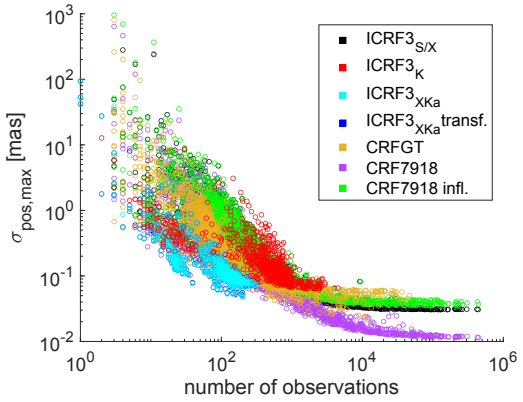

Figure 4.2 Relationship between the semi-major axis of the formal error ellipse, $\sigma_{\mathrm{pos,max}}$, and the number of observations for the sources in each of the CRFs. For comparison, the values for CRF7918 are shown as well (magenta dots). It is clearly visible that its position uncertainties have not been inflated, whereas it was done for ICRF3 (Sect. 2.2.4). Inflating the position uncertainties similar to how it was done for ICRF3 S/X, results in similar scatter as ICRF3 S/X (green dots).

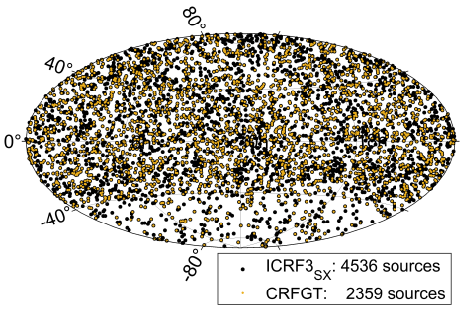

Figure 4.3 Sky distribution of the counterparts between ICRF3 S/X and CRFGT.

The large maximum arc lengths ρ between the ICRF3 S/X positions and the CRF7918 positions for the source observed in only one session, combined with the small mean position difference for all sources, suggests that the number of sessions and observations affects the position difference. Also the uncertainty of this position difference is affected by the number of observations, as shown in Fig. 4.2 for the discussed VLBI-based CRFs. This effect is, of course, due to the least squares method (the square root of the number of observations scales inversely with the formal errors) and with few observations, the estimates are more vulnerable to outliers. When restricting the number of observations to a minimum of 70 for the solution "CRF7918 (>70 obs)", the mean and maximum ρ are considerably smaller, and also the other median quantities are slightly smaller. The CRF7918 with inflated uncertainties, which were determined like those of the ICRF3 S/X, has a slightly larger median $\sigma_{\mathrm{pos,max}}$ than ICRF3 S/X. The median $\sigma_{\mathrm{pos,max}}$ increased by 60 % compared to the CRF7918 without inflated errors.

The CRFGT includes only 52 % of the sources in CRF7918. The sky distribution of the radio sources in ICRF3 S/X and CRFGT is shown in Fig. 4.3. Similar to ICRF3 S/X, CRFGT lacks radio sources in the southern hemisphere, but otherwise the distribution is more or less even. The impact of the reduced observation time span is also present in the source position uncertainties, which are larger by a factor of two in both $\alpha*$ and δ compared to CRF7918 as derived from the median uncertainties in Table 4.1. They

also have a larger scatter when compared to the number of observations as presented in Fig. 4.2. The CRFGT with inflated uncertainties, which were determined like those of the ICRF3 S/X, has a 60 % larger median $\sigma_{\mathrm{pos,max}}$, similar to CRF7918. The median $\sigma_{\mathrm{pos,max}}$ values for the inflated and not inflated versions of CRFGT including only sources with more than 70 observations drop by 20 %.

There are 477 counterparts between ICRF3, CRF7918, and CRFGT.

The crossmatch between VLBI-based CRFs and the Gaia-CRFs is not as straightforward as in the VLBI-only case due to different naming conventions. Therefore, other methods must be used to identify counterparts between VLBI and Gaia with sufficient accuracy considering larger differences in the observation setup and the catalog size. The crossmatching strategy of the Gaia DPAC (Lindegren et al. 2018) was introduced in Sect. 2.3.2. Table 4.2 lists the counterparts for the various VLBI-based CRFs and Gaia DR2 according to this strategy. Because ICRF3 S/X and CRF7918 are almost identical in terms of common sources, only ICRF3 S/X was used for this comparison. The number of counterparts determined for ICRF3 S/X is the same as determined by Charlot et al. (2020). Petrov et al. (2018) introduced another method which is based on the PFA. The PFA is higher in crowded areas in the sky. The counterparts for the various VLBI-based CRFs and Gaia DR2 according to this strategy are listed in Table 4.3.

Both selection strategies provide similar results, and only few sources are in the selection of Lindegren et al. (2018) and not in the selection of Petrov et al. (2018). In fact, the crossmatch with 0.1 as radius is almost identical with the crossmatch with 5 as or 3 as radius and the application of the PFA. For ICRF3 S/X, the difference in the median semi-major axis of the formal error ellipse $\sigma_{\mathrm{pos,max}}$ is the largest between the two selections,

Table 4.2 Counterparts between various CRFs and Gaia DR2 based on the strategy of Lindegren et al. (2018).

	ICRF3 S/X	ICRF3 K	ICRF3 X/Ka	CRFGT
Crossmatch 0.1 as radius	3373	701	604	1781
astrometric_params_solved $\neq 31$	363	46	38	163
astrometric_matched_observations ≤ 8	90	9	7	46
$\lvert(\varpi + 0.029\mathrm{mas})/\sigma_{\varpi}\rvert > 5$	1+363	0+46	0+38	1+163
$(\mu_{\alpha*}/\sigma_{\mu_{\alpha*}})^2 + (\mu_{\delta}/\sigma_{\mu_{\delta}})^2 > 25$	21+363	7+46	6+38	13+163
Number of counterparts	2983	647	558	1602
Median ρ [mas]	0.58	0.45	0.52	0.66
Maximum ρ [mas]	87.39	33.15	13.76	86.76
Median $\sigma_{\mathrm{pos,max}}$, VLBI [mas]	0.19	0.14	0.11	0.28
Median $\sigma_{\mathrm{pos,max}}$, Gaia [mas]	0.29	0.23	0.23	0.26

Notes. The arc lengths ρ and the semi-major axis of the formal error ellipse $\sigma_{\mathrm{pos,max}}$ of the counterparts are investigated.
Note. According to Lunz et al. (2019a).

Table 4.3 Counterparts between various CRFs and Gaia DR2 based on the strategy of Petrov et al. (2018).

	ICRF3 S/X	ICRF3 K	ICRF3 X/Ka	CRFGT
Crossmatch 5 as / 3 as radius	4325	915	762	1942
PFA $> 2 \cdot 10^{-4}$	952	215	158	160
Bad sources[1]	19	4	0	9
Number of counterparts	3354	696	604	1773
Median ρ [mas]	0.66	0.48	0.55	0.73
Maximum ρ [mas]	288.04	43.03	42.08	310.58
Median $\sigma_{\mathrm{pos,max}}$, VLBI [mas]	0.20	0.14	0.11	0.28
Median $\sigma_{\mathrm{pos,max}}$, Gaia [mas]	0.29	0.24	0.24	0.28

Notes. The arc lengths ρ and the semi-major axis of the formal error ellipse $\sigma_{\mathrm{pos,max}}$ o of the counterparts are investigated. [(1)] Radio stars, supernova (remnants) and double or multiple galaxies as found in OCARS catalog (Malkin 2018, catalog version 27-NOV-2018) and other meta data. The up to now newest version of the OCARS catalog (30 July 2022) lists most of these sources as quasars, BL Lac type, galaxies, etc. but not as stellar objects anymore.
Note. According to Lunz et al. (2019a).

Table 4.4 Counterparts between various CRFs and Gaia DR2 based on the combination of the strategies from Petrov et al. (2018) and Lindegren et al. (2018).

	ICRF3 S/X	ICRF3 K	ICRF3 X/Ka	CRFGT
In A but not in B	384	53	46	176
In B but not in A	13	4	0	5
A and B combined	2970	643	558	1596
Median ρ [mas]	0.58	0.45	0.52	0.66
Maximum ρ [mas]	87.39	33.15	13.76	86.76
Median $\sigma_{\mathrm{pos,max}}$, VLBI [mas]	0.19	0.14	0.11	0.28
Median $\sigma_{\mathrm{pos,max}}$, Gaia [mas]	0.26	0.23	0.23	0.26

Notes. The arc lengths ρ and the semi-major axis of the formal error ellipse $\sigma_{\mathrm{pos,max}}$ o of the counterparts are investigated. A is the solution in Table 4.3 and B is the solution in Table 4.2.
Note. According to Lunz et al. (2019a).

Table 4.5 Counterparts between various CRFs and Gaia DR2 based on the combination of the strategies from Petrov et al. (2018) and Lindegren et al. (2018) for the 406 common sources between the catalogs.

	ICRF3 S/X	ICRF3 K	ICRF3 X/Ka	CRFGT
Median ρ [mas]	0.41	0.43	0.51	0.47
Maximum ρ [mas]	9.68	9.67	9.39	80.20
Median $\sigma_{\mathrm{pos,max}}$, VLBI [mas]	0.04	0.12	0.10	0.11
Median $\sigma_{\mathrm{pos,max}}$, Gaia [mas]	0.22	0.22	0.22	0.22

Notes. The arc lengths ρ and the semi-major axis of the formal error ellipse $\sigma_{\mathrm{pos,max}}$ of the counterparts are investigated.

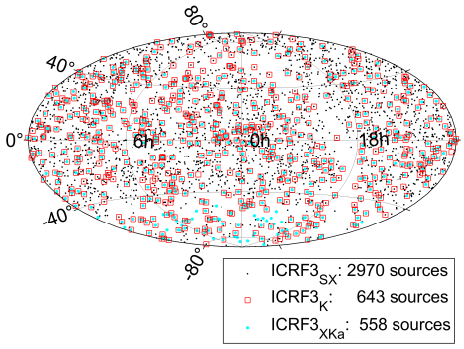

Figure 4.4 Sky distribution of the counterparts between various VLBI-based CRFs and Gaia DR2.

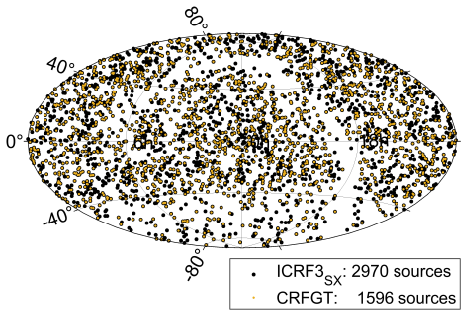

Figure 4.5 Sky distribution of the counterparts between ICRF3 S/X or CRFGT and Gaia DR2.

Table 4.6 Counterparts between various CRFs and Gaia EDR3 based on the filtered selection in Gaia Collaboration et al. (2022).

	ICRF3 S/X	ICRF3 K	ICRF3 X/Ka	CRFGT
Number of counterparts	3142	660	576	1669
Median ρ	0.51	0.37	0.38	0.60
Maximum ρ	87.23	32.94	13.51	149.72
Median $\sigma_{\mathrm{pos,max}}$, VLBI	0.22	0.16	0.12	0.30
Median $\sigma_{\mathrm{pos,max}}$, Gaia	0.24	0.20	0.19	0.23

Notes. The arc lengths ρ and the semi-major axis of the formal error ellipse $\sigma_{\mathrm{pos,max}}$ of the counterparts are investigated. The 1669 counterparts for CRFGT were retrieved simply by cross-matching with the 3142 counterparts of the crossmatch of ICRF3 S/X and Gaia EDR3. Units are in milliarcseconds.

where the selection of Lindegren et al. (2018) has smaller values. The respective results of combining the two selection strategies, which is presumably more rigorous than using just one of them, are given in Table 4.4 and are based on Lunz et al. (2019a). Only 65 % of the radio sources in ICRF3 S/X were found in Gaia DR2, and 68 % of CRFGT. The ratio is 78 % for ICRF3 K and 82 % for ICRF3 X/Ka. Only 54% of the ICRF3 S/X radio sources which have counterparts in Gaia DR2 were observed during Gaia DR2 time interval. For the ICRF3 catalogs, the median $\sigma_{\mathrm{pos,max}}$ is only about 50 % to 70 % from the value of Gaia DR2. For CRFGT these values are about the same. The median arc lengths ρ between the radio and optical position is about 0.5 mas for all catalogs, where the order is CRFGT, ICRF3 S/X, ICRF3 X/Ka, and ICRF3 K, when going from large to small values. The maximum ρ are similar for the S/X catalogs (about 85 mas) and they are 33 mas for ICRF3 K, and 14 mas for ICRF3 X/Ka. Table 4.5 provides quantities for only the 406 common sources between all the discussed catalogs. With this selection,

the sources in ICRF3 S/X have by far the smallest median of the semi-major error axis $\sigma_{\mathrm{pos,max}}$, and CRFGT has similar $\sigma_{\mathrm{pos,max}}$ to ICRF3 K and ICRF3 X/Ka. Furthermore, the median ρ are 0.4 mas to 0.5 mas for all the CRFs.

The crossmatch results from Table 4.4 were used in the following. The heterogeneous distribution of the crossmatches across the sky is shown in Figs. 4.4 and 4.5. Due to Galactic extinction and the PFA function applied, there are fewer counterparts along the Galactic plane. Moreover, due to the sparse VLBI network geometry and therefore fewer observations of southern sources, there are fewer counterparts in the south. Especially for ICRF3 S/X and CRFGT, the heterogeneity is prominent.

For Gaia EDR3, the crossmatch provided in the Gaia archive was taken (Table 4.6). It is the filtered selection from Gaia Collaboration et al. (2022) and is similar to what would be obtained using a strategy similar to Table 4.4. The number of crossmatches increased by 172 sources for ICRF3 S/X, by 17 for ICRF3 K, by 18 for ICRF3 X/Ka, and by 73 for CRFGT. The median ρ decreased more for ICRF3 K and ICRF3 X/Ka than for ICRF3 S/X or CRFGT. The median value of $\sigma_{\mathrm{pos,max}}$ worsened slightly for the VLBI counterparts, as expected since the sample contains more weaker sources compared to the crossmatch with Gaia DR2.

There are 406 common counterparts between all discussed VLBI-based CRFs and Gaia DR2, 410 common counterparts between all discussed VLBI-based CRFs and Gaia EDR3, and 512 common counterparts between ICRF3 and Gaia EDR3.

4.3 Comparison of radio positions

To assess the significance of the differences between the radio positions and the optical positions, the radio positions themselves are briefly compared first.

4.3.1 Differences of counterparts

The radio CRFs are aligned to ICRF3 S/X in terms of NNR using a set of defining sources, as explained above. Thus, the position differences of the counterparts can be directly compared.

The normalized coordinate differences $\mathrm{X}_{\alpha*}$ and X_{δ} for the various VLBI-based CRFs versus ICRF3 S/X are shown in Figs. 4.6 and 4.7 using the equations introduced in Sect. 3.2 for the 477 sources common to these catalogs. The respective arc lengths ρ and normalized arc lengths X_ρ for these data are shown in Figs. 4.8 and 4.9. The X_ρ follow the expected Rayleigh distribution and the $\mathrm{X}_{\alpha*}$ and X_{δ} follow the expected normal distribution for CRFGT. The distributions for CRF7918 are too optimistic, even when inflating the position

uncertainties similar to those of ICRF3 S/X. The data is highly correlated with ICRF3 S/X due to the almost identical database, which can be an explanation. For ICRF3 K, the X_ρ and the $X_{\alpha*}$ also follow the expected distribution, however the X_δ are slightly off. This deviation and also the larger deviation for ICRF3 X/Ka for these quantities can be explained when looking at the VSH parameters in the following section. The ICRF3 X/Ka frequencies shows large systematics of more than 200 µas compared to ICRF3 S/X, which are above the uncertainty of the alignment of the ICRF3 catalogs. After transformation of ICRF3 X/Ka to ICRF3 S/X the X_ρ follow the Rayleigh distribution better, as shown in the figures (labelled 'ICRF3 X/Ka transf.'). Similar exercises can be performed for the ICRF3 K.

Figure 4.10 shows the dependence of the semi-major axis of the formal error ellipse $\sigma_{\mathrm{pos,max}}$ on the number of observations for the 477 counterparts. Clearly, the radio sources have most observations in ICRF3 S/X. A cutoff to exclude high $\sigma_{\mathrm{pos,max}}$ for ICRF3 S/X is about 70 observations per source, although this is a somewhat arbitrarily chosen value. In the following, the subset with at least 70 observations is investigated to learn whether the number of VLBI observations has an impact on the results.

A total of 333 radio sources have more than 70 observations in ICRF3 S/X, ICRF3 K, ICRF3 X/Ka, CRF7918, and CRFGT. The arc lengths ρ compared to the normalized arc lengths X_ρ towards ICRF3 S/X for these radio sources are shown in Fig. 4.12. While the arc lengths ρ slightly depend on the number of observations (Fig. 4.11) and their uncertainties $\sigma_{\mathrm{pos,max}}$ clearly depend on the number of observations (Fig. 4.10), the histograms of normalized arc lengths X_ρ do not change much for this selection compared to the histograms based on all 477 sources, as expected. However, the selection process results in ρ being smaller than 10 mas for all sources in the sample, whereas there are some sources with ρ being larger this threshold when investigating the full sample in each of the CRFs (Fig. 4.13).

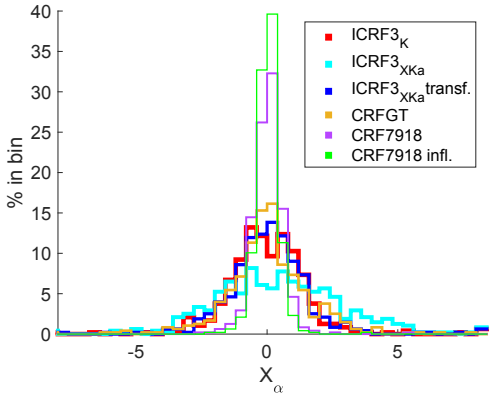

Figure 4.6 Normalized coordinate differences $X_{\alpha*}$ for the 477 sources common to the various VLBI-based CRFs versus ICRF3 S/X.

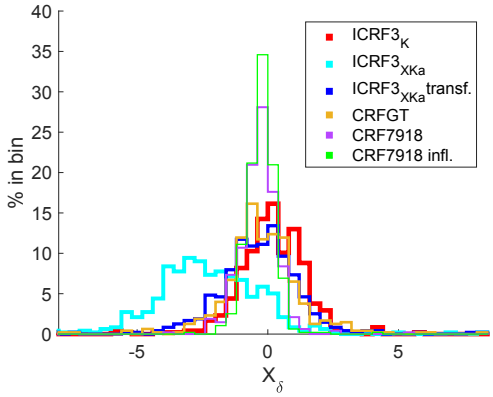

Figure 4.7 Normalized coordinate differences X_δ for the 477 sources common to the various VLBI-based CRFs versus ICRF3 S/X.

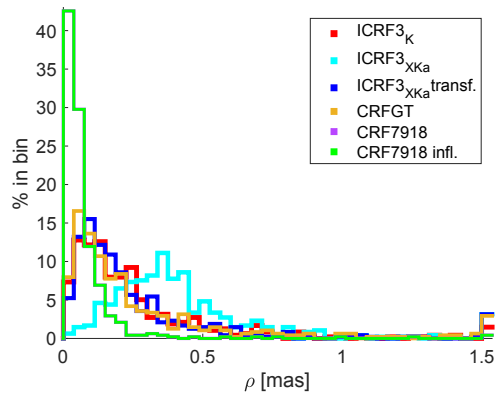

Figure 4.8 Arc lengths ρ for the 477 sources common to the various VLBI-based CRFs versus ICRF3 S/X.

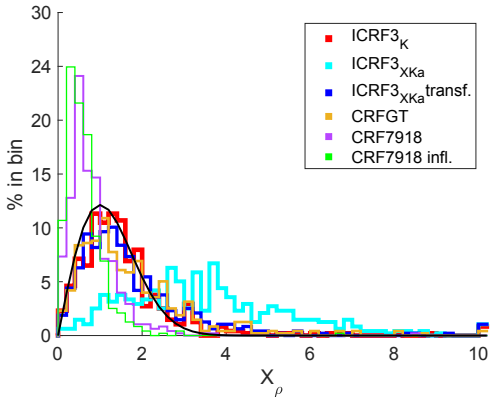

Figure 4.9 Normalized arc lengths X_ρ for the 477 sources common to the various VLBI-based CRFs versus ICRF3 S/X.

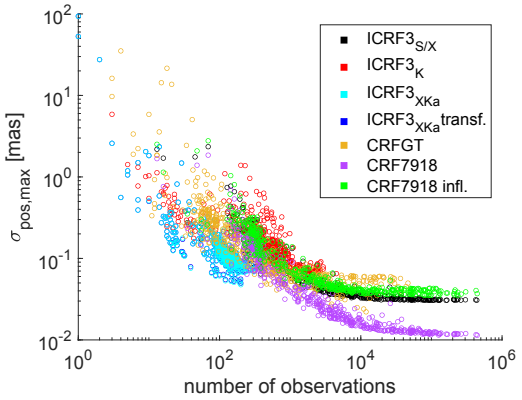

Figure 4.10 Dependence of the semi-major axis of the formal error ellipse $\sigma_{\mathrm{pos,max}}$ on the number of observations for the 477 counterparts to all CRFs shown. This is a selection of Fig. 4.2.

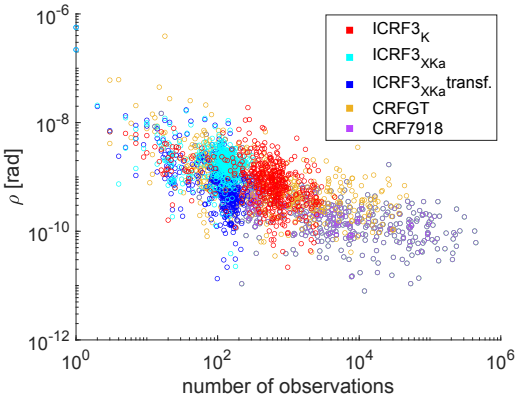

Figure 4.11 Dependence of the arc lengths ρ between the various VLBI-based CRFs and ICRF3 S/X on the number of observations for the 477 counterparts to all CRFs shown. The CRF7918 and the inflated CRF7918 result in the same dots in this graph, thus, only one of them is shown.

Sources with $X_\rho > 3.7$ are outliers according to the Rayleigh distribution for 333 sources. There are 17 sources above the threshold for ICRF3 K, 169 for ICRF3 X/Ka, 26 for ICRF3 X/Ka which was transformed to ICRF3 S/X, and 29 for CRFGT. There are seven sources which pass the threshold for all of these CRFs. They are 0229+131, 0430+052, 0723-008, 2128-123, 2134+004, 2234+282, and 2251+158. Their CARMS values based on basic noise weighting are 0.61, 1.11, 0.90, 0.50, 1.03, 0.54, and 0.54 as determined in Xu et al. (2019a). Any values larger 0.4 indicate very extended source structure. The CARMS values were determined from about the same data as ICRF3 S/X. They show the minimum effect of source structure on the VLBI observables. This finding indicates source structure being the dominant cause for the significant position offsets between the CRF positions discussed.

Thus, in Fig. 4.14 the normalized arc lengths X_ρ are compared to the CARMS values for these 333 radio sources. A clear correlation between the two quantities is visible. The majority of the sources with significant $X_\rho > 3.7$ have CARMS values larger 0.4, which indicate very extended source structure. The significant position offsets between the positions of the various CRFs under discussion appear to be caused by source structure. However, only the minority of sources with CARMS > 0.4 also have $X_\rho > 3.7$, meaning that most sources with significant structure do not show significant position offsets between the positions of the various CRFs under discussion. From Fig. 4.14 histograms such as in Fig. 4.15 can be obtained, which strengthen the finding of larger X_ρ being related to larger CARMS values.

Figure 4.16 shows that the direction angles ψ between the arc from the ICRF3 S/X position in direction of the positive declination axis and from the ICRF3 S/X position to the position in the respective CRF are not evenly distributed. The ψ favor a certain direction due to remaining global systematics between the CRFs. The transformation of the ICRF3 X/Ka to ICRF3 S/X helped reducing the peak around 180°. This finding is similar to the results in Lambert et al. (2021), who tested the ψ for ICRF3. Selecting the same subset of sources as Lambert et al. (2021), the same results for the original ICRF3 were obtained in this work. The ψ do not show such systematic for sources with $X_\rho > 3.7$ except for the original ICRF3 X/Ka (Fig. 4.17). This indicates that the systematic position offsets for all CRFs except ICRF3 X/Ka are very small compared to the position offsets of the individual sources.

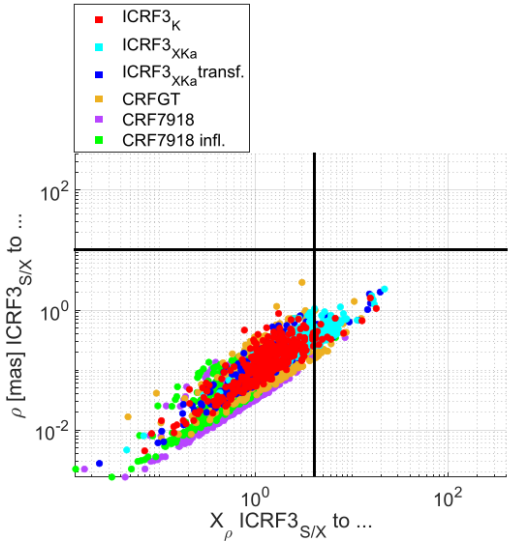

Figure 4.12 Normalized arc lengths X_ρ versus the arc lengths ρ for the 333 sources common to the various VLBI-based CRFs versus ICRF3 S/X with more than 70 observations. The horizontal line is located at $\rho = 10$ mas and the vertical line at $X_\rho = 3.7$.

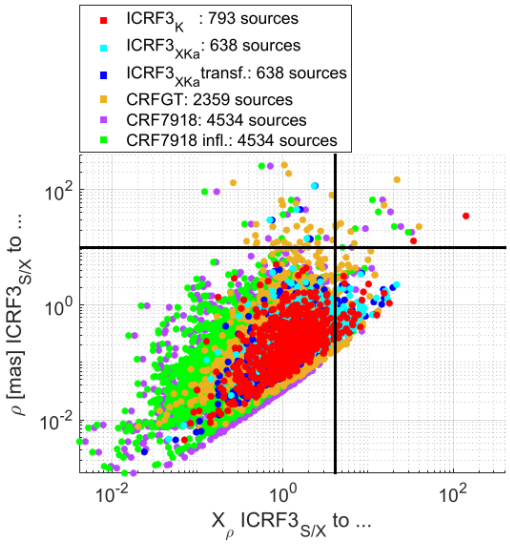

Figure 4.13 Normalized arc lengths X_ρ versus the arc lengths ρ for all sources of the respective VLBI-based CRF versus ICRF3 S/X. The horizontal line is located at $\rho = 10$ mas and the vertical line at $X_\rho = 4.1$.

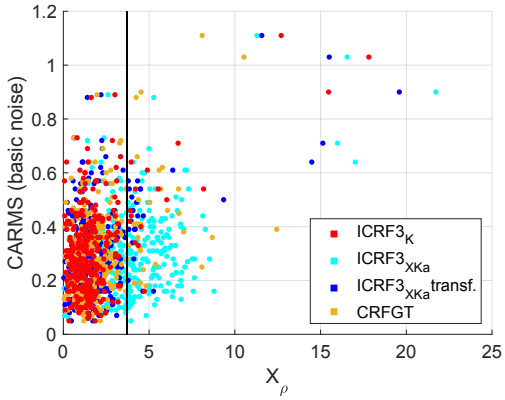

Figure 4.14 Normalized arc lengths X_ρ versus the CARMS values based on basic noise for the 332 of the 333 sources common to the various VLBI-based CRFs versus ICRF3 S/X with more than 70 observations that have CARMS values. The vertical line is located at $X_\rho = 3.7$, which is the threshold for outliers according to the Rayleigh distribution of the sample size. To make the values of the more important CRFs for this work more visible, CRF7918 is not shown.

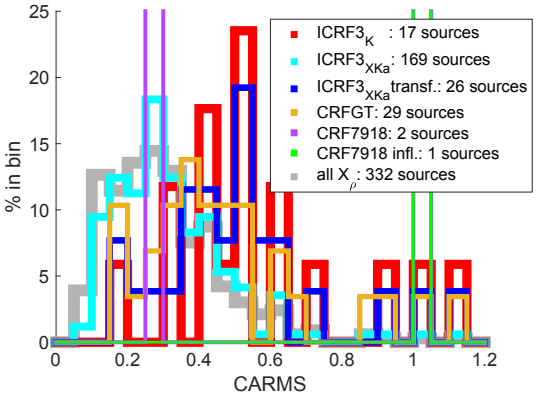

Figure 4.15 Histogram of CARMS values based on basic noise weighting for radio sources with at least 70 observations in each of the VLBI-based CRFs. The grey line depicts the histogram for all 332 counterparts (332 out of the 333 counterparts have CARMS values), while colored histograms depict the sources of the various CRFs with $X_\rho > 3.7$. 22 % of the 333 sources have CARMS > 0.4, while sources with $X_\rho > 3.7$ the share is between 24 % and 100 %.

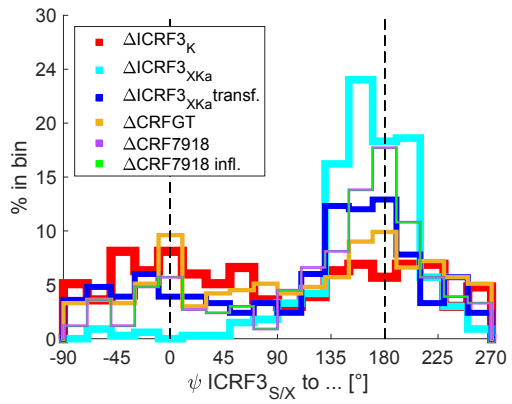

Figure 4.16 Histogram of the direction angles ψ for the 333 sources common to the various VLBI-based CRFs and with more than 70 observations in each of the CRFs.

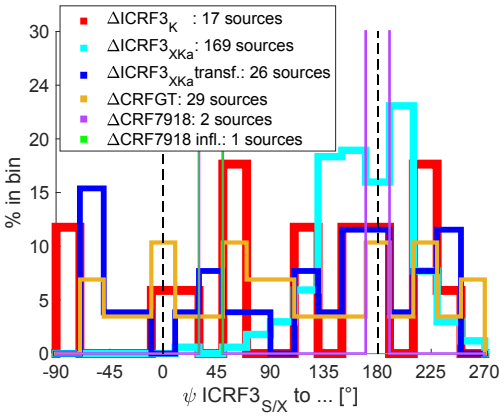

Figure 4.17 Histogram of the direction angles ψ for the sources common to the various VLBI-based CRFs and with more than 70 observations in each of the CRFs and X_ρ towards ICRF3 S/X larger 3.7.

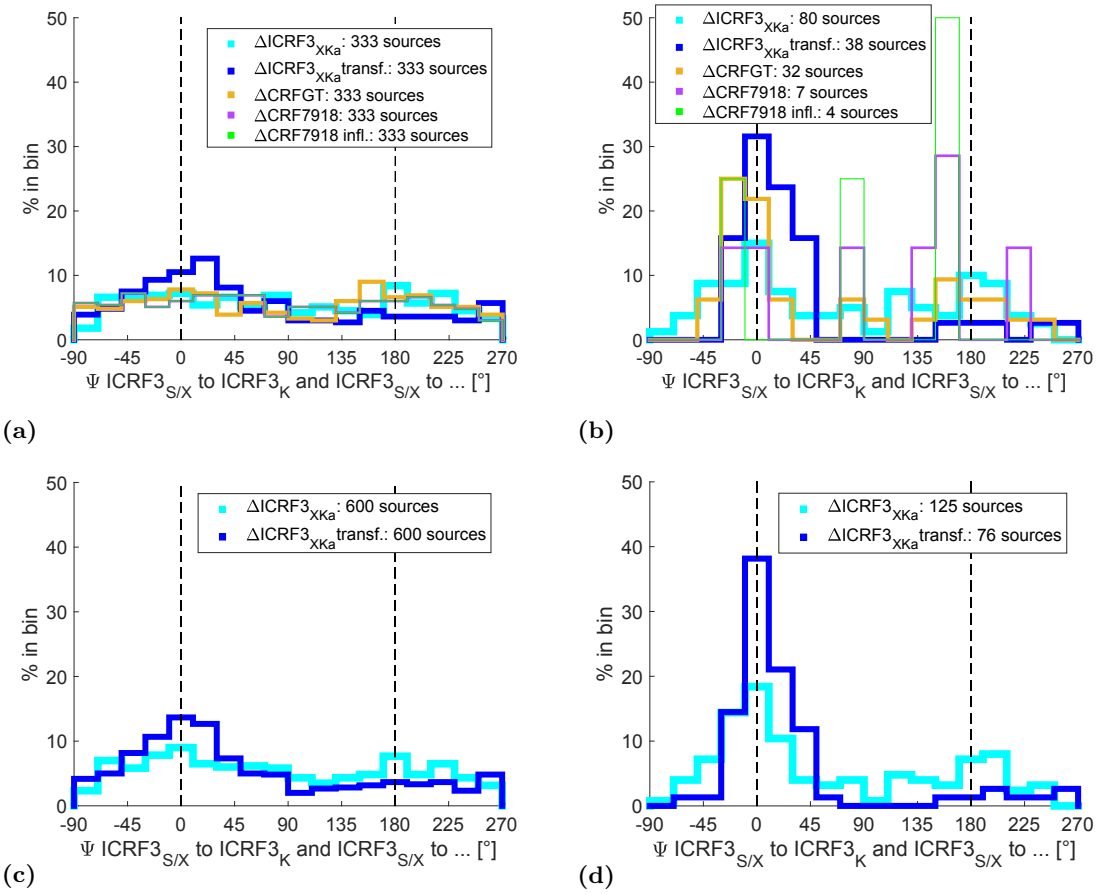

Figure 4.18 Position angle differences Ψ between the arc from the ICRF3 S/X position to the ICRF3 K position versus the other CRFs, as listed in the legend, (a) for radio sources with at least 70 observations in each of the CRFs (333 counterparts), (b) same as (a) but with an uncertainty of Ψ smaller than 30°, (c) for radio sources common to all ICRF3 catalogs (600 counterparts), (d) same as (c) but with an uncertainty of Ψ smaller than 30°.

Looking at the position angle differences Ψ between the arc from the ICRF3 S/X position to the ICRF3 K position versus the arc from the ICRF3 S/X position to the other CRFs in Fig. 4.18a following Eq. 3.9, it can be assumed that the position differences of the other CRFs with respect to the ICRF3 S/X position are mainly in one direction. This assumption is supported by selecting only Ψ with an uncertainty smaller than 30° (Fig. 4.18b), and further by investigating the same quantities for the 600 sources common to only the ICRF3 at different frequencies (Figs. 4.18c and 4.18d). The peak in Ψ for ICRF3 X/Ka is at 0°, indicating a frequency-dependence of the position in the same direction, presumably the jet direction. Only few sources show a frequency-dependence of the position in the opposite direction, as indicated by the small peak at 180°. For CRF7918, the sample size with σ_Ψ <30° is very small, so no clear conclusion can be drawn. For the sample of 333 radio sources, there is no evidence of a preferred direction. This is expected as this CRF was determined from the same set of sessions and frequency as ICRF3 S/X. For CRFGT, also based on S/X frequencies, but with limited time range, a peak in Ψ is visible at both 0° and 180° for the full sample and the sample with σ_Ψ <30°. This finding could indicate that there is a time-dependent position shift along the same or opposite direction as the frequency dependent position offset.

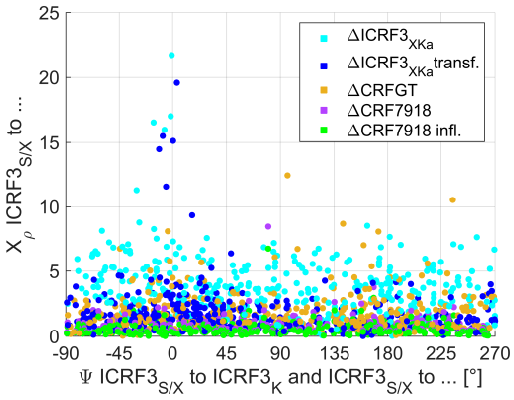

Figure 4.19 Angle differences Ψ as in Fig. 4.18a versus the normalized arc lengths X_ρ between the ICRF3 S/X and respective CRF positions for the 333 radio sources with more than 70 observations in each of the CRFs.

The position angle differences Ψ from the arc between the ICRF3 S/X and ICRF3 K position versus the normalized arc lengths X_ρ between ICRF3 S/X and the respective CRFs (Fig. 4.19) show that the sources with larger X_ρ have Ψ of close to 0° for the ICRF3 X/Ka which was transformed to ICRF3 S/X, whereas those for the original ICRF3 X/Ka only show the clear direction for some outliers with $X_\rho > 10$. Also for CRFGT an increase in X_ρ for the Ψ close to 0° and 180° is visible. For CRF7918 no preference for higher offsets is visible, which is also confirmed by determining histograms of the distribution filtered by bins of X_ρ.

Incorporating the CARMS information from Fig. 4.14 indicates that sources with larger CARMS values have larger X_ρ and Ψ close to zero. Figure 4.20 shows for ICRF3 X/Ka that the subgroup with very large structure (CARMS > 0.6), but also the subgroup with very small structure (CARMS < 0.1) contain noticeably more sources with small Ψ between the ICRF3 S/X to ICRF3 X/Ka arc and the ICRF3 S/X to ICRF3 K arc.

Since CRF7918 is very close to ICRF3 S/X, as determined from the various compar-

ing figures, the differences between CRFGT towards ICRF3 S/X can be assumed to be indications for real differences in source position.

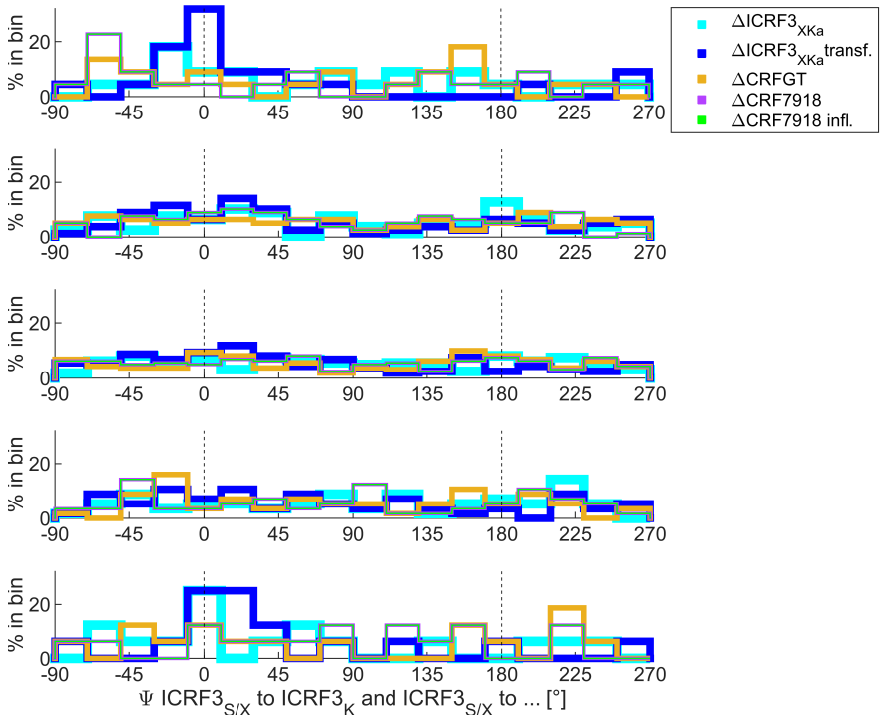

Figure 4.20 Histogram of the number of sources binned by the position angle differences Ψ between the arc from the ICRF3 S/X position to the ICRF3 K position versus the other CRFs, as listed in the legend. The five plots show the results for different subgroups of the 332 out of the 333 radio sources with more than 70 observations in each of the CRFs that have CARMS values. From top to bottom, the selections are: Sources with CARMS ≤ 0.1 (22 sources), $0.1 <$ CARMS ≤ 0.2 (78 sources), $0.2 <$ CARMS ≤ 0.4 (160 sources), $0.4 <$ CARMS ≤ 0.6 (56 sources), CARMS > 0.6 (16 sources).

4.3.2 Systematic global differences

For the determination of the global systematics between the CRFs, outliers with too large normalized arc lengths X_ρ than expected from the Rayleigh distribution of the respective subset were excluded. This results in deformation parameters compared to ICRF3 S/X as presented in Fig. 4.21. Clearly, ICRF3 X/Ka has large-scale deformations in D_3 and $\mathrm{a}^{\mathrm{M}}_{2,0}$ (see Figs. 3.3a and 3.3c for the pattern of their global effect). Combining the individual parameters, the combined position offset in right ascension and declination ranges from 22 µas to 333 µas for the sources used to calculate the transformation parameters. The values are depending on the location on the sky, as shown in Fig. 4.22. ICRF3 K has small deformation in $\mathrm{a}^{\mathrm{E,Im}}_{2,1}$ (see Fig. 3.3d) larger 2σ. The combined position offset ranges from 3 µas to 150 µas for the sources used to calculate the transformation parameters (Fig. 4.23a). The deformations of CRF7918 and CRFGT are not significant at the 2σ-level compared to the noise level of ICRF3 S/X. The minimum and maximum combined position offset is 0.2 µas and 64 µas for CRF7918 and ICRF S/X for the sources used to calculate the transformation parameters (Fig. 4.23b), and 0.4 µas and 93 µas for CRFGT and ICRF3 S/X (Fig. 4.23c), respectively.

The transformation parameters A_1, A_2, D_1, D_2, D_3, $\mathrm{a}^{\mathrm{E}}_{2,0}$, $\mathrm{a}^{\mathrm{E,Im}}_{2,1}$, $\mathrm{a}^{\mathrm{E,Re}}_{2,1}$, and $\mathrm{a}^{\mathrm{M,Im}}_{2,1}$ are correlated to at least one other transformation parameter, as shown in Fig. 4.24. They are most prominent for ICRF3 K ($\leq |0.7|$). The correlation coefficients for the other CRFs follow a weaker but similar pattern ($\leq |0.45|$).

To determine whether a different selection of radio source counterparts would result in a significantly different alignment of the frame, and to determine the accuracy of the alignment, the parameter fitting was iteratively repeated using the equations in Sect. 3.3.4. The resulting transformation parameters towards ICRF3 S/X are shown in Fig. 4.25 for ICRF3 K, in Fig. 4.26 for ICRF3 X/Ka, in Fig. 4.27 for CRF7918, and in Fig. 4.28 for CRFGT for the respective subset of sources which are not outliers in terms of X_ρ. From these, the WM, WRMS, ME, and MS quantities were derived (Fig. 4.29). The transformation parameters of the first solution in Fig. 4.21 are validated to be a good representation of the iterative results, as the WM quantities are almost identical to them. The WRMS scatter of the iterative results is below 15 µas for all parameters and all CRFs. The MS of the various CRFs are below 6 µas, respectively. The MS of CRF7918 and CRFGT are considerably smaller than the MS of the other CRFs because unlike for the other CRFs, the position uncertainties were not inflated for CRF7918 and CRFGT.

Picking ICRF3 K as an example, the impact of choosing different subsets of the full sample of counterparts is shown in Fig. 4.30. The WM values differ by about 6 µas to 35 µas for each parameter, respectively. The scenarios for subsets with CARMS < 0.4 and for subsets with more than 70 observations in ICRF3 K have a small WRMS value

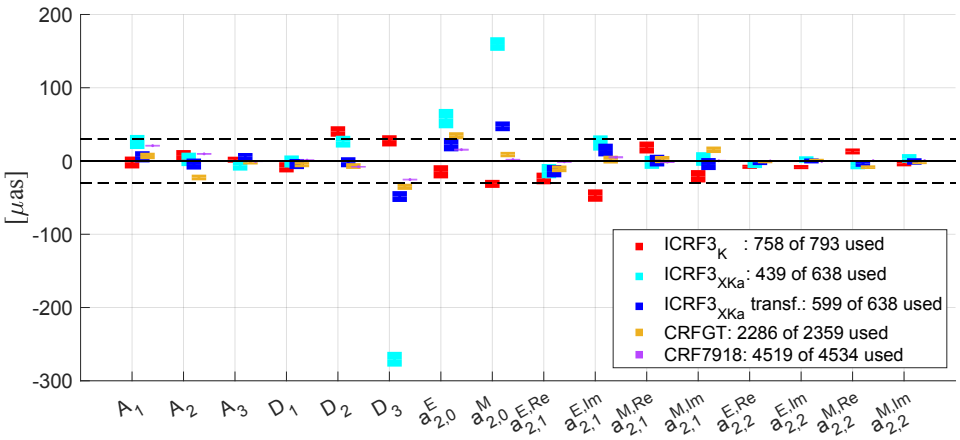

Figure 4.21 Three rotation parameters, three glide parameters, and higher order VSH terms between ICRF3 S/X and various other radio CRFs using all available counterparts except the outliers as determined applying the respective Rayleigh distribution on the arc lengths of the set of counterparts. In the legend, the first number denotes all available counterparts, while the second number represents the sample of counterparts used. The error bars have the size of 1σ. The horizontal dashed line depicts the noise level of ICRF3 S/X.

for most parameters. In general, the WRMS values differ by about 3 µas to 10 µas for each parameter, respectively. The ME values mainly depend on the number of counterparts, as expected. Comparing the ME values for the subgroup with 193 defining sources with those of the other scenarios, they are systematically worse. However, the MS values for the subgroup with 193 defining sources are enhanced considering that they are at the same level as the solution with the 225 ICRF3 defining sources. If only the three rotation parameters were parameterized in the adjustment, the WM values differ by about 15 µas and the WRMS values by about 4 µas to 7 µas.

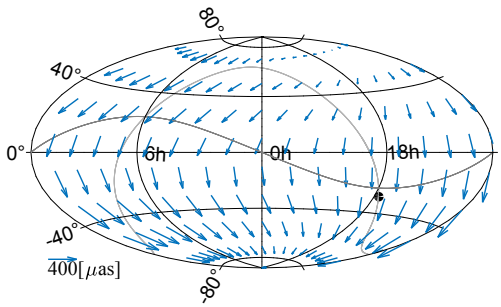

(a)

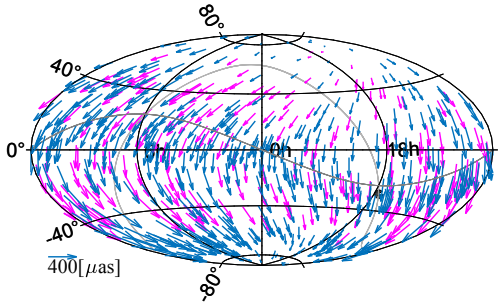

(b)

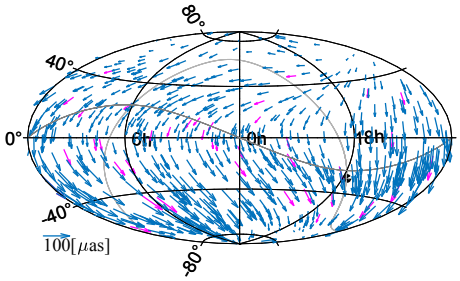

(c)

Figure 4.22 Sky plot of the combined global systematic differences in terms of VSH between ICRF3 X/Ka and ICRF3 S/X for (a) a set of evenly distributed source positions (to better visualize the pattern) and (b) the actual sources used to determine the VSH terms (blue) and the initially removed outliers with respect to their normalized arc length X_ρ (magenta). (c) gives a similar plot to (b), except that the differences are shown for ICRF3 X/Ka already transformed to ICRF3 S/X (labelled "ICRF3 X/Ka transf." in this work). Thus, it is a new iteration of the transformation to ICRF3 S/X with a new set of outlier sources. Note the difference in scale compared to (a) and (b).

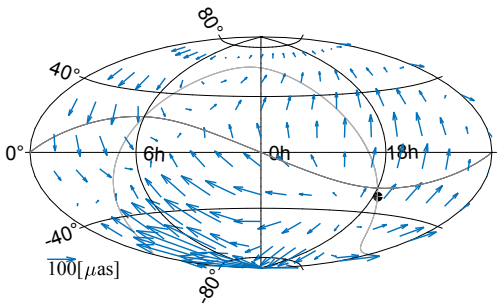

(a)

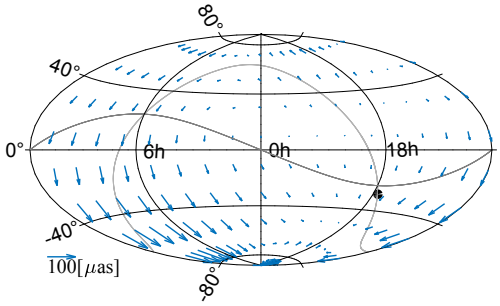

(b)

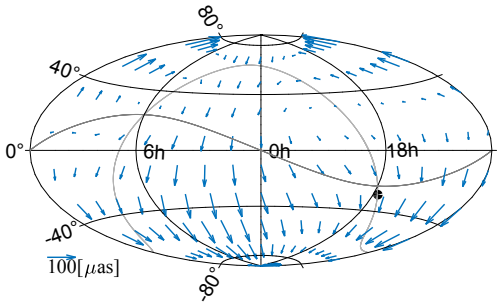

(c)

Figure 4.23 Sky plot of the combined global systematic differences in terms of VSH for a set of evenly distributed source positions (to better visualize the pattern) between (a) ICRF3 K and ICRF3 S/X, (b) CRF7918 and ICRF3 S/X, and (c) CRFGT and ICRF3 S/X.

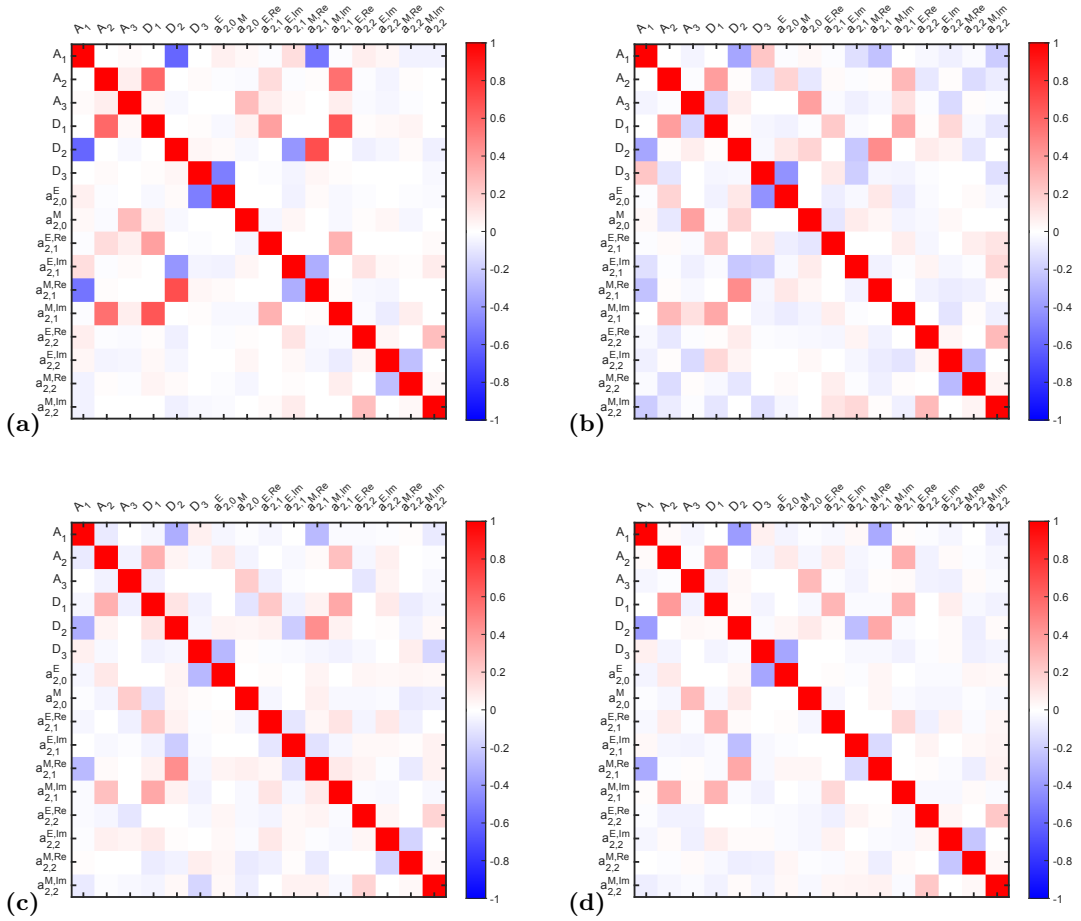

Figure 4.24 Correlation coefficients of the transformation parameters between the various CRFs and ICRF3 S/X. (a) ICRF3 K, (b) ICRF3 X/Ka, (c) CRFGT, and (d) CRF7918.

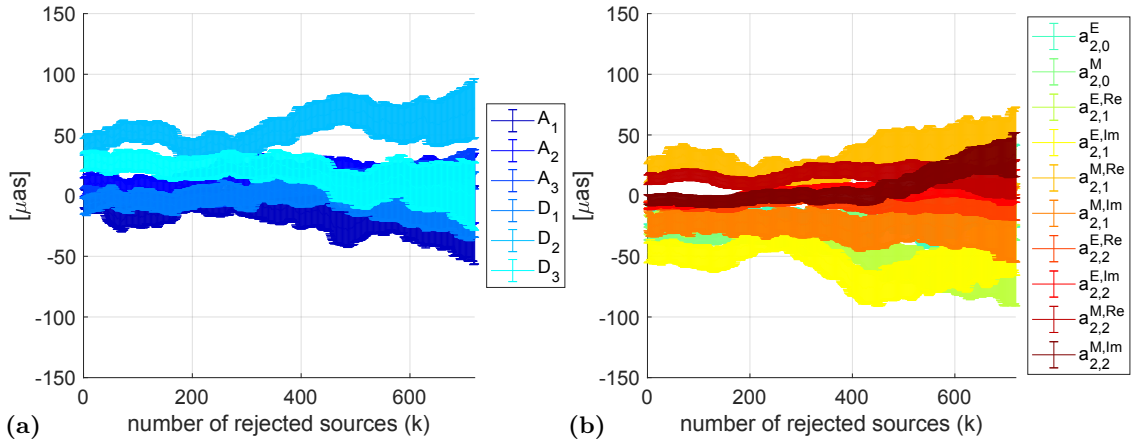

Figure 4.25 Iterative solutions aligning ICRF3 K to ICRF3 S/X by a combined fit of (a) three rotation parameters, three glide parameters, and (b) higher order VSH terms.

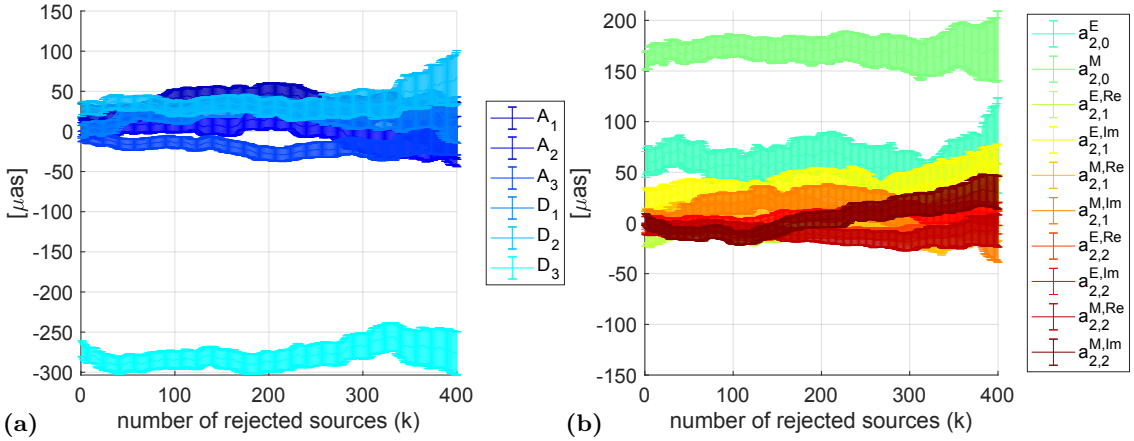

Figure 4.26 Iterative solutions aligning ICRF3 X/Ka to ICRF3 S/X by a combined fit of (a) three rotation parameters, three glide parameters, and (b) higher order VSH terms. Please note the different vertical scale compared to the other figures.

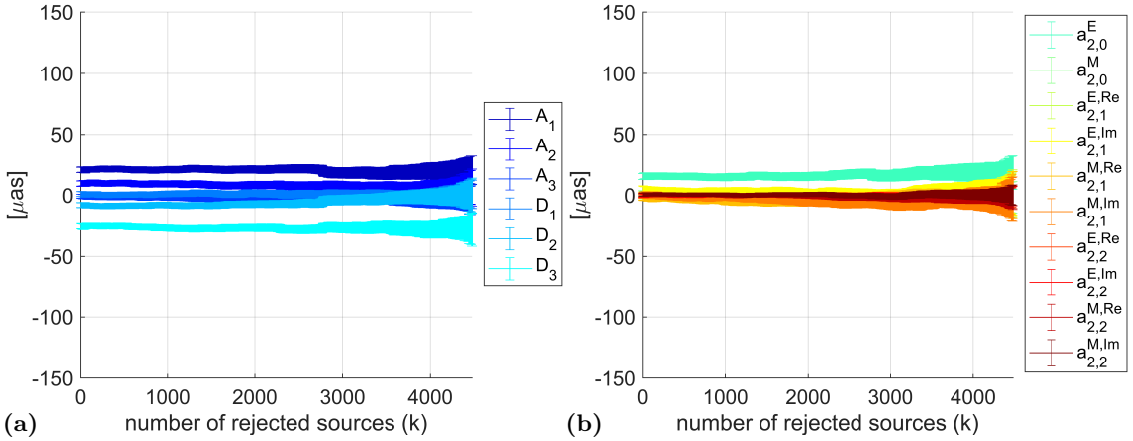

Figure 4.27 Iterative solutions aligning CRF7918 to ICRF3 S/X by a combined fit of (a) three rotation parameters, three glide parameters, and (b) higher order VSH terms.

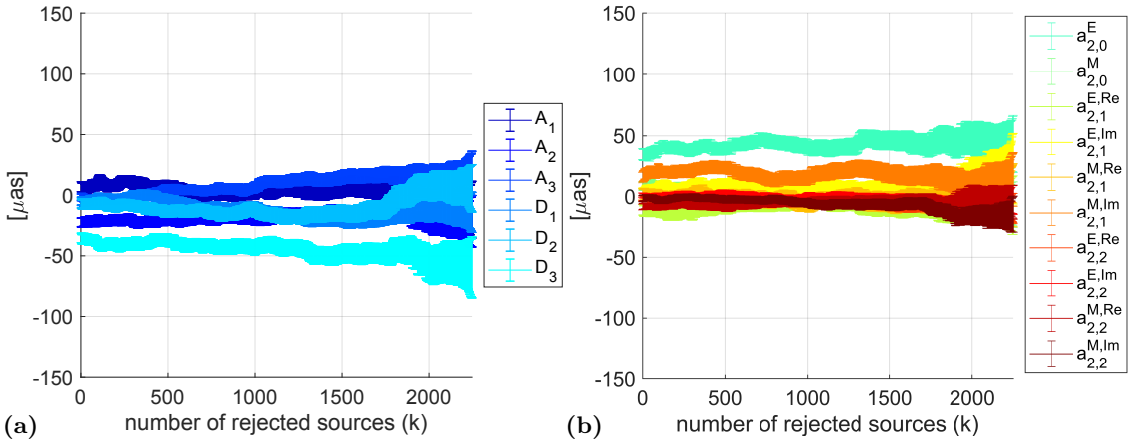

Figure 4.28 Iterative solutions aligning CRFGT to ICRF3 S/X by a combined fit of (a) three rotation parameters, three glide parameters, and (b) higher order VSH terms.

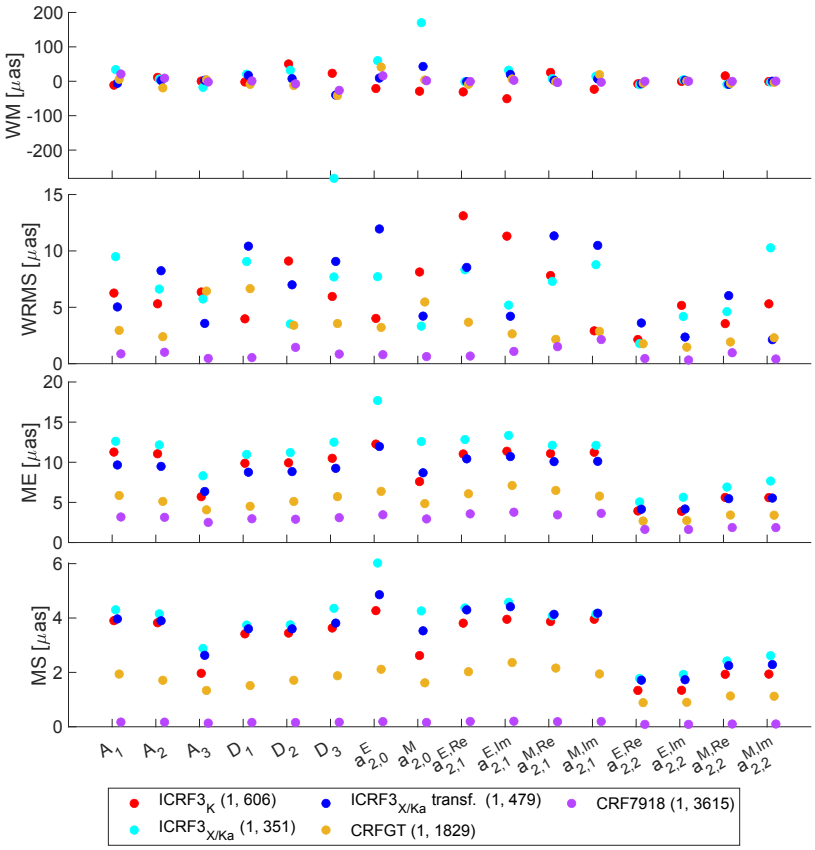

Figure 4.29 WM, WRMS, ME, and MS quantities for the iterative results for the 16 VSH parameters between various VLBI-based CRFs and ICRF3 S/X. All available counterparts for which the normalized arc lengths are not outliers were used. In the legend, the first numbers indicate the number of all available counterparts. The numbers in parentheses indicate the start and end of the iterations used to derive the quantities. Typically, this is the first iteration and the number of suitable counterparts minus the last 20 % of the iterations (to mitigate any effects due to low number of counterparts in those iterations).

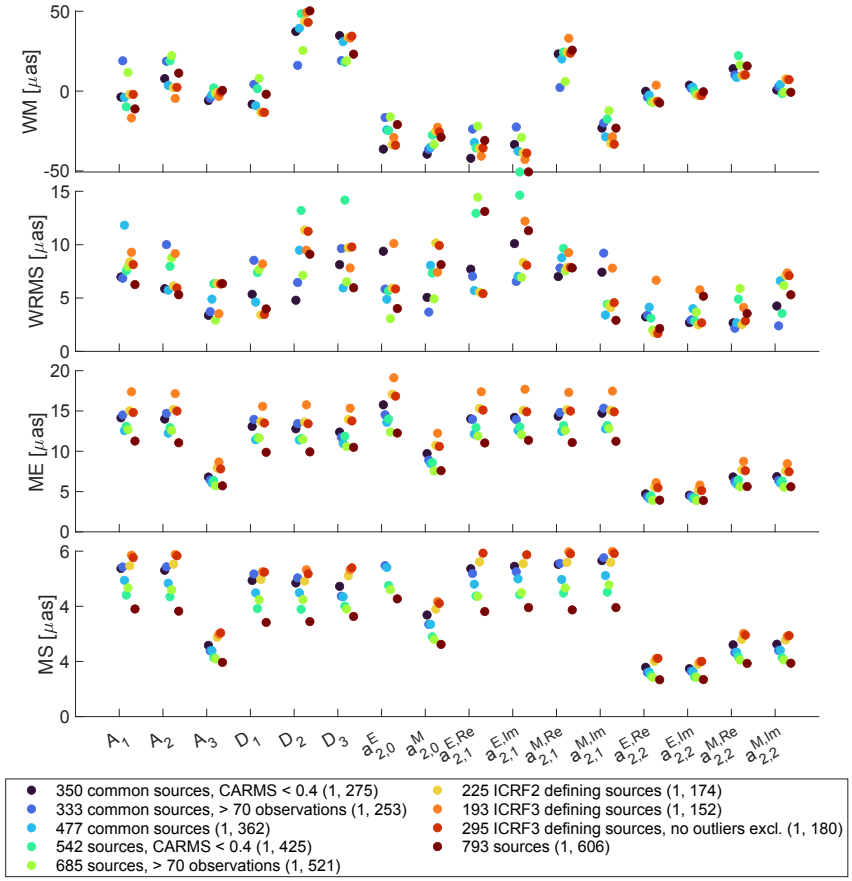

Figure 4.30 WM, WRMS, ME, and MS quantities for the iterative results for the 16 VSH parameters between ICRF3 K and ICRF3 S/X for various subsets of counterparts. All available counterparts in each subset for which the normalized arc lengths are not outliers were used (except for the subset which is labelled differently). In the legend, the first numbers indicate the counterparts in each subset. The numbers in parentheses indicate the start and end of the iterations used to derive the quantities. Typically, this is the first iteration and the number of suitable counterparts minus the last 20 % of the iterations (to mitigate any effects due to low number of counterparts in those iterations).

4.4 Comparison of radio and optical positions

This section examines the radio-optical position offsets of individual sources as well as large scale systematic global deformations. The positions at optical frequencies are dominated by Gaia DR2, while Gaia EDR3 was also tested for comparison. For the positions at radio frequencies, the ICRF3 and the CRFGT are employed.

4.4.1 Differences of counterparts

As explained above, the ICRF3 X/Ka has significant large scale systematic deformations compared to ICRF3 S/X. Thus, the transformed ICRF3 X/Ka towards ICRF S/X is used for the comparison to Gaia DR2 as well. The half-year epoch difference between Gaia DR2 and the VLBI-based CRFs due to Galactocentric acceleration was not corrected because it is negligible compared to the internal systematics of Gaia DR2. For testing the alignment between Gaia EDR3 and ICRF3, the ICRF3 positions were propagated to epoch 2016.0. With this approach, only the galactic aberration in ICRF3, which does not have an uncertainty estimate, needs to be accounted. If the Gaia EDR3 positions had been propagated instead, the individual proper motions including error propagation would have had to be used. Since CRFGT was developed specifically for the Gaia DR2 time interval, it is not included in the discussion for Gaia EDR3.

The normalized coordinate differences $X_{\alpha*}$ and X_δ for the various VLBI-based CRFs versus Gaia DR2 are shown in Figs. 4.31 and 4.32 using the equations introduced in Sect. 3.2 for the 406 sources common to these catalogs. The respective arc lengths ρ and normalized arc lengths X_ρ for these data are shown in Figs. 4.33 and 4.34. The $X_{\alpha*}$ and X_δ follow the expected normal distribution for all CRFs. Similar to the comparison with respect to

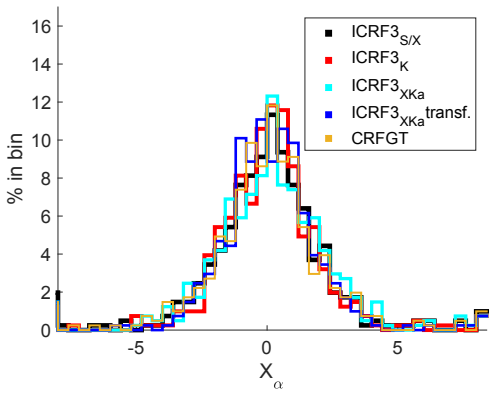

Figure 4.31 Normalized coordinate differences $X_{\alpha*}$ for the 406 sources common to the various VLBI-based CRFs versus GaiaDR2.

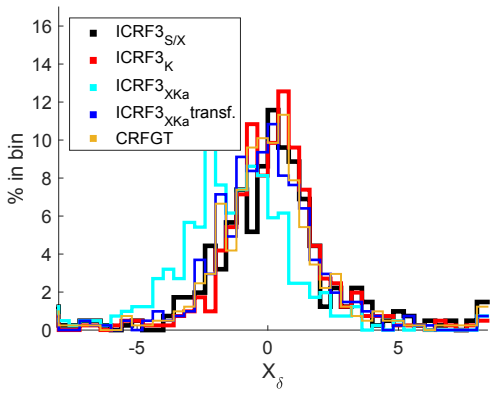

Figure 4.32 Normalized coordinate differences X_δ for the 406 sources common to the various VLBI-based CRFs versus Gaia DR2.

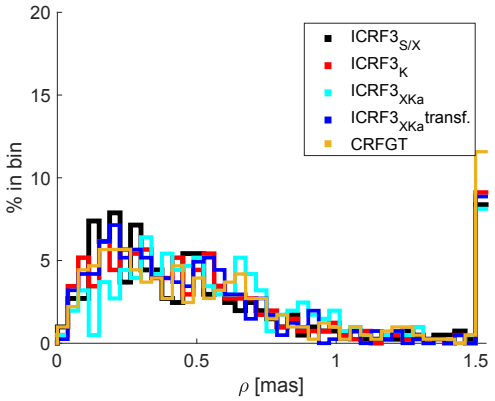

Figure 4.33 Arc lengths ρ for the 406 sources common to the various VLBI-based CRFs versus Gaia DR2.

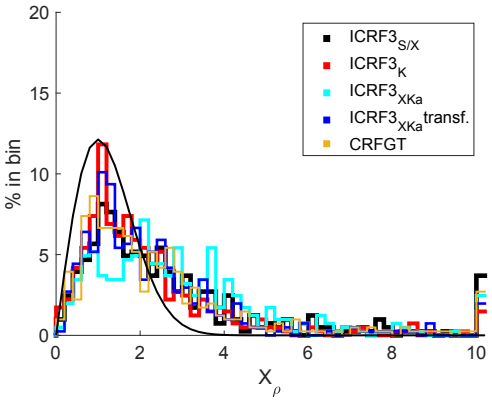

Figure 4.34 Normalized arc lengths X_ρ for the 406 sources common to the various VLBI-based CRFs versus Gaia DR2.

ICRF3 S/X in Sect. 4.3.1, the ICRF3 X/Ka which was transformed to ICRF3 S/X follows the respective distributions better than the original ICRF3 X/Ka. In contrast to the X_ρ of all examined CRFs towards ICRF3 S/X, there is a larger deviation from the expected Rayleigh distribution for the X_ρ of all examined CRFs towards Gaia DR2. This larger deviation is also resulting in more outliers of X_ρ. Apparently, the position uncertainties of the respective CRFs are too optimistic.

As for the comparison of the various VLBI-based CRFs to ICRF3 S/X, the number of observations has no large impact on these quantities. This can be seen from comparing the arc lengths ρ versus the normalized arc lengths X_ρ towards Gaia DR2 for the 289 radio sources with more than 70 observations in all the VLBI-based CRFs in Fig. 4.35 to the previous figures based on all 406 common sources. The histograms of normalized arc lengths X_ρ do not change much for this selection compared to the histograms based on all 406 common sources. Sources with $X_\rho > 3.6$ are outliers according to the Rayleigh distribution for 289 sources. There are 62 sources above the threshold for ICRF3 S/X, 41 for ICRF3 K, 94 for ICRF3 X/Ka, 36 for ICRF3 X/Ka which was transformed to ICRF3 S/X, and 53 for CRFGT. There are 21 sources which pass the threshold for all of these CRFs. They are 0007+106, 0111+021, 0119+115, 0309+411, 0749+540, 1055+018,1143-332, 1514+004, 1652+398, 1730-130, 1803+784, 1800+440, 1921-293, 2106-413, 2126-158, 2131-021, 2150+173, 2223-052, 2254+074, 2344+092, and 0213-026. None of them is in the respective list for the comparison to ICRF3 S/X in Sect. 4.3.1. Only seven out of the 21 sources have CARMS values based on basic noise weighting larger 0.4. As the CARMS values show the minimum effect of source structure on the VLBI observables, this finding indicates radio source structure is not the dominant cause for the significant position offsets between the radio and optical positions discussed. However, in Fig. 4.36 the normalized arc lengths X_ρ are compared to the CARMS values for these 289 radio sources.

A clear correlation between the two quantities is visible as most sources with CARMS $<$ 0.2 do not have a significant $X_\rho > 3.6$. Nevertheless, similar to the radio-only evaluation in Sect. 4.3.1, only the minority of sources with CARMS > 0.4 also have $X_\rho > 3.6$, meaning that most sources with significant radio structure do not show significant position offsets between the positions of the various CRFs and Gaia DR2. All sources but 1803+784 have low declinations, and most of them are located very close to the equator. VLBI could either have systematic errors leading to problems in determining the source positions at low declinations. Or due to, for example, the antenna network configuration, the sources have very poor uv-coverage, and the existing source structure in declination direction is not sampled and therefore not included in the CARMS values of these sources. Source 1803+784 has extended jets in the direction of right ascension (Britzen et al. 2005).

The distribution of the normalized arc lengths X_ρ changes when considering only sources with CARMS values smaller 0.1 (Fig. 4.40, as can be expected from Fig. 4.36). The distribution is more aligned to the expected Rayleigh distribution. In contrast, the selection with CARMS > 0.4 worsened the shape of the distribution. Although the sample size for ICRF3 K and ICRF3 X/Ka is limited, the difference in the distributions of X_ρ is obvious for all CRFs. Using only the ICRF3 defining sources also improved the shape of the distribution, whereas if only more than 70 observations in each VLBI-based CRF were considered, the distribution of the X_ρ does not change compared to using all sources. This finding shows that the radio source structure has an impact on the X_ρ and that for the Gaia to ICRF3 alignment sources with smaller radio source structure could be beneficial. The selection of ICRF3 defining sources results in a more beneficial distribution of X_ρ because the ICRF3 working group intentionally selected radio sources with low radio source structure such that only about one fifth of the defining sources is subject to source structure (Charlot et al. 2020). The number of observations does not appear to have much effect on the distribution at the scale tested.

The same evaluation for Gaia EDR3 instead of Gaia DR2 results in similar conclusions (Figs. 4.37 and 4.38).

Figure 4.41a shows the position angle difference Ψ between the arcs from the Gaia DR2 position to the ICRF3 S/X position and from the Gaia DR2 position to the respective other CRF. The clustering of Ψ around zero for all CRFs shows that the position deviations of VLBI and Gaia prefer the same direction. When only sources with an uncertainty of Ψ smaller than 30° are selected, this signal is even more pronounced. In the opposite direction (by 180 deg) of the arc between the Gaia DR2 and ICRF3 S/X positions, there is no signal for any of the CRFs. The histograms using the 289 sources with more than 70 observations in each VLBI CRF or using all 406 common sources do not diverge much. In the first selection, the signal is even slightly clearer than in the second. For example, in Fig. 4.41b there are 65 % of the sources with Ψ of about zero for CRFGT in the first

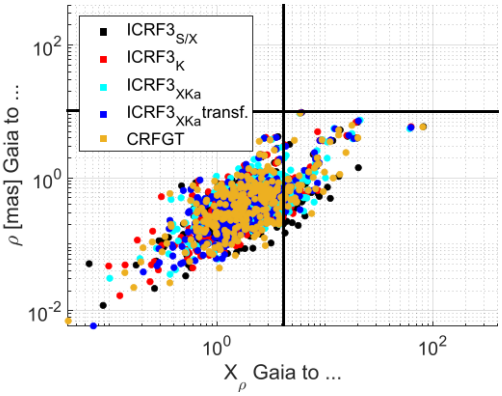

Figure 4.35 Normalized arc lengths X_ρ versus the arc lengths ρ for the 289 sources common to the various VLBI-based CRFs versus Gaia DR2 with more than 70 observations in each of the VLBI-based CRFs. The horizontal line is located at $\rho = 10$ mas and the vertical line at $X_\rho = 3.6$.

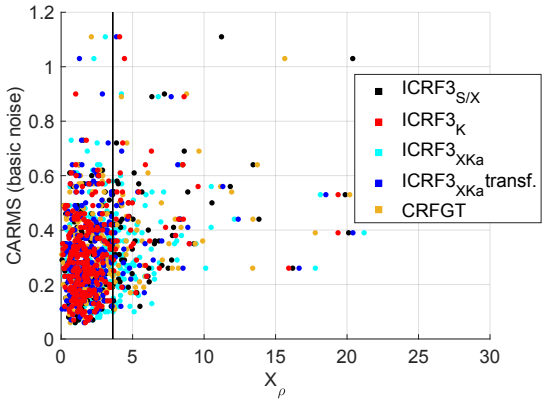

Figure 4.36 Normalized arc lengths X_ρ versus the CARMS values based on basic noise for the 288 of the 289 sources common to the various VLBI-based CRFs versus Gaia DR2 with more than 70 observations in each of the VLBI-based CRFs that have CARMS values. The vertical line is located at $X_\rho = 3.6$, the threshold for outliers according to the Rayleigh distribution of the sample size. One source with $X_\rho > 60$ and CARMS = 0.36 is outside the plot range.

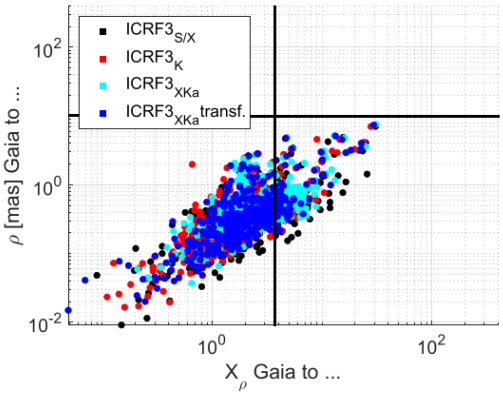

Figure 4.37 Normalized arc lengths X_ρ versus the arc lengths ρ for the 392 sources common to the various VLBI-based CRFs versus Gaia EDR3 with more than 70 observations in each of the VLBI-based CRFs. The horizontal line is located at $\rho = 10$ mas and the vertical line at $X_\rho = 3.7$.

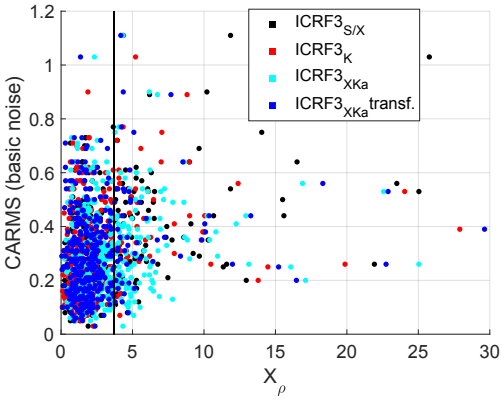

Figure 4.38 Normalized arc lengths X_ρ versus the CARMS values based on basic noise for the 389 of the 392 sources common to the various VLBI-based CRFs versus Gaia EDR3 with more than 70 observations in each of the VLBI-based CRFs that have CARMS values. The vertical line is located at $X_\rho = 3.7$, the threshold for outliers according to the Rayleigh distribution of the sample size.

selection with 289 sources, while in the second selection it would be 60 %.

Figures 4.42 and 4.43 proof that the direction angles ψ between the arc from the Gaia DR2 position in direction of the positive declination axis and from the Gaia DR2 position to the position in the respective CRF are evenly distributed from 0° to 360°, except for the original ICRF3 X/Ka. The ICRF3 X/Ka which was transformed to ICRF3 S/X shows no divergence from the other CRFs under investigation. The angle differences Ψ nevertheless favor the same values for the transformed and original ICRF3 X/Ka, only that for the transformed ICRF3 X/Ka the signal is more pronounced. This supports that the previous investigation is not biased by any global systematic differences of the CRFs towards Gaia DR2 or between the VLBI-based CRFs themselves.

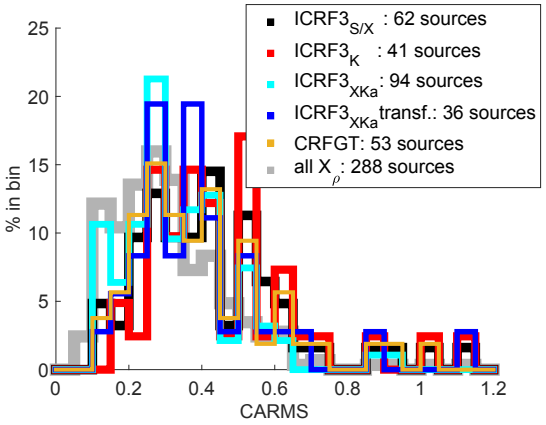

Figure 4.39 Histogram of CARMS values based on basic-noise weighting for radio sources with at least 70 observations in each of the VLBI-based CRFs. The grey line depicts the histogram for all 288 counterparts (288 out of the 289 counterparts have CARMS values), while colored histograms depict the sources of the various CRFs with $X_\rho > 3.6$. 22 % of the 288 sources have CARMS > 0.4, while for sources with $X_\rho > 3.6$ it is between 27 % and 51 %.

Similar patterns for Ψ are derived for Gaia EDR3 (Figs. 4.41c and 4.41d).

The position angle differences Ψ versus the normalized arc lengths X_ρ between Gaia DR2 and the respective CRFs in Fig. 4.46 show that the sources with larger X_ρ have Ψ of close to 0° for all compared CRFs. The X_ρ for the original ICRF3 X/Ka are overall larger, as already shown in Fig. 4.34. Nevertheless, as Fig. 4.44 depicts, the radio-optical position offsets favor about the same direction for all ranges of X_ρ. Incorporating the CARMS information from Fig. 4.36 in Fig. 4.45 indicates that the distribution of Ψ is not largely depending on CARMS. For CARMS ≤ 0.1 the peak is slightly offset from 0°, which could be due to the small sample size.

For Gaia EDR3, the X_ρ for the original ICRF3 X/Ka are overall larger as well. The radio-optical position offsets favor the same direction for all ranges of X_ρ also for Gaia EDR3, and larger X_ρ have Ψ of close to 0° for all compared CRFs (Figs. 4.47 and 4.48). Furthermore, the distribution of Ψ is not largely depending on CARMS (Fig. 4.49), similar to what was found for Gaia DR2.

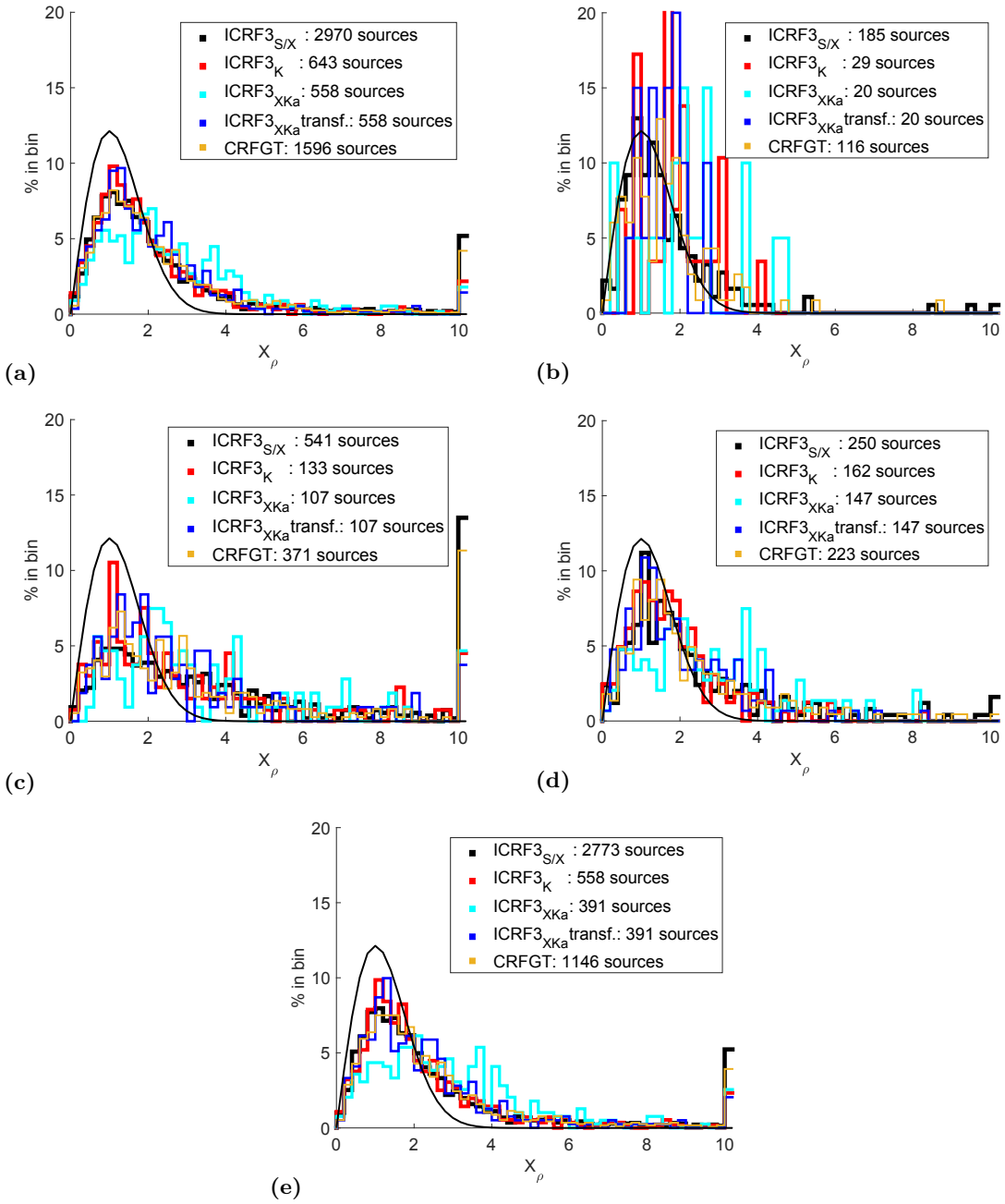

Figure 4.40 Histogram of the normalized arc lengths X_ρ between Gaia DR2 and the VLBI-based CRFs, as listed in the legend, depending on various counterpart subsets. The last bin collects all sources with $X_\rho > 9.8$. (a) all radio sources in each of the CRFs, (b) same as (a) but only for sources with CARMS < 0.1 based on basic noise, (c) same as (a) but only for sources with CARMS > 0.4 based on basic noise, (d) same as (a) but only using the ICRF3 defining sources, (e) same as (a) but showing only sources with at least 70 observations in the respective VLBI-based CRF.

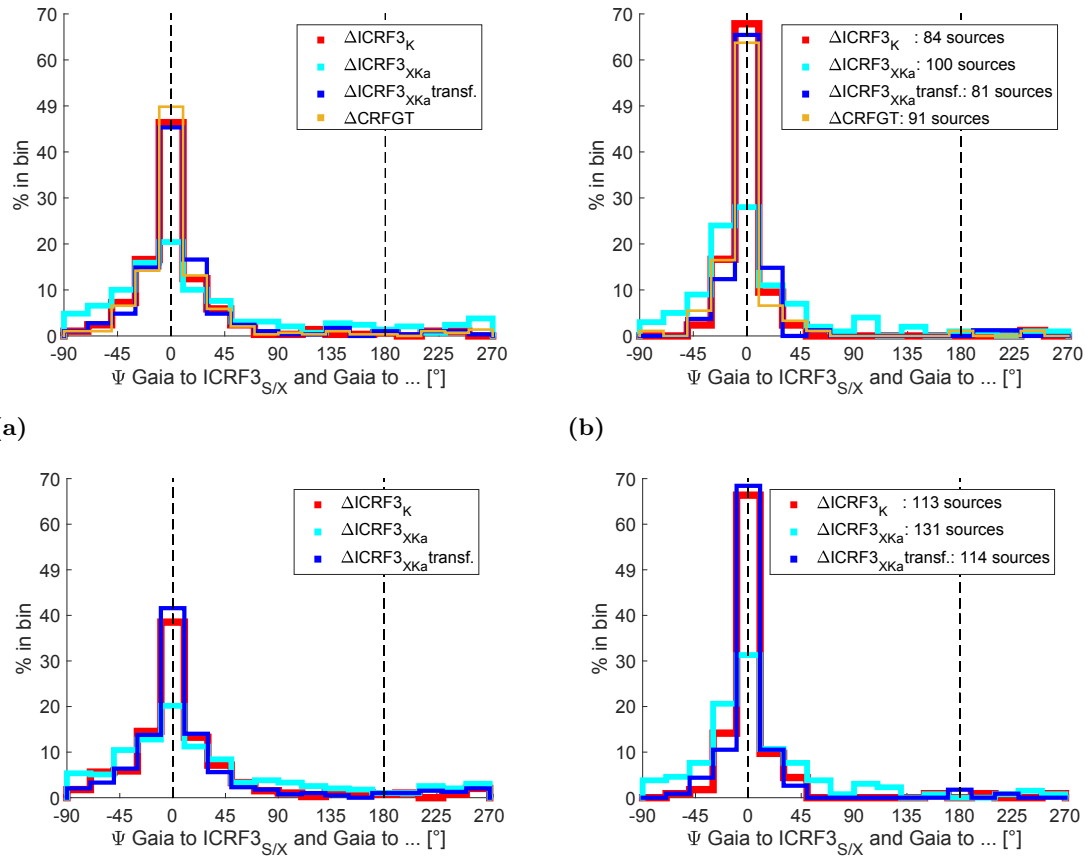

Figure 4.41 Position angle differences Ψ between the arcs from the Gaia position to the ICRF3 S/X position and from the Gaia position to the respective other CRFs, as listed in the legend, (a) for radio sources with at least 70 observations in each of the CRFs and towards Gaia DR2 (289 counterparts), (b) same as (a) but with an uncertainty of Ψ smaller than 30°, (c) for radio sources with at least 70 observations in each of the CRFs and towards Gaia EDR3 (392 counterparts), (d) same as (c) but with an uncertainty of Ψ smaller than 30°.

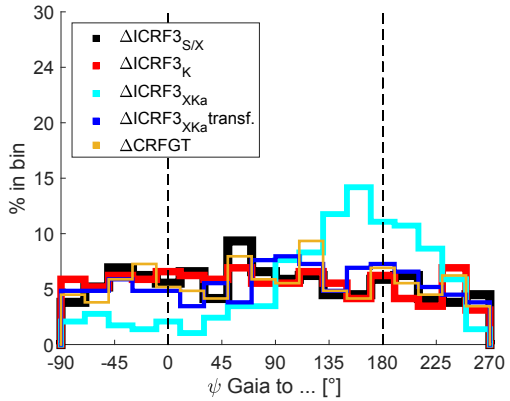

Figure 4.42 Histogram of the direction angles ψ for the 289 sources common to the various VLBI-based CRFs and Gaia DR2 and with more than 70 observations in each of the VLBI-based CRFs.

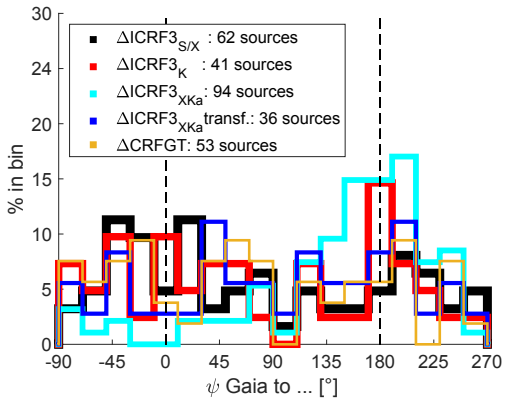

Figure 4.43 Histogram of the direction angles ψ for the sources common to the various VLBI-based CRFs and Gaia DR2, with more than 70 observations in each of the VLBI-based CRFs, and X_ρ towards Gaia DR2 larger 3.6.

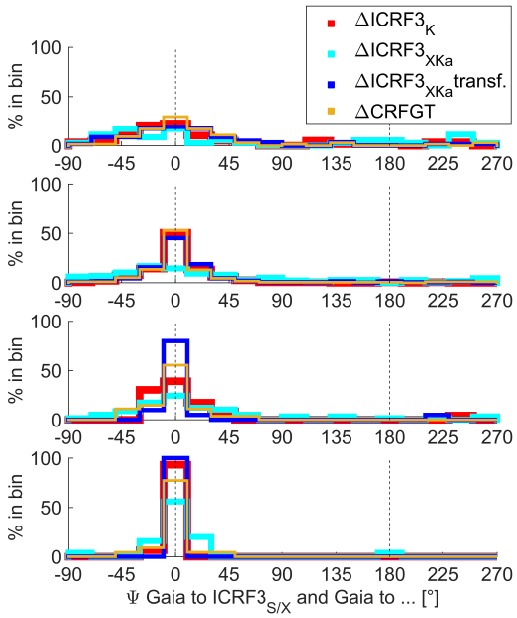

Figure 4.44 Histogram of the number of sources binned by the position angle differences Ψ between the arc from the Gaia DR2 position to the ICRF3 S/X position versus the other CRFs, as listed in the legend. The four plots show the results for different subgroups of the 289 radio sources with more than 70 observations in each of the CRFs. From top to bottom, the selections are: Sources with $X_\rho \leq 1$ (about 65 sources), $1 < X_\rho \leq 3.7$ (about 180 sources), $3.7 < X_\rho \leq 6$ (about 20 sources), and $X_\rho > 6$ (about 20 sources). The selection deviates slightly for the original ICRF3 X/Ka.

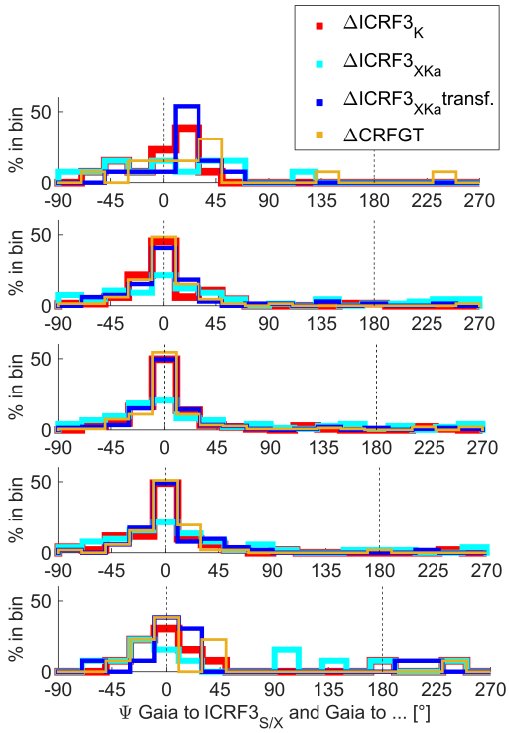

Figure 4.45 Histogram of the number of sources binned by the position angle differences Ψ between the arc from the Gaia DR2 position to the ICRF3 S/X position versus the other CRFs, as listed in the legend. The five plots show the results for different subgroups of the 288 out of the 289 radio sources with more than 70 observations in each of the CRFs that have CARMS values. From top to bottom, the selections are: Sources with CARMS ≤ 0.1 (13 sources), $0.1 <$ CARMS ≤ 0.2 (66 sources), $0.2 <$ CARMS ≤ 0.4 (145 sources), $0.4 <$ CARMS ≤ 0.6 (51 sources), CARMS > 0.6 (13 sources).

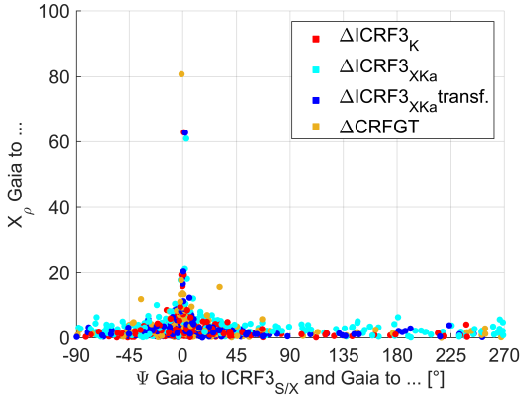

Figure 4.46 Angle differences Ψ as in Fig 4.41a versus the normalized arc lengths X_ρ between the Gaia DR2 and respective CRF positions for the 289 radio sources with more than 70 observations in each of the VLBI-based CRFs.

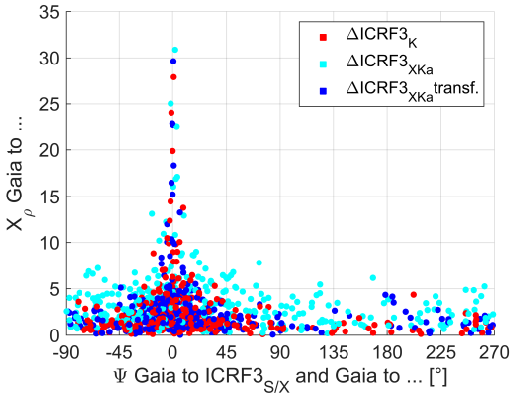

Figure 4.47 Angle differences Ψ as in Fig 4.41c versus the normalized arc lengths X_ρ between the Gaia EDR3 and respective CRF positions for the 392 radio sources with more than 70 observations in each of the VLBI-based CRFs.

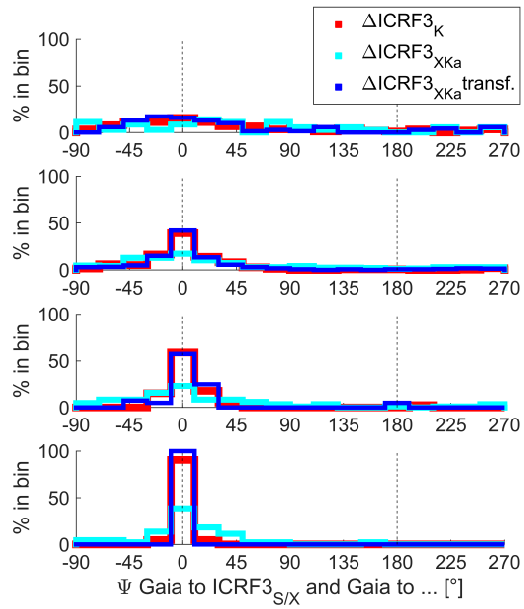

Figure 4.48 Histogram of the number of sources binned by the position angle differences Ψ between the arc from the Gaia EDR3 position to the ICRF3 S/X position versus the other CRFs, as listed in the legend. The four plots show the results for different subgroups of the 392 radio sources with more than 70 observations in each of the CRFs. From top to bottom, the selections are: Sources with $X_\rho \leq 1$ (about 80 sources), $1 < X_\rho \leq 3.7$ (about 260 sources), $3.7 < X_\rho \leq 6$ (about 40 sources), and $X_\rho > 6$ (about 20 sources). The selection deviates slightly for the original ICRF3 X/Ka.

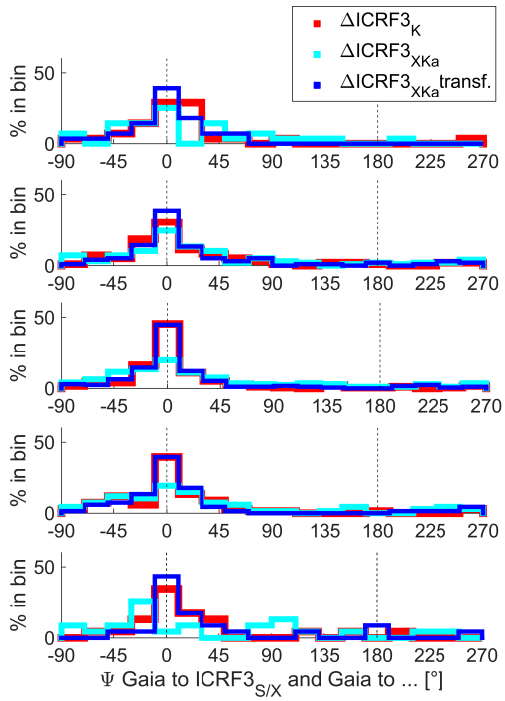

Figure 4.49 Histogram of the number of sources binned by the position angle differences Ψ between the arc from the Gaia EDR3 position to the ICRF3 S/X position versus the other CRFs, as listed in the legend. The five plots show the results for different subgroups of the 389 out of the 392 radio sources with more than 70 observations in each of the CRFs that have CARMS values. From top to bottom, the selections are: Sources with CARMS $\leq$ 0.1 (28 sources), 0.1 < CARMS $\leq$ 0.2 (98 sources), 0.2 < CARMS $\leq$ 0.4 (172 sources), 0.4 < CARMS $\leq$ 0.6 (68 sources), CARMS > 0.6 (23 sources).

4.4.2 Systematic global differences

The VSH parameters of first and second order between the various VLBI-based CRFs and Gaia DR2 were determined. The correlation coefficients between the deformation parameters are most prominent for ICRF3 K ($\leq |0.44|$). The correlation coefficients for the other CRFs are negligible ($\leq |0.30|$), even for ICRF3 S/X, as can be seen in Fig. 4.51. For the ICRF3 X/Ka which was transformed to ICRF3 S/X, the correlations for all parameters except for the correlation between $a_{2,1}^{M,Re}$ and D_2 even reduce to $\leq |0.2|$. For ICRF3 S/X no parameter is significantly determined considering the noise level of ICRF3 S/X. If this level was taken also for the other VLBI-based CRFs, the parameters A_2, D_2, and $a_{2,1}^{M,Re}$ for ICRF3 K are significantly different at the 2σ-level compared to the ICRF3 S/X noise level. The D_2 and $a_{2,1}^{M,Re}$ are very weakly correlated, and A_2 is very weakly correlated with $a_{2,1}^{E,Im}$ and D_1. For ICRF3 X/Ka, D_2, D_3, $a_{2,0}^{E}$, $a_{2,0}^{M}$, and $a_{2,1}^{M,Re}$ are significantly different at the 2σ-level compared to the ICRF3 S/X noise level. The ICRF3 X/Ka which was transformed to ICRF3 S/X and CRFGT have significantly different $a_{2,0}^{E}$ parameters at the 2σ-level compared to the ICRF3 S/X noise level. Interestingly, the CRFGT has very similar transformation parameters to the ICRF3 X/Ka which was transformed to ICRF3 S/X.

Solving these VSH terms iteratively for ICRF3 S/X results in an unstable variation of the $a_{2,0}^{M}$ estimates within the various iterations (Fig. 4.52). This finding is quantified by comparing the WRMS and two times the ME values, as introduced in Sect. 3.3.4.

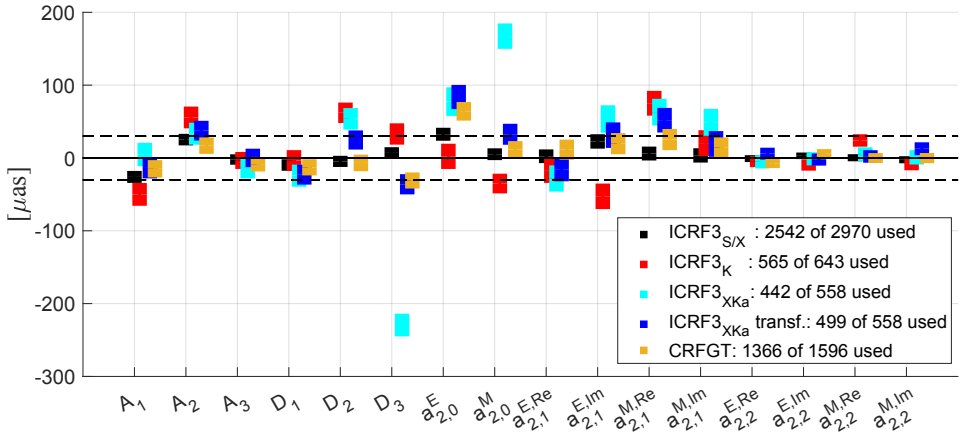

Figure 4.50 Three rotation parameters, three glide parameters, and higher order VSH terms between Gaia DR2 and various radio CRFs using all available counterparts except the outliers as determined applying the respective Rayleigh distribution on the arc lengths of the set of counterparts. In the legend, the first number denotes all available counterparts, while the second number represents the sample of counterparts used. The error bars have the size of 1σ. The horizontal dashed line depicts the noise level of ICRF3 S/X.

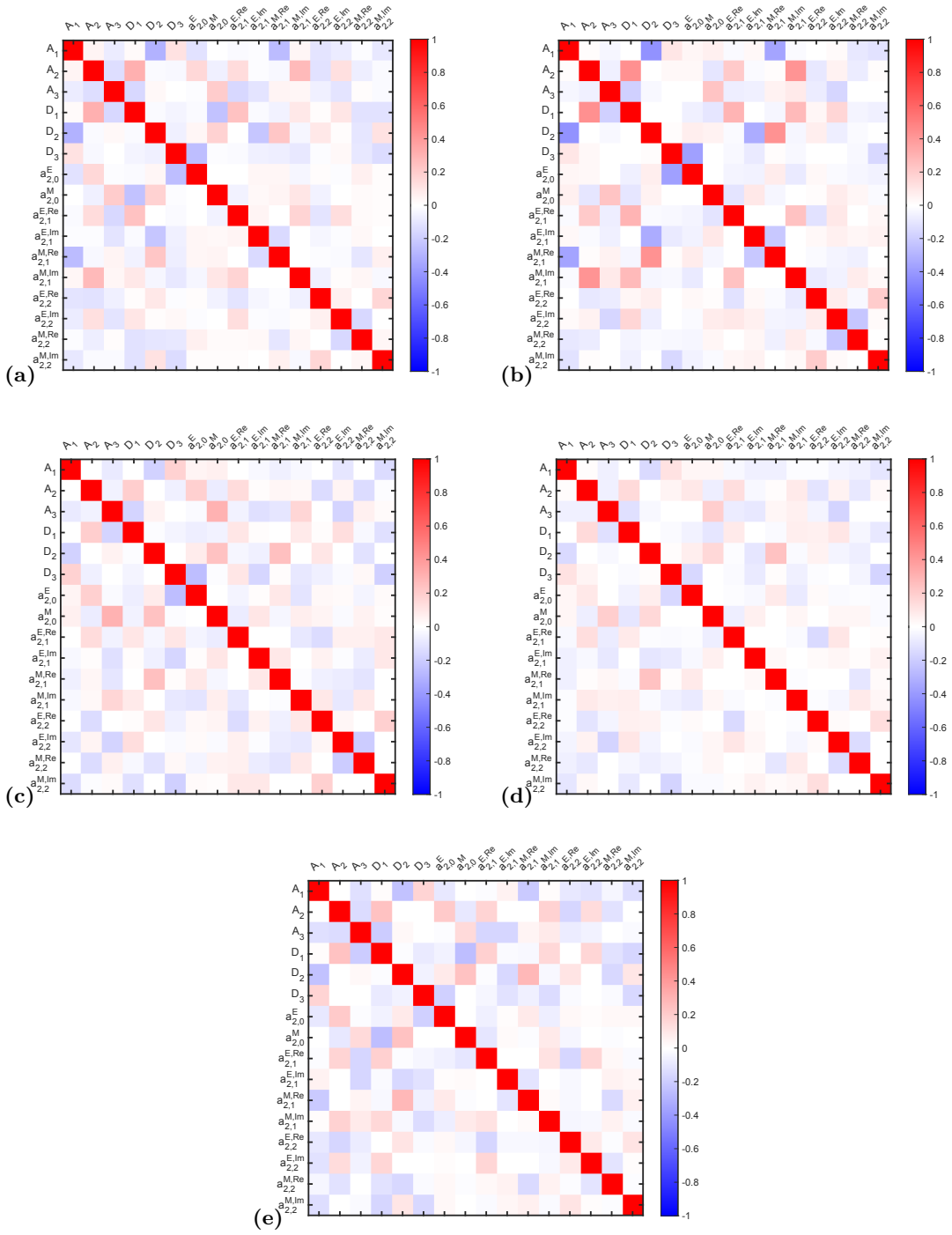

Figure 4.51 Correlation coefficients of the transformation parameters between the various CRFs and Gaia DR2 using all suitable counterparts without outliers. (a) ICRF3 S/X, (b) ICRF3 K, (c) ICRF3 X/Ka, (d) ICRF3 X/Ka which was transformed to ICRF3 S/X, and (e) CRFGT.

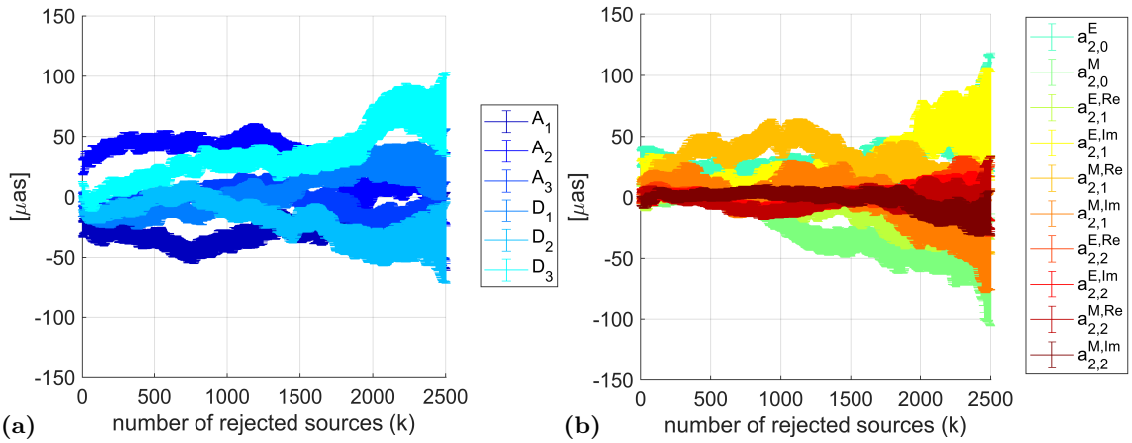

Figure 4.52 Iterative solutions aligning ICRF3 S/X to Gaia DR2 by a combined fit of (a) three rotation parameters, three glide parameters, and (b) higher order VSH terms. All available counterparts where the normalized arc lengths are not outliers were used.

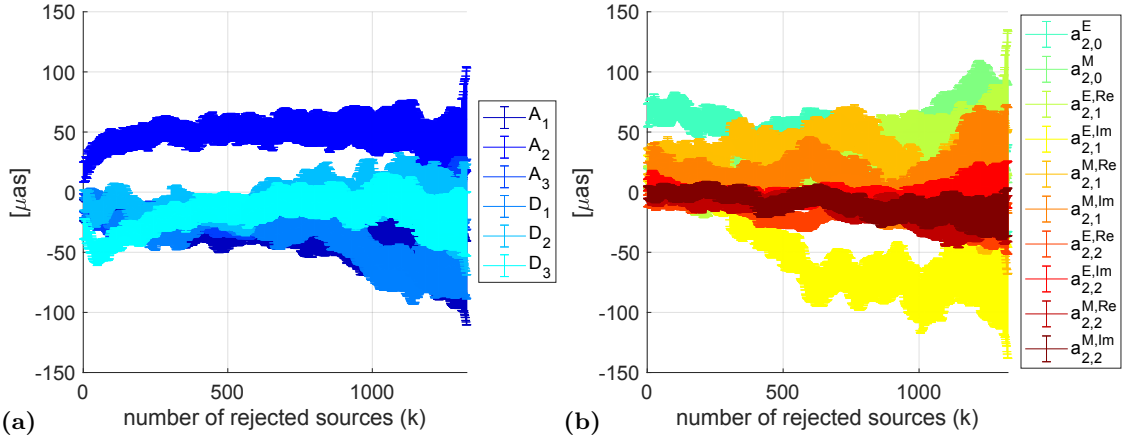

Figure 4.53 Iterative solutions aligning CRFGT to Gaia DR2 by a combined fit of (a) three rotation parameters, three glide parameters, and (b) higher order VSH terms. All available counterparts where the normalized arc lengths are not outliers were used.

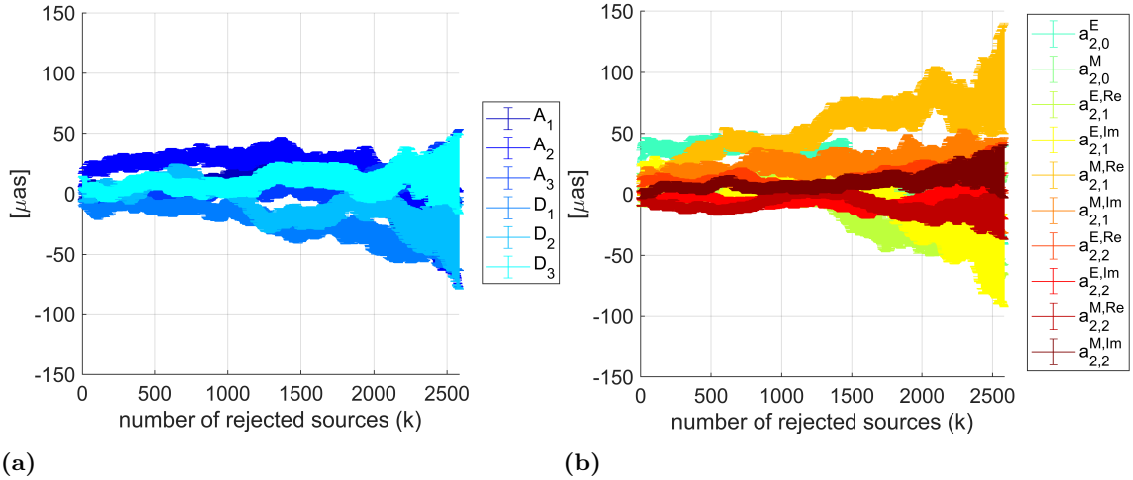

Figure 4.54 Iterative solutions aligning ICRF3 S/X to Gaia EDR3 with positions at epoch 2016.0 by a combined fit of (a) three rotation parameters, three glide parameters, and (b) higher order VSH terms. All available counterparts where the normalized arc lengths are not outliers were used.

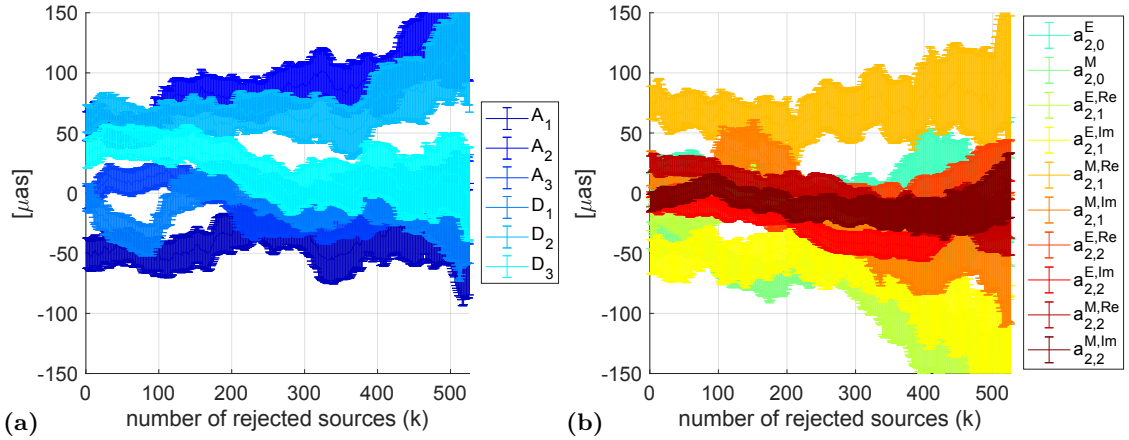

Figure 4.55 Iterative solutions aligning ICRF3 K to Gaia DR2 by a combined fit of (a) three rotation parameters, three glide parameters, and (b) higher order VSH terms. All available counterparts where the normalized arc lengths are not outliers were used.

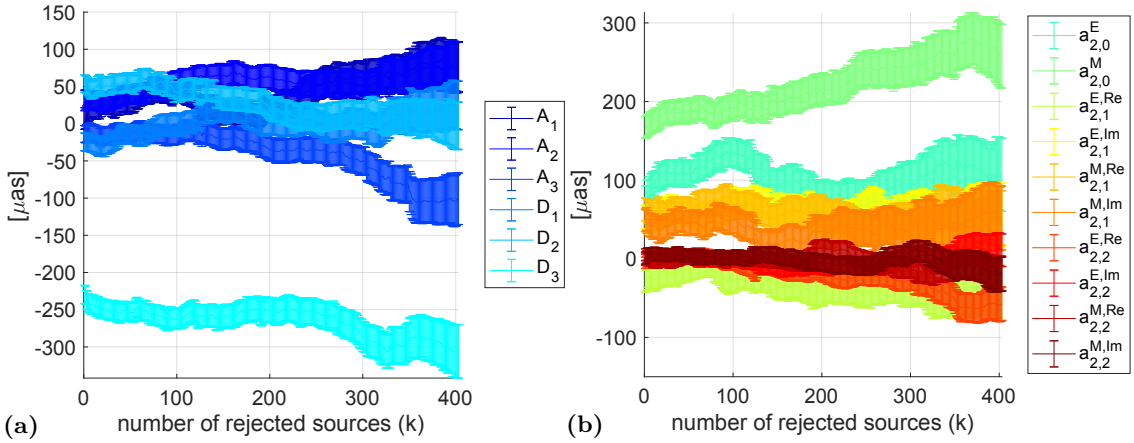

Figure 4.56 Iterative solutions aligning ICRF3 X/Ka to Gaia DR2 by a combined fit of (a) three rotation parameters, three glide parameters, and (b) higher order VSH terms. All available counterparts where the normalized arc lengths are not outliers were used. Please be aware of the different scale compared to the other similar plots.

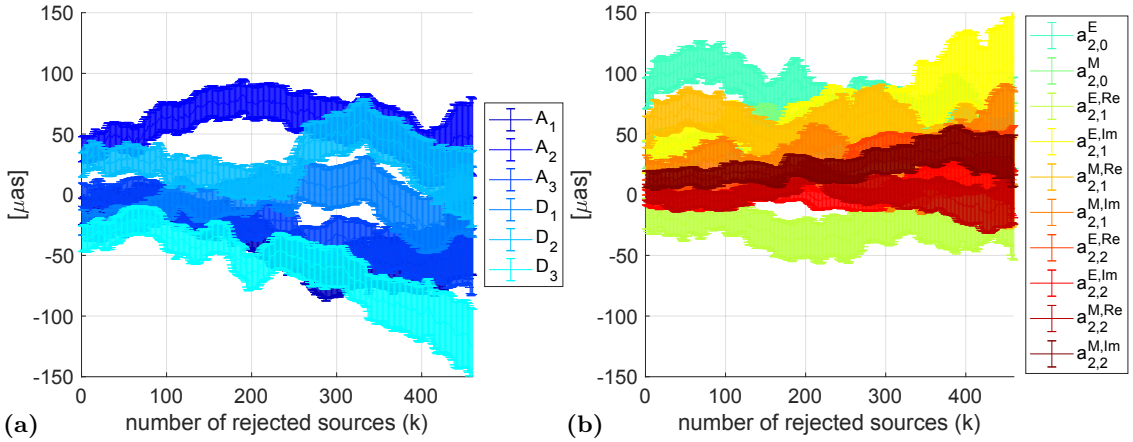

Figure 4.57 Iterative solutions aligning ICRF3 X/Ka which was transformed to ICRF3 S/X to Gaia DR2 by a combined fit of (a) three rotation parameters, three glide parameters, and (b) higher order VSH terms. All available counterparts where the normalized arc lengths are not outliers were used.

Similarly, for CRFGT (Fig. 4.53), the variation of the $a_{2,1}^{E,Im}$ estimates is unstable, and for ICRF3 K (Fig. 4.55) the variation of the $a_{2,1}^{E,Re}$ estimates is unstable. For ICRF3 X/Ka (Fig. 4.56) the variation of the parameter estimates is stable according to this analysis. This supports that the deformation of the ICRF3 X/Ka catalog is not just an artifact, e.g. due to the sky distribution of the counterparts, but a real deformation. It has to be considered that for each VLBI-based catalog, a different set of counterparts was used for this analysis.

The impact of the transformation of ICRF3 X/Ka on ICRF3 S/X before aligning to Gaia DR2 is not systematically smoothing the transformation parameter results in the iterative solution (Fig. 4.57 and 4.58). The smaller D_3 and $a_{2,0}^{M}$ parameters are validated, as expected. Comparing the ME and MS quantities, the VSH parameters for ICRF3 X/Ka which was transformed to ICRF3 S/X have lower ME than for the original ICRF3 X/Ka. Naturally, the magnitude of ME and MS decreases with the number of counterparts. More counterparts could be used for parameter determination for ICRF3 X/Ka transformed into ICRF3 S/X than for the original ICRF3 X/Ka, which may explain the smaller ME quantities.

Using only the counterparts common to all CRFs provides a better comparison without the impact of differing sample size and sky distribution (Fig. 4.59a). Of course the ME and MS are more aligned between the CRFs due to the similar number of counterparts, but also these quantities have larger values due to the fewer counterparts. The iterative results for all parameters are considered as stable because the ratio between WRMS and two times the ME is below unity for all parameters. Nevertheless, the WRMS parameters for ICRF3 S/X are worse for some of the quadrupole terms compared to when using all suitable counterparts, whereas the WRMS for CRFGT clearly reduced for $a_{2,1}^{E,Im}$. The reason for the latter could be the more even distribution of counterparts across the sky. This presumption is further investigated in Sect. 4.4.2. The WRMS quantities for the various CRFs differ for most parameters between 5 µas and 20 µas. No systematic difference between the values for the various CRFs could be identified. The WRMSs of degree and order 2 are about 5 µas lower, and these parameters are also better determined in terms of ME and MS. Furthermore, the scatter of WM values for these parameters for the various CRFs is low. The WM of the three rotations A are very close for the various CRFs when neglecting the WM of the original ICRF3 X/Ka. They vary by 20 µas for A_1 and A_2 and by 10 µas for A_3. The D_1 varies by 30 µas, D_2 by 45 µas, and D_3 by 70 µas. The quadrupole terms of zero and first order vary by 40 µas to 90 µas and those of second order by about 15 µas to 40 µas.

For better comparison, the WM, WRMS, ME, and MS quantities for ICRF3 and Gaia EDR3 are shown in Fig. 4.59b for the same subset of 406 common counterparts as in Fig. 4.59a for Gaia DR2, but in fact there are 512 common counterparts for Gaia EDR3.

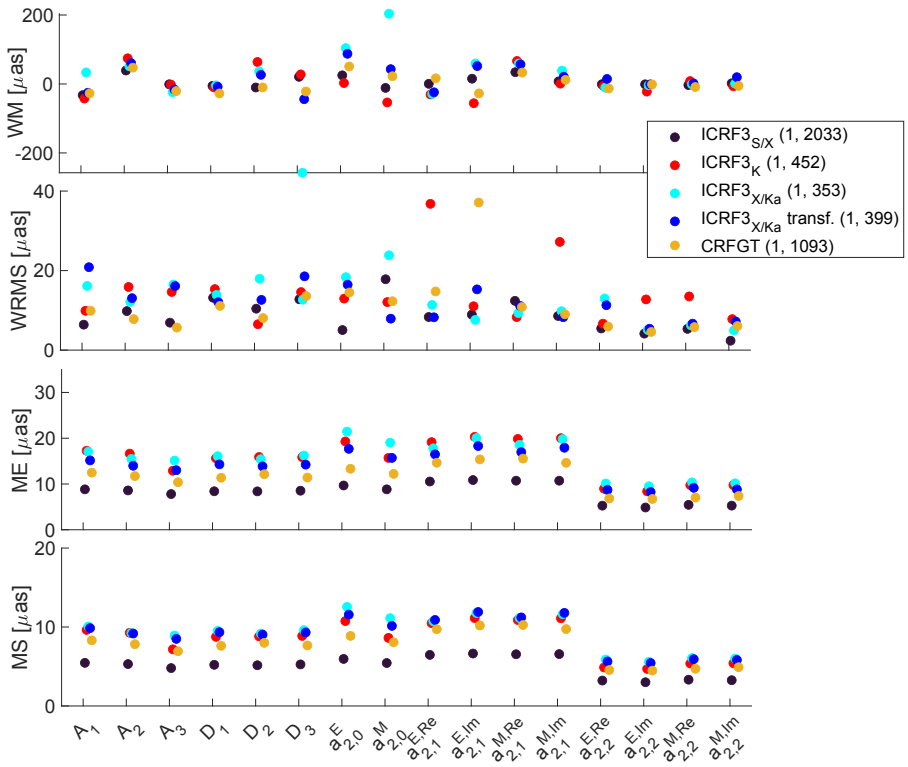

Figure 4.58 WM, WRMS, ME, and MS quantities for the iterative results for the 16 VSH parameters between the various VLBI-based CRFs and Gaia DR2. All available counterparts where the normalized arc lengths are not outliers were used. In the legend, the numbers in parentheses indicate the start and end of the iterations used to derive the quantities. Typically, this is the first iteration and the number of suitable counterparts minus the last 20 % of the iterations (to mitigate any effects due to low number of counterparts in those iterations).

In terms of WMRS, the iterative results for Gaia EDR3 are more stable across iterations than for Gaia DR2 for 13, 10, 7, and 5 parameters for ICRF3 S/X, ICRF3 K, ICRF3 X/Ka, and ICRF3 X/Ka which was transformed to ICRF3 S/X, respectively. The difference is typically below 7 µas. Nevertheless, the WRMS quantities for the various CRFs still differ for most parameters between 5 µas and 20 µas. Although the sample of used counterparts is 10-20 counterparts smaller for Gaia EDR3, the ME are up to 3 µas smaller compared to Gaia DR2. The WM of the three rotations A are very close for the various CRFs except the original ICRF3 X/Ka. They vary by 50 µas for A_1 and by 25 µas for A_2 and A_3. The D_1 varies by 30 µas, D_2 by 45 µas, and D_3 by 50 µas. The quadrupole terms of zero and first order vary by 25 µas to 120 µas and those of second order by about 3 µas to 35 µas. Thus, the rotation parameters vary 15 µas to 40 µas more than compared to Gaia DR2, while D_1 and D_2 variations are the same, and D_3 varies 20 µas less. The main reason for the higher differences of the quadrupole is the $a^{M}_{2,0}$ parameter. For ICRF3 S/X, the iterative results are shown in Fig. 4.54 as an example for using the full sample of counterparts. The corresponding WM, WRMS, ME, and MS plot is not given here. Remarkably, the WRMS of $a^{M,Im}_{2,1}$ for ICRF3 K is again large (about 30 µas) when using the full set of counterparts.

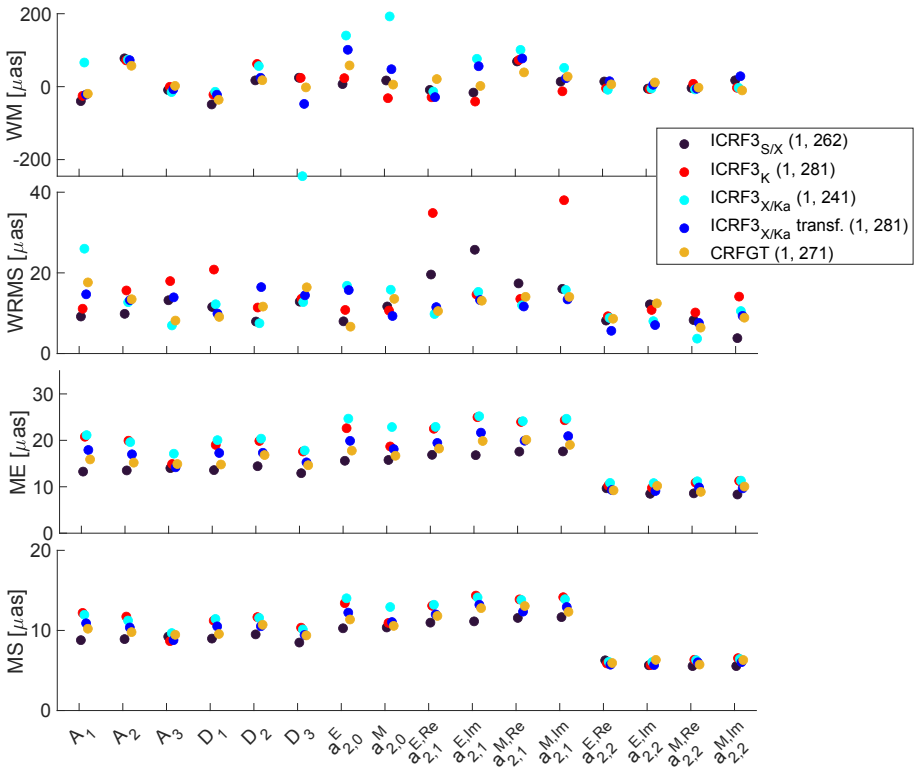

(a)

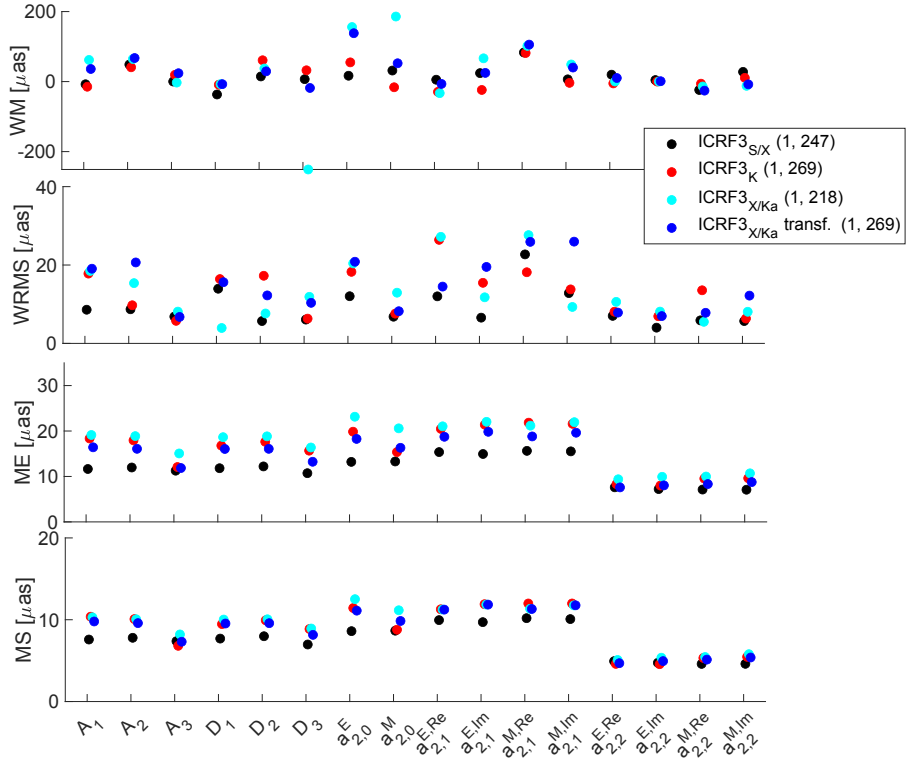

(b)

Figure 4.59 WM, WRMS, ME, and MS quantities for the iterative results for the 16 VSH parameters between the various VLBI-based CRFs and (a) Gaia DR2 or (b) Gaia EDR3. Only the 406 counterparts common to all these CRFs where used to have comparable results, and only the counterparts which are not outliers according to their normalized arc lengths were selected. Thus, the number of counterparts differs slightly for Gaia DR2 and Gaia EDR3. In the legend, the numbers in parentheses indicate the start and end of the iterations used to derive the quantities. Typically, this is the first iteration and the number of suitable counterparts minus the last 20 % of the iterations (to mitigate any effects due to low number of counterparts in those iterations).

Impact of different counterpart subsets

Using all available counterparts of the respective CRFs or only the common 406 sources in the investigation of Gaia DR2 in the previous subsection (Figs. 4.58 and 4.59a) provided similar VSH parameters. The differences in the VSH parameters are up to 40 µas for the two scenarios, and no systematic pattern in the differences for the different CRFs can be discerned. Also, the scatter of the individual parameters from the different CRFs within a scenario does not change significantly if the original ICRF3 X/Ka is not considered. The

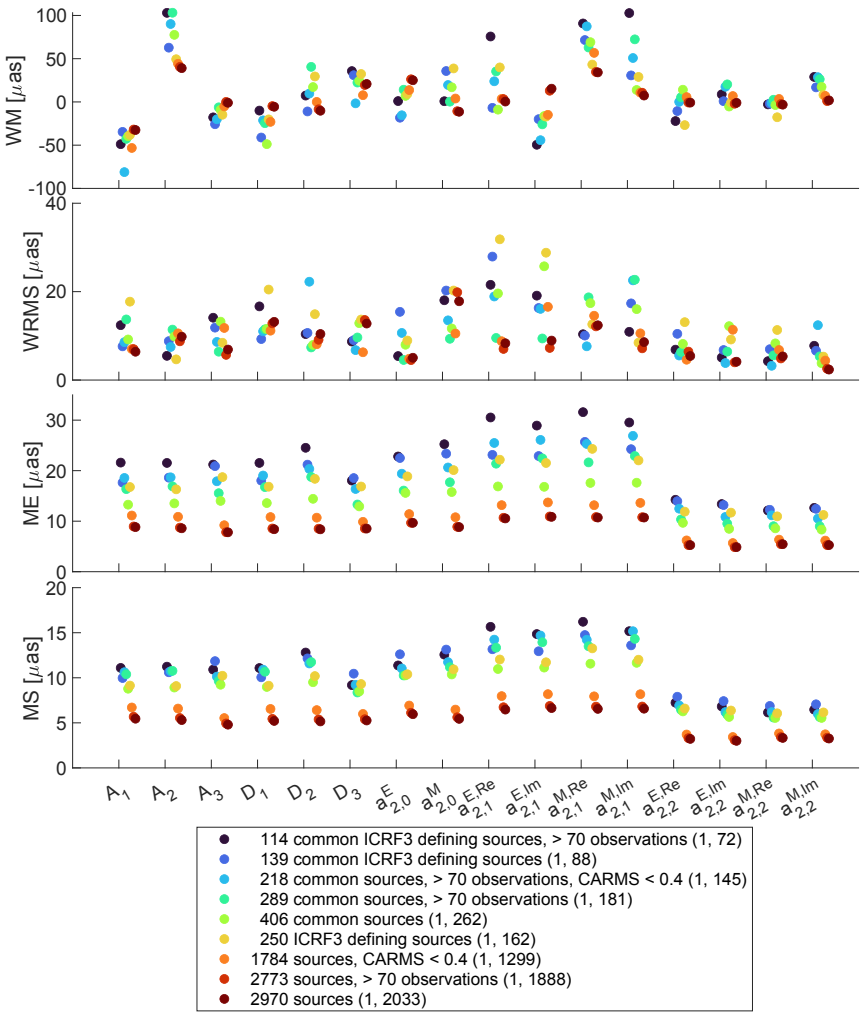

Figure 4.60 WM, WRMS, ME, and MS quantities for the iterative results for the 16 VSH parameters between ICRF3 S/X and Gaia DR2 for various subsets of counterparts. All available counterparts where the normalized arc lengths are not outliers were used. In the legend, the first numbers depict the number of all available counterparts. The numbers in parentheses indicate the start and end of the iterations used to derive the quantities. Typically, this is the first iteration and the number of suitable counterparts minus the last 20 % of the iterations (to mitigate any effects due to low number of counterparts in those iterations).

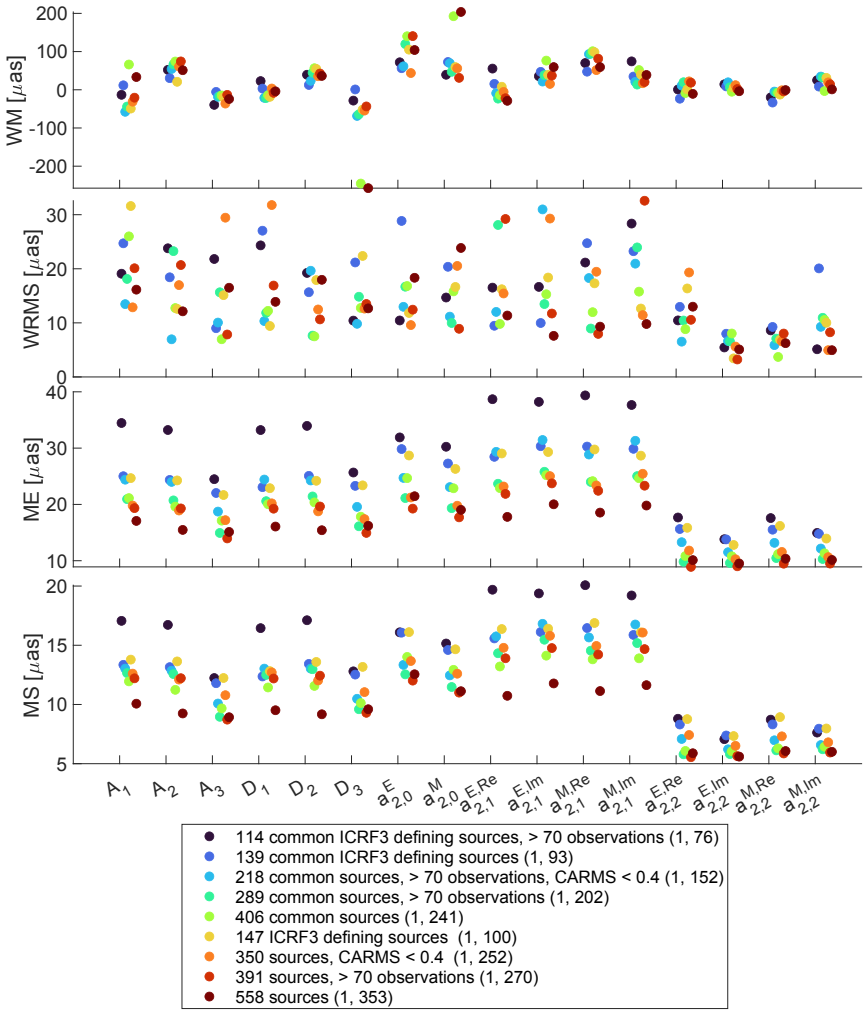

Figure 4.61 WM, WRMS, ME, and MS quantities for the iterative results for the 16 VSH parameters between ICRF3 X/Ka and Gaia DR2 for various subsets of counterparts. All available counterparts where the normalized arc lengths are not outliers were used. In the legend, the first numbers depict the number of all available counterparts. In the legend, the numbers in parentheses indicate the start and end of the iterations used to derive the quantities. Typically, this is the first iteration and the number of suitable counterparts minus the last 20 % of the iterations (to mitigate any effects due to low number of counterparts in those iterations).

largest differences are a reduction of the scatter of 15 µas for A_2 and $a^{M}_{2,0}$, and of 30 µas for D_3 when using the reduced sample of counterparts, whereas the scatter increases by 20 µas for $a^{M,Im}_{2,1}$. The scatter itself is about 15 µas to 100 µas for one scenario. Considering an overall WRMS level of about 5 µas to 20 µas and an overall MS level of about 5 µas to 10 µas, the above differences represent the accuracy of the alignment in terms of differing counterpart subsets. The WRMS parameters for ICRF3 S/X are about 15 µas worse for the $a^{E,Re}_{2,1}$ and $a^{E,Im}_{2,1}$ terms when using all counterparts or the subset of 406 sources, whereas the WRMS for CRFGT clearly reduced by 25 µas for $a^{E,Im}_{2,1}$. The reason for the latter could be the more even distribution of counterparts across the sky.

For the alignment of ICRF3 S/X on Gaia DR2, the impact of different counterpart subsets on the VSH terms is tested to further investigate the accuracy of the alignment (Fig. 4.60). The counterpart subsets were chosen to represent interesting subsets that match the previous investigations. For comparison, the above discussed quantities for the scenarios using all 2970 counterparts or the 406 common sources to all CRFs are shown. The other subsets of the 2970 counterparts are: 2773 sources having at least 70 observations in ICRF3 S/X, 1784 sources having CARMS < 0.4, and 250 ICRF3 defining sources. The other subsets of the 406 counterparts are: 289 sources having more than 70 observations in all VLBI-based CRFs, 218 sources from the latter subset that have CARMS < 0.4, 139 sources that are ICRF3 defining sources, and 114 sources from the latter subset that have more than 70 observations in all VLBI-based CRFs. The ME for the scenarios are depending on the number of counterparts, as expected. Nevertheless, the MS for the scenario with 289 sources with small CARMS values has higher MS than the scenario with 250 ICRF3 defining sources for many parameters. The Q/n of the scenarios equals one if about 20 % of the suitable counterparts were rejected. Thus, this parameter does not indicate any subset to be preferred in terms of reduced systematics.

The maximum differences in WM using one or the other subset for one parameter are 20 µas to 95 µas with a mean of 46 µas and a median of 42 µas. The differences are largest for $a_{2,1}^{M,Im}$ and $a_{2,1}^{E,Re}$. The rotation parameter WM are smallest for the scenarios with most counterparts included in the analysis. Also the other VSH terms are not among the largest for these scenarios. Restricting the number of observations only has a small impact on the results: scenarios with 2970 and 2773 sources are very close to each other in terms of WM, while the scenario with 2773 sources has smaller WRMS values for most parameters.

Section 4.4.1 showed that large X_ρ values are typically connected to large CARMS values. Since outliers in terms of X_ρ were excluded from the analysis, the restriction of CARMS being smaller 0.4 was not expected to have a large impact on the VSH determination when considering the correlation between the two quantities in Fig. 4.36. Furthermore, it is expected that the coordinate differences between two CRFs have random directions on the sky. Thus, the number of counterparts would impact the MS mostly. Indeed, the MS are smaller for the full set of counterparts. For some parameters the WRMS values are smaller than for the solution with all counterparts, but for other scenarios with fewer counterparts they are similarly smaller.

The ICRF3 defining sources are evenly distributed across the sky, thus with this counterpart subset a possible impact of inhomogeneous distribution of counterparts in the VSH terms can be tested, since the counterparts are rather evenly distributed as well. Again, sources with outliers in terms of X_ρ were excluded. No clear conclusion can be drawn from the results.

For ICRF3 K, the larger correlations drop only for the scenarios in which the ICRF3 defining sources were selected. However, this finding might be superimposed by effects due to the small sample size of 163 counterparts.

For ICRF3 X/Ka, the parameters in D_3 and $\mathrm{a}^{\mathrm{M}}_{2,0}$ have the high values only for the subset with all counterparts or with the 406 counterparts (Fig. 4.61). For the other scenarios they are about $-63\,\mu$as to $0\,\mu$as for D_3 and $30\,\mu$as to $70\,\mu$as for $\mathrm{a}^{\mathrm{M}}_{2,0}$. In these scenarios, the counterparts are more evenly distributed across the sky.

Impact of different transformation methods

The different methods typically used to align CRF in astrometry were tested for ICRF3 and Gaia to investigate how much the rotation parameters A differ between the different methods. The methods were introduced in Sect. 3.3. The tested parameterizations are (1) the full set of the 16 VSH terms (three rotations A, three glide terms D, 10 quadrupole terms), (2) the thee rotations A combined with linear trends D_α and D_δ and the bias B_δ, (3) the three rotations A and the three glide terms D, and (4) the three rotations A only.

The respective WM, WRMS, ME, and MS quantities were tested for the 406 sources common to all VLBI-based CRFs and Gaia DR2, as well as for the 2970 sources common to ICRF3 S/X and Gaia DR2 (Fig. 4.63). For the subset of 2970 sources, the rotation parameter differences are $3.5\,\mu$as to $5\,\mu$as for the different transformation methods. The glide parameters are different by $1\,\mu$as to $2.5\,\mu$as only. Thus, for ICRF3 S/X, difference in rotation parameters is larger using either the 406 counterparts or the 2970 counterparts (about $5\,\mu$as to $50\,\mu$as) compared to using additional transformation parameters for the 2970 counterparts. The same conclusion holds for the glide parameters. The rotation and glide parameters are systematically smaller using 2970 instead of 406 counterparts for the transformation. This could be due to the fact that the full set of counterparts was used for the initial alignment between Gaia DR2 and the ICRF3 S/X prototype. Also the WRMS, ME, and MS quantities are smaller for most parameters using the 2970 counterparts. The iterative result of D_α is unstable according to the WRMS divided by two times the ME for both subsets. For the 2970 counterparts, the $\mathrm{a}^{\mathrm{M}}_{2,0}$ is also unstable. The significance of the parameters is shown in Fig. 4.66a. Clearly, the various methods and subsets support a significant rotation in A_2, as well as a significant $\mathrm{a}^{\mathrm{M,Re}}_{2,1}$ term. Also, the rotation in A_1 is significant for all scenarios using the full set of suitable counterparts.

For ICRF3 X/Ka (Fig. 4.64), on the other hand, the difference in the transformation parameters used leads to larger differences in the rotation ($40\,\mu$as to $120\,\mu$as) and glide ($5\,\mu$as to $55\,\mu$as) parameters for the 558 counterparts than the difference due to the different counterpart subsets. Using 406 or 558 counterparts results in a difference of about $5\,\mu$as to $30\,\mu$as. ICRF3 X/Ka has large D_3 and $\mathrm{a}^{\mathrm{M}}_{2,0}$ deformations compared to

Gaia DR2. This is also reflected in the fitted rotations in the sense that the A_1 and A_3 rotations are much closer to zero and the WRMS parameters for all three rotations are systematically smaller for methods that parameterize more than the three rotations. When only three rotations and three glide terms are parameterized, the WRMS and MS of the glide terms are also significantly worse than when the second-order VSH terms are also set up. For both ICRF3 S/X and ICRF3 X/Ka, the WRMS values of the rotation parameters are among the smallest in case the full set of 16 VSH parameters was employed. The lowest MS values of the rotation parameters for ICRF3 X/Ka are determined from the same scenario, whereas for ICRF3 S/X it its the scenario where only the three rotations were estimated. Similar to ICRF3 S/X, the MS of the rotation parameters are similar to those of the other scenarios when D_α, D_δ, and B_δ were estimated, however, the MS and WRMS of D_α are high compared to those of the other parameters. The iterative results of all parameters are stable in terms of the WRMS divided by two times the ME. The large D_3 and $a^{M}_{2,0}$ deformation, or in case D_α, D_δ, and B_δ were set up, the large deformation in D_α and B_δ, disappear when only sources with more than 70 observations were selected (see previous section). Re-consulting the information given in Sect. 3, B_δ describes a global translation in δ direction, which is significant in the presence of declination biases, e.g., due to incorrect modeling of the troposphere at low elevation.

The correlation parameters in Fig. 4.62 and Fig. 4.51 depict the linear correlation between the parameters of interest. As stated earlier, the correlation coefficients for the 16 VSH terms are $\leq |0.30|$. The largest correlations are between A_2 and D_1 (-0.31), between A_1 and D_2 ($+0.30$), and between A_2 and $a^{M,Im}_{2,1}$ ($+0.27$). The correlation coefficients for the rotation parameters, the linear trends D_α and D_δ and the bias B_δ are $\leq |0.18|$ for all parameters except between D_δ and B_δ (-0.35). The correlation coefficients for the three rotations and three glide parameters are $\leq |0.12|$ for all parameters except between

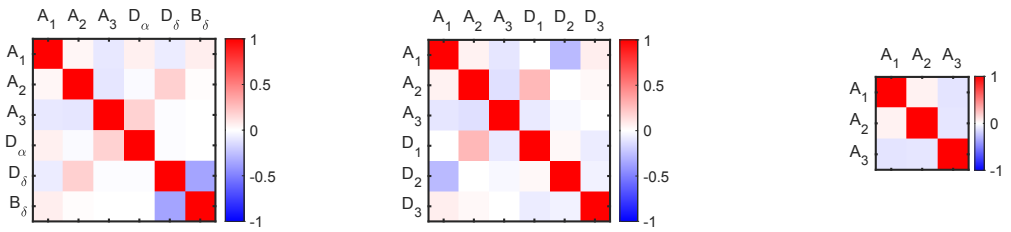

(a) **(b)** **(c)**

Figure 4.62 Correlation coefficients between the transformation parameters between ICRF3 S/X and Gaia DR2 for the first iteration of each scenario. All suitable counterparts without outliers were used. (a) depicts the scenario in which the thee rotations A combined with linear trends D_α and D_δ and the bias B_δ were estimated, (b) the three rotations A and the three glide terms D, and (c) the three rotations A only. The respective correlation parameters of the first iteration of the full VSH terms are shown in Fig. 4.51.

A_1 and D_2 (-0.27) and between A_2 and D_1 ($+0.27$). The correlation coefficients for the rotation parameters only are $\leq |0.10|$. The correlations between the rotation parameters for all scenarios are negligible.

For the alignment of ICRF3 S/X and Gaia EDR3, all (except one) transformation parameters are within about ± 50 µas. Thereby, the rotation parameters vary by 2 µas to 13 µas between the different transformation methods based on the 3142 counterparts, whereas the glide parameters vary by 2 µas to 16 µas based on the same subset. These values are slightly larger than for Gaia DR2. The WRMS scatter is below 20 µas and the MS are below 3 µas to 6 µas for most parameters based on 3142 counterparts, slightly better than for Gaia DR2. Since the WRMS of the two subsets of 512 and 3142 counterparts, respectively, are closer in Gaia EDR3 than the WRMS of the subsets of 406 and 2970 counterparts in Gaia DR2, the question arises whether this is a feature of the known lower systematics in Gaia EDR3 compared to Gaia DR2. This is to be answered in future studies. For the alignment of ICRF3 S/X and Gaia EDR3, on average, the solution with most counterparts (3142 counterparts) and the 16 VSH parameters has the lowest WRMS values for the rotation parameters, while it has about 0.2 µas larger MS than the solution using the other transformation methods for the 3142 counterparts. The smallest MS for the three rotation parameters are derived when only estimating those parameters. The significance of the parameters is shown in Fig. 4.66b. Clearly, the various methods and subsets support a significant rotation in A_2, as well as significant $a_{2,1}^{M,Re}$ and $a_{2,2}^{E,Re}$ terms.

Impact of constraining the VLBI data time interval

The alignment of CRFGT and Gaia DR2 is evaluated in this subsection. CRFGT is a CRF based on VLBI at S/X frequencies and uses only VLBI observations during the Gaia DR2 observation time interval (Sect. 4.1.3). It was specifically created to determine, whether the alignment of the CRFs from Gaia DR2 and VLBI can be improved using the same observation time interval for the CRFs. Using a similar software setup and the same VLBI observations as used for the creation of ICRF3 S/X, a CRF close to ICRF3 S/X was determined (CRF7918, Sect. 4.1.2). The evaluations in Sect. 4.3.1 proved that the differences between ICRF3 S/X and CRF7918 are negligible, and that thus the differences between ICRF3 S/X and CRFGT are not expected to be due to the somewhat different software setup between ICRF3 S/X and this work. Among others, the consistency was visualized by the angle differences Ψ of the arc between the ICRF3 S/X and CRF7918 positions and the arc between the ICRF3 S/X and ICRF3 K positions of the sources being not systematically in the same direction (Fig. 4.18a). Furthermore, the negligible systematic differences between CRF7918 and ICRF3 S/X were visualized by the 16 VSH terms in Fig. 4.21.

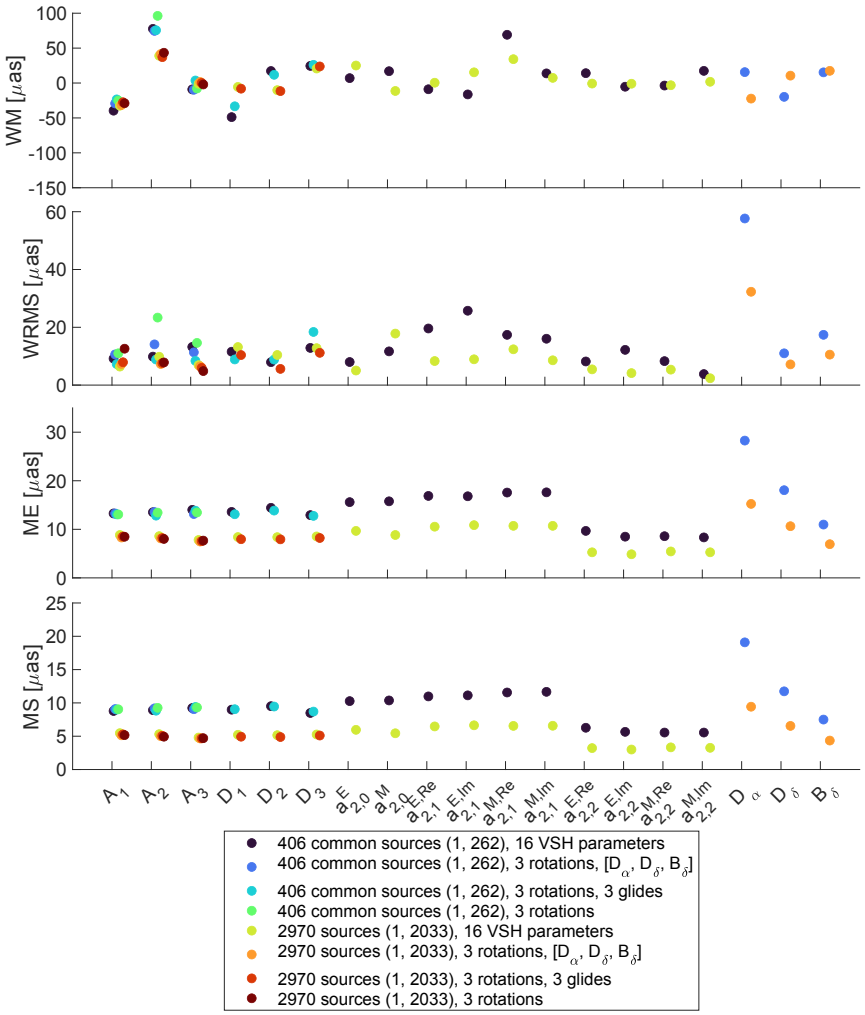

Figure 4.63 WM, WRMS, ME, and MS quantities for the various transformation parameters between ICRF3 S/X and Gaia DR2. Two sets of counterparts were tested: the 406 counterparts common to all VLBI-based CRFs and Gaia DR2 or the 2970 counterparts between ICRF3 S/X and Gaia DR2. Only counterparts for which the normalized arc lengths are not outliers were used. The first iteration and the number of suitable counterparts minus the last 20 % of the iterations (until iteration 262 or 2033) was used to mitigate any effects due to low number of counterparts in those iterations.

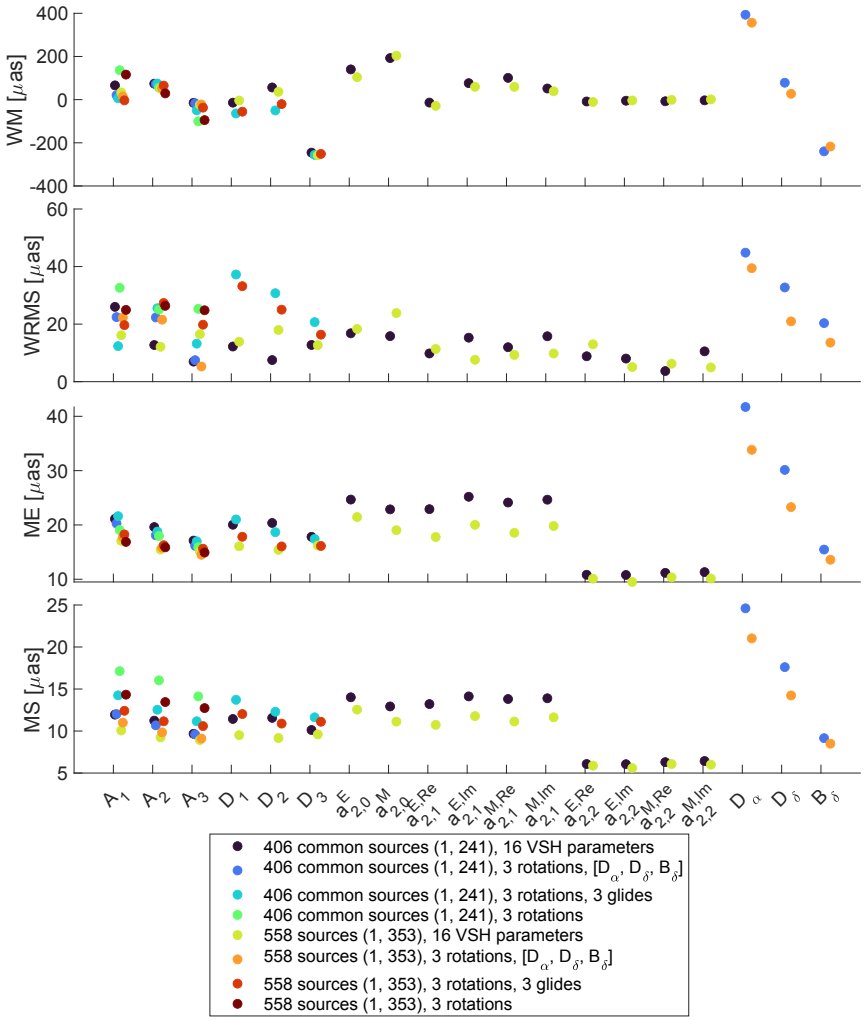

Figure 4.64 WM, WRMS, ME, and MS quantities for the various transformation parameters between ICRF3 X/Ka and Gaia DR2. Two sets of counterparts were tested: the 406 counterparts common to all VLBI-based CRFs and Gaia DR2 or the 558 counterparts between ICRF3 S/X and Gaia DR2. Only counterparts for which the normalized arc lengths are not outliers were used. The first iteration and the number of suitable counterparts minus the last 20 % of the iterations (until iteration 241 or 353) was used to mitigate any effects due to low number of counterparts in those iterations.

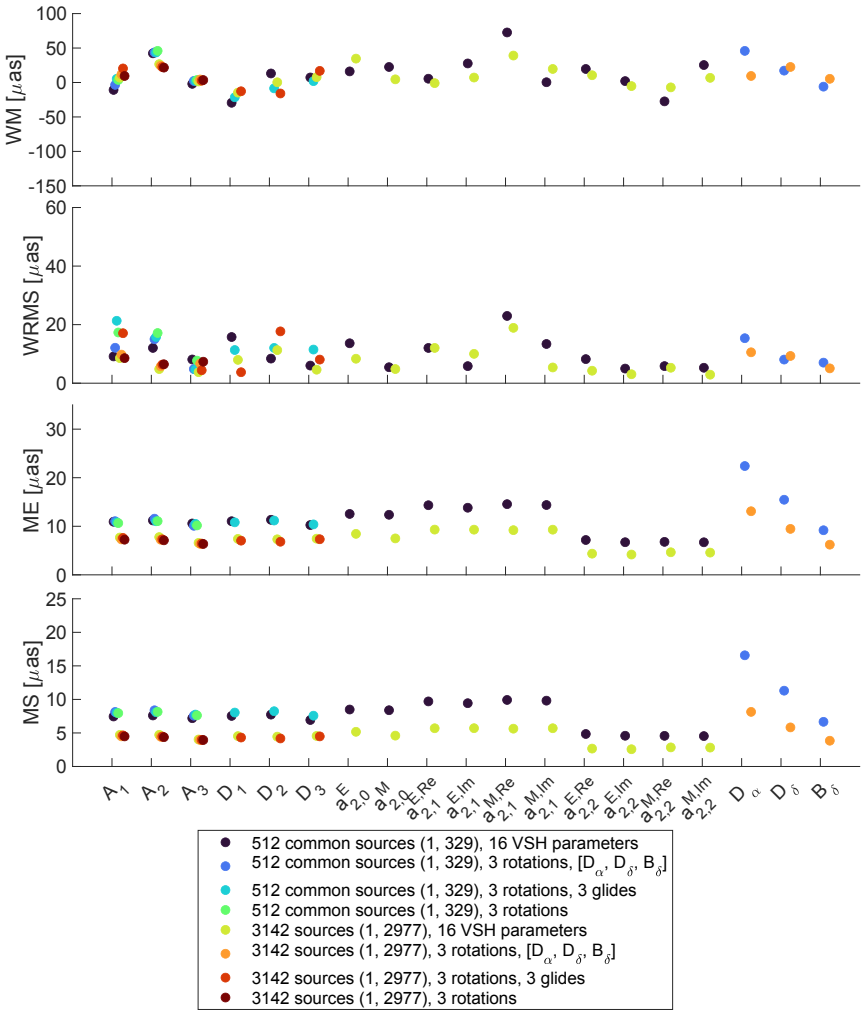

Figure 4.65 WM, WRMS, ME, and MS quantities for the various transformation parameters between ICRF3 S/X and Gaia EDR3. Two sets of counterparts were tested: the 512 counterparts common to all VLBI-based CRFs and Gaia EDR3 or the 3142 counterparts between ICRF3 S/X and Gaia EDR3. Only counterparts for which the normalized arc lengths are not outliers were used. The first iteration and the number of suitable counterparts minus the last 20 % of the iterations (until iteration 329 or 2977) was used to mitigate any effects due to low number of counterparts in those iterations.

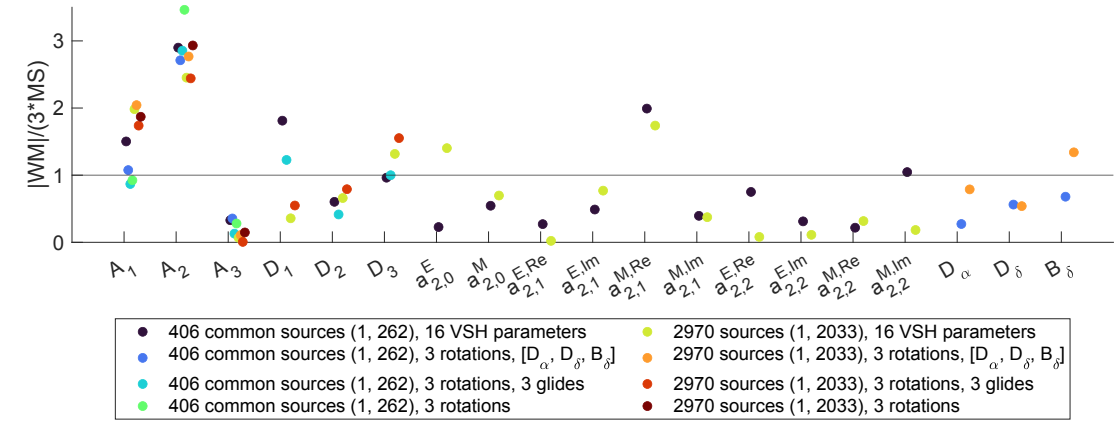

(a)

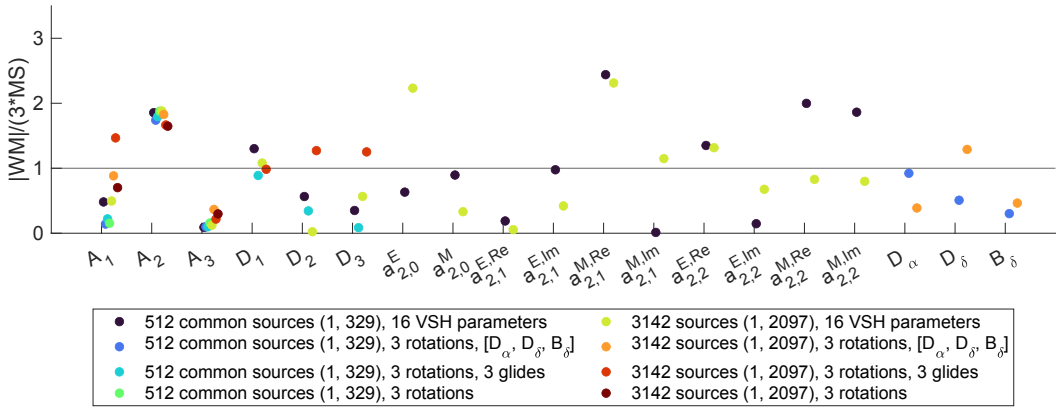

(b)

Figure 4.66 Significance of the transformation parameters, (a) between ICRF3 S/X and Gaia DR2, (b) between ICRF3 S/X and Gaia EDR3. If the value of WM/(3MS) is larger unity, the parameters are considered as significantly determined. The results are shown for the various transformation methods as shown in Figs. 4.63 and 4.65.

From Table 4.1, the median position offset between ICRF3 S/X and CRFGT is 0.31 mas with a median $\sigma_{\mathrm{pos,max}}$ of 0.30 mas, while the normalized arc lengths X_ρ mostly follow the expected Rayleigh distribution. For comparison, the median separation ρ for ICRF3 S/X and CRF7918 is 0.10 mas with a median $\sigma_{\mathrm{pos,max}}$ of 0.16 mas. Likewise, from Table 4.4, the median position offset between Gaia DR2 and CRFGT is 0.66 mas with a median $\sigma_{\mathrm{pos,max}}$ of 0.28 mas, while for ICRF3 S/X, the values are 0.58 mas and 0.19 mas. The normalized arc lengths X_ρ of the 406 sources common to all discussed VLBI-based CRFs and Gaia DR2 follow the expected Rayleigh distribution slightly better for CRFGT than for ICRF3 S/X, as the former has less outliers with $X_\rho > 3.7$ (67 versus 78).

In terms of global systematics it is not possible to determine whether ICRF3 S/X or CRFGT align better to Gaia DR2. In terms of WRMS of the rotation parameters towards Gaia DR2, both ICRF3 S/X and CRFGT have lower WRMS values for some of the parameters. Figure 4.50 suggests that CRFGT and Gaia DR2 have a significant $\mathrm{a}^{\mathrm{E}}_{2,0}$ parameter based on the full set of suitable counterparts, which is confirmed based on the iterative results in Fig. 4.58. Consulting the iterative rotation parameter results in Figs. 4.52 and 4.53, and the correlation parameters in 4.51, it might be that the correlations, although their magnitude is smaller than 0.3, are still too high.

4.5 Discussion

Determining, verifying, and possibly improving the alignment of the ICRFs at various frequencies is an important task. An accurate frame tie is required for a variety of research topics, such as frequency-dependent position offsets of sources or source categorization.

In this chapter, the ICRF3 at K band and at X/Ka band were compared to the ICRF3 S/X. Furthermore, the VLBI-based CRFs were compared to Gaia DR2 and Gaia EDR3. The goal was to determine the accuracy of the alignment between the radio and optical CRFs. For this purpose, the individual source position offsets were examined, and their dependence on radio source structure effects and the number of VLBI observations was studied. Next, global systematic differences such as rotations and glide patterns were determined. Their dependency on various subsets of suitable counterparts, as well as the alignment methods, was demonstrated based on the radio-optical position offsets. Surely, the individual source position differences are typically about one magnitude larger than the global systematic differences. The individual source position differences are correlated with the amount of radio source structure effect, whereas the global systematic differences depend more on the number of counterparts used for the alignment.

To determine the impact of VLBI observations far away in time from the Gaia observation time, the CRFGT was constructed, which is a CRF at S/X band using only observations during the Gaia DR2 time span. It includes only 52 % of the sources in ICRF3 S/X. At the same time, the median position uncertainties are a factor of two larger for CRFGT compared to ICRF3 S/X.

While the normalized arc lengths X_ρ between ICRF3 K, ICRF3 X/Ka after transformation to ICRF3 S/X, or CRFGT towards ICRF3 S/X follow the expected Rayleigh distribution, the distributions of the normalized arc lengths of the VLBI-based CRFs towards Gaia DR2 or Gaia EDR3 deviate more from the expected Rayleigh distribution. This larger deviation is also resulting in more outliers of X_ρ. It shows that the uncertainties of the Gaia or VLBI catalogs are too optimistic and could be inflated to better match the expected distribution (see also Petrov et al. 2018, who determined more realistic uncertainties for the positions in their VLBI-based CRF and Gaia DR2.).

Xu et al. (2021) found that the statistically significant position differences between ICRF3 S/X and Gaia EDR3 are related to large radio source structure based on a comparison of the normalized arc lengths and the CARMS values of these sources. In this work, this finding was approved for position differences between the various VLBI-based CRFs at different frequency bands or observation time intervals and ICRF3 S/X, as well as for the position differences between the various VLBI-based CRFs and Gaia DR2 or Gaia EDR3. Liu et al. (2021) found similar results when comparing ICRF3 to Gaia EDR3 position offsets to the structure index (Charlot 1990; Fey and Charlot 1997).

In this study, the position offset directions ψ between the various VLBI-based CRFs were compared. The ψ are defined as the angles between the declination direction and the arc of the position offset between the ICRF3 S/X positions and the ICRF3 K or ICRF3 X/Ka positions. They have a tendency along the declination direction even after transforming to ICRF3 S/X, similar to what was found in Charlot et al. (2020). They conclude that remaining systematics between the radio catalogs must exist, which cause these declination biases. The angles ψ between the various VLBI-based CRFs and Gaia positions are however evenly distributed, as expected. The VLBI to ICRF3 S/X angles ψ seem to be biased by the small scale systematics as the median distances between the radio positions are small (about 0.2 mas to 0.3 mas). This is not the case for the VLBI to Gaia DR2 positions, which have a larger median of about 0.5 mas.

The angle differences Ψ of the directions ψ of the position offset of the VLBI-based CRF positions and the ICRF3 S/X position of a source favor the same direction as the position offset between the ICRF3 K position and the ICRF3 S/X position. Only for CRFGT, a weak favor also in the opposite direction was found. The offset directions of the VLBI-based positions and the Gaia position however only favor the same direction as the ICRF3 S/X position and the respective Gaia position (Gaia DR2 or Gaia EDR3). Lambert et al. (2021) found using similar data that from the S/X position, the optical position is for most sources downstream the jet, and the K and X/Ka position is upstream the jet. In the future, the evaluation in this thesis can be repeated with respect to the S/X position instead of the Gaia position in order to confirm this finding of Lambert et al. (2021). It was shown that the sources with larger X_ρ favor the same direction for both the radio-only position differences or the radio-optical position differences (only for CRFGT the position differences slightly favor the opposite direction compared to the other radio position differences as well). Only the directions from the ICRF3 S/X position to the ICRF3 K position and the ICRF3 X/Ka position which was transformed to ICRF3 S/X show a slight dependency on very small and very large CARMS values. Comparisons of the position offset directions between VLBI and Gaia DR2 and Gaia EDR3 with jet angles derived from radio images were conducted in Kovalev et al. (2017); Petrov et al. (2018); Plavin et al. (2019); Xu et al. (2021). A comparison of the jet angles with the offset direction between Gaia DR2 and the various ICRF3 catalogs was conducted in Lunz et al. (2019a); Lambert et al. (2021). The comparison of the offset directions with the jet angles derived from images does not show an as clear favor for the same direction as the comparison between the different position offset directions in this work. In general, the jet angles align with the offset directions, however, probably more care has to be taken in solving the 180° ambiguity of the jet angle determination as there appears also a medium peak in the histograms for the opposite direction to the jet angles.

The global systematic differences between the radio and optical catalogs agree well with

those already published in other literature mentioned in the introduction. The global systematic differences between the various VLBI-based CRFs and ICRF3 S/X in terms of the 16 VSH parameters are accurate to a WRMS scatter of below 15 µas as determined from iterative solutions where the most deviating source was rejected in each iteration. Furthermore, their mean standard deviation (MS) is below 6 µas. In contrast, when comparing the various VLBI-based CRFs to Gaia DR2, the WRMS scatter is mostly below 25 µas and the MS values are below 12 µas. The smaller WRMS values for the VLBI-only transformations, although based on different antenna networks, compared to the WRMS values of the VLBI-Gaia transformations may indicate the presence of larger internal systematics in the Gaia CRFs. The correlation coefficients between the deformation parameters are most prominent for ICRF3 K, suggesting a more detailed analysis of the uniformity of the source distribution across the sky.

The selection of different initial subsets, such as using only sources with small source structure at S/X frequency bands or using only sources with more than 70 VLBI observations, results in differences of the weighted mean (WM) of about 6 µas to 35 µas for the comparison between ICRF3 K and ICRF3 S/X and about 20 µas to 95 µas for the comparison between ICRF3 S/X and Gaia DR2. The WM values of the three rotation parameters differ by 8 µas to 30 µas for the comparison between ICRF3 K and ICRF3 S/X and 25 µas to 65 µas for the comparison between ICRF3 S/X and Gaia DR2. The WRMS values for the 16 VSH parameters differ by up to 10 µas for ICRF3 K and ICRF3 S/X and by up to about 30 µas for ICRF3 S/X and Gaia DR2. The mean errors (ME) mainly depend on the number of counterparts, as expected.

The impact of using different functional models for the transformations between catalogs on the rotation parameters was determined to be on the order of a few µas only for the comparison between ICRF3 S/X and Gaia DR2. However, in case of the larger deformations of ICRF3 X/Ka, the rotation parameters are significantly affected by several tens of µas when including more deformation parameters or only the three rotations in the analysis. The correlation coefficients of the different transformation methods based on the alignment between ICRF3 S/X and Gaia DR2 show that the rotations can be very weakly correlated with some of the glide and quadrupole parameters. In contrast, the linear trends and biases are not correlated to the rotation parameters. In the future, simulations can be used to further assess the reason for the correlations and their impact on the rotation parameters, e.g., by using a synthetic data set of evenly distributed and evenly weighted positions. The investigations support the finding from Charlot et al. (2020) and others, which is that the ICRF3 X/Ka is subject to significant large-scale deformations. Using the transformation between ICRF3 X/Ka and Gaia DR2 as an example because ICRF3 X/Ka has large deformations, the sample with most counterparts and the 16 VSH terms is identified as best suitable for the determination of the rotations between the two frames,

as the WRMS values and the MS values of the rotation parameters for this case are the smallest (Fig. 4.64). Again, simulations might help to further assess this finding.

Thus, it can be concluded that the rotations between the ICRF3 catalogs can be determined to a precision of less than 30 µas (the noise of ICRF3 S/X), and that the rotations between ICRF3 S/X and Gaia DR2 can be determined to a precision of less than 65 µas. This finding is a little more pessimistic than the work of Charlot et al. (2020); Liu et al. (2020), who concluded that ICRF3 S/X and Gaia DR2 are consistent at the 30 µas level. The larger level of 65 µas can be explained by the larger variety of tested subsets compared to those in the work of Charlot et al. (2020).

For a more accurate alignment, it is recommended to choose a consistent set of transformation parameters, and more importantly, a fixed set of common counterparts. This holds especially for the definition of any rotations (orientation offsets) between the ICRF realizations to reduce any scatter or inaccuracy of the registration of the CRFs due to different sets of defining sources.

The Gaia DR2 is aligned to the ICRF3 S/X prototype, whereas the various VLBI-based CRFs and Gaia EDR3 are aligned to ICRF3 S/X. Thus, it might be the explanation that the rotations of the VLBI-based CRFs towards Gaia DR2 are a little larger than towards Gaia EDR3. The various methods support a significant rotation in A_2 and, in case the 16 VSH terms were determined, a significant $\mathrm{a}_{2,1}^{\mathrm{M,Re}}$ parameter for both Gaia DR2 and Gaia EDR3 towards ICRF3 S/X, respectively. As a possible significant systematic difference between ICRF3 S/X and Gaia DR2, the $\mathrm{a}_{2,0}^{\mathrm{E}}$ parameter with a value of 35 ± 9 µas was determined in Charlot et al. (2020). The evaluation in this work shows that the scatter of results from different subsets and the iterative solutions is too large to confirm the significance of this parameter.

All VSH parameters between CRFGT and ICRF3 S/X are below 20 µas, except D_3 (-42 µas) and $\mathrm{a}_{2,0}^{\mathrm{E}}$ (41 µas). These are very similar deformations compared to those determined by Charlot et al. (2020) between the ICRF2 with modeled Galactocentric acceleration and the ICRF3 S/X. Furthermore, Mayer (2018) found that including Ray-tracing into the analysis for their VLBI CRF decreased the $\mathrm{a}_{2,0}^{\mathrm{E}}$ value while it increased the D_3 value. On the other hand they found that a correction of a likely systematic effect at VLBI station Hobart12 increased the $\mathrm{a}_{2,0}^{\mathrm{E}}$ value while it decreased the D_3 value (increase and decrease are depending on the direction of the alignment test). A reason for the higher and opposing values in these two parameters could be the slight correlation of D_3 and $\mathrm{a}_{2,0}^{\mathrm{E}}$ in these three cases (Fig. 4.24). The comparisons of the individual source position differences and the global systematic differences towards Gaia DR2 show that no clear indication can be found as to CRFGT being closer to Gaia DR2 in terms of individual source positions than ICRF3 S/X. Only in case of large temporal differences in source structure differences in individual source positions were expected. The global systematic

differences appear to be smaller for ICRF3 S/X when all available counterparts are used. However, this statement is not evident when the counterparts common to all CRFs are used.

There are some limitations of this work. The possible correlation of the results to the number of Gaia observations was not discussed. Only the mean positions over a varying observation time span were used for the comparisons. Position changes of the VLBI core or the photocenter of the sources during the VLBI and Gaia observations were not considered (other than restricting the VLBI data for CRFGT to the Gaia DR2 observation time interval), but only the mean positions were used. It is expected that any temporal changes in the VLBI or Gaia position appear for sources which are randomly distributed across the sky, and that the position changes appear in random directions. Consequently, these position differences will not significantly affect the determination of global systematic differences. The comparison between the radio and optical positions is based on a set of counterparts between the VLBI-based CRFs and Gaia DR2 using the basic selection criteria as developed by the Gaia DPAC and the probability of false detection from the density of the full Gaia sample. A more ambitious selection was determined by Makarov et al. (2019) using, among others, multicolor images. Future work can determine the change in deformation parameters using this selection.

Since the large systematic deformations of ICRF3 X/Ka can be larger than the position uncertainty and the position difference of the individual source, it is recommended to correct for the systematic deformations before the analysis of individual sources. The impact on the analysis of the individual source positions and the offset directions was shown in this work for ICRF3 X/Ka, as it has the largest deformations. However, if arc lengths are small, also small systematic differences can have an impact on the results.

The Gaia astrometric performance[1] predicts standard deviations of about 80 µas to 620 µas in Gaia DR4 for the individual source positions with G magnitudes between $G = 18$ mag and $G = 20.7$ mag. The values are heavily depending on G. Similarly, for Gaia DR5, standard deviations of about 55 µas to 440 µas for sources in the same G magnitude range are expected. Already now, the global systematic differences can be determined to well below these values.

Also the CRF at radio frequencies are constantly improved. For example, the newest version of the X/Ka-band frame (JPL 2022a X/Ka) has an insignificant distortion in the D_3 parameter, and the $a^{M}_{2,0}$ parameter value reduced by about half (Jacobs et al. 2022). The position uncertainties are also comparable to those of ICRF3 S/X for common sources. This suggests that the smaller D_3 and $a^{M}_{2,0}$ estimates found in this work using some subsets of all counterparts between ICRF3 X/Ka and Gaia DR2 should be re-examined using the

[1] https://www.cosmos.esa.int/web/gaia/science-performance#astrometric performance, accessed 24 October 2021.

updated X/Ka band frame and Gaia EDR3. Jacobs et al. (2022) also recommend using the full covariance information to grade this CRF. Also the K-band and S/X-band frames already improved, and both frames are now almost even for the common sources in terms of source position uncertainties (Gordon et al. 2022; de Witt et al. 2022). Currently, ICRF3 S/X is best suited to align the Gaia catalog to ICRF3. However, with the improved CRFs in the K and X/Ka bands, it needs to be evaluated whether they can be superior to the improved CRF in the S/X band for aligning Gaia in the future, as their position uncertainties are already at comparable level with fewer observations compared to those from S/X observations.

Outlook on proper motions: Ideal CRF sources should show no apparent proper motion at all, and sources with significant proper motion in Gaia were excluded from the sample during the selection process of valid counterparts (Sect. 4.2). As a future task, apparent linear proper motions from Gaia and VLBI should nevertheless be compared as well. First attempts in the course of this work did not show a good agreement (Lunz et al. 2019b), which is why they were not presented here. For VLBI, the apparent proper motions were derived from position time series of the sources. Only time series with more than 10 positions spread over at least 1.5 years were employed and the number of scans in each session had to be larger 3. Least squares matching and a more robust estimator against outliers, RANdom SAmple Consensus (Fischler, M. A. and Bolles, R. C. 1981, RANSAC), were tested. In both approaches, the data were weighted according to their uncertainties. The results were then manually filtered for credibility. The position time series were derived from repeating the global solutions in Sect. 4.1.2 and 4.1.3 respectively, where in each repetition a different random small set of source positions was not set up as a global parameter but as a session-wise parameter using the Helmert blocking in Eq. 3.28 via a backwards solution BW. The consistency of the global solutions was checked using the EOP and they are within the ICRF3 S/X error level. An example for the source position time series and the fitted position offsets and linear apparent proper motion is shown in Fig 4.67. The comparison of the direction of the apparent proper motion data from Gaia DR2 and CRFGT can be seen in Fig. 4.68. Clearly, there is no overall tendency of the VLBI and Gaia proper motions facing the same direction. In general, the Gaia DR2 proper motions are much larger than the VLBI-based proper motions and have a higher standard deviation. As future work, a comparison to VLBI proper motions from linear splines using the entire VLBI observation time interval for the respective source can be performed, similar to what was introduced in Karbon et al. (2017), but using position time series from the global solution.

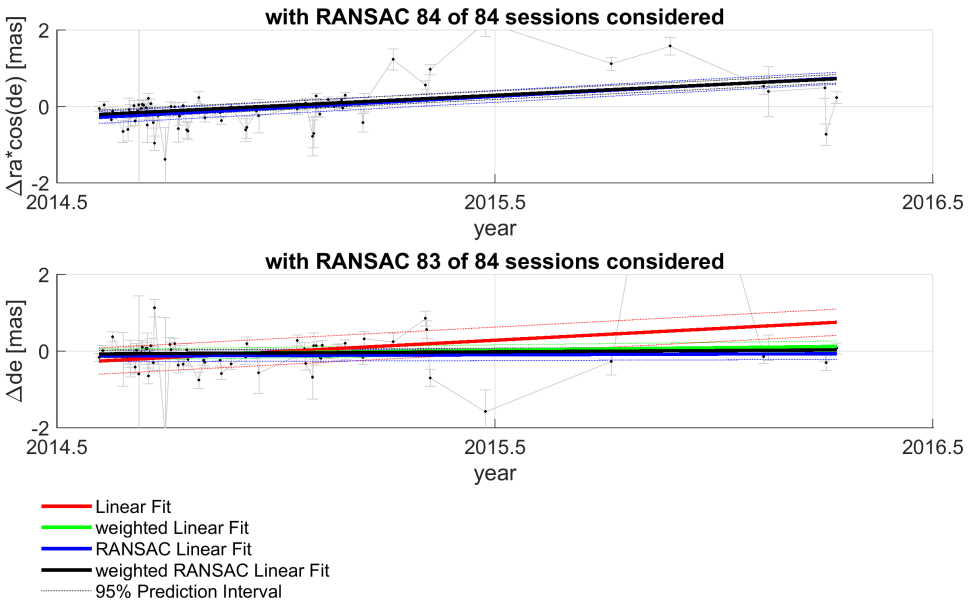

Figure 4.67 Source position time series (black dots, the errorbars describe the uncertainty of the position) and fitted position offsets and linear apparent proper motion for source 0454-463. The fitted models using least-squares adjustment or RANSAC are shown as solid lines. The number of available positions is 84. RANSAC excluded one declination coordinate as an outlier.

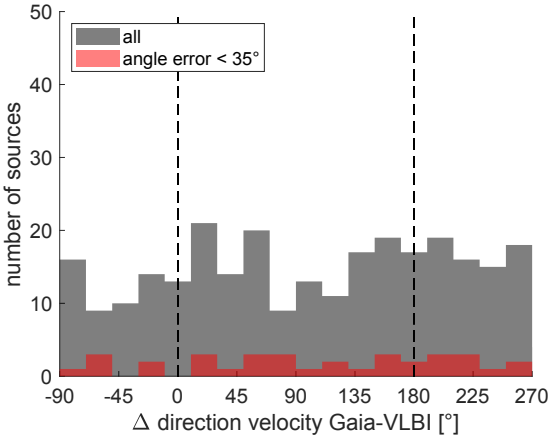

Figure 4.68 Comparison of the selected linear apparent proper motions for 275 AGN from Gaia DR2 and CRFGT based on the weighted RANSAC. For the 625 suitable sources for CRF7918 there is also no clear dependency.

5 Optically bright radio sources

The separate investigation of the alignment of the Gaia optically bright reference frame to the ICRF3 is necessary due to the technical design of Gaia and its internal calibration strategies presented in Sect. 2.3.2. This section documents efforts on the VLBI side to improve the determination of this alignment. The VLBI observations in this section are mainly based on the method of phase referencing relative to a radio-bright calibrator as introduced in Sect. 2.2.3, since the optically bright objects at radio frequencies are usually too faint to be detected in the absolute geodetic mode, as in the case for ICRF3. Only in Sect. 5.5 a few star positions from the absolute geodetic mode were also included. First, the homogenization of existing VLBI data from phase-referencing observations is addressed, which means that all star positions are preferably referenced to calibrator positions in ICRF3. Then, the impact of treating Galactocentric acceleration in the similar way for both Gaia data and VLBI data is examined. Suggestions for suitable new VLBI observations are made, and realized observations are discussed and evaluated in more detail. Since there are few counterparts between VLBI and Gaia for the optically bright data, no VSH, but only rotation parameters in terms of orientation offset and spin between the two catalogs are determined. The global pattern determined by VSH could anyway, in contrast to the evaluation of data from extragalactic objects, be dominated by larger systematic effects within the Galaxy such as Galactic rotation and shear effects (Gaia Collaboration et al. 2021b). The effects of the various steps on the analysis of the rotation parameters are shown, and possible future improvements are described. A discussion concludes this chapter.

5.1 Homogenization of existing data

If two reference frames should get aligned, all data of one catalog must be based on the same reference frame. Otherwise, an artificial bias can distort the results. The main goal of this work is to test the alignment of the Gaia catalog to ICRF3. However, star positions from the archive are usually given relative to a calibrator position in one of the predecessors of ICRF3 or even in CRFs which were not adopted conventionally, simply because the ICRF3 did not exist at the time of their analysis. Consequently, the principle of homogenization is quite simple: if the difference between the historical

calibrator position and the position of the same calibrator in ICRF3 is applied to the original star position, the updated star position is then also given in ICRF3. For this point tie no uncertainty is assumed.

The basis for the data treated in this section is the literature search of historic VLBI data from Table 1 in Lindegren (2020a). Most of these data are estimates of a model of stellar motion from time series of relative star positions. The model consists of a maximum of five astrometric parameters, position, proper motion, and parallax. Parallax and proper motion are in general not dependent on the CRF and therefore do not need to be homogenized. According to Lindegren (2020a), some of the star positions in his collection were already shifted to ICRF3. Thereby, the ICRF3 coordinates at epoch 2015.0 were employed, which means that the effect of Galactocentric acceleration was neglected in the context of his work (More on the handling of this topic in Sect. 5.2). Not all publications provided easy access to the required historical calibrator positions, thus, not all stars were referred to ICRF3. Therefore, in this work, emphasis was placed on homogenizing all star positions. This was accomplished using auxiliary data from online archives or metadata in the respective publications to find the historic calibrator positions.

"If not found in the publication or in a cited catalog, the positions from .vex files or, if missing, from the .crd files in the VLBA observing archive[1] were collected in order to obtain the calibrator positions most likely used. For some publications only the observed fields were given, but it was possible to connect each star to a field and then to identify the calibrator used by cross-referencing some of the tables in the respective publications. For one publication contradictory information was sorted out with the help of the main author.

The calibrator positions were not listed in all publications with a sufficient level of accuracy. Thus, some assumptions were made, and cross-checks with the VLBA observation archive, where metadata of the observation sessions are stored, were performed. We assume that if the calibrator positions would have been changed after the scheduling or .vex file creation, it would have been mentioned in the respective publication. All original calibrator positions were identified and the differences to the ICRF3 positions were determined. They are listed in Table 5.1 as α_{original} and δ_{original}. With this information, all star model positions were transformed to ICRF3 by applying the shifts Δ_α and Δ_δ between the original calibrator position and the ICRF3 S/X catalog position. The ICRF3 catalog position uncertainties were applied as calibrator position uncertainties $\sigma_{\alpha,\text{CRF}}$ or $\sigma_{\delta,\text{CRF}}$ to the star position uncertainties. All star positions thereby have a consistent error budget. For S Per, the calibrator position and uncertainty from the rfc_2018b catalog (Petrov 2018) were taken, as the calibrator is not present in ICRF3. It is indicated in Table 5.1. As shown in Lunz et al. (2019a), the rfc_2018b and ICRF3 S/X are aligned

[1] www.vlba.nrao.edu/astro/VOBS/astronomy/, accessed 10 July 2021.

Table 5.1 Subset of stars from Table 1 of Lindegren (2020a) along with the corresponding phase-referencing calibrators and the corrections to be applied in order to homogenize the dataset. Listed are only the stars which need homogenization.

Star	Phase-referencing calibrator			Shift to ICRF3 [mas]				Resource	Ref.
Name	Name	$\alpha_{original}$ [°]	$\delta_{original}$ [°]	$\Delta\alpha$	$\sigma_{\alpha,\mathrm{CRF}}$	$\Delta\delta$	$\sigma_{\delta,\mathrm{CRF}}$		
SY Scl	J0011 − 2612	2.755194738	−26.209271344	−0.0039	0.0382	+0.2940	0.0360	publication	1
S Per	J0222 + 5848[1]	35.639670150	+58.803873460	+1.9950	0.8600	+0.5850	1.0400	publication	2
UX Ari	J0329 + 2756	52.490289271	+27.937638614	+0.2220	0.1130	−0.2555	0.1108	publication	3
HD 283447	J0408 + 3032	62.084906562	+30.541802731	+0.0369	0.2728	−0.1985	0.4248	VLBA o. a.	4
V410 Tau	J0429 + 2724	67.470669867	+27.410521200	+0.0167	0.0411	+0.1813	0.0443	VLBA o. a.	5
V1023 Tau	J0429 + 2724	67.470669825	+27.410521189	−0.1333	0.0411	+0.1413	0.0443	VLBA o. a.	6
HD 283572	J0429 + 2724	67.470669825	+27.410521189	−0.1333	0.0411	+0.1413	0.0443	VLBA o. a.	6, 5
T Tau	J0428 + 1732	67.148473662	+17.539885553	−0.0353	0.1173	+0.4301	0.2328	publication	7
HD 283641	J0429 + 2724	67.470669867	+27.410521200	+0.0167	0.0411	+0.1813	0.0443	VLBA o. a.	5
V1110 Tau	J0435 + 2532	68.894095596	+25.549915803	−0.1518	0.1214	−1.6523	0.2062	VLBA o. a.	5
HD 282630	J0459 + 3106	74.887640446	+31.109524306	−0.6429	0.1211	−0.7672	0.1622	VLBA o. a.	5
T Lep	J0513 − 2159	78.454643017	−21.987803342	+0.0123	0.0748	+0.0920	0.1159	publication	8
V1961 Ori	J0529 − 0519	82.473056042	−5.328226883	−0.7522	0.1145	+0.1458	0.2271	publication	9
Brun 334	J0529 − 0519	82.473056042	−5.328226883	−0.7522	0.1145	+0.1458	0.2271	publication	9
V1321 Ori	J0529 − 0519	82.473056042	−5.328226883	−0.7522	0.1145	+0.1458	0.2271	publication	9
MT Ori	J0539 − 0514	84.999738300	−5.244806039	+0.8051	0.3541	−1.1310	0.7662	publication	9
V1046 Ori	J0539 − 0514	84.999738300	−5.244806039	+0.8051	0.3541	−1.1310	0.7662	publication	9
HD 37150	J0539 − 0514	84.999738300	−5.244806039	+0.8051	0.3541	−1.1310	0.7662	publication	9
TY C5346-538-1	J0542 − 0913	85.732822533	−9.225279611	−0.9450	0.1595	−1.0675	0.2860	publication	9
HD 290862	J0558 − 0055	89.684964417	−0.918589931	−1.8798	0.2988	+5.3974	0.4889	publication	9
[SSC75] M 78 11	J0558 − 0055	89.684964417	−0.918589931	−1.8798	0.2988	+5.3974	0.4889	publication	9
VY CMa	J0725 − 2640	111.351721250	−26.675744444	−0.9074	0.1500	−0.5828	0.3357	publication[2]	10
S Crt	J1147 − 0724	176.964808479	−7.411428081	+0.0022	0.0331	+0.0866	0.0364	publication	11
Haro 1-6	J1627 − 2426[3]	246.750025782	−24.444573598	−0.3121	0.1971	−2.0066	0.4999	VLBA o. a.	12
DoAr 51	J1627 − 2426[3]	246.750025782	−24.444573598	−0.3121	0.1971	−2.0066	0.4999	VLBA o. a.	12
W 40 IRS 5	J1826 + 0149	276.604421567	+1.827810811	+0.5072	0.0912	−0.5268	0.1718	VLBA o. a.	13
SS Cyg	J2136 + 4301	324.100026608	+43.028464750	+0.4542	0.1515	−0.5418	0.1450	VLBA o. a.	14
IM Peg	J2253 + 1608	343.490616401	+16.148211374	−0.0594	0.0340	+0.0665	0.0357	publication[4]	15
PZ Cas	J2339 + 6010	354.838021708	+60.169958056	+0.2008	0.1773	−0.5795	0.0864	publication	16

Notes. Right ascension $\alpha_{\mathrm{original}}$ and declination $\delta_{\mathrm{original}}$ were used in the original publications. The shift in right ascension $\Delta\alpha$ and declination $\Delta\delta$ has to be subtracted in order to match the ICRF3 coordinates. The variables $\sigma_{\alpha,\mathrm{CRF}}$ and $\sigma_{\delta,\mathrm{CRF}}$ are the uncertainties of the calibrator coordinates in ICRF3, to be applied as uncertainties for the star coordinates. The last two columns list the resource where the coordinates most likely used in the original publication were found, which can be the VLBA observation archive (VLBA o. a.) or the original publication, and the reference of the original publication. (1) Not in ICRF3. The position used is from rfc_2018b and is (α, δ) = (35.639 669 596° ± 0.86 mas, 58.803 873 297° ± 1.04 mas). (2) Correct position, obtained from correspondence with main author.(3) The position used is from the ICRF3 K band catalog. (4) Publication directs to ICRF2 which was therefore used as original position.

References. Nyu et al. (2011); (2) Asaki et al. (2010); (3) Peterson et al. (2011); (4) Torres et al. (2012); (5) Galli et al. (2018); (6) Torres et al. (2007); (7) Loinard et al. (2007); (8) Nakagawa et al. (2014); (9) Kounkel et al. (2017); (10) Zhang et al. (2012); (11) Nakagawa et al. (2008); (12) Ortiz-León et al. (2017b); (13) Ortiz-León et al. (2017a); (14) Miller-Jones et al. (2013); (15) Bartel et al. (2015); (16) Kusuno et al. (2013).

Note. According to Lunz et al. (2020a, Table 1).

within about 50 µas in orientation, which is acceptable at the current stage of analysis, considering the error level involved (see below). It is assumed that for the stars from references 3, 5, 14, and 17 in Table 1 of Lindegren (2020a) the model positions already were transformed to ICRF3, and the calibrator uncertainties from ICRF3 were applied, as stated in the publication. Furthermore, the two data entries for the star HD 283572 are based upon the same observational data but different calibration strategies (Galli et al. 2018), therefore they are highly correlated[2]"(Lunz et al. 2020a).

The error budget for these homogenized absolute star positions from models of stellar motion in ICRF3 is labeled $\sigma_{\text{model pos}}$. When utilizing these positions for comparison to an independent measurement system like Gaia, additional error budget items have to be considered in order to obtain realistic values. For the sake of brevity, the error budget of the absolute star positions in ICRF3 will be revised in more detail in the later Sect. 5.4.5. There, the error budget of the absolute star position from models of stellar motion and from single-epoch phase-referencing (as used in Sect. 5.4.4) will be directly compared. The reader is referred to that section for more information, but it should be revealed here that the upper limit of additional noise to $\sigma_{\text{model pos}}$ to obtain the realistic error budget for the absolute positions from models of stellar motion is 0.21 mas in $\alpha*$ and δ, respectively.

5.2 Impact of Galactocentric acceleration on phase-referencing results

While the homogenization of the underlying reference frame is only relevant for the calibrator positions and thus for the star positions, the global systematic effect of Galactocentric acceleration affects both the positions and the proper motions. Although the effect is tiny compared to the individual star proper motions, it affects all objects in a systematic way (see Eq. 3.63).

In Gaia DR2, it was not possible to determine this effect due to internal systematics of the Gaia DR2 dataset being well above its magnitude. In Gaia EDR3 however, the effect was found to be of magnitude $|D| = 5.05 \pm 0.35\,\mu\text{as}\,\text{yr}^{-1}$ towards ($\alpha_D = 269.1° \pm 5.1°, \delta_D = -31.6° \pm 4.1°$) derived from the proper motions of extragalactic compact objects (Gaia Collaboration et al. 2021b).

The star positions at various epochs from VLBI in Sect. 5.1 do not yet account for the Galactocentric acceleration because positions listed in the ICRF3 at epoch 2015.0 were used for the homogenization in all cases. In addition, the star proper motions, based on time series of relative positions from phase-referencing, need to be investigated. This is because at historic times the same (static) calibrator position was used for the fringe-fitting

[2]Both data entries were used for this work to be consistent with Lindegren (2020a).

to determine the position time series from phase-referencing, since the historical CRF did not take the effect of Galactocentric acceleration into account, which was only newly introduced into the CRF with ICRF3. Both the VLBI and Gaia datasets should include or not include this effect in all positions and proper motions to be consistent. In this work, the VLBI data is corrected to also include the effect of Galactocentric acceleration to be fully consistent with ICRF3 and thereby also with Gaia. The magnitude for the time-dependent correction in the shape of a dipole pattern is chosen to be $|D| = 5.8\,\mu\mathrm{as\,yr}^{-1}$ in the Galactocentric direction ($\alpha_D = 266.4°, \delta_D = -29.0°$) following the values employed in the creation of ICRF3. They are based on VLBI results from the IVS Working Group on Galactic Aberration (WG8), published in MacMillan et al. (2019). These results agree with the Gaia-based result within the error limits. However, to be fully consistent, the same values should be used in future data releases of the two measurement techniques.

"Considering this relation, the homogenized star positions in ICRF3 at epoch 2015.0 can be corrected for the effect of Galactocentic acceleration (see e.g., Titov et al. 2011; MacMillan et al. 2019) by

$$\begin{aligned}\Delta\alpha =& \Delta t \cdot (-D_1 \sin\alpha + D_2 \cos\alpha)/\cos\delta,\\ \Delta\delta =& \Delta t \cdot (-D_1 \cos\alpha \sin\delta - D_2 \sin\alpha \sin\delta + D_3 \cos\delta),\end{aligned} \tag{5.1}$$

where $D_1 = |D| \cdot \cos\delta_D \cos\alpha_D, D_2 = |D| \cdot \cos\delta_D \sin\alpha_D, D_3 = |D| \cdot \sin\delta_D$ and $\Delta t = t_B - 2015.0$, with t_B as the barycentric times of the barycentric star positions, and α and δ as the calibrator coordinates. The correction needs to be added to the star positions.

[...] The correction of

$$\begin{aligned}\Delta\mu_{\alpha*} =& -D_1 \sin\alpha + D_2 \cos\alpha,\\ \Delta\mu_\delta =& -D_1 \cos\alpha \sin\delta - D_2 \sin\alpha \sin\delta + D_3 \cos\delta,\end{aligned} \tag{5.2}$$

needs to be added to the star proper motions $\mu_{\alpha*}$ and μ_δ to correct for the time-varying calibrator coordinates that should have been used during the data processing with respect to ICRF3" (Lunz et al. 2021b).

The stars in this work are located at distances between about 23 pc for σ^2 CrB and 2 500 pc for PZ Cas. Therefore about three orders of magnitude larger systematic effects within the Galaxy such as Galactic rotation and shear effects dominate the evaluation of the Galactocentric acceleration (Gaia Collaboration et al. 2021b). Therefore, it is currently impossible to infer the Galactocentric acceleration effect from star proper motions using this method.

5.3 Proposals for new observations of radio stars

Analyses of Lindegren (2020a,b) showed that more observations of known radio stars and more optically bright counterparts are necessary to improve the determination of the alignment between VLBI and Gaia. For this reason, three types of proposals have been worked out in Lunz et al. (2020b) that can be observed from theVLBA, located in the U.S. It is an excellent antenna network for high-precision radio interferometry of objects that are generally expected to be weak at radio frequencies and it is strongly interconnected with the IVS antenna network. Together, they provide the main data for ICRF3 S/X. This section reflects the findings from Lunz et al. (2020b).

The detection limit for possible counterparts was intended to be 1 mJy at X-band and 0.45 mJy at C-band. The C-band should only be used if suitable historical observations have also been made at C-band. The star positions at C-band are potentially differently connected to the ICRF3 S/X than observations at X-band. However, due to the expected error budget for absolute star positions from phase-referencing, a consistent frequency band for the absolute positions of all stars was judged to be secondary to the consistency of the more precise relative positions of one star. Thus, systematic errors that could be attributed to a possible frequency-dependent position of the calibrator could be excluded when determining the proper motion from time series of relative positions. The detection limit was chosen to represent a compromise between observation time with the VLBA and good astrometric results. It was determined based on results from the relevant literature, where the instrument was used in a similar way as in this work.

All stars for the proposed observations lie within the declination limit of the VLBA and are optically brighter than $G = 13$ mag, as is required for the Gaia bright frame. In Fig. 5.1, the sky coverage for the different proposals is shown, and the corresponding brightness histograms are presented in Fig. 5.2. Unless otherwise stated, the selected stars have a fully valid 5-parameter solution in Gaia DR2. Moreover, as indicated by the RUWE parameter (re-normalized unit weight error calculated from Gaia DR2 data, Lindegren et al. 2018) smaller than 1.4, which means that they are not resolved as binary stars in Gaia DR2 and they show a good fit to a single star model from these data. The final main criterion for all proposals is that the stars were selected to provide good sky coverage, i.e. in areas with many stars, only the brightest ones were selected.

Proposal A: Re-observation of already known radio stars

Re-observing radio stars that have been previously observed with VLBI not only has the advantage of obtaining improved proper motions and parallaxes for them, but also provides the opportunity to determine their VLBI positions during Gaia's observing pe-

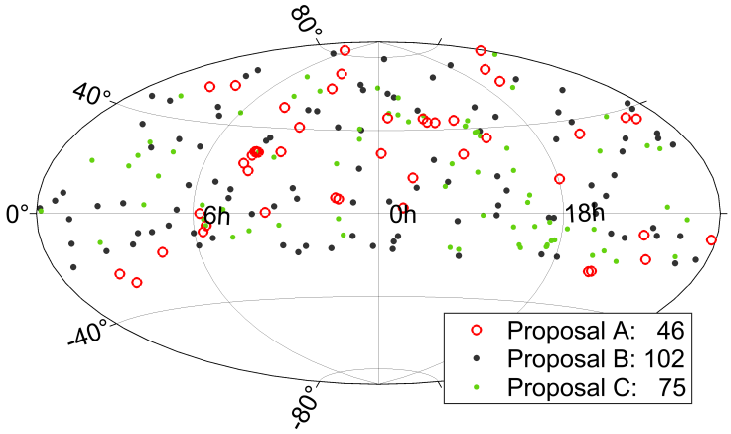

Figure 5.1 Stars selected for observations with color-coding according to the type of proposal.
Note. According to Lunz et al. (2020b, Fig. 1). Reproduced with permission from C. Bizouard.

riod. This is achieved with little investment of new observing time and the probability of successful detection is high. Compared to extragalactic radio sources normally used for geodetic VLBI, optically bright stars are highly variable and faint at radio frequencies. In this work, the emphasis is on continuum observations, so stars detected by spectral line observations only are excluded. Suitable spectral types for the link between optical and radio frequencies are main sequence stars with two exceptions. First, O and B type stars, because of the higher probability of radio-optical shifts due to stellar winds and complex structures, and second, M and L type stars due to the higher probability of resolved binaries in VLBI observations (Lindegren, L., June 2019, private communication). Therefore, 40 candidate radio stars which were detected in continuum mode in Benaglia

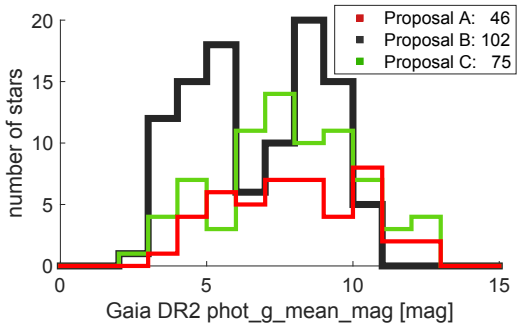

Figure 5.2 Histogram of G-magnitude of the stars selected for the observations.
Note. According to Lunz et al. (2020b, Fig. 2). Reproduced with permission from C. Bizouard.

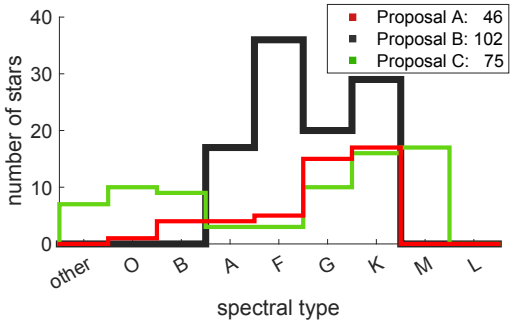

Figure 5.3 Histogram of the spectral types of the stars selected for the observations. For proposal C, a stricter selection for the most suitable spectral types would be possible.
Note. According to Lunz et al. (2020b, Fig. 3). Reproduced with permission from C. Bizouard.

(2010), were rejected because they are of O or B type. As recommended by Lindegren (2020a), Mira-type stars and red supergiants are also not selected. The spectral class information was taken from the SIMBAD database (Wenger et al. 2000).

As described in Lunz et al. (2020b), the final selection of 46 stars includes:

- 17 stars from the list of recommended candidates for Gaia-VLBI link in (Lindegren 2020a). Four of them are of spectral type O or B, but they were exceptionally selected because they fit well into a single-star model and therefore higher priority was given to the valuable longer data set available when combining the new data with data from the archive. One of the 17 stars (DoAr 51, also known as V2248 Oph) shows a small discrepancy between VLBI and Gaia as determined from its low RUWE parameter, but is known to be a triple star system. Further monitoring will help to improve the study of the VLBI and Gaia offsets for this object.
- Four other stars in Lindegren (2020a) were selected with a view of future Gaia DRs, where orbital parameters for some objects may also be available, and verification of these orbits by VLBI, namely T Tau, HD 283447, UX Ari and σ^2 CrB. They are likely to have a binary companion indicated by their high RUWE values and thus it is likely that along with VLBI positions from the archive, orbital parameters can also be estimated from VLBI.
- Two other stars, namely CoKu HP Tau G2 and bet Per, were selected from the Xu et al. (2019b) list, which are not in Lindegren (2020a). The star bet Per is the only one of the eleven link stars for the Hipparcos mission not yet in the selected sample, since a complete astrometry solution was not available for this star in Gaia DR2. The exception was made because it is likely that if the star was detected by Hipparcos, it would also be well observed by Gaia[3]. Moreover, it would then be possible in future Gaia DRs to perform tests on the same stars used for Hipparcos comparisons. Also for this star, new observations together with the positions from the 1980s and 1990s would give a long position time series. Searching for other possible stars for the Gaia-VLBI connection that have an extensive VLBI observing history and have been discovered by Gaia, but for which a complete astrometric solution is not yet available will remain a future task. Star CoKu HP Tau G2 was chosen because it fulfills all selection criteria and does not have any other stars nearby.
- Boboltz et al. (2003) and Boboltz et al. (2007) performed phase-referenced continuum observations at X-band of 52 radio stars for the Hipparcos CRF link using the VLA and Pie Town telescopes. With the same selection approach, 23 suitable stars for the Gaia-VLBI link were found.

[3]Later investigations revealed that the star is simply too bright for Gaia.

Proposal B: Detection of nearby stars

The second proposal aims to increase the number of radio-optical counterparts to improve their sky distribution. Optically bright stars included in both the Hipparcos and Gaia DR2 catalogs were selected in terms of having a reasonable chance of accurate Gaia data at a later phase of the mission. Stars identified by Hipparcos as double or multiple star systems were excluded, and SIMBAD data were used to filter for main sequence stars that have suitable spectral types. Based on the inverse square law, the nearest stars are assumed to be the brightest. The nearest stars thus are the preferred observables if new detections at radio frequencies are to be more likely. Therefore, the distance requirement was set to less than 20 pc from Earth. The final selection consists of 102 stars that, to our knowledge, have not yet been observed with VLBI. The data set was selected to achieve uniform sky coverage in terms of geometry, using equal area grids (Malkin 2016b,a). In addition, stars with spectral types from SIMBAD that were most suitable for alignment were preferred in each grid cell. The distribution of the latter is shown in Fig. 5.3.

Proposal C: VLBI-observation of previously detected stars

The third proposal targets the re-observation of stars that have been previously detected by continuum radio observations. The Wendker (2015) catalog, a collection of radio detections up to the late 1990s, was utilized to find promising objects for successful re-observation with the VLBA. The selected stars must be listed with a minimum flux density of 0.5 mJy in a frequency range from 1 to 100 GHz. It is assumed that the continuum emission does not vary substantially over a wide frequency range. Because it is expected that the stellar brightness variations can be large, a lower detection limit than targeted for the VLBA observations was chosen to not exclude any stars prematurely. In total 75 stars were selected. No further filtering was done for suitable spectral classes, as seen in Fig. 5.3, because a higher priority was given to non-binarity and the higher number of possible new counterparts. A more stringent selection is however possible. As to the authors' knowledge, the objects have not been observed in phase-referencing mode before and are therefore not included in the selection of proposal A.

5.4 New observations of radio stars

Proposal A was prioritized for realization in this work because the probability for successful detection is higher for known radio stars than for stars that have not yet been observed by VLBI. The observations were designed as a survey to determine the peak intensities of candidate stars with the VLBA. The star positions were determined whenever possible

and used for the subsequent analyses. This section describes the selection of suitable calibrators for phase-referencing, the observation setup, and the data analysis. Furthermore, the determined peak intensities and star positions are reported. The error budget for these absolute star positions obtained at a single observation epoch is compared in detail to the error budget of absolute star positions from models of stellar motion (see Sect. 5.1), where both types of position are based on continuum phase-referencing observations.

5.4.1 Calibrator selection

Table 5.2 Calibrators, observation setup and metadata for the 46 radio stars observed with the VLBA.

			Phase-referencing calibrator		Secondary calibrator				
Star	Type	Gaia DR2 match	$P1$	$P2$	$S1$	$S2$	Exp	Freq	Ref.
UV Psc	bL*	2576772264960362112	J0121+0422	...	J0110+0714	J0105+0600	A, C	X	1
HD 8357	XB*	2566277181659646208	J0121+0422	...	J0110+0714	J0130+0842	A, C	X	1
LS I +61 303	HXB	465645515129855872	J0244+6228	...	J0306+6243	...	A, C	X	2, 3
RZ Cas	Al*	541801332594262912	J0243+7120	...	J0319+6949	...	A, C	X	1
bet Per	Al*	239863001382455424	J0313+4120	...	J0310+3814	...	A	X	2, 3
UX Ari	RS*	1189860602778361 60	J0316+2733[1]	J0329+2756	...	...	A	X	2, 3
HD 22468[2]	RS*	3263936692671872384	J0339−0146	...	J0337+0137	...	A	X	2, 3
HD 283447	TT*	163184366130809984	J0408+3032	J0403+2600	J0421+2606[1]	...	A	C	4
B Per	SB*	270632486391536512	J0359+5057	...	J0413+5250	...	A	X	1
V410 Tau	TT*	164518589131083136	J0429+2724	...	J0421+2606[1]	J0433+2905	A	C	5, 3
HD 283572	TT*	164536250037820160	J0429+2724	...	J0421+2606[1]	J0433+2905	A	X	6
T Tau Sb	TT*	48192969034959232	J0428+1732	...	J0423+2108	...	A	C	7, 3
HD 283641	TT*	152104381299305600	J0429+2724	...	J0421+2606[1]	J0433+2905	A	C	5, 3
CoKu HP Tau G2	TT*	145213192171159552	J0438+2153	J0426+2350	...	...	A	C	8
V1961 Ori	Or*	3209424108758593408	J0529-0519	...	J0541−0541	...	A	C	9, 3
Brun 334	pr*	3017270879709003520	J0529−0519	...	J0541−0541	...	A	C	9, 3
TYC 5346-538-1	Star	3015742318025842944	J0542−0913	...	J0541−0541	...	A	C	9, 3
HD 290862	Star	3219148872492984192	J0541−0211[1]	...	J0552+0313	...	A	C	9, 3
SV Cam	Al*	1143477013259041920	J0626+8202	...	J0637+8125	...	A, B	X	1
R CMa	Al*	3030977013710528768	J0721−1530	...	J0725−1904	...	A, B	X	1
54 Cam	RS*	1081565094046074624	J0811+5714	...	J0752+5808	...	B	X	1
TY Pyx	RS*	5648046341168575616	J0900−2808	...	J0854−2540	...	B	X	1
XY UMa	RS*	1023682919309621632	J0902+5402	...	J0903+5151	...	B	X	1
IL Hya	RS*	5674681804189819648	J0923−2135	...	J0921−2618	...	B	X	1
HU Vir	RS*	3582095053777917952	J1216−1033	...	J1204−0710	...	B	X	1
DK Dra	RS*	1690218825255945216	J1220+7105	...	J1243+7442	...	B	X	1
RS CVn	Al*	1474194339773131648	J1308+3546	...	J1317+3425	...	B	X	1
BH CVn	RS*	1475118788534734592	J1324+3622	J1340+3754	J1322+3912	...	B	X	2, 3
RV Lib	RS*	6285122413593372032	J1436−1846	...	J1432−1801	...	B	X	1
del Lib	Al*	6332277920392457472	J1510−0843[1]	J1456−0617	J1512−0905	...	B, C	X	1
AG Dra	Sy*	1642955252784454144	J1623+6624	...	J1604+6722[1]	...	B, C	X	1
σ^2 CrB	RS*	1328866562170960512	J1613+3412	...	J1558+3323	...	B, C	X	2, 3
Haro 1-6	TT*	6049142032584969088	J1633−2557	...	J1625−2527	...	C	C	10, 3
DoAr 51	TT*	6047570826172040960	J1633−2557	...	J1625−2527	...	C	C	10, 3
WW Dra	RS*	1624551008683167616	J1635+5955	...	J1645+6330	...	C	X	1

Table 5.2 continued.

Star	Type	Gaia DR2 match	Phase-referencing calibrator $P1$	$P2$	Secondary calibrator $S1$	$S2$	Exp	Freq	Ref.
Z Her	RS*	4501439984674494080	J1756+1535	...	J1758+1429	...	C	X	1
HD 226868	HXB	2059383668236814720	J1953+3537	...	J1957+3338	...	C	X	2, 3
HD 199178	Ro*	2162964329341318656	J2102+4702	...	J2114+4634	...	C	X	2, 3
ER Vul	Ae*	1845206534070618624	J2114+2832	...	J2105+2920[1]	...	C	X	1
SS Cyg	DN*	1972957892448494592	J2136+4301	...	J2153+4322	...	C	X	11
RT Lac	RS*	1961028607902617216	J2153+4322	J2202+4216	J2207+4316[1]	...	C	X	1
AR Lac	RS*	1962909425622345728	J2153+4322	J2202+4216	J2207+4316[1]	...	C	X	2, 3
IM Peg	RS*	2829193299742131328	J2253+1608	...	J2253+1942	...	C	X	2, 3
SZ Psc	RS*	2658507622907361536	J2311+0205	J2320+0513	...	...	C	X	1
lam And	RS*	1939115478596951296	J2322+4445	...	J2354+4553	...	C	X	1
HD 224085	RS*	2855095251072482432	J2347+2719	...	J2352+3030	...	C	X	1

Notes. The columns indicate the star names and types as listed in the SIMBAD database (Wenger et al. 2000), their *Gaia* DR2 match and the respective calibrators that were observed. In order to be able to distinguish the calibrators better in the further work, they were also assigned variables – $P1$, $P2$, $S1$, and $S2$. For each star, the experiment(s) (see Table 5.3), the frequency band, and the literature reference for a priori positional data used for scheduling are given as well. In case that two literature references are given, the first one describes the original data and the second one points to improved data as given in the respective reference. In this case the improved data were used. An ellipsis (...) indicates the omission of an entry. [(1)] Not in ICRF3. The position in rfc_2018b (given in the format of (α, δ)) is (49.120 883 046°±0.36 mas, 27.552 263 194°±0.45 mas) for J0316+2733, (65.263 952 933°±0.37 mas, 26.110 132 133°±0.48 mas) for J0421+2606, (85.340 401 167°±0.15 mas, −2.185 662 947°±0.29 mas) for J0541-0211, (227.727 671 113°±0.21 mas, −8.722 588 583°±0.46 mas) for J1510-0843, (241.192 478 767°±1.96 mas, 67.371 391 931°±0.66 mas) for J1604+6722, (316.431 623 725°±0.67 mas, 29.347 996 394°±0.77 mas) for J2105+2920, (331.789 686 825°±0.23 mas, 43.274 276 806°±0.28 mas) for J2207+4316.
[(2)] Also known as HR 1099.
References. (1) Boboltz et al. (2007); (2) Lestrade et al. (1999); (3) Lindegren (2020a); (4) Torres et al. (2012); (5) Galli et al. (2018); (6) Torres et al. (2007); (7) Loinard et al. (2007); (8) Torres et al. (2009); (9) Kounkel et al. (2017); (10) Ortiz-León et al. (2017b); (11) Miller-Jones et al. (2013).
Note. According to Lunz et al. (2020a, Table 2).

For the 46 stars in Proposal A, phase-referencing calibrators P were selected that are located near the target star, are compact in their structure, and are radio-bright. The NRAO VLBA calibrator search tool[4], the RFC calibrator search tool[5], and the Astrogeo VLBI FITS image database[6] were used for this purpose. Several criteria were considered for the identification of suitable calibrators, as suggested by the 'Guide to Proposing for the VLBA (and HSA/Global VLBI)'[7]. Phase calibrators were selected that were

- bright enough to be detected with an SNR suitable for self-calibration. This thresh-

[4] www.vlba.nrao.edu/astro/calib/, accessed 20 October 2021.
[5] astrogeo.org/calib/search.html, accessed 20 October 2021.
[6] astrogeo.org/vlbi_images/, accessed 20 October 2021.
[7] https://science.nrao.edu/facilities/vlba/docs/manuals/propvlba/calibration-considerations, accessed 20 October 2021.

old is determined by looking up the baseline sensitivity of the VLBA, which is given for a fringe-fit interval of 2 minutes, and the 2 Gbps recording rate for continuum observations in Table 3 of the VLBA Observational Status Summary 2020A[8], which was the current state of information at the time the observations in this work were planned. The values are 1.2 mJy in X-band and 0.7 mJy in C-band. The SNR in geodetic VLBI is usually set to about 20. The scan length is chosen to be 30 seconds. Therefore, the minimum flux density for a calibrator in X-band is determined to be $\left(1.2\,\mathrm{mJy} \cdot \sqrt{2\,\mathrm{min}/30\,\mathrm{s}} \cdot 20\right)/\sqrt{6} = 20\,\mathrm{mJy}$, where 6 is the number of baselines per antenna, assuming not all antennas in the VLBA were observing mutually. The respective value for C-band is 11.5 mJy. Accounting for changing source structure and other time-dependent variables, the values were multiplied by a factor of 1.5, and to secure detections (because the whole star observation would otherwise be lost) the values were doubled. The resulting limit for unresolved flux density was set to 60 mJy at X-band and 34 mJy at C-band for the calibrators. Only calibrators with expected values greater than this threshold and reasonably large correlated flux density values on the long baselines were considered. This is to ensure that the radio source is visible even on the longest baseline, which is necessary in order to achieve the desired resolution.

- closest to the target star. It is preferred to select calibrators that are closer to the target but fainter than using a calibrator that is brighter but further away. As shown by Martí-Vidal et al. (2010, 2011) and Peterson et al. (2011) the atmospheric difference between the two objects is limiting the dynamic range, which is inversely proportional to the sine of their position offset. Similar behavior is shown for the peak flux densities of the targets. In general, the calibrators should not be more than 2° to 3° away from the target star, with a maximum of 5°.
- listed with a CRF catalog position uncertainty of less than 10 mas and better less than 1 mas, where the lowest uncertainties are preferred (Reid and Honma 2014).

Furthermore, known radio bright and compact calibrators on the order of 10 Jy are needed for fringe-finding to calibrate the phases and delays, and for bandpass calibration of the data channels. For both calibration purposes, the same radio source and scan can be utilized. Radio sources J0927+3902, J2253+1608, J0359+5057, and J1927+7358 were selected as calibrators for the different patches of the sky.

Atmospheric calibration is performed using geodetic blocks, for each of which on the order of 15 calibrators are randomly selected from a pool of suitable geodetic point sources distributed across the sky to sample the atmosphere.

[8] https://science.nrao.edu/facilities/vlba/docs/manuals/oss2020A/referencemanual-all-pages, accessed 20 October 2021.

Also, in addition to the primary calibrators, secondary calibrators S can be picked for each target star. With their supplementary observations, residual phase gradients can be removed during data processing. In selecting appropriate secondary calibrators for each star, the recommendations on the geometrical arrangement of the secondary calibrators with respect to the phase calibrator and the star in Fomalont and Kogan (2005) were followed. Occasionally, however, suitable calibrators were not available, so no secondary calibrator could be chosen.

As described in Lunz et al. (2020a), both phase calibrators $P1$ and secondary calibrators $S1$, $S2$ were selected, preferring calibrators already used in previous observations from the literature. If the calibrator is compact, its position from phase-referencing best matches the ICRF3 catalog position. Using the CARMS values of Xu et al. (2019a) (basic-noise weighting), the compactness of the primary calibrators was evaluated. If the calibrator $P2$ chosen in the older historical observations had significant structure, another, more compact, but then often weaker calibrator $P1$ was chosen as the alternative to be tested (except for del Lib where both calibrators $P1$ and $P2$ were newly selected). The groups of stars, calibrators and the references can be found in Table 5.2.

Some of the calibrators are not part of ICRF3 S/X, and therefore the coordinates had to be taken from a different resource. The coordinates from rfc_2018b CRF were chosen as was done for the homogenized data in Sect. 5.1.

5.4.2 Observations and data analysis

The observations were designed to detect stars brighter than about 1 mJy. A valid detection is achieved if the dynamic range, which is the ratio between peak intensity and the RMS noise of the image, is larger 5. For determination of the required on-source time to achieve this goal with the VLBA, the image sensitivity of the network is needed. It is taken from the EVN sensitivity calculator[9], and the required on-source time is determined to be 5 minutes for a recording rate of 2 Gbps assuming the longest baseline of the VLBA is available. Then, the detection limit is 1 mJy in X-band and 0.45 mJy in C-band. Shortly before the planned observations, it was possible to double the recording rate due to new Mark 6 recorders, and thereby to achieve an increase in sensitivity by a factor of $\sqrt{2}$.

The content of the following two paragraphs is essentially based on the information given in (Lunz et al. 2020a). In order to observe all stars within only 14 hours of VLBA time and still achieve sufficient uv-coverage, the schedule was divided into three experiments spanning over various blocks of Local Sidereal Time (LST) as seen in Table 5.3. Each star was observed three times, with the antennas pointing at the primary calibrator for 30 s, at

[9] http://old.evlbi.org/cgi-bin/EVNcalc, accessed 20 October 2021.

the target star for 100 s and at the primary calibrator again for 30 s. Criteria for scheduling in this nodding-style are described in Wrobel et al. (2000). Since the calibrators were manually scheduled with a fixed scan duration of 30 s per scan, some may be observed with a higher SNR value than the desired value of about 20. The time intervals were chosen considering the degradation of quality of the results with the size of the target-calibrator separations, as published in Martí-Vidal et al. (2010, 2011), and not to lose phase-coherence between the scans of the primary calibrator at the given frequencies for typical weather. Furthermore, elevations below 10° were neglected (Ulvestad 1999; Beasley et al. 1994). The three observing blocks for each star were distributed over one or two of the three experiments, as documented in Table 5.2. The time difference between first and last scan was adapted to prevent any significant smearing effects in case of known high proper motion. This was the case for star HD 224085, which has a proper motion of approximately 577 mas yr^{-1} according to literature, and with the time interval set to 23 minutes, the smearing effect is limited to 25 µas. No jitter due to high-frequency orbital motion of a star was considered. "In one of the blocks, the secondary calibrators were observed with one 30 s scan between the respective target and primary calibrator scans. Within an experiment, frequency setups were depending on the observed star. The center frequencies were 8.11225 GHz for observations at X-band and 4.61175 GHz for C-band. Four subbands with a bandwidth of 128 MHz each were used. Dual-polarization observations were recorded with a total data rate of 4 Gbit s^{-1}. With this setup, stars fainter than 1 mJy beam^{-1} can be detected" (Lunz et al. 2020a).

Table 5.3 Date and time of experiments.

Exp	Date	Start (UTC)	End (UTC)
UL005B (B)	06 January 2020	09:40:41	13:35:10
UL005C (C)	06 January 2020	16:54:30	21:48:40
UL005A (A)	07 January 2020	01:08:09	06:06:27

Note. According to Lunz et al. (2020a, Table 3).

The bandpass calibrators and fringe finders were scheduled for each experiment in two 3 minute scans per frequency setting, one near the beginning and one near the end of the experiment. In experiment UL005A the calibrator was J0359+5057, in experiment UL005B it was J0927+3902, in experiment UL005C it was J2253+1608 at X-band, and J1927+7358 at C-band. At the end of the first third and the second third of each experiment, two geodetic blocks of 30 minute duration each were recorded. These consist of observations to bright radio sources at various elevations to enable atmospheric corrections in the data processing using group delays as specified by Mioduszewski (2009). The recorded data were correlated at the VLBA correlator in Socorro, New Mexico (USA).

The data were processed with the help of the NRAO Astronomical Image Processing Sys-

tem (AIPS; Greisen 2003) as described in the AIPS cookbook[10] and by using ParselTongue (Kettenis et al. 2006). Detailed information on the general data calibration, including the use of the different calibrator observations, can be found in the appendix A.

After the general data calibration, several processing steps are needed to determine peak intensities, absolute star positions, and star positions relative to the corresponding primary calibrator.

- The primary calibrator was assumed to be a point source during the fringe fit, as it was done for geodetic VLBI analysis that was used for the creation of the ICRF3. In this way it was attempted to best connect the phase-referenced positions of the stars to the absolute positions of the primary calibrators from ICRF3. "The ICRF3 calibrator positions are in general neither referring to the core nor to the jet. Therefore, we won't be able to correct the calibrator source structure sufficiently because [...][it cannot be assumed that] the ICRF3 position is in the core (or in the jet). Moreover, without correcting calibrator source structure, the derived position of a star would refer to a point somewhere between the core and the jet of the calibrator, as in the case of the ICRF3 positions" (Lunz et al. 2021b). The position differences between the primary calibrator and the star from this method were added to the calibrator positions to derive the 'absolute star positions' at a single epoch. Here, self-calibration was dispensed with in order not to falsify the reference to the calibrator position. For the determination of the peak intensities, these primary calibrator data were used for self-calibration (see appendix A) to derive a CLEANed image (Högbom 1974; Clark 1980) with a high dynamic range. The clean component model of the source, which describes its source structure as seen from the observations, was created in the process of constructing the self-calibrated CLEANed image. It was used in the second type of fringe fitting as described below.
- A clean component model was applied for the primary calibrator during the fringe fit in order to model its source structure. The clean component model was derived from self-calibration of the primary calibrator data (from a fringe fit with a point source model applied). Following this method, the 'relative star positions' were derived, which were inserted in the adjustment of models of stellar motion from VLBI position time series. Compared to the fringe fitting on a point source calibrator model, this method eliminates any scatter in the relative position time series due to the source structure of the primary calibrator. "This re-analysis allows the best connection to positions from other studies, where the same procedure was applied. [...] As long as the common feature within the images of the calibrator is used as reference, there is no need to involve the ICRF3 at all and there is no need to define which feature was used as reference" (Lunz et al. 2021b).

[10] www.aips.nrao.edu/CookHTML/CookBook.html, accessed 20 October 2020.

For each star, one calibrated data set was derived for each of the above fringe fitting methods. If a star was observed relative to two different primary calibrators $P1$ and $P2$, the file per fringe fitting method was derived for each calibrator separately, e.g., one file referencing the star's data to the first primary calibrator $P1$ and another file referencing the star's data to the second primary calibrator $P2$. These data were used in the following Sects. 5.4.3 and 5.4.4.

5.4.3 Peak intensities

For the determination of peak intensities in the radio source images, the data from the fringe fit with the point source model of the primary calibrator used were employed, and various self-calibrations were performed. From these data final clean images were derived, which have a high-dynamic range due to the self-calibration of the phases and amplitudes. What is even more important is that due to the self-calibration, the phase-coherence of the stars is improved and the accuracy of the peak intensity measurement is increased. However, due to the self-calibration, the absolute position information of the calibrator and thus also of the stars is lost.

The peak intensities PI of the radio emission in the images of all objects were determined (using task JMFIT in AIPS). A separate run was conducted in case multiple centers of radio emission were visible. Radio source J1456−0617 was used as the final phase-referencing calibrator for the star del Lib because it had more valid fringes than the observations of radio source J1510−0843 (Lunz et al. 2020a). J1510−0843 is also not in ICRF3 catalog. The PI of the detected stars and their calibrators are given in Table 5.4. Some of the stars were observed by VLBI (VLBA) for the first time. Also provided are the dynamic ranges DR for the images of the stars, which are obtained by dividing the PI by the RMS of the image residuals. According to Lunz et al. (2020a), 32 out of the 46 observed stars were detected, which means they had a DR $\geq 5\,\sigma$ of the image noise level. The non-detected stars were HD 283641, V1961 Ori, HD 290862, R CMa, XY UMa, RV Lib, AG Dra, WW Dra, HD 226868, ER Vul, RT Lac, lam And, Z Her, and TY Pyx. The sky distribution of the observed and detected stars is shown in Fig. 5.7.

"The mean (median) peak intensity for the detected target stars is 11 (1.5) mJy beam^{-1}. Their mean (median) standard deviations σ_{PI}, which represent the RMS noise of the images, are 0.17 (0.09) mJy beam^{-1}. Dynamic ranges DR vary from 5.5 for star SV Cam to 349.6 for SZ Psc." (Lunz et al. 2020a) If a star is that bright, theoretically no other calibrators are needed to detect it and it could be observed by geodetic VLBI using group delays. However, it is known that the emission of stars can be very variable at radio frequencies (Hjellming and Wade 1971).

Three of the detected stars (HD 283447, DoAr 51, and UX Ari) are close binary star sys-

Table 5.4 Peak intensities for the 32 detected stars and their respective calibrators, determined from the January 2020 observations.

Star	PI	σ_{PI}	DR	$P1$	PI	σ_{PI}	$P2$	PI	σ_{PI}	$S1$	PI	σ_{PI}	$S2$	PI	σ_{PI}
UV Psc	0.62	0.08	7	J0121+0422	807.58	0.61	...	...	...	J0110+0714	67.72	0.20	J0105+0600	116.37	0.33
HD 8357	0.85	0.09	9	J0121+0422	807.58	0.61	...	...	...	J0110+0714	67.72	0.20	J0130+0842	230.50	0.55
LS I +61 303	8.47	0.13	64	J0244+6228	260.92	0.14	...	...	...	J0306+6243	147.06	0.46	...	...	...
RZ Cas	1.29	0.09	14	J0243+7120	71.22	0.06	...	...	...	J0319+6949	154.53	0.54	...	...	...
bet Per	2.16	0.10	23	J0313+4120	573.17	0.39	...	...	...	J0310+3814	367.41	0.94	...	...	...
UX Ari	10.00	0.14	72	J0316+2733	176.58	0.14	J0329+2756	194.00	0.84	...	...	...	...	...	...
HD 22468	57.99	1.36	43	J0339−0146	541.15	0.09	...	...	...	J0337+0137	26.67	0.22	...	...	...
HD 283447 Ab	1.74	0.07	23	J0408+3032	138.46	0.14	J0403+2600	597.28	3.51	J0421+2606	43.85	0.13	...	...	...
HD 283447 Aa	1.54	0.07	21												
B Per	0.95	0.09	11	J0359+5057	5586.50	7.69	...	...	...	J0413+5250	80.94	0.37	...	...	...
V410 Tau	1.66	0.06	27	J0429+2724	224.89	0.16	...	...	...	J0421+2606	43.85	0.13	J0433+2905	95.94	0.22
HD 283572	1.30	0.09	14	J0429+2724	126.58	0.09	...	...	...	J0421+2606	80.94	0.37	J0433+2905	71.08	0.09
T Tau N	2.31	0.06	41	J0428+1732	159.75	0.16	...	...	...	J0423+2108	137.31	0.44	...	...	...
CoKu HP Tau G2	1.25	0.05	24	J0438+2153	119.40	0.13	J0426+2350	190.85	19.09	...	...	...	...	...	...
Brun 334	6.90	0.13	55	J0529−0519	132.23	0.14	...	...	...	J0541−0541	462.99	0.94	...	...	...
TYC 5346-538-1	0.53	0.06	9	J0542−0913	242.02	0.18	...	...	...	J0541−0541	462.99	0.94	...	...	...
SV Cam	0.45	0.08	5	J0626+8202	639.00	0.70	...	...	...	J0637+8125	37.51	0.20	...	...	...
54 Cam	1.48	0.08	19	J0811+5714	341.35	0.25	...	...	...	J0752+5808	31.63	0.14	...	...	...
IL Hya	1.24	0.11	12	J0923−2135	171.68	0.25	...	...	...	J0921−2618	918.36	6.25	...	...	...
HU Vir	1.33	0.09	15	J1216−1033	178.52	0.14	...	...	...	J1204−0710	95.84	0.69	...	...	...
DK Dra	3.62	0.09	40	J1220+7105	315.64	0.13	...	...	...	J1243+7442	248.67	0.58	...	...	...
RS CVn	1.52	0.08	20	J1308+3546	693.90	0.65	...	...	...	J1317+3425	289.24	0.23	...	...	...
BH CVn	3.96	0.10	38	J1324+3622	62.61	0.07	J1340+3754	52.36	0.02	J1322+3912	89.55	0.23	...	...	...
del Lib	0.75	0.09	8	J1456−0617	75.14	0.06	J1510−0843	288.43	1.47	J1512−0905	1686.30	1.66	...	...	...
σ^2 CrB	9.45	0.20	48	J1613+3412	2917.40	1.27	...	...	...	J1558+3323	111.30	0.17	...	...	...
Haro 1-6	4.23	0.15	29	J1633−2557	176.83	0.07	...	...	...	J1625−2527	692.65	0.69	...	...	...
DoAr 51 Aa	1.08	0.07	16	J1633−2557	176.83	0.07	...	...	...	J1625−2527	692.65	0.69	...	...	...
DoAr 51 Ab	1.06	0.07	15												
HD 199178	51.90	0.89	58	J2102+4702	121.17	0.09	...	...	...	J2114+4634	134.96	0.29	...	...	...
SS Cyg	0.83	0.11	8	J2136+4301	165.23	0.10	...	...	...	J2153+4322	213.60	0.12	...	...	...
AR Lac	1.24	0.09	14	J2153+4322	213.60	0.12	J2202+4216	1462.50	5.33	J2207+4316	55.49	3.06	...	...	...
IM Peg	25.32	0.35	73	J2253+1608	12360.00	2.63	...	...	...	J2253+1942	188.37	0.49	...	...	...
SZ Psc	172.00	0.49	350	J2311+0205	41.35	0.46	J2320+0513	706.05	6.26	...	...	...	...	...	...
HD 224085	1.26	0.10	13	J2347+2719	143.57	0.07	...	...	...	J2352+3030	28.44	0.19	...	...	...

Notes. Peak intensity PI and its standard deviation σ_{PI}, both in units of mJy beam^{-1}, for detected stars along with information about the dynamic range DR of the image. For their calibrators $P1$, $P2$, $S1$, and $S2$, as explained in Table 5.2, PI and σ_{PI} are given as well. The information was derived from fitting a Gaussian shape to the object's image, on which the corrections derived from self-calibration of the respective $P1$ calibrator, and additional self-calibration whenever possible, were applied. For the fitting process AIPS task JMFIT was used. An ellipsis (...) indicates the omission of an entry.

Note. According to Lunz et al. (2020a, Table B.1)

tems and have resolved components when observed by VLBI. The identification of their components Aa and Ab was based on their images in Figs. 5.4, 5.5, and 5.6.

"Stars HD 283447 (V773 Tau) and DoAr 51 (V2248 Oph) consist of two close components of almost equal peak intensity. As Torres et al. (2012) summarize, HD 283447 is at least a quadruple system. The subsystem HD 283447 A is a strong radio source and a spectroscopic binary consisting of components Aa and Ab (Phillips et al. 1996; Boden et al. 2007; Massi et al. 2008). Its trajectory is gravitationally influenced by other components, mainly by subsystem HD 283447 B, which has an apparent [maximum] separation of about 150 mas. From comparison of Fig. [...][5.4] with the orbit (Fig. 4 of Torres et al. 2012), it could be determined that the west (right) component is the primary component Aa, and the east (left) component is the secondary component Ab. DoAr 51 is a triple system with a close binary of about 60 mas maximum separation and a third component about 0.″8 away (Barsony et al. 2003; Ortiz-León et al. 2017b). From comparison of the image in Fig. [...][5.5] with the orbit in Fig. 3 of Ortiz-León et al. (2017b), it could be determined that the east (left) component is the primary component Aa, and the west (right) component is the secondary component Ab. In addition, structure was detected for UX Ari as shown in Fig. [...][5.6], which could represent the close inner binary system A of the triple system described in Hummel et al. (2017). Then the large east (left) component is the subgiant primary star Aa, and the small west (right) component is its main-sequence companion Ab as reported in Carlos and Popper (1971). JMFIT was unable to fit two separate Gaussians, which is why only one component is shown in Table [...][5.4]" (Lunz et al. 2020a).

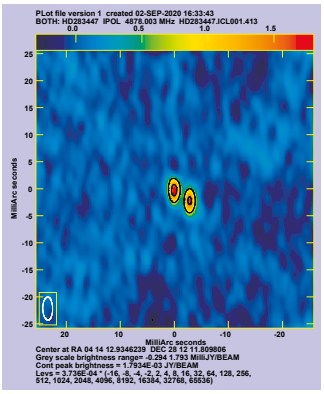

Figure 5.4 Phase-referenced map of star HD 283447 where self-calibration of the calibrator J0408+3032 was applied.
Note. According to Lunz et al. (2020a, Fig. C.1-C.3).

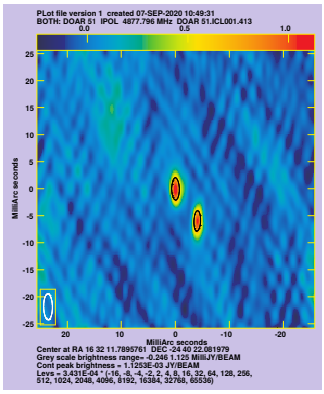

Figure 5.5 Phase-referenced map of star DoAr 51 where self-calibration of the calibrator J1633−2557 was applied.

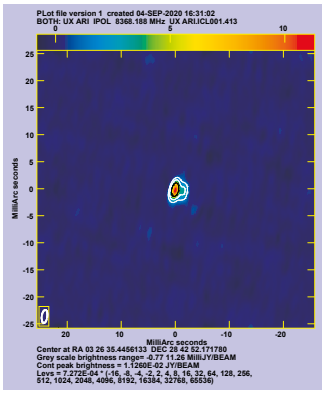

Figure 5.6 Phase-referenced map of star UX Ari where self-calibration of the calibrator J0316+2733 was applied.

For multiple star systems, it must be checked in detail from which component Gaia de-

livers the trajectory and from which component VLBI delivers the trajectory. Due to the expectation that the Gaia spacecraft will not be able to resolve any sources below 100 mas even in its final DR, these three close binaries require more research. This means that Gaia is detecting the photocenter of the binary for these close binaries. Apart from any radio-optical shifts, it is not certain whether the multiple star systems also emit optical emission similar to radio emission. It is possible that a component does not emit at all at optical frequencies while emitting radio emission, and it is possible that a component is much brighter or fainter compared to the other components. This would pull the unresolved Gaia position more toward one component or the other. Therefore, close binary or multiple star systems need special attention if their astrometry is used for the alignment between VLBI and Gaia (see Sect. 5.4.4).

5.4.4 Positions

Although the observations were designed to obtain realistic peak intensities and not very precise positions, the star positions were derived and tested to be used already for comparison between VLBI and Gaia.

Absolute and relative single-epoch star positions

From the phase-referencing VLBI data of one epoch, two types of target positions can be retrieved: single-epoch absolute star positions and single epoch relative star positions. Only the fringe-fitting of the calibrator data is different, as described in Sect. 5.4.2. In Lunz et al. (2020a) and in the appendix B, it was found that based on the UL005 experiment data modelfit in the Caltech Difmap imaging package (Shepherd 1997) is more robust in determining the position of the centroid of emission compared to JMFIT in AIPS if structure or multiple close components are present, so its results were used in this analysis. The positions of the stars $\alpha(t)$ and $\delta(t)$ were determined at the observation epoch t, which is the mean of the first and last scans of the epoch. "The epochs of observation t are displayed with five digits after the decimal point of the Julian year to represent 6 minutes time difference. This higher precision compared to information in other publications such as Lindegren (2020a) is needed, because star HD 224085 in our list has a combined proper motion of approximately 577 mas yr^{-1} according to literature, which reflects in an acceptable position error of about 0.007 mas only at this level of time accuracy" (Lunz et al. 2020a). The position uncertainties $\sigma_{\alpha*,\mathrm{random}}$ and $\sigma_{\delta,\mathrm{random}}$ were derived from the beam shape and the RMS noise of the image based on equations for elliptical Gaussians in Condon (1997). They reflect the thermal noise of the observations.

The absolute star positions are listed in Table 5.5 and the relative star positions (used in Sect. 5.5) are listed in Table 5.6.

Table 5.5 [Absolute] positions estimated for the 32 radio stars detected with the VLBA on 6-7 January 2020, along with the respective phase-referencing calibrators used.

Star	Calibrator	Δ_c [°]	t [Julian year]	$\alpha(t)$ [°]	$\sigma_{\alpha*,\mathrm{random}}$ [mas]	$\sigma_{\alpha*,\mathrm{absolute}}$ [mas]	$\delta(t)$ [°]	$\sigma_{\delta,\mathrm{random}}$ [mas]	$\sigma_{\delta,\mathrm{absolute}}$ [mas]
UV Psc	J0121+0422	2.7	J2020.01506	19.230136917	0.051	0.336	6.811818183	0.113	0.769
HD 8357	J0121+0422	3.1	J2020.01507	20.737009593	0.032	0.334	7.420541599	0.072	0.764
LS I +61 303	J0244+6228	1.3	J2020.01520	40.131930495	0.007	0.361	61.229330180	0.030	0.770
RZ Cas	J0243+7120	1.8	J2020.01520	42.231326331	0.011	0.361	69.634498545	0.041	0.782
bet Per	J0313+4120	1.0	J2020.01541	47.042232516	0.014	0.333	40.955640671	0.042	0.763
UX Ari Aa	J0316+2733	2.5	J2020.01542	51.647690075	0.016	0.464	28.714492103	0.040	0.885
...	J0329+2756	1.1	J2020.01542	51.647689970	0.017	0.346	28.714491777	0.043	0.770
UX Ari Ab	J0316+2733	2.5	J2020.01542	51.647689596	0.041	0.465	28.714492021	0.103	0.890
...	J0329+2756	1.1	J2020.01542	51.647689491	0.038	0.347	28.714491711	0.096	0.775
HD 22468	J0339−0146	2.5	J2020.01545	54.196857481	0.017	0.333	0.586857856	0.041	0.762
HD 283447 Aa	J0408+3032	2.7	J2020.01544	63.553893394	0.070	0.415	28.203279915	0.174	0.888
...	J0403+2600	3.3	J2020.01544	63.553893460	0.071	0.341	28.203280346	0.175	0.782
HD 283447 Ab	J0408+3032	2.7	J2020.01544	63.553894285	0.069	0.415	28.203280449	0.171	0.888
...	J0403+2600	3.3	J2020.01544	63.553894350	0.070	0.341	28.203280911	0.175	0.782
B Per	J0359+5057	3.1	J2020.01544	64.561289604	0.025	0.334	50.295190728	0.077	0.765
V410 Tau	J0429+2724	2.7	J2020.01546	64.629671674	0.053	0.337	28.454348214	0.127	0.772
HD 283572	J0429+2724	2.0	J2020.01547	65.495256404	0.030	0.334	28.301662284	0.073	0.765
T Tau	J0428+1732	2.5	J2020.01548	65.497657029	0.054	0.353	19.534875498	0.126	0.805
CoKu HP Tau G2	J0438+2153	1.2	J2020.01549	68.975719888	0.056	0.350	22.903662821	0.133	0.791
...	J0426+2350	2.3	J2020.01549	68.975720024	0.056	0.351	22.903662788	0.135	0.789
Brun 334	J0529−0519	1.2	J2020.01560	83.665661456	0.055	0.354	−5.407113861	0.135	0.805
TYC 5346-538-1	J0542−0913	1.1	J2020.01561	85.640320727	0.102	0.381	−8.120884591	0.252	0.850
SV Cam	J0626+8202	0.6	J2020.01461	100.331305792	0.010	0.334	82.266505083	0.074	0.765
54 Cam	J0811+5714	1.1	J2020.01358	120.648721430	0.026	0.348	57.273297738	0.050	0.770
IL Hya	J0923−2135	2.2	J2020.01348	141.203985240	0.023	0.350	−23.826489202	0.067	0.806
HU Vir	J1216−1033	1.7	J2020.01371	183.336147857	0.029	0.353	−9.079682807	0.072	0.806
DK Dra	J1220+7105	1.5	J2020.01362	183.922718144	0.006	0.355	72.551058090	0.045	0.771
RS CVn	J1308+3546	0.5	J2020.01370	197.653442180	0.023	0.333	35.934999284	0.067	0.764
BH CVn	J1324+3622	2.1	J2020.01370	203.699807328	0.016	0.365	37.182358583	0.050	0.793
...	J1340+3754	1.3	J2020.01370	203.699807107	0.020	0.363	37.182358180	0.059	0.803
del Lib	J1456−0617	2.1	J2020.01405	225.242763734	0.036	0.359	−8.518981969	0.081	0.772
...	J1510−0843	2.5	J2020.01405	225.242763508	0.035	0.392	−8.518981571	0.078	0.887
σ^2 CrB	J1613+3412	0.4	J2020.01416	243.668436106	0.015	0.333	33.858120828	0.031	0.762
Haro 1-6	J1633−2557	2.3	J2020.01429	246.512495673	0.050	0.364	−24.393536461	0.147	0.852
DoAr 51 Aa	J1633−2557	1.3	J2020.01429	248.049123210	0.071	0.368	−24.672800585	0.209	0.865
DoAr 51 Ab	J1633−2557	1.3	J2020.01429	248.049121991	0.077	0.369	−24.672802148	0.228	0.869
HD 199178	J2102+4702	3.0	J2020.01452	313.473754647	0.014	0.432	44.386404314	0.037	0.818
SS Cyg	J2136+4301	1.3	J2020.01451	325.679208442	0.052	0.352	43.586257891	0.113	0.782
AR Lac	J2153+4322	3.5	J2020.01460	332.169653346	0.020	0.345	45.742508506	0.046	0.770
...	J2202+4216	3.6	J2020.01460	332.169653266	0.021	0.333	45.742508577	0.047	0.762
IM Peg	J2253+1608	0.7	J2020.01469	343.259318421	0.018	0.333	16.841040559	0.041	0.762
SZ Psc	J2311+0205	0.8	J2020.01475	348.349199758	0.029	0.503	2.675591665	0.065	1.151
...	J2320+0513	3.1	J2020.01475	348.349199839	0.022	0.333	2.675591802	0.047	0.762
HD 224085	J2347+2719	2.1	J2020.01471	358.770517712	0.038	0.351	28.633868049	0.062	0.790

Notes. The apparent separation between star and calibrator is Δ_c. Uncertainties $\sigma_{\alpha*,\mathrm{random}}$ and $\sigma_{\delta,\mathrm{random}}$ refer to the random error from observations, whereas $\sigma_{\alpha*,\mathrm{absolute}}$ and $\sigma_{\delta,\mathrm{absolute}}$ are inflated uncertainties as described in Sect. 5.4.5. The parameters $Roe\,(t)$, $\Delta\alpha$, and $\Delta\delta$ need to be applied if the effect of parallax should be corrected. Thereby, the Römer delay Roe needs to be subtracted from the epoch t in column 4, which is the mean epoch between the first and the last scans. In addition, the parallax effects $\Delta\alpha$, and $\Delta\delta$ need to be added to the positions in Cols. 5 and 8.
Note. According to Lunz et al. (2020a, Table 4).

Table 5.6 Relative positions in ICRF3 for 14 stars based on observations conducted in January 2020 which are including correction of the phase calibrator structure.

Star	Calibrator	Δ_c [°]	t [Julian year]	$\alpha(t)$ [°]	$\sigma_{\alpha*,\mathrm{random}}$ [mas]	$\delta(t)$ [°]	$\sigma_{\delta,\mathrm{random}}$ [mas]
HD 283572	J0429+2724	2.0	J2020.01547	65.495256413	0.033	+28.301662253	0.072
V410 Tau	J0429+2724	2.7	J2020.01546	64.629671673	0.059	+28.454348213	0.126
SS Cyg	J2136+4301	1.3	J2020.01451	325.679208442	0.071	+43.586257890	0.112
Brun 334	J0529−0519	1.2	J2020.01560	83.665661454	0.055	−5.407113858	0.134
TYC 5346-538-1	J0542−0913	1.1	J2020.01561	85.640320721	0.101	−8.120884576	0.248
Haro 1-6	J1633−2557	2.3	J2020.01429	246.512495679	0.055	−24.393536459	0.148
CoKu HP Tau G2	J0438+2153	1.2	J2020.01549	68.975719883	0.061	+22.903662815	0.134
BH CVn	J1324+3622	2.1	J2020.01370	203.699807328	0.020	+37.18235859	0.050
...	J1340+3754	1.3	J2020.01370	203.699807118	0.019	+37.18235822	0.046
σ^2 CrB	J1613+3412	0.4	J2020.01416	243.668436110	0.018	+33.85812083	0.031
HD 199178	J2102+4702	3.0	J2020.01452	313.473754649	0.019	+44.38640432	0.037
AR Lac	J2153+4322	3.5	J2020.01460	332.169653348	0.029	+45.74250851	0.046
IM Peg	J2253+1608	0.7	J2020.01469	343.259318422	0.019	+16.84104056	0.041
HD 22468	J0339−0146	2.5	J2020.01545	54.196857495	0.016	+0.58685785	0.038
del Lib	J1456−0617	2.1	J2020.01405	225.242763738	0.037	−8.51898195	0.082

Notes. Position $\alpha(t)$ and $\delta(t)$ at epoch t and respective uncertainties $\sigma_{\alpha*,\mathrm{random}}$ and $\sigma_{\delta,\mathrm{random}}$. The apparent distance between star and primary calibrator is Δ_c.
Note. According to Lunz et al. (2021b, Table 1).

The differences in star positions between Tables 5.5 and 5.6 are small and the differences in the dynamic range are negligible. Figure 5.8 shows the star position offsets for the 32 stars using one or the other method for fringe-fitting, sorted by the dynamic range. Their RMS is 19 µas in $\alpha*$ and 35 µas in δ (Lunz et al. 2021b). None of the position differences is larger than two times their uncertainty. The position difference is highest with 0.112 ± 0.103 mas in δ for the star HD 283572. All other position offsets are within ±73 µas in δ and ±57 µas in $\alpha*$.

"Star bet Per, although successfully detected in VLBI, was not used for the adjustment computations. In our VLBI observations in January 2020, star bet Per was scheduled although it only had a matching object in *Gaia* DR2 with a two parameter solution (position only). It was assumed that in *Gaia* EDR3 a five parameter solution would be available for the object assumed to be bet Per due to the longer data time span and therefore presumably more observations for the parameter fit. The assumption was supported by the fact that the star was also detected by its predecessor spacecraft Hipparcos. However, in *Gaia* EDR3, no counterpart was found for bet Per. This position will however be useful if comparing to future *Gaia* data releases, should a counterpart with a full five-parameter solution be available for the star" (Lunz et al. 2020a).

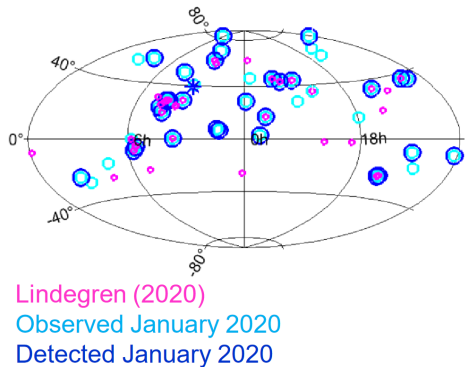

Figure 5.7 Sky plot of the Lindegren (2020a) stars, the observed stars, and the detected stars in January 2020 (this work).
Note. According to Lunz et al. (2021a).

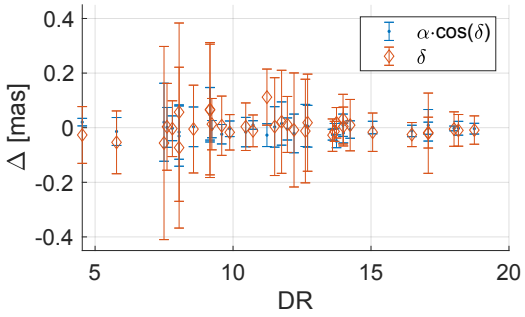

Figure 5.8 Differences between the two types of positions in Tables 5.5 and 5.6 for the 32 detected stars. The tables are based on different fringe fits of the primary calibrators $P1$. The differences are plotted versus the dynamic range DR from Difmap modelfit of the images with structure correction of the primary calibrator applied. The two stars of the close binary systems are plotted as two separate dots.

Unresolved binaries as seen by Gaia - center of luminosity versus barycenter

For close binary or multiple star systems that are not resolved by Gaia but are resolved by VLBI, a stable reference point must be defined which is the same for both measurement methods and that can ideally be modeled by the simple five astrometric parameters. The Gaia spacecraft detects the photocenter of the star system, while VLBI has the potential to detect one, some, or all of the components of the star system individually. In the example for the observations from this work, they can be detected individually if the separations are larger than the milliarcsecond scale. In a standard analysis, the barycenter would be determined from the astrometric measurements and used to represent the trajectory of the whole star system, but for comparison with the Gaia-sensed photocenter, this might not be the ideal reference point because the ratio between stellar masses and brightness need not be the same. Thus, the photocenter observed by Gaia and the barycenter determined by VLBI differ. In fact, the luminosity increases faster than the mass. In addition, the location of the radio emission of a star does not need to coincide with the center of mass of the star. As an alternative, the center of luminosity was determined in Lunz et al. (2020a), which takes into account their brightness at the observing frequency rather than the masses of the components. The comparison between the two types of reference points for the VLBI astrometry from Lunz et al. (2020a) is reproduced in the following.

As a start, the apparent separation **r** between the two best-fitting Gaussian components of the binary star from VLBI needs to be known. These were derived from the star positions based on a point source fringe fit of the primary calibrator. For HD 283447, it

was determined to be 2.824 ± 0.070 mas in $\alpha*$ and 1.975 ± 0.174 mas in δ, which is the mean of the result for the apparent separation between the two components from the observations relative to the first and the second primary calibrators, respectively. The corresponding values for DoAr 51 are -4.031 ± 0.105 mas in $\alpha*$ and -5.626 ± 0.309 mas in δ, and for UX Ari the two components differ on average -1.514 ± 0.030 mas in $\alpha*$ and -0.268 ± 0.076 mas in δ. Since only two components of the close unresolved star systems were detected in this work, the binary star model was applied as an approximation, even if the close binary system is part of a multiple star system.

"For calculation of barycenter coordinates of a binary system, the masses of the two components, m_1 for the primary and m_2 for the secondary, are needed. For HD 283447 Aa and Ab the masses are given in Torres et al. (2012), for DoAr 51 they are given in Ortiz-León et al. (2017b) and for UX Ari they are given in Hummel et al. (2017). Then, the vector $\mathbf{r_1}$ between the primary star position and the barycenter is (Torres et al. 2012)

$$\mathbf{r_1} = \frac{m_1}{m_2 + m_1}\mathbf{r}, \tag{5.3}$$

where $\mathbf{r}$ is the separation between the primary and secondary star as mentioned above.

The center of luminosity was calculated in the same manner, but instead of the masses the luminosities of the stars were used for the calculations. For HD 283447 the optical luminosities for components Aa and Ab are given in Welty (1995) and for UX Ari, they are given in Hummel et al. (2017). For DoAr 51 we determined the factor equivalent to $\frac{m_1}{m_1+m_2}$ from the flux ratio in Schaefer et al. (2018), assuming that both stars are equally distant, since we could not find the luminosities directly. We use the J-band flux ratio because it is the closest to the *Gaia* bands" (Lunz et al. 2020a).

The components for the vector $\mathbf{r_1}$ in the direction of α and δ are listed in Table 5.7 for the offset of the barycenter or the offset of the center of luminosity from the primary star. Their differences are given as well and they are several hundred microarcseconds in magnitude. These displacements were added to the position of the primary star of the binary system to obtain the absolute position of the center of luminosity and the barycenter. As expected, the separations between the components derived from the solution with or without considering the source structure of the phase calibrator during the fringe fit are not significantly different. Also, they are not significantly different when using the $P1$ or the $P2$ calibrator for phase referencing as it was done for HD 283447 and UX Ari. The differences between the two types of centers conclude that position offsets between VLBI and Gaia for these close binaries of up to 0.7 mas can be explained by the offsets between photocentric position and barycenter or center of luminosity. At this stage, no clear indication could be found as to the trajectory of which of the two centers better

Table 5.7 Components in α and δ for the vector $\mathbf{r_1}$ including the uncertainties $\sigma_{r_{1,\alpha*}}$ and $\sigma_{r_{1,\delta}}$ from the calculation of the position of the barycenter and center of luminosity, respectively, with respect to the position of the primary star of the close binary system in UX Ari, HD 283447 and DoAr51 based on Eq. 5.3.

	Barycenter				Center of Luminosity				Difference			
	$r_{1,\alpha*}$	$\sigma_{r_{1,\alpha*}}$	$r_{1,\delta}$	$\sigma_{r_{1,\delta}}$	$r_{1,\alpha*}$	$\sigma_{r_{1,\alpha*}}$	$r_{1,\delta}$	$\sigma_{r_{1,\delta}}$	$r_{1,\alpha*}$	$\sigma_{r_{1,\alpha*}}$	$r_{1,\delta}$	$\sigma_{r_{1,\delta}}$
UX Ari, $P1$	−0.707	0.020	−0.139	0.052	−0.304	0.009	−0.060	0.022	−0.403	0.022	−0.079	0.056
UX Ari, $P2$	−0.708	0.019	−0.111	0.049	−0.305	0.008	−0.048	0.021	−0.403	0.021	−0.063	0.053
HD 283447, $P1$	+1.286	0.045	+0.873	0.111	+0.568	0.020	+0.386	0.049	+0.717	0.049	+0.487	0.121
HD 283447, $P2$	+1.283	0.045	+0.924	0.113	+0.567	0.020	+0.408	0.050	+0.716	0.050	+0.515	0.123
DoAr 51, $P1$	−2.003	0.052	−2.795	0.153	−2.169	0.057	−3.028	0.166	+0.167	0.077	+0.233	0.226

Notes. If two primary calibrators – $P1$ and $P2$ – were available for phase-referencing, the results from referencing to each of them are shown. The standard deviations $\sigma_{r_{1,\alpha*}}$ and $\sigma_{r_{1,\delta}}$ are based on the random error σ_{random} and variance propagation. Units are in milliarcseconds.
Note. According to Lunz et al. (2020a, Table 6).

matches the Gaia trajectory, and the center of luminosity was used in the following.

In addition to the information provided in Lunz et al. (2020a), it has to be noted that for UX Ari the five astrometric parameters of the center of mass of the triple system were taken from Peterson et al. (2011) and used in the estimation of rotation parameters between VLBI and Gaia in Lindegren (2020a). The outer binary has a semi-major axis of 648.0 ± 0.7 mas (Peterson et al. 2011), thus it can be resolved by Gaia. It should be checked, whether the center of the mass from the inner binary only, with a semi-major axis of 1.71 mas (Peterson et al. 2011), would be more suitable for matching with Gaia. Also from the VLBI side further homogenization of the data is needed. For example, in the adjustment of the rotation parameters between VLBI and Gaia, triple system astrometric parameters should not be mixed with parameters from the inner binary only as it was done in Lindegren (2020a) when using both the Peterson et al. (2011) data and the data from Lestrade et al. (1999). This kind of homogenization is out of the scope of this work, however this gross error will not affect the results of the rotation parameter analysis much, because UX Ari is one of the first rejected stars and therefore the rotation parameters including its data were not used for any of the statistics.

Stars phase-referenced to multiple primary calibrators

From the star positions based on a point source fringe fit of the primary calibrator another investigation was done.

"Seven of the detected target stars, UX Ari, HD 283447, CoKu HP Tau G2, BH CVn, del Lib, AR Lac, and SZ Psc, were observed along with two different primary calibrators within the same respective observing block as indicated in Table 5.2. The pat-

tern was $P1$-$P2$-star-$P1$-$P2$. Therefore the star positions relative to $P1$ and $P2$ are highly correlated in terms of error sources like earth orientation, atmosphere, and uv-coverage; however both are valid results considering an appropriate error budget. This observational setup provides the opportunity to study the accuracy of the absolute positions of these stars. The positions derived with MODELFIT in DIFMAP were obtained from the same data set once with phase referencing all objects of the group, consisting of the star and the associated calibrators, to the primary calibrator $P1$ and once with phase referencing all objects of the group to $P2$. The results are also reported in Table [...]5.5. The differences between the positional fits to $P1$ and $P2$, $\Delta\alpha*$ and $\Delta\delta$, are presented in Table [...]5.8. These quantities can be used to quantify potential systematic errors in the absolute star positions, which is further investigated in Sect. [...]5.4.5.

Table 5.8 Difference $\Delta\alpha*$ and $\Delta\delta$ in the absolute positions of seven stars when phase-referenced to two different primary calibrators.

Name	$\Delta\alpha*$	$\sigma_{\Delta\alpha*,\mathrm{CRF}}$	$\Delta\delta$	$\sigma_{\Delta\delta,\mathrm{CRF}}$
UX Ari Aa	+0.33	0.34	+1.18	0.46
UX Ari Ab	+0.33	0.34	+1.12	0.46
HD 283447 Aa	−0.21	0.24	−1.55	0.43
HD 283447 Ab	−0.20	0.24	−1.66	0.43
CoKu HP Tau G2	−0.45	0.14	+0.12	0.24
BH CVn	+0.63	0.21	+1.45	0.33
del Lib	+0.80	0.25	−1.43	0.46
AR Lac	+0.20	0.10	−0.26	0.12
SZ Psc	−0.29	0.38	−0.49	0.86
RMS	+0.47	0.26	+1.08	0.47

Notes. Uncertainties $\sigma_{\Delta\alpha*,\mathrm{CRF}}$ and $\sigma_{\Delta\delta,\mathrm{CRF}}$ were derived from the coordinate uncertainties of the primary calibrators $P1$ and $P2$ as described in Sect. 5.4.5 into account. The last lines indicates the RMS of the quantities, where double stars (UX Ari, HD 283447) were accounted only once in the calculations. Units are in milliarcseconds.
Note. According to Lunz et al. (2020a, Table 5).

The RMS of the offsets $\Delta\alpha*$ and $\Delta\delta$ is 0.47 mas in $\alpha*$ and 1.08 mas in δ. For comparison, the RMS of the standard deviations of the catalog positions of the calibrators $\sigma_{\Delta\alpha*,\mathrm{CRF}}$ and $\sigma_{\Delta\delta,\mathrm{CRF}}$ is 0.26 mas and 0.47 mas respectively, which is a factor of 2 smaller than the RMS of the offsets. The RMS of the offsets in the α direction is only half that in the δ direction. This could be due to the poor uv-coverage of our observations in the δ direction due to network geometry, as indicated by the beam sizes, and the short observation time span for most objects. For double stars only one component was considered for these calculations in order not to bias the results. Furthermore, for both UX Ari and del Lib, one of the calibrators is not included in ICRF3, so its position and uncertainty were taken from the rfc_2018b catalog. However, the offsets for these two stars are not significantly different than those for the other stars. The offsets of the respective other primary and secondary calibrators observed along with the stars, as listed in Table [...]5.2, do not differ significantly from those of the stars" (Lunz et al. 2020a). No systematics could be identified between offsets of stars observed at X-band or at C-band.

Correction of the absolute single-epoch star positions for parallactic displacement and Römer delay

As described in Sect. 2.2.3, the source positions determined by phase-referencing VLBI at an epoch t must be corrected for the parallactic displacement (Eq. 2.9), and the observation epoch t must be corrected by the Römer delay *Roe* (Eq. 2.10) to obtain Solar System barycentric positions $\boldsymbol{s}(t_B)$ at the time of arrival at the Solar System barycenter t_B that are comparable to the positions from Gaia, the positions for extragalactic objects in ICRF3, and the positions from models of stellar motion. For these reductions, the Solar System barycentric coordinates of the Earth's center $\boldsymbol{b}(t)$ at the time of observation t were derived from the DE 421 ephemeris (Folkner et al. 2009) employing the VieVS@GFZ VLBI software developed by the German Research Centre for Geosciences (GFZ) in Potsdam.

"For the evaluation of the *Gaia* DR2 dataset, the *Gaia* parallax was applied to all stars, as the VLBI parallax is not available for all objects (for example, for the stars in Boboltz et al. 2007), and a unified result was aimed for. The parallaxes of *Gaia* DR2 are known to be biased by a few tens of μas (Arenou et al. 2018). For faint quasars an offset of −0.03 mas was determined by Lindegren et al. (2018), but for brighter objects this parameter was determined to be larger. A variety of studies examining this topic by using different sets of stars and methods already exist (Riess et al. 2018; Schönrich et al. 2019; Zinn et al. 2019). Following Lindegren (2020a), the parallax offset of −0.05 mas was used to keep results comparable. In the last columns of Table 4 [in Lunz et al. (2020a)],the calculated Römer delay Roe (t) and the shifts to mitigate the parallax effect $\Delta\alpha\,(t)$ and $\Delta\delta\,(t)$ at the epoch of observation t, both using the *Gaia* DR2 parallax, are listed [...].For *Gaia* EDR3, the parallax correction is not static and the python implementation calculating the bias function provided in Lindegren et al. (2021a) was used instead. Therefore, corrections $\Delta\alpha\,(t)$ and $\Delta\delta\,(t)$ for *Gaia* DR2 in Table 4 [in Lunz et al. (2020a)]are slightly different in case of *Gaia* EDR3" (Lunz et al. 2020a). They are given, also for the additional stars discussed in Sect. 5.5, in Table 4 of Lunz et al. (2021b).

5.4.5 Error budget of absolute star positions from phase-referencing VLBI

The difference in the error budget of the star positions in ICRF3 from phase-referencing VLBI when the star positions are used as absolute positions for the analysis of the rotation parameters between VLBI and Gaia is described below. This subsection was taken from Lunz et al. (2020a), and references to other sections, tables and figures were adjusted to match the outline of this work.

The positions derived in the previous sections are of two kinds that is the model positions from Sect. 5.1 and the single-epoch positions from Sect. 5.4.4. The single-epoch positions

describe the star positions at a specific epoch in time. For these positions no averaging or correction for non-visible binary companions and other disturbances could be applied. In contrast, the uncertainties of the model positions from a fit of relative position time series to models of stellar motion (usually mean position, linear proper motion, and parallax) are affected by such disturbances. They would increase the uncertainty of the estimated astrometric parameters because the formal errors are usually adjusted by variance component estimation during the fit, so that the reduced χ^2 of the adjustment equals unity. The impact is minimized by selecting stars with a small RUWE parameter [...] indicating that the *Gaia* data fits the five-parameter astrometric model well, and by the iterative approach, where deviating stars get rejected first. Nevertheless, the difference of the error budget for the two types of positions needs further investigation, which is given in the following.

In general, positions derived from phase-referencing measurements, as in the present study, are affected by the following errors:

- Random error σ_{random} [thermal] due to thermal noise calculated based on the SNR and the shape of the elliptical Gaussian fitted to the central map component (e.g., Thompson et al. 1986; Condon 1997). Mean (Median) values of 0.034 (0.026) mas in $\alpha*$ and 0.087 (0.067) mas in δ were determined from the data of this study.
- CRF calibrator position uncertainty σ_{CRF} [thermal]. The median position uncertainty in ICRF3 S/X is 0.1 mas in α and 0.2 mas in δ. Additional error due to absolute position wander of individual calibrators, for example quantified by Allan variance in Gattano, C. et al. (2018), is ignored.
- Delay model error $\sigma_{\text{delay model}}$ [systematic] from residual ionospheric and tropospheric errors, antenna and source position errors, and the accuracy of the earth orientation parameters used for calibration; mostly depending on the declination of the source and the calibrator-target separation. Pradel et al. (2006) determined this error is roughly between 0.015 mas to 0.284 mas per coordinate direction for a calibrator-target separation of 1° from a simulation without residual ionospheric delay but with calibrator position uncertainty considered. The uncertainty due to residual ionospheric delay for JPL TEC maps is below 0.1 mas.
- Source structure error $\sigma_{\text{structure}}$ [systematic] due to non-point like and possibly varying calibrator structure. The larger the structure, the higher the effect. When modeling calibrator structure, the positions of the stars estimated in our analysis show a mean difference of -0.003 mas in $\alpha*$ and 0.002 mas in δ, while the RMS of the differences is 0.019 mas mas in $\alpha*$ and 0.035 mas in δ.
- Uncertainty $\sigma_{\text{phase-group}}$ [systematic] due to the difference between calibrator group- and phase-delay positions in the presence of core shift (possibly varying with time).

The value is the order of 0.036 mas to 0.326 mas for a source with core shift median value of 0.44 mas between S- and X-band (Kovalev et al. 2008) and for a variety of power-law exponents (Porcas 2009). We anticipate the impact of core shift on C-band to be smaller since it lies between the frequency bands of S and X. In practice, it is possible that $\sigma_{\text{phase-group}}$ is also affected by structure at S-band, which impacts the S/X-band positions, but this is only a second order effect.

All of these effects are unique in magnitude and direction in the sky from radio sources to radio sources.

A possible way to get insights into the magnitude of unaccounted systematic errors in the single-epoch positions may be obtained by comparing absolute star positions determined by phase-referencing with respect to two different calibrators (see Sect. 5.4.4). In principle, i.e. in the absence of systematic errors, the difference in the absolute positions of a star measured in such a case should have the uncertainties derived from a combination of the positions uncertainties of the two calibrators in the ICRF3, $\sigma_{\Delta\alpha*,\text{CRF}}$ and $\sigma_{\Delta\delta,\text{CRF}}$. Any difference larger than that reveals the presence of systematic errors. In our analysis (see Sect. 5.4.4 and Table 5.8), the RMS of the differences of the star positions, $\Delta\alpha*$ and $\Delta\delta$, is on average twice as large as the combined calibrator uncertainties, $\sigma_{\Delta\alpha*,\text{CRF}}$ and $\sigma_{\Delta\delta,\text{CRF}}$. Thus, our analysis is not free of systematic errors. To evaluate the magnitude of such systematic errors, we subtracted in quadrature the RMS of $\sigma_{\Delta\alpha*,\text{CRF}}$ and $\sigma_{\Delta\delta,\text{CRF}}$, respectively, from the RMS of $\Delta\alpha*$ and $\Delta\delta$, as $\sqrt{0.47^2 - 0.26^2}/\sqrt{2} = 0.28$ mas for $\alpha*$ and $\sqrt{1.08^2 - 0.47^2}/\sqrt{2} = 0.69$ mas for δ. The errors thus determined can then be added to the thermal errors σ_{random} and σ_{CRF} to get the absolute star position uncertainties, expressed as

$$\sigma^{single\,epoch}_{\alpha*,\text{absolute}} = \sqrt{\sigma^2_{\alpha*,\text{random}} + \left[\sigma_{\alpha,\text{CRF}} \cdot \cos(\delta)\right]^2 + 0.28^2}\,\text{mas} \tag{5.4}$$

and

$$\sigma^{single\,epoch}_{\delta,\text{absolute}} = \sqrt{\sigma^2_{\text{random}} + \sigma^2_{\delta,\text{CRF}} + 0.69^2}\,\text{mas}. \tag{5.5}$$

The mean (median) of $\sigma^{single\,epoch}_{\text{absolute}}$ quantity for our data is 0.315 (0.305) mas in $\alpha*$ and 0.738 (0.714) mas in δ respectively.

In case of star positions derived from fitting models of stellar motion to multi-epoch relative positions, many systematic errors were accounted for by inflating the formal errors such that the χ^2 of the fit equals one. However, not all systematic errors can be accounted for by this method. Such inflated errors are labeled $\sigma_{modelpos}$ if the σ_{CRF} were added (as it was done for the homogenization efforts in Sect. 5.1). To complete the realistic absolute position error budget for the model positions, an average value for $\sigma_{\text{phase-group}}$ still needs to

be applied. We found three approaches to determine an average value for this uncertainty. First, the difference between group-delay position and phase-delay position determined from simulations in Porcas (2009) is 0.166 mas for a core shift of 0.440 mas between 2.3 GHz and 8.4 GHz, and in the case of an ideal source having no jet. Second, Fomalont et al. (2011) studied the difference between ICRF2 positions and positions from phase-referencing at 8.6 GHz for four compact radio sources by using the VLBA. The conclusion was that the positions in ICRF2 can be offset from the phase-referenced positions (materialized by the core of the sources) by up to 0.5 mas. The mean difference between ICRF2 positions and 8.6 GHz peak positions in the images is 0.42 mas. Dividing by $\sqrt{2}$ a $\sigma_{\text{phase-group}}$ of 0.30 mas per coordinate direction is obtained. Third, the trajectory of the Cassini spacecraft was observed at 8.4 GHz relative to various primary calibrators by VLBA as well (Jones et al. 2020). From this study, $\sigma_{\text{phase-group}}$ was determined to be in the range of 0.18 mas to 0.20 mas, similar to the above values. The mean value of the three approaches is 0.21 mas. For star positions observed at C-band, this value might be smaller due to the C-band being closer to the frequency between S- and X-bands. However, this is not considered in this study. The 0.21 mas are added as an average extra noise for $\sigma_{\text{model pos}}$ to obtain a more realistic error budget for the absolute positions derived from models of stellar motions:

Table 5.9 Realistic error budget for the one-epoch positions of the additional stars used in in Sect. 5.5.

Star	t [Julian year]	$\sigma_{\alpha*,\text{absolute}}$ [mas]	$\sigma_{\delta,\text{absolute}}$ [mas]
HD 167971	J2020.21812	2.410	2.036
HD 167971	J2020.53120	4.899	5.147
V479 Sct	J2020.21812	0.364	0.826
EI Eri	J2020.21812	0.345	0.793
YY Men	J2020.53120	0.348	0.779
YY Men	J1990.94045	4.350	13.600

Notes. Realistic error budget $\sigma_{\alpha*,\text{absolute}}$ and $\sigma_{\delta,\text{absolute}}$ for the star positions $\alpha\ (t)$ and $\delta\ (t)$ at epoch t in Table 3 in Lunz et al. (2021b) when used as absolute positions in ICRF3 for the comparison to Gaia positions.
Note. According to Lunz et al. (2021b, Table 5).

$$\sigma^{model}_{\alpha*,\text{absolute}} = \sqrt{\sigma^2_{\alpha*,\text{model pos}} + 0.21^2}\,\text{mas} \tag{5.6}$$

and

$$\sigma^{model}_{\delta,\text{absolute}} = \sqrt{\sigma^2_{\text{model pos}} + 0.21^2}\,\text{mas}. \tag{5.7}$$

The more realistic error budget for the absolute positions presented in this section has to be used when comparing the two kinds of absolute positions from VLBI to an independent measurement system like *Gaia*.

In addition to the above cited information from Lunz et al. (2020a) for the detected stars

of this experiment UL005, additional stars from other projects are discussed in Lunz et al. (2021b) and therefore also in Sect. 5.5 of this work. Their absolute position uncertainties are reproduced in Table 5.9 for completion.

In this work, the σ_{CRF} are considered twice, as the RMS of $\sigma_{\Delta\alpha*,CRF}$ and $\sigma_{\Delta\delta,CRF}$ were not subtracted from the RMS of $\Delta\alpha*$ and $\Delta\delta$, respectively. Instead, the RMS of $\Delta\alpha*$ and $\Delta\delta$ were taken directly as $0.47 mas/\sqrt{2} = 0.33$ mas for $\alpha*$ and $1.08 mas/\sqrt{2} = 0.76$ mas for δ. The mean (median) of $\sigma_{absolute}^{single\,epoch}$ quantity for the data is 0.360 (0.351) mas in $\alpha*$ and 0.805 (0.782) mas in δ respectively. The correct error assessment was applied to the affected scenarios in Lunz et al. (2020a). The star positions remained the same as in the results presented in the previous manuscript version, and only the star position uncertainties of the single-epoch VLBA observations in 2020 were changed. For "55,EDR3" The order of rejected stars only changes slightly: UX Ari and V1023 Tau (iterations 5 and 6) are switched, HD 8357 is not rejected at iterations 26 but iteration 22, del Lib and IL Hya (iterations 27 and 28) are switched, and the order of the following rejected stars is also slightly different. Other than that, the plots of the iterative parameter estimates do not change, as can be seen comparing relevant figures in this work and in Lunz et al. (2020a). The baseline solution at $k = 13$ rejected stars changes from (ϵ_X, ϵ_Y, ϵ_Z, ω_X, ω_Y, ω_Z) = (+0.212, +0.319, +0.175, +0.020, +0.065, -0.017) ± (0.073, 0.098, 0.057, 0.010, 0.011, 0.011) mas or mas yr^{-1} with $Q/n = 5.5$ to (+0.226, +0.327, +0.168, +0.022, +0.065, -0.016) ± (0.070, 0.091, 0.054, 0.010, 0.011, 0.010) mas or mas yr^{-1} with $Q/n = 5.6$. The uncertainties combining the formal error and $\sqrt{Q/n}$ are (0.172, 0.230, 0.134, 0.023, 0.027, 0.025) mas or mas yr^{-1} for the first and (0.165, 0.215, 0.127, 0.023, 0.027, 0.024) mas or mas yr^{-1} for the latter parameter set. Thus, the uncertainties of ϵ decrease, but only by 4 % to 7 %. The parameter estimates themselves do not change significantly. The decrease in correlation parameter magnitude for the two baseline solutions is minor. The WM, WRMS, and ME quantities based on the same iterations change as shown in Table 5.10. Thus, there is no significant difference in the WM, only a slight reduction in the WRMS for ϵ_X, and only 7 % to 8 % reduction of the ME values in ϵ (but when applying the $\sqrt{Q/n}$, the reduction is 4 % to 6 %, similar to the uncertainties of the baseline solution).

Similarly, for "55,DR2" only small changes in the rejection process occur using one or the other error budget. RR Aql and HD 224085 are switched (iterations 17 and 18), HD 8357 is excluded in iteration 16 instead of 18, BH Cvn and Il Hya switch place with V1110 Tau and SY Scl (iterations 32-35), and so forth. The WM, WRMS, and ME quantities, the baseline solution, and the correlation coefficients similarly only slightly change. For example, the ME values only reduce by 2 % to 5 % for ϵ.

Table 5.10 WM, WRMS, and ME of scenario "55,EDR3".

Scenario	Parameter	$\epsilon_X(T)$	$\epsilon_Y(T)$	$\epsilon_Z(T)$	ω_X	ω_Y	ω_Z
55,EDR3 this work	WM	0.292	0.337	0.086	0.033	0.054	−0.019
	WRMS	0.058	0.071	0.083	0.016	0.014	0.013
	ME	0.083	0.107	0.064	0.012	0.013	0.012
55,EDR3, Lunz et al. (2020a)	WM	0.294	0.340	0.077	0.034	0.055	−0.020
	WRMS	0.049	0.074	0.084	0.016	0.014	0.012
	ME	0.079	0.099	0.060	0.011	0.013	0.012

Notes. The epoch T is 2016.0 for Gaia EDR3. Units are in milliarcseconds for $\epsilon_X(T)$, $\epsilon_Y(T)$, and $\epsilon_Z(T)$. They are milliarcseconds per year for ω_X, ω_Y, and ω_Z.

5.5 New estimates for models of stellar motion

The new topocentric single-epoch relative positions from Table 5.6 were used in this section to produce improved estimates for models of stellar motion whenever possible or they were used to determine such estimates from VLBI data for the first time. The relevant formulas and methods for estimating the main astrometric parameters – position, proper motion, and parallax – from position time series and for testing the significance of additional linear acceleration parameters are introduced in Sect. 2.2.3.

"Each star position was corrected to be referenced to the calibrator position in ICRF3 by accounting for the difference between the calibrator position in ICRF3 and the calibrator position used in the literature" (Lunz et al. 2021b). Using Eq. 2.11 or Eq. 2.15 as the functional model, a linear least squares fit as described in Sect. 3.3.1 was performed to these position time series. The positions were weighted by variances determined from the thermal noise σ_{random}. In the case where the empirical variance of the weight unit $s^2_{0,\alpha*}$, $s^2_{0,\delta}$ for the residuals in the coordinate direction α and δ was greater than one, the variances $E^2_{\alpha*}$ and E^2_δ were added to the variances of the respective observations in the weight matrix in Eq. 3.17 such that the $s^2_{0,\alpha*}$, $s^2_{0,\delta}$ approach unity in the fit. This method leads to realistic uncertainty estimates for the parameters and is often used in astrometry projects such as Loinard et al. (2007). Compared to multiplying the square sum of residuals Q with the empirical variance of the weight unit s^2_0 for all residuals to obtain the covariance matrix $\boldsymbol{\Sigma_{xx}}$ of the estimated parameters as in Eq. 3.23, this method recognizes different weights in α and δ directions and equalizes the weights of the individual observations in the presence of large additional variances.

"The new estimates for models of stellar motion obtained in this study are listed in Table 5.12 along with corresponding estimates found in the literature. Their sky motion including the astrometric models and the positions are shown in [...][the respective figures in each of the subsections]. The estimates for the models of the five astrometric parameters α_0, δ_0, ϖ, $\mu_{\alpha*}$, and μ_δ derived using only data from the literature are denoted M_{old}, while

the estimates for the models containing the 2020 positions are labeled M_{new}. [If the acceleration terms $a_{\alpha*}$ and a_δ were also estimated, the models are denoted $M_{old,a}$ and $M_{new,a}$, respectively.] The table also provides information on the additional uncertainties $E_{\alpha*}$ and E_δ. The RMS of the post-fit residuals v is denoted by RMS_v, specifically $RMS_{v,\alpha*}$ and $RMS_{v,\delta}$ for the two coordinate directions. The epoch of α_0 and δ_0 was chosen as the mean epoch t_0 of the observation epochs t to minimize the correlations between the parameters. For the projection of the parallax ellipse in Eq. 2.13, the barycentric coordinates of the Earth's center of mass at the observation epoch were derived from the DE 421 ephemeris (Folkner et al. 2009).

Considering the difference between positions determined from group delays, as used for the determination of ICRF3, and positions from phase delays, as determined from phase-referencing, special attention should be paid to the combination of star positions referenced to different phase-calibrators. For the VLBA observations in 2020, position differences with a RMS of 0.47 mas in $\alpha*$ and 1.08 mas in δ were determined from referencing seven stars to two different phase-calibrators (Lunz et al. 2020a). To account for this effect on the position time series, all observations not referenced to a primary phase calibrator can be down-weighted by adding the respective additional uncertainties to the star position uncertainties through variance propagation. A mean value of 0.5 mas in both directions is assumed to be not too pessimistic in the presence of different uv-coverage, source structure, difference between group- and phase-delay position, and residual delay model errors in the historical observations. The resulting models are denoted 'w0.5' "(Lunz et al. 2021b).

In the following, a detailed description of the input positions from various resources, the homogenization of the input data, and model estimates of various analysis cases are given separately for each star. The results are compared to the parameter values from Gaia and from literature. The subsections were mainly taken from Lunz et al. (2021b), and references to other sections, tables and figures were adjusted to match the outline of this work.

HD 283572

The star HD 283572 (HDE 283572) was observed relative to J0429+2724 at 6 epochs from September 2004 to December 2005 at 8.4 GHz (Torres et al. 2007). These data were reprocessed in Galli et al. (2018) using the same scheme as that described in Sect. 5.4.2. Observations in the same band and using the same primary calibrator were carried out in experiment UL005. The shifts of $-0.133\,3$ mas in $\alpha*$ and $0.141\,3$ mas in δ were subtracted from the single-epoch star positions from Galli et al. (2018) to reference them to ICRF3.

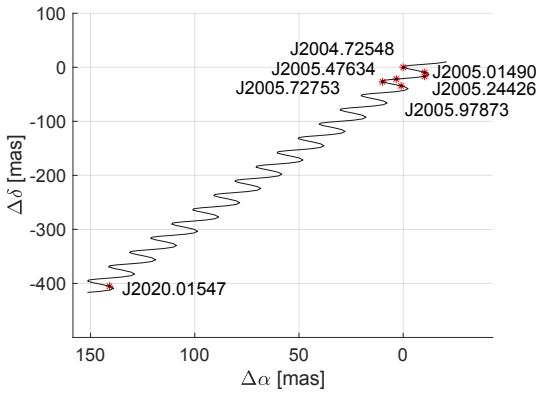

Figure 5.9 Observed positions, selected model in Table 5.12, and adjusted positions for HD 283572. The observed positions are marked with the red stars and their uncertainties are visualized by the black ellipses. The adjusted positions are labeled by the black dots and their uncertainties by the blue ellipses. The model is indicated by a black line. If no ellipses are visible, they are too small for the scale of the image.
Note. According to Lunz et al. (2021b, Fig. 1).

The work of Galli et al. (2018) does not report a model position, whereas Lindegren (2020a) determined a full five-parameter model for the star using the single-epoch positions of Galli et al. (2018). The solution M_{old} is not significantly different from Galli et al. (2018) – however, the formal errors of M_{old} are larger. Adding the 2020 position to the analysis (M_{new}) reduces the formal errors by 10 % to 20 % for α_0, δ_0, and ϖ, and by about 90 % for $\mu_{\alpha*}$ and μ_δ compared to M_{old}. The latter is due to the longer time span involved for the estimation. The additional uncertainties $E_{\alpha*}$ and E_δ decrease by 10 % to 15 %, while the values of RMS_v do not change significantly. The differences in model estimates between M_{new} and Galli et al. (2018) are not significant" (Lunz et al. 2021b). Higher order terms were not significant.

V410 Tau

"The 2020 position of V410 Tau (HD 283518) was added to the 9 epochs listed in Galli et al. (2018). These epochs span from October 2014 to September 2017, used the same antenna network as the January 2020 observations, and used a self-calibrated image of the phase-calibrator as a model during the fringe fit. The first 5 epochs were observed at 8.4 GHz, whereas the last 4 epochs were observed at 5.0 GHz, consistent with the January 2020 observation at 4.6 GHz. The same phase calibrator, J0429+2724, was used. The

shifts of 0.016 7 mas in $\alpha*$ and 0.181 3 mas in δ were subtracted from the star positions from Galli et al. (2018) to reference them to ICRF3.

The formal errors are not improved between M_{old} and M_{new}. The additional observation uncertainties increase from $E_{\alpha*}$ = 116 µas and E_δ = 79 µas to $E_{\alpha*}$ = 199 µas and E_δ = 93 µas when the January 2020 position is included in the analysis, and the scatter of the residuals increases. The residuals at X-band and C-band however do not differ. Compared to the estimates in Galli et al. (2018), the new values are not significantly different but the proper motion is closer to the *Gaia* one" (Lunz et al. 2021b).

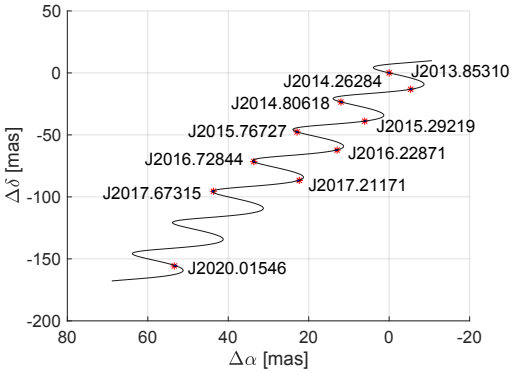

Figure 5.10 Observed positions, selected model in Table 5.12, and adjusted positions for V410 Tau. For a description of the plot, see Fig. 5.9.
Note. According to Lunz et al. (2021b, Fig. 1).

V410 Tau is a multiple star system (Harris et al. 2012) where one component is detected at radio frequencies. While Galli et al. (2018) could not determine a signature of orbital motion using their data, the inclusion of the January 2020 position provided a significant acceleration term in the $\alpha*$ direction (0.062 ± 0.024 mas/yr^2) applying Student's t-test at a significance level of 5 % (this level indicates the probability that the hypothesis is false when it is actually true). The $RMS_{v,\alpha*}$ and $RMS_{v,\delta}$ are reduced by about 25 % when comparing $M_{new,a}$ with M_{new}. Gaia EDR3 only provides a fit of five astrometric parameters. To be consistent, the M_{new} estimates are used for the frame alignment.

SS Cyg

"SS Cyg was observed by Miller-Jones et al. (2013) from April 2010 to October 2012 in 7 epochs with the VLBA at 8.4 GHz and in 2 epochs at 5 GHz with the European VLBI Network (EVN). In the publication, the phase-calibrator position of the EVN observations was already corrected to match that used by the VLBA. The 2020 position was referenced to the same phase-calibrator, J2136+4301, and observed at 8.1 GHz. All star positions were referred to the same ICRF3 phase-calibrator position by subtracting 0.454 2 mas in $\alpha*$ and 0.541 8 mas in δ from the 9 epochs in Miller-Jones et al. (2013). In all 10 epochs, the phase-calibrator data were processed by taking the self-calibrated image of the phase-calibrator as a structure model.

For M_{new}, the formal errors were reduced by 10 % to 20 % (for α and δ), 40 % (for ϖ) and by 70 % (for $\mu_{\alpha*}$ and μ_δ) compared to M_{old}. The additional observation uncertainty $E_{\alpha*}$

is 184 µas, while in the δ direction no uncertainty was added, since the reduced χ^2 was already below 1. The correlations between all parameters decrease when the new epoch in 2020 is included, especially those between α and δ, and between $\mu_{\alpha*}$ and μ_δ. Only the correlation between parallax and proper motion increases slightly. This indicates that more observations sensitive to the parallax determination are needed to decorrelate the parameters. The residuals at X-band and C-band do not differ" (Lunz et al. 2021b).

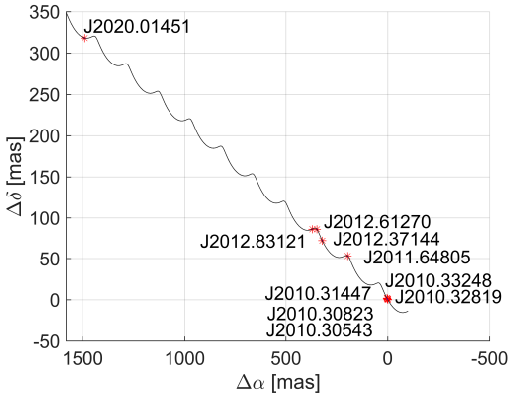

Figure 5.11 Observed positions, selected model in Table 5.12, and adjusted positions for SS Cyg. For a description of the plot, see Fig. 5.9.
Note. According to Lunz et al. (2021b, Fig. 1).

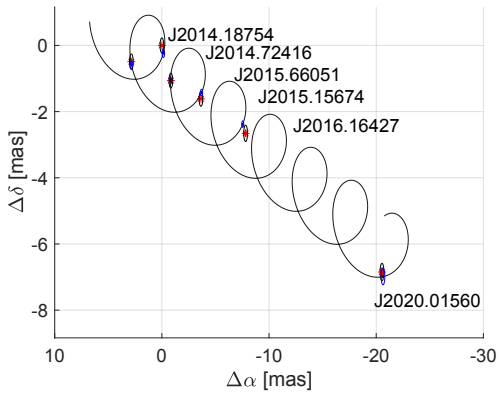

Figure 5.12 Observed positions, selected model in Table 5.12, and adjusted positions for Brun 334. For a description of the plot, see Fig. 5.9.
Note. According to Lunz et al. (2021b, Fig. 1).

Brun 334

"Brun 334 (VLBA 19, Parenago 1540) was observed by Kounkel et al. (2017) using the VLBA in 5 epochs between March 2014 and March 2016 at 5 GHz. The publication only gives the observation epochs to the precision of a full day. Therefore, the positions could be imprecise by up to 0.005 mas, considering the proper motion in *Gaia* EDR3 of 3.840 mas yr^{-1}. The star was observed in one epoch in January 2020 at 4.6 GHz relative to the same phase-calibrator, J0529−0519. The shifts of −0.752 2 mas in $\alpha*$ and 0.145 8 mas in δ were subtracted from the single-epoch star positions from Kounkel et al. (2017) to reference them to ICRF3. The phase-calibrator data were processed using the self-calibrated image of the phase-calibrator as a structure model at all epochs.

When the January 2020 position is included in the analysis, the formal errors of the proper motion parameters improve by 60 % and 40 %, respectively, while those of the position and parallax degrade (in δ 50 %). However, the residual scatter in each coordinate direction doubles and the additive variances (mostly in δ) need to be increased to obtain χ^2

equal one. [In contrast, when additional acceleration parameters are added in solution $M_{new,a}$, the same level of residuals as in M_{old} is reached and the Student's t-test with a significance level of 5 % reveals both acceleration terms to be significant.] Although Brun 334 is a spectroscopic binary (Marschall and Mathieu 1988), these short-term orbital parameters were not considered in this work. Comparing the model estimates to *Gaia* EDR3, which fit five astrometric parameters only, shows that the five-astrometric parameter model is in good agreement (2-σ level) [, whereas the $M_{new,a}$ model deviates more]. Therefore, the M_{new} model is used for the calculations in Sect. 5.6.4" (Lunz et al. 2021b). More observations should be conducted for this star to confirm the existence of long-term acceleration.

TYC 5346-538-1

"Star TYC 5346-538-1 (VLBA 45) was observed in 5 epochs between March 2014 and March 2016 by Kounkel et al. (2017) at 5 GHz. As for Brun 334, the epoch was only given to the precision of a full day. Considering the small proper motion in *Gaia* EDR3 of 0.610 mas yr^{-1}, this aspect is negligible for this study. The new observation in January 2020 was also observed at 4.6 GHz and the same phase-calibrator calibrator was used as for the historical observations, J0542−0913. All positions are based on an analysis with source structure corrections applied to the phase-calibrator data. The shifts of −0.945 0 mas in $\alpha*$ and −1.067 5 mas in δ were subtracted from the single-epoch star positions from Kounkel et al. (2017) to reference them to ICRF3. In addition, Kounkel et al. (2017) applied corrections of 0.256 mas in $\alpha*$ and 0.771 mas in δ to the positions of the first epoch and of 0.204 mas in $\alpha*$ and 0.659 mas in δ to the positions of the fourth epoch. It is believed that the reason is a pointing error due to calibration. These corrections were also imposed to the data to achieve the positions shown in Fig. 4 in Kounkel et al. (2017).

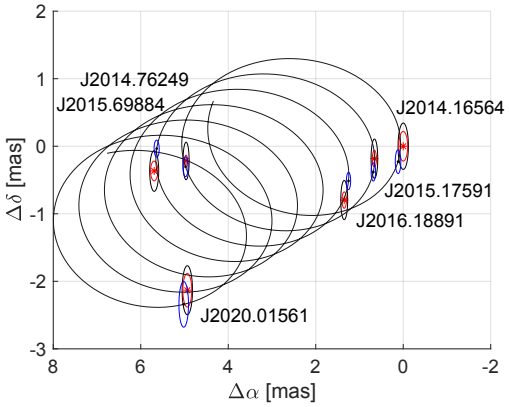

Figure 5.13 Observed positions, selected model in Table 5.12, and adjusted positions for TYC 5346-538-1. For a description of the plot, see Fig. 5.9.
Note. According to Lunz et al. (2021b, Fig. 1).

The reduced χ^2 in α direction is already 0.07 without adding additional weights to the data in model M_{old}. M_{old} and M_{new} differ by 0.299 ± 0.142 mas yr^{-1} in μ_δ, which is about 60 % of its value, and by -0.102 ± 0.049 mas yr^{-1} in $\mu_{\alpha*}$. Both parameters are closer to

the *Gaia* EDR3 solution for M_{new}. The formal errors for $\mu_{\alpha*}$ and μ_δ decrease by about 40 % compared to M_{old}, whereas the formal error in ϖ increases. $M_{old,orig}$ and $M_{new,orig}$ are solutions without applying the above corrections from Kounkel et al. (2017). They agree with the parameters M_{old}, M_{new}, and *Gaia* EDR3 within the uncertainty bounds, except for μ_δ which differs at the 1.4-σ level between M_{old} and $M_{old,orig}$" (Lunz et al. 2021b).

The various tests performed on the data have shown that further VLBI observations are needed to improve the determination of the proper motion in the declination direction as well as the position shifts in the first and fourth epochs.

BH CVn

"Star BH CVn (HR 5110) was observed at 15 epochs from May 1987 to May 1994 relative to J1317+3425 or relative to J1340+3754 in Lestrade et al. (1999). The 6 sessions relative to J1340+3754 were conducted at 8.4 GHz (observed after 01 January 1992), while the frequency of the other observations is 5.0 GHz for the four sessions before 01 January 1992 and 8.4 GHz for the sessions thereafter. The star was observed in January 2020 at 8.1 GHz relative to J1324+3622 and J1340+3754. A second reference source was chosen because J1340+3754 has significant structure and is relatively faint considering the sensitivity of the observations at the given frequency bands. Therefore, J1324+3622 was chosen as a backup calibrator, which is closer to the target star than the second historical calibrator J1317+3425, but also relatively faint. In Lestrade et al. (1999) the phase-calibrator data were corrected for source structure only for the positions relative to J1340+3754 because of its significant structure. The structure correction was applied for both positions in 2020. The star positions were referenced to the ICRF3 position of the respective calibrators at all epochs. This results in the shift of −0.285 0 mas in $\alpha*$ and 0.170 0 mas in δ subtracted from positions referenced to J1317+3425, and −0.866 2 mas in $\alpha*$ and 1.376 8 mas in δ from positions referenced to J1340+3754. The 2020 positions was already in ICRF3, so no correction was needed.

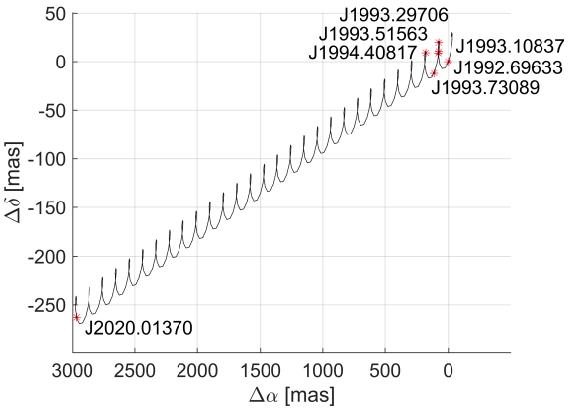

Figure 5.14 Observed positions, selected model in Table 5.12, and adjusted positions for BH CVn. For a description of the plot, see Fig. 5.9.
Note. According to Lunz et al. (2021b, Fig. 1).

As with the other stars in this study, several solutions with five astrometric parameters

were determined based on three different selections of observations to show the reliability of the final solution. M_{old} and M_{new} are based on the observations relative to all calibrators, whereas $M_{J1340+3754}$ contains only positions relative to calibrator J1340+3754 and M_{others} contains only positions referenced to the other two calibrators. Because $M_{J1340+3754}$ has the least residual scatter, this calibrator was used as the primary calibrator without additional weights in $M_{w0.5,new}$. Comparing the various solutions, no significant differences can be found for $\mu_{\alpha*}$. The estimate for parameter μ_δ converges to the *Gaia* EDR3 value when the 2020 position is added. The formal error of both parameters deceases by 80 % when the 2020 position is added. It decreases by more than 90 % for solution $M_{J1340+3754}$, but only by about 60 % for solution M_{others}. The result indicates that even though source structure was present for a calibrator and this was corrected during in the data analysis, the relative positions are more consistent than referencing to several more compact calibrators (without consistent calibration of their structure). The latter is the solution which determines the parallax worst in terms of formal error. Solution $M_{w0.5,new}$ is not significantly different from $M_{J1340+3754}$ and M_{new}, but $M_{J1340+3754}$ clearly has the lowest formal errors in all parameters. Thus, it is used for the analysis of the rotation parameters in Sect. 5.6.4, and the additional observations relative to other calibrators are thereby neglected. This is not possible for all corresponding stars in this study, as these stars do not have as many positions in the time series to choose from and therefore the solutions deteriorate more by neglecting a subset of the positions" (Lunz et al. 2021b).

Haro 1-6

"Star Haro 1-6 (DoAr 21) was observed in 9 epochs from September 2005 to August 2006 relative to J1625−2527 at 8.42 GHz in Loinard et al. (2008), where 7 epochs were of good quality. Another 8 epochs were conducted at the same frequency from December 2006 to September 2007 relative to J1625−2527. Three of the epochs were discarded due to influence of bad weather (Ortiz-León et al. 2017b). Then Ortiz-León et al. (2017b) observed the star in 2 epochs at 8 GHz and in 5 epochs at 5 GHz from August 2012 to October 2015 relative

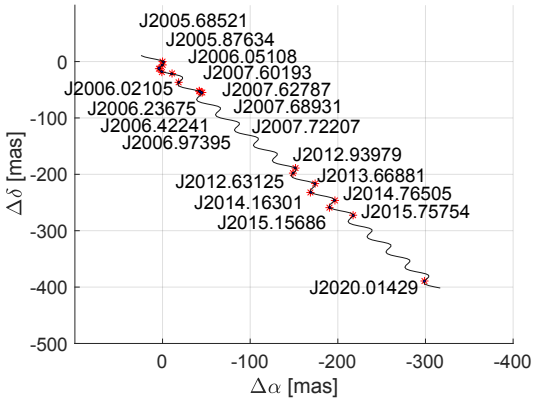

Figure 5.15 Observed positions, selected model in Table 5.12, and adjusted positions for Haro 1-6. For a description of the plot, see Fig. 5.9.
Note. According to Lunz et al. (2021b, Fig. 1).

to J1627−2426[11]. In the following, the re-
processed data from Ortiz-León et al. (2017b) is used, who referenced the star positions from all these observations to the same calibrator position of J1627−2426. In January 2020, the star was observed at 4.6 GHz relative to J1633−2557, since J1627−2426 is not in ICRF3 and probably too faint for the observation setup, and J1625−2527 has developed structure in the meantime. Just as in Ortiz-León et al. (2017b), the phase-calibrator data were processed by considering source structure correction.

To reference the star positions to the ICRF3 position of J1633−2557 at all epochs, the shifts of −0.345 mas in $\alpha*$ and −1.2 mas in δ between J1627−2426 and J1625−2527, as determined by Ortiz-León et al. (2017b) from observations between 2005 and 2007, were subtracted from the star positions in Ortiz-León et al. (2017b). Another shift of −0.030 0 mas in $\alpha*$ and 0.060 0 mas in δ was subtracted, corresponding to the position offset between the calibrator position of J1625−2527 from Ortiz-León et al. (2017b) and the rfc_2018b catalog used in the 2020 observation. Finally, a third shift of 0.755 0 mas in $\alpha*$ and −0.020 7 mas in δ was subtracted, which represents the difference between the observed calibrator position of J1625−2527 in the 2020 experiment (when phase-referenced to J1633−2557) and the rfc_2018b catalog position. This workaround is not ideal, however it reduces the $\mathrm{RMS}_{v,\delta}$ by 10 %. Calibrator J1627−2426 should get added to the next ICRF to resolve this issue.

To show the robustness of the final solution, several solutions based on three different subsets of the time series were obtained. $\mathrm{M_{all}}$ includes all the above mentioned positions as input data in the fitting process, while $\mathrm{M_{wo7}}$ excludes the position at the seventh epoch, since that position showed the largest residuals (about 6 mas for $\alpha*$) and was considered as an outlier. $\mathrm{M_{>2012}}$ includes only the more precise latest observations, similar to what was used for the final selection in Ortiz-León et al. (2017b). For each of the three different selections, a solution with (*new*) or without (*old*) the January 2020 position was obtained. Down-weighting the 2020 position by 0.5 mas, because it is relative to a different calibrator (similar to what was tested for the observations of BH CVn), does not change the results significantly, which is to be expected as the positions were previously homogenised to one calibrator position.

Comparing the model estimates $\mathrm{M_{all}}$ with $\mathrm{M_{wo7}}$, the additional noise required to achieve a χ^2 of 1 and the scatter of residuals decrease significantly in $\alpha*$. The proper motion estimates do not change, but the formal errors of $\mu_{\alpha*}$ decrease by 60 %. Furthermore ϖ decreases by 8 % and its formal error by 60 %. The ϖ of *Gaia* EDR3 lies between these two VLBI-based estimates and the ϖ of $\mathrm{M_{wo7}}$ deviates significantly from the *Gaia* EDR3

[11]Positions α = 246°.750025782, δ = -24°.444573598 are given in the VLBA archive for radio source J1627−2427. It is assumed to be the radio source J1627−2426 (α = 246°.750025121, δ = -24°.4445743194) in catalog rfc_2018b, whose position only differs by 2.38 mas and 2.60 mas.

result due to the decreased formal error. Employing only the more precise positions in $M_{>2012}$ reduces the residual scatter by more than half, and ϖ matches the *Gaia* EDR3 result. However, μ_δ deviates significantly compared to *Gaia* EDR3, even though the observation selection is closest in time to the *Gaia* EDR3 observations compared to the other selections. Since the formal error in proper motion parameters is smallest for the $M_{wo7,new}$ solution due to the long time interval between first and last observation employed, this solution is used in Sect. 5.6.4" (Lunz et al. 2021b).

σ^2 CrB

"Star σ^2 CrB was observed at 12 epochs from May 1987 to November 1994 relative to J1613+3412 in Lestrade et al. (1999) at 5.0 GHz in the first three epochs and at 8.4 GHz thereafter. In January 2020 the star was observed at 8.1 GHz relative to the same calibrator with positions in ICRF3. For calculation of the new estimates for the model of stellar motion, the position without structure correction during the fringe fit of the phase-calibrator is employed, since the correction was also not made in Lestrade et al. (1999). The subtraction of 0.101 7 mas in $\alpha*$ and 0.196 5 mas in δ is required to reference the star positions from the historical observations to ICRF3.

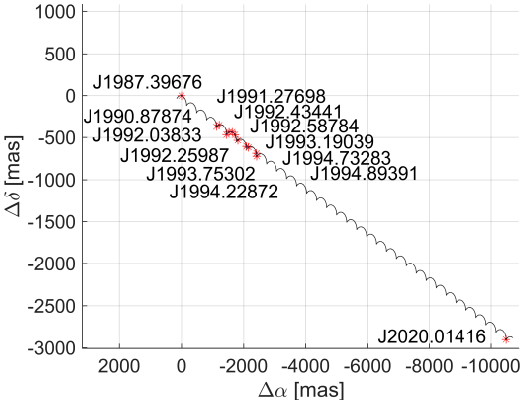

Figure 5.16 Observed positions, selected model in Table 5.12, and adjusted positions for σ^2 CrB. For a description of the plot, see Fig. 5.9.
Note. According to Lunz et al. (2021b, Fig. 1).

Additional weights are only needed in case of M_{new}. [The RMS of residual scatter decreases by about two thirds in α and about half in δ when acceleration terms are set up. They are highly significant in both coordinate directions.] Due to the large time difference between the historical observations and the 2020 position, small but significant linear acceleration terms [...] are needed to align the proper motion values from VLBI to *Gaia* EDR3, as shown by the better agreement of the proper motion and parallax parameters and the reduction of residual scatter in the case of $M_{new,a}$, where the estimated acceleration terms are $-0.046 \pm 0.004\,\mathrm{mas/yr^2}$ in $\alpha*$ and $-0.018 \pm 0.004\,\mathrm{mas/yr^2}$ in δ. The estimates for M_{old} and $M_{new,a}$ differ by $-1.137 \pm 0.060\,\mathrm{mas\,yr^{-1}}$ in μ_δ. Also $\mu_{\alpha*}$ changes by $-0.451 \pm 0.061\,\mathrm{mas\,yr^{-1}}$. Both estimates are closer to the *Gaia* EDR3 solution for $M_{new,a}$. Their formal errors decrease by more than 20 %, whereas the formal error of ϖ increases by about 15 % and those of the positions by about 100 % to 120 %. This could be due to the

change in epochs from about 1993 to 2016. Compared to values in Lestrade et al. (1999), the proper motion values were brought closer to those of *Gaia* EDR3" (Lunz et al. 2021b).

HD 199178

"Star HD 199178 was observed at 6 epochs from September 1992 to May 1994 relative to J2102+4702 in Lestrade et al. (1999) at 8.4 GHz. In January 2020, the star was observed at 8.1 GHz relative to the same calibrator with positions in ICRF3. For calculation of the new estimates for the model of stellar motion, the position without structure correction during the fringe fit of the phase-calibrator was employed, since the correction was also not made in Lestrade et al. (1999). The subtraction of 0.376 0 mas in $\alpha*$ and 1.386 1 mas in δ is required to reference the star positions from the historical observations to ICRF3.

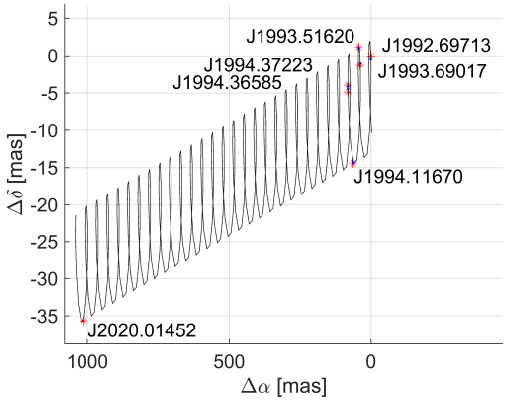

Figure 5.17 Observed positions, selected model in Table 5.12, and adjusted positions for HD 199178. For a description of the plot, see Fig. 5.9.
Note. According to Lunz et al. (2021b, Fig. 1).

The scatter of the residuals does not change comparing M_{old} and M_{new}. This shows that the observations fit each other well. Moreover, the formal errors decrease by about 97 % for proper motion and by 30 % for ϖ. The estimates M_{new} are closer to the *Gaia* EDR3 parameters than the ones from Lestrade et al. (1999), however because of the smaller formal errors, the differences for M_{new} are significant. No additional weights were added in either solution, and the χ^2 was 0.5. This is suggesting that the uncertainties were too pessimistic for the single-epoch positions" (Lunz et al. 2021b).

AR Lac

"Star AR Lac was observed at 6 epochs from July 1990 to May 1994 relative to J2202+4216 in Lestrade et al. (1999) at 5.0 GHz in the first two epochs and at 8.4 GHz thereafter. In January 2020, the star was observed at 8.1 GHz relative to the same calibrator with positions in ICRF3. The star was additionally observed relative to J2153+4322 because J2202+4216 shows a lot of structure and future observations could benefit from a more compact calibrator, which can nowadays be used due to the increased sensitivity of the antenna network compared to historical observations. The position without structure correction during the fringe fit of the phase-calibrator is employed because the correction was also not made in Lestrade et al. (1999). The epoch in July 1990 was observed

with poor uv-coverage (Lestrade et al. 1999). The subtraction of 0.173 0 mas in $\alpha*$ and 0.083 7 mas in δ is required to reference the star positions from the historical observations to ICRF3.

Adding the new position in 2020 to all available observations relative to J2202+4216 decreases the formal errors of the proper motions decrease by 90 % compared to solution M_{old}. Furthermore, the first epoch in July 1990, which was affected by poor uv-coverage, was removed in $M_{wo90,J2202+4216,new}$, which provides about 50 % less residual scatter and formal errors of all parameters compared to a solution including this epoch. Adding the star position relative to J2153+4322 in 2020 in solution $M_{wo90,w0.5,new}$ with an additional uncertainty of 0.5 mas in quadrature, the additional position has almost no influence on the estimates, which is verified by the position with respect to J2202+4216 having residuals of zero, while the position with respect to J2153+4322 has residuals of about ±0.28 mas. If no additional uncertainty was added, the uncertainties of the model parameters would double. Solution $M_{wo90,w0.5,new}$ is used for the analysis of the rotation parameters in Sect. 5.6.4 as the observation relative to J2153+4322 should not be completely excluded as it is technically not an outlier. Compared to the parameter values in Lestrade et al. (1999), $\mu_{\alpha*}$ is closer to *Gaia* EDR3. However, (similar for μ_δ) the formal error reduced considerably, which is why the selected solution shows a $> 3\sigma$ offset relative to *Gaia* EDR3, while it is $< 2\sigma$ for Lestrade et al. (1999). In contrast, ϖ of $M_{wo90,w0.5,new}$ is significantly off from *Gaia* EDR3 and ϖ of Lestrade et al. (1999) agrees with the one from *Gaia* EDR3 within about one standard deviation" (Lunz et al. 2021b).

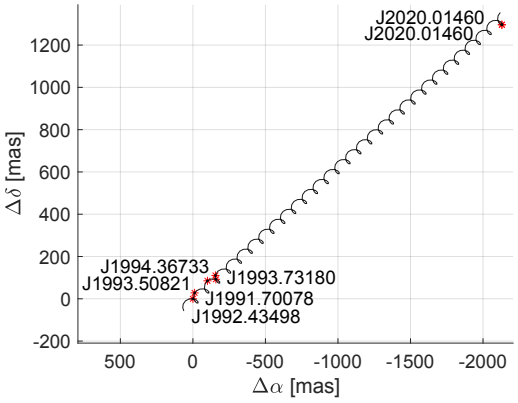

Figure 5.18 Observed positions, selected model in Table 5.12, and adjusted positions for AR Lac. For a description of the plot, see Fig. 5.9.
Note. According to Lunz et al. (2021b, Fig. 1).

IM Peg

"Star IM Peg was observed at 4 epochs from December 1991 to July 1994 relative to J2253+1608 in Lestrade et al. (1999) at 5.0 GHz in the first epoch and at 8.4 GHz thereafter. The subtraction of −0.031 8 mas in $\alpha*$ and −0.000 5 mas in δ is required for these star positions to reference them to ICRF3. In addition, 35 positions between January 1997 and July 2005 from the Gravity Probe B experiment at 8.3 GHz could be used (Ratner et al. 2012). They are referenced to point C1 in J2253+1608 with coordinates

$\alpha = 22\mathrm{h}53\mathrm{m}57\overset{\mathrm{s}}{.}7479573, \delta = 16°8'53\overset{''}{.}561281$ (Bartel et al. 2012), and the calibrator structure was corrected during the fringe-fit (Lebach et al. 2012). The subtraction of 0.257 7 mas in $\alpha*$ and 0.400 5 mas in δ is needed for these star positions to be referenced to ICRF3. To weight the positions relative to the data obtained in other studies, the 0.06 mas WRMS scatter of residuals of the astrometric check source determined in Ratner et al. (2012) was used as the position uncertainties $\sigma_{\alpha*,random}, \sigma_{\delta,random}$ of the star. In January 2020, the star was observed at 8.1 GHz relative to the same calibrator. For calculation of the new estimates for the model of stellar motion, the position obtained after correcting the phases of the calibrator for structure is used, since this correction was also used in the latest observations.

Adding the 2020 position, the formal errors of the proper motions in $\alpha*$ and δ decreased by 30 %, while the formal error in ϖ remained stable. The radio emission from star IM Peg has an orbital motion with a semi-major axis of 0.89 mas and an axis ratio of 0.30 (Ratner et al. 2012). The orbital motion has a period of 24.64877 days (Marsden et al. 2005). The reduction of the orbital pattern in the positions by subtracting the model values derived from the functional model for the linear orbital parameters in Table 3 of Ratner et al. (2012) resulted in a decrease in $\mathrm{RMS}_{v,\alpha*}$ of about 0.15 mas and in $\mathrm{RMS}_{v,\delta}$ of about 0.05 mas in the corresponding solution (labelled $\mathrm{M}_{\mathrm{orb,new}}$ in Table 5.12). Less additive errors were needed and thus the formal errors of all parameters decreased. However, the astrometric parameters did not change significantly (they remain within 1σ). Since the binary cannot be resolved by *Gaia*, the following analysis uses the estimates for the model without correction for the binary orbit trajectory, $\mathrm{M}_{\mathrm{new}}$. The new model estimates are not significantly different from those presented in previous studies, but the formal error of the proper motion values is significantly smaller" (Lunz et al. 2021b).

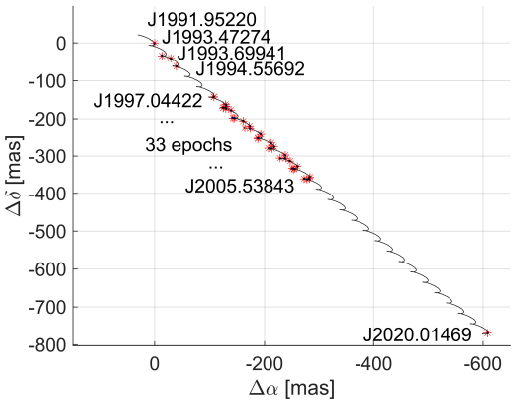

Figure 5.19 Observed positions, selected model in Table 5.12, and adjusted positions for IM Peg. For a description of the plot, see Fig. 5.9.
Note. According to Lunz et al. (2021b, Fig. 1).

HD 22468

"Star HD 22468 (HR 1099) was observed at 8 epochs from March 1991 to August 1994 relative to J0339−0146 in Lestrade et al. (1999) at 5.0 GHz in the first 3 sessions and

at 8.4 GHz thereafter. The subtraction of −0.012 0 mas in $\alpha*$ and −0.279 2 mas in δ is required for these star positions to be referenced to ICRF3. In addition, one position was obtained during experiment V515C (July 2018) relative to the same calibrator by the Long Baseline Array (LBA) supported by the ATNF (CSIRO), by Russian antennas operated by the Institute of Applied Astronomy of Russian Academy of Sciences (Shuygina et al. 2019), and by the HartRAO antenna in South Africa as described in Titov et al. (2020). The calibrator position was in ICRF3. Additional three positions in ICRF3 between May 2015 and July 2016 from absolute astrometry in S/X mode are published in Titov et al. (2020). Further details are given in Table 5.11. In January 2020, the star was observed at 8.1 GHz relative to the same calibrator, J0339−0146, with the VLBA. For calculation of the new estimates for the model of stellar motion, the position determined without correcting the phases of the calibrator for structure is employed, since the correction was not applied in the observations from the archive.

Several estimates of astrometric models were produced to test the impact of the new positions compared to using only the Lestrade et al. (1999) positions in solution M_{old}. The additional use of the 2018 and 2020 positions for the solution M_{new} leads to a reduction in the formal errors of the proper motions of more than 90 %, but also to a decrease of 40 % in those of ϖ. This can be justified by the two positions being located at the opposite extremes of the parallax pattern of the star.

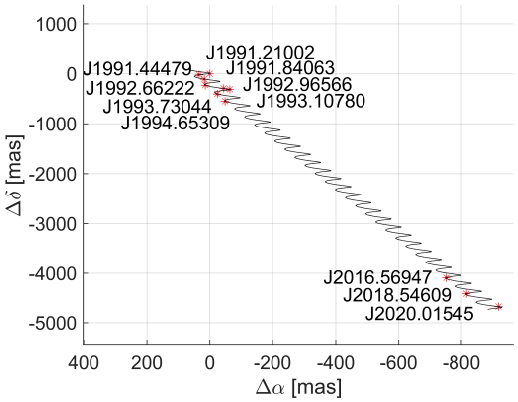

Figure 5.20 Observed positions, selected model in Table 5.12, and adjusted positions for HD 22468. For a description of the plot, see Fig. 5.9.

Note. According to Lunz et al. (2021b, Fig. 1).

As a final test, the three positions from absolute astrometry were included in the analysis, thus all 13 epochs were used. However, the first two epochs from absolute astrometry were discarded in solution $M_{abs,wo9\&10,new}$ because they had large residuals of several milliarcseconds after iterative rejection. Only the third epoch from experiment AOV010 was a good fit to the phase-referenced data. The number of observations in this epoch is 56 compared to 6 and 10 for the rejected epochs (Titov et al. 2020). Adding this position to the phase-referencing dataset does not change the results within the error bounds, but improves the formal errors by another 5 % to 10 % for the five parameters. These estimates are used as the model for comparison with *Gaia* in the following section" (Lunz et al. 2021b).

Star HD 22468 is a close binary with a period of about 2.8 days (Fekel 1983; García-Alvarez, D. et al. 2003). It is located in another binary system ADS 2644A with an

orbital period of 2101 years and 6.″2 orbital diameter (Lestrade et al. 1999). In solution $M_{abs,wo9\&10,new,a}$ the acceleration terms were added to the fitting process. The acceleration is not significant according to Student's t-test. The greater agreement of the parameter estimates for ϖ and $\mu_{\alpha*}$ with the *Gaia* EDR3 parameters and the reduction in $E_{\alpha*}$ as well as $RMS_{v,\alpha*}$ suggests that a long-term acceleration in α should be tested by adding more observations in a few years from now.

CoKu HP Tau G2

"Star CoKu HP Tau G2 (HP Tau/G2) was observed during 8 epochs between September 2005 and December 2007 with the VLBA at 8.42 GHz by Torres et al. (2009) relative to the calibrator J0426+2327. In addition, Galli et al. (2018) detected the star in 5 epochs at 8.4 GHz and in 4 epochs at 5.0 GHz between December 2012 and October 2017 relative to J0438+2153. They corrected the 8 epochs from Torres et al. (2009) for the shift of the calibrator position and combined the time series. The homogenized data are used for astrometric fitting and the star position obtained relative to J0438+2153 at 4.6 GHz, including correction for source structure, is added. The star positions from Galli et al. (2018) were corrected by subtracting −0.428 7 mas in $\alpha*$ and −0.049 2 mas in δ, to refer them to the calibrator position in ICRF3 as used for the position from UL005.

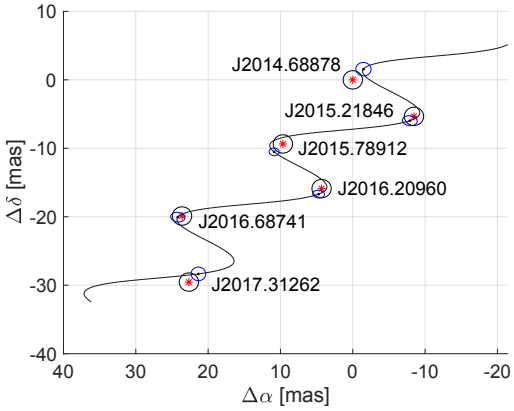

Figure 5.21 Observed positions, selected model in Table 5.12, and adjusted positions for CoKu HP Tau G2. For a description of the plot, see Fig. 5.9.
Note. According to Lunz et al. (2021b, Fig. 1).

The young star is the primary star in a gravitationally bound system with HP Tau G3 AB which has a separation of about 10" (Harris et al. 2012; Nguyen et al. 2012). HP Tau G3 AB itself is a close binary (Richichi et al. 1994). Linear acceleration terms are not sufficient to model the trajectory of CoKu HP Tau G2 given the above observations, as can be seen from the large residual scatter and the deviation from the *Gaia* EDR3 values for solutions based on all observations towards J0438+2153 (M_{new}). The non-linear model is supported by the RUWE parameter (re-normalized unit weight error, calculated from *Gaia* data; Lindegren et al. 2018) in *Gaia* EDR3, which is 3.85 for this star. [...] Galli et al. (2018) estimated orbital parameters in addition to position, proper motion, and parallax. In this work, orbital parameters are not considered. To compare the proper motion with

Gaia EDR3, the VLBI time series were therefore trimmed to match the *Gaia* EDR3 observations between 25 July 2014 and 28 May 2017" (Lunz et al. 2021b). Significant linear acceleration parameters $M_{Gaia,a}$ can still be detected and verified by Student's t-test. Comparing the model at *Gaia* EDR3 time $M_{Gaia,a}$ with acceleration terms, and M_{Gaia} without acceleration terms, to *Gaia* EDR3 parameters provides no clear indication which one better fits the *Gaia* EDR3 results. The proper motions of $M_{Gaia,a}$ are referenced to the *Gaia* epoch. Therefore the bias due to linear accelerations is limited.

M_{Gaia} is applied in the following analysis to best match the *Gaia* EDR3 model parameterization. No difference in residuals for X-band and C-band observations can be found, thus frequency dependent position offsets are not considered.

del Lib

"Star del Lib (HD 132742) was observed at 3 epochs from July 2016 to July 2020. The positions in experiment UL005 (January 2020) were obtained relative to two different calibrators, J1456−0617 and J1510−0843, at 8.1 GHz. During experiment AOV010 (July 2016) it was observed relative to J1456−0617 with the Asia-Oceania VLBI network (AOV) and during experiment V583B (July 2020) it was observed relative to J1512−0905 by the LBA, both at about 8.4 GHz. The positions are listed in Table 5.11. The star position derived without correcting the calibrator phases for structure was used for this fit because the other experiments did not use it either. To reference all observations to ICRF3, −0.457 2 mas in $\alpha*$ and 0.209 2 mas in δ were subtracted from the position of J1512−0905, which was originally $\alpha = 15\mathrm{h}12\mathrm{m}50\overset{\mathrm{s}}{.}5329, \delta = -9°5'59''.830$. All observations relative to J1456−0617 have already been in ICRF3.

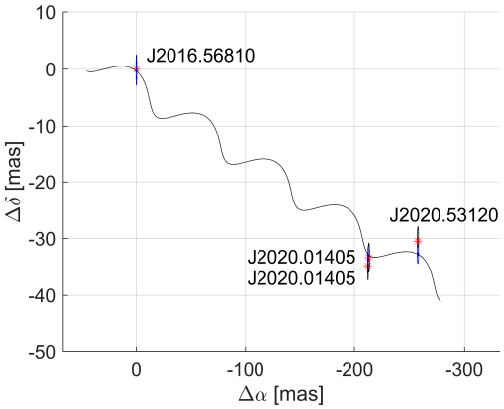

Figure 5.22 Observed positions, selected model in Table 5.12, and adjusted positions for del Lib. For a description of the plot, see Fig. 5.9.
Note. According to Lunz et al. (2021b, Fig. 1).

An additional uncertainty of 0.5 mas was applied to the star positions that are not relative to J1456−0617 to test the impact of a potential star position offset from referencing to one or the other calibrator. The resulting solution $M_{w0.5,new}$ is not significantly different from a solution without the additional uncertainties M_{new}. The VLBI model estimates differ from those of *Gaia* EDR3, but for comparison, those of *Gaia* DR2 differ again.

$M_{w0.5,new}$ was used in the following" (Lunz et al. 2021b).

HD 142184

"Star HD 142184 (HR 5907, 1550−238) was not in the sample of VLBA observations in January 2020 because it is a Be-type star and therefore may exhibit radio emission from stellar winds leading to radio-optical offsets. The star is one of the fastest rotating stars. Data from absolute astrometry performed with the LBA, VLBA, AOV, and other networks were collected. During experiment V583B (July 2020) it was furthermore observed relative to J1553−2422 with the LBA at about 8.4 GHz. To reference the observation to ICRF3, −0.209 8 mas in $\alpha*$ and −0.049 1 mas in δ were subtracted from the position of J1512−0905, which was originally $\alpha = 15^h53^m31^s.6278, \delta = -24°22'6''.036$. They are listed in Table [...][2 in Lunz et al. (2021b)]. The proper motion and parallax [of M_{new}] are in agreement with the *Gaia* EDR3 values within the error bounds. Because most of the data is not referenced to ICRF3 but the aus2020b[12] reference frame, the positions were not included in the analysis of the rotation parameters in the following section, and only the remaining model parameters from M_{new} were used[13]. For propagation of the *Gaia* parameters to the VLBI epoch, the radial velocity $v_r = -9.2\,km\,s^{-1}$ was taken from the SIMBAD database (Wenger et al. 2000)" (Lunz et al. 2021b). The model estimates $M_{new,a}$ indicate a linear acceleration in the trajectory of the star. However, the proper motion and parallax from the solution without acceleration terms, M_{new}, fit the *Gaia* EDR3 data better. This star certainly is a candidate for more detailed comparison of radio and optical emission.

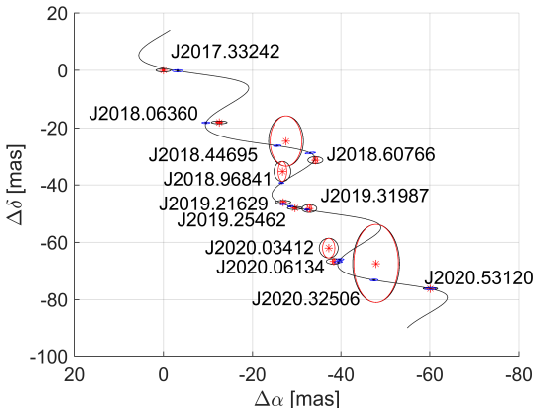

Figure 5.23 Observed positions, selected model in Table 5.12, and adjusted positions for HD 142184. For a description of the plot, see Fig. 5.9.
Note. According to Lunz et al. (2021b, Fig. 1).

Additional single-epoch positions

"For four additional stars, only one or two epochs were available from experiments observed at 8.4 GHz by the LBA. They are listed in Table 5.11. In experiments V583A

[12] ftp://ivs.bkg.bund.de/pub/vlbi/ivsproducts/crf/aus2020b.crf.txt, accessed 13 December 2021.
[13] In future work, the position from V583B can be added to the rotation parameter analysis as an absolute position. However, for this work, it was not considered.

(March 2020) and V583B (July 2020), star HD 167971 was observed, but relative to two different calibrators. The shift of 0.042 8 mas in $\alpha*$ and $-0.010\,2$ mas in δ is subtracted for the star position relative to J1818−1108 and the shift of 0.001 1 mas in $\alpha*$ and 0.000 5 mas in δ is subtracted for the star position relative to J1832−1035 to transfer them to ICRF3. Because the time interval between first and last scan of a radio star in experiment V583A was only about 20 to 30 minutes, the uv-coverage was sparse, so the side lobes were large and so is the uncertainty of the position. The same is true for stars V479 Sct (shift of $-0.000\,5$ mas in $\alpha*$ and $-0.000\,4$ mas in δ) and EI Eri (shift of $-0.000\,6$ mas in $\alpha*$ and 0.000 4 mas in δ), which were also observed in experiment V583A. Star YY Men was observed in absolute geodetic mode in two single-baseline experiments in 1990 and 1991, from which the position from 1990 could be restored. In addition, it was detected in experiment V583B relative to J0529−7245. The shift of 0.003 6 mas in $\alpha*$ and 0.005 0 mas in δ is subtracted to reference the position to ICRF3" (Lunz et al. 2021b).

Recapitulation

"The RMS of the residual scatter shows that modern phase-referencing observations can reach levels of 0.1 mas to 0.2 mas and below, whereas inclusion of historical observations from around the 1990s (case of BH CVn, HD 199178, AR Lac, IM Peg, HD 22468) yields RMS levels of about 0.2 mas to 0.6 mas. Other reasons, such as orbital jitter (see Lestrade et al. 1999), may account for the differences as well. This effect is specific to each source and can be studied in detail. For the present study it is negligible, since the long-term linear proper motions are of interest.

At the present stage, accelerations are not considered in the rotation parameter analysis. However, six stars were found to have signs of non-linear proper motion from their VLBI data verified by Student's t-test with significance level of 5 % (V410 Tau, Brun 334, σ^2 CrB, HD 22468, CoKu HP Tau G2, and HD 142184). For some stars, the model estimates better fit the values of the astrometric *Gaia* model when the same parameterization is applied (i.e. with no acceleration terms). This is usually the case when the VLBI mean epoch is close in time to the *Gaia* observations, such as for V410 Tau, Brun 334, and HD 142184. In the case of σ^2 CrB, the proper motion estimates are closer to the *Gaia* estimates when the accelerations are also estimated. This star is representative of those objects for which the mean epoch of the VLBI observations is temporally more distant from the *Gaia* observation time interval. Star CoKu HP Tau G2 has a more complicated trajectory. Restricting the VLBI time interval to the time interval of the Gaia EDR3 observations, significant acceleration parameters can be detected, however there are no significant proper motion differences between models with and without acceleration terms. Star HD 22468 is a close binary with a period of about 2.8 days (Fekel 1983; García-Alvarez, D. et al.

Table 5.11 Star positions from other research works used in this study. The references are given in the two last columns.

Star	Calibrator	Epoch t [Julian year]	$\alpha(t)$ [h m s]	$\sigma_{\alpha*,\mathrm{random}}$ [s]	$\delta(t)$ [° ′ ″]	$\sigma_{\delta,\mathrm{random}}$ [″]	Calibrator α [h m s]	Calibrator δ [° ′ ″]	Ref.	Project code	Network
HD 142184	absolute	2457875.66760	15 53 55.8473903	0.0000217	-23 58 41.562171	0.000406	...	...	Titov et al. (2020)	AUA020	AUA(1)
HD 142184	absolute	2458142.72890	15 53 55.8465556	0.0000466	-23 58 41.580231	0.000314	...	...	Titov et al. (2020)	AOV019	AOV
HD 142184	absolute	2458282.74890	15 53 55.8455544	0.0002387	-23 58 41.586771	0.008776	...	...	This work	18JUN13XW	VLBA
HD 142184	absolute	2458341.44780	15 53 55.8451101	0.0000348	-23 58 41.593428	0.001182	...	...	This work	UG002O	VLBA
HD 142184	absolute	2458473.21000	15 53 55.8456092	0.0000647	-23 58 41.597420	0.003519	...	...	This work	UG002V	VLBA
HD 142184	absolute	2458563.75110	15 53 55.8455989	0.0000405	-23 58 41.608241	0.000496	...	...	Titov et al. (2020)	AOV033	AOV
HD 142184	absolute	2458577.75080	15 53 55.8454197	0.0000353	-23 58 41.610263	0.000351	...	...	Titov et al. (2020)	AOV034	AOV
HD 142184	absolute	2458601.58380	15 53 55.8452023	0.0000334	-23 58 41.610419	0.001328	...	...	This work	UG003H	VLBA
HD 142184	absolute	2458862.46170	15 53 55.8449085	0.0000928	-23 58 41.624139	0.003391	...	...	This work	UG003T	VLBA
HD 142184	absolute	2458872.40590	15 53 55.8448337	0.0000232	-23 58 41.628742	0.000865	...	...	This work	UG03T1	VLBA
HD 142184	absolute	2458968.72980	15 53 55.8441951	0.0003340	-23 58 41.629517	0.013609	...	...	This work	AOV046	AOV(1)
HD 142184	J1553−2422	2459044.02083	15 53 55.8433673	0.0000022	-23 58 41.638212	0.000133	15 53 31.62780000	-24 22 6.0360000	This work	V583B	LBA
HD 167971	J1818−1108	2458929.66667	18 18 5.8926205	0.0001457	-12 14 33.308782	0.001516	18 18 19.31660000	-11 8 48.3290000	This work	V583A	LBA
HD 167971	J1832−1035	2459044.02083	18 18 5.8798553	0.0000224	-12 14 33.360195	0.000321	18 32 20.83640000	-10 35 11.2000000	This work	V583B	LBA
V479 Sct	J1838−1833	2458929.66667	18 26 15.0661506	0.0000003	-14 50 54.408599	0.000022	18 38 37.69160000	-18 33 55.2600000	This work	V583A	LBA
EI Eri	J0408−0529	2458929.66667	4 9 40.9432071	0.0000007	-7 53 32.068041	0.000039	4 8 59.64990000	-5 29 40.5380000	This work	V583A	LBA
YY Men	J0529−7245	2459044.02083	4 58 17.9152711	0.0000271	-75 16 38.050921	0.000166	5 29 30.04220000	-72 45 28.5070000	This work	V583B	LBA
YY Men	absolute	2448236.00000	4 58 17.9479200	0.0002900	-75 16 38.085200	0.013600	...	...	This work	South-12	DSS45-Hobart26
del Lib	J1456−0617	2457596.50000	15 0 58.2774500	0.0000130	-8 31 8.300300	0.000120	14 56 41.39265522	-6 17 43.2039727	Titov et al. (2020)	AOV010	AOV
del Lib	J1512−0905	2459044.02083	15 0 58.2602504	0.0000031	-8 31 8.330971	0.000161	15 12 50.53290000	-9 5 59.8300000	This work	V583B	LBA
HD 22468	J0339−0146	2458318.95833	3 36 47.2525900	0.0000060	0 35 12.948100	0.000080	3 39 30.93778633	-01 46 35.8041892	Titov et al. (2020)	V515C	LBA(2)
HD 22468	absolute	2457160.00000	3 36 47.2573000	0.0008000	0 35 13.470000	0.004000	...	...	This work	AOV003	AOV
HD 22468	absolute	2457582.00000	3 36 47.2562000	0.0003400	0 35 13.308000	0.002000	...	...	This work	AUA011	AUA(1)
HD 22468	absolute	2457597.00000	3 36 47.2569000	0.0000300	0 35 13.269000	0.000300	...	...	This work	AOV010	AOV

Notes. Position α (t) and δ (t) at epoch t and respective uncertainties $\sigma_{\alpha*,\mathrm{random}}$ and $\sigma_{\delta,\mathrm{random}}$, information about the observing network and frequency as well as the position type ("absolute" in case of absolute geodetic VLBI and a calibrator name given in case of phase-referencing observations as collected from the respective references. The original calibrator positions "Calibrator α" and "Calibrator δ" taken from the references "Ref." are also given. $\alpha* = \alpha \cdot \cos(\delta)$.
(1)The network was enlarged with more participating stations. Details can be found in the IVS master schedules available at https://ivscc.gsfc.nasa.gov/program/master.html.
(2) See Titov et al. (2020).
Note. According to Lunz et al. (2021b, Table 3).

2003). It is located in another binary system ADS 2644A with an orbital period of 2101 years and 6.″2 orbital diameter (Lestrade et al. 1999). For this star, the acceleration terms are not determined significant according to Student's t-test. The greater agreement of the parameter estimates with the *Gaia* EDR3 parameters and the reduction in $E_{\alpha*}$ as well as $\mathrm{RMS}_{v,\alpha*}$ however suggests that a long-term acceleration in α should be tested by adding more observations in a few years from now.

The detailed investigation of the various star time series showed that for some stars more observations would help proving the existence of long-term accelerations (V410 Tau, Brun 334, HD 22468), decorrelating the model parameters (SS Cyg, Haro 1-6), or investigating the reason for significant model differences between VLBI and Gaia (AR Lac)" (Lunz et al. 2021b).

Table 5.12 Newly derived estimates for the astrometric models of stellar motion.

model	$E_{\alpha*}$	E_δ	$\mathrm{RMS}_{v,\alpha*}$	$\mathrm{RMS}_{v,\delta}$	Σn	t_0	α_0	$\sigma_{\alpha*_0}$	δ_0	σ_{δ_0}	ϖ	σ_ϖ	$\mu_{\alpha*}$	$\sigma_{\mu_{\alpha*}}$	μ_δ	σ_{μ_δ}	$a_{\alpha*}$	$\sigma_{a_{\alpha*}}$	a_δ	σ_{a_δ}
	[μas]		[mas]			[Julian year]	[°]	[mas]	[°]	[mas]	[mas]		[mas yr^{-1}]		[mas yr^{-1}]		[mas yr^{-2}]		[mas yr^{-2}]	
HD 283572																				
ref. (1,2)	...	...	...	...	...	2005.36000	65.495216803	0.032	+28.301769751	0.035	+7.841	0.057	+9.023	0.061	−26.445	0.077	...	...	...	...
ref. (1)	...	...	...	...	...	...	...	...	...	...	+7.722	0.057	+8.853	0.096	−26.491	0.113	...	...	...	...
Gaia EDR3	...	...	...	...	...	2016.00000	65.495246613	0.018	+28.301691618	0.009	+7.873	0.019	+8.837	0.027	−26.426	0.017	...	...	...	...
$\mathrm{M_{old}}$	122	185	0.102	0.161	6	2005.36121	65.495216801	0.054	+28.301769680	0.080	+7.736	0.068	+8.865	0.114	−26.502	0.190	...	...	...	...
$\mathrm{M^{(1)}_{new}}$	105	165	0.097	0.159	7	2007.45467	65.495222674	0.043	+28.301754339	0.068	+7.745	0.059	+8.892	0.008	−26.386	0.013	...	...	...	...
V410 Tau																				
ref. (1)	...	...	...	...	...	...	...	...	...	...	+7.751	0.027	+8.703	0.017	−24.985	0.020	...	...	...	...
Gaia EDR3	...	...	...	...	...	2016.00000	64.629661927	0.019	+28.454376079	0.009	+7.730	0.021	+8.846	0.025	−25.129	0.016	...	...	...	...
$\mathrm{M_{old}}$	116	79	0.102	0.075	9	2015.75818	64.629661280	0.040	+28.454377875	0.029	+7.749	0.043	+8.705	0.028	−24.985	0.024	...	...	...	...
$\mathrm{M^{(1)}_{new}}$	199	93	0.175	0.100	10	2016.18390	64.629662471	0.064	+28.454374915	0.033	+7.707	0.067	+8.786	0.033	−25.010	0.022	...	...	...	...
$\mathrm{M_{new,a}}$	151	90	0.125	0.075	10	2016.00000	64.629661934	0.059	+28.454376202	0.038	+7.732	0.052	+8.738	0.030	−24.996	0.023	+0.062	0.024	−0.031	0.021
SS Cyg																				
ref. (3,2)	108	91	...	...	...	2011.56610	325.678846337	0.065	+43.586181392	0.070	+8.800	0.120	+112.420	0.070	+33.380	0.070	...	...	...	...
Gaia EDR3	...	...	...	...	...	2016.00000	325.679037286	0.022	+43.586222469	0.026	+8.854	0.030	+112.385	0.029	+33.315	0.033	...	...	...	...
$\mathrm{M_{old}}$	164	0	0.229	0.145	9	2011.22802	325.678831631	0.101	+43.586178393	0.050	+8.841	0.094	+112.449	0.064	+33.399	0.049	...	...	...	...
$\mathrm{M^{(1)}_{new}}$	184	0	0.243	0.136	10	2012.10667	325.678869501	0.081	+43.586186535	0.043	+8.896	0.054	+112.415	0.019	+33.353	0.014	...	...	...	...
Brun 334																				
ref. (4,2)[(2)]	...	...	...	...	...	2015.18000	83.665666567	0.023	−5.407112221	0.048	+2.591	0.046	−4.010	0.080	−1.170	0.070	...	...	...	...
Gaia EDR3	...	...	...	...	...	2016.00000	83.665665932	0.009	−5.407112470	0.008	+2.569	0.014	−3.736	0.012	−0.887	0.010	...	...	...	...
$\mathrm{M_{old}}$	150	132	0.061	0.093	5	2015.17864	83.665666765	0.069	−5.407112250	0.063	+2.524	0.070	−3.943	0.098	−1.221	0.094	...	...	...	...
$\mathrm{M^{(1)}_{new}}$	169	226	0.132	0.181	6	2015.98480	83.665665922	0.072	−5.407112466	0.097	+2.502	0.079	−3.766	0.037	−0.995	0.055	...	...	...	...
$\mathrm{M_{new,a}}$	120	125	0.065	0.082	6	2016.00000	83.665665867	0.076	−5.407112524	0.086	+2.529	0.052	−3.868	0.048	−1.127	0.054	+0.080	0.033	+0.109	0.037
TYC 5346-538-1																				
ref. (4,2)	...	...	...	...	...	2015.20000	85.640319910	0.058	−8.120884301	0.140	+2.348	0.069	+0.680	0.090	−0.510	0.250	...	...	...	...
Gaia EDR3	...	...	...	...	...	2016.00000	85.640320285	0.009	−8.120884072	0.010	+2.363	0.013	+0.580	0.012	−0.189	0.012	...	...	...	...
$\mathrm{M_{old}}$	0	114	0.012	0.013	5	2015.19836	85.640320180	0.022	−8.120884015	0.078	+2.348	0.026	+0.686	0.043	−0.524	0.121	...	...	...	...
$\mathrm{M^{(1)}_{new}}$	61	264	0.076	0.235	6	2016.00123	85.640320310	0.037	−8.120884063	0.126	+2.328	0.039	+0.584	0.024	−0.225	0.075	...	...	...	...
$\mathrm{M_{old,orig}}$	139	398	0.111	0.302	5	2015.19836	85.640320157	0.070	−8.120884022	0.189	+2.336	0.071	+0.739	0.099	−0.092	0.274	...	...	...	...
$\mathrm{M_{new,orig}}$	167	331	0.142	0.283	6	2016.00123	85.640320289	0.076	−8.120884058	0.151	+2.336	0.083	+0.603	0.041	−0.166	0.086	...	...	...	...

Table 5.12 continued.

model	$E_{\alpha*}$ [μas]	E_δ [μas]	$\mathrm{RMS}_{v,\alpha*}$ [mas]	$\mathrm{RMS}_{v,\delta}$ [mas]	Σn	t_0 [Julian year]	α_0 [°]	$\sigma_{\alpha*_0}$ [mas]	δ_0 [°]	σ_{δ_0} [mas]	ϖ [mas]	σ_ϖ	$\mu_{\alpha*}$ [mas yr^{-1}]	$\sigma_{\mu_{\alpha*}}$	μ_δ [mas yr^{-1}]	σ_{μ_δ}	$a_{\alpha*}$ [mas yr^{-2}]	$\sigma_{a_{\alpha*}}$	a_δ [mas yr^{-2}]	σ_{a_δ}
BH CVn																				
ref.(6,2)	...	...	...	...	...	1993.10880	203.698997828	0.373	+37.182433334	0.455	+22.210	0.450	+85.496	0.131	−9.220	0.160	...	...	...	...
Gaia EDR3	...	...	...	...	...	2016.00000	203.699680762	0.044	+37.182371955	0.048	+21.327	0.089	+85.609	0.043	−9.549	0.051	...	...	...	...
$\mathrm{M}_{\mathrm{old}}$	1043	1373	1.656	1.649	14	1992.05054	203.698966582	0.580	+37.182435878	0.580	+22.475	0.683	+85.618	0.179	−9.351	0.228	...	...	...	...
$\mathrm{M}_{\mathrm{new}}$	869	1422	1.575	1.696	16	1995.54593	203.699070754	0.445	+37.182426495	0.511	+22.294	0.655	+85.504	0.037	−9.673	0.044	...	...	...	...
$\mathrm{M}^{(1)}_{\mathrm{J1340+3754}}$	0	0	0.687	0.468	7	1997.25288	203.699121926	0.282	+37.182421740	0.224	+21.578	0.333	+85.482	0.018	−9.696	0.012	...	...	...	...
$\mathrm{M}_{\mathrm{others}}$	168	2053	1.282	2.015	9	1994.21831	203.699031029	0.614	+37.182430076	1.025	+23.092	1.146	+85.503	0.055	−9.618	0.085	...	...	...	...
$\mathrm{M}_{\mathrm{w0.5,new}}$	785	1348	1.575	1.698	16	1995.54593	203.699070762	0.443	+37.182426490	0.503	+22.268	0.646	+85.502	0.036	−9.675	0.044	...	...	...	...
Haro 1-6																				
ref. (5,2)	...	...	...	...	...	2007.99000	246.512566654	0.399	−24.393446456	0.356	+7.385	0.234	−19.630	0.190	−26.920	0.130	...	...	...	...
Gaia EDR3	...	...	...	...	...	2016.00000	246.512518670	0.026	−24.393506245	0.014	+7.344	0.031	−19.798	0.045	−27.146	0.033	...	...	...	...
$\mathrm{M}_{\mathrm{all,old}}$	1759	595	1.640	0.561	19	2009.45441	246.512557797	0.421	−24.393457135	0.139	+7.592	0.435	−19.606	0.099	−27.047	0.037	...	...	...	...
$\mathrm{M}_{\mathrm{all,new}}$	1716	589	1.605	0.556	20	2009.98241	246.512554617	0.395	−24.393461095	0.134	+7.521	0.417	−19.636	0.082	−27.034	0.031	...	...	...	...
$\mathrm{M}_{\mathrm{wo7,old}}$	680	642	0.633	0.608	18	2009.61057	246.512556911	0.167	−24.393458297	0.153	+6.961	0.187	−19.675	0.039	−27.049	0.041	...	...	...	...
$\mathrm{M}^{(1)}_{\mathrm{wo7,new}}$	659	628	0.617	0.597	19	2010.15813	246.512553621	0.156	−24.393462404	0.146	+6.947	0.177	−19.680	0.032	−27.037	0.034	...	...	...	...
$\mathrm{M}_{>2012,\mathrm{old}}$	340	220	0.270	0.184	7	2014.15461	246.512529655	0.128	−24.393492465	0.084	+7.385	0.134	−19.631	0.108	−26.928	0.083	...	...	...	...
$\mathrm{M}_{>2012,\mathrm{new}}$	340	190	0.286	0.178	8	2014.88707	246.512525240	0.120	−24.393497950	0.072	+7.381	0.136	−19.732	0.053	−26.949	0.036	...	...	...	...
σ^2CrB																				
ref.(6,2)	...	...	...	...	...	1990.00140	243.671114605	0.104	+33.858853887	0.124	+43.930	0.100	−267.048	0.037	−86.660	0.050	...	...	...	...
Gaia EDR3	...	...	...	...	...	2016.00000	243.668787168	0.033	+33.858226431	0.041	+44.057	0.046	−268.216	0.043	−87.282	0.058	...	...	...	...
$\mathrm{M}_{\mathrm{old}}$	0	0	0.341	0.280	12	1992.47265	243.670893774	0.110	+33.858794346	0.092	+43.844	0.108	−267.078	0.047	−86.671	0.049	...	...	...	...
$\mathrm{M}_{\mathrm{new}}$	1596	344	1.527	0.543	13	1994.59123	243.670704024	0.472	+33.858743174	0.164	+43.496	0.280	−267.725	0.049	−86.947	0.016	...	...	...	...
$\mathrm{M}^{(1)}_{\mathrm{new,a}}$	0	0	0.415	0.272	13	2016.00000	243.668787173	0.215	+33.858226371	0.206	+43.809	0.124	−268.215	0.037	−87.122	0.036	−0.046	0.004	−0.018	0.004
HD 199178																				
ref.(6,2)	...	...	...	...	...	1993.79330	313.473486712	0.332	+44.386412565	0.397	+8.590	0.330	+26.595	0.407	−1.240	0.430	...	...	...	...
Gaia EDR3	...	...	...	...	...	2016.00000	313.473714681	0.011	+44.386407243	0.013	+8.891	0.015	+26.451	0.015	−0.877	0.015	...	...	...	...
$\mathrm{M}_{\mathrm{old}}$	0	0	0.576	0.226	6	1993.79305	313.473486760	0.263	+44.386412351	0.200	+8.637	0.285	+26.555	0.389	−1.221	0.326	...	...	...	...
$\mathrm{M}^{(1)}_{\mathrm{new}}$	0	0	0.548	0.277	7	1997.53897	313.473525218	0.210	+44.386411488	0.152	+8.768	0.206	+26.421	0.008	−0.819	0.011	...	...	...	...

Table 5.12 continued.

model	$E_{\alpha*}$	E_δ	$\mathrm{RMS}_{v,\alpha*}$	$\mathrm{RMS}_{v,\delta}$	Σn	t_0	α_0	$\sigma_{\alpha*_0}$	δ_0	σ_{δ_0}	ϖ	σ_ϖ	$\mu_{\alpha*}$	$\sigma_{\mu_{\alpha*}}$	μ_δ	σ_{μ_δ}	$a_{\alpha*}$	$\sigma_{a_{\alpha*}}$	a_δ	σ_{a_δ}
	[μas]		[mas]			[Julian year]	[°]	[mas]	[°]	[mas]	[mas]		[mas yr^{-1}]		[mas yr^{-1}]		[mas yr^{-2}]		[mas yr^{-2}]	
AR Lac																				
ref.(6,2)	...	...	...	...	...	1992.43530	332.170232910	0.274	+45.742153188	0.361	+23.970	0.370	−52.080	0.126	+47.030	0.190	...	...	...	...
Gaia EDR3	...	...	...	...	...	2016.00000	332.169742736	0.018	+45.742460766	0.017	+23.525	0.023	−52.310	0.021	+46.931	0.020	...	...	...	...
$\mathrm{M_{old}}$	0	0	0.684	0.469	6	1992.70656	332.170227205	0.432	+45.742156681	0.339	+24.125	0.409	−52.023	0.192	+47.297	0.196	...	...	...	...
$\mathrm{M_{wo90,J2202+4216,new}}$	0	0	0.355	0.248	6	1997.62628	332.170124990	0.180	45.742221000	0.139	24.275	0.216	−52.233	0.010	47.032	0.011	...	...	...	...
$\mathrm{M^{(1)}_{wo90,w0.5,new}}$	0	0	0.346	0.249	7	2000.82461	332.170058496	0.164	45.742262784	0.121	24.275	0.238	−52.233	0.011	47.032	0.013	...	...	...	...
IM Peg																				
ref.(6,2)	...	...	...	...	...	1992.91720	343.259484359	0.360	+16.841247861	0.392	+10.280	0.620	−20.587	0.459	−27.530	0.400	...	...	...	...
ref.(7,2)	...	...	...	...	...	2005.08690	343.259410883	0.400	+16.841155569	0.390	+10.370	0.074	−20.833	0.090	−27.267	0.095	...	...	...	...
Gaia EDR3	...	...	...	...	...	2016.00000	343.259344951	0.056	+16.841072625	0.049	+10.166	0.065	−21.185	0.063	−27.444	0.060	...	...	...	...
$\mathrm{M_{old}}$	572	635	0.558	0.640	39	2000.48153	343.259438677	0.096	+16.841190373	0.106	+10.424	0.117	−20.847	0.031	−27.306	0.034	...	...	...	...
$\mathrm{M^{(1)}_{new}}$	570	631	0.556	0.632	40	2000.96986	343.259435726	0.094	+16.841186666	0.103	+10.408	0.113	−20.826	0.021	−27.322	0.024	...	...	...	...
$\mathrm{M_{orb,new}}$	382	545	0.401	0.584	40	2000.96986	343.259435710	0.064	+16.841186652	0.090	+10.352	0.080	−20.805	0.015	−27.302	0.021	...	...	...	...
HD 22468																				
ref.(6,2)	...	...	...	...	...	1992.00000	54.197113376	0.406	+0.588121131	0.401	+33.880	0.470	−31.588	0.330	−161.690	0.310	...	...	...	...
ref. (8)	...	...	...	...	...	...	...	...	...	...	...	...	−31.350	0.300	−160.900	0.300	...	...	...	...
Gaia EDR3	...	...	...	...	...	2016.00000	54.196900130	0.027	+0.587041811	0.026	+33.978	0.035	−32.246	0.036	−162.073	0.032	...	...	...	...
$\mathrm{M_{old}}$	0	662	0.630	0.967	8	1992.70183	54.197107163	0.312	+0.588089854	0.372	+33.838	0.432	−31.574	0.303	−161.693	0.338	...	...	...	...
$\mathrm{M_{new}}$	438	1125	0.781	1.131	10	1998.01762	54.197059930	0.282	0.587850689	0.411	34.307	0.280	−31.973	0.017	−161.966	0.033	...	...	...	...
$\mathrm{M^{(1)}_{abs,wo9\&10,new}}$	428	1027	0.689	1.073	11	1999.70415	54.197044944	0.263	0.587774811	0.366	34.220	0.256	−31.976	0.016	−161.965	0.028	...	...	...	...
$\mathrm{M_{abs,wo9\&10,new,a}}$	322	1105	0.657	1.075	11	2016.00000	54.19690029	0.700	0.587041623	0.939	34.186	0.342	−32.071	0.187	−161.921	0.267	−0.009	0.018	0.004	0.025
CoKu HP Tau G2																				
ref. (5)	...	...	...	...	...	...	...	...	...	...	+6.145	0.029	+11.248	0.022	−15.686	0.013	...	...	...	...
Gaia EDR3	...	...	...	...	...	2016.00000	68.975704541	0.055	+22.903678923	0.032	+5.979	0.059	+13.459	0.074	−11.399	0.054	...	...	...	...
$\mathrm{M_{new}}$	4986	5379	4.627	4.992	18	2011.81055	68.975691744	1.191	22.903697677	1.268	5.769	1.471	11.103	0.221	−16.085	0.257				
$\mathrm{M^{(1)}_{Gaia}}$	1333	1337	1.018	1.023	6	2015.98433	68.975704603	0.545	22.903678775	0.547	6.353	0.583	11.830	0.586	−10.812	0.624				
$\mathrm{M_{Gaia,a}}$	468	366	0.302	0.239	6	2016.00000	68.975704363	0.284	22.903679029	0.224	6.247	0.205	11.827	0.206	−10.838	0.174	2.563	0.503	−2.804	0.432
del Lib																				
Gaia DR2	...	...	...	...	...	2015.50000	225.242843762	0.269	−8.518973195	0.238	+8.328	0.334	−60.564	0.552	−3.651	0.457	...	...	...	...
Gaia EDR3	...	...	...	...	...	2016.00000	225.242834573	0.290	−8.518974108	0.324	+9.282	0.472	−63.051	0.385	−6.024	0.326	...	...	...	...
$\mathrm{M_{new}}$	469	2633	0.288	1.605	4	2019.28185	225.242775374	0.240	−8.518979155	1.314	+6.616	0.311	−64.411	0.175	−8.205	0.832	...	...	...	...
$\mathrm{M^{(1)}_{w0.5,new}}$	311	2531	0.334	1.569	4	2019.28185	225.242775406	0.217	−8.518979160	1.276	+6.755	0.342	−64.418	0.178	−8.201	0.804	...	...	...	...

Table 5.12 continued.

model	$E_{\alpha*}$	E_δ	$\mathrm{RMS}_{v,\alpha*}$	$\mathrm{RMS}_{v,\delta}$	Σn	t_0	α_0	$\sigma_{\alpha*_0}$	δ_0	σ_{δ_0}	ϖ	σ_ϖ	$\mu_{\alpha*}$	$\sigma_{\mu_{\alpha*}}$	μ_δ	σ_{μ_δ}	$a_{\alpha*}$	$\sigma_{a_{\alpha*}}$	a_δ	σ_{a_δ}
	[μas]		[mas]			[Julian year]	[°]	[mas]	[°]	[mas]	[mas]		[mas yr^{-1}]		[mas yr^{-1}]		[mas yr^{-2}]		[mas yr^{-2}]	
HD 142184																				
Gaia EDR3	...	...	...	...	...	2016.00000	238.482700570	0.069	−23.978202542	0.050	+6.990	0.074	−13.406	0.083	−24.111	0.064	...	...	...	...
$\mathrm{M}_{\mathrm{new}}^{(1)}$	1630	384	1.672	2.496	12	2019.18013	238.482688156	0.594	−23.978223981	0.220	+7.690	0.712	−13.663	0.533	−24.339	0.195	...	...	...	...
$\mathrm{M}_{\mathrm{new,a}}$	1284	544	1.355	2.510	12	2016.00000	238.482703642	3.856	−23.978202276	2.044	+8.043	0.627	−19.350	2.521	−24.880	1.493	1.911	0.844	0.181	0.496

Notes. Estimates for astrometric models of stellar motions M with mean positions at mean epoch t_0. In case linear acceleration terms were estimated, the proper motions also refer to t_0. The number of single-epoch positions employed for derivation of the respective model is given in column Σn for the fifteen stars discussed in this study. The parameters from literature references (ref.) and *Gaia* EDR3 are indicated in the first lines of each star segment. In case two literature references are given in one line, the first one describes the original data, and the second one points to improved data as given in the respective reference (e.g. positions were shifted to ICRF3 or positions were determined as they were not provided in the first reference). An ellipsis (...) indicates the omission of an entry. [(1)]Chosen as best solution for rotation parameter estimation in the following sections. [(2)]Including orbital fit.

References. (1) Galli et al. (2018); (2) Lindegren (2020a); (3) Miller-Jones et al. (2013); (4) Kounkel et al. (2017); (5) Ortiz-León et al. (2017b); (6) Lestrade et al. (1999); (7) Ratner et al. (2012); (8) Titov et al. (2020).

Note. All model except those including accelerations according to Lunz et al. (2021b, Table 2).

5.6 Various rotation parameter solutions

In this section, the solutions for different iterative rotation parameter scenarios between VLBI and Gaia are presented and evaluated using the method introduced in Sect. 3.3.2. The algorithm allows simultaneous estimation of the orientation offset $\epsilon(T)$ at epoch T and the spin ω for the case where multiple positions or position and proper motion information are given by VLBI for some of the counterparts under investigation. In each iteration the star with the largest discrepancy measure, $max\,(Q_i/n_i)$, sensitive to radio-optical offsets and long-term perturbations of the linear proper motion model, was rejected. As described earlier, only stars that have a five-parameter astrometric model in the Gaia data set were considered, as this is required for propagation of the Gaia data to the VLBI epoch using Eq. 3.33. In addition, the radial velocity v_r is used for the propagation. The values for v_r adopted from the SIMBAD database are given in Table 5.13 for the stars in this work.

The results for the scenarios s are compared using among others the weighted mean WM_s, weighted root mean square WRMS_s, and mean formal error ME_s statistics as presented in Sect. 3.3.4. The respective results are listed in Table 5.14 for Gaia DR2 and in Table 5.15 for Gaia EDR3.

For each scenario, a representative iteration, called the baseline solution, is selected. As many stars as possible are included in the selected iteration, with the offset of the rotation parameters from the previous iteration being within their formal errors and representative for the following iterations. Furthermore, Q/n should no longer show large jumps in the following iterations and stars with very large Q_i/n_i should be excluded. The respective results are listed in Table 5.16.

The various scenarios s consisting of different VLBI and Gaia datasets are labeled consistently by "a,b,c,..." in the following, where a is the number of stars in the dataset, b

Table 5.13 Radial velocities (v_r) from the SIMBAD database (Wenger et al. 2000) used to calculate the rotation parameters.

Star	v_r [km s^{-1}]
UV Psc	+6.5
HD 8357	+12.7
LS I +61 303	−41.4
RZ Cas	−39.4
bet Per	+4.0
UX Ari	+50.7
HD 22468	−15.3
HD 283447	+16.0
B Per	+19.8
V410 Tau	+19.9
HD 283572	+14.2
T Tau	+19.2
CoKu HP Tau G2	+16.6
Brun 334	+20.3
TYC 5346-538-1	+0.0
SV Cam	−13.8
54 Cam	+27.5
IL Hya	−7.3
HU Vir	−0.7
DK Dra	−45.3
RS CVn	−13.6
BH CVn	+6.4
del Lib	−38.7
σ^2 CrB	−14.7
Haro 1-6	−3.7
DoAr 51	+0.0
HD 199178	−30.8
SS Cyg	−62.0
AR Lac	−33.8
IM Peg	−14.4
SZ Psc	+12.0
HD 224085	−20.5
HD 142184	−9.20
HD 167971	+14.2
V479 Sct	+0.0
EI Eri	+17.6
YY Men	−8.5

Note. According to Lunz et al. (2020a, Table 4).

is the Gaia data release used, and the optional identifiers
starting from c are used when, e.g., not the homogenized dataset with realistic absolute position uncertainties was used (see Sect. 5.4.5) or corrections to the positions were made (such as considering Galactocentric acceleration).

The whole analysis is inspired by the scenario given in Fig. 3 of Lindegren (2020a) for the rotation parameters between his collection of models of stellar motion from VLBI and Gaia DR2 for 41 stars. This scenario is denoted "41,DR2,Lind2020" in this work. Possible future improvements to the rotational parameter analysis between VLBI and Gaia are presented and a discussion of the various results concludes the section.

Table 5.14 WM, WRMS, and ME of the various rotation parameter scenarios for Gaia DR2.

Scenario	Parameter	$\epsilon_X(T)$	$\epsilon_Y(T)$	$\epsilon_Z(T)$	ω_X	ω_Y	ω_Z
41,DR2,Lind2020	$\mathrm{WM}_{41,\mathrm{DR2,Lind2020}}$	0.055	1.273	0.537	−0.047	−0.081	0.028
	$\mathrm{WRMS}_{41,\mathrm{DR2,Lind2020}}$	0.105	0.237	0.087	0.050	0.037	0.030
	$\mathrm{ME}_{41,\mathrm{DR2,Lind2020}}$	0.031	0.073	0.025	0.023	0.028	0.028
41,DR2,shift	$\mathrm{WM}_{41,\mathrm{DR2,shift}}$	−0.165	0.390	0.005	−0.083	−0.139	0.027
	$\mathrm{WRMS}_{41,\mathrm{DR2,shift}}$	0.115	0.131	0.103	0.044	0.012	0.019
	$\mathrm{ME}_{41,\mathrm{DR2,shift}}$	0.029	0.070	0.024	0.022	0.029	0.027
41,DR2,$\sigma_{\mathrm{model\ pos}}$	$\mathrm{WM}_{41,\mathrm{DR2},\sigma_{\mathrm{model\ pos}}}$	−0.152	0.393	−0.017	−0.077	−0.145	0.046
	$\mathrm{WRMS}_{41,\mathrm{DR2},\sigma_{\mathrm{model\ pos}}}$	0.102	0.055	0.035	0.025	0.010	0.025
	$\mathrm{ME}_{41,\mathrm{DR2},\sigma_{\mathrm{model\ pos}}}$	0.059	0.107	0.051	0.023	0.030	0.027
41,DR2	$\mathrm{WM}_{41,\mathrm{DR2}}$	0.038	0.391	−0.025	−0.061	−0.150	0.045
	$\mathrm{WRMS}_{41,\mathrm{DR2}}$	0.090	0.051	0.047	0.022	0.013	0.029
	$\mathrm{ME}_{41,\mathrm{DR2}}$	0.104	0.182	0.087	0.024	0.032	0.028
55,DR2	$\mathrm{WM}_{55,\mathrm{DR2}}$	0.057	0.387	−0.014	−0.068	−0.134	0.037
	$\mathrm{WRMS}_{55,\mathrm{DR2}}$	0.048	0.050	0.077	0.016	0.010	0.021
	$\mathrm{ME}_{55,\mathrm{DR2}}$	0.083	0.113	0.066	0.022	0.026	0.024
55,DR2,NM	$\mathrm{WM}_{55,\mathrm{DR2,NM}}$	0.080	0.368	−0.037	−0.064	−0.121	0.019
	$\mathrm{WRMS}_{55,\mathrm{DR2,NM}}$	0.079	0.063	0.037	0.014	0.013	0.025
	$\mathrm{ME}_{55,\mathrm{DR2,NM}}$	0.102	0.139	0.079	0.021	0.027	0.024

Notes. For scenarios "41" not including the January 2020 positions iterations 9 to 34 were used for calculation, whereas for scenarios "55" including the January 2020 positions iterations 12 to 47 were considered. For derivation of values $\mathrm{ME_s}$ the last 10 iterations were rejected because the formal errors of the rotation parameters increase substantially if only few stars are available for calculations. The epoch T is 2015.5 for Gaia DR2. Units are in milliarcseconds for $\epsilon_X(T)$, $\epsilon_Y(T)$, and $\epsilon_Z(T)$. They are milliarcseconds per year for ω_X, ω_Y, and ω_Z.
Note. Some scenarios are according to Lunz et al. (2020a, Table 8 and D.1).

Table 5.15 WM, WRMS, and ME of the various rotation parameter scenarios for Gaia EDR3.

Scenario	Parameter	$\epsilon_X(T)$	$\epsilon_Y(T)$	$\epsilon_Z(T)$	ω_X	ω_Y	ω_Z
41,EDR3,Lind2020	$\mathrm{WM}_{41,\mathrm{EDR3,Lind2020}}$	0.028	1.137	0.574	0.010	0.117	−0.008
	$\mathrm{WRMS}_{41,\mathrm{EDR3,Lind2020}}$	0.111	0.227	0.070	0.019	0.018	0.011
	$\mathrm{ME}_{41,\mathrm{EDR3,Lind2020}}$	0.025	0.051	0.019	0.010	0.011	0.011
37,EDR3,Lind2020	$\mathrm{WM}_{37,\mathrm{EDR3,Lind2020}}$	0.778	−0.123	0.521	0.045	0.055	−0.027
	$\mathrm{WRMS}_{37,\mathrm{EDR3,Lind2020}}$	0.150	0.295	0.201	0.049	0.032	0.033
	$\mathrm{ME}_{37,\mathrm{EDR3,Lind2020}}$	0.042	0.079	0.031	0.012	0.012	0.013
41,EDR3	$\mathrm{WM}_{41,\mathrm{EDR3}}$	0.204	0.221	0.067	0.024	0.050	−0.027
	$\mathrm{WRMS}_{41,\mathrm{EDR3}}$	0.094	0.129	0.079	0.016	0.015	0.014
	$\mathrm{ME}_{41,\mathrm{EDR3}}$	0.110	0.189	0.087	0.013	0.016	0.013
41,EDR3,GA	$\mathrm{WM}_{41,\mathrm{EDR3,GA}}$	0.203	0.217	0.074	0.022	0.047	−0.023
	$\mathrm{WRMS}_{41,\mathrm{EDR3,GA}}$	0.092	0.128	0.078	0.016	0.015	0.014
	$\mathrm{ME}_{41,\mathrm{EDR3,GA}}$	0.110	0.189	0.087	0.013	0.016	0.013
55,EDR3	$\mathrm{WM}_{55,\mathrm{EDR3}}$	0.292	0.337	0.086	0.033	0.054	−0.019
	$\mathrm{WRMS}_{55,\mathrm{EDR3}}$	0.058	0.071	0.083	0.016	0.014	0.013
	$\mathrm{ME}_{55,\mathrm{EDR3}}$	0.083	0.107	0.064	0.012	0.013	0.012
55,EDR3,GA	$\mathrm{WM}_{55,\mathrm{EDR3,GA}}$	0.288	0.337	0.087	0.030	0.052	−0.016
	$\mathrm{WRMS}_{55,\mathrm{EDR3,GA}}$	0.058	0.071	0.083	0.016	0.014	0.013
	$\mathrm{ME}_{55,\mathrm{EDR3,GA}}$	0.083	0.107	0.064	0.012	0.013	0.012
49,EDR3,GA	$\mathrm{WM}_{49,\mathrm{EDR3,GA}}$	0.318	0.342	0.057	0.037	0.037	−0.004
	$\mathrm{WRMS}_{49,\mathrm{EDR3,GA}}$	0.035	0.049	0.068	0.014	0.010	0.013
	$\mathrm{ME}_{49,\mathrm{EDR3,GA}}$	0.088	0.111	0.066	0.013	0.014	0.013
55,EDR3,GA,NM	$\mathrm{WM}_{55,\mathrm{EDR3,GA,NM}}$	0.302	0.395	0.081	0.029	0.063	−0.013
	$\mathrm{WRMS}_{55,\mathrm{EDR3,GA,NM}}$	0.059	0.094	0.085	0.010	0.013	0.014
	$\mathrm{ME}_{55,\mathrm{EDR3,GA,NM}}$	0.098	0.125	0.073	0.010	0.012	0.010
55,EDR3,GA,NM,modelpos	$\mathrm{WM}_{55,\mathrm{EDR3,GA,NM,modelpos}}$	0.188	0.438	0.117	0.028	0.061	−0.008
	$\mathrm{WRMS}_{55,\mathrm{EDR3,GA,NM,modelpos}}$	0.031	0.061	0.100	0.008	0.015	0.016
	$\mathrm{ME}_{55,\mathrm{EDR3,GA,NM,modelpos}}$	0.082	0.106	0.069	0.010	0.012	0.010
49,EDR3,GA,NM	$\mathrm{WM}_{49,\mathrm{EDR3,GA,NM}}$	0.272	0.498	0.094	0.024	0.043	0.005
	$\mathrm{WRMS}_{49,\mathrm{EDR3,GA,NM}}$	0.038	0.051	0.078	0.009	0.007	0.005
	$\mathrm{ME}_{49,\mathrm{EDR3,GA,NM}}$	0.104	0.134	0.077	0.011	0.014	0.011
60,EDR3,GA,NM	$\mathrm{WM}_{60,\mathrm{EDR3,GA,NM}}$	0.347	0.365	0.086	0.032	0.064	−0.015
	$\mathrm{WRMS}_{60,\mathrm{EDR3,GA,NM}}$	0.112	0.098	0.084	0.011	0.011	0.013
	$\mathrm{ME}_{60,\mathrm{EDR3,GA,NM}}$	0.096	0.122	0.072	0.010	0.011	0.010
53,EDR3,GA,NM	$\mathrm{WM}_{53,\mathrm{EDR3,GA,NM}}$	0.287	0.476	0.112	0.024	0.042	0.006
	$\mathrm{WRMS}_{53,\mathrm{EDR3,GA,NM}}$	0.046	0.060	0.097	0.009	0.009	0.007
	$\mathrm{ME}_{53,\mathrm{EDR3,GA,NM}}$	0.104	0.132	0.076	0.011	0.014	0.011

Notes. For scenarios "41" not including the January 2020 positions iterations 9 to 34 were used for calculation, whereas for scenarios "55" including the January 2020 positions iterations 12 to 47 were considered. For the scenarios where stars were excluded beforehand, the iterations 11 to 41 for "49,EDR3,GA" and "49,EDR3,GA,NM", and 45 for "53,EDR3,GA,NM" were employed. For scenario "60,EDR3,GA,NM" iterations 11 to 52, and for scenario "37,EDR3,Lind2020" iterations 9 to 30 were used. For derivation of values $\mathrm{ME_s}$ the last 10 iterations were rejected because the formal errors of the rotation parameters increase substantially if only few stars are available for calculations. The epoch T is 2016.0 for Gaia EDR3. Units are in milliarcseconds for $\epsilon_X(T)$, $\epsilon_Y(T)$, and $\epsilon_Z(T)$. They are milliarcseconds per year for ω_X, ω_Y, and ω_Z.

Note. Some scenarios are according to Lunz et al. (2020a, Table 8 and D.1) and Lunz et al. (2021b, Table 6).

Table 5.16 Baseline solutions of the various scenarios.

Scenario	k	ki	$\epsilon_X(T)$	$\epsilon_Y(T)$	$\epsilon_Z(T)$	ω_X	ω_Y	ω_Z	$\sigma_{\epsilon_X(T)}$	$\sigma_{\epsilon_Y(T)}$	$\sigma_{\epsilon_Z(T)}$	σ_{ω_X}	σ_{ω_Y}	σ_{ω_Z}	Q/n
41,DR2,Lind2020[1]	15	26	−0.019	+1.304	+0.553	−0.068	−0.051	−0.014	0.032	0.074	0.026	0.023	0.027	0.028	5.68
41,DR2	9	32	+0.100	+0.405	−0.044	−0.045	−0.141	+0.023	0.099	0.177	0.082	0.022	0.029	0.026	4.75
55,DR2	11	44	+0.095	+0.477	+0.022	−0.054	−0.114	+0.033	0.077	0.105	0.061	0.020	0.024	0.022	5.79
55,DR2,NM	11	44	+0.089	+0.414	−0.022	−0.061	−0.119	+0.024	0.091	0.125	0.070	0.019	0.024	0.021	6.08
41,EDR3	9	32	+0.100	+0.146	+0.159	+0.011	+0.055	−0.023	0.098	0.171	0.082	0.011	0.014	0.012	6.54
55,EDR3	13	42	+0.212	+0.319	+0.175	+0.020	+0.065	−0.017	0.073	0.098	0.057	0.010	0.011	0.011	5.50
55,EDR3,GA	13	42	+0.209	+0.319	+0.176	+0.019	+0.062	−0.014	0.073	0.098	0.057	0.010	0.011	0.011	5.49
49,EDR3,GA	11	38	+0.311	+0.356	+0.133	+0.041	+0.022	+0.013	0.082	0.107	0.061	0.012	0.014	0.012	4.92
55,EDR3,GA,NM	12	43	+0.274	+0.285	+0.180	+0.032	+0.073	−0.027	0.086	0.113	0.065	0.009	0.010	0.009	5.88
49,EDR3,GA,NM	13	35	+0.289	+0.510	+0.175	+0.027	+0.032	+0.010	0.097	0.128	0.070	0.011	0.013	0.011	4.88
60,EDR3,GA,NM	15	45	+0.308	+0.233	+0.172	+0.033	+0.072	−0.027	0.085	0.107	0.065	0.009	0.010	0.009	6.28
53,EDR3,GA,NM	13	40	+0.332	+0.426	+0.162	+0.028	+0.031	+0.010	0.095	0.121	0.070	0.011	0.013	0.011	6.08

Notes. The epoch T is 2015.5 for Gaia DR2 and 2016.0 for Gaia EDR3. Units are in milliarcseconds for $\epsilon_X(T)$, $\epsilon_Y(T)$, and $\epsilon_Z(T)$. They are milliarcseconds per year for ω_X, ω_Y, and ω_Z. The uncertainties σ are in the same units as the parameters. The parameter Q/n describes the quality of the fit, similar to s_0^2, in the iteration with k discarded stars. For better comparison, the number of included stars, ki is provided as well.
[1] Taken from Table 3 in Lindegren (2020b), solution A.

5.6.1 Homogenization of existing data

To better compare the effects of the homogenization steps of the VLBI data from Lindegren (2020a) in Sect. 5.1, this section is first based on Gaia DR2, since the rotation parameter analysis in Lindegren (2020a,b) is also based on this Gaia data release.

Gaia DR2

Re-calculating the rotation parameters as shown in Fig. 3 of Lindegren (2020b) results in Figs. 5.24 and 5.25. For scenario "41,DR2,shift" (Fig. 5.24) only the position shifts of the historic calibrator positions to the positions in ICRF3 S/X, were applied (see Table 5.1), whereas for scenario "41,DR2,$\sigma_{\text{model pos}}$" (Fig. 5.25) also the calibrator catalog uncertainties σ_{CRF} were considered in the star position uncertainties consistently for all stars. For scenario "41,DR2" (Fig. 5.26), the more realistic error budgets for absolute star positions from the VLBI phase-referencing, σ_{absolute}, were used.

For this collection of only 41 stars, the small position shifts of mostly less than a milliarcsecond had a large impact on the steadiness of the iterative solutions, as shown by comparing the WRMS of scenarios "41,DR2,Lind2020" and "41,DR2,shift". Both the orientation and spin in Y are determined with less scatter between the iterative solutions, which is visible from the plots, but also from the WRMS statistics being about 70 %

smaller for ω_Y and 50 % smaller for ϵ_Y. Also the WRMS of ω_Z decreased by about 40 %, whereas it increased slightly for ϵ_Z. While the ME did not change significantly, the WM of all estimated parameters except ω_Z changes significantly as determined by the t-test. The large ϵ_Y decreases to about one third of its value, 0.390 mas, and the large ϵ_Z (0.537 mas)to about zero. The ϵ_X changes direction and triples its magnitude to -0.165 mas. The spin in X and Y increases about 70 %, which is several tens of $\mu\text{as}\,\text{yr}^{-1}$.

Increasing the position uncertainties to a common level for all stars in scenario "41,DR2,$\sigma_{\text{model pos}}$" deceased the WRMS values by a factor of 2 to 4 for ϵ_Y, ϵ_Z, ω_X, and ω_Y compared to "41,DR2,Lind2020", which is expected. In this scenario, the effect of position shifts on the spin parameters is smaller; the star LSI +61 303 apparently had a large effect on the spin in X in "41,DR2,shift", as can be seen from the different level in the spin parameters after its rejection, which is reduced in scenario "41,DR2,$\sigma_{\text{model pos}}$". Compared to scenario "41,DR2,Lind2020", if the mean $\sqrt{Q/n}$ over the respective iterations was considered, the ME of the orientation parameters increase by 30 % to 90 %, and the ME of the spin parameters decrease by 10 % to 20 %. If the mean $\sqrt{Q/n}$ was not considered, the ME behave like in Table 5.14, where the "formal errors of the orientation parameters are increased by a factor of about 1.5 to 2 while the formal errors of the spin parameters are only marginally affected. Except for ϵ_X, the WRMS values are equal or smaller than the ME values, whereas they were larger (by up to a factor of 3.5) in scenario "41,DR2,Lind2020" " (Lunz et al. 2020a). The WM are similar to "41,DR2,shift".

The introduction of the more realistic error budget for absolute star positions from VLBI phase-referencing in scenario "41,DR2" did not change the results considerably compared to solution "41,DR2,$\sigma_{\text{model pos}}$" except for the WM of ϵ_X and ω_X. As expected due to the inflated VLBI position uncertainties, mainly the ME in the orientation parameters raise noticeably, by about 60 %, if the mean $\sqrt{Q/n}$ over the respective iterations was considered.

The parameter Q/n is below unity with $k = 33$ rejected stars for "41,DR2,Lind2020", $k = 32$ for "41,DR2,shift", $k = 29$ for "41,DR2,$\sigma_{\text{model pos}}$", and $k = 26$ for "41,DR2". The decrease in rejected stars to reach $Q/n = 1$ for "41,DR2,Lind2020" and "41,DR2,shift" shows that the VLBI and Gaia datasets align better for more stars with the homogenization efforts. The differences when inflating the VLBI position uncertainties can be expected. The order of rejected stars is almost the same.

For "41,DR2", the solution with $k = 9$ rejected stars was selected as the baseline solution. Its Q/n "is 4.75, slightly lower than the value in Lindegren (2020b) of 5.68. However, if rejecting 15 stars as done in Lindegren (2020b), the Q/n from our solution is as low as 2.26, which reflects the improvement resulting from the homogenization and the increase in uncertainties for the absolute positions in scenario "41,DR2". The correlation coefficients

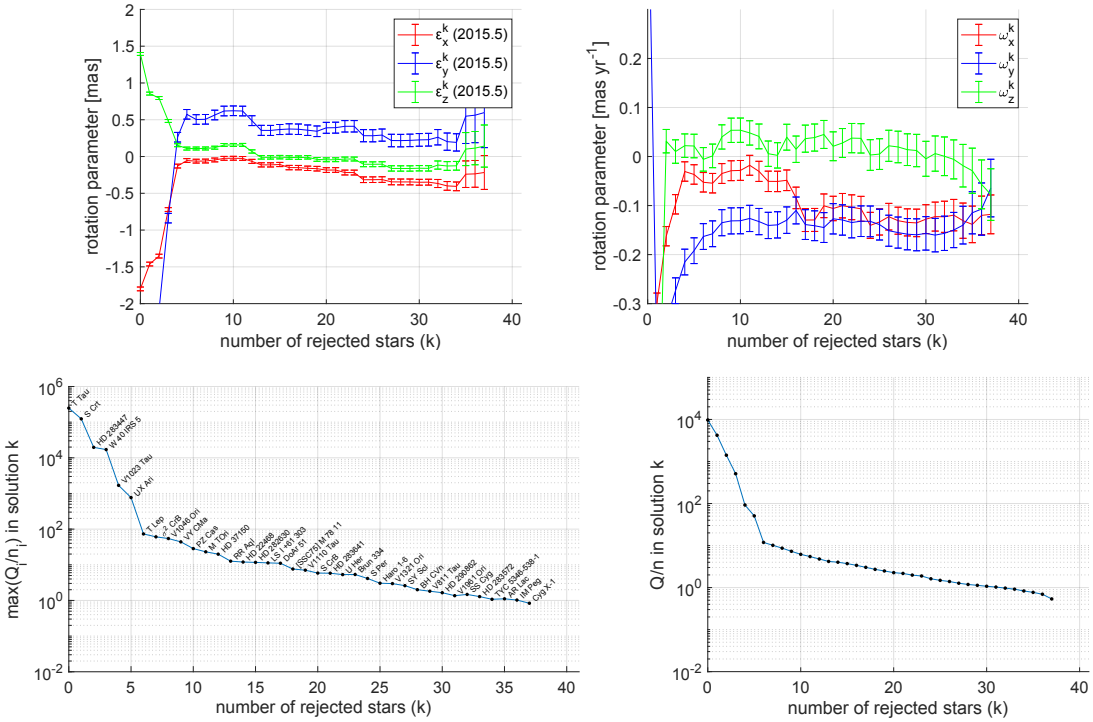

Figure 5.24 Rotation parameter results for the partly homogenized Lindegren (2020a) dataset "41,DR2,shift" when introducing only the phase-referencing calibrator shift from Table 5.1 to the star positions to refer to ICRF3 S/X. The top row shows the orientation (left) and spin (right) parameters from 38 iterative adjustments, where for each fit the star with the largest (Q_i/n_i) was discarded in the following iteration. The respective $max\,(Q_i/n_i)$ and the star's name are shown in the lower left plot. The lower right plot provides information about the quality of the fit Q/n, equivalent to χ^2. All plots are relative to the number of rejected stars k in the iteration. The order of the rejected stars is individual to each scenario.

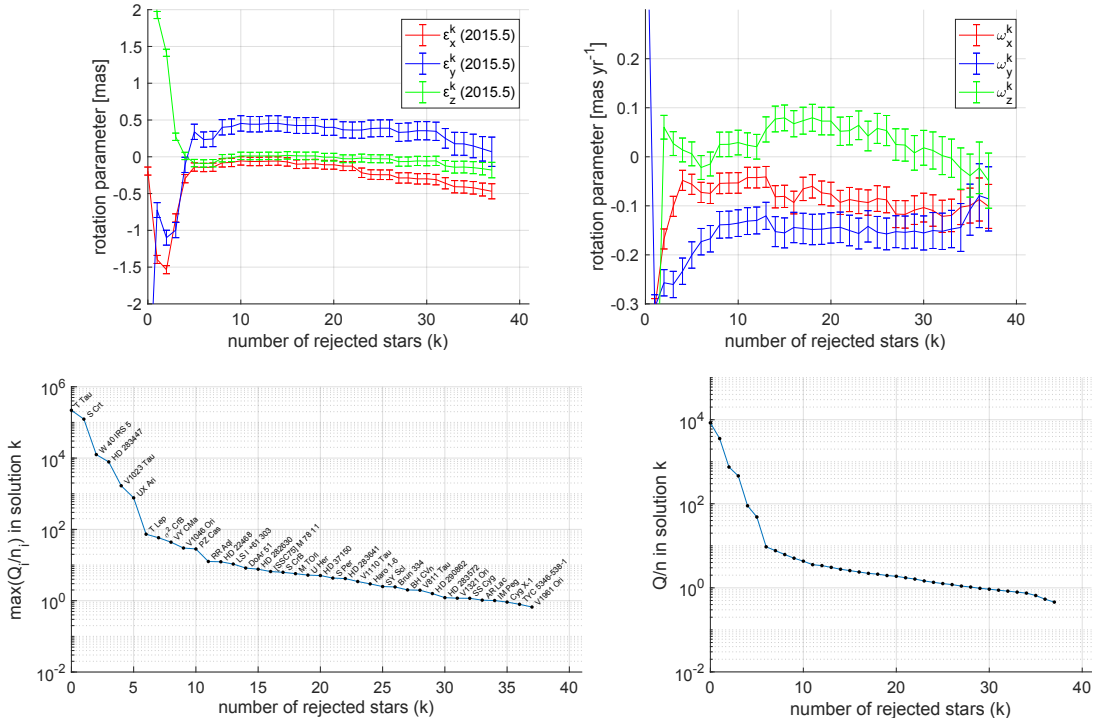

Figure 5.25 Rotation parameter results for the homogenized Lindegren (2020a) dataset "41,DR2,$\sigma_{\text{model pos}}$" when introducing the phase-referencing calibrator shift as in "41,DR2,shift", as well as accounting for the calibrator catalog position uncertainties σ_{CRF} in the star position uncertainties. For a description of the plots refer to Fig. 5.24.
Note. According to Lunz et al. (2020a, Fig. D1).

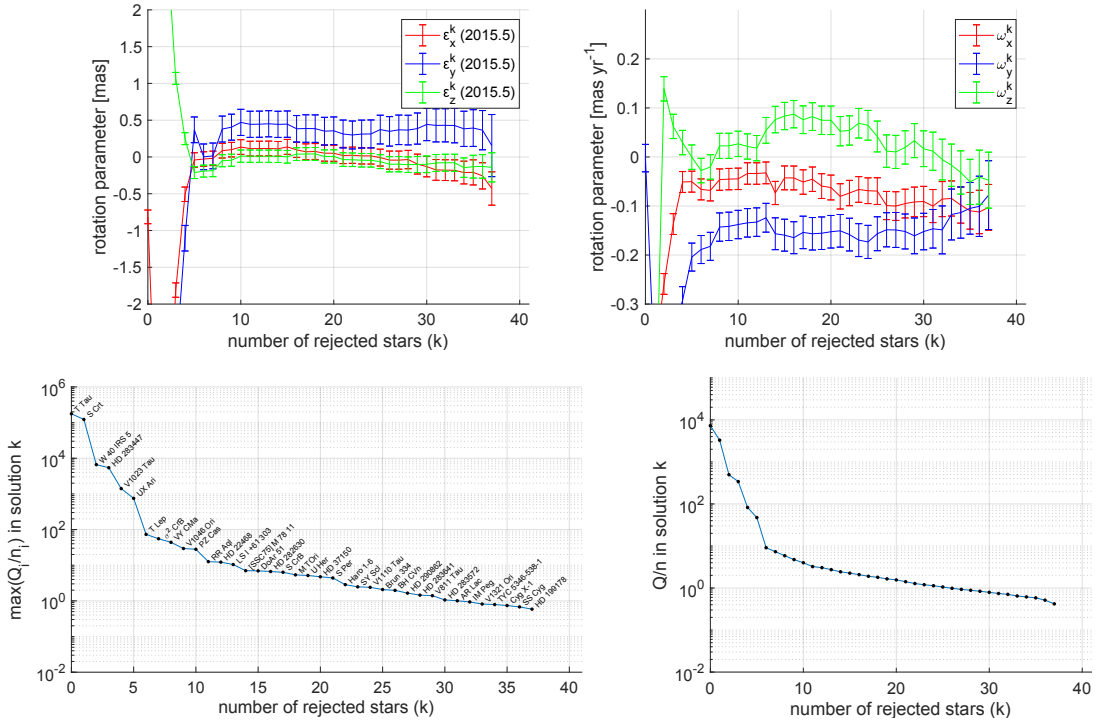

Figure 5.26 Rotation parameter results for the homogenized Lindegren (2020a) dataset "41,DR2" where more realistic uncertainties for the absolute star positions from VLBI phase-referencing, σ_{absolute}, were accounted for. For a description of the plots refer to Fig. 5.24.
Note. According to Lunz et al. (2020a, Fig. 1).

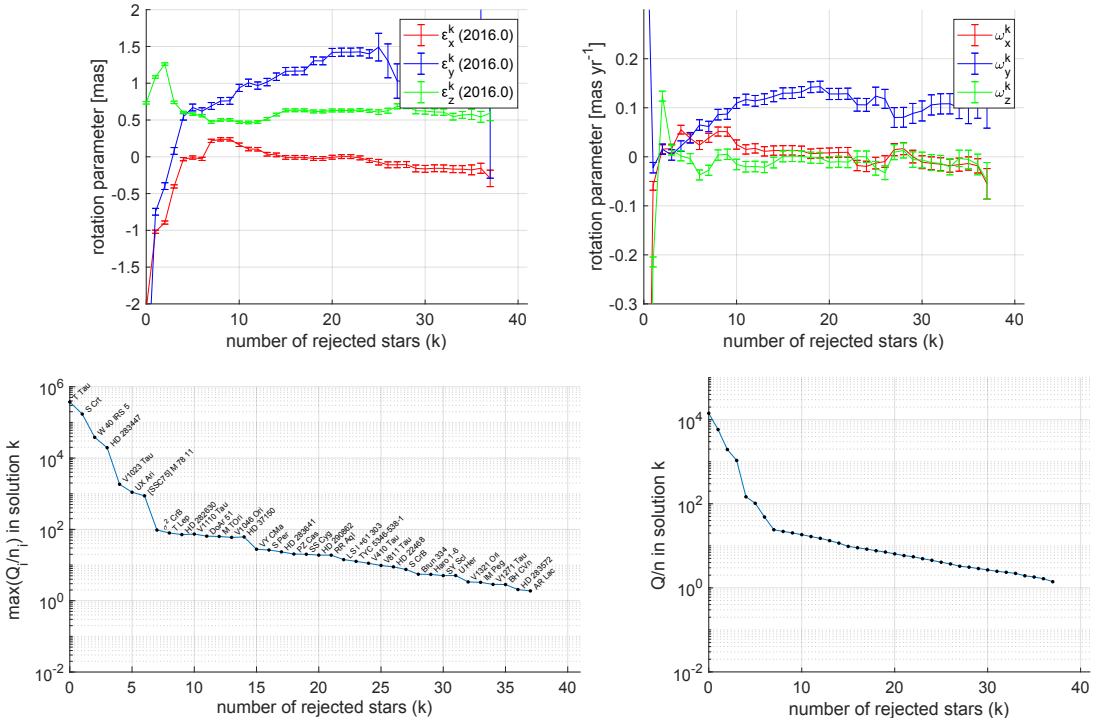

Figure 5.27 Rotation parameter results for the Lindegren (2020a) dataset "41,EDR3,Lind2020" but for Gaia EDR3. The parallax correction was applied to the Gaia data. For a description of the plots refer to Fig. 5.24.

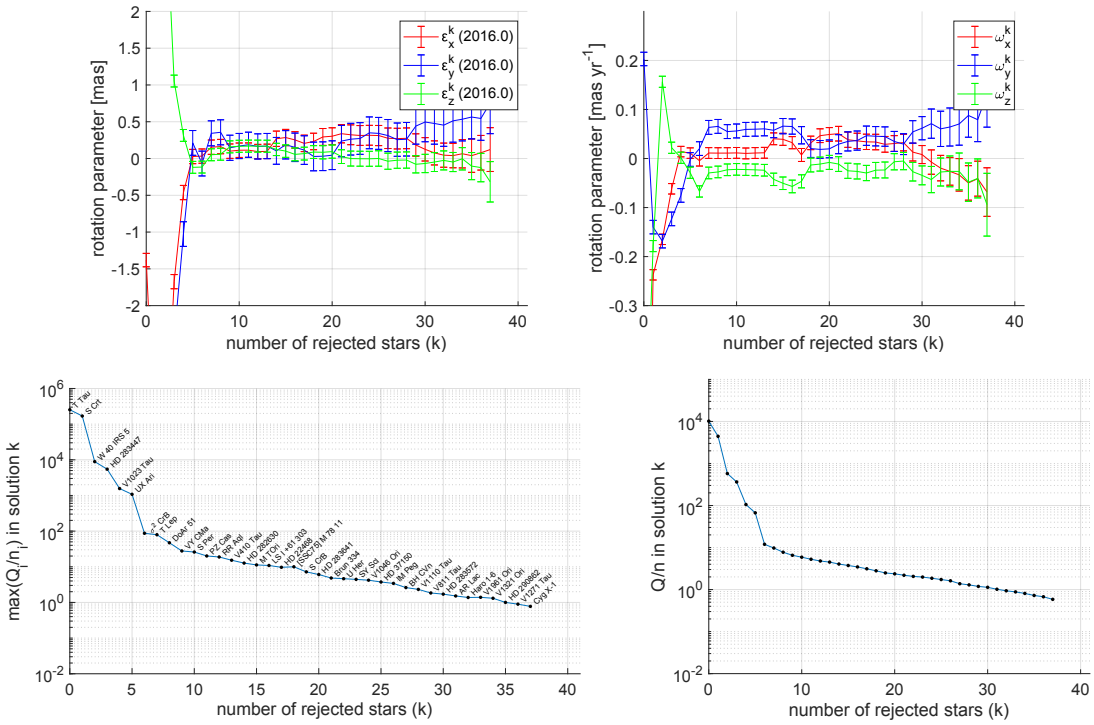

Figure 5.28 Rotation parameter results for the homogenized Lindegren (2020a) dataset "41,EDR3" where more realistic uncertainties for the absolute star positions from VLBI phase-referencing, σ_{absolute}, were accounted for. For a description of the plots refer to Fig. 5.24.
Note. According to Lunz et al. (2020a, Fig. 2).

between the rotation parameters from the baseline solution are

$$\begin{aligned}&\mathrm{corr}[\epsilon_X(T), \epsilon_Y(T), \epsilon_Z(T), \omega_X, \omega_Y, \omega_Z] \\ &= \begin{bmatrix} +1.000 & +0.419 & +0.276 & +0.173 & +0.119 & +0.031 \\ \dots & +1.000 & +0.372 & +0.052 & +0.315 & +0.046 \\ \dots & \dots & +1.000 & +0.033 & +0.125 & +0.113 \\ \dots & \dots & \dots & +1.000 & -0.007 & +0.345 \\ \dots & \dots & \dots & \dots & +1.000 & -0.065 \\ \dots & \dots & \dots & \dots & \dots & +1.000 \end{bmatrix},\end{aligned} \tag{5.8}$$

which show that the orientation parameters are still weakly correlated (correlation coefficients up to 0.4). The largest changes in correlation coefficient compared to the Lindegren (2020b) baseline solution happened for that between the orientation and spin parameters in Y (increase by 0.184), and for that between the Y and Z orientation parameters (increase by 0.166). " (Lunz et al. 2020a).

For each source i a formal weight E_i was determined, which quantifies the contribution of the source to the estimation of $\epsilon(T)$, and formal weight Ω_i the contribution to ω, respectively. For the baseline solution in Lindegren (2020a,b) and "41,DR2", the minimum, maximum, and median values for the weights are given in Table 5.17. The positions in "41,DR2" were given a lower weight relative to the proper motion information compared to "41,DR2,Lind2020" because of the more realistic error budget for the star positions from VLBI phase-referencing observations. However for the spin determination, stars LSI +61 303, V410 Tau, CygX-1, HD 199178, and AR Lac have a weight above 300 $\mathrm{mas}^{-2}\,\mathrm{yr}^2$ also for the baseline solution of Lindegren (2020a,b).

Table 5.17 Formal weights E_i and Ω_i of the various scenarios.

		E_i [mas^{-2}]			Ω_i [$\mathrm{mas}^{-2}\,\mathrm{yr}^2$]	
		max	median	min	max	median
41,DR2,Lind2020	0.01	1156	10	0.68	933	96
41,DR2	0.01	42	6	0.68	898	84
55,DR2	0.01	51	8	0.68	908	98
55,DR2,NM	0.01	36	8	0.68	981	103
41,EDR3,Lind2020	0.01	2074	15	5	5097	464
41,EDR3	0.01	43	7	5	4096	255
55,EDR3	0.01	53	11	5	4168	153
55,EDR3,GA,NM	0.01	38	10	5	6425	153
55,EDR3,GA,NM,modelpos	0.01	41	10	5	6715	153

Notes. The formal weights quantify the contribution of the source to the estimation of $\epsilon(T)$ and ω, respectively, as defined in Eq. 3.59. The three stars without position information are not considered.

Gaia EDR3

"Also in *Gaia* EDR3 no matched ICRF3 S/X radio sources are brighter than $G = 13$ mag and optically bright radio stars are needed for the link of the bright *Gaia* reference frame to ICRF.

Gaia EDR3 is based on a longer observation time span than DR2, and the epoch of the catalog changed to $T = 2016.0$. Velocities are still only modelled linearly. Higher order terms or orbits due to multiple star systems are neglected. Therefore, differences in proper motion of *Gaia* EDR3 and DR2 can not only be due to better sampling but also due to non-linear motions. The red supergiant VY CMa shows very large differences between *Gaia* DR2 and EDR3. Its *Gaia* EDR3 proper motions better match the VLBI data in Zhang et al. (2012). In addition its negative parallax of approximately -6 mas in *Gaia* DR2 disappeared. *Gaia* EDR3 was corrected for its spin offset during the *Gaia* data processing. Therefore, the rotation parameters are the orientation and residual spin of *Gaia* EDR3 as determined by VLBI. The uncertainty in the *Gaia* EDR3 spin correction is at least 0.024 mas yr^{-1} per axis (Lindegren et al. 2021b)" (Lunz et al. 2020a).

The scenario "41,EDR3" (Fig.,5.28) produces the rotation parameters for Gaia EDR3 relative to the same homogenized VLBI dataset with more realistic uncertainties as for "41,DR2". The scenario for Gaia EDR3 relative to the VLBI dataset from Lindegren (2020a) is called "41,EDR3,Lind2020" (Fig. 5.27).

All weighted mean parameters change significantly in solution "41,EDR3" compared to "41,EDR3,Lind2020". The orientation parameters change their magnitude by about 0.18 mas to 0.92 mas, and the spin parameters by about 0.01 mas yr^{-1} to 0.07 mas yr^{-1}. The WRMS values decrease for all rotation parameters except those in Z where they increase. The ME of "41,EDR3" are about 4-fold for the orientation parameters and about 1.3-fold for the spin parameters compared to "41,EDR3,Lind2020". While the ratio between WRMS and ME was larger two for all orientation parameters in "41,EDR3,Lind2020", indicating that the scatter between iterations is larger than the formal errors of the individual iterations, the ratio is below one for "41,EDR3".

Also for scenarios with Gaia EDR3, the basic statistics of the weights are given in Table 5.17. For "41,EDR3,Lind2020", the ranges of the weights become larger compared to "41,DR2,Lind2020", especially for the spin. The stars LSI +61 303, V410 Tau, HD 283572, CygX-1, HD 199178, and AR Lac have the highest weights above 2500 mas^{-2} yr^2 in the spin determination. These are the same stars as for "41,DR2", where the threshold was 300 mas^{-2} yr^2, plus HD 283572. Stars LSI +61 303, HD 283572, HD 199178, and CygX-1 have a weight above 4000 mas^{-2} yr^2. These stars have one of the largest epoch differences between the VLBI position and the Gaia position. For "41,EDR3", the weights related to the orientation offset are clearly smaller due to the higher but more realistic error budget.

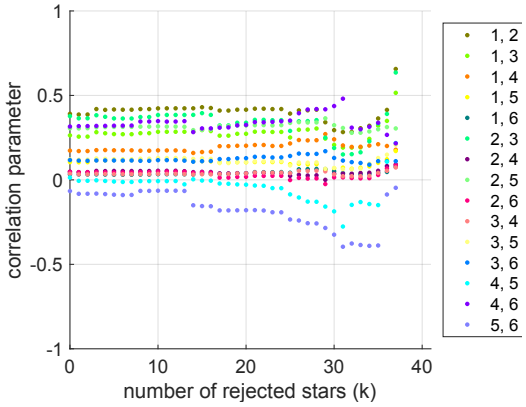

Figure 5.29 Correlation parameters for all iterations of "41,DR2". The numbers 1 to 6 represent the rotation parameters in the order $[\epsilon_X(T), \epsilon_Y(T), \epsilon_Z(T), \omega_X, \omega_Y, \omega_Z]$.

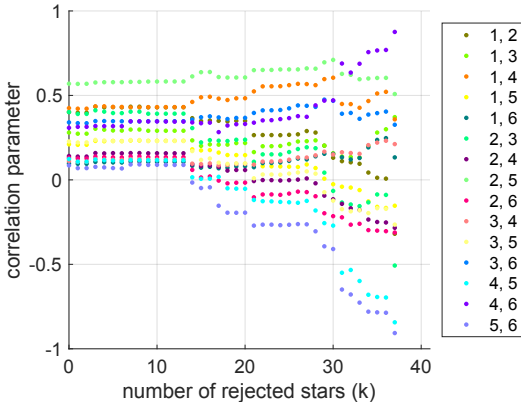

Figure 5.30 Correlation parameters for all iterations of "41,EDR3". The numbers 1 to 6 represent the rotation parameters in the order $[\epsilon_X(T), \epsilon_Y(T), \epsilon_Z(T), \omega_X, \omega_Y, \omega_Z]$.

But also the weights related to the spin were reduced due to the same reason. The stars LSI +61 303, HD 22468, V410 Tau, HD 283572, CygX-1, HD 199178, and AR Lac have the highest weights above 2500 $\mathrm{mas}^{-2}\,\mathrm{yr}^2$ in the spin determination. These are the same stars as for "41,EDR3,Lind2020", plus HD 22468. Stars LSI +61 303 and CygX-1 have a weight above 4000 $\mathrm{mas}^{-2}\,\mathrm{yr}^2$.

Another scenario, "37,EDR3,Lind2020" was produced, where the four stars V410 Tau, V1961 Ori, HD 283572, Brun 334 with very precise positions below 50 µas were excluded from the sample to test their impact on the large orientation offset and spin components of the not fully homogenized dataset. The components of the orientation offset vector change their magnitude by up to 1.26 mas, and those of the spin by up to 0.06 $\mathrm{mas\,yr}^{-1}$ compared to "41,EDR3,Lind2020". The WM change significantly according to the t-test for all parameters except ϵ_Z and ω_X, and the differences are even larger than the WRMS and ME combined. The ME worsen to be about 1.6-fold for the orientation and about 1.1-fold for the spin. The reason might be the reduced number of counterparts, but also the reduced amount of precise VLBI data. What is surprising is that the WRMS values raise compared to "41,EDR3,Lind2020". Still, the WM are different from the WM of "41,EDR3". This proofs that the difference in results between "41,EDR3" and "41,EDR3,Lind2020" is not only due to the four stars with the very precise positions.

For scenario "41,EDR3" 12 stars are still included to reach a Q/n below one, which indicates that the accuracy of the input data is overrated. The ratio between $\mathrm{WRMS}_{41,\mathrm{EDR3}}$ and $\mathrm{ME}_{41,\mathrm{EDR3}}$ demonstrates that for no parameters significant variations between the iterative solutions are present. In contrast, for "41,EDR3,Lind2020", Q/n less than one cannot be achieved, and the ratio between $\mathrm{WRMS}_{41,\mathrm{EDR3}}$ and $\mathrm{ME}_{41,\mathrm{EDR3}}$ is greater than three for all orientation parameters. The baseline solution for "41,EDR3" is also deter-

mined at $k = 9$, just like for "41,DR2". The correlation coefficients are

$$\begin{aligned}&\mathrm{corr}[\epsilon_X(T), \epsilon_Y(T), \epsilon_Z(T), \omega_X, \omega_Y, \omega_Z] \\ &= \begin{bmatrix} +1.000 & +0.429 & +0.291 & +0.431 & +0.231 & +0.106 \\ \dots & +1.000 & +0.391 & +0.157 & +0.582 & +0.135 \\ \dots & \dots & +1.000 & +0.121 & +0.229 & +0.347 \\ \dots & \dots & \dots & +1.000 & +0.117 & +0.346 \\ \dots & \dots & \dots & \dots & +1.000 & +0.088 \\ \dots & \dots & \dots & \dots & \dots & +1.000 \end{bmatrix}.\end{aligned} \tag{5.9}$$

Compared to "41,DR2", all correlation parameters increased for Gaia EDR3; especially the correlations between the orientation and spin parameter of each coordinate axis.

The evolution of the correlation parameters across iterations is shown for "41,DR2" and "41,EDR3" in Figs. 5.29 and 5.30. When V410 Tau is rejected for "41,EDR3", the correlations between iterations diverge more than in the preceding iterations. This is also the case for "41,EDR3,Lind2020", but there the offset is much larger, the spread between coefficients increases, and some of the correlation coefficients are larger ± 0.5 afterward, whereas before they were all smaller 0.5. Obviously, this one star still has an influence on the result.

5.6.2 Impact of Galactocentric acceleration

As discussed earlier, the internal systematics are too large for Gaia DR2 to detect the effect of Galactocentric acceleration. Therefore, the impact of correction of this effect in the phase-referencing VLBI data as introduced in Sect. 5.2 is shown using Gaia EDR3 only.

The homogenized VLBI data with more realistic position uncertainties was used for this task. This scenario called "41,EDR3,GA" (where "GA" indicates that the effect of Galactocentric acceleration was corrected) results in rotation parameters, $max(Q_i/n_i)$, and Q/n which are not visibly different from those of "41,EDR3". Therefore their plots are not presented. In particular the order of rejected stars is identical to "41,EDR3". The respective WM_s, WRMS_s, and ME_s statistics are not significantly different from those of "41,EDR3". As for "41,EDR3" there are no significant variations between the iterative solutions of the parameters and $k = 32$ stars need to get discarded to reach a Q/n below one.

5.6.3 Adding new observations as single-epoch positions

This subsection is based on Lunz et al. (2020a), and references to other sections, tables and figures were adjusted to match the outline of this work. *However, a slightly different error budget was used compared to Lunz et al. (2020a), as outlined in Sect. 5.4.5. Therefore, the corresponding numbers in the citations to Lunz et al. (2020a) have been replaced with the numbers of the results of this work where necessary.*

The newly derived single-epoch star positions determined with the VLBA were inserted into the analysis. If the stars were observed relative to two different primary calibrators, both positions were employed in the adjustment. This will, if only two positions are present as observations for the star, result in a weighted mean position. For close binaries the center of luminosity was used.

In total, the observations of 55 stars in both VLBI and *Gaia* were utilized for the adjustment of the rotation parameters. There were 21 stars that had more than one entry of positions or proper motions. Eleven stars had only a position measurement and no proper motion or parallax. Three stars had only a proper motion and parallax entry but no position. The remaining stars had one position, proper motion, and parallax entry.

Gaia EDR3

The scenario for the 55 stars and the alignment to *Gaia* EDR3 is labelled "55,EDR3" (Fig. 5.31). "Comparing "55,EDR3" with "41,EDR3", the ME values reduce by [20 to 40%] for the orientation parameters, and by 10 to 20% for the spin parameters. This decrease can be explained by the increase in the volume of observations. In both orientation and spin, the ME in Y decrease most but are still the largest compared to the ME values for the parameters in X and Z. For "55,EDR3" the Q/n of unity is reached when [16] stars are still in the sample, whereas for "41,EDR3" it is 9 stars. The WRMS values decrease by about 40% for the orientation parameters in X and Y, while they remain similar for the other rotation parameters. The WM values change significantly (by about 0.1 mas) for parameters ϵ_X and ϵ_Y" (Lunz et al. 2020a).

The uncertainties of the baseline solution at $k = 13$ "show a similar behavior as those predicted by Lindegren (2020b) – that is that the spin parameter uncertainties should decrease if updated *Gaia* data releases were used, even without adding further VLBI observations. This is due to smaller uncertainties in the *Gaia* EDR3 positions and proper motions. However, the Q/n equals [5.50] for this solution, which is larger than that for the baseline solution of "55,DR2" at iteration $k = 13$ [(4.54)] and signalizing the presence of systematic errors" (Lunz et al. 2020a).

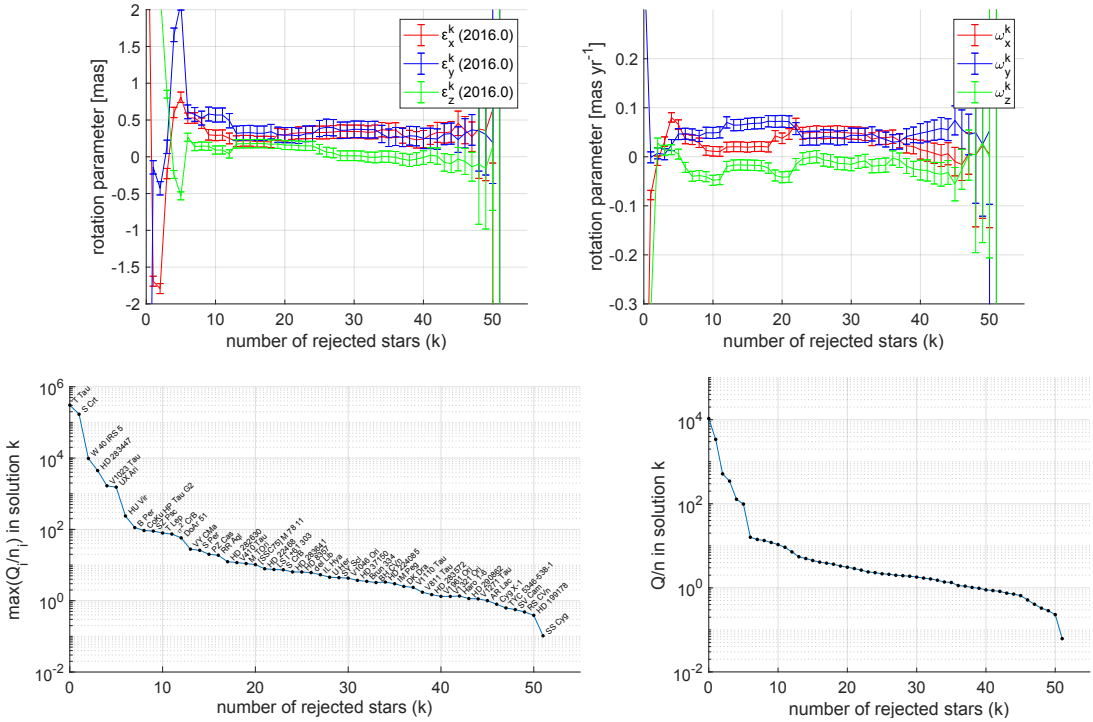

Figure 5.31 Rotation parameter results for Gaia EDR3 in scenario "55,EDR3" when using the homogenized data explained in Sect. 5.1 as well as the data of this work as explained in Sect. 5.4.4 applying the more realistic error budget from Sect. 5.4.5. For a description of the plots refer to Fig. 5.24.
Note. Similar to Lunz et al. (2020a, Fig. 3).

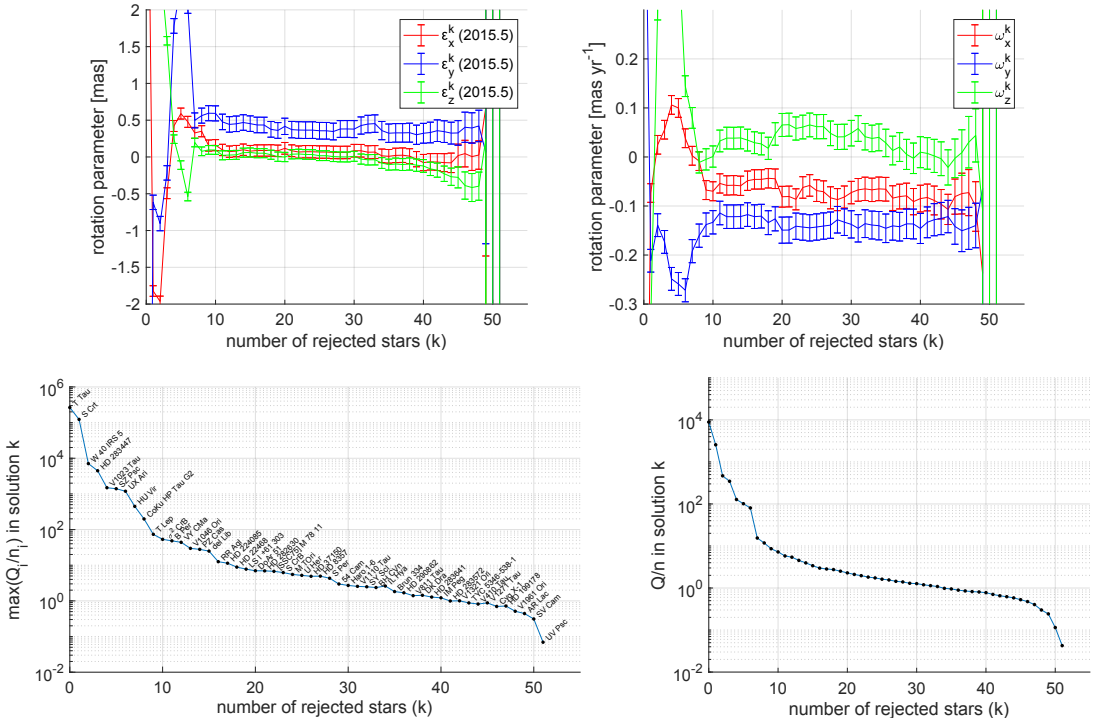

Figure 5.32 Rotation parameter results for Gaia DR2 in scenario "55,DR2" when using the homogenized data explained in Sect. 5.1 as well as the data of this work as explained in Sect. 5.4.4 applying the more realistic error budget from Sect. 5.4.5. For a description of the plots refer to Fig. 5.24.

The correlation coefficients between the rotation parameters from the baseline solution are

$$\begin{aligned}&\mathrm{corr}[\epsilon_X(T), \epsilon_Y(T), \epsilon_Z(T), \omega_X, \omega_Y, \omega_Z] \\ &= \begin{bmatrix} +1.000 & +0.244 & +0.212 & +0.238 & +0.040 & +0.011 \\ \dots & +1.000 & +0.195 & +0.033 & +0.232 & +0.019 \\ \dots & \dots & +1.000 & +0.010 & +0.052 & +0.076 \\ \dots & \dots & \dots & +1.000 & +0.047 & +0.328 \\ \dots & \dots & \dots & \dots & +1.000 & +0.020 \\ \dots & \dots & \dots & \dots & \dots & +1.000 \end{bmatrix}.\end{aligned} \tag{5.10}$$

Except between ω_X and ω_Z, there are only negligible correlations (i.e., correlation coefficients smaller than 0.3) between the rotation parameters. Compared to those of "41,EDR3" all of them decreased.

For "55,EDR3", the stars LSI +61 303, HD 22468, V410 Tau, HD 283572, CygX-1, HD 199178, and AR Lac have the highest weights above 1000 $\mathrm{mas}^{-2}\,\mathrm{yr}^2$ in the spin determination. They are the same stars as for "41,EDR3". In addition to LSI +61 303, star CygX-1 has an Ω_i above 4000 $\mathrm{mas}^{-2}\,\mathrm{yr}^2$. As can be seen from Table 5.17, the maximum values for E_i and Ω_i increased slightly.

Another scenario "55,EDR3,GA" was computed, where "GA" represents the correction for Galactocentric acceleration. No significant changes compared to "55,EDR3" occurred in any of the WM, WRMS, and ME quantities. Its baseline solution at $k = 13$ including the correlation coefficients are similar to those of the baseline solution from "55,EDR3" at $k = 13$, and the weights are the same.

Gaia DR2

The scenario for 55 stars and the alignment to Gaia DR2 is labelled "55,DR2" (Fig. 5.32). Comparing "55,DR2" with "41,DR2", the ME values for the orientation and spin parameters decrease similarly as for EDR3. The WRMS decreases for ϵ_X by 50 %, while it increases for ϵ_Z by 60 %. For the spin parameters the WRMS values decrease by about 20 % to 30 %. The WM values only change significantly for ω_Y according to the t-test. The ratio between $\mathrm{WRMS}_{55,\mathrm{DR2}}$ and $\mathrm{ME}_{55,\mathrm{DR2}}$ indicates that the variation of the rotation parameters is stable over the given intervals. The Q/n is smaller one at the iteration with $k = 34$ rejected stars for "55,DR2", and with $k = 39$ rejected stars for "55,EDR3".

The baseline solution for "55,DR2" was chosen to be at $k = 11$ stars ($Q/n = 5.79$). There are no significant changes in the orientation and spin parameters compared to the baseline solution of "41,DR2", however, the uncertainties of all rotation parameters improved. The

correlation coefficients between the rotation parameters from the baseline solution are

$$\begin{aligned}&\mathrm{corr}[\epsilon_X(T), \epsilon_Y(T), \epsilon_Z(T), \omega_X, \omega_Y, \omega_Z] \\ &= \begin{bmatrix} +1.000 & +0.259 & +0.239 & -0.018 & -0.029 & -0.034 \\ \dots & +1.000 & +0.192 & -0.010 & -0.079 & +0.015 \\ \dots & \dots & +1.000 & -0.046 & +0.016 & -0.108 \\ \dots & \dots & \dots & +1.000 & -0.007 & +0.296 \\ \dots & \dots & \dots & \dots & +1.000 & -0.049 \\ \dots & \dots & \dots & \dots & \dots & +1.000 \end{bmatrix}.\end{aligned} \tag{5.11}$$

There remain only negligible correlations (i.e., correlation coefficients smaller than 0.3) between the orientation parameters.

For "55,DR2", the weights are slightly larger than for "41,DR2" (Table 5.17). The same stars as for "41,DR2" and "41,DR2,Lind2020" have a weight above $300\,\mathrm{mas}^{-2}\,\mathrm{yr}^2$ in the spin determination.

"The proper motion values and uncertainties did not change between Lindegren (2020b) and our work. Thus, if the spin was determined only from the proper motion information, it is the same when using the proper motions of either the "55,DR2" or the "41,DR2,Lind2020" dataset. The latter is scenario B in Lindegren (2020b) and the determined spin is $(-0.050,\ -0.139,\ 0.002) \pm (0.036,\ 0.055,\ 0.038)\ \mathrm{mas\,yr}^{-1}$. The spin from the baseline solution of "55,DR2" (including the information coming from the positions) can thus be compared directly to the spin from scenario B to see if the positions have an effect on the determination of the spin, although their uncertainties were inflated in our work. The parameter estimates do not differ significantly, however the formal errors were about halved. Thus, the positions have a large impact on the spin determination. For the spin in Y, our baseline solution ($-0.113 \pm 0.240\,\mathrm{mas\,yr}^{-1}$) is closer to scenario B than the baseline solution of "41,DR2,Lind2020" ($-0.051 \pm 0.270\,\mathrm{mas\,yr}^{-1}$, equivalent to scenario A in Lindegren (2020b)). However, compared to "41,DR2,Lind2020", the positions of these stars in "55,DR2" were given lower weights relative to the proper motion information due to the inflated position uncertainties. The effect of the inflated position uncertainties was compensated by the increased number of star positions so that the formal errors for the spin parameters in "55,DR2" are as large as that of the original baseline solution "41,DR2,Lind2020" " (Lunz et al. 2020a).

The evolution of the correlation parameters across iterations is shown for "55,DR2" and "55,EDR3" in Figs 5.33 and 5.34. Their evolution is approximately the same for all scenarios where the new observations from experiment UL005 were added.

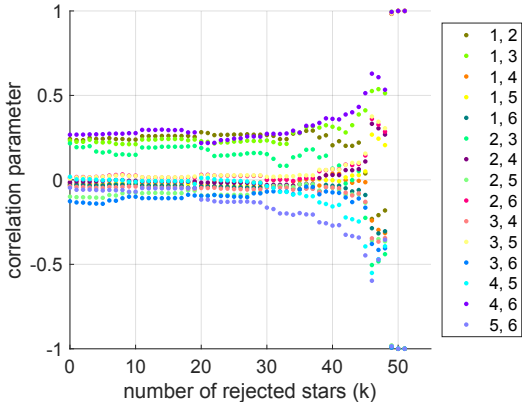

Figure 5.33 Correlation parameters for all iterations of "55,DR2". The numbers 1 to 6 represent the rotation parameters in the order $[\epsilon_X(T), \epsilon_Y(T), \epsilon_Z(T), \omega_X, \omega_Y, \omega_Z]$.

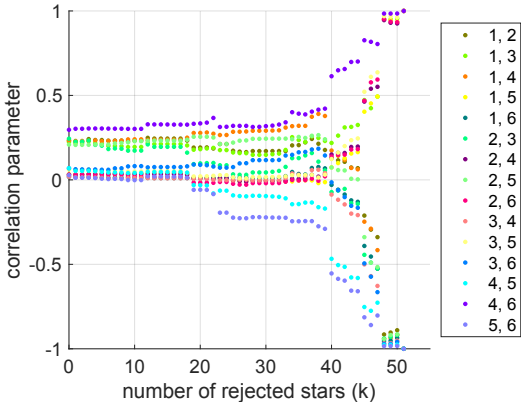

Figure 5.34 Correlation parameters for all iterations of "55,EDR3". The numbers 1 to 6 represent the rotation parameters in the order $[\epsilon_X(T), \epsilon_Y(T), \epsilon_Z(T), \omega_X, \omega_Y, \omega_Z]$.

Residuals

Figure 5.35 shows the position and proper motion residuals from VLBI with respect to those from Gaia at the VLBI epoch and corrected for the rotation parameters for the baseline solutions of "55,DR2" and "55,EDR3" with 44 included stars (similar to Figs. 4 and 5 in Lunz et al. (2020a)). The residuals of T Tau and S Crt are too large to be in the plotting window. There are significant differences between Gaia DR2 and Gaia EDR3, but most residuals are not significant within 2 to 3 times their standard deviation. The improvement of Gaia parameters of VY CMa is confirmed.

5.6.4 Adding new observations as single-epoch positions and improved estimates of models of stellar motion

If not stated otherwise, the text of this subsection was taken from Lunz et al. (2021b), and references to other sections, tables and figures were adjusted to match the outline of this work.

Gaia EDR3

We use the new models of stellar motion determined in Sect. 5.5 for the 12 stars HD 283572, V410 Tau, SS Cyg, Brun 334, TYC 5346-538-1, Haro 1-6, BH CVn, σ^2 CrB, HD 199178, AR Lac, IM Peg, and HD 22468 to replace the VLBI data of the respective star in the rotation parameter analysis "55,EDR3,GA". This way, the change of the rotation parameters due to the new model estimates can be directly compared. Instead of using the positions from the model of stellar motion at the mean epoch of the respective star time

series, the corrected positions from the fringe fit of the calibrator to a point source model, as described in Sect. 5.4.4, were used to best connect to ICRF3. Furthermore, the new data was also corrected for the effect of Galactocentric acceleration. The resulting rotation parameter estimates "55,EDR3,GA,NM" (where "NM" indicates that star data was replaced with the new models of stellar motion) are shown in Fig. 5.38.

The new scenario still shows some offsets for iterations $10 \leq k \leq 35$ (same range as for "55,EDR3,GA" for comparison) in both orientation and spin parameters. This indicates that data from individual stars still has an impact on the derived rotation parameters. Small offsets in orientation occur after iteration $k = 11$ when DoAr 51, LS I +61 303, and HD 283641 are rejected. For LS I +61 303 also offsets appear for the spin. It is a binary star with an orbit of a few milliarcseconds diameter (Albert et al. 2006, 2008; Wu et al. 2018). We observed the star in UL005 and collected additional positions for the star. However, because of the more complicated trajectory, it was not considered for the new model estimates in this work. Offsets in spin appear for the iterations when stars HD 22468 ($k = 20$), LSI +61 303 ($k = 21$), V410 Tau ($k = 27$), and AR Lac ($k = 32$) are

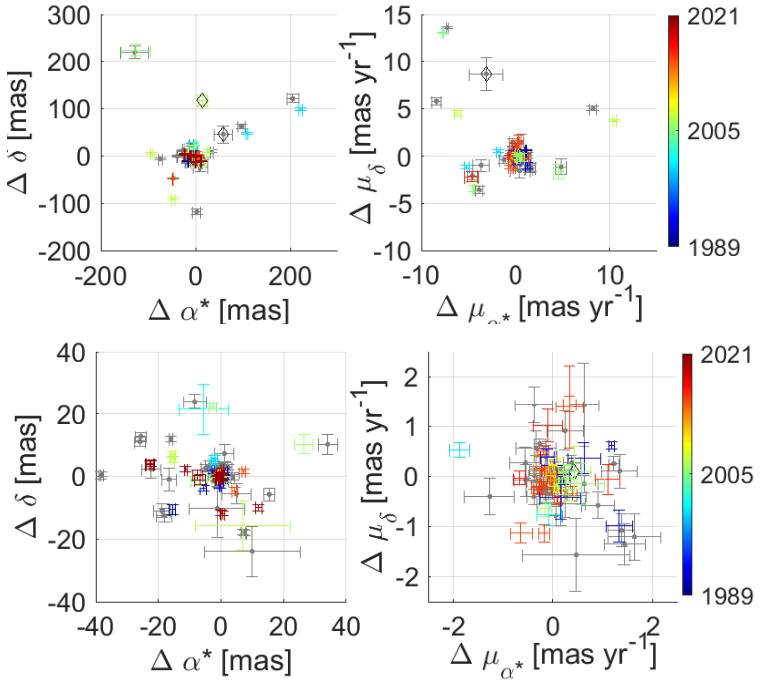

Figure 5.35 Residuals of the VLBI positions and proper motions from the adjustment of orientation and spin. They are with respect to the *Gaia* values at the VLBI epoch and are corrected for the rotation parameters. Values are given for the baseline solutions with $k = 11$ rejected stars employing *Gaia* DR2 ("55,DR2", grey) and for the baseline solutions with $k = 13$ rejected stars employing EDR3 ("55,EDR3", color coded by the epoch of the VLBI position of the respective data). The lower plots are zoomed in from the upper plots. The position residuals for T Tau and S Crt are not shown, as they are far outside the plot area. The residuals for VY CMa are marked with a black diamond.

rejected. The introduction of the new estimates for the stellar motion model reduced the offsets in the iterative spin parameter results for σ^2 CrB but added AR Lac instead. This suggests that more emphasis has to be put on the detailed VLBI-*Gaia* comparison for these objects.

Significant deviations in WM occur in both orientation and spin in Y direction and in ω_Z when comparing "55,EDR3,GA,NM" to "55,EDR3,GA". The new estimates for models of stellar motion reduced the scatter in ω_X and increased it in ϵ_Y (Figs. 5.37 and 5.38), which is also reflected by the WRMS statistics. The ME decreased by about 15 % for the spin, while the orientation parameters increased by about 15 %. The "55,EDR3,GA" scenario has a lower ME for the orientation parameters because more VLBI positions are involved in the adjustment than in "55,EDR3,GA,NM". At the same time, the uncertainties of the spin parameters are lower for "55,EDR3,GA,NM" because improved VLBI proper motion estimates were used.

The new baseline solution is chosen to be at $k = 12$ rejected stars because both orientation and spin parameters are stable for some iterations thereafter. [...] The spin tends to be smaller compared to the baseline solution of "55,EDR3,GA". Correlation coefficients for $k = 12$ and $T = 2016.0$ are

$$\begin{aligned}&\mathrm{corr}[\epsilon_X(T), \epsilon_Y(T), \epsilon_Z(T), \omega_X, \omega_Y, \omega_Z] \\ &= \begin{bmatrix} +1.000 & +0.225 & +0.196 & +0.031 & +0.011 & -0.040 \\ \dots & +1.000 & +0.187 & +0.003 & +0.010 & -0.019 \\ \dots & \dots & +1.000 & -0.038 & +0.008 & -0.054 \\ \dots & \dots & \dots & +1.000 & -0.035 & +0.336 \\ \dots & \dots & \dots & \dots & +1.000 & -0.101 \\ \dots & \dots & \dots & \dots & \dots & +1.000 \end{bmatrix},\end{aligned} \tag{5.12}$$

which show that no strong correlations are present, and that the spin in the X and Z components still show a low correlation. Compared to the scenario with the old models, "55,EDR3,GA", the correlation coefficient of the orientation parameter and the spin parameter of each axis is now also reduced to close to zero.

In addition to Lunz et al. (2021b), the formal weights of the stars for the rotation parameter determination were evaluated, as given in Table 5.17. The median and maximum values for E_i are smaller than those of "55,EDR3,GA". The maximum value for Ω_i is larger, although the median value is the same. The stars LSI +61 303, V410 Tau, HD 283572, CygX-1, HD 199178, and AR Lac have weights above 2000 $\mathrm{mas}^{-2}\,\mathrm{yr}^2$. All of them were used in the baseline solution. Star HD 199178 has the highest weight. Out of these six stars, four were given new estimates for the models of stellar motion in this work. Additionally, four stars have the highest weights above 1000 $\mathrm{mas}^{-2}\,\mathrm{yr}^2$ in the spin deter-

mination. They are HD 22468, Brun 334, TYC 5346-538-1, SS Cyg, which all obtained new estimates for the model of stellar motion in "55,EDR3,GA,NM".

In addition to Lunz et al. (2021b), the difference in residuals of the VLBI data with respect to the Gaia data at the VLBI epoch and corrected for the rotations it shown in Fig. 5.36 for scenarios "55,EDR3,GA" and "55,EDR3,GA,NM". From this residual plot it can be seen that e.g. star HD 283447 is a candidate for detailed studies of its trajectory as seen by VLBI and by Gaia — in the rotation parameter analysis it is one of the first rejected stars and therefore is not in the presented baseline solutions and does not corrupt the

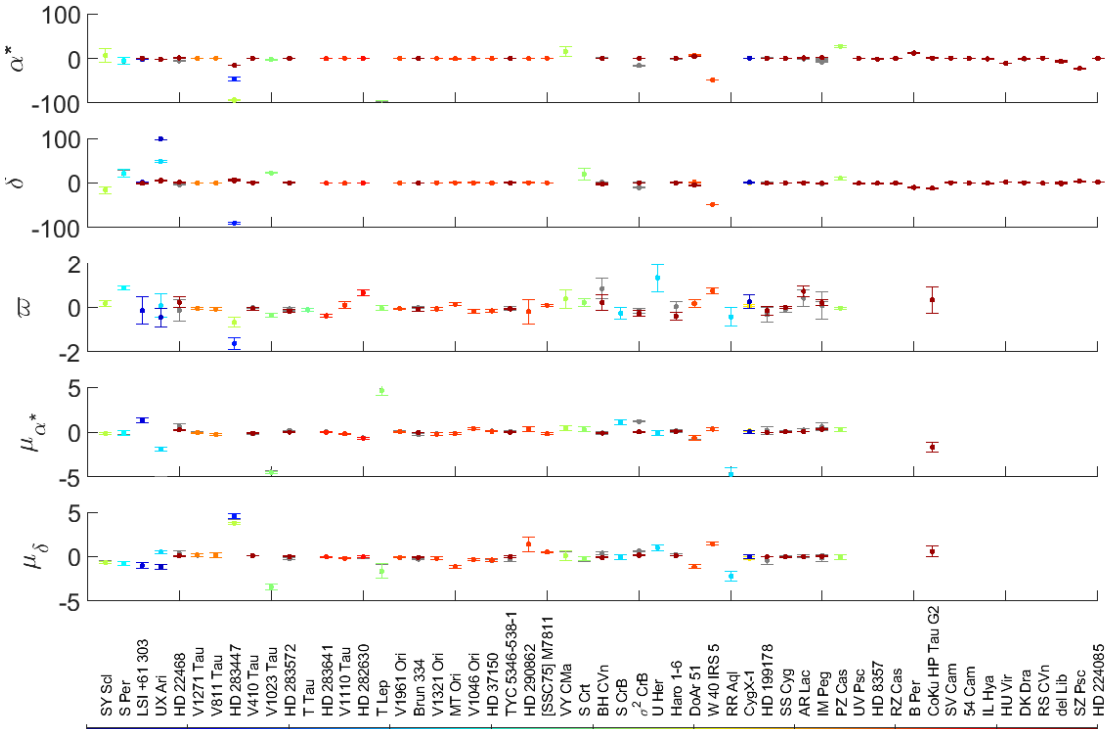

Figure 5.36 Residuals of the VLBI positions, parallaxes, and proper motions from the adjustment of orientation and spin for the baseline solutions of "55,EDR3,GA" (grey) and "55,EDR3,GA,NM" (color coded by the epoch of the VLBI position of the respective data). The residuals are with respect to the Gaia values at the VLBI epoch and are corrected for the rotation parameters. Units are in milliarcseconds for the residuals of positions and parallaxes, and milliarcseconds per year for the residuals of the proper motions. The $\alpha*$ of about 1 889 mas for S Crt, the $\alpha*$ of about 109 mas and 223 mas and the $\mu_{\alpha*}$ of about $-5.2\,\mathrm{mas\,yr^{-1}}$ for UX Ari, the $\alpha*$ of about -149 mas, δ of about -651 mas and -593 mas, $\mu_{\alpha*}$ of about $-8\,\mathrm{mas\,yr^{-1}}$, and μ_δ of about $13\,\mathrm{mas\,yr^{-1}}$ for T Tau, the $\alpha*$ of about -126 mas, and δ of about 226 mas for T Lep, the δ of about 117 mas for VY CMa, and the $\mu_{\alpha*}$ of about $10\,\mathrm{mas\,yr^{-1}}$ and $-6\,\mathrm{mas\,yr^{-1}}$ for HD 283447, are outside the plot range.

results. Furthermore, most of the residuals for stars that have received new estimates for stellar motion models in this work are smaller compared to the residuals using the original homogenized dataset. The discrepancy measure Q_i/n_i is reduced for some stars with the new model estimates applied. The largest reductions in Q_i/n_i appeared for σ^2 CrB (from 77 to 2), V410 Tau (from 11 to 6), Brun 334 (from 4 to 1), and S Crt and T Tau which both still have values on the order of 10^5. For AR Lac and Haro 1-6, the values worsen from about 1 to about 3 to 4. This could be due to the larger residuals in parallax, meaning that the VLBI parallax estimates were closer to the Gaia ones.

Inserting model positions instead of single-epoch positions

In addition to Lunz et al. (2021b), the impact of using model positions instead of single-epoch positions was investigated in this work. In literature, such as in Lindegren (2020a), the alignment between a VLBI-based CRF and another astrometric catalog by employing radio star observations was done by inserting the positions from the model of stellar motions into the rotation parameter analysis. For comparison to the method in this work, a scenario "55,EDR3,GA,NM,modelpos" was run where instead of the January 2020 absolute single-epoch positions based on a point source fringe fit, the positions from the models of stellar motion estimates were inserted into the analysis whenever possible. It is important to not apply the Römer delay and parallax correction in case the model positions are used. In addition, the uncertainties of the positions were adjusted to match Eqs. 5.6 and 5.7 instead of 5.4 and 5.5. For the model positions, only the σ_{CRF} of one of the primary calibrators was considered in case there were multiple. For BH CVn and AR Lac the calibrators which were not excluded or down-weighted were employed. The resulting rotation parameters are presented in Fig. 5.39. The order of rejected stars is only mixed by less than about 10 places for a star.

The differences in WM for ϵ_X (0.114 mas) compared to "55,EDR3,GA,NM" are significant according to the t-test. The scatter of the parameters decreased in ϵ_X and ϵ_Y by about 40 % while it changed for the others by up to 25 %. Only the WRMS ω_X also improved. While the ME of the orientation offsets decreased by 6 % to 16 % compared to "55,EDR3,GA,NM", the ME of the spin remained similar with an increase of 1 % to 2 %.

The maximum values for E_i and Ω_i are slightly larger than those of "55,EDR3,GA,NM" (Table 5.17), but the median values are the same. The stars LSI +61 303, HD 283572, CygX-1, HD 199178, and AR Lac have weights above 2000 $\mathrm{mas}^{-2}\,\mathrm{yr}^2$ for the spin determination. These are all stars except V410 Tau which fulfilled the selection criteria in "55,EDR3,GA,NM". Star HD 199178 also has the highest weight. Out of these five stars, three were given new estimates for the models of stellar motion in this work. Additionally, four stars have the highest weights above 1000 $\mathrm{mas}^{-2}\,\mathrm{yr}^2$ in the spin determination. They

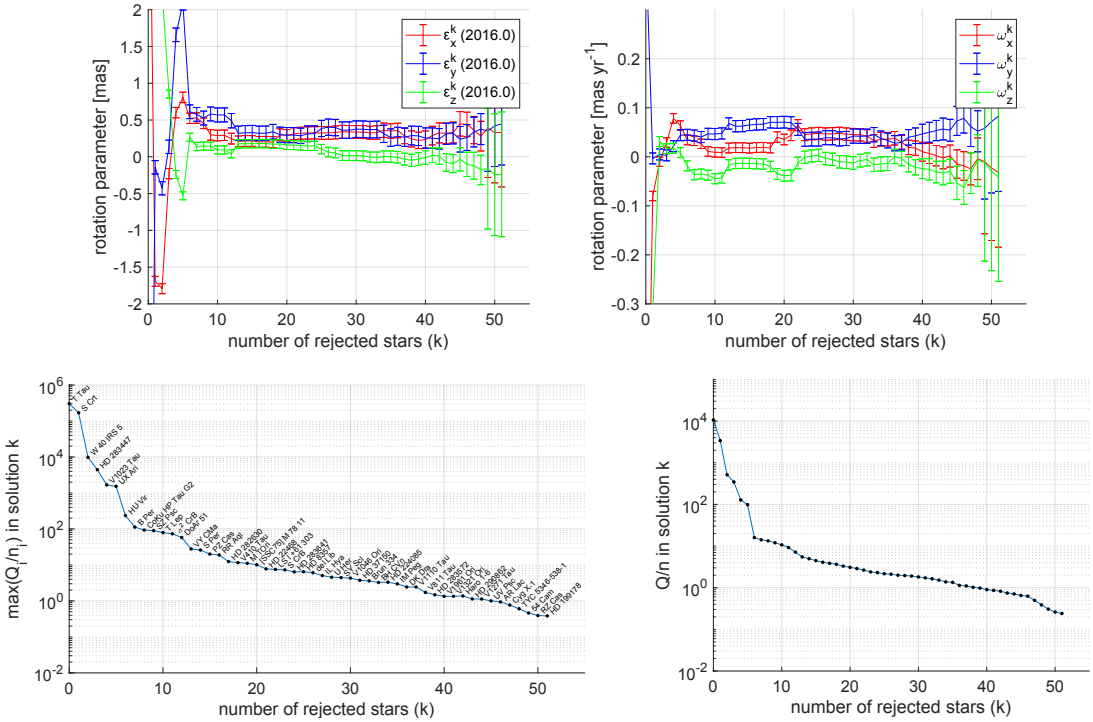

Figure 5.37 Results "55,EDR3,GA" when using the VLBI data and *Gaia* EDR3 as in Fig. 5.31 but correcting for the effect of Galactocentric acceleration. For a description of the plots refer to Fig. 5.24

Note. According to Lunz et al. (2021b, Fig. 2).

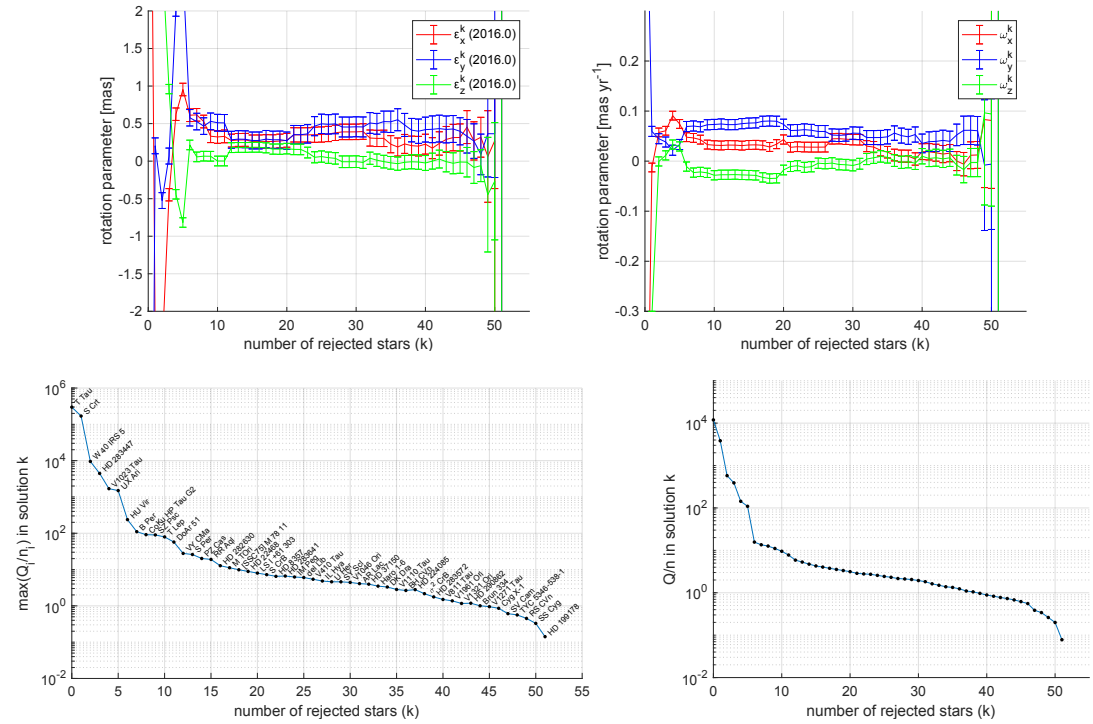

Figure 5.38 Results "55,EDR3,GA,NM" using the VLBI data and *Gaia* EDR3 as in Fig. 5.37, but replacing the VLBI data of stars HD 283572, V410 Tau, SS Cyg, Brun 334, TYC 5346-538-1, Haro 1-6, BH CVn, σ^2 CrB, HD 199178, AR Lac, IM Peg, and HD 22468 with newly determined models of stellar motion and newly corrected absolute positions as described in Sect. 5.5. For a description of the plots refer to Fig. 5.24.

Note. According to Lunz et al. (2021b, Fig. 3).

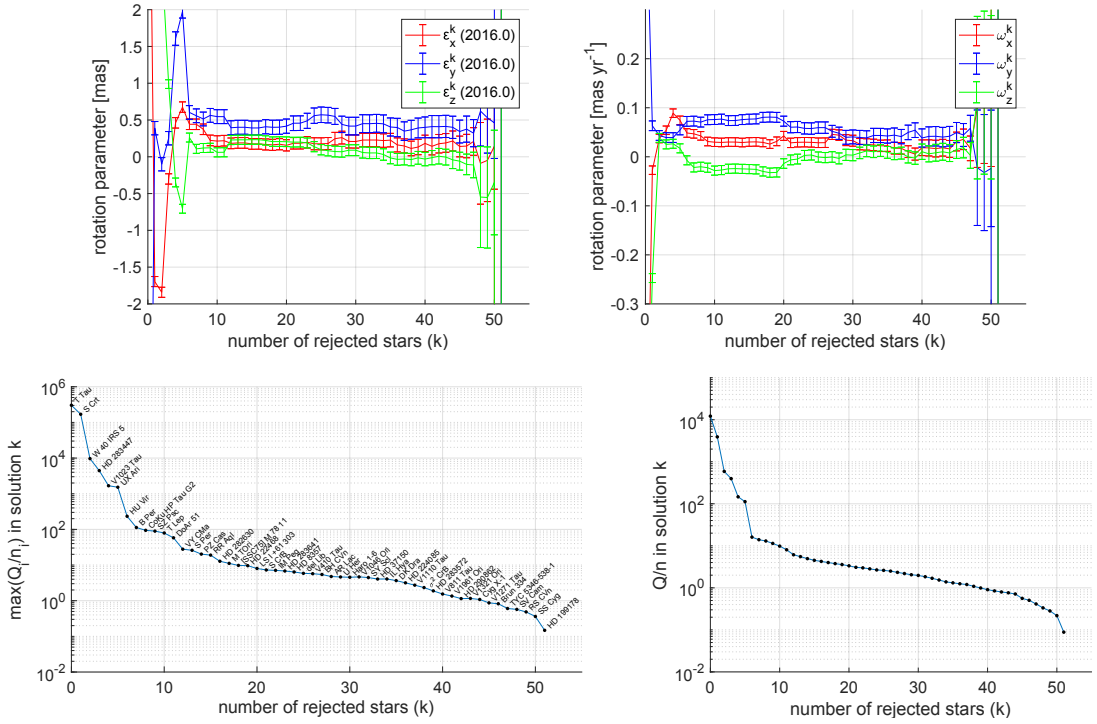

Figure 5.39 Results "55,EDR3,GA,NM,modelpos" when using the same data as for "55,EDR3,GA,NM" but using the model positions as input for the rotation parameter analysis instead of the January 2020 single-epoch positions. For a description of the plots refer to Fig. 5.24.

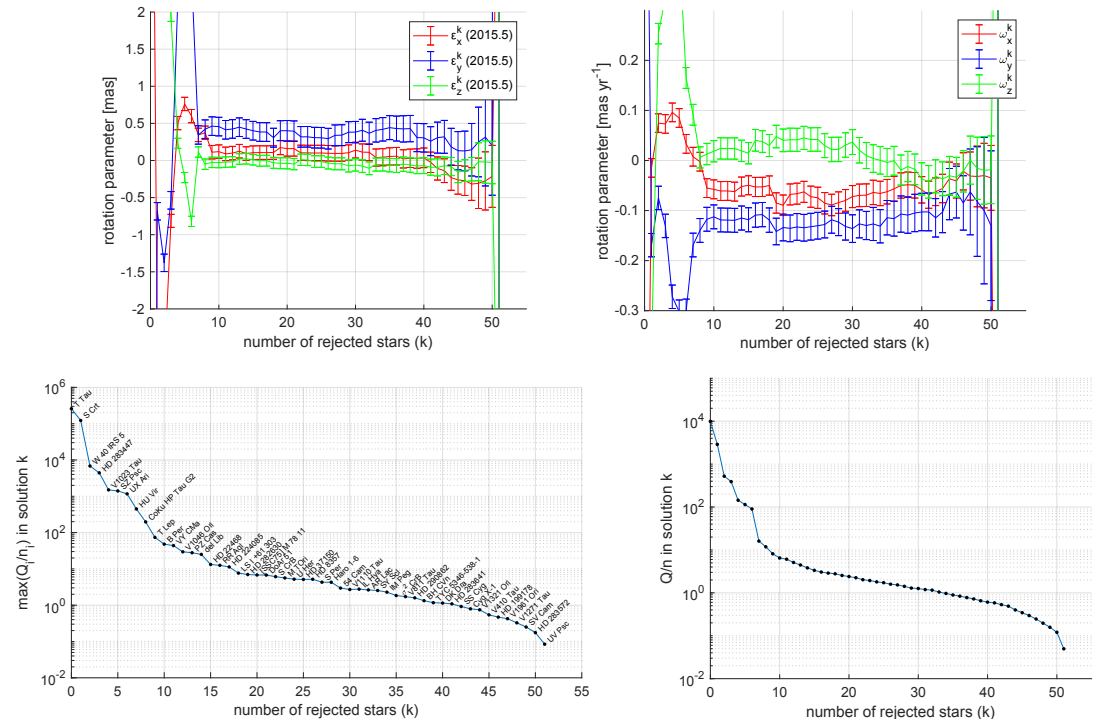

Figure 5.40 Results"55,DR2,NM" using the VLBI data and *Gaia* DR2 as in Fig. 5.32, but replacing the VLBI data of stars HD 283572, V410 Tau, SS Cyg, Brun 334, TYC 5346-538-1, Haro 1-6, BH CVn, σ^2 CrB, HD 199178, AR Lac, IM Peg, and HD 22468 with newly determined models of stellar motion and newly corrected absolute positions as described in Sect. 5.5. For a description of the plots refer to Fig. 5.24.

are HD 22468, V410 Tau, TYC 5346-538-1, SS Cyg, which all obtained new estimates for the model of stellar motion in "55,EDR3,GA,NM". Brun 334 does not fulfill the selection criteria anymore.

From this analysis it can be concluded that for the purpose of aligning the VLBI dataset and Gaia EDR3, the method of this work is equal in terms of spin determination and in terms of the scatter of the resulting rotation parameters. Most likely because the model positions inserted into the analysis have smaller uncertainties than the absolute single-epoch positions, the ME of the orientation parameters are smaller for "55,EDR3,GA,NM,modelpos".

The residuals show that there are differences between the two scenarios for some of the stars. IM Peg has a residual in α of -5.068 mas for "55,EDR3,GA,NM,modelpos" and of 1.532 mas for "55,EDR3,GA,NM", whereas the one in δ remains similar. Here, the single-epoch position seems to fit the Gaia data better. HD 22468 has a residual in δ of -2.027 mas for "55,EDR3,GA,NM,modelpos" and of 1.319 mas for "55,EDR3,GA,NM", whereas the one in α is -3.514 mas for "55,EDR3,GA,NM,modelpos" and 1.151 mas for "55,EDR3,GA,NM". Here, again the single-epoch position seems to fit the Gaia data better. BH CVn has a residual in α of 2.033 mas for "55,EDR3,GA,NM,modelpos" and of 0.232 mas and -0.402 mas for "55,EDR3,GA,NM", whereas the one in δ is -0.482 mas for "55,EDR3,GA,NM,modelpos" and -1.486 mas and -2.937 mas for "55,EDR3,GA,NM". Here, no clear decision can be made. For the latter two stars significant correlations between the model estimates are present and more observations are suggested to decorrelate the estimates and thereby improve this evaluation. Furthermore, the reader should keep in mind that the magnitude of the position difference of a star from referencing to two different calibrators is about 0.47 mas in α and about 1.08 mas in δ as listed in Table 5.8. The difference between model position and single-epoch position can be influenced by this budget.

Gaia DR2

In addition to the analysis for Gaia EDR3 in Lunz et al. (2021b), Fig. 5.40 shows the results for Gaia DR2, called "55,DR2,NM". In this scenario, the parallaxes from the new estimates from models of stellar motion were used for the correction of the absolute star positions and the Römer delay whenever possible. Otherwise, the Gaia DR2 parallax was used for consistency with "55,DR2". According to the t-test, the mean of the spin in X, Y, and Z is different between "55,DR2" and "55,DR2,NM", although the differences are only -0.004, -0.013, and $+0.018$ mas yr^{-1} respectively. The Q/n is smaller one at the iteration with $k = 34$ rejected stars for "55,DR2,NM", the same as for "55,DR2". The WRMS decreased for ϵ_Z by 50 %, and in ω_X by 10 %, while it increased or remained

similar for the other rotation parameters. The ME increased in all orientation parameters by about 20 %, which is expected due to the change in the set of input positions.

The baseline solution for "55,DR2,NM" was chosen to be at the same iteration as the baseline solution of "55,DR2". Similar to "55,EDR3,GA" and "55,EDR3,GA,NM", the estimates do not differ and the formal errors of the orientation offset parameters increase, while those of the spin parameters remain similar or decrease slightly. The Q/n also marginally increases. The correlation parameters are similar for the two scenarios.

The median and maximum values for E_i are smaller than of those of "55,DR2" (Table 5.17). The values for Ω_i are slightly larger. The same stars as for "41,DR2", "41,DR2,Lind2020", and "55,DR2" have a weight above 300 $\mathrm{mas}^{-2}\,\mathrm{yr}^2$ in the spin determination.

5.6.5 Additional VLBI observations from other resources

The five stars HD 142184 (HR 5907), EI Eri, HD 167971, V479 Sct, and YY Men observed in additional experiments as described in Sect. 5.5 were added to the dataset "55,EDR3,GA,NM". In addition, the new proper motion and parallax information was appended to the two 2020 positions from point source fringe fit for CoKu HP Tau G2 and del Lib respectively. The effect of Galactocentric acceleration was corrected in the new data as well. A more realistic error budget of the positions was considered, as introduced in Sect. 5.4.5 and given in Table 5 in Lunz et al. (2021b). The position uncertainty from absolute geodetic observations, such as for star YY Men in the last line of the table, remain unchanged. The scenario is labelled "60,EDR3,GA,NM" (Fig. 5.41).

"Star EI Eri is rejected at $k = 7$, HD 167971 at $k = 8$, V479 Sct at $k = 10$, and YY Men at $k = 16$. For the first three stars and CoKu HP Tau G2 (rejected at $k = 14$), small shifts occur in both orientation offset and spin when they are excluded. Star del Lib is rejected at $k = 24$, and no shift can be identified. HD 142184 gets excluded as one of the last stars. Furthermore, the offsets in orientation for DoAr 51 and HD 283641 and in spin for HD 22468, V410 Tau, AR Lac, and LSI +61 303 remain similar to those in scenario "55,EDR3,GA,NM".

Comparing "60,EDR3,GA,NM" to "55,EDR3,GA,NM", the inclusion of new stars in the analysis leads to a small improvement in the ME values of 1 % to 2 %. The WM and WRMS values do not significantly change, except for the WRMS of ϵ_X. Its increase from 0.059 mas to 0.112 mas can be explained by the offset in ϵ_X due to the exclusion of CoKu HP Tau G2 being included in the latter statistic" (Lunz et al. 2021b). The baseline solution at $k = 15$, including the correlation coefficients, is similar to the baseline solution of "55,EDR3,GA,NM".

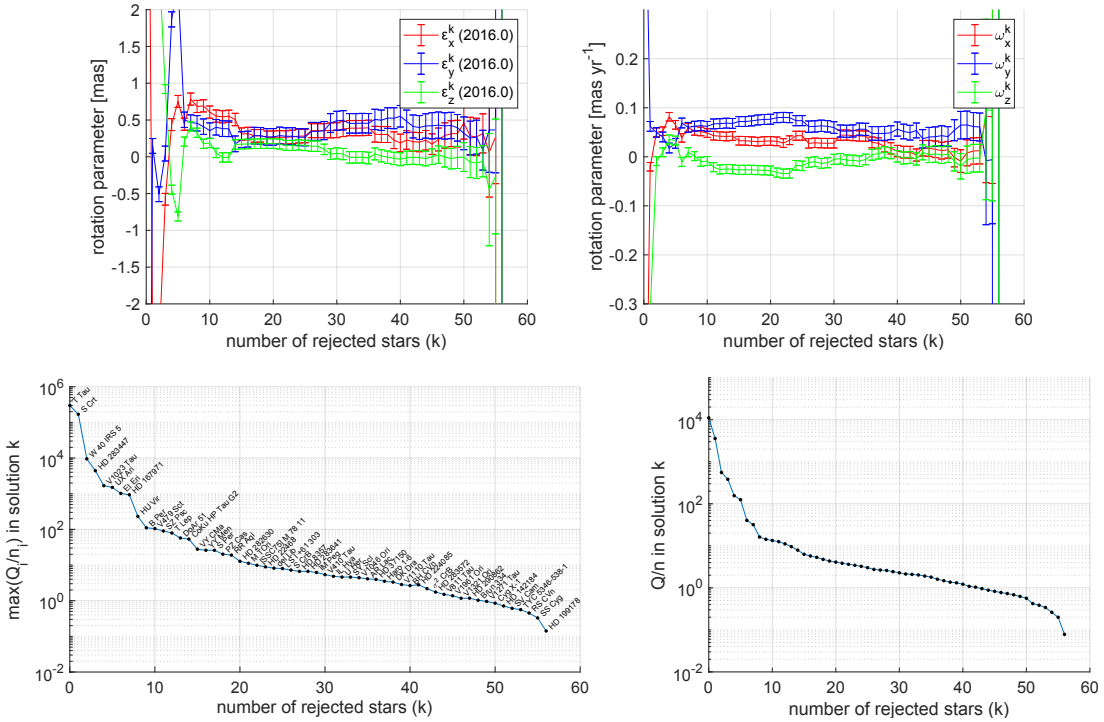

Figure 5.41 Results "60,EDR3,GA,NM" using the VLBI data and *Gaia* EDR3 as for "55,EDR3,GA,NM" and adding additional counterparts and astrometric information. For a description of the plots refer to Fig. 5.24.
Note. According to Lunz et al. (2021b, Fig. 4).

Unresolved binaries as seen by Gaia - center of luminosity versus barycenter

Solutions employing the barycenter instead of the center of luminosity as a reference point for the new observations of close unresolved binaries as seen by *Gaia* were additionally produced for "60,EDR3,GA,NM". The rotation parameter solutions do not differ much, the order of rejected stars is almost the same, and in both baseline solutions, the three binaries under discussion are excluded from the rotation parameter determination already. The differences of the residuals between the baseline solutions using the barycenter and center of luminosity are similar to the differences between the two types of centers as given in Table 5.7, as expected. In δ direction they are smaller than the difference in residuals when using calibrator $P1$ or $P2$ for the stars under discussion. All differences are within the uncertainty limits. The statement from Lunz et al. (2020a) still holds, which was made from the data of scenario "55,DR2": "[...] historical data from Lindegren (2020a) were already available for the three binaries, and the mean positions there were not calculated as the center of luminosity. Therefore, at this point, no clear decision can be made as to of which of the centers is closer to the *Gaia* photocenter. A more detailed study needs to be conducted, where also the reference position for the data from the archive is changed from the barycenter to the center of luminosity".

Table 5.18 Difference in residuals between the baseline solution of "60,EDR3,GA,NM" where the center of luminosity is employed for the three unresolved binaries as seen by Gaia, and the rotation parameter solution at the same iteration where their barycenter position was employed instead.

	Barycenter				Center of Luminosity				Difference			
	$\alpha*$	$\sigma_{\alpha*}$	δ	σ_δ	$\alpha*$	$\sigma_{\alpha*}$	δ	σ_δ	$\alpha*$	$\sigma_{\alpha*}$	δ	σ_δ
UX Ari, $P1$	−2.519	0.773	+5.837	1.003	−2.216	0.773	+5.916	1.002	+0.403	1.093	+0.079	1.417
UX Ari, $P2$	−2.850	0.709	+4.690	0.903	−2.447	0.708	+4.753	0.902	+0.403	1.002	+0.063	1.276
HD 283447, $P1$	−14.861	0.768	+6.127	1.005	−15.578	0.767	+5.640	1.001	−0.717	1.085	−0.487	1.418
HD 283447, $P2$	−14.653	0.730	+7.729	0.913	−15.369	0.729	+7.214	0.907	−0.716	1.032	−0.515	1.287
DoAr 51, $P1$	+4.559	0.902	−4.461	1.104	+4.392	0.902	−4.694	1.106	−0.167	1.275	−0.233	1.563

Notes. If two primary calibrators – $P1$ and $P2$ – were available for phase-referencing, the results from referencing to each of them are shown. The difference is center of luminosity minus barycenter scenario. Units are in milliarcseconds.

5.6.6 Dependence on subsets and weighting

The dependence of the rotation parameter results on various subsets and weighting schemes was tested. The baseline solutions of the various scenarios are provided in Table 5.20. The WM, WRMS, and ME values are given in Table 5.19.

Dependence on visual magnitude

As shown in Lindegren et al. (2018) for Gaia DR2 and in Cantat-Gaudin and Brandt (2021) for Gaia EDR3, the alignment of the Gaia bright frame itself is also G magnitude dependent. In the following, the magnitude dependence of the results based on Gaia EDR3 in this work is tested.

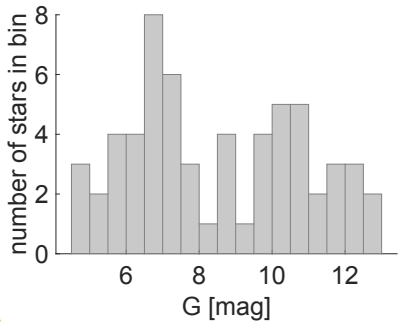

Figure 5.42 Histogram of the G magnitude of the 60 stars in "60,EDR3,GA,NM".

For Gaia DR2, Lindegren (2020b) tested a magnitude dependent function to the frame rotation in Eq. 3.45 based on his selected baseline solution, where the bright stars with 11 mag$< G \leq$ 13 mag were down-weighted with $(13 - G)/2$. The fit with respect to Q was improved (leaving n unchanged), but there is no clear indication whether this is really due to G, given the sparse data and the different peculiarities of each star. Also for "60,EDR3,GA,NM" this magnitude dependent function was tested, labelled "60,EDR3,GA,NM,Gweighting". A histogram of the G magnitudes of the sample is given in Fig. 5.42. The order of rejected stars did not change until $k = 15$, therefore the base-

line solution at $k = 15$ is based on the same subset of stars as the baseline solution of "60,EDR3,GA,NM". The estimates of both baseline solutions and correlation coefficients are similar and the Q only improved from 1269.2 to 1262.8. Also the WM, WRMS, and ME values do not differ from "60,EDR3,GA,NM" according to the t-test.

Cantat-Gaudin and Brandt (2021) used a sample of wide-separation binaries and open cluster members, in which both optically faint and bright objects were included, to determine the spin between the bright and faint frame of Gaia. Thereby, they could separate the data into several G magnitude bins and show that within the bright fraction of Gaia EDR3 with $G < 13\,\mathrm{mag}$, the spin can deviate up to $(20,\ 45,\ 20)\,\mu\mathrm{as\,yr}^{-1}$ for $(\omega_X,\ \omega_Y,\ \omega_Z)$. The binned spin estimates can roughly be grouped into stars brighter $G = 10.5$ mag and stars fainter $G = 10.5$ mag. The binning was possible due to the large number of counterparts between the faint and the bright frame, several ten thousand. In the present work, only 60 counterparts are used. Therefore, here a binning into two separated groups of G magnitude was tested only. The threshold was chosen to be $G = 10.5\,\mathrm{mag}$ according to the findings in Cantat-Gaudin and Brandt (2021). Scenario "60,EDR3,GA,NM" contains 15 stars with $G \geq 10.5\,\mathrm{mag}$ and $G < 13\,\mathrm{mag}$. Excluding them results in scenario "45,EDR3,GA,NM,<10.5mag". Inverting the selection results in scenario "15,EDR3,GA,NM,G>10.5mag".

All spin parameters and ϵ_Y of "15,EDR3,GA,NM,G>10.5mag" are significantly different from those of "60,EDR3,GA,NM". The statistics are based on only 4 iterative results due to the small sample of 15 stars. The sample in the relevant iterations is dominated by 5 stars in the direction of the Y axis ($\alpha \approx 84°$ and $\delta \approx -5°$). Thus, the difference in Y can be explained compared to the scenario using the full dataset. The correlation coefficients for the baseline solution at $k = 5$ are

$$\begin{aligned}&\mathrm{corr}[\epsilon_X(T), \epsilon_Y(T), \epsilon_Z(T), \omega_X, \omega_Y, \omega_Z] \\ &= \begin{bmatrix} +1.000 & +0.558 & +0.390 & +0.063 & -0.025 & -0.056 \\ \ldots & +1.000 & +0.437 & -0.078 & +0.121 & -0.138 \\ \ldots & \ldots & +1.000 & -0.028 & -0.052 & -0.009 \\ \ldots & \ldots & \ldots & +1.000 & +0.088 & +0.207 \\ \ldots & \ldots & \ldots & \ldots & +1.000 & -0.090 \\ \ldots & \ldots & \ldots & \ldots & \ldots & +1.000 \end{bmatrix},\end{aligned} \tag{5.13}$$

The correlations between the orientation offsets increased considerably by more than 0.2 compared to those of "60,EDR3,GA,NM" while the others remained similar.

In "45,EDR3,GA,NM,<10.5mag", ϵ_Z and also all spin parameters are significantly different from those of "60,EDR3,GA,NM". The WRMS in ω_Z increased. The correlation

coefficients for the baseline solution at $k = 10$ are

$$\begin{aligned}&\mathrm{corr}[\epsilon_X(T), \epsilon_Y(T), \epsilon_Z(T), \omega_X, \omega_Y, \omega_Z] \\ &= \begin{bmatrix} +1.000 & +0.044 & +0.149 & -0.023 & +0.039 & -0.074 \\ \dots & +1.000 & +0.061 & +0.039 & -0.068 & +0.033 \\ \dots & \dots & +1.000 & -0.075 & +0.033 & -0.110 \\ \dots & \dots & \dots & +1.000 & -0.074 & +0.387 \\ \dots & \dots & \dots & \dots & +1.000 & -0.128 \\ \dots & \dots & \dots & \dots & \dots & +1.000 \end{bmatrix},\end{aligned} \tag{5.14}$$

The correlations between the orientation offsets reduced slightly compared to those of "60,EDR3,GA,NM" while the others increased slightly.

Deselecting in addition all stars that also were deselected in "53,EDR3,GA,NM" is leaving 41 stars in the sample. For the baseline solution at $k = 10$ the spin in the Y and Z directions decreases and the orientation offset in the Y direction increases, similar to the comparison of "60,EDR3,GA,NM" and "53,EDR3,GA,NM".

Dependence on RUWE

A look at the order of the rejected stars shows that stars with a larger RUWE value in Gaia EDR3 were excluded early. Therefore, another test was performed where all stars with RUWE values greater than 3 and greater than 1.4 were excluded before analysis. This prevented stars with larger RUWE values but low weight from remaining in the sample for the baseline solution and the WM, WRMS, and ME quantities and potentially corrupting them. In case of RUWE > 3, 49 stars stay in the sample ("49,EDR3,GA,NM,RUWE3"), and in case of RUWE > 1.4, 32 stars, respectively ("32,EDR3,GA,NM,RUWE1.4"). The WM, WRMS, and ME quantities for "49,EDR3,GA,NM,RUWE3" do not significantly differ from "60,EDR3,GA,NM". The correlation coefficients at $k = 6$ are very similar to those of the baseline solution in "60,EDR3,GA,NM". Even though less stars are in the baseline solution compared to the one of "60,EDR3,GA,NM", the formal errors are basically the same and the Q/n is smaller (5.65 compared to 6.28). This is due to most stars with RUWE > 3 were rejected in the baseline solution of "60,EDR3,GA,NM" as well (all except VY CMa and del Lib).

Likewise, for the baseline solution of "32,EDR3,GA,NM,RUWE1.4", the formal errors are only slightly worse than for the baseline solution of "60,EDR3,GA,NM" and the Q/n is reduced considerably (4.78 compared to 6.28). The correlation coefficients of this baseline solution are similar to those of the baseline solution in "60,EDR3,GA,NM". Most of the most deviating stars were excluded, as shown in Fig. 5.43. There are eight stars with $G > 10.5$ mag in "32,EDR3,GA,NM,RUWE1.4", meaning that no clear dependence be-

tween higher RUWE and higher G magnitude is present. The ϵ_X and ϵ_Z iterative results are significantly different according to the t-test. The WRMS values decreased for the orientation offset while they increased for the spin.

A solution "24,EDR3,GA,NM,RUWE1.4,<10.5mag" where in addition the eight stars with $G > 10.5$ mag were excluded did not improve the results in the sense that the spin results are more aligned to the respective results of Cantat-Gaudin and Brandt (2021) or that they have considerably less WRMS scatter as shown in Table 5.19. However, the correlation coefficients between the orientation offsets are reduced to below ± 0.095 for the baseline solution at $k = 0$ compared to the above scenarios. This can be an effect of geometry, but also of G magnitude because the results in Cantat-Gaudin and Brandt (2021) show that even within the range of $G > 10.5$ mag and $G < 13$ mag there is a significant variation in the spin results. Therefore, it is likely that such a variation can also occur in the orientation offset.

Excluding maser stars

In the VLBI dataset there are some stars with a very different uncertainty of their absolute positions, the maser stars. In "60,EDR3,GA,NM" 9 such maser stars are present (SY Scl, S Per, T Lep, VY CMa, S Crt, S CrB, U Her, RR Aql, PZ Cas). They each have a position uncertainty of several milliarcseconds, except for S CrB, U Her, and RR Aql, whose positions were not used. The nine masers have G magnitudes between 6.3 and 9.7. Their RUWEs are 2.0, 1.9, 2.3, 14.3, 1.4, 1.6, 1.3, 1.5, 1.1, respectively, thus, seven out of the nine maser stars were already excluded in "32,EDR3,GA,NM,RUWE1.4" and "24,EDR3,GA,NM,RUWE1.4,G<10.5mag", and only one position from masers (PZ Cas) was actually used. Thus, the expected difference in iterative rotation parameter results is expected to be small when running the scenario "22,EDR3,GA,NM,RUWE1.4,G<10.5mag,nomaser", where in addition to all stars with RUWE > 1.4 and $G < 10.5$ mag also all masers were excluded. This is verified by the WM, WRMS, and ME quantities as shown in Table 5.19 and 5.20.

5.6.7 Accuracy of the final results

The various rotation parameter iterative solutions can be tested to further determine the accuracy of the final result. In a first test, stars producing visible deviations in the iterative results of the parameter estimates were excluded a priori to simulate that they were never observed with VLBI. Another, less rigorous option would be to down-weight the respective stars, but this was not tested here.

For "55,EDR3,GA", the scenario "49,EDR3,GA" was tested, in which the four stars

Table 5.19 WM, WRMS, and ME of the various rotation parameter scenarios for Gaia EDR3 when investigating the dependence of the results on different subsets or weighting.

Scenario	Parameter	$\epsilon_X(T)$	$\epsilon_Y(T)$	$\epsilon_Z(T)$	ω_X	ω_Y	ω_Z
60,EDR3,GA,NM,Gweighting	$\mathrm{WM}_{60,\mathrm{EDR3,GA,NM,Gweighting}}$	0.371	0.337	0.129	0.031	0.070	−0.017
	$\mathrm{WRMS}_{60,\mathrm{EDR3,GA,NM,Gweighting}}$	0.119	0.132	0.106	0.012	0.011	0.014
	$\mathrm{ME}_{60,\mathrm{EDR3,GA,NM,Gweighting}}$	0.105	0.130	0.080	0.010	0.012	0.011
15,EDR3,GA,NM,G>10.5mag	$\mathrm{WM}_{15,\mathrm{EDR3,GA,NM,G>10.5mag}}$	0.249	−0.197	0.049	0.070	−0.004	0.006
	$\mathrm{WRMS}_{15,\mathrm{EDR3,GA,NM,G>10.5mag}}$	0.277	0.104	0.074	0.029	0.016	0.003
	$\mathrm{ME}_{15,\mathrm{EDR3,GA,NM,G>10.5mag}}$	0.176	0.289	0.123	0.022	0.032	0.016
45,EDR3,GA,NM,G<10.5mag	$\mathrm{WM}_{45,\mathrm{EDR3,GA,NM,G<10.5mag}}$	0.348	0.397	0.187	0.013	0.077	−0.027
	$\mathrm{WRMS}_{45,\mathrm{EDR3,GA,NM,G<10.5mag}}$	0.100	0.150	0.097	0.014	0.011	0.024
	$\mathrm{ME}_{45,\mathrm{EDR3,GA,NM,G<10.5mag}}$	0.116	0.135	0.088	0.010	0.012	0.012
49,EDR3,GA,NM,RUWE3	$\mathrm{WM}_{49,\mathrm{EDR3,GA,NM,RUWE3}}$	0.303	0.373	0.082	0.029	0.063	−0.014
	$\mathrm{WRMS}_{49,\mathrm{EDR3,GA,NM,RUWE3}}$	0.059	0.100	0.082	0.011	0.012	0.014
	$\mathrm{ME}_{49,\mathrm{EDR3,GA,NM,RUWE3}}$	0.099	0.126	0.074	0.010	0.012	0.010
32,EDR3,GA,NM,RUWE1.4	$\mathrm{WM}_{32,\mathrm{EDR3,GA,NM,RUWE1.4}}$	0.293	0.370	0.021	0.028	0.067	−0.009
	$\mathrm{WRMS}_{32,\mathrm{EDR3,GA,NM,RUWE1.4}}$	0.067	0.093	0.055	0.013	0.015	0.016
	$\mathrm{ME}_{32,\mathrm{EDR3,GA,NM,RUWE1.4}}$	0.102	0.132	0.079	0.010	0.012	0.010
24,EDR3,GA,NM,RUWE1.4,G<10.5mag	$\mathrm{WM}_{24,\mathrm{EDR3,GA,NM,RUWE1.4,G<10.5mag}}$	0.383	0.360	0.052	0.016	0.075	-0.024
	$\mathrm{WRMS}_{24,\mathrm{EDR3,GA,NM,RUWE1.4,G<10.5mag}}$	0.098	0.109	0.037	0.012	0.014	0.022
	$\mathrm{ME}_{24,\mathrm{EDR3,GA,NM,RUWE1.4,G<10.5mag}}$	0.117	0.140	0.094	0.010	0.012	0.012
22,EDR3,GA,NM,RUWE1.4,G<10.5mag,nomaser	$\mathrm{WM}_{22,\mathrm{EDR3,GA,NM,RUWE1.4,G<10.5mag,nomaser}}$	0.374	0.365	0.052	0.016	0.074	-0.022
	$\mathrm{WRMS}_{22,\mathrm{EDR3,GA,NM,RUWE1.4,G<10.5mag,nomaser}}$	0.103	0.118	0.039	0.013	0.015	0.024
	$\mathrm{ME}_{22,\mathrm{EDR3,GA,NM,RUWE1.4,G<10.5mag,nomaser}}$	0.116	0.138	0.093	0.010	0.011	0.012

Notes. For scenario "60,EDR3,GA,NM,Gweighting" iterations 11 to 52 were used for calculation. For "45,EDR3,GA,NM,G<10.5mag" iterations 7 to 37 were used, whereas for "15,EDR3,GA,NM,G>10.5mag" iterations 5 to 9 were used. For "49,EDR3,GA,NM,RUWE3" iterations 6 to 41, and for "32,EDR3,GA,NM,RUWE1.4" iterations 1 to 24 were employed. For "24,EDR3,GA,NM,RUWE1.4,G<10.5mag" iterations 1 to 16, and for "22,EDR3,GA,NM,RUWE1.4,G<10.5mag,nomaser" iterations 1 to 14 were used. For derivation of values $\mathrm{ME_s}$ the last 10 iterations were rejected (except for "15,EDR3,GA,NM,G>10.5mag" due to the small sample) because the formal errors of the rotation parameters increase substantially if only few stars are available for calculations. The epoch T is 2016.0 for Gaia EDR3. Units are in milliarcseconds for $\epsilon_X(T)$, $\epsilon_Y(T)$, and $\epsilon_Z(T)$. They are milliarcseconds per year for ω_X, ω_Y, and ω_Z.

Table 5.20 Baseline solutions of the various scenarios.

Scenario	k	ki	$\epsilon_X(T)$	$\epsilon_Y(T)$	$\epsilon_Z(T)$	ω_X	ω_Y	ω_Z	$\sigma_{\epsilon_X(T)}$	$\sigma_{\epsilon_Y(T)}$	$\sigma_{\epsilon_Z(T)}$	σ_{ω_X}	σ_{ω_Y}	σ_{ω_Z}	Q/n
60,EDR3,GA,NM	15	45	+0.308	+0.233	+0.172	+0.033	+0.072	−0.027	0.085	0.107	0.065	0.009	0.010	0.009	6.28
60,EDR3,GA,NM, Gweighting	15	45	+0.334	+0.217	+0.207	+0.034	+0.077	−0.030	0.091	0.112	0.071	0.009	0.010	0.010	6.25
15,EDR3,GA,NM, G>10.5mag	5	10	+0.134	−0.170	+0.110	+0.053	+0.003	+0.007	0.164	0.278	0.116	0.021	0.031	0.016	3.54
45,EDR3,GA,NM, G<10.5mag	10	35	+0.378	+0.245	+0.201	+0.024	+0.082	−0.043	0.106	0.120	0.082	0.010	0.011	0.011	7.10
41,EDR3,GA,NM, G<10.5mag	10	31	+0.384	+0.432	+0.219	+0.021	+0.037	+0.010	0.117	0.137	0.090	0.012	0.015	0.014	7.04
49,EDR3,GA,NM, RUWE3	6	43	+0.319	+0.238	+0.168	+0.033	+0.072	−0.028	0.085	0.108	0.065	0.009	0.010	0.009	5.65
32,EDR3,GA,NM, RUWE1.4	1	31	+0.323	+0.241	+0.030	+0.030	+0.080	−0.028	0.092	0.117	0.073	0.009	0.011	0.010	4.78
24,EDR3,GA,NM, RUWE1.4,G<10.5mag	0	24	+0.422	+0.187	+0.077	+0.023	+0.086	−0.045	0.109	0.126	0.091	0.010	0.011	0.012	5.40
22,EDR3,GA,NM, RUWE1.4,G<10.5mag, nomaser	0	22	+0.390	+0.171	+0.086	+0.024	+0.088	−0.046	0.109	0.127	0.091	0.010	0.011	0.012	4.68

Notes. The epoch T is 2016.0 for Gaia EDR3. Units are in milliarcseconds for $\epsilon_X(T)$, $\epsilon_Y(T)$, and $\epsilon_Z(T)$. They are milliarcseconds per year for ω_X, ω_Y, and ω_Z. The uncertainties σ are in the same units as the parameters. The parameter Q/n describes the quality of the fit, similar to s_0^2, in the iteration with k discarded stars. For better comparison, the number of included stars, ki is provided as well.

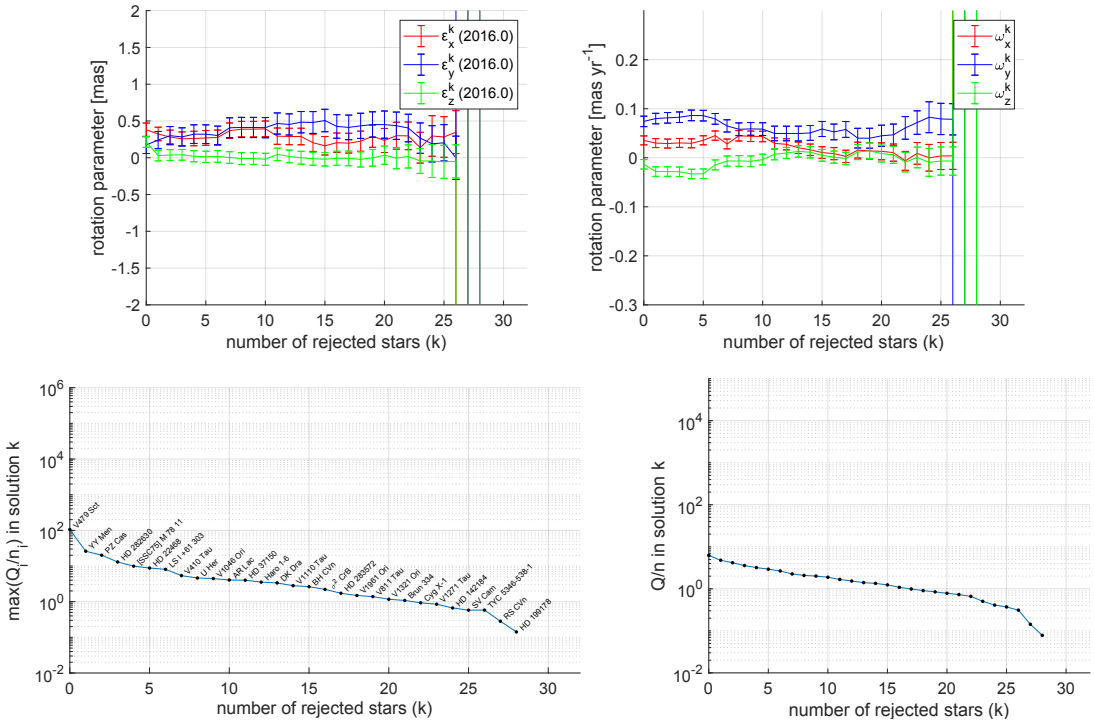

Figure 5.43 Rotation parameter results for Gaia EDR3 in scenario "32,EDR3,GA,NM,RUWE1.4" when using the same data as for "60,EDR3,GA,NM" and excluding stars with a RUWE larger 1.4 in Gaia EDR3. For a description of the plots refer to Fig. 5.24.

σ^2 CrB, HD 22468, LSI +61 303, and V410 Tau, which produce jumps in the iterative spin parameter results, and the two stars DoAr 51 and HD 283641, which produce jumps in the iterative orientation parameter results, were excluded at the beginning. The WM, WRMS, and ME quantities for this scenario are provided in Table 5.15. "The $\mathrm{WRMS}_{49,\mathrm{EDR3,GA}}$ of the orientation parameters reduced by 20 % to 40 % compared to $\mathrm{WRMS}_{55,\mathrm{EDR3,GA}}$. For ω_Y it decreased by 30 % and the difference in the parameter values was also tested significant. The mean standard deviations only deteriorate by up to 10 %, which can be explained by the reduced number of objects in the dataset. The χ^2 is smaller than one for both "49,EDR3,GA" and "55,EDR3,GA" when there are still 16 stars in the sample" (Lunz et al. 2021b).

"Another scenario "49,EDR3,GA,NM" was tested where the four stars HD 22468, LSI +61 303, V410 Tau, and AR Lac, which produce jumps in the iterative results of the spin parameters, and the two stars DoAr 51 and HD 283641, which produce jumps in the iterative results of the orientation parameters, were excluded from the beginning. The WRMS statistics for all parameters dropped by 10 % to 65 % compared to those for the scenario "55,EDR3,GA,NM". At the same time, the WM values changed significantly for ϵ_Y, ω_Y, and ω_Z. The larger spin in Y direction is still present. The correlations between parameters did not really change compared to scenario "55,EDR3,GA,NM" except for a decrease of the correlation coefficients between ω_X and ω_Z to +0.261 and an increase of the correlation coefficient between ω_Y and ω_Z to −0.260" (Lunz et al. 2021b).

For "60,EDR3,GA,NM" another scenario "53,EDR3,GA,NM" was tested where the same seven stars as for "49,EDR3,GA,NM" and CoKu HP Tau G2 were excluded, because they also produce jumps in the iterative results of the rotation parameters of "60,EDR3,GA,NM". "The WRMS statistics dropped by 20 % to 60 % for all parameters except for ϵ_Z compared to "60,EDR3,GA,NM". Otherwise, the same conclusions can be drawn as for the difference between "55,EDR3,GA,NM" and "49,EDR3,GA,NM", so they are not repeated here. This shows that the new data has little impact on this investigation" (Lunz et al. 2021b).

The baseline solutions for these scenarios are given in Table 5.16. The differences in the baseline solutions of the respective full sample and manually reduced sample of counterparts are up to 0.1 mas for ϵ_X and up to 0.2 mas for ϵ_Y. For the spin, the differences are up to 0.02 mas yr^{-1} for ω_X and up to 0.04 mas yr^{-1} for ω_Y and ω_Z. These values, although at the level of significance, are already indicative of the accuracy of the final result, since they show how much the result would have been affected if a (rather random) selection of stars had never been used to test the alignment.

Accuracy test - Gaia EDR3

To test whether a different group of four stars rejected from "60,EDR3,GA,NM" instead of stars HD 22468, V410 Tau, AR Lac, and LSI +61 303, which produce jumps in the iterative results of the spin parameters, would provide better statistics, additional scenarios were set up similar to the work in Lunz et al. (2022). In these scenarios, the 11 most deviating stars of "60,EDR3,GA,NM" and in addition an individual selection of four other stars were excluded from the beginning, so that in total 15 stars were rejected (similar to the baseline solution of "60,EDR3,GA,NM"). The selection of four stars is furthermore a trade-off between computing time and the amount of tested solutions. Thus, there are $\frac{49!}{(49-4)!4!} = 211876$ solutions to be tested.

The 11 most deviant stars were excluded at the beginning of the iterations in all scenarios in which they are included: The first two rejected stars in all of the following scenarios were T Tau and S Crt, which have with more than 170 000 the highest discrepancy measure Q_i/n_i. T Tau is located in a triple star system. While the VLBI observations detected star T Tau Sb in Loinard et al. (2007) and in this work, the Gaia data corresponds to the optically dominant component T Tau N. This is indicated by the residuals of about -150 mas in α and -600 mas in δ from the rotation parameter analysis in this work, which align with, i.e., the offsets between T Tau Sb and T Tau N shown in Fig. 1 in Schaefer et al. (2020). Obviously, this star is not suitable for testing the alignment with the given data and approach.

S Crt is an AGB star whose VLBI astrometric parameters were determined from water maser spots (Nakagawa et al. 2008). The residual of about $-1\,900$ mas in α from the rotation parameter analysis in this work is consistent to the difference of $-1\,926$ mas between the absolute coordinate of the reference maser spot (which was determined relative to the ICRF1 (Ma et al. 1998) position of J1147−0724) and the a priori coordinates of the star given in the publication. It is likely that the unit conversion between milliarcseconds and hour angle for the position offset between phase tracking center and the reference maser spot was not done correctly. This suggests that the VLBI position should be revised[14].

The next set of rejected stars is W 40 IRS 5 ($Q_i/n_i = 10794$), HD 283447, V1023 Tau, and UX Ari. The latter three stars have a Q_i/n_i between 1 600 and 4 550 and point in the similar direction on the sky to T Tau. Their parameters in Gaia have larger standard deviations than the other stars, and their RUWE parameters are between 5.0 and 7.5, where values larger 1.4 are indicating that the Gaia data does not fit the 5-parameter astrometric model well. W 40 IRS 5 (J183114.82-020350.1) has a residual both in α and

[14] Unfortunately, this possibility was only uncovered at a late stage of this work. Because the star gets excluded at a very early stage, it does not corrupt the evaluation of the rotation parameter analysis in this work.

in δ of about -48 mas. The VLBI proper motion and parallax were determined by Ortiz-León et al. (2017a) and the position by Lindegren (2020a) using the same VLBI position time series. Shuping et al. (2012) find a close binary likely due to the star's He I spectra. The star is of B1 spectral type and an X-ray emitter, and therefore could be affected by radio-optical position offsets due to stellar winds (Cassinelli et al. 1994). This can be the reason for the larger RUWE parameter. UX Ari and HD 283447 are resolved close binaries as seen by VLBI and unresolved by Gaia. It is likely that both binary components of the respective star also emit at optical frequencies at comparable brightness because the stars' RUWE values are large. It is questionable whether these stars should be used for the alignment test due to the possible inaccuracy between the positions of the photocenter as seen by Gaia and the barycenter or center of luminosity as determined from the two components' positions from VLBI observations. Because other stars are well known in this direction of the sky which seem more suitable, less priority can be given to UX Ari and HD 283447. V1023 Tau is also a close binary system which was resolved in VLBI observations by Torres et al. (2007); Galli et al. (2018), but not observed in this work because more suitable stars in this area on the sky were prioritized. The same discussion applies as for UX Ari and HD 283447.

EI Eri and HD 167971 are stars which were included into the rotation parameter analysis for the first time in this work. They were both observed in experiment V538 where the uv-coverage was sparse and therefore their positions are possibly not accurately determined. More observations are especially tempting because the stars are located in areas of the sky where the VLBI dataset is sparse. However it should be considered that HD 167971 is an O-type star where the radio emission stems from the colliding wind region between a spectral binary with about 0.1 mas separation and a third component (Blomme, R. et al. 2007; De Becker et al. 2012; Sanchez-Bermudez, J. et al. 2019). The binary and the third component, a O8 supergiant, are about 8 mas to 15 mas apart in the 3 years of observations in (De Becker et al. 2012). Sanchez-Bermudez, J. et al. (2019) confirmed that for the observations in 2016 the Gaia DR2 position is also located between the spectral binary and the third component, close to the peak of the radio emission. The residuals from this work are on the order of -78 mas in α and 54 mas in δ for the epoch in 2020.2, and -223 mas in α and -7 mas in δ for the epoch in 2020.5. These offsets are much larger than in the previous studies. Comparing the positions in 2020 to the positions in 2006 and 2016 from Fig. 4 in Sanchez-Bermudez, J. et al. (2019) shows that the star's trajectory detected by Gaia is likely to be a mixture of the orbital motion of the wind-collision region and the proper motion of the multiple star system. Therefore, more detailed analysis would be needed for this star to properly use it for the alignment of VLBI and Gaia reference frames (For the dedicated observations in experiment UL005, O-type stars were not observed for this reason). This physical nature can also be a reason for the

larger RUWE of 3.1 in Gaia EDR3 for this star. EI Eri is a close binary which has signs of a third component in its long-term barycentric velocities, suggesting an orbital motion with a period of about 19 years (Washuettl et al. 2009). Therefore it can be assumed that modeling of non-linear proper motions is needed to properly include this star in the future. Also the Gaia EDR3 data might express this need with the slightly higher RUWE of 1.9.

The next rejected stars are HU Vir, B Per and V479 Sct. With values between 110 and 250 they still have noticeably high discrepancy measures. These stars also only have one positional measurement from VLBI. HU Vir and B Per were observed in experiment UL005, and their parameters in Gaia have larger standard deviations than many of the other stars in the sample. B Per has a RUWE of 2.7 in Gaia EDR3 and HU Vir of 3.9. HU Vir is, similar to EI Eri, a binary star in a triple system with an orbital period of about 6 years for the large orbit (Fekel, F. C. et al. 1999). The same holds for B Per, where the orbital period of the large orbit is about 2 years (Hill et al. 1976). The short periods of the large orbits being in similar length to the Gaia observation time span could explain the larger standard deviations of the Gaia data and the large RUWEs. Therefore future observations have to show whether modeling of non-linear proper motions or orbits will be required to properly include these stars into the analysis. V479 Sct was also observed in experiment V538A, which is why another observation might improve the usefulness of the star. This is especially feasible since its Gaia EDR3 data has very low standard deviations and the RUWE value is 0.75 and therefore following the single-star model well. However, V479 Sct is a O-type X-ray binary where VLBA observations in 1999 showed that it has a bipolar jet emerging from the core, and is therefore a galactic microquasar (Paredes et al. 2000). Its core has a diameter of about 2 mas and the jets extend over 16 mas. Therefore, the residuals of -5 mas in α and 3 mas in δ could be due to radio-optical position offsets.

From this evaluation all 11 stars have reasons not to be included in the sample for testing the accuracy of the alignment task. Position offsets can however also occur due to offsets between the calibrator position from phase- and group delays and other error sources as discussed in Sect. 5.4.5.

Other stars that get discarded at early iterations of many scenarios, and therefore also in the baseline solution of "60,EDR3,GA,NM", also have reasons to be rejected. They are are SZ Psc, T Lep, DoAr 51, and CoKu HP Tau G2. Their RUWE values are between 2.4 and 9.2. The parameters of SZ Psc have larger standard deviations in both VLBI and Gaia. It is a close binary in a tertiary system with a period of 3 or 4 years (Eaton and Henry 2007). The same discussion applies as for HU Vir and B Per. Star T Lep has large position uncertainties from VLBI because only its masers can be detected in certain spectral lines at radio frequencies. Also its Gaia parameters have larger standard deviations. With the maser spots spanning about 100 mas in α and 50 mas in δ, and the infrared image

from ground-based VLTI measurements being in their center (Nakagawa et al. 2014), radio-optical offsets are not proven to be the reason of the residuals of −126 mas in α and 226 mas in δ. DoAr 51 is a resolved close binary as seen by VLBI but unresolved by Gaia. The close binary has a semi-major axis of about 32 mas (Ortiz-León et al. 2017b), and a third component is located in a distance of about 790 mas at their time of observation (Barsony et al. 2003). Due to the increased RUWE value, the same discussion applies as for UX Ari and HD 283447. CoKu HP Tau G2 is a component of a multiple star system (Harris et al. 2012). New model estimates were determined in Sect. 5.5, however without considering the orbital motion between CoKu HP Tau G2 and CoKu HP Tau G3 AB. The significance of the orbital motion was demonstrated in Torres et al. (2009) and Galli et al. (2018). In this work, the time interval was limited to match the Gaia time interval instead, and a standard 5-parameter astrometric model was fit to the data. Surely, this is not an ideal approach, but it should be tested whether this method would better align the VLBI model estimates to the Gaia parameters. However, still significant linear accelerations were tested for the limited time interval, and the star still shows large residuals in the rotation parameter analysis. Therefore, as long as orbits cannot be considered in the Gaia processing, it might be suitable to neglect this star.

The latter two stars show variations in the orientation parameter estimates in the subsequent iteration of their rejection. It is consequently to be expected that they are represented in the selections with low WRMS values.

"All possible combinations of four stars from the data set were tested. From each of the 211 876 individual scenarios iterative solutions for the rotation parameters were obtained and the WM, WRMS, and ME statistics were calculated, discarding the last 10 iterations because the formal errors became too large due to the small sample. The orientation offset WM values range from $(\epsilon_X, \epsilon_Y, \epsilon_Z) = (0.128, 0.131, -0.016)$mas to $(0.542, 0.545, 0.225)$mas, and the spin WM values range from $(\omega_X, \omega_Y, \omega_Z) = (-0.000, 0.020, -0.041)$mas yr^{-1} to $(0.106, 0.098, 0.015)$mas yr^{-1}. Their mean values coincide with $\mathrm{WM}_{60,\mathrm{EDR3,GA,NM}}$ in Table 5.15. The Q/n for the baseline solution with $k = 15$ rejected stars varies between 6.28 and 14.08, with a median of 12.91, for the various solutions. [There is a clear gradient in the mean Q/n visible in the scatter of each rotation parameter, which suggests that the rotation parameter solutions are not random but statistically significant (Lindegren 2020a).] The scenario with the minimum sum of all Q/n of the selected iterations for the calculation of the WM is the scenario where T Lep, DoAr 51, CoKu HP Tau G2, and SZ Psc were the four additional excluded stars. These are the same stars that were excluded in the base solution of "60,EDR3,GA,NM", proving that the rejection process is sound. The four stars have RUWE parameters greater than 1.4, indicating that the *Gaia* data do not fit the standard model of stellar motion well.

The minimum magnitudes[15] of WRMS values are 0.098 mas for the orientation offset and 0.009 mas yr^{-1} for the spin, and the minimum magnitudes of the ME values are 0.177 mas and 0.018 mas yr^{-1} respectively. The minimum magnitude of the orientation offset WRMS of 0.098 mas is reached, if LSI +61 303, HD 283641, DoAr 51, CoKu HP Tau G2 are excluded. Similarly, the minimum magnitude of the spin WRMS of 0.009 mas yr^{-1} is reached, if LSI +61 303, HD 22468, CoKu HP Tau G2, and AR Lac are rejected from the sample. Except CoKu HP Tau G2 for the spin they are the same stars as from the manual selection in "53,EDR3,GA,NM". It was expected that there would be a large overlap between the two samples.

From the scatter of these results and the minimum ME and WRMS values, it is concluded that the lowest level of the uncertainty of WM is $\gtrapprox 0.12$ mas for each of the orientation offset rotations and $\gtrapprox 0.01$ mas yr^{-1} for each of the three spin rotations for "60,EDR3,GA,NM" (Lunz et al. 2021b).

Figures 5.44a, 5.44b, 5.44c, and 5.44d show the scatter plots of the WM, WRMS, ME, and the mean standard deviation (MS) of the 211 876 individual scenarios. The MSs are calculated as the mean of each iteration series' formal errors re-normalized with the $\sqrt{Q/n}$ of the respective iteration. The values for the rotations around the three different axes X, Y, Z are plotted against each other to illustrate possible correlations.

In general the WM and WRMS statistics for the rotation about the Z axis show the smallest scatter, while for the other two axes the scatter is similar. The solutions with the lowest mean Q/n are located in the central region of the scatter. If the distribution of the rotation parameter results is visualized as a histogram, the solutions cluster around the solution with the minimum sum of all Q/n of their iterations. An exception is the scatter of WRMS$_{\epsilon_X}$, which is slightly separated into two scatter clouds and where only one of them is including the solutions with the lowest mean Q/n. The lower WRMS$_{\epsilon_X}$ scatter cloud appears when CoKu HP Tau G2 is excluded from the sample.

For the Y axis, the scatter in ME and MS for both ϵ and ω is larger than for the other two axes. Figure 5.44d shows that solutions with the lowest mean Q/n also have the lowest MS values. Solutions with the lowest ME values however, not surprisingly, do not have the lowest MS values. Thus, the solutions with the lowest mean Q/n are preferred.

The 10 solutions with the lowest ME values in ϵ are compactly grouped. They are offset for WRMS$_{\epsilon_X}$ from the solutions with the lowest mean Q/n and are located in a rather central region of the WRMS scatter. Also in the scatter of WM$_{\epsilon_X}$ they are slightly off from the solutions with the lowest mean Q/n. For comparison, the 10 solutions with the lowest WRMS values in $\boldsymbol{\epsilon}$ or $\boldsymbol{\omega}$ have only very small ME differences compared to the ME

[15] Magnitudes in this context are defined as the square-root of the quadratically added values for the three rotation axes. This value can be understood as a combined value for the total rotation and should provide a better comparison between the various solutions.

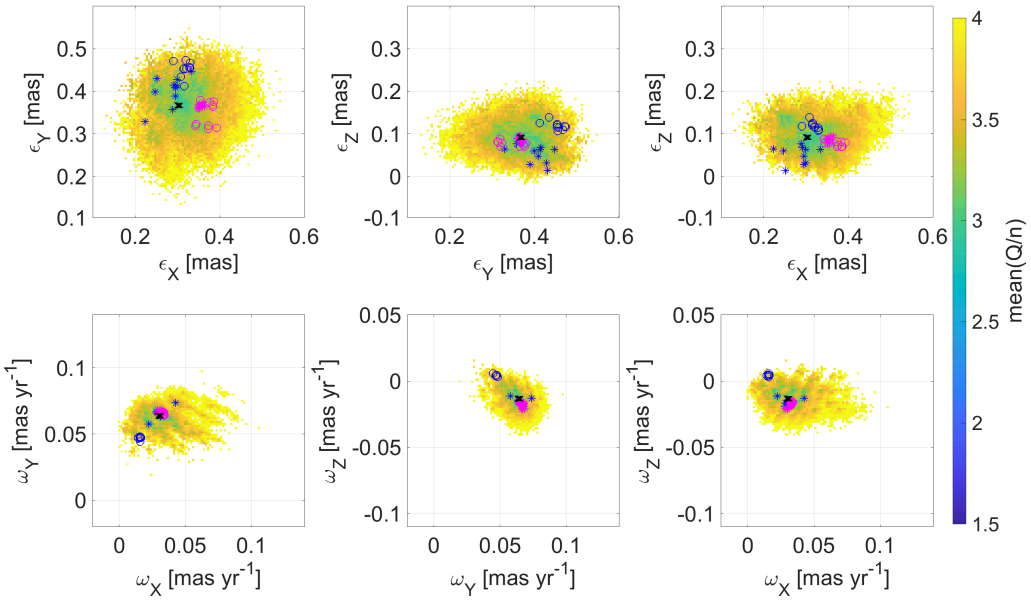

(a) WM for "60,EDR3,GA,NM".

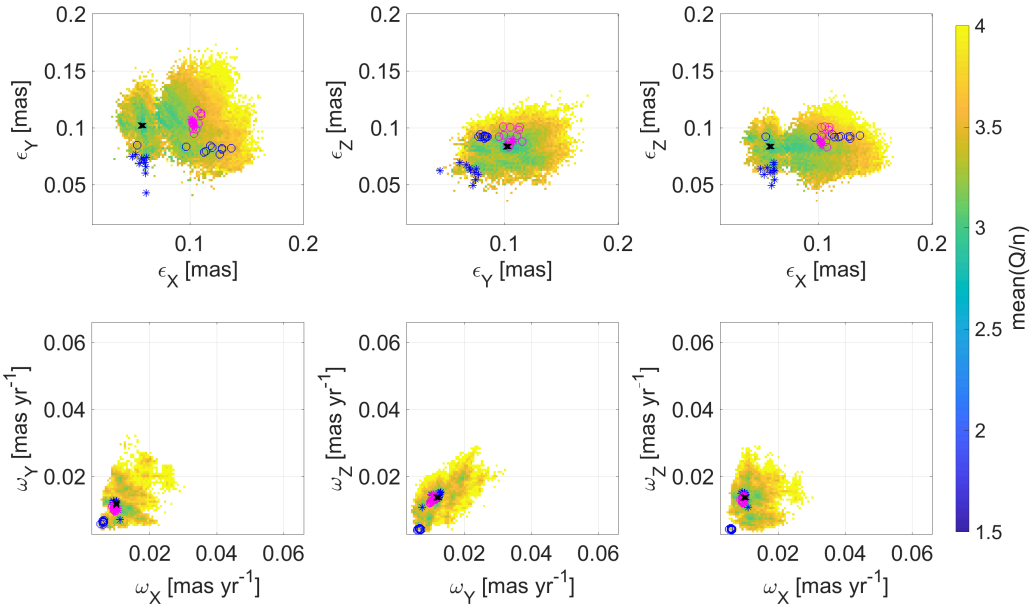

(b) WRMS for "60,EDR3,GA,NM".

Figure 5.44 WM, WRMS, ME, and MS statistics of the rotations around the X, Y, and Z axes for the 211 876 individual solutions based on "60,EDR3,GA,NM". The colors of the scatter points indicate the minimum value of the respective mean Q/n in each bin. In each of the subplots, the upper plots show the statistics for the orientation offset $\boldsymbol{\epsilon(T)}$ and the lower plots for the spin $\boldsymbol{\omega}$. The black crosses label the solution with the minimum mean Q/n. The blue stars depict the 10 solutions with the lowest WRMS in $\epsilon(T)$, whereas the blue circles depict the 10 solutions with the lowest WRMS in ω. Similarly, the respective magenta symbols show the 10 iterations with the lowest respective ME.

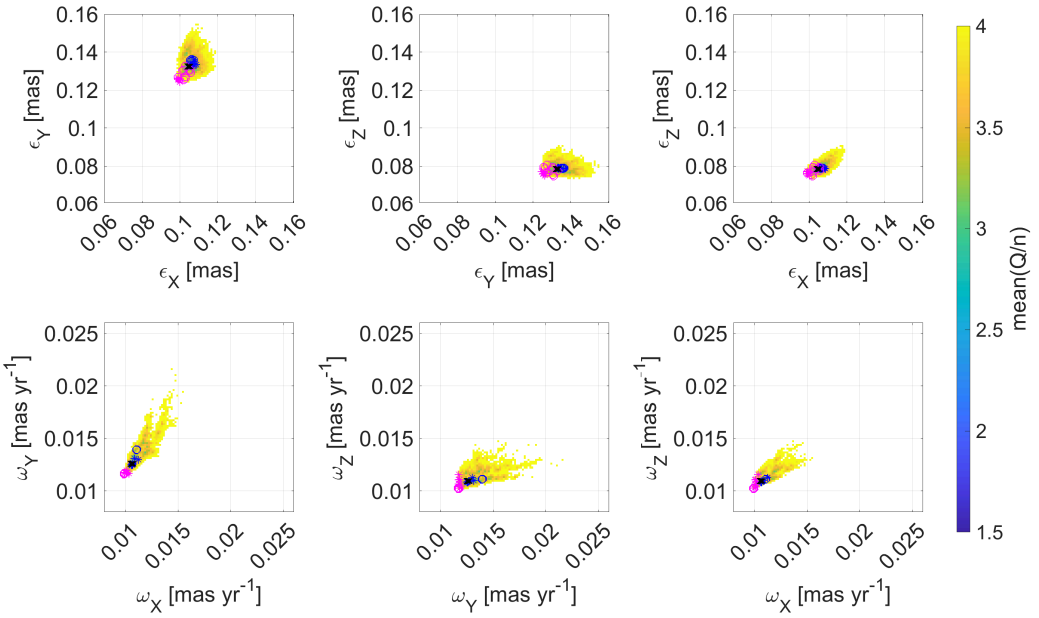

(c) ME for "60,EDR3,GA,NM".

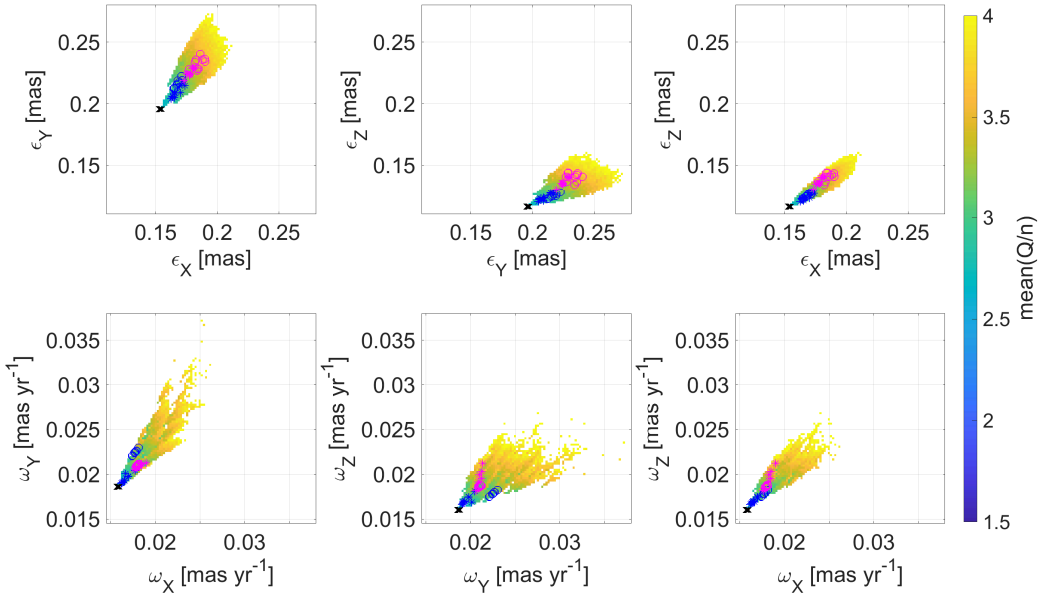

(d) MS for "60,EDR3,GA,NM".

Figure 5.44 WM, WRMS, ME, and MS statistics of the rotations around the X, Y, and Z axes for the 211 876 individual solutions based on "60,EDR3,GA,NM" (cont.).

values of the solutions with the lowest Q/n. What is interesting from the ME and MS plots is that the solutions with the lowest WRMS in $\boldsymbol{\omega}$ have higher ME and MS values in ω_Y than the other solutions.

Another test case where instead of the 11 most deviating stars the 15 most deviating stars were excluded from the beginning showed only WRMS values for ϵ_X smaller 0.09 mas, which can be explained by CoKu HP Tau G2 being among the 15 stars. The WRMS scatter of ϵ_Y elongates to smaller values which in turn can be explained by the exclusion of DoAr 51. Apart from this, and the fact that the mean Q/n is naturally smaller, the scatter plots do not change significantly and are therefore not presented and discussed here.

In Fig. 5.45, the WM values of the rotations around each axis divided by three times their MS are shown. Therefore, any value with a magnitude larger 1 indicates a significance better than 3 σ. The determination of $\boldsymbol{\epsilon}$ is not significant. The scatter is more compact for $\boldsymbol{\epsilon}$ than for $\boldsymbol{\omega}$. For $\boldsymbol{\omega}$, the scatter cloud is well within ± 1 for ω_Z, between about 0.0 and 1.3 for ω_X and between about 0.4 and 1.3 for ω_Y. The spin reaches a 3-σ significance in the Y-axis for solutions with low mean Q/n and low ME. However, the 10 solutions with the lowest WRMS or WM values in ω do not support a significant spin signal. This result is in line with the iterative rotation parameter results of "53,EDR3,GA,NM".

Figure 5.46 discusses the same data and representation as Fig. 5.45 except that the color coding is representing the minimum value of the respective mean sum of the absolute values of the correlation coefficients r_{ij} for one solution of the iterative solutions in each bin. It can be seen that the solutions with a significant spin in ω_Y and the lowest Q/n do not have the smallest average correlations. A similar plot to Fig. 5.44a but with the mean sum of absolute correlation coefficients as color coding shows that all rotation parameters from the solution with the color depicting the minimum value have higher magnitudes of the rotation parameters except for ω_Y, which is similar. Thus, the difference in significance between the solution with the lowest Q/n and the lowest mean absolute correlation coefficient is mainly driven by the larger MS in the latter. It is good to see that in general the mean absolute correlation coefficients do not diverge much between the solutions.

The 10 solutions with the lowest correlations have stars HD 199178 (all 10 solutions), 54 Cam (8 solutions), HD 283641 (6 solutions), V1271 Tau (5 solutions), UV Psc (5 solutions), and V811 Tau (3 solutions) excluded in more than one solution. Stars HD 283641, V1271 Tau, and V811 Tau are located at the same direction in the sky and have one of the highest weights E_i for the orientation offset and also relatively high weights Ω_i for the spin in the adjustment. HD 199178 contributes most information to the spin adjustment as it has the highest Ω_i. For the new model estimates from Sect. 5.5, no additional error budget was needed in order to obtain a reduced χ^2 in the adjustment, meaning that the single-epoch relative position uncertainties were already too pessimistic. The other two stars have, besides RZ Cas, the smallest Q_i/n_i, below 0.2, in the baseline solution of "60,EDR3,GA,NM" and they only have one VLBI position. The solutions with the lowest

mean correlation have high MS values due to higher ME and Q/n. They furthermore support a higher $\mathrm{WRMS}_{\epsilon_X}$ of about 0.12 mas.

Taking only the first iteration results of each scenario (instead of the WM, WRMS, and ME statistics), where the number of rejected stars is equivalent to those of the baseline solution of "60,EDR3,GA,NM", results in scatter plots similar to Fig. 4 in Lindegren (2020b), but of course with different values as shown in Fig. 5.47. Also for this work, the baseline solution is the solution with the smallest value of Q/n from the given sample. According to Lindegren (2020a), who did a similar test with their data set, this suggests that the resulting rotation parameters are not a chance result from the given sample of few counterparts but show a statistically significant signal. From comparing the scatter plots for the first iteration results and the WM statistics of the various solutions for scenario "60,EDR3,GA,NM" it can be concluded that the resulting scatter plots are similar for $\boldsymbol{\omega}$ (slightly smaller values for the WM statistics), and $\boldsymbol{\epsilon}$ (more homogeneous), as expected.

For "55,EDR3,GA,NM" the nine most deviant stars were excluded from the beginning because no more seemed necessary from looking at the steadiness of its baseline solution. The excluded stars are T Tau, S Crt, W 40 IRS 5, HD 283447, V1023 Tau, UX Ari, HU Vir, and B Per, which are also included in the group of excluded stars in "60,EDR3,GA,NM".

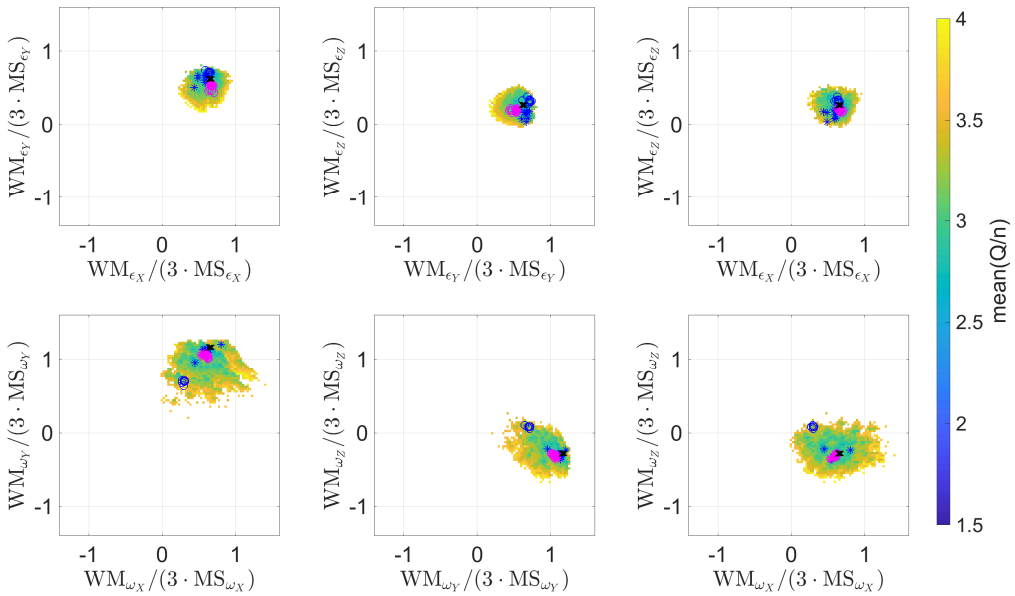

Figure 5.45 Significance of the 211 876 individual solutions based on "60,EDR3,GA,NM" determined as $\mathrm{WM}/(3\cdot\mathrm{MS})$. The colors indicate the minimum value of the respective mean Q/n in each bin. The upper plots show the statistics for the orientation offset $\boldsymbol{\epsilon(T)}$ and the lower plots for the spin $\boldsymbol{\omega}$. The black crosses label the solution with the minimum mean Q/n. The blue stars depict the 10 solutions with the lowest WRMS in $\epsilon(T)$, whereas the blue circles depict the 10 solutions with the lowest WRMS in ω. Similarly, the respective magenta symbols show the 10 iterations with the lowest respective ME.

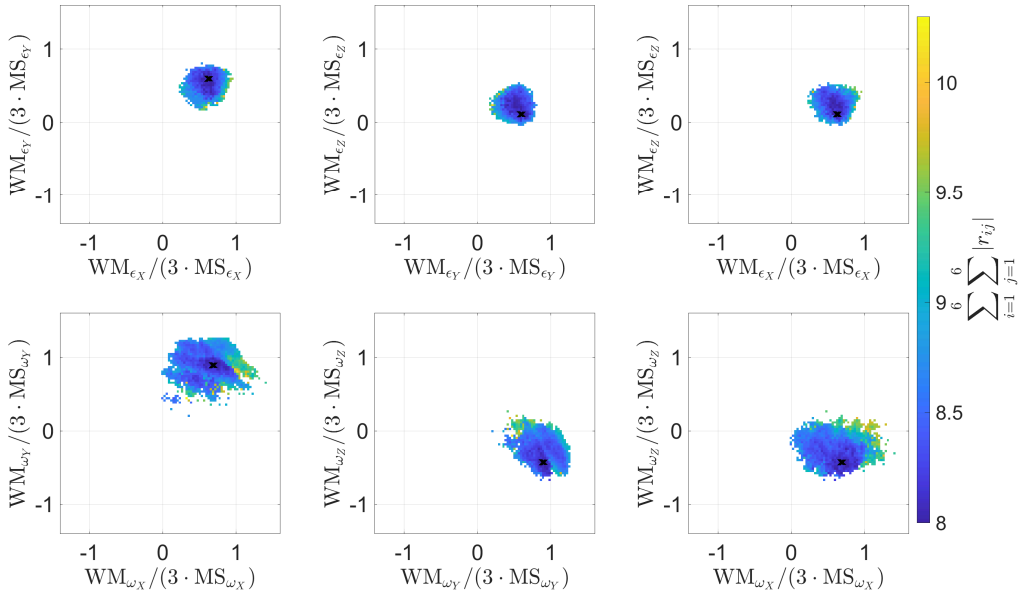

Figure 5.46 Significance of the 211 876 individual solutions based on "60,EDR3,GA,NM" determined as WM/(3 · MS). The colors indicate the minimum value of the respective mean sum of the absolute values of the correlation coefficients r_{ij} for one solution of the iterative solutions in each bin. Thus, e.g. a value of 9 represents the correlation coefficients with value 1 for the six diagonal elements of the correlation matrix and for the 30 off-diagonal elements on average a value of 0.1. The solution with the minimum value might be a different one than the solution with the minimum Q/n per bin as shown in Fig. 5.45. The upper plots show the statistics for the orientation offset $\boldsymbol{\epsilon(T)}$ and the lower plots for the spin $\boldsymbol{\omega}$. The black crosses label the solution with the minimum mean sum of the absolute values of the correlation coefficients.

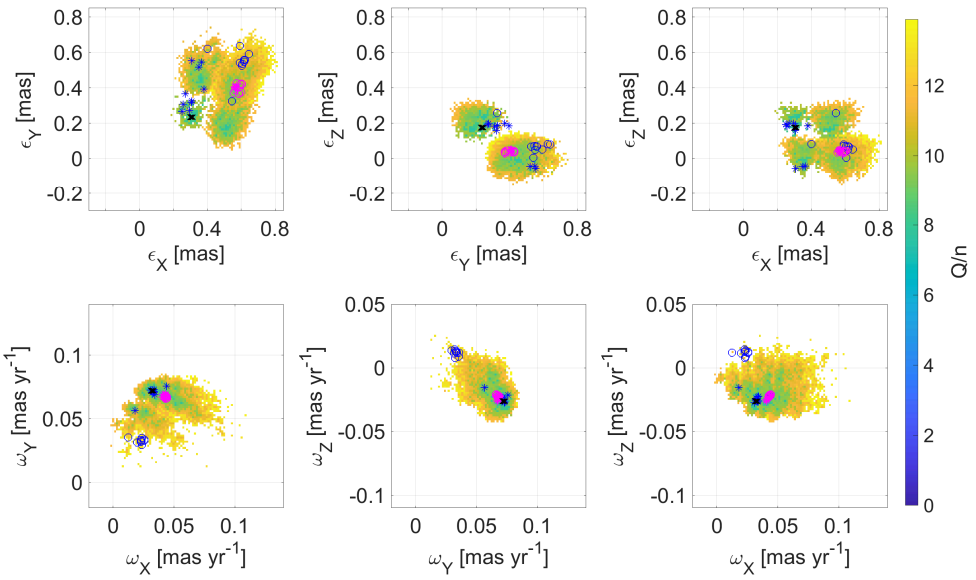

Figure 5.47 Rotation parameters of the first iteration of the 211 876 individual solutions based on "60,EDR3,GA,NM" for the X, Y, and Z axes. The color is chosen by the minimum value of each bin, where the values are the Q/n of the selected iterations. The upper plots show the parameters for the orientation offset $\boldsymbol{\epsilon(T)}$ and the lower plots for the spin $\boldsymbol{\omega}$. The black crosses label the solution with the minimum mean Q/n. This is also the baseline solution of "60,EDR3,GA,NM". The blue stars depict the 10 solutions with the lowest WRMS in $\epsilon(T)$, whereas the blue circles depict the 10 solutions with the lowest WRMS in ω. Similarly, the respective magenta symbols show the 10 iterations with the lowest respective ME.

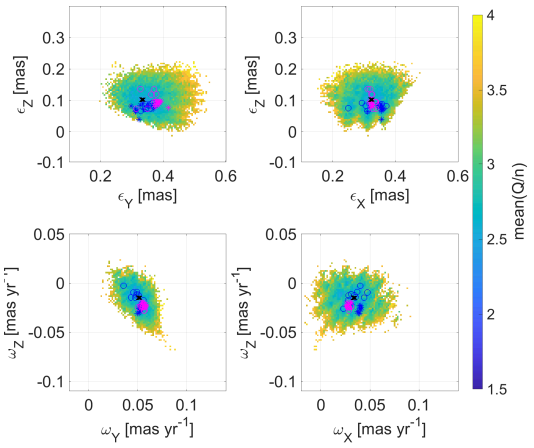

(a) WM for "55,EDR3,GA".

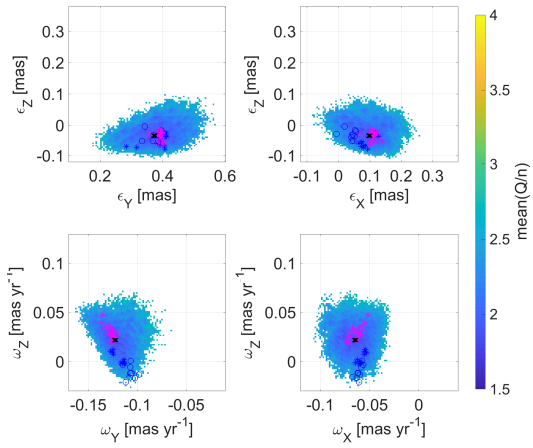

(b) WM for "55,DR2,NM".

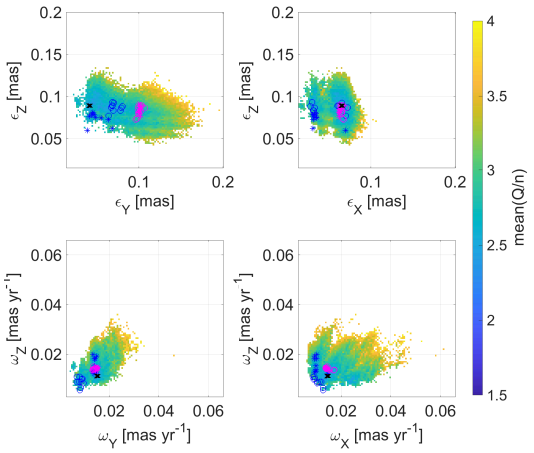

(c) WRMS for "55,EDR3,GA".

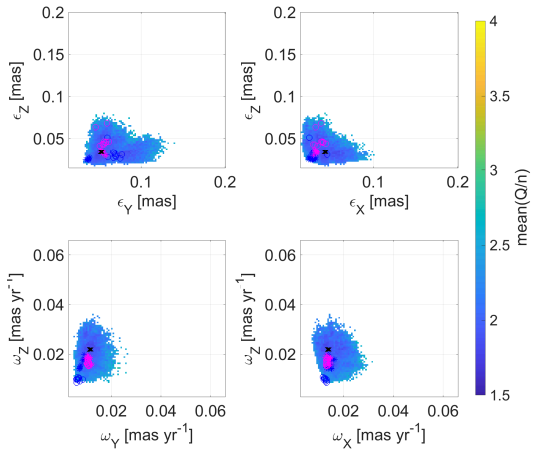

(d) WRMS for "55,DR2,NM".

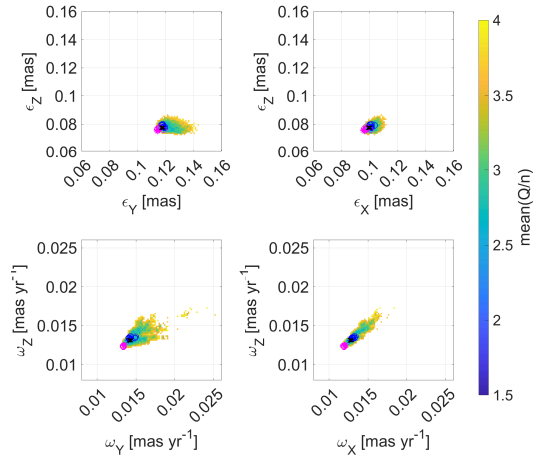

(e) ME for "55,EDR3,GA".

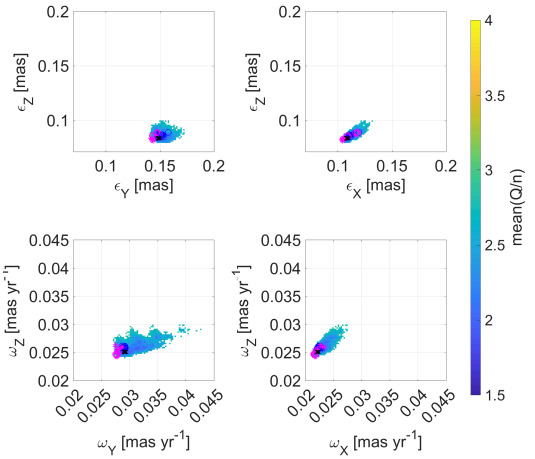

(f) ME for "55,DR2,NM".

Figure 5.48 WM, WRMS, and ME statistics of the rotations around the X, Y, and Z axes for the 163 185 individual solutions based on the respective scenario. For a description of the plots see Figs. 5.44a to 5.44c. Note the different axis limits for the two scenarios.

In addition, CoKu HP Tau G2 is excluded, which has also been discussed previously as it was also excluded in the baseline solution of "60,EDR3,GA,NM". The scatter plots for WM, WRMS and ME are similar to those of "60,EDR3,GA,NM", thus, they are not reported here. Only the scatter in WRMS of ϵ_X is more compact between 0.01 mas and 0.09 mas which is because CoKu HP Tau G2 was excluded a priori. Therefore, also the 10 solutions with the lowest WRMS and ME in ω also have lower WRMS values in ϵ_X. The mean values for the magnitude of the WRMS (0.148 mas for ϵ and 0.022 mas yr^{-1} for ω) and ME (0.189 mas for ϵ and 0.020 mas yr^{-1} for ω) are almost identical to those of "60,EDR3,GA,NM". The mean values of the WM of the six rotations coincide with $\mathrm{WM}_{55,\mathrm{EDR3,GA,NM}}$ in Table 5.19 and are very similar to those of "60,EDR3,GA,NM". The main difference is the mean Q/n, which is between 2.41 and 3.91, instead of between 2.59 and 4.23 for "60,EDR3,GA,NM", a 7 % reduction.

For "55,EDR3,GA" the scatter plots are shown in Figs. 5.48a, 5.48c, and 5.48e. The nine most deviant stars were excluded from the beginning. The stars are identical to those of "55,EDR3,GA,NM" in the previous paragraph. The orientation offset WM for "55,EDR3,GA" ranges from $(\epsilon_X, \epsilon_Y, \epsilon_Z) = (0.155, 0.198, -0.010)$mas to $(0.478, 0.547, 0.224)$mas, and the spin ranges from $(\omega_X, \omega_Y, \omega_Z) = (-0.016, 0.013, -0.067)$mas yr^{-1} to $(0.091, 0.087, 0.024)$mas yr^{-1}. The mean values for ω coincide with $\mathrm{WM}_{55,\mathrm{EDR3,GA}}$ in Table 5.15, while they are with (0.318, 0.373, 0.104) about 10 % larger for ϵ. The mean values for the magnitude of the WRMS and ME are 0.148 and 0.175 mas for ϵ, and 0.027 and 0.023 mas yr^{-1} for ω. The mean ME is larger for ϵ when the new model estimates are applied and the scatter in WM is also larger. This indicates that ϵ is determined better in "55,EDR3,GA". It can be explained by larger number of VLBI positions that were included in the rotation parameter analysis compared to the scenarios with the new model estimates, where multiple VLBI positions, if any, were replaced by the new absolute positions. The $\mathrm{WRMS}_{\epsilon_Z}$ is similar, but the $\mathrm{WRMS}_{\epsilon_X}$ and $\mathrm{WRMS}_{\epsilon_Y}$ are smaller in size and in scatter for "55,EDR3,GA,NM" compared to "55,EDR3,GA". For ω the ME and WRMS are smaller and the scatter in WM is slightly more compact for ω when the new model estimates are applied. This shows the improvement of the spin determination due to the new estimates. The mean Q/n has with a range of 2.33 to 4.05 a larger range than for "55,EDR3,GA,NM" (2.41 and 3.91). In "55,EDR3,GA" there are 44 solutions with ME_{ω_Y} larger 0.020 mas yr^{-1} which stand out from the main scatter of the solutions ME_{ω_Y}. In all of them HD 199178 and AR Lac were removed, and in 43 of them Cyg X-1. The three stars are located in the same direction in the sky (approx. α =310°, δ =40°) and have besides LSI +61 303 the highest weights Ω in the spin determination. The minimum magnitudes of the WRMS values for "55,EDR3,GA" are 0.093 mas for the orientation offset and 0.015 mas yr^{-1} for the spin, and the minimum magnitudes of the ME values are 0.167 mas and 0.022 mas yr^{-1}

respectively. Thus, the new and improved models improved the spin solutions as these four minimum values are only 0.098 mas, 0.009 mas yr^{-1}, 0.177 mas, and 0.018 mas yr^{-1} for "60,EDR3,GA,NM" respectively. The minimum magnitude of the orientation offset WRMS of 0.093 mas is reached, if V410 Tau, σ^2 CrB, DoAr 51, and HD 8357 are excluded. Similarly, the minimum magnitude of the spin WRMS of 0.015 mas yr^{-1} is reached, if LSI +61 303, V410 Tau, σ^2 CrB, and [SSC75] M 78 11 are rejected from the sample. From the manual selection in "49,EDR3,GA,NM" it is expected that HD 283641 would be excluded for the minimum WRMS of the orientation offset, as it was one of the two excluded stars besides DoAr 51 which produce jumps in the orientation offsets. Similarly HD 22468 was expected to be excluded instead of [SSC75] M 78 11 for the spin.

Plots for "55,EDR3,GA" similar to Fig. 5.45 for "60,EDR3,GA,NM" (which are almost identical to those of "55,EDR3,GA,NM") show that ω_Y is not yet determined with a 3-σ significance. The significance for the solution with the lowest mean Q/n is at 2.6-σ for "55,EDR3,GA" compared to 3.5-σ for "55,EDR3,GA,NM".

Similar plots for "45,EDR3,GA,NM,G<10.5mag" (where seven stars were excluded a priori as outliers) show that the scatter in ϵ_X, ω_X, and in ω_Z is slightly larger but still the ω_Y is significantly determined. The plots for "24,EDR3,GA,NM,RUWE1.4,G<10.5mag" (where no stars were excluded a priori as outliers) provide similar results to "45,EDR3,GA,NM,G<10.5mag".

Accuracy test - Gaia DR2

In the same fashion as for Gaia EDR3 plots for scenario "55,DR2,NM" were produced which are shown in Figs. 5.48b, 5.48d, and 5.48f. Also for this scenario the nine most deviating stars were excluded before the analysis. The nine excluded stars are identical to those of "55,EDR3,GA,NM" except that instead of B Per SZ Psc was excluded. SZ Psc was also excluded for the baseline solution of "60,EDR3,GA,NM" and was therefore discussed earlier.

The scatter in $\boldsymbol{\omega}$ WM is larger compared to the scenarios with Gaia EDR3. This is explained by the improved proper motion estimates in Gaia EDR3 compared to Gaia DR2. The scatter in ME, especially of ω_Y, is larger for "55,DR2,NM". Again, the 10 scenarios with the lowest WRMS in ϵ or ω have small ME values. The outlying patch with approximately $\mathrm{ME}_{\omega_Y} \geq 0.38$ mas yr^{-1} includes 45 solutions where in each of them Cyg X-1 was rejected, and in 44 of them both HD 199178 and AR Lac. The same reasoning applies as for "55,EDR3,GA". The mean values for the magnitude of the WRMS and ME are 0.082 and 0.205 mas for the ϵ and 0.026 and 0.045 mas yr^{-1} for ω. The mean WRMS for ϵ therefore is only half of the value for "55,EDR3,GA,NM". The mean Q/n vary between 1.77 and 2.93, which are smaller values than for for "55,EDR3,GA,NM" (2.41 and 3.91). The

mean values for ϵ and ω for the respective axes coincide with $\mathrm{WM}_{55,\mathrm{DR2,NM}}$ in Table 5.14. The minimum magnitudes of the WRMS values are 0.049 mas for the orientation offset and 0.017 mas yr^{-1} for the spin, and the minimum magnitudes of the ME values are 0.195 mas and 0.043 mas yr^{-1} respectively. The minimum magnitude of the orientation offset WRMS of 0.049 mas is reached, if V1110 Tau, V1961 Ori, HD 8357, and HD 224085 are excluded. Similarly, the minimum magnitude of the spin WRMS of 0.017 mas yr^{-1} is reached, if V811 Tau, V1110 Tau, HD 37150, and RS CVn are rejected from the sample. They are mostly different stars compared to those of the respective solutions based on Gaia EDR3.

From the scatter of these results and the minimum ME and WRMS values, it is concluded that the lowest level of the uncertainty of WM is $\gtrapprox$0.12 mas for each of the orientation offset rotations and $\gtrapprox$0.03 mas yr^{-1} for each of the spin rotations. In the future it can be tested how much the additional observations as used in "60,EDR3,GA,NM" would improve the result for Gaia DR2. Plots similar to Fig. 5.45 for "60,EDR3,GA,NM" show that ω_Y is determined with a 3.4-σ significance for the solution with the lowest mean Q/n. This solution is usually in the scatter range where most of the solutions are found.

5.7 Possible future improvements

Three main works can be done to improve the above analysis. First, the VLBI celestial reference frame has to be updated to include all relevant primary calibrators. Positions of calibrators already included in the ICRF3 should be updated with more observations if necessary to improve the calibrator catalog position. This topic is discussed in the first subsection. Second, new Gaia data releases are expected to provide better astrometric information for the stars at optical frequencies. This is discussed in the subsequent subsection. In the last subsection, recommendations for follow-on phase-referencing observations of the known radio stars are outlined to further improve the VLBI database.

5.7.1 VLBI celestial reference frame

An item in the error budget of the VLBI positions is the catalog position uncertainty σ_{CRF} of the primary calibrator as indicated in Sect. 5.4.5. The σ_{CRF} of the primary calibrators in this work are presented in Fig. 5.49 in directions of $\alpha*$ and δ. It can be seen that not only the positions from other catalogs than ICRF3 S/X have larger position uncertainties, but also some of the ICRF3 S/X positions. Furthermore, the uncertainty in δ direction tends to be higher than in $\alpha*$ direction, which is similar to, e.g., the random errors of the star position measurements.

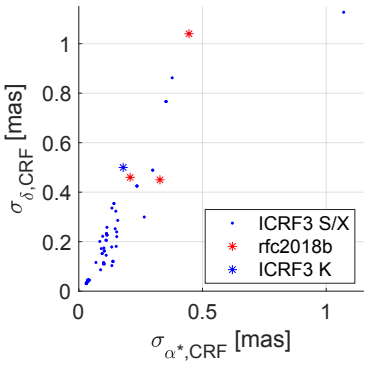

Figure 5.49 Uncertainties of the primary calibrator catalog positions $\sigma_{\mathrm{CRF}} = \sqrt{\sigma^2_{\alpha*,\mathrm{CRF}} + \sigma^2_{\delta,\mathrm{CRF}}}$ in directions of $\alpha*$ and δ for all observations in "60,EDR3,GA,NM". The uncertainty of one primary calibrator (J1832-1035, one position for star HD 167971) with $(\sigma_{\alpha*}, \sigma_\delta)$ of (4.9,5.1) mas from ICRF3 S/X is outside the plot range.

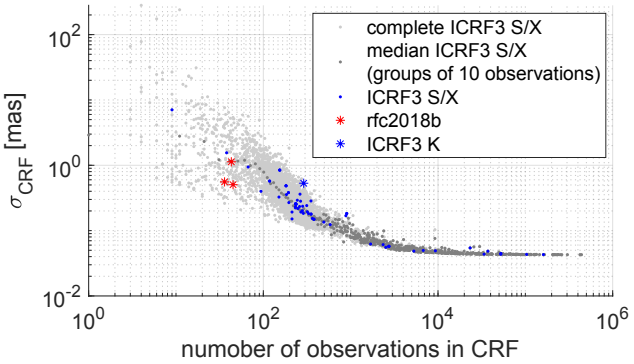

Figure 5.50 Uncertainties of the primary calibrator catalog positions $\sigma_{\mathrm{CRF}} = \sqrt{\sigma^2_{\alpha*,\mathrm{CRF}} + \sigma^2_{\delta,\mathrm{CRF}}}$ for all observations in "60,EDR3,GA,NM" versus the number of observations of the object in the respective CRF along with the values for all objects in ICRF3 S/X. The dark grey points are the median values of all ICRF3 S/X values per bin of 10 observations. The axes are logarithmic.

To test the maximum impact on the rotation parameter analysis that can be achieved by improving the calibrator catalog uncertainties, they are excluded from the error budget $\sigma_{\mathrm{absolute}}$ in scenario "60,EDR3,GA,NM,nosigmaCRF". The resulting statistics when employing all available VLBI data are presented in Table 5.21. The six rotation parameters of the baseline solution at the same iteration as the baseline solution of "60,EDR3,GA,NM", $k = 15$, are (+0.215, +0.229, +0.213, +0.035, +0.076, -0.026)±(0.064, 0.101, 0.055, 0.009, 0.010, 0.009) mas or mas yr^{-1} with $Q/n = 6.48$. While the uncertainties of the spin parameters remain similar to the baseline solution of "60,EDR3,GA,NM" and the Q/n only increases slightly, the uncertainties of the orientation parameters decrease by (0.050, 0.011, 0.023) mas if $Q/n = 1$. This is also supported by the $\mathrm{ME}_{\mathrm{60,EDR3,GA,NM,nosigmaCRF}}$, which are reduced by (19, 6, 11, 0, 0, 0) % compared to $\mathrm{ME}_{\mathrm{60,EDR3,GA,NM}}$.

Another scenario is presented Table 5.21 as well, where the seven stars HD 22468, LSI +61 303, V410 Tau, AR Lac, DoAR 51, CoKu HP Tau G2, HD 283641 which produce offsets in the iterative rotation parameter results were excluded. The six rotation parameters of the baseline solution at the same iteration as the baseline solution of "53,EDR3,GA,NM", $k = 13$, are (+0.221, +0.391, +0.219, +0.030, +0.039, +0.010)±(0.069, 0.112, 0.058, 0.011, 0.013, 0.010) mas or mas yr^{-1} with $Q/n = 6.31$. The uncertainties, Q/n, and $\mathrm{ME}_{\mathrm{53,EDR3,GA,NM,nosigmaCRF}}$ behave similar to the previous scenario.

Of course, calibrator catalog uncertainties of zero are not realistic. Thus, their data from

Table 5.21 WM, WRMS, and ME of the various rotation parameter scenarios for Gaia EDR3 when assuming σ_{CRF} to be zero.

Scenario	Parameter	$\epsilon_X(T)$	$\epsilon_Y(T)$	$\epsilon_Z(T)$	ω_X	ω_Y	ω_Z
60,EDR3,GA,NM, nosigmaCRF	$\mathrm{WM}_{60,\mathrm{EDR3,GA,NM,nosigmaCRF}}$	0.258	0.378	0.118	0.027	0.066	-0.013
	$\mathrm{WRMS}_{60,\mathrm{EDR3,GA,NM,nosigmaCRF}}$	0.078	0.105	0.087	0.014	0.012	0.015
	$\mathrm{ME}_{60,\mathrm{EDR3,GA,NM,nosigmaCRF}}$	0.078	0.115	0.064	0.010	0.011	0.010
53,EDR3,GA,NM, nosigmaCRF	$\mathrm{WM}_{53,\mathrm{EDR3,GA,NM,nosigmaCRF}}$	0.225	0.457	0.144	0.024	0.042	0.007
	$\mathrm{WRMS}_{53,\mathrm{EDR3,GA,NM,nosigmaCRF}}$	0.038	0.064	0.117	0.009	0.007	0.008
	$\mathrm{ME}_{53,\mathrm{EDR3,GA,NM,nosigmaCRF}}$	0.082	0.124	0.067	0.011	0.014	0.011

Notes. For scenario "60,EDR3,GA,NM,nosigmaCRF" iterations 11 to 52 were used for calculation, whereas for scenario "53,EDR3,GA,NM,nosigmaCRF" where stars were excluded beforehand, the iterations 11 to 45 were employed. For derivation of values $\mathrm{ME_s}$ the last 10 iterations were rejected because the formal errors of the rotation parameters increase substantially if only few stars are available for calculations. The epoch T is 2016.0 for Gaia EDR3. Units are in milliarcseconds for $\epsilon_X(T)$, $\epsilon_Y(T)$, and $\epsilon_Z(T)$. They are milliarcseconds per year for ω_X, ω_Y, and ω_Z.

Table 5.22 ME and difference to $\mathrm{ME}_{53,\mathrm{EDR3,GA,NM}}$ in percent, labeled as Δ, of various rotation parameter scenarios with different threshold of maximum σ_{CRF}.

Scenario	$\epsilon_X(T)$	$\epsilon_Y(T)$	$\epsilon_Z(T)$	ω_X	ω_Y	ω_Z
$\mathrm{ME}_{53,\mathrm{EDR3,GA,NM}}$	0.104	0.132	0.076	0.011	0.014	0.011
$\mathrm{ME}_{53,\mathrm{EDR3,GA,NM,nosigmaCRF}}$	0.082	0.124	0.067	0.011	0.014	0.011
Δ [%]	21	6	12	1	2	1
$\mathrm{ME}_{53,\mathrm{EDR3,GA,NM,0.10maxsigmaCRF}}$	0.081	0.122	0.068	0.011	0.013	0.011
Δ [%]	22	8	11	2	3	2
$\mathrm{ME}_{53,\mathrm{EDR3,GA,NM,0.22maxsigmaCRF}}$	0.090	0.128	0.074	0.011	0.014	0.011
Δ [%]	14	3	3	1	1	1

Notes. Iterations 11 to 35 were considered for calculation of the $\mathrm{ME_s}$ of the various scenarios s, because the formal errors of the rotation parameters increase substantially if only few stars are available for calculations. If the square root of the mean Q/n were considered as well for the respective iterations, the Δ [%] are 2 % lower for $\mathrm{ME}_{53,\mathrm{EDR3,GA,NM,nosigmaCRF}}$ and $\mathrm{ME}_{53,\mathrm{EDR3,GA,NM,0.10maxsigmaCRF}}$, and 1 % lower for $\mathrm{ME}_{53,\mathrm{EDR3,GA,NM,0.22maxsigmaCRF}}$. The epoch T is 2016.0 for Gaia EDR3. Units are in milliarcseconds for $\epsilon_X(T)$, $\epsilon_Y(T)$, and $\epsilon_Z(T)$. They are milliarcseconds per year for ω_X, ω_Y, and ω_Z.

ICRF3 S/X was evaluated to find suitable assumptions for achievable uncertainty levels. When comparing the combined position uncertainty $\sqrt{\sigma^2_{\alpha*,\mathrm{CRF}} + \sigma^2_{\delta,\mathrm{CRF}}}$, labeled as σ_{CRF}, to the number of observations in the respective CRF in Fig. 5.50, it can be seen that the primary calibrators with larger σ_{CRF} values have a smaller number of observations. The median position uncertainty of ICRF3 S/X in bins of 10 observations is plotted in darker grey for comparison. The median position uncertainty for the bin of 250 observations is 0.22 mas. A level of 0.10 mas can only be reached with more than about 600 observations of the radio source. Only 30 % of the primary calibrators in this work have a position determined from more than 600 observations in the respective catalogs. Surely, since ICRF3 and rfc2018b, more observations have been conducted by the IVS and other communities to improve the future CRF. Since ICRF3 where 6206 sessions at S/X bands were included (Charlot et al. 2020), more suitable sessions have been observed, such as the R1/R4 sessions observed twice per week by the IVS. For example, for the preparation of ITRF2020, already more than 6500 sessions could be submitted by the VLBI community[16]. However, for linking the radio star positions to ICRF3 S/X the specific calibrators are needed out of which some are even not yet in ICRF3 S/X. Of course a requirement of 0.10 mas, meaning about 600 observations per primary calibrator, would require an enormous effort of the VLBI community. Therefore, it might be more realistic to target 0.22 mas, meaning about 250 observations, for each primary calibrator first, where 57 % of the primary calibrators already reach this target.

With this information in mind, two more scenarios were prepared, where the $\sigma_{\alpha*,\mathrm{CRF}}$ and $\sigma_{\delta,\mathrm{CRF}}$ were capped at $0.10/\sqrt{2}$ mas and $0.22/\sqrt{2}$ mas respectively, equal to 0.10 mas and 0.22 mas for σ_{CRF}. This means the uncertainties of any star positions with σ_{CRF} smaller the threshold were not changed, and the uncertainties of any star positions with σ_{CRF} larger the threshold were set to the threshold value. With a limitation to 0.10 mas 18 stars needed no capping, and with a limitation of 0.22 mas 35 stars needed no capping. Furthermore, to derive a better comparison of the ME statistics, the seven stars which produce offsets in the spin and orientation parameters similar to "53,ERD3,GA,NM" were excluded. The resulting mean formal errors $\mathrm{ME}_{53,\mathrm{EDR3,GA,NM,0.10maxsigmaCRF}}$, $\mathrm{ME}_{53,\mathrm{EDR3,GA,NM,0.22maxsigmaCRF}}$, and $\mathrm{ME}_{53,\mathrm{EDR3,GA,NM,nosigmaCRF}}$ are listed in Table 5.22 along with the percentage of improvement compared to "53,ERD3,GA,NM". As expected, the greatest decrease in ME is seen when σ_{CRF} was set to zero or a maximum of 0.10 mas. Both give similar results, with the greatest reduction in ME for ϵ_X by 20 %. The ME of the other orientation parameters also reduce considerably, whereas the ME of the spin parameters do not. When σ_{CRF} was set to a maximum of 0.22 mas, the reduction in ME for ϵ_X is still 14 %, whereas it is negligible for the other rotation parameters. Of course these results only apply to the given dataset that means to the given sky distribution

[16] https://ivscc.gsfc.nasa.gov/IVS_AC/IVS-AC_ITRF2020.htm, accessed 20 October 2021.

of the counterparts, the differences between VLBI and Gaia parameters, and the given uncertainties.

Some of the primary calibrators are not yet included in ICRF3. Therefore, when processing a new CRF with the updated list of VLBI sessions, it should be checked whether the sessions used to create the rfc catalogs can also be added. In this way, all calibrator positions are given in a common frame and any degradation of results due to calibrator positions in different CRF is eliminated. However, the orientation offset between rfc_2018b and ICRF3 S/X was tested to be below 50 µas (Lunz et al. 2019a), smaller than the position offsets seen in the iterative rotation parameter results, such as for the scenario "60,EDR3,GA,NM". For the current datasets, no unexpected offsets in the rotation parameters can be found when rejecting a star whose position was referenced to a primary calibrator that is not in ICRF3.

Special sessions to improve the positions of the primary calibrators can be proposed. In particular, if it is not possible to use VLBI sessions from rfc catalogs to create a new CRF, this should be considered.

5.7.2 Upcoming Gaia data release

Not only the VLBI-based CRF but also the Gaia dataset will improve with time. According to Lindegren (2020a), the new Gaia data releases are expected to improve as $L^{-1/2}$ for positions and parallax, and as $L^{-3/2}$ for proper motions. Thereby $L = 1.8\,\mathrm{yr}$ for Gaia DR2 at epoch $T = 2015.5$. In the further calculations, the correlations are not changed. Gaia EDR3 is based on the time period between 25 July 2014 and 28 May 2017 (Fabricius et al. 2021), which is equal to $L = 2.8\,\mathrm{yr}$ and the epoch is $T = 2016.0$.

The evolution of the formal errors of the baseline solutions of scenarios "60,EDR3,GA,NM" and "53,EDR3,GA,NM" was tested for possible future Gaia DRs as reported in Table 5.23. The exact time span and epochs for upcoming Gaia DRs are not yet known. Therefore, the test scenarios were chosen similar to Lindegren (2020a). For one test, the nominal period of 5 years with epoch $T = 2017.1$ of the corresponding DR is expected and is denoted DR4 for simplicity. For the other test, the maximum achievable extended period of 10 years[17] with epoch $T = 2019.6$ was chosen and is denoted as DR5. The maximum reduction in the formal errors of the spin parameters is about 40% for the 10-year period compared to the 2.8-year period. The formal errors of the orientation parameters remain similar for the three time intervals tested. In fact, the inclusion of five more stars has, with about 10 % reduction, a larger impact on the formal errors of the orientation parameters than the upcoming Gaia DRs, when comparing results for the baseline solutions of "60,EDR3,GA,NM" and "53,EDR3,GA,NM" containing 45 and 40 stars, respectively.

[17] https://www.cosmos.esa.int/web/gaia/faqs#missionend, accessed 20 October 2021.

The decrease in formal errors of the spin is also about 15 % when comparing the two scenarios.

Table 5.23 Expected change in the formal errors of the rotation parameters of the baseline solutions of scenarios "60,EDR3,GA,NM" and "53,EDR3,GA,NM" from employing future Gaia DRs.

Scenario	T	$\sigma_{\boldsymbol{\epsilon}(T)}$ [μas]	$\sigma_{\boldsymbol{\omega}}$ [μas yr^{-1}]
60,EDR3,GA,NM	2016.0	87.4	9.4
60,DR4,GA,NM	2017.1	85.4	6.6
60,DR5,GA,NM	2019.6	86.4	5.5
53,EDR3,GA,NM	2016.0	97.7	11.6
53,DR4,GA,NM	2017.1	94.8	7.9
53,DR5,GA,NM	2019.6	95.8	6.4

Notes. The formal errors $\sigma_{\boldsymbol{\epsilon}(T)}$ and $\sigma_{\boldsymbol{\omega}}$ are presented as the quadratic mean of the uncertainty components in X, Y, and Z. Thereby T is the assumed epoch of the Gaia DR. Therefore, solutions with T = 2016.0 correspond to the respective baseline solutions presented in Table 5.16.

5.7.3 Follow-on star observations

To simulate the effect of new one-epoch observations, another scenario was tested in which a new single-epoch position from phase-referencing observations was added to the baseline solution of "60,EDR3,GA,NM" at epoch t = 2022, 2023, 2025, and 2030, respectively, for each star in the baseline solution. The uncertainty of the additional position for each of the stars was derived with the formulas given in Eqs. 5.4 and 5.5. Thereby the σ_{random} were chosen to be the median values as given in Sect. 5.4.5. The calibrator used for the existing data was chosen as the primary calibrator for the simulated positions, and $\sigma_{\alpha,\text{CRF}}$ and $\sigma_{\delta,\text{CRF}}$ were chosen accordingly. In case positions referenced to multiple primary calibrators were available, one of them was randomly selected. Any masers (SY Scl, S Per, T Lep, VY CMa, S Crt, S CrB, U Her, RR Aql, PZ Cas) in the accepted stars of the baseline solution were ignored, which means no additional position was simulated for them. This is because it is not expected to obtain a phase-referencing position for them in the continuum mode. In total, a new position was added for 37 of the accepted stars.

Table 5.24 Expected change in the formal errors of the rotation parameters of the baseline solution of scenario "60,EDR3,GA,NM" when adding new single-epoch positions for 37 of the accepted stars which are no masers and have VLBI positions in "60,EDR3,GA,NM" already. The results are also shown for the expected Gaia DR4 and Gaia DR5.

Scenario	T	t	$\sigma_{\boldsymbol{\epsilon}(T)}$ [μas]	$\sigma_{\boldsymbol{\omega}}$ [μas yr^{-1}]
60,EDR3,GA,NM	2016.0	none	87.4	9.4
60,EDR3,GA,NM	2016.0	2022	70.7	8.9
60,EDR3,GA,NM	2016.0	2023	71.5	8.7
60,DR4,GA,NM	2017.1	2023	67.2	6.3
60,DR5,GA,NM	2019.6	2023	66.0	5.3
60,EDR3,GA,NM	2016.0	2025	73.0	8.4
60,DR4,GA,NM	2017.1	2025	68.0	6.1
60,DR5,GA,NM	2019.6	2025	65.9	5.1
60,EDR3,GA,NM	2016.0	2030	76.2	7.6
60,DR4,GA,NM	2017.1	2030	70.4	5.6
60,DR5,GA,NM	2019.6	2030	66.5	4.7
60,EDR3,GA,NM	2016.0	2023+2030	67.9	7.5
60,DR4,GA,NM	2017.1	2023+2030	61.7	5.5
60,DR5,GA,NM	2019.6	2023+2030	57.0	4.7

Notes. The formal errors $\sigma_{\boldsymbol{\epsilon}(T)}$ and $\sigma_{\boldsymbol{\omega}}$ are presented as the quadratic mean of the uncertainty components in X, Y, and Z. Thereby t is the assumed epoch of the newly added VLBI positions and T is the epoch of the Gaia DR. The Gaia DR covering the nominal mission period of 5 years is denoted DR4, and the Gaia DR covering the extended mission period of 10 years is denoted DR5.

In Table 5.24 the results of the formal errors of the rotation parameters are presented as the quadratic mean of the uncertainty components in X, Y, and Z. As expected, the scenarios where the epoch of the new VLBI observations t is closer to the Gaia epoch T lead to lower formal errors for the orientation parameters, but higher formal errors for the spin parameters compared to the scenario where t is further away in time from T. Observing the 37 stars in both 2023 and 2030 would lead to improvements in both

orientation and spin determination. Moreover, this behavior of the formal errors of the rotation parameters remains similar when tested on possible future Gaia DRs, where of course the formal errors will additionally decrease due to the improved Gaia dataset. The test with a new observation in 2023 and 2030 shows that there is no advantage to observing the stars in 2023 in addition to 2030, provided the given data, if only the spin determination of the Gaia DR with $T = 2019.6$ would be of interest. From a practical point of view, however, it is advantageous to observe the stars in several epochs. First, it is then possible to determine if a position is an outlier in the position time series, and second, acceleration terms or other nonlinear motions become visible. Third, $\sqrt{Q/n}$, similar to s_0^2, cannot be investigated in the simulations due to unknown residuals.

Moreover, for the determination of the residual spin, it is usually advantageous to determine estimates for the stellar motion model of a star. Models of stellar motion are derived from relative positions, which are much more precise than absolute single epoch positions and therefore carry more weight in the adjustment procedure. Thus, another simulation was computed in which model estimates were assumed for some of the stars for which a stellar motion model is not yet available. Candidates for deriving estimates of models of stellar motion for the first time from VLBI data only are the 12 stars from Boboltz et al. (2007) which were detected in the January 2020 VLBA observations of this work. They are UV Psc, HD 8357, RZ Cas, B Per, SV Cam, 54 Cam, IL Hya, Hu Vir, DK Dra, RS Cvn, SZ Psc, and HD 224085. Deriving appropriate estimates for models of stellar motion for stars for which very precise estimates are not yet available requires enough phase-referencing VLBI observations of these stars in continuum mode at X-band or C-band. For the above 12 stars only the positions at one epoch

Table 5.25 Expected change in the formal errors of the rotation parameters of the baseline solution of scenario "60,EDR3,GA,NM" when adding proper motions with different uncertainties for 9 of the accepted stars which were detected in Boboltz et al. (2007) and in this work and which do not yet have a VLBI-based proper motion. The results are also shown for the expected Gaia DR4 and Gaia DR5.

Scenario	T	$\sigma_{\mu_{\alpha*,\delta}}$ [μas yr^{-1}]	$\sigma_{\boldsymbol{\epsilon}(T)}$ [μas]	$\sigma_{\boldsymbol{\omega}}$ [μas yr^{-1}]
60,EDR3,GA,NM	2016.0	0.1	87.4	9.2
60,DR4,GA,NM	2017.1	0.1	85.4	6.5
60,DR5,GA,NM	2019.6	0.1	86.4	5.4
60,EDR3,GA,NM	2016.0	0.05	87.3	8.7
60,DR4,GA,NM	2017.1	0.05	85.4	6.3
60,DR5,GA,NM	2019.6	0.05	86.3	5.3
60,EDR3,GA,NM	2016.0	0.03	87.2	8.1
60,DR4,GA,NM	2017.1	0.03	85.4	5.8
60,DR5,GA,NM	2019.6	0.03	86.1	5.0

Notes. The formal errors $\sigma_{\boldsymbol{\epsilon}(T)}$ and $\sigma_{\boldsymbol{\omega}}$ are presented as the quadratic mean of the uncertainty components in X, Y, and Z. Thereby $\sigma_{\mu_{\alpha*,\delta}}$ is the assumed uncertainty of the newly added VLBI proper motion in $\alpha*$ and δ directions, and T is the epoch of the Gaia data. The Gaia DR covering the nominal mission period of 5 years is denoted DR4, and the Gaia DR covering the extended mission period of 10 years is denoted DR5.

in 2020 are collected at present. Assuming altogether four more observations of each of the stars in the second half of 2022 and the first half of 2023 at the maxima and minima of the parallax signal, a time span of about three years is covered by five VLBI observations per star. Taking the median σ_{random} from Sect. 5.4.5 of 0.026 mas in $\alpha*$ and 0.067 mas in δ, this would result in formal errors for $\sigma_{\mu_{\alpha*}}$ of roughly 0.01 mas yr^{-1} and for σ_{μ_δ} of roughly 0.03 mas yr^{-1}. Similar values are expected when observing with EVN, although the north-south geometry can be improved by including stations like Hartebeesthoek. When comparing to the results from Table 5.12, it is clear that this is a very optimistic uncertainty estimate and that it is likely that they need inflation to obtain a $s_0^2 = 1$.

To not be over-optimistic, $\sigma_{\mu_{\alpha*}} = \sigma_{\mu_\delta} = 0.1$ mas yr^{-1} or 0.05 mas yr^{-1} were assumed for a simulated scenario. For the determination of the rotation parameters the proper motions for the above 12 stars were added to "60,EDR3,GA,NM". However, those of B Per, HU Vir, and SZ Psc have no effect on the results, because they are not in the baseline solution of "60,EDR3,GA,NM". They get excluded beforehand because their VLBI and Gaia data based on the given parameterizations with position, proper motion, and parallax diverge largely. That the parameterization is not sufficient for the given data is also expressed by the larger RUWE values in Gaia EDR3 for these stars. This can be explained, as all three stars are located in the larger orbit of a triple system, where the larger orbit has a period of 2 to 6 years, close to the Gaia EDR3 observation time interval. In Gaia DR2, their RUWE value was below 1.4, which is why they were selected as suitable stars for the Gaia VLBI alignment.

The resulting formal errors of the rotation parameters are presented in Table 5.25. There is less than 14 % improvement in the formal error of the spin compared to the original baseline solution, which is presented in Table 5.23, even if $\sigma_{\mu_{\alpha*}} = \sigma_{\mu_\delta} = 0.03$ mas yr^{-1} was applied. The formal errors of the orientation offset reduced only insignificantly.

Despite the formal errors from the $\boldsymbol{Q_{xx}}$ matrix in the adjustment, the residuals affect the final parameter uncertainties because the formal errors must be inflated so that $\sigma_0^2/s_0^2 = 1$, where σ_0^2 is the unknown variance of the weight unit. Only real measurements can can provide information about this. Therefore, it is of interest to further investigate the reason for large residuals in, e.g., Fig. 5.36 and to plan new observations for stars with large residuals if they cannot be explained with the already known information. In this way, linear accelerations or motions due to multiple star systems can be uncovered. Furthermore, the correlations between the astrometric parameters in the stellar motion model are large for some stars in this study. To decorrelate the parameters, additional geometrically sensitive observations are needed for these stars. For the planning of the re-observations, the peak intensities from Sect. 5.4.3 should be used in order to obtain a suitable SNR for astrometric observations. Furthermore, the secondary calibrators can be observed in order to improve the atmosphere correction. In addition, a better uv-coverage

will reduce side-lobes. These actions will improve the consistency of the relative positions.

The inclusion of new counterparts would provide the possibility to better identify stars that produce offsets in the iterative rotation parameter solutions and enable further investigations of possible magnitude dependence of the alignment. The formal errors of the rotation parameters are moreover very sensitive to the number of counterparts included, since their number is small. More counterparts can be searched for by making use of the proposals B and C in Sect. 5.3 and it is possible to cross-check the selection of stars with detections from the NRAO VLA Sky Survey (Condon et al. 1998) and Gaia EDR3 beforehand.

Of lower priority for the alignment between a VLBI-based CRF and the Gaia bright frame are further observations for additional investigations on the topic of unresolved binaries as seen by Gaia but resolved by VLBI. As shown in Table 5.18 the difference between the Gaia position and the barycenter and the center of luminosity is individual for each binary and at the level of the position uncertainty of an absolute single-epoch position in this work. Given the limited amount of observing time, these objects therefore should be taken aside and instead individual objects with expected linear motion, which are more suitable for the task, should be observed instead.

If dedicated observations were planned, the expected effect on the rotation parameter analysis can be tested using the algorithm of Lindegren (2020a) and of this work.

5.8 Discussion

The alignment of the Gaia bright frame to ICRF3 S/X using radio stars was improved through several ways in this work, but the result is still limited by the small number of counterparts and the heterogeneity of the reference points of the absolute positions for both the calibrator AGNs and the stars.

5.8.1 Various rotation parameter solutions

The aim of this chapter was to evaluate and improve the alignment of the optically bright fraction of the Gaia data releases 2 and 3 to ICRF3 S/X in terms of three rotations. Both the static part of the rotation and its time derivative were determined. The static part is called orientation offset $\epsilon(T) = [\epsilon_X(T), \epsilon_Y(T), \epsilon_Z(T)]'$ about the three axes of the ICRF3 S/X X, Y, and Z at epoch T of the Gaia DR, and the time derivative is called the linear spin $\omega = [\omega_X, \omega_Y, \omega_Z]'$.

For this task, VLBI observations of optically bright radio stars relative to radio bright extragalactic primary calibrators in the phase-referencing mode were employed. Various

scenarios were tested where the impact of the homogenization of the VLBI data, the impact of a more realistic error budget, the impact of the Galactocentric acceleration, the impact of the new observations from this work in two different fashions (absolute or relative positions), and the inclusion or deletion of various counterparts on the six rotation parameters was tested. For each scenario, iterative rotation parameter results were derived, where in each iteration the most deviating star was excluded from the sample. Weighted mean (WM), weighted RMS (WRMS), and mean formal error (ME) statistics of a representative range of the iterative rotation parameter results were used for comparison of the various scenarios.

The determination of residual rotation parameters for Gaia DR2 was improved to have less scatter in the iterative results, especially in ϵ_Y, ω_X, and ω_Y, after homogenizing the VLBI data.

- First, the reduced scatter in Y results mainly from consistently shifting all phase-calibrator coordinates (and thus star coordinates) from the partly homogenized VLBI data collection in Lindegren (2020a) to those from ICRF3 S/X (or rfc_2018b if not in ICRF3), even though the shifts are mostly less than a milliarcsecond in magnitude. Metadata from publications and the VLBI data repository were used for this effort. This scenario was labeled "41,DR2,shift". Also, the WM changed substantially during this homogenization step. The large WM in ϵ_Y of 1.273 mas decreased by 0.883 mas and the large WM in ϵ_Z of 0.537 mas decreased by 0.532 mas, whereas the WM in ϵ_X increased from 0.055 mas to -0.152 mas. The WM in ω_X increased from $-0.047\,\mathrm{mas\,yr^{-1}}$ by $-0.036\,\mathrm{mas\,yr^{-1}}$ and the WM in ω_Y increased from $-0.081\,\mathrm{mas\,yr^{-1}}$ by $-0.058\,\mathrm{mas\,yr^{-1}}$, while the WM in ω_Z remained the same ($-0.001\,\mathrm{mas\,yr^{-1}}$ difference).
- Second, the catalog position uncertainty of the primary calibrator, σ_{CRF}, was not consistently applied for all star positions in Lindegren (2020a). The consistent handling of this error budget item in scenario "41,DR2,$\sigma_{\mathrm{model\ pos}}$" smoothed the results as indicated by the lower WRMS values. The homogeneous handling of the position uncertainties compared to the original solution in Lindegren (2020a) equalized the weights of the positions in the adjustment computation, so the decreased scatter is not surprising.
- Third, a more realistic error budget for absolute star positions from continuum phase-referencing was determined in this work. It was separately evaluated for positions from single epochs and from models of stellar motion (which usually consist of position, proper motion and parallax) because both are mixed in the computation of the rotations between VLBI and Gaia frames. The detailed discussion in Sect. 5.4.5 identified five error budget items that must be considered, and general orders of magnitude were provided for each of them. The largest error budget items are the

calibrator catalog position uncertainty, the delay model error, and the position difference of the primary calibrator determined from group delays or phase delays. Some of these items were already considered in the previous analyses, some had to be added on top to obtain the total more realistic error budget. Because of the added uncertainties, positions from models of stellar motion (and single-epoch positions in case they were inserted) contributed less to the spin determination compared to the approach in "41,DR2,Lind2020". The result is a 2.5- to 3.5-fold increase in ME of the orientation offset compared to "41,DR2,Lind2020" and a 1.7-fold increase compared to "41,DR2,$\sigma_{\text{model pos}}$". The ME of the spin are only marginally affected. The Q/n, similar to s_0^2, however decreased due to the higher uncertainties of the VLBI positions. The Q/n was less than one for "41,DR2" when there were still 15 stars in the sample, compared to 8 stars for "41,DR2,Lind2020". This result shows that the error budget for absolute positions applied in this work is more realistic. Combining ME and $\sqrt{Q/n}$, the uncertainties of the orientation offsets increased by 60 %. The resulting rotation parameters support a magnitude lowered by 0.114 mas in ϵ_X compared to "41,DR2,$\sigma_{\text{model pos}}$" and a lower magnitude in ω_X by 0.016 mas yr^{-1}. They are furthermore significantly different from the results without full homogenization. Therefore, it shows that careful handling of historic data is necessary for ensuring that all positions are in the same reference frame, but also realistic uncertainties must be considered for the comparison between VLBI and Gaia.

The same conclusions apply to Gaia EDR3, where the orientation offset WM magnitudes similarly decreased for Y and Z and increased for X after homogenization. The WM of ω_Y however decreased compared to the results from Gaia DR2. Again, the increase in position uncertainties reduced the Q/n so that unity was reached in "41,EDR3" when there were still 12 stars in the sample, while it could not be reached at all in "41,EDR3,Lind2020".

In the next step, new absolute single-epoch positions from VLBA observations (experiment UL005) were added to the rotation parameter analysis. The more realistic error budget for these positions has a median of 0.351 mas in $\alpha*$ and 0.782 mas in δ, which is substantially higher than the 0.1 mas expected in simulations of the impact of future VLBI observations by Lindegren (2020a). Adding the new positions for the 32 stars in this work nevertheless improved the ME of the rotation parameters due to the higher number of observations and the new counterparts between VLBI and Gaia, as expected.

The new observations in scenario "55,DR2" changed the magnitude of the WM of ω_Y significantly by about 0.016 mas yr^{-1} compared to the value for "41,DR2" and the correlations between parameters reduced to be negligible. The WRMS values were improved for most rotation parameters. For Gaia EDR3 ("55,EDR3"), the new single-epoch positions likewise decreased the ME of the rotation parameters compared to the scenario with 41 stars. The WM values of ϵ_X and ϵ_Y changed significantly by about 0.1 mas and the

correlations between the parameters become negligible (Later analyses show that the exclusion of stars that produce offsets in the analysis of the rotation parameters can lead to a change in the WM of similar magnitudes.). The inclusion of the new data even slightly changed the ratio of the rotation parameter values of the X, Y and Z axes and the size of the orientation offset. The WRMS values of ϵ_X and ϵ_Y further improved by 40 %, while they remained similar for the other rotation parameters. Furthermore, the iteration with Q/n equal to one for both Gaia DR2 and Gaia EDR3 includes 6 or 7 more stars than the corresponding iteration for scenarios without the new observations. These aspects show that the new observations have a positive impact on the analysis of the rotation parameters.

In another test case "55,EDR3,GA", the effect of the Galactocentric acceleration of $5.8\,\mu\mathrm{as\,yr}^{-1}$ in the Galactocentric direction was applied to the VLBI positions and proper motions of scenario "55,EDR3", as it was not previously considered in the processing of the VLBI data from phase referencing. Thus, this effect was consistently taken into account for both VLBI and Gaia positions and proper motions in "55,EDR3,GA". The rotation parameter estimates demonstrate that the consistent handling of the effect of the Galactocentric acceleration had no significant impact on the alignment of the bright Gaia frame to ICRF3 using the data and method in this work. This was to be expected, since the maximum effect on the proper motions of the objects with $5.8\,\mu\mathrm{as\,yr}^{-1}$ is smaller than the spin ME and WRMS values of the bright part of Gaia determined in this work.

Since the more realistic error budget mitigates the influence of the absolute VLBI positions on the spin determination, it can be suggested that more and refined VLBI proper motions should be determined instead of one-epoch positions to obtain further improved spin parameters. The proper motions can be determined from the more precise relative positions towards the primary calibrator, which is thereby assumed to have a stable position based on phase delays. Thus, it was assessed whether it would be more effective for the spin determination to use the new data from the UL005 experiment to derive relative star positions rather than absolute positions and to improve the estimates for models of stellar motion whenever possible. New model estimates for position, proper motion, and parallax were derived for 12 stars. Linear acceleration terms were also tested and found to be significant for four out of the 12 stars. For some stars, estimates from constrained VLBI observation intervals or estimates for only five astrometric parameters were used, although the accelerations were significant because the fits were in better agreement with the Gaia EDR3 values. Since the Gaia data are always based on the five astrometric parameters and the largest possible time interval of observations in the respective Gaia DR, this approach makes sense. The VLBI data for the 12 stars from the scenarios "55,DR2" and "55,EDR3,GA" were replaced with the new model estimates in the scenarios "55,DR2,NM" and "55,EDR3,GA,NM". Instead of the model positions, the

single-epoch absolute position(s) from experiment UL005 were inserted because they are likely to be better connected to the group delay positions of the primary calibrators in ICRF3 S/X due to the same handling of calibrator source structure in the VLBI analysis.

For Gaia DR2, the WRMS and WM values do not change much between "55,DR2" and "55,DR2,NM", however the orientation offset ME values increased 1.2-fold due to the lower number of positions inserted into the analysis. Only the WRMS in ϵ_Z changed noteworthy (decrease by 50 %). For Gaia EDR3, the orientation offset ME values also increased, due to the same reasons as for Gaia DR2. However, the WRMS and ME values of the spin decreased. These results confirm that replacing the VLBI data with the absolute one-epoch star positions and the updated VLBI proper motions determined from the precise relative positions has a greater impact on the spin determination than simply adding the absolute one-epoch positions to the existing dataset, when a realistic error budget is considered. However, when the determination of the orientation offset is of interest, it might be interesting to set up a scenario, where as many independent absolute positions are included as possible to decrease the orientation offset ME. For both "55,EDR3,GA" and "55,EDR3,GA,NM", the Q/n of one is reached when there are still 16 stars in the sample, indicating that other effects dominate the error budget.

Further scenarios based on Gaia EDR3 with the inclusion of more stars or rejection of stars leading to offsets in the determination of the orientation and spin showed that the WRMS scatter of the orientation parameters can be reduced to below 0.078 mas per rotation axis and the WRMS scatter of the spin can be reduced to below 0.009 mas yr^{-1} respectively. This is a large difference compared to the WRMS of the rotation parameters using the original Lindegren (2020a) dataset of 0.227 mas and 0.019 mas yr^{-1} respectively. As shown for Gaia DR2, a large fraction of this reduction is due to the additional error budget of the observations in the present study. The WM between the various scenarios "49,EDR3,GA,NM", "53,EDR3,GA,NM", "55,EDR3,GA,NM", and "60,EDR3,GA,NM" change for each of the three orientation offset estimates ϵ_X, ϵ_Y, and ϵ_Z at maximum by 0.075, 0.133, and 0.026 mas and for each of the three spin estimates ω_X, ω_Y, and ω_Z at maximum by 0.008, 0.022, and 0.021 mas yr^{-1}. The scenarios in which the stars that lead to offsets in the iterative rotation parameters were excluded a priori, namely "49,EDR3,GA", "49,EDR3,GA,NM", and "53,EDR3,GA,NM", show a smaller magnitude in ω_Y than the scenarios in which all available stars were included, irrespective of whether the new estimates for the stellar motion models were used or not (Lunz et al. 2021b).

In similar analyses of rotation parameters, such as Lestrade et al. (1999); Lindegren (2020a), only the model positions were used as absolute positions from VLBI. Accordingly, using the model positions instead of the one-epoch positions from experiment UL005 in "55,EDR3,GA,NM,modelpos", the difference in WM for ϵ_X (comparing "55,EDR3,GA,NM" and "55,EDR3,GA,NM,modelpos") is significant and the orientation

offset ME is slightly reduced. This is probably due to the lower error budget of the absolute model positions compared to the one-epoch positions of experiment UL005. Nevertheless, the position residuals show that for individual stars the residuals of one or the other scenario are smaller and therefore fit the Gaia data better. This finding suggests that more detailed studies are needed for the stars in question. Furthermore, the differences of the rotation parameters between the two solutions are smaller than the differences of the rotation parameters in the scatter plots in Fig. 5.44a. These scatter plots show the WM, WRMS, and ME statistics for 211876 individual scenarios, where in each scenario the first eleven rejected stars from "60,EDR3,GA,NM" and an individual set of four stars were deleted before the analysis run to show the accuracy of a representative range of the results (A detailed discussion of these plots follows in the next subsection.). The WM values of the orientation offset and spin for "55,EDR3,GA,NM,modelpos" are within the scatter of the WM values in the plots.

5.8.2 Accuracy of the final results

For the scenarios with the more realistic error budget, scatter plots were created from solutions in each of which the obvious outliers and an additional individual group of four stars were excluded before the analysis of the rotation parameters. In this way, it was simulated that from the representative set of stars, some stars had never been observed by VLBI or Gaia. For "60,EDR3,GA,NM" the orientation offset WM values are variable by $(\epsilon_X, \epsilon_Y, \epsilon_Z) = (0.414, 0.414, 0.266)$mas and the spin WM values are variable by $(\omega_X, \omega_Y, \omega_Z) = (0.126, 0.078, 0.056)\mathrm{mas\,yr^{-1}}$. The WRMS and ME scatter further support this accuracy; their minimum values are on average $\gtrapprox 0.12$ mas per axis for the orientation offset and $\gtrapprox 0.01\,\mathrm{mas\,yr^{-1}}$ per axis for the spin. The values provide an average lower level of the uncertainty of the WM values of Gaia EDR3. For "55,DR2,NM", the respective values are $\gtrapprox 0.19$ mas and $\gtrapprox 0.04\,\mathrm{mas\,yr^{-1}}$.

Comparing "55,EDR3,GA,NM' to "55,EDR3,GA", the scatter in spin WM values, the minimum spin WRMS values, and the spin ME values are smaller for "55,EDR3,GA,NM", while they generally increase for the orientation offset. The scatter of the WRMS values is also smaller for "55,EDR3,GA,NM". This again shows that the new model estimates improve the accuracy of the spin results. Proper motions, based on the far more accurate VLBI relative positions, contribute more to the spin determination than single-epoch absolute positions with large uncertainties. Furthermore, the scatter plots of the ME for "55,EDR3,GA" show that there are stars in the sample that have a large effect on lowering the ME, as can be seen from the small clusters of points next to the main field of ME results. These stars are HD 199178, AR Lac, and CygX-1, which are located in the same direction in the sky and have high weights in the spin determination due to small

uncertainties in the Gaia dataset. Also for "55,EDR3,GA,NM" and future Gaia DRs, stars with more precise proper motions are desirable to similarly lower the ME.

For both Gaia EDR3 and Gaia DR2, the ω_Y is determined with a 3.4-σ significance or more from these statistics for the solutions with the lowest mean Q/n when the new model estimates were applied ("55,DR2,NM", "55,EDR3,GA,NM", and "60,EDR3,GA,NM"). If the new model estimates were not applied, the significance of ω_Y is 2.6-σ ("55,EDR3,GA").

Another interesting evaluation is comparing the maximum difference of the WM values from all the scenarios based on Gaia EDR3 and 55 stars in Table 5.15 to the WRMS of the scenario "55,EDR3,GA,NM". Here, the former represents the variability of the solutions based on the different setups of the VLBI data (none of which can be considered wrong), and the latter represents the variability of the representative range of iterative rotation parameter results within the scenario. When the ratio is small, the different scenarios vary less than the iterative solutions in scenario "55,EDR3,GA,NM", which means that the individual counterparts need to be examined in more detail rather than deciding on an approach to setting up the VLBI data. The ratio is larger one only for ϵ_X (1.9), because "55,EDR3,GA,NM,modelpos" has a small value for this rotation parameter compared to the other scenarios and its WRMS is small.

With the discussion of the WM, WRMS, and ME statistics in mind, the final baseline solution for Gaia DR2 and Gaia EDR3 can be assessed. For each scenario, one iteration, called baseline solution, was selected as listed in Table 5.16. The baseline solution represents the scenario after the obvious outliers have been excluded and the maximum Q_i/n_i of the rejected stars no longer show large deviations from the value of the previous iteration.

The final baseline solution for Gaia DR2 is taken from scenario "55,DR2,NM" with 44 included stars and is $(\epsilon_X,\epsilon_Y,\epsilon_Z,\omega_X,\omega_Y,\omega_Z) = (+0.089, +0.414, -0.022, -0.061, -0.119, +0.024) \pm (0.224, 0.309, 0.173, 0.047, 0.059, 0.052)$ mas or mas yr^{-1}. Thereby, the formal errors were already inflated with $Q/n = 6.08$, indicating that the uncertainties of the input data are underestimated by a factor of about 2.4. The ω_Y is a 2.0-σ detection. The final baseline solution for Gaia EDR3 taken from scenario "60,EDR3,GA,NM" with 45 included stars and is $(\epsilon_X,\epsilon_Y,\epsilon_Z,\omega_X,\omega_Y,\omega_Z) = (+0.308, +0.233, +0.172, +0.033, +0.072, -0.027) \pm (0.213, 0.268, 0.163, 0.023, 0.025, 0.023)$ mas or mas yr^{-1} with $Q/n = 6.28$ already applied. The ω_Y is a 2.9-σ detection. For comparison, the ω_Y in the baseline solution of "55,EDR3,GA,NM" it is a 3.0-σ detection. Without the new model estimates from this work, in scenario "55,EDR3,GA", ω_Y is a 2.5-σ detection. This is also supported by the scatter plots of the WM, WRMS, and ME values.

In contrast, the baseline solution of "53,EDR3,GA,NM", ω_Y is not significantly determined, since ω_Y is only $+0.031 \pm 0.032$ mas yr^{-1}. The difference in significance is mainly

due to the different value of ω_Y. However, for this solution deviating stars were manually excluded, which is one of the most rigorous approaches in the adjustment calculus. Evidence of the rejection process using the highest Q_i/n_i is sound is provided by the fact that the baseline solution of each scenario is at the global minimum of the Q/n values in the scatter plots of the WM, WRMS, and ME values, as shown for "60,EDR3,GA,NM" in Fig. 5.47. Thus, the baseline solution without manual outlier deletion is a statistically significant signal and ω_Y is significant at about the 3-σ level. The largest correlations remain between the three orientation offsets, albeit at less than +0.2 below significance, and between ω_X and ω_Z (significant with +0.335).

5.8.3 Comparison with external results

The spin parameter estimates can be compared with values from the literature that are not based on VLBI. Those for Gaia DR2 can be compared to results from Brandt (2018), who "derived proper motions of 115 662 stars by dividing the differences of positions from *Gaia* DR2 and Hipparcos by the time difference of their respective epochs, which is 24.25 years. In addition, he reduced systematics by cross-calibrating these proper motions with the proper motions from the *Gaia* and Hipparcos catalogs themselves. This includes the correction of global rotations between the catalogs. The spin parameters he derived are $(\omega_X, \omega_Y, \omega_Z) = (-0.081, -0.113, -0.038)$ mas yr^{-1}. Lindegren (2020a) estimated the corresponding uncertainties to be 0.03 mas yr^{-1}" (Lunz et al. 2020a). These spin parameters need to be corrected for the misalignment of the *Gaia* bright frame and ICRF3 as described in Lindegren (2020a) in order to be able to compare them with the spin parameters from "55,DR2,NM". This is done by adding the orientation parameters of "55,DR2,NM" divided by the time difference of 24.25 yr to the spin parameters of Brandt (2018). The corrected spin parameters are $(\omega_X, \omega_Y, \omega_Z) = (-0.078, -0.096, -0.039)$ mas yr^{-1}. The corrections and the differences are not significant. However, the difference in ω_Y between the Brandt (2018) solution and "55,DR2,NM" is increased. The $\mathrm{WRMS}_{55,\mathrm{DR2,NM}}$ for this parameter is 0.013 mas yr^{-1}, the $\mathrm{WM}_{55,\mathrm{DR2,NM}}$ is -0.121 mas yr^{-1}, and the $\mathrm{MS}_{55,\mathrm{DR2}}$ is 0.027 mas yr^{-1}. This means that iteration solutions that agree with the results of Brandt (2018) within the error bounds exist, similar to what was found for "55,DR2" in Lunz et al. (2020a).

Bobylev (2019) determined the spin of Gaia DR2 from VLBI proper motions of 81 stars, including e.g. red supergiants and masers. The spin he determined is $(\omega_X, \omega_Y, \omega_Z) = (-0.14, +0.03, -0.33) \pm (0.15, 0.22, 0.16)$ mas yr^{-1} using the VLBI and Gaia uncertainties as weights, which is much larger than the spin magnitude determined from the cleaned set of stars in Lindegren (2020a) and this work. Stars with proper motion differences between VLBI and Gaia DR2 larger 6 mas yr^{-1} were excluded beforehand, but no indication is

given in Bobylev (2019) whether an outlier detection similar to the iterative rejections of Lindegren (2020a) and this work was conducted or not. Because the magnitude of the spin reaches similar values for the early iterations in this work, this might be a reason why his results deviate from those presented in this work.

For Gaia EDR3, the spin of the various rotation parameter solutions can be compared with independent estimates from Cantat-Gaudin and Brandt (2021). Their analysis determined the spin between optically bright and faint Gaia EDR3 data by selecting open clusters and binaries with a bright and faint component and determining the spin between the two G magnitude sets. Because the sample has many counterparts, a magnitude dependence of the optically bright frame itself could be taken into account. They tested the spin for bins of 0.5 mag and less. The resulting rotation parameters can be divided into two groups. The spin values from the magnitude range $G \geq 10.5$ mag from Cantat-Gaudin and Brandt (2021) are between 16.2 μas yr^{-1} to 34.9 μas yr^{-1} for ω_X, 50.0 μas yr^{-1} to 76.6 μas yr^{-1} for ω_Y, and -2.9 μas yr^{-1} to 2.1 μas yr^{-1} for ω_Z. Those from the magnitude range $G \leq 10.5$ mag are between 12.8 μas yr^{-1} to 18.4 μas yr^{-1} for ω_X, 30.7 μas yr^{-1} to 35.7 μas yr^{-1} for ω_Y, and -19.4 μas yr^{-1} to -10.5 μas yr^{-1} for ω_Z. The uncertainty of their estimates is on the order of 2 μas yr^{-1} to 5 μas yr^{-1}, better than using the method in this work. The results for the magnitude range $G \leq 10.5$ mag are similar to those of scenarios "49,EDR3,GA", "49,EDR3,GA,NM", and "53,EDR3,GA,NM" in which stars which produce offsets in the rotation parameters were manually excluded before the rotation parameter analysis. "The stars DoAr 51, CoKu HP Tau G2, and HD 283641, which were excluded a priori because they lead to offsets in the iterative orientation offset parameter results, are fainter than the threshold of $G = 10.5$ mag. This could indicate that the alignment tests in this work are as well sensitive to the G. However, the RUWE parameters of these stars are also larger 1.4, which indicates that the standard model of stellar motion does not fit their *Gaia* data well. Therefore, this could as well be the effect seen when excluding the stars from the analysis. Fifteen stars in the sample have $G \geq 10.5$ mag, and 28 stars have a RUWE$\geq$ 1.4, almost 50 %. The stars producing the offsets in spin do not show any conspicuousness from the *Gaia* data but indicate linear acceleration or orbital motion from the VLBI data" (Lunz et al. 2021b).

For all scenarios, whether based on Gaia EDR3 or Gaia DR2, the estimates for Y are still the least well determined. It is plausible that in the case of the orientation offset this result is due to the precise VLBI data from recent years, which are not evenly distributed across the sky but roughly in the direction of the Y axis, as already mentioned by Lindegren (2020a). In the case of "60,EDR3,GA,NM" these stars with the highest weights in the orientation offset determination are those of the Pleiades from Melis et al. (2014), of the Taurus from Galli et al. (2018), and of the Orion from Kounkel et al. (2017). Those stars have not been replaced with new single-epoch positions in this work but use the homog-

enized positions based on the original, more precise model positions. Knowing about the magnitude dependence of the spin for the Gaia bright frame, which is determined with an almost linear trend in Y across bins of G magnitude according to Cantat-Gaudin and Brandt (2021), this could also be a reason for the larger formal errors in Y. Therefore, G magnitude dependence was tested on scenario "60,EDR3,GA,NM" despite the small number of counterparts in the relevant subsets.

Excluding the 15 stars with $G \geq 10.5$ mag in scenario "45,EDR3,GA,NM,G<10.5mag" resulted in a similar shape of the iterative results to those of "60,EDR3,GA,NM" and the uncertainty for ϵ_Y is still the largest. However, the uncertainties are more aligned. The t-test of the iterative results claims that the spin is different between the iterative results of "45,EDR3,GA,NM,G<10.5mag" and "60,EDR3,GA,NM" for the three axes. Using only the baseline solutions for comparison, the spin is not significantly different from that of "60,EDR3,GA,NM". However, it differs in ω_Z more than other scenarios, such as "60,EDR3,GA,NM,Gweighting" or "32,EDR3,GA,NM,RUWE1.4", from "60,EDR3,GA,NM". The WRMS in ω_Z increased compared to "60,EDR3,GA,NM". This is due to offsets between the iteration results when HD 22468 and AR Lac are excluded. Both stars have very accurate VLBI proper motions. The deselection of the two stars which produce offsets in the rotation parameter iterative solutions (similar to what was done for "53,EDR3,GA,NM") also produced significantly smaller spin in Y direction, similar to what was obtained for "53,EDR3,GA,NM". The ω_Y is similar to the spin from Cantat-Gaudin and Brandt (2021). In contrast, the ω_Z deviates more from the value in Cantat-Gaudin and Brandt (2021). Nevertheless, the scenarios meet the spin expected from the similar magnitude range in Cantat-Gaudin and Brandt (2021) within 2.3σ. The correlation coefficients between the orientation offsets are reduced. This can be an effect of G magnitude but also of geometry.

If instead the 45 stars with $G \leq 10.5$ mag from "60,EDR3,GA,NM" were excluded in the "15,EDR3,GA,NM,G>10.5mag" scenario, the t-test indicated that the spin parameters were also different compared to those of "60,EDR3,GA,NM". However, for "15,EDR3,GA,NM,G>10.5mag" the statistics are based on only 4 iterative results due to the small sample of 15 stars. The statistics and the baseline solution are dominated by five stars in the direction of the Y axis, which is an explanation for the difference in Y compared to the scenario using the full dataset and to the spin values from the respective magnitude range from Cantat-Gaudin and Brandt (2021). These results for "15,EDR3,GA,NM,G>10.5mag" should be evaluated with caution because the correlations between the orientation offset estimates increase and the sample is also very small.

In addition to the discussion of the magnitude dependence, Cantat-Gaudin and Brandt (2021) found evidence for a possible second-order dependence of the spin on the source color. They estimate this effect to be on the order of $10\,\mu\mathrm{as\,yr}^{-1}$, which is below the

current uncertainty of the baseline solution from comparing to VLBI as in this work.

The down-weighting of stars in magnitude range $11 < G \leq 13$ by $(13 - G)/2$ or the exclusion of stars with RUWE > 3 (11 stars rejected) or RUWE > 1.4 (28 stars rejected) did not noticeably change the rotation parameter solution. It was expected that stars with large RUWE would have a larger effect on the rotation parameter analysis, however the result shows that the selection of the iteration for the baseline solution of the respective scenarios is reasonable. A solution where in addition to all stars with RUWE > 1.4 the eight stars with $G > 10.5$ mag were excluded, "24,EDR3,GA,NM,RUWE1.4,G<10.5mag", did not improve the results in the sense that the spin results are more aligned to the respective results of Cantat-Gaudin and Brandt (2021) or that they have considerably less WRMS scatter. The results are more similar to those of "45,EDR3,GA,NM,G<10.5mag" than "32,EDR3,GA,NM,RUWE1.4". Excluding in addition the two remaining maser stars (which have very large position uncertainties) in "22,EDR3,GA,NM,RUWE1.4,G<10.5mag,nomaser" provides similar results to "24,EDR3,GA,NM,RUWE1.4,G<10.5mag" except a very small improvement in the ME values.

The results indicate that for the present analysis using VLBI and Gaia, the larger uncertainty in Y might really stem from the heterogeneity of the VLBI data and of the sky location of the counterparts rather than the magnitude dependence of the spin in Y.

For the bright Gaia EDR3 reference frame, a correction of $(-0.016\,6, -0.095\,0, +0.0283)$ mas yr^{-1} with an uncertainty of about 0.024 mas yr^{-1} per axis was applied to the spin in one of the middle iterations of the data processing, as explained in Sect. 2.3.1. No orientation offset was considered. Due to this correction, the spin determined for Gaia EDR3 in this work can be understood as residual spin of the corrected Gaia bright frame. Reversing the correction by adding it back to the baseline solution, for example of scenario "60,EDR3,GA,NM", results in an original, uncorrected spin in Gaia EDR3 of (0.016, -0.023, $+0.001$) $\pm$ (0.023, 0.025, 0.023) mas yr^{-1} if $Q/n = 6.28$ was considered. Thus, the current accuracy level of aligning the spin of the bright Gaia EDR3 reference frame to ICRF3 using VLBI observations of radio stars is about on par with using the Hipparcos positions instead.

In this work, the orientation offset of Gaia EDR3 could be determined with formal errors below 0.2 mas using available relative VLBI observations based on phase delays and an additional 14 hours of observing time. Malkin (2016b) found that this accuracy level can also be reached using geodetic VLBI, with a reasonable amount of observing time. However, the (equally distributed) stars need to be brighter than a few mJy to be detectable by geodetic VLBI, and large antennas (such as the 100 m Effelsberg antenna) need to be included in the network to ensure sufficient sensitivity. The assumption for his estimates is that the statistics of number of observations versus position uncertainty are similar for

the radio faint stars and the radio bright extragalactic objects, which is questionable.

5.8.4 Possible future improvements

While existing phase-referenced VLBI data have already been improved in this work, there are several possibilities for enhancing the alignment between the bright Gaia frame and ICRF3 through VLBI observations of radio stars. Three possible cases have been investigated in this work:

- First, the effect of reducing the error budget of the ICRF3 positions of the primary calibrators was determined. Reducing the error budget item of the primary calibrator catalog position σ_{CRF} to zero drops only the formal errors of the orientation parameters appreciably, by 6 % to 21 % for "53,EDR3,GA,NM", with the largest decrease in X. The formal errors of the spin are not affected (up to 2 % only). When ICRF3 is used as a template, about 600 observations per primary calibrator are similar to σ_{CRF} of about 0.10 mas. This minimum σ_{CRF} for each primary calibrator is sufficient to obtain similar results in improvement of the rotation parameter formal errors than when attempting that σ_{CRF} was zero for all of them. If instead the primary calibrators were observed with minimum about 250 observations each, which is similar to σ_{CRF} of about 0.22 mas, a larger decrease of 14 % is observed only for ϵ_X, while the decrease of formal errors of the other rotation parameters is 3 % and below.
- Second, the improved Gaia astrometric data according to expected future Gaia data releases was tested. Future Gaia data releases with extended observing time intervals of 5 or 10 years, will not change the orientation parameter formal errors much (3 % and below). This effect arises because they are limited by the number of counterparts and the VLBI position uncertainty. Tests showed that including five more counterparts already has a larger impact of about 10 % lower formal error for the orientation parameters. The reduced error budget of future Gaia data releases however largely impacts the formal errors of the spin, which are reduced by about 40 % for the Gaia DR based on 10 years of observation.
- Third, the impact of future observations as shown in two case studies was investigated. Adding one position measurement for 37 suitable accepted stars to "60,EDR3,GA,NM" was tested for several epochs. Additional positions in the year 2030 would result in an improvement of the spin formal error of 19 %. If instead the new positions were taken in 2023, the improvement would only be 7 %. This is to be expected because the value of the time interval between the VLBI and Gaia positions in the functional model for the spin is larger, and therefore the spin can be determined with a lower formal error. The orientation offset has a contradicting

behavior, where the improvement is 18 % for positions in 2023 and 13 % for positions in 2030. This is to be expected because the additional uncertainty in the Gaia data propagated to the VLBI epoch is smaller when the difference between VLBI and Gaia epochs is smaller. Adding a position in both 2023 and 2030 is advantageous for both parameters. The percentage improvements change only slightly for the upcoming Gaia DRs, indicating that the new observations will also be worth for the future Gaia DRs alignment verification with VLBI. Nine stars in the baseline solution of "60,EDR3,GA,NM" do not have proper motion values from VLBI. In another test scenario new estimates for proper motion were assumed for them with an uncertainty of $0.03\,\mathrm{mas\,yr^{-1}}$ based on four new positions in 2022 and 2023. The improvement in spin is 14 %. This effect of $9 \cdot 4 = 36$ additional positions is less than what would be achieved from 37 additional positions for the 37 stars in 2030, given this dataset. For comparison, the reduction in the formal error of both the orientation offset and the spin of Gaia EDR3 from the various measures done in this work are more than 40 % when looking at Table 5.15 ("41,EDR3" vs. "60,EDR3,GA,NM").

The simulations do not take into account the residual-based value Q/n, which is above one for the selected baseline solutions in Table 5.16. It seems possible that the high values of Q/n arose due to radio-optical offsets, extended structure or non-linear motion of the stars. The introduction of the new model estimates has helped to lower the single star discrepancy measure Q_i/n_i for some of the stars. It seems possible that further studies of individual stars will be fruitful in bringing more Q_i/n_i close to unity. Possible candidates are the stars where the correlation between astrometric parameters in the stellar motion model estimates is significant. If this is not possible, and these systematic errors dominate, the determination of the rotation parameters can only be improved by increasing the number of counterparts, as already suggested by Lindegren (2020a). As the scenario based on "60,EDR3,GA,NM" but excluding stars with RUWE larger 1.4 ("32,EDR3,GA,NM,RUWE1.4") showed, the selection criteria for new counterparts should be considered if possible. This conclusion also seems obvious after the discussion in Sect. 5.6.7 about the individual properties of the first rejected stars, most of which have large RUWE values. An extension of the functional model of the rotation parameter analysis by including linear accelerations for stars whenever needed should be tested in future work. This would make it possible to exclude fewer stars in order to obtain the baseline solution. Furthermore, the individual properties of the star types were not yet considered in full detail. For example, the accuracy in proper motions and parallaxes of AGB stars could be limited due to their large diameter and their variability of the radio emission Xu et al. (2019b). Thus, the inaccuracy of the reference point of the star position could be considered for single-epoch positions in future work.

The various simulations show that with improved calibrator position uncertainties, one additional absolute VLBI position for each star in the baseline solution, or precise VLBI proper motions for suitable candidates, which not yet have a VLBI proper motions, the uncertainties of the spin estimates in Cantat-Gaudin and Brandt (2021) of $2\,\mu\mathrm{as\,yr}^{-1}$ to $5\,\mu\mathrm{as\,yr}^{-1}$ (which are even subdivided into G magnitude bins of mostly 0.5 mag) are not reached. Nevertheless, the approach of Cantat-Gaudin and Brandt (2021) cannot detect the orientation offset between ICRF3 and the Gaia bright frame.

The Gaia science performance website[18] provides predictions for the standard errors of the astrometric performance of the expected Gaia DR4 for the nominal 5 year period and Gaia DR5 for the extended 10 year period, based on Gaia EDR3. For Gaia EDR3, the astrometric performance for $G < 13$ mag with a five-parameter solution is $\sigma_{\alpha*} = 14\,\mu\mathrm{as}$, $\sigma_\delta = 13\,\mu\mathrm{as}$, $\sigma_{\mu_{\alpha*}} = 18\,\mu\mathrm{as\,yr}^{-1}$, and $\sigma_{\mu_\delta} = 16\,\mu\mathrm{as\,yr}^{-1}$ from the respective data (Lindegren et al. 2021b). As introduced in Sect. 2.3.2, the predicted average uncertainties for Gaia DR4 are determined as $\sigma_{\alpha*} = 8.0\,\mu\mathrm{as}$, $\sigma_\delta = 7.0\,\mu\mathrm{as}$, $\sigma_{\mu_{\alpha*}} = 5.8\,\mu\mathrm{as\,yr}^{-1}$, and $\sigma_{\mu_\delta} = 5.0\,\mu\mathrm{as\,yr}^{-1}$. For Gaia DR5, the respective values are $\sigma_{\alpha*} = 5.6\,\mu\mathrm{as}$, $\sigma_\delta = 4.9\,\mu\mathrm{as}$, $\sigma_{\mu_{\alpha*}} = 2.0\,\mu\mathrm{as\,yr}^{-1}$, and $\sigma_{\mu_\delta} = 1.8\,\mu\mathrm{as\,yr}^{-1}$. However, due to shorter CCD integration times to limit the saturation of the bright objects, and the high impact of the actual performance of the respective Gaia DR for these G magnitudes, the performance predictions for bright stars are very uncertain.

Ideally, the uncertainties of the rotation parameter estimates in this work should match with the respective Gaia DRs uncertainty levels of the individual objects. For Gaia EDR3, the orientation offset level is about an order of magnitude larger than required and the spin level is almost reached. A look at the Table 5.23 shows that the formal errors of the orientation parameters using the method and VLBI data from this work on Gaia DR4 will still be an order of magnitude larger than required, while those of the spin will be close. Nevertheless, the Q/n most likely will worsen the uncertainties of the rotation parameters. For Gaia DR5, the method or the VLBI data need to be improved to meet the required uncertainty limit. Neither the addition of a new position for all 37 stars in the baseline solution in 2023 and 2030, nor the addition of precise proper motions for nine suitable stars without proper motions in the current data set could improve the formal errors to reach these uncertainty limits.

[18] https://www.cosmos.esa.int/web/gaia/science-performance#astrometric performance, accessed 24 October 2021.

6 Conclusions and outlook

This chapter presents the general conclusions drawn from the summary and discussion in the Sects. 4.5 and 5.8, as well as an outlook for future work.

6.1 General conclusions

Both VLBI observations at radio frequencies and Gaia observations at optical frequencies to AGN are employed to realize the ICRS. With Gaia-CRF3, ICRF3 K, and ICRF3 X/Ka, the traditional ICRF at S/X frequencies (ICRF3 S/X) can be compared to other internationally recognized CRFs with comparable precision for the first time in the history of ICRFs. At the same time, by design the Gaia data releases require an alignment to the ICRS using the radio CRFs due to their degrees of freedom.

In this work, the ICRF3 S/X, the ICRF3 K, and the ICRF3 X/Ka were studied and compared to Gaia-CRF3 as part of Gaia EDR3 as well as to its predecessor Gaia DR2. The AGN in ICRF3 are optically faint as determined from the Gaia G magnitudes. The evaluation of the counterparts between the Gaia DRs and the ICRF3 showed that the differences of the position offset directions tend to be aligned in the same directions as expected from the chromatic model of AGN. This is although the various CRFs are based on different data time spans and the observed positions could change with time. Restricting the minimum number of VLBI observations did not have an effect on these results. Furthermore, all sources with larger normalized differences between the radio CRFs and ICRF3 S/X, Gaia DR2, or Gaia EDR3 have large CARMS values, meaning that they show a significant minimum level of source structure at S/X bands.

The systematic global differences provide insight into possible deformations of the CRFs. A large deformation was clearly shown for ICRF3 X/Ka towards all other CRFs. For the alignment of the various CRFs, the rule "the more, the better" showed validity in terms of more counterparts providing smaller uncertainties, in general less scatter of the iterative results, and often smaller deformation parameters. Using different subsets of counterparts yielded different results of the deformation parameters, but it is likely that this is largely due to the geometric distribution of the counterparts. Since the position differences of a source in the various CRFs are assumed to be in random directions across

the sky, the systematic global differences are not affected by larger position offsets due to source structure for instance.

The VLBI-based CRF with observations restricted to the Gaia DR2 time interval failed to provide better alignment or position smaller differences with Gaia DR2. The largest caveat was that the position uncertainties became larger due to the much smaller number of VLBI observations and that only about 50 % of the sources in ICRF3 S/X were detected during that time interval.

The optically bright fraction of Gaia DRs was compared using phase-referencing VLBI observations of optically bright radio stars relative to radio bright calibrators in ICRF3 S/X. It was shown that it is crucial to homogenize data from the literature by relating all star positions to their respective calibrator positions in ICRF3 S/X and by considering a realistic error budget for the star positions. This is only possible if astrometric studies provide all relevant meta information in the respective publications. The main components of the error budget for the absolute star position are the position uncertainty of the calibrator in ICRF3 S/X, the delay model error, and the difference of the primary calibrator's position as determined from group or phase delays. The consistent treatment of the Galactocentric acceleration for both the VLBI and Gaia data sets had no impact at the current accuracy level.

New one-epoch positions were added to the VLBI dataset from the literature, and improved stellar motion models were created for the stars whenever possible. It is likely that future astrometric missions will be able to benefit even more than Gaia from these data, since the time span between the first and last VLBI observations will then be larger and proper motions and long-term accelerations can be more accurately determined.

The number of optically bright counterparts is still very small. Therefore, it was not possible to determine higher-order systematic deformations between the bright Gaia frame and ICRF3 S/X. Due to the same reason, it was also not possible to determine a variation in the orientation of the bright frame within $G \leq 13\,\mathrm{mag}$, the existence of which was shown by Cantat-Gaudin and Brandt (2021). Many additional VLBI observations would be needed to achieve an accuracy of the spin determination close to their results based only on the readily available Gaia data. This is especially true should their initial indications of the need for color correction be substantiated. However, the method of Cantat-Gaudin and Brandt (2021) cannot provide an estimate for the orientation offset. At this stage, this is only possible using VLBI products.

Clearly, reducing the largest error budget items of the VLBI phase-referencing observations would help to determine the rotation parameters more precisely. The results in this work nevertheless already provide spin parameters as accurate as the lowest estimate for the uncertainty of the method for the spin correction applied during Gaia EDR3 process-

ing in Lindegren et al. (2021b). In the absence of suitable data, no orientation offset was even corrected for the bright portion of Gaia EDR3. The orientation offset of future Gaia DRs can be determined using the VLBI data provided in this work.

When all available counterparts are employed, the alignment between ICRF3 S/X and the optically faint fraction of Gaia DR2 results in smaller estimates of rotation parameters and other deformation parameters than when a smaller subset is used. As a result, the estimates of the rotation parameters for the bright frame might also be larger than they would be if more counterparts were available.

There are no counterparts for the G magnitude range between 13 mag and 16 mag, so the alignment could not be tested for this G magnitude range.

The validation of the alignment of the ICRFs, including possible deformations or temporal dependencies, is critical for all studies using these data as a reference. Otherwise, the user might not recognize possible systematic shifts when comparing the individual positions of a source in the ICRFs or with other astrometric products. Also, users need to be reminded of the differences in the mean positions associated with the nature of the sources and a different data acquisition, a different observation period, and a different number of observations of each ICRFs.

At the end, when it is a matter of comparing individual counterparts, the alignment between the individual CRFs is not much better than the differences of the astrometric parameters of the individual sources which cannot be explained (cf. Brosche and Schuh (1999)). This applies, for example, to very close unresolved binaries or to AGN with multiple components if their components cannot be unambiguously identified due to lack of resolution or observational data.

6.2 Future prospects and recommendations

Extending the parameterization for the model of stellar motion in the rotation parameter analysis for stars with known linear accelerations or orbits might as well help when acceleration terms, orbits, or position time series become available in future Gaia DRs. Then, also the Gaia data can get propagated to the VLBI epoch properly for the relevant stars. VLBI data of the more complicated trajectories might help to verify this additional Gaia data product. At the present stage, the discrepancies between VLBI and Gaia astrometric parameters for the individual star are mostly larger than the residual systematic global rotations.Some of them can be explained by expected radio-optical offsets due to the star's physics and structure (which can also be variable), by multiplicity, by lack of parameterization of a more complex trajectory than the 5-parameter model, or sparse observations. For the other stars a re-observation is beneficial to find out more about their

trajectory. Cross-checking with the HIPPARCOS-Gaia Catalog of Accelerations (Brandt 2021) can help to identify any stars that could show signs of non-linear proper motion in the future Gaia DRs.

The new model estimates determined in this work are significantly correlated for some stars. Therefore, a few additional geometrically sensitive observations are needed to decorrelate the parameters. Future work should test whether including the correlations of the astrometric model estimates of the stars would improve the rotation parameter analysis. Improved on-source observation time can be determined using the peak intensities as determined in previous observations.

Furthermore, all calibrators should get included in the next radio ICRF and the impact of calibrator apparent proper motion on the rotation parameter analysis can be studied. The finding in Sect. 5.8.3 suggests that searching for more counterparts is an additional task that should be done in parallel to improving the data for known stars. New counterparts can also help to identify outlier counterparts.

Due to these reasons, more dedicated observations with EVN (125 hours, EL065/E22B005 and EL066/E22B006) were applied for and granted. The aim is to re-observe all suitable stars in this work in one epoch, to re-observe all suitable stars without proper motion and parallax information in this work in enough epochs to determine these parameters, and to search for a few new counterparts at radio frequencies using the strategy in proposal B of this work.

Simulations for new observations with the LBA in project P583 observed in February 2022 showed, that stars with α perpendicular to the Y axis improve the formal error of the rotation around Y most, as expected.

Nevertheless, the analysis in Cantat-Gaudin and Brandt (2021) showed that the alignment of the bright Gaia frame itself is magnitude dependent and thus, if it is aimed to verify this effect with the help of VLBI, more counterparts with various G magnitudes are needed. Currently, there are only 15 counterparts with $G > 10.5$ mag, so this sample needs to be expanded. Furthermore, the G magnitude range 13 to 16 should also get verified and only very few stars in this magnitude range are known to be observed by VLBI up to date.

A large error budget item in the determination of the absolute position of the star in ICRF3 from phase-referencing is the position difference of the calibrator as determined from VLBI group delays or phase delays in the presence of core-shift. This suggests to investigate on this topic individually for each calibrator, starting with the ones that are least compact. Furthermore, the atmospheric error budget can be improved by using advanced atmosphere calibration observations and analysis strategies. The Galactocentric acceleration should be handled consistently (magnitude and direction) for both VLBI and Gaia CRFs.

The new VGOS observation style requires the modeling of source structure of the four frequency bands (Xu et al. 2020; Xu et al. 2022). For alignment of the radio positions across frequencies for VGOS and for the legacy VLBI, observations of the planned co-location satellite GENESIS could be helpful (Delva et al. 2022). It could serve as a phase calibrator and as a calibrator for multi-frequency observations.

It is important to know more about the possible rotation of the Gaia frame because any successor astrometric probe, such as GaiaNIR (Hobbs et al. 2016), will not provide the next CRF at optical frequencies for several decades, assuming the same time difference between the launch of Gaia and that of its predecessor, the HIPPARCOS spacecraft.

Bibliography

Albert, J., Aliu, E., Anderhub, H., Antoranz, P., Armada, A., Asensio, M., Baixeras, C., Barrio, J. A., Bartelt, M., Bartko, H., Bastieri, D., Bavikadi, S. R., Bednarek, W., Berger, K., Bigongiari, C., Biland, A., Bisesi, E., Bock, R. K., Bordas, P., Bosch-Ramon, V., Bretz, T., Britvitch, I., Camara, M., Carmona, E., Chilingarian, A., Ciprini, S., Coarasa, J. A., Commichau, S., Contreras, J. L., Cortina, J., Curtef, V., Danielyan, V., Dazzi, F., Angelis, A. D., de los Reyes, R., Lotto, B. D., Domingo-Santamaria, E., Dorner, D., Doro, M., Errando, M., Fagiolini, M., Ferenc, D., Fernandez, E., Firpo, R., Flix, J., Fonseca, M. V., Font, L., Fuchs, M., Galante, N., Garczarczyk, M., Gaug, M., Giller, M., Goebel, F., Hakobyan, D., Hayashida, M., Hengstebeck, T., Höhne, D., Hose, J., Hsu, C. C., Isar, P. G., Jacon, P., Kalekin, O., Kosyra, R., Kranich, D., Laatiaoui, M., Laille, A., Lenisa, T., Liebing, P., Lindfors, E., Lombardi, S., Longo, F., Lopez, J., Lopez, M., Lorenz, E., Lucarelli, F., Majumdar, P., Maneva, G., Mannheim, K., Mansutti, O., Mariotti, M., Martinez, M., Mase, K., Mazin, D., Merck, C., Meucci, M., Meyer, M., Miranda, J. M., Mirzoyan, R., Mizobuchi, S., Moralejo, A., Nilsson, K., na Wilhelmi, E. O., na, R. O., Otte, N., Oya, I., Paneque, D., Paoletti, R., Paredes, J. M., Pasanen, M., Pascoli, D., Pauss, F., Pavel, N., Pegna, R., Persic, M., Peruzzo, L., Piccioli, A., Poller, M., Pooley, G., Prandini, E., Raymers, A., Rhode, W., Ribo, M., Rico, J., Riegel, B., Rissi, M., Robert, A., Romero, G. E., Rügamer, S., Saggion, A., Sanchez, A., Sartori, P., Scalzotto, V., Scapin, V., Schmitt, R., Schweizer, T., Shayduk, M., Shinozaki, K., Shore, S. N., Sidro, N., Sillanpää, A., Sobczynska, D., Stamerra, A., Stark, L. S., Takalo, L., Temnikov, P., Tescaro, D., Teshima, M., Tonello, N., Torres, A., Torres, D. F., Turini, N., Vankov, H., Vitale, V., Wagner, R. M., Wibig, T., Wittek, W., Zanin, R., and Zapatero, J. (2006). Variable very-high-energy gamma-ray emission from the microquasar LS I +61 303. *Science*, 312(5781):1771–1773.

Albert, J., Aliu, E., Anderhub, H., Antoranz, P., Backes, M., Baixeras, C., Barrio, J. A., Bartko, H., Bastieri, D., Becker, J., Bednarek, W., Berger, K., Bigongiari, C., Biland, A., Bock, R., Bonnoli, G., Bordas, P., Bosch-Ramon, V., Bretz, T., and Diamond, a. (2008). Multiwavelength (radio, X-ray, and γ-ray) observations of the γ-ray binary LS I +61 303. *The Astrophysical Journal*, 684:1351.

Alef, W. (1989). *Introduction to Phase-Reference Mapping*, pages 261–274. Springer Netherlands, Dordrecht.

Altamimi, Z., Rebischung, P., Métivier, L., and Collilieux, X. (2016). ITRF2014: A new release of the International Terrestrial Reference Frame modeling nonlinear station motions. *Journal of Geophysical Research (Solid Earth)*, 121(8):6109–6131.

Andersen, J., editor (1999). *Chapter IV: Resolutions of the General Assembly.* Proceedings of the 23rd General Assembly. Cambridge University Press.

Anderson, J. M. and Xu, M. H. (2018). Source structure and measurement noise are as important as all other residual sources in geodetic VLBI combined. *Journal of Geophysical Research: Solid Earth*, 123(11):10,162–10,190.

Antonucci, R. (1993). Unified models for active galactic nuclei and quasars. *ARA&A*, 31:473–521.

Arenou, F., Luri, X., Babusiaux, C., Fabricius, C., Helmi, A., Muraveva, T., Robin, A. C., Spoto, F., Vallenari, A., Antoja, T., Cantat-Gaudin, T., Jordi, C., Leclerc, N., Reylé, C., Romero-Gómez, M., Shih, I.-C., Soria, S., Barache, C., Bossini, D., Bragaglia, A., Breddels, M. A., Fabrizio, M., Lambert, S., Marrese, P. M., Massari, D., Moitinho, A., Robichon, N., Ruiz-Dern, L., Sordo, R., Veljanoski, J., Eyer, L., Jasniewicz, G., Pancino, E., Soubiran, C., Spagna, A., Tanga, P., Turon, C., and Zurbach, C. (2018). Gaia Data Release 2 - Catalogue validation. *A&A*, 616:A17.

Arias, E. F., Charlot, P., Feissel, M., and Lestrade, J. F. (1995). The extragalactic reference system of the International Earth Rotation Service, ICRS. *A&A*, 303:604–608.

Arias, E. F., Cionco, R. G., Orellana, R. B., and Vucetich, H. (2000). A comparison of the SAO-Hipparcos reference frames. *A&A*, 359:1195–1200.

Asaki, Y., Deguchi, S., Imai, H., Hachisuka, K., Miyoshi, M., and Honma, M. (2010). Distance and proper motion measurement of the red supergiant, S Persei, with VLBI H_2O maser astrometry. *ApJ*, 721(1):267–277.

Barsony, M., Koresko, C., and Matthews, K. (2003). A search for close binaries in the ρ Ophiuchi star-forming region. *ApJ*, 591(2):1064–1074.

Bartel, N., Bietenholz, M. F., Lebach, D. E., Lederman, J. I., Petrov, L., Ransom, R. R., Ratner, M. I., and Shapiro, I. I. (2012). VLBI for Gravity Probe B. III. A limit on the proper motion of the "core" of the quasar 3C 454.3. *The Astrophysical Journal Supplement Series*, 201(1):3.

Bartel, N., Bietenholz, M. F., Lebach, D. E., Ransom, R. R., Ratner, M. I., and Shapiro, I. I. (2015). VLBI for Gravity Probe B: The guide star, IM Pegasi. *Classical and Quantum Gravity*, 32(22):224021.

Beasley, A. J. and Conway, J. E. (1995). Vlbi phase-referencing. In Zensus, A., Diamond, P., and Napier, P., editors, *Proceedings of the NRAO VLBA Summer School*, volume 82 of *ASP Conference Series*, page 327.

Beasley, A. J., Conway, J. E., Diamond, P. J., Cotton, W. D., and Vermeulen, R. C. (1994). VLBA phase-referencing. In Robertson, J. G. and Tango, W. J., editors, *Very High Angular Resolution Imaging*, pages 105–108, Dordrecht. Springer Netherlands.

Benaglia, P. (2010). Non-thermal radio emission from OB stars: An observer's view. In Martí, J., Luque-Escamilla, P. L., and Combi, J. A., editors, *High Energy Phenomena in Massive Stars*, volume 422 of *Astronomical Society of the Pacific Conference Series*, page 111.

Bizouard, C., Lambert, S., Gattano, C., Becker, O., and Richard, J.-Y. (2019). The IERS EOP 14C04 solution for Earth orientation parameters consistent with ITRF 2014. *Journal of Geodesy*, 93(5):621–633.

Blomme, R., De Becker, M., Runacres, M. C., Van Loo, S., and Setia Gunawan, D. Y. A. (2007). Non-thermal radio emission from O-type stars - II. HD 167971. *A&A*, 464(2):701–708.

Boboltz, D. A., Fey, A. L., Johnston, K. J., Claussen, M. J., de Vegt, C., Zacharias, N., and Gaume, R. A. (2003). Astrometric positions and proper motions of 19 radio stars. *The Astronomical Journal*, 126(1):484–493.

Boboltz, D. A., Fey, A. L., Puatua, W. K., Zacharias, N., Claussen, M. J., Johnston, K. J., and Gaume, R. A. (2007). Very Large Array plus Pie Town astrometry of 46 radio stars. *AJ*, 133(3):906–916.

Bobylev, V. V. (2019). Parameters of the link between the optical and radio frames from Gaia DR2 data and VLBI measurements. *Astronomy Letters*, 45(1):10–19.

Boden, A. F., Torres, G., Sargent, A. I., Akeson, R. L., Carpenter, J. M., Boboltz, D. A., Massi, M., Ghez, A. M., Latham, D. W., Johnston, K. J., Menten, K. M., and Ros, E. (2007). Dynamical masses for pre-main-sequence stars: A preliminary physical orbit for V773 Tau A. *ApJ*, 670(2):1214–1224.

Boehm, J., Werl, B., and Schuh, H. (2006). Troposphere mapping functions for GPS and very long baseline interferometry from European Centre for Medium-Range Weather Forecasts operational analysis data. *Journal of Geophysical Research: Solid Earth*, 111(B2).

Böhm, J., Urquhart, L., Steigenberger, P., Heinkelmann, R., Nafisi, V., and Schuh, H. (2013). A priori gradients in the analysis of space geodetic observations. In Altamimi, Z. and Collilieux, X., editors, *Reference Frames for Applications in Geosciences*, pages 105–109, Berlin, Heidelberg. Springer Berlin Heidelberg.

Bourda, G., Charlot, P., and Le Campion, J.-F. (2008). Astrometric suitability of optically-bright ICRF sources for the alignment with the future Gaia celestial reference frame. *A&A*, 490(1):403–408.

Brandt, T. D. (2018). The Hipparcos – Gaia Catalog of Accelerations. *ApJS*, 239(2):31.

Brandt, T. D. (2021). The Hipparcos – Gaia Catalog of Accelerations: Gaia EDR3 Edition. *The Astrophysical Journal Supplement Series*, 254(2):42.

Britzen, S., Witzel, A., Krichbaum, T. P., Beckert, T., Campbell, R. M., Schalinski, C., and Campbell, J. (2005). The radio structure of S5 1803+784. *MNRAS*, 362(3):966–974.

Brosche, P. and Schuh, H. (1999). Neue Entwicklungen in der Astrometrie und ihre Bedeutung für die Geodäsie. *Zeitschrift für Vermessungswesen*, 124(11):343–350.

Brown, A. G. A. (2017). The Gaia sky: version 1.0. *Proceedings of the International Astronomical Union*, 12(S330):13–22.

Brunthaler, A., Reid, M. J., and Falcke, H. (2005). Atmosphere-corrected phase-referencing. In Romney, J. and Reid, M., editors, *Future Directions in High Resolution Astronomy*, volume 340 of *Astronomical Society of the Pacific Conference Series*, page 455.

Cantat-Gaudin, T. and Brandt, T. D. (2021). Characterizing and correcting the proper motion bias of the bright Gaia EDR3 sources. *A&A*, 649:A124.

Capitaine, N., Wallace, P. T., and Chapront, J. (2003). Expressions for IAU 2000 precession quantities. *A&A*, 412:567–586.

Carlos, R. C. and Popper, D. M. (1971). HD 21242, a spectroscopic binary with H and K emission. *PASP*, 83(494):504.

Cassinelli, J. P., Cohen, D. H., Macfarlane, J. J., Sanders, W. T., and Welsh, B. Y. (1994). X-ray emission from near–main-sequence B stars. *ApJ*, 421:705.

Charlot, P. (1990). Radio-source structure in astrometric and geodetic very long baseline interferometry. *The Astronomical Journal*, 99:1309–1326.

Charlot, P., Jacobs, C. S., Gordon, D., Lambert, S., de Witt, A., Böhm, J., Fey, A. L., Heinkelmann, R., Skurikhina, E., Titov, O., Arias, E. F., Bolotin, S., Bourda, G., Ma, C., Malkin, Z., Nothnagel, A., Mayer, D., MacMillan, D. S., Nilsson, T., and Gaume, R. (2020). The third realization of the International Celestial Reference Frame by very long baseline interferometry. *A&A*, 644(A159):28.

Clark, B. G. (1980). An efficient implementation of the algorithm 'CLEAN'. *A&A*, 89(3):377.

Condon, J. J. (1997). Errors in elliptical gaussian FITS. *PASP*, 109:166–172.

Condon, J. J., Cotton, W. D., Greisen, E. W., Yin, Q. F., Perley, R. A., Taylor, G. B., and Broderick, J. J. (1998). The NRAO VLA Sky Survey. *AJ*, 115(5):1693–1716.

De Becker, M., Sana, H., Absil, O., Le Bouquin, J.-B., and Blomme, R. (2012). The long-period eccentric orbit of the particle accelerator HD 167971 revealed by long baseline interferometry. *Monthly Notices of the Royal Astronomical Society*, 423(3):2711–2717.

de Witt, A., Charlot, P., Gordon, D., and Jacobs, C. S. (2022). Overview and status of the International Celestial Reference Frame as realized by VLBI. *Universe*, 8(7).

Delva, P., Altamimi, Z., Blazquez, A., Blossfeld, M., Böhm, J., Bonnefond, P., Boy, J.-P., Bruinsma, S., Bury, G., Chatzinikos, M., Couhert, A., Courde, C., Dach, R., Dehant, V., Dell'Agnello, S., Elgered, G., Enderle, W., Exertier, P., Glaser, S., Haas, R., Huang, W., Hugentobler, U., Jäggi, A., Karatekin, O., Lemoine, F. G., Le Poncin-Lafitte, C., Lunz, S., Männel, B., Mercier, F., Métivier, L., Meyssignac, B., Müller, J., Nothnagel, A., Perosanz, F., Rietbroek, R., Rothacher, M., Sert, H., Sosnica, K., Testani, P., Ventura-Traveset, J., Wautelet, G., and Zajdel, R. (2022). GENESIS: Co-location of Geodetic Techniques in Space. *arXiv e-prints*, page arXiv:2209.15298.

Desai, S. D. (2002). Observing the pole tide with satellite altimetry. *Journal of Geophysical Research: Oceans*, 107(C11):7–1–7–13.

Dick, W. R. and Thaller, D. e. (2018). *IERS annual report 2017*. International Earth Rotation and Reference Systems Service, Central Bureau. Verlag des Bundesamts für Kartographie und Geodäsie, Frankfurt am Main.

DIN Deutsches Institut für Normung e.V. (2010). DIN ISO 18709-4:2010-09, Begriffe, Kurzzeichen und Formelzeichen in der Geodäsie - Teil 4: Ausgleichungsrechnung und Statistik. *Beuth Verlag GmbH*.

Eaton, J. A. and Henry, G. W. (2007). The distribution of activity on the RS CVn-type star SZ Piscium. *PASP*, 119(853):259–273.

Egbert, G. D. and Erofeeva, S. Y. (2002). Efficient inverse modeling of barotropic ocean tides. *Journal of Atmospheric and Oceanic Technology*, 19(2):183 – 204.

ESA, editor (1997). *The HIPPARCOS and TYCHO catalogues. Astrometric and photometric star catalogues derived from the ESA HIPPARCOS Space Astrometry Mission*, volume 1200 of *ESA Special Publication*.

Eubanks, M., Treuhaft, R., Thomas, J., Hellings, R., Soffel, M., Groten, E., Fukushima, T., and Zhu, S. (1991). *Proceedings of the U.S. Naval Observatory Workshop on Relativistic Models for use in Space Geodesy*. U.S. Naval Observatory.

Fabricius, C., Luri, X., Arenou, F., Babusiaux, C., Helmi, A., Muraveva, T., Reylé, C., Spoto, F., Vallenari, A., Antoja, T., Balbinot, E., Barache, C., Bauchet, N., Bragaglia, A., Busonero, D., Cantat-Gaudin, T., Carrasco, J. M., Diakité, S., Fabrizio, M., Figueras, F., Garcia-Gutierrez, A., Garofalo, A., Jordi, C., Kervella, P., Khanna, S., Leclerc, N., Licata, E., Lambert, S., Marrese, P. M., Masip, A., Ramos, P., Robichon, N., Robin, A. C., Romero-Gómez, M., Rubele, S., and Weiler, M. (2021). Gaia Early Data Release 3 - Catalogue validation. *A&A*, 649:A5.

Feissel, M. and Mignard, F. (1998). The adoption of ICRS on 1 January 1998: meaning and consequences. *A&A*, 331:L33–L36.

Feissel-Vernier, M., Ma, C., Gontier, A. M., and Barache, C. (2006). Analysis strategy issues for the maintenance of the ICRF axes. *A&A*, 452(3):1107–1112.

Fekel, F. C., J. (1983). Spectroscopy of V711 Tauri (= HR 1099) : fundamental properties and evidence for starspots. *ApJ*, 268:274–281.

Fekel, F. C., Strassmeier, K. G., Weber, M., and Washuettl, A. (1999). Orbital elements and physical parameters of ten chromospherically active binary stars. *Astron. Astrophys. Suppl. Ser.*, 137(2):369–383.

Fey, A. L. and Charlot, P. (1997). VLBA observations of radio reference frame sources. II. astrometric suitability based on observed structure. *ApJS*, 111(1):95–142.

Fey, A. L., Gordon, D., Jacobs, C. S., Ma, C., Gaume, R. A., Arias, E. F., Bianco, G., Boboltz, D. A., Böckmann, S., Bolotin, S., Charlot, P., Collioud, A., Engelhardt, G., Gipson, J., Gontier, A. M., Heinkelmann, R., Kurdubov, S., Lambert, S., Lytvyn, S., MacMillan, D. S., Malkin, Z., Nothnagel, A., Ojha, R., Skurikhina, E., Sokolova, J., Souchay, J., Sovers, O. J., Tesmer, V., Titov, O., Wang, G., and Zharov, V. (2015). The second realization of the International Celestial Reference Frame by very long baseline interferometry. *AJ*, 150(2):58.

Fischler, M. A. and Bolles, R. C. (1981). Random sample consensus: A paradigm for model fitting with applications to image analysis and automated catography. *Communications of the ACM*, 24(6):381–395.

Folkner, W. M., Williams, J. G., and Boggs, D. H. (2009). The Planetary and Lunar Ephemeris DE 421. *IPN Progress Report*, 178(42).

Fomalont, E., Johnston, K., Fey, A., Boboltz, D., Oyama, T., and Honma, M. (2011). The position/structure stability of four ICRF2 sources. *AJ*, 141(3):91.

Fomalont, E. and Kogan, L. (2005). ATMCA: phase referencing with more than one calibrator. *AIPS Memo 111, NRAO.*

Fomalont, E. B. (1999). Lecture 14: Image Analysis. In Taylor, G. B., Carilli, C. L., and Perley, R. A., editors, *Synthesis Imaging in Radio Astronomy II*, volume 180 of *Astronomical Society of the Pacific Conference Series.*

Fricke, W., Schwan, H., Lederle, T., Bastian, U., Bien, R., Burkhardt, G., Du Mont, B., Hering, R., Jährling, R., Jahreiß, H., Röser, S., Schwerdtfeger, H.-M., and Walter, H. G. (1988). Fifth fundamental catalogue (FK5). Part 1: The basic fundamental stars. In *Veröffentlichung No. 32.* Astronomisches Rechen-Insitut Heidelberg.

Gaia Collaboration, Brown, A. G. A., Vallenari, A., Prusti, T. et al.and de Bruijne, J. H. J., Babusiaux, C., Biermann, M., Creevey, O. L., Evans, D. W., Eyer, L., Hutton, A., Jansen, F., Jordi, C., Klioner, S. A., Lammers, U., Lindegren, L., Luri, X., Mignard, F., Panem, C., Pourbaix, D., Randich, S., Sartoretti, P., Soubiran, C., Walton, N. A., Arenou, F., Bailer-Jones, C. A. L., Bastian, U., Cropper, M., Drimmel, R., Katz, D., Lattanzi, M. G., van Leeuwen, F., Bakker, J., Cacciari, C., Castañeda, J., De Angeli, F., Ducourant, C., Fabricius, C., Fouesneau, M., Frémat, Y., Guerra, R., Guerrier, A., Guiraud, J., Jean-Antoine Piccolo, A., Masana, E., Messineo, R., Mowlavi, N., Nicolas, C., Nienartowicz, K., Pailler, F., Panuzzo, P., Riclet, F., Roux, W., Seabroke, G. M., Sordo, R., Tanga, P., Thévenin, F., Gracia-Abril, G., Portell, J., Teyssier, D., Altmann, M., Andrae, R., Bellas-Velidis, I., Benson, K., Berthier, J., Blomme, R., Brugaletta, E., Burgess, P. W., Busso, G., Carry, B., Cellino, A., Cheek, N., Clementini, G., Damerdji, Y., Davidson, M., Delchambre, L., Dell´Oro, A., Fernández-Hernández, J., Galluccio, L., García-Lario, P., Garcia-Reinaldos, M., González-Núñez, J., Gosset, E., Haigron, R., Halbwachs, J.-L., Hambly, N. C., Harrison, D. L., Hatzidimitriou, D., Heiter, U., Hernández, J., Hestroffer, D., Hodgkin, S. T., Holl, B., Janßen, K., Jevardat de Fombelle, G., Jordan, S., Krone-Martins, A., Lanzafame, A. C., Löffler, W., Lorca, A., Manteiga, M., Marchal, O., Marrese, P. M., Moitinho, A., Mora, A., Muinonen, K., Osborne, P., Pancino, E., Pauwels, T., Petit, J.-M., Recio-Blanco, A., Richards, P. J., Riello, M., Rimoldini, L., Robin, A. C., Roegiers, T., Rybizki, J., Sarro, L. M., Siopis, C., Smith, M., Sozzetti, A., Ulla, A., Utrilla, E., van Leeuwen, M., van Reeven, W., Abbas, U., Abreu Aramburu, A., Accart, S., Aerts, C., Aguado, J. J., Ajaj, M., Altavilla, G., Álvarez, M. A., Álvarez Cid-Fuentes, J., Alves, J., Anderson, R. I., Anglada Varela, E., Antoja, T., Audard, M., Baines, D., Baker, S. G., Balaguer-Núñez, L., Balbinot, E., Balog, Z., Barache, C., Barbato, D., Barros, M., Barstow, M. A., Bartolomé, S., Bassilana, J.-L., Bauchet, N., Baudesson-Stella, A., Becciani, U., Bellazzini, M., Bernet,

M., Bertone, S., Bianchi, L., Blanco-Cuaresma, S., Boch, T., Bombrun, A., Bossini, D., Bouquillon, S., Bragaglia, A., Bramante, L., Breedt, E., Bressan, A., Brouillet, N., Bucciarelli, B., Burlacu, A., Busonero, D., Butkevich, A. G., Buzzi, R., Caffau, E., Cancelliere, R., Cánovas, H., Cantat-Gaudin, T., Carballo, R., Carlucci, T., Carnerero, M. I, Carrasco, J. M., Casamiquela, L., Castellani, M., Castro-Ginard, A., Castro Sampol, P., Chaoul, L., Charlot, P., Chemin, L., Chiavassa, A., Cioni, M.-R. L., Comoretto, G., Cooper, W. J., Cornez, T., Cowell, S., Crifo, F., Crosta, M., Crowley, C., Dafonte, C., Dapergolas, A., David, M., David, P., de Laverny, P., De Luise, F., De March, R., De Ridder, J., de Souza, R., de Teodoro, P., de Torres, A., del Peloso, E. F., del Pozo, E., Delbo, M., Delgado, A., Delgado, H. E., Delisle, J.-B., Di Matteo, P., Diakite, S., Diener, C., Distefano, E., Dolding, C., Eappachen, D., Edvardsson, B., Enke, H., Esquej, P., Fabre, C., Fabrizio, M., Faigler, S., Fedorets, G., Fernique, P., Fienga, A., Figueras, F., Fouron, C., Fragkoudi, F., Fraile, E., Franke, F., Gai, M., Garabato, D., Garcia-Gutierrez, A., García-Torres, M., Garofalo, A., Gavras, P., Gerlach, E., Geyer, R., Giacobbe, P., Gilmore, G., Girona, S., Giuffrida, G., Gomel, R., Gomez, A., Gonzalez-Santamaria, I., González-Vidal, J. J., Granvik, M., Gutiérrez-Sánchez, R., Guy, L. P., Hauser, M., Haywood, M., Helmi, A., Hidalgo, S. L., Hilger, T., Hladczuk, N., Hobbs, D., Holland, G., Huckle, H. E., Jasniewicz, G., Jonker, P. G., Juaristi Campillo, J., Julbe, F., Karbevska, L., Kervella, P., Khanna, S., Kochoska, A., Kontizas, M., Kordopatis, G., Korn, A. J., Kostrzewa-Rutkowska, Z., Kruszy´nska, K., Lambert, S., Lanza, A. F., Lasne, Y., Le Campion, J.-F., Le Fustec, Y., Lebreton, Y., Lebzelter, T., Leccia, S., Leclerc, N., Lecoeur-Taibi, I., Liao, S., Licata, E., Lindstrøm, E. P., Lister, T. A., Livanou, E., Lobel, A., Madrero Pardo, P., Managau, S., Mann, R. G., Marchant, J. M., Marconi, M., Marcos Santos, M. M. S., Marinoni, S., Marocco, F., Marshall, D. J., Martin Polo, L., Martín-Fleitas, J. M., Masip, A., Massari, D., Mastrobuono-Battisti, A., Mazeh, T., McMillan, P. J., Messina, S., Michalik, D., Millar, N. R., Mints, A., Molina, D., Molinaro, R., Molnár, L., Montegriffo, P., Mor, R., Morbidelli, R., Morel, T., Morris, D., Mulone, A. F., Munoz, D., Muraveva, T., Murphy, C. P., Musella, I., Noval, L., Ordénovic, C., Orrù, G., Osinde, J., Pagani, C., Pagano, I., Palaversa, L., Palicio, P. A., Panahi, A., Pawlak, M., Peñalosa Esteller, X., Penttilä, A., Piersimoni, A. M., Pineau, F.-X., Plachy, E., Plum, G., Poggio, E., Poretti, E., Poujoulet, E., Prsa, A., Pulone, L., Racero, E., Ragaini, S., Rainer, M., Raiteri, C. M., Rambaux, N., Ramos, P., Ramos-Lerate, M., Re Fiorentin, P., Regibo, S., Reylé, C., Ripepi, V., Riva, A., Rixon, G., Robichon, N., Robin, C., Roelens, M., Rohrbasser, L., Romero-Gómez, M., Rowell, N., Royer, F., Rybicki, K. A., Sadowski, G., Sagristà Sellés, A., Sahlmann, J., Salgado, J., Salguero, E., Samaras, N., Sanchez Gimenez, V., Sanna, N., Santoveña, R., Sarasso, M., Schultheis, M., Sciacca, E., Segol, M., Segovia, J. C., Ségransan, D., Semeux, D., Shahaf, S., Siddiqui, H. I., Siebert, A., Siltala, L., Slezak, E., Smart, R. L., Solano, E., Solitro, F., Souami, D., Souchay, J., Spagna, A., Spoto, F., Steele, I. A., Steidelmüller, H., Stephenson, C. A., Süveges, M., Szabados, L., Szegedi-Elek, E., Taris, F., Tauran, G., Taylor, M. B., Teixeira, R., Thuillot, W., Tonello, N., Torra, F., Torra, J., Turon, C., Unger, N., Vaillant, M., van Dillen, E., Vanel, O., Vecchiato, A., Viala, Y., Vicente, D., Voutsinas, S., Weiler, M., Wevers, T., Wyrzykowski, L., Yoldas, A., Yvard, P., Zhao, H., Zorec, J., Zucker, S., Zurbach, C., and Zwitter, T. (2021a). Gaia Early Data Release 3 - Summary of the contents and survey properties. *A&A*, 649:A1.

Gaia Collaboration, Klioner, S. A., Lindegren, L., Mignard, F., J., H., Ramos-Lerate, M., Bastian, U., Biermann, M., Bombrun, A., de Torres, A., Gerlach, E., Geyer, R., Hilger, T., Hobbs, D., Lammers, U. L., McMillan, P. J., Steidelmüller, H., Teyssier, D., Raiteri, C. M., Bartolomé, S., Bernet, M., Castañeda, J., Clotet, M., Davidson, M., Fabricius, C., Torres, N. G., González-Vidal, J. J., Portell, J., Rowell, N., Torra, F., Torra, J., Brown, A. G. A., Vallenari, A., Prusti, T., de Bruijne, J. H. J., Arenou, F., Babusiaux, C., Creevey, O. L., Ducourant, C., Evans, D. W., Eyer, L., Guerra, R., Hutton, A., Jordi, C., Luri, X., Panem, C., Pourbaix, D., Randich, S., Sartoretti, P., Soubiran, C., Tanga, P., Walton, N. A., Bailer-Jones, C. A. L., Drimmel, R., Jansen, F., Katz, D., Lattanzi, M. G., van Leeuwen, F.,

Bakker, J., Cacciari, C., De Angeli, F., Fouesneau, M., Frémat, Y., Galluccio, L., Guerrier, A., Heiter, U., Masana, E., Messineo, R., Mowlavi, N., Nicolas, C., Nienartowicz, K., Pailler, F., Panuzzo, P., Riclet, F., Roux, W., Seabroke, G. M., Sordo, R., Thévenin, F., Gracia-Abril, G., Altmann, M., Andrae, R., Audard, M., Bellas-Velidis, I., Benson, K., Berthier, J., Blomme, R., Burgess, P. W., Busonero, D., Busso, G., Cánovas, H., Carry, B., Cellino, A., Cheek, N., Clementini, G., Damerdji, Y., de Teodoro, P., Campos, M. N., Delchambre, L., Dell'Oro, A., Esquej, P., Fernández-Hernández, J., Fraile, E., Garabato, D., García-Lario, P., Gosset, E., Haigron, R., Halbwachs, J. L., Hambly, N. C., Harrison, D. L., Hestroffer, D., Hodgkin, S. T., Holl, B., Janßen, K., de Fombelle, G. J., Jordan, S., Krone-Martins, A., Lanzafame, A. C., Löffler, W., Marchal, O., Marrese, P. M., Moitinho, A., Muinonen, K., Osborne, P., Pancino, E., Pauwels, T., Recio-Blanco, A., Reylé, C., Riello, M., Rimoldini, L., Roegiers, T., Rybizki, J., Sarro, L. M., Siopis, C., Smith, M., Sozzetti, A., Utrilla, E., van Leeuwen, M., Abbas, U., Ábrahám, P., Aramburu, A. A., Aerts, C., Aguado, J. J., Ajaj, M., Aldea-Montero, F., Altavilla, G., Álvarez, M. A., Alves, J., Anderson, R. I., Varela, E. A., Antoja, T., Baines, D., Baker, S. G., Balaguer-Núñez, L., Balbinot, E., Balog, Z., Barache, C., Barbato, D., Barros, M., Barstow, M. A., Bassilana, J. L., Bauchet, N., Becciani, U., Bellazzini, M., Berihuete, A., Bertone, S., Bianchi, L., Binnenfeld, A., Blanco-Cuaresma, S., Boch, T., Bossini, D., Bouquillon, S., Bragaglia, A., Bramante, L., Breedt, E., Bressan, A., Brouillet, N., Brugaletta, E., Bucciarelli, B., Burlacu, A., Butkevich, A. G., Buzzi, R., Caffau, E., Cancelliere, R., Cantat-Gaudin, T., Carballo, R., Carlucci, T., Carnerero, M. I., Carrasco, J. M., Casamiquela, L., Castellani, M., Castro-Ginard, A., Chaoul, L., Charlot, P., Chemin, L., Chiaramida, V., Chiavassa, A., Chornay, N., Comoretto, G., Contursi, G., Cooper, W. J., Cornez, T., Cowell, S., Crifo, F., Cropper, M., Crosta, M., Crowley, C., Dafonte, C., Dapergolas, A., David, P., de Laverny, P., De Luise, F., De March, R., De Ridder, J., de Souza, R., del Peloso, E. F., del Pozo, E., Delbo, M., Delgado, A., Delisle, J. B., Demouchy, C., Dharmawardena, T. E., Diakite, S., Diener, C., Distefano, E., Dolding, C., Enke, H., Fabre, C., Fabrizio, M., Faigler, S., Fedorets, G., Fernique, P., Fienga, A., Figueras, F., Fournier, Y., Fouron, C., Fragkoudi, F., Gai, M., Garcia-Gutierrez, A., Garcia-Reinaldos, M., García-Torres, M., Garofalo, A., Gavel, A., Gavras, P., Giacobbe, P., Gilmore, G., Girona, S., Giuffrida, G., Gomel, R., Gomez, A., González-Núñez, J., González-Santamaría, I., Granvik, M., Guillout, P., Guiraud, J., Gutiérrez-Sánchez, R., Guy, L. P., Hatzidimitriou, D., Hauser, M., Haywood, M., Helmer, A., Helmi, A., Sarmiento, M. H., Hidalgo, S. L., Hładczuk, N., Holland, G., Huckle, H. E., Jardine, K., Jasniewicz, G., Piccolo, A. J.-A., Jiménez-Arranz, ., Campillo, J. J., Julbe, F., Karbevska, L., Kervella, P., Khanna, S., Kordopatis, G., Korn, A. J., Kóspál, ., Kostrzewa-Rutkowska, Z., Kruszyńska, K., Kun, M., Laizeau, P., Lambert, S., Lanza, A. F., Lasne, Y., Campion, J. F. L., Lebreton, Y., Lebzelter, T., Leccia, S., Leclerc, N., Lecoeur-Taibi, I., Liao, S., Licata, E. L., Lindstrøm, H. E. P., Lister, T. A., Livanou, E., Lobel, A., Lorca, A., Loup, C., Pardo, P. M., Romeo, A. M., Managau, S., Mann, R. G., Manteiga, M., Marchant, J. M., Marconi, M., Marcos, J., Santos, M. M. S. M., Pina, D. M., Marinoni, S., Marocco, F., Marshall, D. J., Polo, L. M., Martín-Fleitas, J. M., Marton, G., Mary, N., Masip, A., Massari, D., Mastrobuono-Battisti, A., Mazeh, T., Messina, S., Michalik, D., Millar, N. R., Mints, A., Molina, D., Molinaro, R., Molnár, L., Monari, G., Monguió, M., Montegriffo, P., Montero, A., Mor, R., Mora, A., Morbidelli, R., Morel, T., Morris, D., Muraveva, T., Murphy, C. P., Musella, I., Nagy, Z., Noval, L., Ocaña, F., Ogden, A., Ordenovic, C., Osinde, J. O., Pagani, C., Pagano, I., Palaversa, L., Palicio, P. A., Pallas-Quintela, L., Panahi, A., Payne-Wardenaar, S., Esteller, X. P., Penttilä, A., Pichon, B., Piersimoni, A. M., Pineau, F. X., Plachy, E., Plum, G., Poggio, E., Prša, A., Pulone, L., Racero, E., Ragaini, S., Rainer, M., Rambaux, N., Ramos, P., Fiorentin, P. R., Regibo, S., Richards, P. J., Diaz, C. R., Ripepi, V., Riva, A., Rix, H. W., Rixon, G., Robichon, N., Robin, A. C., Robin, C., Roelens, M., Rogues, H. R. O., Rohrbasser, L., Romero-Gómez, M., Royer, F., Mieres, D. R., Rybicki, K. A., Sadowski, G., Núñez, A. S., Sellés, A. S., Sahlmann, J., Salguero, E., Samaras, N., Gimenez, V. S., Sanna, N., Santoveña, R., Sarasso, M., Schultheis, M.,

Sciacca, E., Segol, M., Segovia, J. C., Ségransan, D., Semeux, D., Shahaf, S., Siddiqui, H. I., Siebert, A., Siltala, L., Silvelo, A., Slezak, E., Slezak, I., Smart, R. L., Snaith, O. N., Solano, E., Solitro, F., Souami, D., Souchay, J., Spagna, A., Spina, L., Spoto, F., Steele, I. A., Stephenson, C. A., Süveges, M., Surdej, J., Szabados, L., Szegedi-Elek, E., Taris, F., Taylor, M. B., Teixeira, R., Tolomei, L., Tonello, N., Elipe, G. T., Trabucchi, M., Tsounis, A. T., Turon, C., Ulla, A., Unger, N., Vaillant, M. V., van Dillen, E., van Reeven, W., Vanel, O., Vecchiato, A., Viala, Y., Vicente, D., Voutsinas, S., Weiler, M., Wevers, T., Wyrzykowski, ., Yoldas, A., Yvard, P., Zhao, H., Zorec, J., Zucker, S., and Zwitter, T. (2022). Gaia Early Data Release 3: The celestial reference frame (Gaia-CRF3).

Gaia Collaboration, Klioner, S. A., Mignard, F., Lindegren, L., Bastian, U., McMillan, P. J., Hernández, J., Hobbs, D., Ramos-Lerate, M., Biermann, M., Bombrun, A., de Torres, A., Gerlach, E., Geyer, R., Hilger, T., Lammers, U., Steidelmüller, H., Stephenson, C. A., Brown, A. G. A., Vallenari, A., Prusti, T., de Bruijne, J. H. J., Babusiaux, C., Creevey, O. L., Evans, D. W., Eyer, L., Hutton, A., Jansen, F., Jordi, C., Luri, X., Panem, C., Pourbaix, D., Randich, S., Sartoretti, P., Soubiran, C., Walton, N. A., Arenou, F., Bailer-Jones, C. A. L., Cropper, M., Drimmel, R., Katz, D., Lattanzi, M. G., van Leeuwen, F., Bakker, J., Castañeda, J., De Angeli, F., Ducourant, C., Fabricius, C., Fouesneau, M., Frémat, Y., Guerra, R., Guerrier, A., Guiraud, J., Jean-Antoine Piccolo, A., Masana, E., Messineo, R., Mowlavi, N., Nicolas, C., Nienartowicz, K., Pailler, F., Panuzzo, P., Riclet, F., Roux, W., Seabroke, G. M., Sordo, R., Tanga, P., Thévenin, F., Gracia-Abril, G., Portell, J., Teyssier, D., Altmann, M., Andrae, R., Bellas-Velidis, I., Benson, K., Berthier, J., Blomme, R., Brugaletta, E., Burgess, P. W., Busso, G., Carry, B., Cellino, A., Cheek, N., Clementini, G., Damerdji, Y., Davidson, M., Delchambre, L., Dell´Oro, A., Fernández-Hernández, J., Galluccio, L., García-Lario, P., Garcia-Reinaldos, M., González-Núñez, J., Gosset, E., Haigron, R., Halbwachs, J.-L., Hambly, N. C., Harrison, D. L., Hatzidimitriou, D., Heiter, U., Hestroffer, D., Hodgkin, S. T., Holl, B., Janßen, K., Jevardat de Fombelle, G., Jordan, S., Krone-Martins, A., Lanzafame, A. C., Löffler, W., Lorca, A., Manteiga, M., Marchal, O., Marrese, P. M., Moitinho, A., Mora, A., Muinonen, K., Osborne, P., Pancino, E., Pauwels, T., Recio-Blanco, A., Richards, P. J., Riello, M., Rimoldini, L., Robin, A. C., Roegiers, T., Rybizki, J., Sarro, L. M., Siopis, C., Smith, M., Sozzetti, A., Ulla, A., Utrilla, E., van Leeuwen, M., van Reeven, W., Abbas, U., Abreu Aramburu, A., Accart, S., Aerts, C., Aguado, J. J., Ajaj, M., Altavilla, G., Álvarez, M. A., Álvarez Cid-Fuentes, J., Alves, J., Anderson, R. I., Anglada Varela, E., Antoja, T., Audard, M., Baines, D., Baker, S. G., Balaguer-Núñez, L., Balbinot, E., Balog, Z., Barache, C., Barbato, D., Barros, M., Barstow, M. A., Bartolomé, S., Bassilana, J.-L., Bauchet, N., Baudesson-Stella, A., Becciani, U., Bellazzini, M., Bernet, M., Bertone, S., Bianchi, L., Blanco-Cuaresma, S., Boch, T., Bossini, D., Bouquillon, S., Bramante, L., Breedt, E., Bressan, A., Brouillet, N., Bucciarelli, B., Burlacu, A., Busonero, D., Butkevich, A. G., Buzzi, R., Caffau, E., Cancelliere, R., Cánovas, H., Cantat-Gaudin, T., Carballo, R., Carlucci, T., Carnerero, M. I., Carrasco, J. M., Casamiquela, L., Castellani, M., Castro-Ginard, A., Castro Sampol, P., Chaoul, L., Charlot, P., Chemin, L., Chiavassa, A., Comoretto, G., Cooper, W. J., Cornez, T., Cowell, S., Crifo, F., Crosta, M., Crowley, C., Dafonte, C., Dapergolas, A., David, M., David, P., de Laverny, P., De Luise, F., De March, R., De Ridder, J., de Souza, R., de Teodoro, P., del Peloso, E. F., del Pozo, E., Delgado, A., Delgado, H. E., Delisle, J.-B., Di Matteo, P., Diakite, S., Diener, C., Distefano, E., Dolding, C., Eappachen, D., Enke, H., Esquej, P., Fabre, C., Fabrizio, M., Faigler, S., Fedorets, G., Fernique, P., Fienga, A., Figueras, F., Fouron, C., Fragkoudi, F., Fraile, E., Franke, F., Gai, M., Garabato, D., Garcia-Gutierrez, A., García-Torres, M., Garofalo, A., Gavras, P., Giacobbe, P., Gilmore, G., Girona, S., Giuffrida, G., Gomez, A., Gonzalez-Santamaria, I., González-Vidal, J. J., Granvik, M., Gutiérrez-Sánchez, R., Guy, L. P., Hauser, M., Haywood, M., Helmi, A., Hidalgo, S. L., Hladczuk, N., Holland, G., Huckle, H. E., Jasniewicz, G., Jonker, P. G., Juaristi Campillo, J., Julbe, F., Karbevska, L., Kervella, P., Khanna, S., Kochoska, A., Kordopatis, G., Korn, A. J., Kostrzewa-Rutkowska, Z., Kruszy´nska, K., Lambert, S., Lanza, A. F., Lasne, Y., Le Campion, J.-F., Le Fustec,

Y., Lebreton, Y., Lebzelter, T., Leccia, S., Leclerc, N., Lecoeur-Taibi, I., Liao, S., Licata, E., Lindstrøm, H. E. P., Lister, T. A., Livanou, E., Lobel, A., Madrero Pardo, P., Managau, S., Mann, R. G., Marchant, J. M., Marconi, M., Marcos Santos, M. M. S., Marinoni, S., Marocco, F., Marshall, D. J., Martin Polo, L., Martín-Fleitas, J. M., Masip, A., Massari, D., Mastrobuono-Battisti, A., Mazeh, T., Messina, S., Michalik, D., Millar, N. R., Mints, A., Molina, D., Molinaro, R., Molnár, L., Montegriffo, P., Mor, R., Morbidelli, R., Morel, T., Morris, D., Mulone, A. F., Munoz, D., Muraveva, T., Murphy, C. P., Musella, I., Noval, L., Ordénovic, C., Orrù, G., Osinde, J., Pagani, C., Pagano, I., Palaversa, L., Palicio, P. A., Panahi, A., Pawlak, M., Peñalosa Esteller, X., Penttilä, A., Piersimoni, A. M., Pineau, F.-X., Plachy, E., Plum, G., Poggio, E., Poretti, E., Poujoulet, E., Prsa, A., Pulone, L., Racero, E., Ragaini, S., Rainer, M., Raiteri, C. M., Rambaux, N., Ramos, P., Re Fiorentin, P., Regibo, S., Reylé, C., Ripepi, V., Riva, A., Rixon, G., Robichon, N., Robin, C., Roelens, M., Rohrbasser, L., Romero-Gómez, M., Rowell, N., Royer, F., Rybicki, K. A., Sadowski, G., Sagristà Sellés, A., Sahlmann, J., Salgado, J., Salguero, E., Samaras, N., Sanchez Gimenez, V., Sanna, N., Santoveña, R., Sarasso, M., Schultheis, M., Sciacca, E., Segol, M., Segovia, J. C., Ségransan, D., Semeux, D., Siddiqui, H. I., Siebert, A., Siltala, L., Slezak, E., Smart, R. L., Solano, E., Solitro, F., Souami, D., Souchay, J., Spagna, A., Spoto, F., Steele, I. A., Süveges, M., Szabados, L., Szegedi-Elek, E., Taris, F., Tauran, G., Taylor, M. B., Teixeira, R., Thuillot, W., Tonello, N., Torra, F., Torra, J., Turon, C., Unger, N., Vaillant, M., van Dillen, E., Vanel, O., Vecchiato, A., Viala, Y., Vicente, D., Voutsinas, S., Weiler, M., Wevers, T., Wyrzykowski, L., Yoldas, A., Yvard, P., Zhao, H., Zorec, J., Zucker, S., Zurbach, C., and Zwitter, T. (2021b). Gaia Early Data Release 3 - Acceleration of the Solar System from Gaia astrometry. *A&A*, 649:A9.

Gaia Collaboration, Mignard, F., Klioner, S. A., Lindegren, L., Hernández, J., Bastian, U., Bombrun, A., Hobbs, D., Lammers, U., Michalik, D., Ramos-Lerate, M., Biermann, M., Fernández-Hernández, J., Geyer, R., Hilger, T., Siddiqui, H. I., Steidelmüller, H., Babusiaux, C., Barache, C., Lambert, S., Andrei, A. H., Bourda, G., Charlot, P., Brown, A. G. A., Vallenari, A., Prusti, T., de Bruijne, J. H. J., Bailer-Jones, C. A. L., Evans, D. W., Eyer, L., Jansen, F., Jordi, C., Luri, X., Panem, C., Pourbaix, D., Randich, S., Sartoretti, P., Soubiran, C., van Leeuwen, F., Walton, N. A., Arenou, F., Cropper, M., Drimmel, R., Katz, D., Lattanzi, M. G., Bakker, J., Cacciari, C., Castañeda, J., Chaoul, L., Cheek, N., De Angeli, F., Fabricius, C., Guerra, R., Holl, B., Masana, E., Messineo, R., Mowlavi, N., Nienartowicz, K., Panuzzo, P., Portell, J., Riello, M., Seabroke, G. M., Tanga, P., Thévenin, F., Gracia-Abril, G., Comoretto, G., Garcia-Reinaldos, M., Teyssier, D., Altmann, M., Andrae, R., Audard, M., Bellas-Velidis, I., Benson, K., Berthier, J., Blomme, R., Burgess, P., Busso, G., Carry, B., Cellino, A., Clementini, G., Clotet, M., Creevey, O., Davidson, M., De Ridder, J., Delchambre, L., Dell´Oro, A., Ducourant, C., Fouesneau, M., Frémat, Y., Galluccio, L., García-Torres, M., González-Núñez, J., González-Vidal, J. J., Gosset, E., Guy, L. P., Halbwachs, J.-L., Hambly, N. C., Harrison, D. L., Hestroffer, D., Hodgkin, S. T., Hutton, A., Jasniewicz, G., Jean-Antoine-Piccolo, A., Jordan, S., Korn, A. J., Krone-Martins, A., Lanzafame, A. C., Lebzelter, T., Löffler, W., Manteiga, M., Marrese, P. M., Martín-Fleitas, J. M., Moitinho, A., Mora, A., Muinonen, K., Osinde, J., Pancino, E., Pauwels, T., Petit, J.-M., Recio-Blanco, A., Richards, P. J., Rimoldini, L., Robin, A. C., Sarro, L. M., Siopis, C., Smith, M., Sozzetti, A., Süveges, M., Torra, J., van Reeven, W., Abbas, U., Abreu Aramburu, A., Accart, S., Aerts, C., Altavilla, G., Álvarez, M. A., Alvarez, R., Alves, J., Anderson, R. I., Anglada Varela, E., Antiche, E., Antoja, T., Arcay, B., Astraatmadja, T. L., Bach, N., Baker, S. G., Balaguer-Núñez, L., Balm, P., Barata, C., Barbato, D., Barblan, F., Barklem, P. S., Barrado, D., Barros, M., Barstow, M. A., Bartholomé Muñoz, L., Bassilana, J.-L., Becciani, U., Bellazzini, M., Berihuete, A., Bertone, S., Bianchi, L., Bienaymé, O., Blanco-Cuaresma, S., Boch, T., Boeche, C., Borrachero, R., Bossini, D., Bouquillon, S., Bragaglia, A., Bramante, L., Breddels, M. A., Bressan, A., Brouillet, N., Brüsemeister, T., Brugaletta, E., Bucciarelli, B., Burlacu, A., Busonero, D., Butkevich, A. G., Buzzi, R., Caffau, E., Cancelliere, R., Cannizzaro, G., Cantat-Gaudin, T., Carballo, R., Carlucci, T., Carrasco,

J. M., Casamiquela, L., Castellani, M., Castro-Ginard, A., Chemin, L., Chiavassa, A., Cocozza, G., Costigan, G., Cowell, S., Crifo, F., Crosta, M., Crowley, C., Cuypers, J., Dafonte, C., Damerdji, Y., Dapergolas, A., David, P., David, M., de Laverny, P., De Luise, F., De March, R., de Souza, R., de Torres, A., Debosscher, J., del Pozo, E., Delbo, M., Delgado, A., Delgado, H. E., Diakite, S., Diener, C., Distefano, E., Dolding, C., Drazinos, P., Durán, J., Edvardsson, B., Enke, H., Eriksson, K., Esquej, P., Eynard Bontemps, G., Fabre, C., Fabrizio, M., Faigler, S., Falcão, A. J., Farràs Casas, M., Federici, L., Fedorets, G., Fernique, P., Figueras, F., Filippi, F., Findeisen, K., Fonti, A., Fraile, E., Fraser, M., Frézouls, B., Gai, M., Galleti, S., Garabato, D., García-Sedano, F., Garofalo, A., Garralda, N., Gavel, A., Gavras, P., Gerssen, J., Giacobbe, P., Gilmore, G., Girona, S., Giuffrida, G., Glass, F., Gomes, M., Granvik, M., Gueguen, A., Guerrier, A., Guiraud, J., Gutié, R., Haigron, R., Hatzidimitriou, D., Hauser, M., Haywood, M., Heiter, U., Helmi, A., Heu, J., Hofmann, W., Holland, G., Huckle, H. E., Hypki, A., Icardi, V., Janßen, K., Jevardat de Fombelle, G., Jonker, P. G., Juhász, A. L., Julbe, F., Karampelas, A., Kewley, A., Klar, J., Kochoska, A., Kohley, R., Kolenberg, K., Kontizas, M., Kontizas, E., Koposov, S. E., Kordopatis, G., Kostrzewa-Rutkowska, Z., Koubsky, P., Lanza, A. F., Lasne, Y., Lavigne, J.-B., Le Fustec, Y., Le Poncin-Lafitte, C., Lebreton, Y., Leccia, S., Leclerc, N., Lecoeur-Taibi, I., Lenhardt, H., Leroux, F., Liao, S., Licata, E., Lindstrøm, H. E. P., Lister, T. A., Livanou, E., Lobel, A., López, M., Managau, S., Mann, R. G., Mantelet, G., Marchal, O., Marchant, J. M., Marconi, M., Marinoni, S., Marschalkó, G., Marshall, D. J., Martino, M., Marton, G., Mary, N., Massari, D., Matijevic, G., Mazeh, T., McMillan, P. J., Messina, S., Millar, N. R., Molina, D., Molinaro, R., Molnár, L., Montegriffo, P., Mor, R., Morbidelli, R., Morel, T., Morris, D., Mulone, A. F., Muraveva, T., Musella, I., Nelemans, G., Nicastro, L., Noval, L., O´Mullane, W., Ordénovic, C., Ordóñez-Blanco, D., Osborne, P., Pagani, C., Pagano, I., Pailler, F., Palacin, H., Palaversa, L., Panahi, A., Pawlak, M., Piersimoni, A. M., Pineau, F.-X., Plachy, E., Plum, G., Poggio, E., Poujoulet, E., Prsa, A., Pulone, L., Racero, E., Ragaini, S., Rambaux, N., Regibo, S., Reylé, C., Riclet, F., Ripepi, V., Riva, A., Rivard, A., Rixon, G., Roegiers, T., Roelens, M., Romero-Gómez, M., Rowell, N., Royer, F., Ruiz-Dern, L., Sadowski, G., Sagristà Sellés, T., Sahlmann, J., Salgado, J., Salguero, E., Sanna, N., Santana-Ros, T., Sarasso, M., Savietto, H., Schultheis, M., Sciacca, E., Segol, M., Segovia, J. C., Ségransan, D., Shih, I.-C., Siltala, L., Silva, A. F., Smart, R. L., Smith, K. W., Solano, E., Solitro, F., Sordo, R., Soria Nieto, S., Souchay, J., Spagna, A., Spoto, F., Stampa, U., Steele, I. A., Stephenson, C. A., Stoev, H., Suess, F. F., Surdej, J., Szabados, L., Szegedi-Elek, E., Tapiador, D., Taris, F., Tauran, G., Taylor, M. B., Teixeira, R., Terrett, D., Teyssandier, P., Thuillot, W., Titarenko, A., Torra Clotet, F., Turon, C., Ulla, A., Utrilla, E., Uzzi, S., Vaillant, M., Valentini, G., Valette, V., van Elteren, A., Van Hemelryck, E., van Leeuwen, M., Vaschetto, M., Vecchiato, A., Veljanoski, J., Viala, Y., Vicente, D., Vogt, S., von Essen, C., Voss, H., Votruba, V., Voutsinas, S., Walmsley, G., Weiler, M., Wertz, O., Wevers, T., Wyrzykowski, L., Yoldas, A., Zerjal, M., Ziaeepour, H., Zorec, J., Zschocke, S., Zucker, S., Zurbach, C., and Zwitter, T. (2018). Gaia Data Release 2 - The celestial reference frame (Gaia-CRF2). *A&A*, 616:A14.

Gaia Collaboration, Prusti, T., de Bruijne, J. H. J., Brown, A. G. A., Vallenari, A., Babusiaux, C., Bailer-Jones, C. A. L., Bastian, U., Biermann, M., Evans, D. W., Eyer, L., Jansen, F., Jordi, C., Klioner, S. A., Lammers, U., Lindegren, L., Luri, X., Mignard, F., Milligan, D. J., Panem, C., Poinsignon, V., Pourbaix, D., Randich, S., Sarri, G., Sartoretti, P., Siddiqui, H. I., Soubiran, C., Valette, V., van Leeuwen, F., Walton, N. A., Aerts, C., Arenou, F., Cropper, M., Drimmel, R., Høg, E., Katz, D., Lattanzi, M. G., O´Mullane, W., Grebel, E. K., Holland, A. D., Huc, C., Passot, X., Bramante, L., Cacciari, C., Castañeda, J., Chaoul, L., Cheek, N., De Angeli, F., Fabricius, C., Guerra, R., Hernández, J., Jean-Antoine-Piccolo, A., Masana, E., Messineo, R., Mowlavi, N., Nienartowicz, K., Ordóñez-Blanco, D., Panuzzo, P., Portell, J., Richards, P. J., Riello, M., Seabroke, G. M., Tanga, P., Thévenin, F., Torra, J., Els, S. G., Gracia-Abril, G., Comoretto, G., Garcia-Reinaldos, M., Lock, T.,

Mercier, E., Altmann, M., Andrae, R., Astraatmadja, T. L., Bellas-Velidis, I., Benson, K., Berthier, J., Blomme, R., Busso, G., Carry, B., Cellino, A., Clementini, G., Cowell, S., Creevey, O., Cuypers, J., Davidson, M., De Ridder, J., de Torres, A., Delchambre, L., Dell´Oro, A., Ducourant, C., Frémat, Y., García-Torres, M., Gosset, E., Halbwachs, J.-L., Hambly, N. C., Harrison, D. L., Hauser, M., Hestroffer, D., Hodgkin, S. T., Huckle, H. E., Hutton, A., Jasniewicz, G., Jordan, S., Kontizas, M., Korn, A. J., Lanzafame, A. C., Manteiga, M., Moitinho, A., Muinonen, K., Osinde, J., Pancino, E., Pauwels, T., Petit, J.-M., Recio-Blanco, A., Robin, A. C., Sarro, L. M., Siopis, C., Smith, M., Smith, K. W., Sozzetti, A., Thuillot, W., van Reeven, W., Viala, Y., Abbas, U., Abreu Aramburu, A., Accart, S., Aguado, J. J., Allan, P. M., Allasia, W., Altavilla, G., Álvarez, M. A., Alves, J., Anderson, R. I., Andrei, A. H., Anglada Varela, E., Antiche, E., Antoja, T., Antón, S., Arcay, B., Atzei, A., Ayache, L., Bach, N., Baker, S. G., Balaguer-Núñez, L., Barache, C., Barata, C., Barbier, A., Barblan, F., Baroni, M., Barrado y Navascués, D., Barros, M., Barstow, M. A., Becciani, U., Bellazzini, M., Bellei, G., Bello García, A., Belokurov, V., Bendjoya, P., Berihuete, A., Bianchi, L., Bienaymé, O., Billebaud, F., Blagorodnova, N., Blanco-Cuaresma, S., Boch, T., Bombrun, A., Borrachero, R., Bouquillon, S., Bourda, G., Bouy, H., Bragaglia, A., Breddels, M. A., Brouillet, N., Brüsemeister, T., Bucciarelli, B., Budnik, F., Burgess, P., Burgon, R., Burlacu, A., Busonero, D., Buzzi, R., Caffau, E., Cambras, J., Campbell, H., Cancelliere, R., Cantat-Gaudin, T., Carlucci, T., Carrasco, J. M., Castellani, M., Charlot, P., Charnas, J., Charvet, P., Chassat, F., Chiavassa, A., Clotet, M., Cocozza, G., Collins, R. S., Collins, P., Costigan, G., Crifo, F., Cross, N. J. G., Crosta, M., Crowley, C., Dafonte, C., Damerdji, Y., Dapergolas, A., David, P., David, M., De Cat, P., de Felice, F., de Laverny, P., De Luise, F., De March, R., de Martino, D., de Souza, R., Debosscher, J., del Pozo, E., Delbo, M., Delgado, A., Delgado, H. E., di Marco, F., Di Matteo, P., Diakite, S., Distefano, E., Dolding, C., Dos Anjos, S., Drazinos, P., Durán, J., Dzigan, Y., Ecale, E., Edvardsson, B., Enke, H., Erdmann, M., Escolar, D., Espina, M., Evans, N. W., Eynard Bontemps, G., Fabre, C., Fabrizio, M., Faigler, S., Falcão, A. J., Farràs Casas, M., Faye, F., Federici, L., Fedorets, G., Fernández-Hernández, J., Fernique, P., Fienga, A., Figueras, F., Filippi, F., Findeisen, K., Fonti, A., Fouesneau, M., Fraile, E., Fraser, M., Fuchs, J., Furnell, R., Gai, M., Galleti, S., Galluccio, L., Garabato, D., García-Sedano, F., Garé, P., Garofalo, A., Garralda, N., Gavras, P., Gerssen, J., Geyer, R., Gilmore, G., Girona, S., Giuffrida, G., Gomes, M., González-Marcos, A., González-Núñez, J., González-Vidal, J. J., Granvik, M., Guerrier, A., Guillout, P., Guiraud, J., Gúrpide, A., Gutiérrez-Sánchez, R., Guy, L. P., Haigron, R., Hatzidimitriou, D., Haywood, M., Heiter, U., Helmi, A., Hobbs, D., Hofmann, W., Holl, B., Holland, G., Hunt, J. A. S., Hypki, A., Icardi, V., Irwin, M., Jevardat de Fombelle, G., Jofré, P., Jonker, P. G., Jorissen, A., Julbe, F., Karampelas, A., Kochoska, A., Kohley, R., Kolenberg, K., Kontizas, E., Koposov, S. E., Kordopatis, G., Koubsky, P., Kowalczyk, A., Krone-Martins, A., Kudryashova, M., Kull, I., Bachchan, R. K., Lacoste-Seris, F., Lanza, A. F., Lavigne, J.-B., Le Poncin-Lafitte, C., Lebreton, Y., Lebzelter, T., Leccia, S., Leclerc, N., Lecoeur-Taibi, I., Lemaitre, V., Lenhardt, H., Leroux, F., Liao, S., Licata, E., Lindstrøm, H. E. P., Lister, T. A., Livanou, E., Lobel, A., Löffler, W., López, M., Lopez-Lozano, A., Lorenz, D., Loureiro, T., MacDonald, I., Magalhães Fernandes, T., Managau, S., Mann, R. G., Mantelet, G., Marchal, O., Marchant, J. M., Marconi, M., Marie, J., Marinoni, S., Marrese, P. M., Marschalkó, G., Marshall, D. J., Martín-Fleitas, J. M., Martino, M., Mary, N., Matijevic, G., Mazeh, T., McMillan, P. J., Messina, S., Mestre, A., Michalik, D., Millar, N. R., Miranda, B. M. H., Molina, D., Molinaro, R., Molinaro, M., Molnár, L., Moniez, M., Montegriffo, P., Monteiro, D., Mor, R., Mora, A., Morbidelli, R., Morel, T., Morgenthaler, S., Morley, T., Morris, D., Mulone, A. F., Muraveva, T., Musella, I., Narbonne, J., Nelemans, G., Nicastro, L., Noval, L., Ordénovic, C., Ordieres-Meré, J., Osborne, P., Pagani, C., Pagano, I., Pailler, F., Palacin, H., Palaversa, L., Parsons, P., Paulsen, T., Pecoraro, M., Pedrosa, R., Pentikäinen, H., Pereira, J., Pichon, B., Piersimoni, A. M., Pineau, F.-X., Plachy, E., Plum, G., Poujoulet, E., Prsa, A., Pulone, L., Ragaini, S., Rago, S., Rambaux, N., Ramos-

Lerate, M., Ranalli, P., Rauw, G., Read, A., Regibo, S., Renk, F., Reylé, C., Ribeiro, R. A., Rimoldini, L., Ripepi, V., Riva, A., Rixon, G., Roelens, M., Romero-Gómez, M., Rowell, N., Royer, F., Rudolph, A., Ruiz-Dern, L., Sadowski, G., Sagristà Sellés, T., Sahlmann, J., Salgado, J., Salguero, E., Sarasso, M., Savietto, H., Schnorhk, A., Schultheis, M., Sciacca, E., Segol, M., Segovia, J. C., Segransan, D., Serpell, E., Shih, I-C., Smareglia, R., Smart, R. L., Smith, C., Solano, E., Solitro, F., Sordo, R., Soria Nieto, S., Souchay, J., Spagna, A., Spoto, F., Stampa, U., Steele, I. A., Steidelmüller, H., Stephenson, C. A., Stoev, H., Suess, F. F., Süveges, M., Surdej, J., Szabados, L., Szegedi-Elek, E., Tapiador, D., Taris, F., Tauran, G., Taylor, M. B., Teixeira, R., Terrett, D., Tingley, B., Trager, S. C., Turon, C., Ulla, A., Utrilla, E., Valentini, G., van Elteren, A., Van Hemelryck, E., van Leeuwen, M., Varadi, M., Vecchiato, A., Veljanoski, J., Via, T., Vicente, D., Vogt, S., Voss, H., Votruba, V., Voutsinas, S., Walmsley, G., Weiler, M., Weingrill, K., Werner, D., Wevers, T., Whitehead, G., Wyrzykowski, L., Yoldas, A., Zerjal, M., Zucker, S., Zurbach, C., Zwitter, T., Alecu, A., Allen, M., Allende Prieto, C., Amorim, A., Anglada-Escudé, G., Arsenijevic, V., Azaz, S., Balm, P., Beck, M., Bernstein, H.-H., Bigot, L., Bijaoui, A., Blasco, C., Bonfigli, M., Bono, G., Boudreault, S., Bressan, A., Brown, S., Brunet, P.-M., Bunclark, P., Buonanno, R., Butkevich, A. G., Carret, C., Carrion, C., Chemin, L., Chéreau, F., Corcione, L., Darmigny, E., de Boer, K. S., de Teodoro, P., de Zeeuw, P. T., Delle Luche, C., Domingues, C. D., Dubath, P., Fodor, F., Frézouls, B., Fries, A., Fustes, D., Fyfe, D., Gallardo, E., Gallegos, J., Gardiol, D., Gebran, M., Gomboc, A., Gómez, A., Grux, E., Gueguen, A., Heyrovsky, A., Hoar, J., Iannicola, G., Isasi Parache, Y., Janotto, A.-M., Joliet, E., Jonckheere, A., Keil, R., Kim, D.-W., Klagyivik, P., Klar, J., Knude, J., Kochukhov, O., Kolka, I., Kos, J., Kutka, A., Lainey, V., LeBouquin, D., Liu, C., Loreggia, D., Makarov, V. V., Marseille, M. G., Martayan, C., Martinez-Rubi, O., Massart, B., Meynadier, F., Mignot, S., Munari, U., Nguyen, A.-T., Nordlander, T., Ocvirk, P., O´Flaherty, K. S., Olias Sanz, A., Ortiz, P., Osorio, J., Oszkiewicz, D., Ouzounis, A., Palmer, M., Park, P., Pasquato, E., Peltzer, C., Peralta, J., Péturaud, F., Pieniluoma, T., Pigozzi, E., Poels, J., Prat, G., Prod´homme, T., Raison, F., Rebordao, J. M., Risquez, D., Rocca-Volmerange, B., Rosen, S., Ruiz-Fuertes, M. I., Russo, F., Sembay, S., Serraller Vizcaino, I., Short, A., Siebert, A., Silva, H., Sinachopoulos, D., Slezak, E., Soffel, M., Sosnowska, D., Straizys, V., ter Linden, M., Terrell, D., Theil, S., Tiede, C., Troisi, L., Tsalmantza, P., Tur, D., Vaccari, M., Vachier, F., Valles, P., Van Hamme, W., Veltz, L., Virtanen, J., Wallut, J.-M., Wichmann, R., Wilkinson, M. I., Ziaeepour, H., and Zschocke, S. (2016). The Gaia mission. *A&A*, 595:A1.

Galli, P. A. B., Loinard, L., Ortiz-Léon, G. N., Kounkel, M., Dzib, S. A., Mioduszewski, A. J., Rodríguez, L. F., Hartmann, L., Teixeira, R., Torres, R. M., Rivera, J. L., Boden, A. F., II, N. J. E., Briceño, C., Tobin, J. J., and Heyer, M. (2018). The Gould's Belt Distances Survey (GOBELINS). IV. Distance, depth, and kinematics of the Taurus star-forming region. *ApJ*, 859(1):33.

García-Alvarez, D., Foing, B. H., Montes, D., Oliveira, J., Doyle, J. G., Messina, S., Lanza, A. F., Rodonò, M., Abbott, J., Ash, T. D. C., Baldry, I. K., Bedding, T. R., Buckley, D. A. H., Cami, J., Cao, H., Catala, C., Cheng, K. P., A. Domiciano de Souza Jr, Donati, J.-F., Hubert, A.-M., Janot-Pacheco, E., Hao, J. X., Kaper, L., Kaufer, A., Leister, N. V., Neff, J. E., Neiner, C., Orlando, S., O'Toole, S. J., Schäfer, D., Smartt, S. J., Stahl, O., Telting, J., and Tubbesing, S. (2003). Simultaneous optical and X-ray observations of flares and rotational modulation on the RS CVn binary HR 1099 (V711 Tau) from the MUSICOS 1998 campaign. *A&A*, 397(1):285–303.

Gattano, C., Lambert, S. B., and Le Bail, K. (2018). Extragalactic radio source stability and VLBI celestial reference frame: insights from the Allan standard deviation. *A&A*, 618:A80.

Gordon, D., de Witt, A., and Jacobs, C. S. (2022). Current CRF Status at X/S and K Bands. In *Proc. 12th IVS General Meeting*, page 2.

Greisen, E. W. (2003). Processing and archiving of AIPS, the VLA, and the VLBA. In (ed), H. A., editor,

Information handling in astronomy— Historical vistas, volume 285, chapter 7, pages 109–125. Springer Netherlands, Astrophys and Space Sci Lib. doi: 10.1007/0-306-48080-8.

Gwinn, C. R., Eubanks, T. M., Pyne, T., Birkinshaw, M., and Matsakis, D. N. (1997). Quasar proper motions and low-frequency gravitational waves. *The Astrophysical Journal*, 485(1):87–91.

Hada, K., Doi, A., Kino, M., Nagai, H., Hagiwara, Y., and Kawaguchi, N. (2011). An origin of the radio jet in M87 at the location of the central black hole. *Nature*, 477(7363):185–187.

Harris, R. J., Andrews, S. M., Wilner, D. J., and Kraus, A. L. (2012). A resolved census of millimeter emission from Taurus multiple star systems. *ApJ*, 751(2):115.

Høg, E. (2014). Interferometry from space: A great dream.

Hill, G., Aikman, G. C. L., Cowley, A. P., Bolton, C. T., and Thomas, J. C. (1976). The radio-flaring triple system b Persei. *ApJ*, 208:152–164.

Hilton, J. L., Capitaine, N., Chapront, J., Ferrandiz, J. M., Fienga, A., Fukushima, T., Getino, J., Mathews, P., Simon, J. L., Soffel, M., Vondrak, J., Wallace, P., and Williams, J. (2006). Report of the International Astronomical Union Division I Working Group on Precession and the Ecliptic. *Celestial Mechanics and Dynamical Astronomy*, 94(3):351–367.

Hjellming, R. M. and Wade, C. M. (1971). Radio stars. *Science*, 173(4002):1087–1092.

Hobbs, D., Høg, E., Mora, A., Crowley, C., McMillan, P., Ranalli, P., Heiter, U., Jordi, C., Hambly, N., Church, R., Anthony, B., Tanga, P., Chemin, L., Portell, J., Jiménez-Esteban, F., Klioner, S., Mignard, F., Fynbo, J., Wyrzykowski, u., Rybicki, K., Anderson, R. I., Cellino, A., Fabricius, C., Davidson, M., and Lindegren, L. (2016). GaiaNIR: Combining optical and Near-Infra-Red (NIR) capabilities with Time-Delay-Integration (TDI) sensors for a future Gaia-like mission.

Högbom, J. A. (1974). Aperture synthesis with a non-regular distribution of interferometer baselines. *A&AS*, 15:417.

Hummel, C. A., Monnier, J. D., Roettenbacher, R. M., Torres, G., Henry, G. W., Korhonen, H., Beasley, A., Schaefer, G. H., Turner, N. H., Brummelaar, T. T., Farrington, C. D., Sturmann, J., Sturmann, L., Baron, F., and Kraus, S. (2017). Orbital elements and stellar parameters of the active binary UX Arietis. *ApJ*, 844(2):115.

Jacobs, C. S., Horiuchi, S., Firre, D., Murata, Y., Takeuchi, H., Uchimura, T., and Asmar, S. (2022). The JPL 2022a X/Ka Celestial Reference Frame. In *Proc. 12th IVS General Meeting*, page 4.

Jones, D. L., Folkner, W. M., Jacobson, R. A., Jacobs, C. S., Romney, J., and Dhawan, V. (2020). Very Long Baseline Array astrometry of Cassini: The final epochs and an improved orbit of Saturn. *The Astronomical Journal*, 159(2):72.

Karbon, M., Heinkelmann, R., Mora-Diaz, J., Xu, M., Nilsson, T., and Schuh, H. (2017). The extension of the parametrization of the radio source coordinates in geodetic VLBI and its impact on the time series analysis. *Journal of Geodesy*, 91(7):755–765.

Karbon, M. and Nothnagel, A. (2019). Realization of a multifrequency celestial reference frame through a combination of normal equation systems. *A&A*, 630:A101.

Kardashev, N. S., Khartov, V. V., Abramov, V. V., Avdeev, V. Y., Alakoz, A. V., Aleksandrov, Y. A., Ananthakrishnan, S., Andreyanov, V. V., Andrianov, A. S., Antonov, N. M., Artyukhov, M. I., Arkhipov, M. Y., Baan, W., Babakin, N. G., Babyshkin, V. E., Bartel', N., Belousov, K. G., Belyaev, A. A., Berulis, J. J., Burke, B. F., Biryukov, A. V., Bubnov, A. E., Burgin, M. S., Busca, G., Bykadorov, A. A., Bychkova, V. S., Vasil'kov, V. I., Wellington, K. J., Vinogradov, I. S., Wietfeldt, R., Voitsik,

P. A., Gvamichava, A. S., Girin, I. A., Gurvits, L. I., Dagkesamanskii, R. D., D'Addario, L., Giovannini, G., Jauncey, D. L., Dewdney, P. E., D'yakov, A. A., Zharov, V. E., Zhuravlev, V. I., Zaslavskii, G. S., Zakhvatkin, M. V., Zinov'ev, A. N., Ilinen, Y., Ipatov, A. V., Kanevskii, B. Z., Knorin, I. A., Casse, J. L., Kellermann, K. I., Kovalev, Y. A., Kovalev, Y. Y., Kovalenko, A. V., Kogan, B. L., Komaev, R. V., Konovalenko, A. A., Kopelyanskii, G. D., Korneev, Y. A., Kostenko, V. I., Kotik, A. N., Kreisman, B. B., Kukushkin, A. Y., Kulishenko, V. F., Cooper, D. N., Kut'kin, A. M., Cannon, W. H., Larionov, M. G., Lisakov, M. M., Litvinenko, L. N., Likhachev, S. F., Likhacheva, L. N., Lobanov, A. P., Logvinenko, S. V., Langston, G., McCracken, K., Medvedev, S. Y., Melekhin, M. V., Menderov, A. V., Murphy, D. W., Mizyakina, T. A., Mozgovoi, Y. V., Nikolaev, N. Y., Novikov, B. S., Novikov, I. D., Oreshko, V. V., Pavlenko, Y. K., Pashchenko, I. N., Ponomarev, Y. N., Popov, M. V., Pravin-Kumar, A., Preston, R. A., Pyshnov, V. N., Rakhimov, I. A., Rozhkov, V. M., Romney, J. D., Rocha, P., Rudakov, V. A., Räisänen, A., Sazankov, S. V., Sakharov, B. A., Semenov, S. K., Serebrennikov, V. A., Schilizzi, R. T., Skulachev, D. P., Slysh, V. I., Smirnov, A. I., Smith, J. G., Soglasnov, V. A., Sokolovskii, K. V., Sondaar, L. H., Stepan'yants, V. A., Turygin, M. S., Turygin, S. Y., Tuchin, A. G., Urpo, S., Fedorchuk, S. D., Finkel'shtein, A. M., Fomalont, E. B., Fejes, I., Fomina, A. N., Khapin, Y. B., Tsarevskii, G. S., Zensus, J. A., Chuprikov, A. A., Shatskaya, M. V., Shapirovskaya, N. Y., Sheikhet, A. I., Shirshakov, A. E., Schmidt, A., Shnyreva, L. A., Shpilevskii, V. V., Ekers, R. D., and Yakimov, V. E. (2013). "RadioAstron"-A telescope with a size of 300 000 km: Main parameters and first observational results. *Astronomy Reports*, 57(3):153–194.

Kettenis, M., van Langevelde, H. J., Reynolds, C., and Cotton, B. (2006). ParselTongue: AIPS Talking Python. In Gabriel, C., Arviset, C., Ponz, D., and Enrique, S., editors, *Astronomical Data Analysis Software and Systems XV*, volume 351 of *Astronomical Society of the Pacific Conference Series*, page 497.

Kopeikin, S. M. and Makarov, V. V. (2006). Astrometric Effects of Secular Aberration. *AJ*, 131(3):1471–1478.

Kounkel, M., Hartmann, L., Loinard, L., Ortiz-León, G. N., Mioduszewski, A. J., Rodríguez, L. F., Dzib, S. A., Torres, R. M., Pech, G., Galli, P. A. B., Rivera, J. L., Boden, A. F., II, N. J. E., Briceño, C., and Tobin, J. J. (2017). The Gould's Belt Distances Survey (GOBELINS). II. Distances and structure toward the Orion molecular clouds. *ApJ*, 834(2):142.

Kovalev, Y. Y., Lobanov, A. P., Pushkarev, A. B., and Zensus, J. A. (2008). Opacity in compact extragalactic radio sources and its effect on astrophysical and astrometric studies. *A&A*, 483(3):759–768.

Kovalev, Y. Y., Petrov, L., and Plavin, A. V. (2017). VLBI-Gaia offsets favor parsec-scale jet direction in active galactic nuclei. *A&A*, 598:L1.

Kovalevsky, J., Lindegren, L., Perryman, M. A. C., Hemenway, P. D., Johnston, K. J., Kislyuk, V. S., Lestrade, J. F., Morrison, L. V., Platais, I., Röser, S., Schilbach, E., Tucholke, H.-J., de Vegt, C., Vondrák, J., Arias, F., Gontier, A. M., Arenou, F., Brosche, P., Florkowski, D. R., Garrington, S. T., Preston, R. A., Ron, C., Rybka, S. P., Scholz, R.-D., and Zacharias, N. (1997). The Hipparcos Catalogue as a realisation of the extragalactic reference system. *Astronomy and Astrophysics - A&A*, 323:620–633.

Kovalevsky, J. and Seidelmann, P. K. (2004). *Fundamentals of Astrometry*. Cambridge University Press.

Kozai, Y. (1991). Chapter ii: Twenty-first general assembly. In Bergeron, J., editor, *Transactions of the International Astronomical Union Vol. XXI B*, Proceedings of the 21st General Assembly, page 11–83. Cambridge University Press.

Kusuno, K., Asaki, Y., Imai, H., and Oyama, T. (2013). Distance and proper motion measurement of the red supergiant, PZ CAS, in very long baseline interferometry H2O maser astrometry. *ApJ*, 774(2):107.

Lagler, K., Schindelegger, M., Böhm, J., Krásná, H., and Nilsson, T. (2013). Gpt2: Empirical slant delay model for radio space geodetic techniques. *Geophysical Research Letters*, 40(6):1069–1073.

Lambert, S., Liu, N., Arias, E. F., Barache, C., Souchay, J., Taris, F., Liu, J. C., and Zhu, Z. (2021). Parsec-scale alignments of radio-optical offsets with jets in AGNs from multifrequency geodetic VLBI, Gaia EDR3, and the MOJAVE program. *A&A*, 651:A64.

Lebach, D. E., Bartel, N., Bietenholz, M. F., Campbell, R. M., Gordon, D., Lederman, J. I., Lestrade, J.-F., Ransom, R. R., Ratner, M. I., and Shapiro, I. I. (2012). VLBI for Gravity Probe B. IV. A new astrometric analysis technique and a comparison with results from other techniques. *The Astrophysical Journal Supplement Series*, 201(1):4.

Lefèvre, F., Lyard, F. H., Le Provost, C., and Schrama, E. J. O. (2002). FES99: A global tide finite element solution assimilating tide gauge and altimetric information. *Journal of Atmospheric and Oceanic Technology*, 19(9):1345–1356.

Lestrade, J. F. (1991). VLBI phase-referencing for observations of weak radio sources. In Cornwell, T. J. and Perley, R. A., editors, *IAU Colloq. 131: Radio Interferometry. Theory, Techniques, and Applications*, volume 19 of *Astronomical Society of the Pacific Conference Series*, pages 289–297.

Lestrade, J. F., Preston, R. A., Jones, D. L., Phillips, R. B., Rogers, A. E. E., Titus, M. A., Rioja, M. J., and Gabuzda, D. C. (1999). High-precision VLBI astrometry of radio-emitting stars. *A&A*, 344:1014–1026.

Lindegren, L. (2018). Re-normalising the astrometric chi-square in Gaia DR2. GAIA-C3-TN-LU-LL-124.

Lindegren, L. (2020). The bright reference frame of Gaia and VLBI observations of radio stars. In Bizouard, C., editor, *Astrometry, Earth Rotation, and Reference Systems in the GAIA era*, pages 3–8.

Lindegren, L. (2020a). The Gaia reference frame for bright sources examined using VLBI observations of radio stars. *A&A*, 633:A1.

Lindegren, L. (2020b). The Gaia reference frame for bright sources examined using VLBI observations of radio stars (Corrigendum). *A&A*, 637:C5.

Lindegren, L., Bastian, U., Biermann, M., Bombrun, A., de Torres, A., Gerlach, E., Geyer, R., Hernández, J., Hilger, T., Hobbs, D., Klioner, S. A., Lammers, U., McMillan, P. J., Ramos-Lerate, M., Steidelmüller, H., Stephenson, C. A., and van Leeuwen, F. (2021a). Gaia Early Data Release 3 - Parallax bias versus magnitude, colour, and position. *A&A*, 649:A4.

Lindegren, L., Hernández, J., Bombrun, A., Klioner, S., Bastian, U., Ramos-Lerate, M., de Torres, A., Steidelmüller, H., Stephenson, C., Hobbs, D., Lammers, U., Biermann, M., Geyer, R., Hilger, T., Michalik, D., Stampa, U., McMillan, P.J., Castañeda, J., Clotet, M., Comoretto, G., Davidson, M., Fabricius, C., Gracia, G., Hambly, N.C., Hutton, A., Mora, A., Portell, J., van Leeuwen, F., Abbas, U., Abreu, A., Altmann, M., Andrei, A., Anglada, E., Balaguer-Núñez, L., Barache, C., Becciani, U., Bertone, S., Bianchi, L., Bouquillon, S., Bourda, G., Brüsemeister, T., Bucciarelli, B., Busonero, D., Buzzi, R., Cancelliere, R., Carlucci, T., Charlot, P., Cheek, N., Crosta, M., Crowley, C., de Bruijne, J., de Felice, F., Drimmel, R., Esquej, P., Fienga, A., Fraile, E., Gai, M., Garralda, N., González-Vidal, J.J., Guerra, R., Hauser, M., Hofmann, W., Holl, B., Jordan, S., Lattanzi, M.G., Lenhardt, H., Liao, S., Licata, E., Lister, T., Löffler, W., Marchant, J., Martin-Fleitas, J.-M., Messineo, R., Mignard, F., Morbidelli, R., Poggio, E., Riva, A., Rowell, N., Salguero, E., Sarasso, M., Sciacca, E., Siddiqui, H., Smart, R.L., Spagna, A., Steele, I., Taris, F., Torra, J., van Elteren, A., van Reeven, W., and Vecchiato, A. (2018). Gaia Data Release 2 - The astrometric solution. *A&A*, 616:A2.

Lindegren, L., Klioner, S. A., Hernández, J., Bombrun, A., Ramos-Lerate, M., Steidelmüller, H., Bastian, U., Biermann, M., de Torres, A., Gerlach, E., Geyer, R., Hilger, T., Hobbs, D., Lammers, U., McMillan,

P. J., Stephenson, C. A., Castañeda, J., Davidson, M., Fabricius, C., Gracia-Abril, G., Portell, J., Rowell, N., Teyssier, D., Torra, F., Bartolomé, S., Clotet, M., Garralda, N., González-Vidal, J. J., Torra, J., Abbas, U., Altmann, M., Anglada Varela, E., Balaguer-Núñez, L., Balog, Z., Barache, C., Becciani, U., Bernet, M., Bertone, S., Bianchi, L., Bouquillon, S., Brown, A. G. A., Bucciarelli, B., Busonero, D., Butkevich, A. G., Buzzi, R., Cancelliere, R., Carlucci, T., Charlot, P., Cioni, M.-R. L., Crosta, M., Crowley, C., del Peloso, E. F., del Pozo, E., Drimmel, R., Esquej, P., Fienga, A., Fraile, E., Gai, M., Garcia-Reinaldos, M., Guerra, R., Hambly, N. C., Hauser, M., Janßen, K., Jordan, S., Kostrzewa-Rutkowska, Z., Lattanzi, M. G., Liao, S., Licata, E., Lister, T. A., Löffler, W., Marchant, J. M., Masip, A., Mignard, F., Mints, A., Molina, D., Mora, A., Morbidelli, R., Murphy, C. P., Pagani, C., Panuzzo, P., Peñalosa Esteller, X., Poggio, E., Re Fiorentin, P., Riva, A., Sagristà Sellés, A., Sanchez Gimenez, V., Sarasso, M., Sciacca, E., Siddiqui, H. I., Smart, R. L., Souami, D., Spagna, A., Steele, I. A., Taris, F., Utrilla, E., van Reeven, W., and Vecchiato, A. (2021b). Gaia Early Data Release 3 - The astrometric solution. *A&A*, 649:A2.

Lindegren, L. and Kovalevsky, J. (1995). Linking the HIPPARCOS Catalogue to the extragalactic reference system. *A&A*, 304:189.

Lindegren, L., Lammers, U., Bastian, U., Hernández, J., Klioner, S., Hobbs, D., Bombrun, A., Michalik, D., Ramos-Lerate, M., Butkevich, A., Comoretto, G., Joliet, E., Holl, B., Hutton, A., Parsons, P., Steidelmüller, H., Abbas, U., Altmann, M., Andrei, A., Anton, S., Bach, N., Barache, C., Becciani, U., Berthier, J., Bianchi, L., Biermann, M., Bouquillon, S., Bourda, G., Brüsemeister, T., Bucciarelli, B., Busonero, D., Carlucci, T., Castañeda, J., Charlot, P., Clotet, M., Crosta, M., Davidson, M., de Felice, F., Drimmel, R., Fabricius, C., Fienga, A., Figueras, F., Fraile, E., Gai, M., Garralda, N., Geyer, R., González-Vidal, J. J., Guerra, R., Hambly, N. C., Hauser, M., Jordan, S., Lattanzi, M. G., Lenhardt, H., Liao, S., Löffler, W., McMillan, P. J., Mignard, F., Mora, A., Morbidelli, R., Portell, J., Riva, A., Sarasso, M., Serraller, I., Siddiqui, H., Smart, R., Spagna, A., Stampa, U., Steele, I., Taris, F., Torra, J., van Reeven, W., Vecchiato, A., Zschocke, S., de Bruijne, J., Gracia, G., Raison, F., Lister, T., Marchant, J., Messineo, R., Soffel, M., Osorio, J., de Torres, A., and O'Mullane, W. (2016). Gaia Data Release 1. Astrometry: one billion positions, two million proper motions and parallaxes. *A&A*, 595:A4.

Lindegren, L., Lammers, U., Hobbs, D., O´Mullane, W., Bastian, U., and Hernández, J. (2012). The astrometric core solution for the Gaia mission - Overview of models, algorithms, and software implementation. *A&A*, 538:A78.

Lindegren, L. and Perryman, M. A. C. (1994). GAIA: Global Astrometric Interferometer for Astrophysics (A concept for an ESA cornerstone mission). *Internal report submitted to the ESA Horizon 2000+ Survey Committee.*

Lindegren, L. and Perryman, M. A. C. (1996). Gaia: Global astrometric interferometer for astrophysics. *Astron. Astrophys. Suppl. Ser.*, 116(3):579–595.

Lister, M. L., Aller, M. F., Aller, H. D., Hodge, M. A., Homan, D. C., Kovalev, Y. Y., Pushkarev, A. B., and Savolainen, T. (2018). MOJAVE. XV. VLBA 15 GHz total intensity and polarization maps of 437 parsec-scale AGN jets from 1996 to 2017. *ApJS*, 234(1):12.

Liu, N., Lambert, S. B., Charlot, P., Zhu, Z., Liu, J. C., Jiang, N., Wan, X. S., and Ding, C. Y. (2021). Comparison of multifrequency positions of extragalactic sources from ICRF3 and Gaia EDR3. *A&A*, 652:A87.

Liu, N., Lambert, S. B., Zhu, Z., and Liu, J.-C. (2020). Systematics and accuracy of VLBI astrometry: A comparison with Gaia Data Release 2. *A&A*, 634:A28.

Liu, N., Zhu, Z., and Liu, J.-C. (2018). Possible systematics in the VLBI catalogs as seen from Gaia. *A&A*, 609:A19.

Loinard, L., Torres, R. M., Mioduszewski, A. J., and Rodríguez, L. F. (2008). A preliminary VLBA distance to the core of Ophiuchus, with an accuracy of 4%. *The Astrophysical Journal*, 675(1):L29–L32.

Loinard, L., Torres, R. M., Mioduszewski, A. J., Rodriguez, L. F., Gonzalez-Lopezlira, R. A., Lachaume, R., Vazquez, V., and Gonzalez, E. (2007). VLBA determination of the distance to nearby star-forming regions. I. The distance to T Tauri with 0.4% accuracy. *ApJ*, 671(1):546–554.

Lunz, S., Anderson, J., Heinkelmann, R., Xu, M. H., Gong, S., and Schuh, H. (2019a). Radio source position offsets among various radio frames and Gaia. Poster-presentation at the 24th Meeting of the European VLBI Group for Geodesy and Astrometry, 17-19 March 2019, Gran Canaria.

Lunz, S., Anderson, J., Xu, M., Heinkelmann, R., Titov, O., Lestrade, J. F., Johnson, M. C., Shu, F., Chen, W., Melnikov, A., McCallum, J., Lopez, Y., Mikhailov, A., Abad, P. d. V., and Schuh, H. (2021a). On the alignment of the optically bright Gaia frame to ICRF3 and the impact of new models of stellar motion from VLBI. In *European Astronomical Society Annual Meeting 2021, Online, Gaia/GREAT Science Symposium*.

Lunz, S., Anderson, J., Xu, M., Heinkelmann, R., Titov, O., Lestrade, J. F., Johnson, M. C., Shu, F., Chen, W., Melnikov, A., McCallum, J., Lopez, Y., Mikhailov, A., Abad, P. d. V., and Schuh, H. (2022). The impact of new estimates of models of stellar motion from VLBI on the alignment of the optically bright Gaia frame to ICRF3. In *European VLBI Network Mini-Symposium and Users' Meeting 2021*, page 32.

Lunz, S., Anderson, J. M., Xu, M. H., Heinkelmann, R., Titov, O., Lestrade, J.-F., Johnson, M. C., Shu, F., Chen, W., Melnikov, A., Mikhailov, A., McCallum, J., Lopez, Y., de Vicente Abad, P., and Schuh, H. (2021b). The impact of improved estimates of radio star astrometric models on the alignment of the *Gaia* bright reference frame to ICRF3. *A&A*. submitted to A&A in 2021, version of 22.06.2022.

Lunz, S., Anderson, J. M., Xu, M. H., Titov, O., Heinkelmann, R., Johnson, M. C., and Schuh, H. (2020a). Enhancing the link of the optically bright Gaia reference frame towards ICRS. *A&A*. submitted to A&A in 2020, version of 23.08.2022.

Lunz, S., Heinkelmann, R., Anderson, J., Johnson, M., Fey, A., and Titov, O. (2020b). Gaia-VLBI: phase-referencing continuum emission observations of optically bright stars with the VLBA (planned proposal). In Bizouard, C., editor, *Astrometry, Earth Rotation, and Reference Systems in the GAIA era*, pages 49–54.

Lunz, S., Heinkelmann, R., Anderson, J., Xu, M. H., and Schuh, H. (2019b). Vergleich der Positionen und scheinbaren Eigenbewegungen von Radioquellen aus Gaia- und VLBI-Beobachtungen. Presentation at Frontiers of Geodetic Science conference, 17-19 September 2019, Stuttgart.

Lyard, F., Lefevre, F., Letellier, T., and Francis, O. (2006). Modelling the global ocean tides: modern insights from FES2004. *Ocean Dynamics*, 56(5-6):394–415.

Ma, C., Arias, E. F., Eubanks, T. M., Fey, A. L., Gontier, A. M., Jacobs, C. S., Sovers, O. J., Archinal, B. A., and Charlot, P. (1998). The International Celestial Reference Frame as realized by Very Long Baseline Interferometry. *AJ*, 116(1):516–546.

Ma, C. and Feissel, M., editors (1997). *Definition and realization of the International Celestial Reference System by VLBI astrometry of extragalactic objects, IERS Technical Note 23*. Observatiore de Paris, Paris.

MacMillan, D. S., Fey, A., Gipson, J. M., Gordon, D., Jacobs, C. S., Krásná, H., Lambert, S. B., Malkin, Z., Titov, O., Wang, G., and Xu, M. H. (2019). Galactocentric acceleration in VLBI analysis. Findings of IVS WG8. *A&A*, 630:A93.

Makarov, V. V., Berghea, C. T., Frouard, J., Fey, A., and Schmitt, H. R. (2019). The precious set of radio-optical reference frame objects in the light of Gaia DR2 data. *ApJ*, 873(2):132.

Makarov, V. V. and Murphy, D. W. (2007). The local stellar velocity field via vector spherical harmonics. *AJ*, 134(1):367–375.

Malkin, Z. (2016a). A new method to subdivide a spherical surface into equal-area cells. *arXiv e-prints, arXiv:1612.03467*.

Malkin, Z. (2016b). Using radio stars to link the Gaia and VLBI reference frames. *Monthly Notices of the Royal Astronomical Society*, 461(2):1937–1942.

Malkin, Z. (2018). A new version of the OCARS catalog of optical characteristics of astrometric radio sources. *The Astrophysical Journal Supplement Series*, 239(2):20.

Marcaide, J. M. and Shapiro, I. I. (1984). VLBI study of 1038+528A and B : discovery of wavelength dependence of peak brightness location. *ApJ*, 276:56–59.

Marschall, L. A. and Mathieu, R. D. (1988). Parenago 1540: A pre-main-sequence double-lined spectroscopic binary near the Orion Trapezium. *AJ*, 96:1956.

Marsden, S. C., Berdyugina, S. V., Donati, J.-F., Eaton, J. A., Williamson, M. H., Ilyin, I., Fischer, D. A., Muñoz, M., Isaacson, H., Ratner, M. I., Semel, M., Petit, P., and Carter, B. D. (2005). A sun in the spectroscopic binary IM Pegasi, the guide star for the Gravity Probe B mission. *The Astrophysical Journal*, 634(2):L173–L176.

Martí-Vidal, I., Ros, E., Pérez-Torres, M. A., Guirado, J. C., Jiménez-Monferrer, S., and Marcaide, J. M. (2010). Coherence loss in phase-referenced VLBI observations. *A&A*, 515:A53.

Martí-Vidal, I., Ros, E., Pérez-Torres, M. A., Guirado, J. C., Jiménez-Monferrer, S., and Marcaide, J. M. (2011). Coherence loss in phase-referenced VLBI observations (Corrigendum). *A&A*, 533:C1.

Martin-Mur, T. J., Zhai, C., Jacobs, C., Turyshev, S. G., Shao, M., Peng, M., McCandless, S. E., and Karimi, R. R. (2017). Using optical communications links for deep-space navigation. In *2017 IEEE International Conference on Space Optical Systems and Applications (ICSOS)*, pages 176–182.

Massi, M., Ros, E., Menten, K. M., Kaufman Bernadó, M., Torricelli-Ciamponi, G., Neidhöfer, J., Boden, A., Boboltz, D., Sargent, A., and Torres, G. (2008). Interacting coronae of two T Tauri stars: first observational evidence for solar-like helmet streamers. *A&A*, 480(2):489–494.

Mathews, J. (1981). *Tensor Spherical Harmonics*. Pasadena: California Institute of Technology.

Mathews, P. M., Herring, T. A., and Buffett, B. A. (2002). Modeling of nutation and precession: New nutation series for nonrigid Earth and insights into the Earth's interior. *Journal of Geophysical Research (Solid Earth)*, 107(B4):2068.

Mayer, D. (2018). *VLBI celestial reference frames and assessment with Gaia*. PhD thesis, Wien.

Melis, C., Reid, M. J., Mioduszewski, A. J., Stauffer, J. R., and Bower, G. C. (2014). A VLBI resolution of the Pleiades distance controversy. *Science*, 345(6200):1029–1032.

Mignard, F. and Klioner, S. (2012). Analysis of astrometric catalogues with vector spherical harmonics. *A&A*, 547:A59.

Mignard, F., Klioner, S., Lindegren, L., Bastian, U., Bombrun, A., Hernández, J., Hobbs, D., Lammers, U., Michalik, D., Ramos-Lerate, M., Biermann, M., Butkevich, A., Comoretto, G., Joliet, E., Holl, B., Hutton, A., Parsons, P., Steidelmüller, H., Andrei, A., Bourda, G., and Charlot, P. (2016). Gaia Data Release 1 - Reference frame and optical properties of ICRF sources . *A&A*, 595:A5.

Mignard, F. and Morando, B. (1990). Journées 1990, Systèmes de Référence spatio-temporels, ed. N. Capitaine. *Observatoire de Paris*, page 151.

Miller-Jones, J. C. A., Sivakoff, G. R., Knigge, C., Körding, E. G., Templeton, M., and Waagen, E. O. (2013). An accurate geometric distance to the compact binary SS Cygni Vindicates accretion disc theory. *Science*, 340(6135):950–952.

Mioduszewski, A. J. (2009). Strategy for removing tropospheric and clock errors using DELZN. *AIPS Memo 110*.

Nakagawa, A., Omodaka, T., Handa, T., Honma, M., Kawaguchi, N., Kobayashi, H., Oyama, T., Sato, K., Shibata, K. M., Shizugami, M., Tamura, Y., and Ueno, Y. (2014). VLBI astrometry of AGB variables with VERA: A Mira-type variable T Lepus. *PASJ*, 66(6). 101.

Nakagawa, A., Tsushima, M., Ando, K., Bushimata, T., Choi, Y. K., Hirota, T., Honma, M., Imai, H., Iwadate, K., Jike, T., Kameno, S., Kameya, O., Kamohara, R., Kan-Ya, Y., Kawaguchi, N., Kijima, M., Kim, M. K., Kobayashi, H., Kuji, S., Kurayama, T., Maeda, T., Manabe, S., Maruyama, K., Matsui, M., Matsumoto, N., Miyaji, T., Nagayama, T., Nakamura, K., Nyu, D., Oh, C. S., Omodaka, T., Oyama, T., Pradel, N., Sakai, S., Sasao, T., Sato, K., Sato, M., Shibata, K. M., Suda, H., Tamura, Y., Ueda, K., Ueno, Y., and Yamashita, K. (2008). VLBI astrometry of AGB variables with VERA — A semiregular variable S Crateris. *PASJ*, 60(5):1013–1021.

Nguyen, D. C., Brandeker, A., van Kerkwijk, M. H., and Jayawardhana, R. (2012). Close companions to young stars. I. A large spectroscopic survey in Chamaeleon I and Taurus-Auriga. *ApJ*, 745(2):119.

Niemeier, W. (2008). Ausgleichungsrechnung. *De Gruyter*.

Nothnagel, A. (2009). Conventions on thermal expansion modelling of radio telescopes for geodetic and astrometric VLBI. *Journal of Geodesy*, 83(8):787–792.

Nothnagel, A. (2020). *Very Long Baseline Interferometry*, pages 1257–1314. Springer Berlin Heidelberg, Berlin, Heidelberg.

Nothnagel, A. (2022). Elements of geodetic and astrometric very long baseline interferometry. https://www.vlbi.at/data/publications/2022_Nothnagel_Elements_of_VLBI_20220221.pdf. Version: 21 February 2022.

Nothnagel, A., Artz, T., Behrend, D., and Malkin, Z. (2017). International VLBI Service for Geodesy and Astrometry. *Journal of Geodesy*, 91:711–721.

Nyu, D., Nakagawa, A., Matsui, M., Imai, H., Sofue, Y., Omodaka, T., Kurayama, T., Kamohara, R., Hirota, T., Honma, M., Shibata, K. M., Kobayashi, H., Iwadate, K., and Miyaji, T. (2011). Astrometry of AGB variables with VERA: Annual parallax and the orbit of SY Sculptoris in the Galaxy. *PASJ*, 63(1):63–70.

Ortiz-León, G. N., Dzib, S. A., Kounkel, M. A., Loinard, L., Mioduszewski, A. J., Rodríguez, L. F., Torres, R. M., Pech, G., Rivera, J. L., Hartmann, L., Boden, A. F., II, N. J. E., Briceño, C., Tobin, J. J., and Galli, P. A. B. (2017a). The Gould's Belt Distances Survey (GOBELINS). III. The distance to the Serpens/Aquila molecular complex. *ApJ*, 834(2):143.

Ortiz-León, G. N., Loinard, L., Kounkel, M. A., Dzib, S. A., Mioduszewski, A. J., Rodríguez, L. F., Torres, R. M., González-Lópezlira, R. A., Pech, G., Rivera, J. L., Hartmann, L., Boden, A. F., II, N. J. E., Briceño, C., Tobin, J. J., Galli, P. A. B., and Gudehus, D. (2017b). The Gould's Belt Distances Survey (GOBELINS). i. Trigonometric parallax, distances, and depth of the Ophiuchus complex. *ApJ*, 834(2):141.

Paredes, J. M., Martí, J., Ribó, M., and Massi, M. (2000). Discovery of a high-energy gamma-ray-emitting persistent microquasar. *Science*, 288(5475):2340–2342.

Perryman, M. (2012). The history of astrometry. *European Physical Journal H*, 37(5):745–792.

Perryman, M. A. C., de Boer, K. S., Gilmore, G., Høg, E., Lattanzi, M. G., Lindegren, L., Luri, X., Mignard, F., Pace, O., and de Zeeuw, P. T. (2001). Gaia: Composition, formation and evolution of the galaxy. *A&A*, 369(1):339–363.

Peterson, W. M., Mutel, R. L., Lestrade, J.-F., Güdel, M., and Goss, W. M. (2011). Radio astrometry of the triple systems Algol and UX Arietis. *ApJ*, 737(2):104.

Petit, G. and Luzum, B. (2010). IERS Conventions (2010). *IERS Technical Note*, 36:1.

Petrachenko, W. T., Niell, A. E., Corey, B. E., Behrend, D., Schuh, H., and Wresnik, J. (2012). VLBI2010: Next generation VLBI system for geodesy and astrometry. In Kenyon, S., Pacino, M. C., and Marti, U., editors, *Geodesy for Planet Earth*, pages 999–1005, Berlin, Heidelberg. Springer Berlin Heidelberg.

Petrov, L. (2018). VLBI global solution rfc_2018b. http://astrogeo.org/vlbi/solutions/rfc_2018b/, accessed 12 June 2019.

Petrov, L. and Boy, J.-P. (2004). Study of the atmospheric pressure loading signal in very long baseline interferometry observations. *Journal of Geophysical Research: Solid Earth*, 109(B3).

Petrov, L. and Kovalev, Y. Y. (2017). Observational consequences of optical band milliarcsec-scale structure in active galactic nuclei discovered by Gaia. *MNRAS*, 471(4):3775–3787.

Petrov, L. and Kovalev, Y. Y. (2017). On significance of VLBI/Gaia position offsets. *Monthly Notices of the Royal Astronomical Society: Letters*, 467(1):L71–L75.

Petrov, L., Kovalev, Y. Y., and Plavin, A. V. (2018). A quantitative analysis of systematic differences in the positions and proper motions of Gaia DR2 with respect to VLBI. *Monthly Notices of the Royal Astronomical Society*, 482(3):3023–3031.

Phillips, R. B., Lonsdale, C. J., Feigelson, E. D., and Deeney, B. D. (1996). Polarized radio emission from the multiple T Tauri system HD 283447. *AJ*, 111:918.

Plavin, A. V., Kovalev, Y. Y., and Petrov, L. Y. (2019). Dissecting the AGN disk-jet system with joint VLBI-Gaia analysis. *ApJ*, 871(2):143.

Plavin, A. V., Kovalev, Y. Y., Pushkarev, A. B., and Lobanov, A. P. (2019). Significant core shift variability in parsec-scale jets of active galactic nuclei. *Monthly Notices of the Royal Astronomical Society*, 485(2):1822–1842.

Porcas, R. W. (2009). Radio astrometry with chromatic AGN core positions. *A&A*, 505(1):L1–L4.

Pradel, N., Charlot, P., and Lestrade, J.-F. (2006). Astrometric accuracy of phase-referenced observations with the VLBA and EVN. *A&A*, 452(3):1099–1106.

Ratner, M. I., Bartel, N., Bietenholz, M. F., Lebach, D. E., Lestrade, J.-F., Ransom, R. R., and Shapiro, I. I. (2012). VLBI for Gravity Probe B. V. Proper motion and parallax of the guide star, IM Pegasi. *The Astrophysical Journal Supplement Series*, 201(1):5.

Ray, R. D. and Ponte, R. M. (2003). Barometric tides from ECMWF operational analyses. *Annales Geophysicae*, 21(8):1897–1910.

Reid, M. and Honma, M. (2014). Microarcsecond radio astrometry. *ARA&A*, 52(1):339–372.

Richichi, A., Leinert, C., Jameson, R., and Zinnecker, H. (1994). New binary young stars in the Taurus and Ophiuchus star-forming regions. *A&A*, 287:145–153.

Riess, A. G., Casertano, S., Yuan, W., Macri, L., Bucciarelli, B., Lattanzi, M. G., MacKenty, J. W., Bowers, J. B., Zheng, W., Filippenko, A. V., Huang, C., and Anderson, R. I. (2018). Milky Way Cepheid Standards for measuring cosmic distances and application to Gaia DR2: Implications for the Hubble Constant. *ApJ*, 861(2):126.

Rioja, M. J., Dodson, R., Orosz, G., Imai, H., and Frey, S. (2017). MultiView high precision VLBI astrometry at low frequencies. *The Astronomical Journal*, 153(3):105.

Rogers, A. E. E. (1970). Very long baseline interferometry with large effective bandwidth for phase-delay measurements. *Radio Science*, 5(10):1239–1247.

Ryan, J. and Ma, C. (1998). NASA-GSFC's geodetic VLBI program: a twenty-year retrospective. *Physics and Chemistry of the Earth*, 23(9):1041–1052.

Sanchez-Bermudez, J., Alberdi, A., Schödel, R., Brandner, W., Galván-Madrid, R., Guirado, J. C., Herrero-Illana, R., Hummel, C. A., Marcaide, J. M., and Pérez-Torres, M. A. (2019). A VLBI study of the wind-wind collision region in the massive multiple HD 167971. *A&A*, 624:A55.

Schaefer, G. H., Beck, T. L., Prato, L., and Simon, &. M. (2020). Orbital motion, variability, and masses in the T Tauri triple system. *The Astronomical Journal*, 160(1):35.

Schaefer, G. H., Prato, L., and Simon, M. (2018). Orbital motion of young binaries in Ophiuchus and Upper Centaurus–Lupus. *AJ*, 155(3):109.

Schartner, M. (2019). *Optimizing geodetic VLBI schedules with VieSched++*. PhD thesis, Wien.

Schönrich, R., McMillan, P., and Eyer, L. (2019). Distances and parallax bias in Gaia DR2. *MNRAS*, 487(3):3568–3580.

Schuh, H. and Behrend, D. (2012). VLBI: A fascinating technique for geodesy and astrometry. *Journal of Geodynamics*, 61:68–80.

Schuh, H. and Böhm, J. (2013). *Very Long Baseline Interferometry for geodesy and astrometry*, page 339–376. Springer Berlin Heidelberg, Berlin, Heidelberg.

Schuh, H., Heinkelmann, R., Beyerle, G., Anderson, J. M., Balidakis, K., Belda, S., Dhar, S., Glaser, S., Jenie, O. S., Karbon, M., Kitpracha, C., Nehbit, P. K., Liu, L., Lunz, S., Mammadaliyev, N., Modiri, S., Nilsson, T. J., Raut, S., Soja, B., Wang, J., and Xu, M. H. (2021). The Potsdam Open Source Radio Interferometry Tool (PORT). *Publications of the Astronomical Society of the Pacific*, 133(1028):104503.

Secrest, N. J., Dudik, R. P., Dorland, B. N., Zacharias, N., Makarov, V., Fey, A., Frouard, J., and Finch, C. (2015). Identification of 1.4 Million Active Galactic Nuclei in the Mid-Infrared using WISE Data. *ApJS*, 221(1):12.

Secrest, N. J., Dudik, R. P., Dorland, B. N., Zacharias, N., Makarov, V., Fey, A., Frouard, J., and Finch, C. (2016). VizieR Online Data Catalog: AGNs in the MIR using AllWISE data (Secrest+, 2015). *VizieR Online Data Catalog*, page J/ApJS/221/12.

Seidelmann, P. K. (1992). *Explanatory supplement to the Astronomical almanac.* Mill Valley: University Science Books, [rev. ed.] edition.

Shepherd, M. C. (1997). Difmap: an interactive program for synthesis imaging. In Hunt, G. and Payne, H., editors, *Astronomical Data Analysis Software and Systems VI*, volume 125 of *Astronomical Society of the Pacific Conference Series*, page 77.

Shuping, R. Y., Vacca, W. D., Kassis, M., and Yu, K. C. (2012). Spectral classification of the brightest objects in the galactic star-forming region W40. *AJ*, 144(4):116.

Shuygina, N., Ivanov, D., Ipatov, A., Gayazov, I., Marshalov, D., Melnikov, A., Kurdubov, S., Vasilyev, M., Ilin, G., Skurikhina, E., Surkis, I., Mardyshkin, V., Mikhailov, A., Salnikov, A., Vytnov, A., Rakhimov, I., Dyakov, A., and Olifirov, V. (2019). Russian VLBI network "Quasar": Current status and outlook. *Geodesy and Geodynamics*, 10(2):150–156. From Space Geodesy to Astro-Geodynamics.

Sovers, O. J., Fanselow, J. L., and Jacobs, C. S. (1998). Astrometry and geodesy with radio interferometry: experiments, models, results. *Rev. Mod. Phys.*, 70:1393–1454.

Sparks, W. B., Fraix-Burnet, D., Macchetto, F., and Owen, F. N. (1992). A counterjet in the elliptical galaxy M87. *Nature*, 355(6363):804–806.

Thompson, A. R., Moran, J. M., and Swenson, G. W. (1986). *Interferometry and synthesis in radio astronomy*. Wiley, New York.

Titov, O. and Lambert, S. (2013). Improved VLBI measurement of the solar system acceleration. *A&A*, 559:A95.

Titov, O., Lambert, S. B., and Gontier, A. M. (2011). VLBI measurement of the secular aberration drift. *A&A*, 529:A91.

Titov, O. and Malkin, Z. (2009). Effect of asymmetry of the radio source distribution on the apparent proper motion kinematic analysis. *A&A*, 506(3):1477–1485.

Titov, O., Shu, F., and Chen, W. (2020). Observations of radio stars in geodetic VLBI experiments. In Bizouard, C., editor, *Astrometry, Earth Rotation, and Reference Systems in the GAIA era*, pages 173–178.

Torres, R. M., Loinard, L., Mioduszewski, A. J., Boden, A. F., Franco-Hernández, R., Vlemmings, W. H. T., and Rodríguez, L. F. (2012). VLBA determination of the distance to nearby star-forming regions. V. Dynamical mass, distance, and radio structure of V773 Tau A. *ApJ*, 747(1):18.

Torres, R. M., Loinard, L., Mioduszewski, A. J., and Rodriguez, L. F. (2007). VLBA determination of the distance to nearby star-forming regions. II. Hubble 4 and HDE 283572 in Taurus. *ApJ*, 671(2):1813–1819.

Torres, R. M., Loinard, L., Mioduszewski, A. J., and Rodríguez, L. F. (2009). VLBA determination of the distance to nearby star-forming regions. III. HP TAU/G2 and the three-dimensional structure of Taurus. *ApJ*, 698(1):242–249.

Ulvestad, J. (1999). VLBA Scientific Memorandum 20: Phase-referencing cycle times. *VLBA Scientific Memorandum*, 20.

Ulvestad, J. and Schmitt, H. (2001). VLBA Test Memorandum 68: The need for ionospheric corrections at 5 GHz. *VLBA Test Memorandum*, 68.

Walker, R. C. (2014). VLBA Scientific Memorandum 37: Flux density calibration on the VLBA. *VLBA Scientific Memorandum*.

Washuettl, A., Strassmeier, K., Granzer, T., Weber, M., and Oláh, K. (2009). The chromospherically active binary star EI Eridani: I. Absolute dimensions. *Astronomische Nachrichten*, 330(1):27–41.

Welty, A. D. (1995). Discovery of a pre-main-sequence spectrscopic binary: V773 Tauri. *AJ*, 110:776.

Wendker, H. J. (2015). VizieR Online Data Catalog: Catalogue of radio stars (Wendker, 2001). *VizieR Online Data Catalog*, page VIII/99.

Wenger, M., Ochsenbein, F., Egret, D., Dubois, P., Bonnarel, F., Borde, S., Genova, F., Jasniewicz, G., Laloë, S., Lesteven, S., and Monier, R. (2000). The SIMBAD astronomical database. The CDS reference database for astronomical objects. *A&AS*, 143:9–22.

Wolf, H. (1978). The Helmert block method — its origins and development. In *Proceedings of the second International Symposium on Problems Related to the Redefinition of North American Geodetic Networks*, pages 319–326. Arlington, Virginia: U.S. Dept. of Commerce.

Wrobel, J. M., Walker, R. C., Benson, J. M., and Beasley, A. J. (2000). VLBA Scientific Memorandum 24: Strategies for phase referencing with the VLBA. *VLBA Scientific Memorandum*, 24.

Wu, Y. W., Torricelli-Ciamponi, G., Massi, M., Reid, M. J., Zhang, B., Shao, L., and Zheng, X. W. (2018). Revisiting LS I +61 303 with VLBI astrometry. *MNRAS*, 474(3):4245–4253.

Xu, M. H., Anderson, J. M., Heinkelmann, R., Lunz, S., Schuh, H., and Wang, G. L. (2019a). Structure effects for 3417 celestial reference frame radio sources. *ApJS*, 242(1):5.

Xu, M. H., Lunz, S., Anderson, J. M., Savolainen, T., Zubko, N., and Schuh, H. (2021). Evidence of the Gaia–VLBI position differences being related to radio source structure. *Astronomy and Astrophysics*, 647.

Xu, M. H., Savolainen, T., Anderson, J. M., Kareinen, Niko, Zubko, Nataliya, Lunz, Susanne, and Schuh, Harald (2022). Impact of the image alignment over frequency for the VLBI Global Observing System. *A&A*, 663:A83.

Xu, M. H., Savolainen, T., Zubko, N., Poutanen, M., Lunz, S., Schuh, H., and Wang, G. (2020). Imaging VGOS observations and investigating source structure effects. *Earth and Space Science Open Archive*, page 42.

Xu, S., Zhang, B., Reid, M. J., Zheng, X., and Wang, G. (2019b). Comparison of Gaia DR2 parallaxes of stars with VLBI astrometry. *ApJ*, 875(2):114.

Zhang, B., Reid, M. J., Menten, K. M., and Zheng, X. W. (2012). Distance and kinematics of the red supergiant VY CMa: Very Long Baseline Array and Very Large Array astrometry. *ApJ*, 744(1):23.

Zinn, J. C., Pinsonneault, M. H., Huber, D., and Stello, D. (2019). Confirmation of the Gaia DR2 parallax zero-point offset using asteroseismology and spectroscopy in the Kepler Field. *ApJ*, 878(2):136.

A New VLBA observations (UL005) - data processing with AIPS and DIFMAP

This section contains detailed information about the data processing of the phase-referenced observations in AIPS and DIFMAP. This information is not crucial for the general reader of this publication, but anyone who wants to use the positions or even use them in other ways should be able to know about the data processing applied.

Data cleaning and calibration in AIPS: "The data were processed using the NRAO Astronomical Image Processing System (AIPS; Greisen 2003) as outlined in the AIPS cookbook[1] and with the help of ParselTongue (Kettenis et al. 2006). In X-band strong radio frequency interference (RFI) happened at the Pie Town antenna, and in addition the observations of the antenna had very low SNR. We obtained better results after flagging the antenna entirely. In C-band RFI happened at the Brewster antenna and the respective subband (IF 1 at 4.6118 GHz in AIPS) was flagged.

The amplitude calibration was based on Walker (2014). The a priori Earth Orientation Parameters were corrected using the finals series from the United States Naval Observatory (USNO). Then the dispersive delay from the ionosphere was removed utilizing global maps of total electron content (TEC) derived from GPS observables and provided by the Jet Propulsion Laboratory (JPL). After the purely geometric parallactic angle correction was applied, the digital sampling correction to amplitudes was carried out. In the next step, instrumental delays and phases were corrected. Pulse-calibration information was used except for antennas with ambiguities in those data. For those antennas the corrections were done manually using the known bright compact radio source J0359+5057 in experiment UL005A, J0927+3902 in experiment UL005B, J2253+1608 in experiment UL005C in X-band, and J1927+7358 in experiment UL005C in C-band. Then bandpass calibration was performed, auto-correlations were calibrated to be unity, and a priori amplitude calibration was applied using system temperature and gain curve tables. Atmospheric opacity correction was negligible at the given frequencies. Multi-band delays for the observations of the geodetic blocks were produced [with task MBDLY] and used to correct for elevation- and time-dependent delay errors for each antenna as described

[1] www.aips.nrao.edu/CookHTML/CookBook.html

in Mioduszewski (2009) by interpolation over all scans [using task DELZN]. [In Mioduszewski (2009) the example shows a difference in position of a weak < 2 mJy target of 0.4 mas when applying DELZN or not. Furthermore, the peak is higher. The memo says that with low elevations, a weak target source could well be undetectable without correcting for atmosphere.] The secondary calibrators are in principle used to calculate residual phase gradients between the phase-calibrator and the secondary calibrator. With this additional information, the correction of the target positions can be improved using the task ATMCA in AIPS (Fomalont and Kogan 2005). However, it was not possible to employ this feature for our observations since the secondary calibrators were only scheduled in one of the three phase-referencing blocks in order to obtain their peak intensities for the follow-on observations, as noted above" (Lunz et al. 2020a).

Fringe-fitting: A final fringe fit of each primary calibrator was made using the full scan length of 30 s. In fringe-fitting, corrections for the observed phases get determined by solving for the antenna-based instrumental phase, fringe rate, and delay, so that the observed phases fit the modeled phases well. It is a form of phase self-calibration. The derived corrections were applied to the respective calibrator itself as well as to its associated secondary calibrators and target star. Then the AIPS task SPLIT was used to pipe the data of an object from the multi-source file into a single data file for further use, such as imaging and determining positions. If a set of calibrators and stars was observed in two experiments, their respective data were first combined after the fringe fit to prepare a single file per object. The fringe fitting was done in two different ways, depending on what kind of position should be achieved:

- The primary calibrator was assumed to be a point source during the fringe fit, as was done for the geodetic VLBI analysis that was used for the creation of the ICRF3. In this way it was attempted to best connect the phase-referenced positions of the stars to the absolute positions of the primary calibrators from ICRF3. These data were used for self-calibration to derive CLEAN images with a high dynamic range for peak intensity determination and for insertion into the second type of fringe fitting as described below. In addition, the position differences between the primary calibrator and the star from this method were added to the calibrator positions to derive the absolute star positions of a single epoch.
- A clean component model was applied for the primary calibrator during the fringe fit. The clean component model was derived from self-calibration of the calibrator's data (from a fringe fit with a point source model applied). Following this method, the relative star positions were derived, which were inserted in the adjustment of models of stellar motion from VLBI position time series later on. Compared to the fringe fitting using a point source model, this method eliminates any scatter in the relative star position time series due to source structure of the calibrator.

Frequency averaging: In order to be able to process the data in the Caltech DIFMAP imaging package (DIFMAP; Shepherd (1997)) later on, the subbands needed to get frequency averaged. This however would result in bandwidth smearing, and therefore in a reduction of dynamic range because the a priori positions of the target stars deviated from the approximate positions used for correlation in some cases more than several tens of milliarcseconds. We therefore corrected the u, v, w terms of the target stars to match the positions of the brightest peak in the image created from the uncorrected data by using task UVFIX in AIPS. This allowed splitting the objects from the multi-source file while combining all channels of each subband without loss of dynamic range. If using AIPS instead of DIFMAP for imaging, the channels can be combined during the IMAGR task in AIPS itself.

Multiple primary calibrators: If a star was observed by multiple phase-referencing calibrators, the fringe fit of the calibrator data and subsequent steps were repeated for each of the calibrators so that multiple single source files were derived for the star. This was possible because of the incremental calibration philosophy of AIPS software.

Imaging in AIPS: The objects were imaged with a cell size of 0.2 mas and natural weighting (robust = 5).

Self-calibration: Self-calibration is performed on the data of an individual source after fringe-fitting. During this process, a clean component model is fit to the data and then this model is applied to the data. In the following round, a new clean component model is fit to the previously calibrated data, and so forth. Usually, first the phases are self-calibrated in several rounds. After the result converges, the phases and amplitudes are calibrated together. In case sources were observed in multiple experiments, the data of the sources were combined before self-calibration. For deriving peak intensities in Sect. 5.4.3, each phase-calibrators data was self-calibrated. Then these corrections were applied to the target star data, and, if possible, another round of phase-self-calibration was performed on the star's data. These processing steps had to be done manually, as automation was not possible due to the sparseness of the data and the faintness of the objects.

B Comparison of software approaches for the determination of radio source positions

There is a variety of software available for analyzing astrometric VLBI data for position determination. Two commonly used software packages were compared in this subsection to determine if they produce different results and if one is more suitable for the position determination of faint objects.

From the fringe fit with the point source model applied (see Sect. 5.4.2), and without self-calibration, CLEANed images (Högbom 1974; Clark 1980) with "a cell size of 0.2 mas and natural weighting [...] were produced in AIPS from which positions were derived using the task JMFIT. It fits two-dimensional Gaussians to a given area including the source in the image. The position uncertainty resulting from this task is based on the expected theoretical precision of the interferometer and the RMS noise of the image.

An independent comparison was done with the modelfit in the Caltech Difmap imaging package (Shepherd 1997)[1]. This task determines Gaussian model parameters of the radio source from the visibility data directly instead of from the image. The model can consist of multiple components. The uncertainty σ_{random} of a model component position was calculated from the beam shape and RMS noise of the image based on formulas for elliptical Gaussians in Condon (1997)" (Lunz et al. 2020a).

Section 2.3 in Condon (1997) provides the relevant equations:

$$\begin{aligned}
\mu_{x_0} &= \theta_M \mathrm{RMS}_{\mathrm{image}} / (\sqrt{8 \ln 2} \mathrm{PF}), \\
\mu_{y_0} &= \theta_m \mathrm{RMS}_{\mathrm{image}} / (\sqrt{8 \ln 2} \mathrm{PF}), \\
\sigma_{\alpha*,\mathrm{random}} &= \sqrt{\mu_{x_0}^2 \sin(\Theta)^2 + \mu_{y_0}^2 \cos(\Theta)^2}, \\
\sigma_{\delta,\mathrm{random}} &= \sqrt{\mu_{x_0}^2 \cos(\Theta)^2 + \mu_{y_0}^2 \sin(\Theta)^2},
\end{aligned} \tag{B.1}$$

[1] [...] The u, v, w terms of the target stars [were corrected] to match the positions of the brightest peak in the image created from the uncorrected data by using task UVFIX in AIPS. This allowed combining all channels of each subband, which is needed for Difmap, without loss of SNR due to potential bandwidth smearing in case the a priori position of the target star deviated from the approximate positions used for correlation by more than several tens of mas.

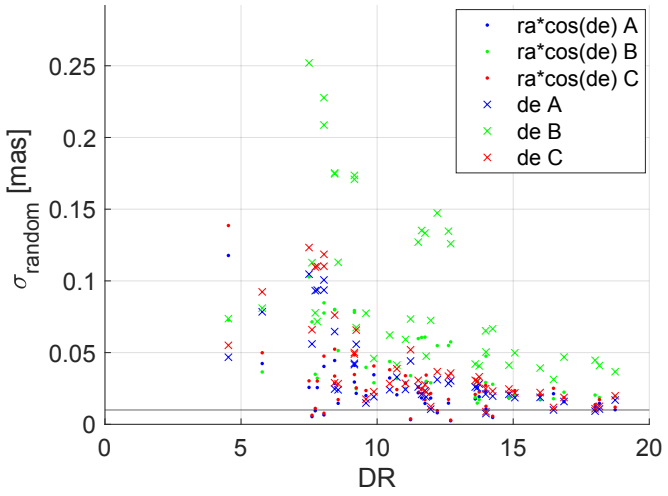

Figure B.1 Possible values for uncertainties σ_{random} as determined from (A) equations in Condon (1997) based on the model shape, (B) equations in Condon (1997) based on the beam shape, and (C) equations in Fomalont (1999) based on the model shape. The horizontal black line is at σ_{random}=10 µas. The results are given for the stars with corrections from a fringe fit using a point source model of the respective primary calibrator applied.

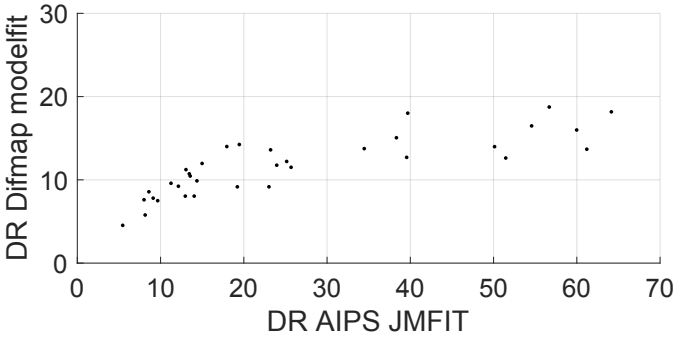

Figure B.2 Dynamic range DR from Difmap modelfit results versus the DR from AIPS JMFIT results for the stars with corrections from a fringe fit using a point source model of the respective primary calibrator applied. The two stars of the close binary systems HD 283447 and DoAr 51 are plotted as two separate dots.

where μ_{x_0} and μ_{y_0} are the uncertainties of the beam in x and y directions, which are the directions of the major and minor axis of the beam. Furthermore, θ_M is the full width at half maximum (FWHM) major diameter of the beam, θ_m is the FWHM minor diameter of the beam, Θ is the position angle of the major axis, PF is the model's peak flux density, and RMS_{image} is the image RMS. This uncertainty calculation represents the position uncertainty of the model component, rather than the uncertainty the model itself, as do equations which depend on the size of the estimated radio source model, such as equations in Fomalont (1999). To support this decision, in Fig. B.1, various σ_{random} are shown for the detected stars, sorted by the respective dynamic range DR of the stars' images. The uncertainties based on the beam shape from Eq. B.1 are show as solution B in green color.

The solution A uses the same equations as B, but is based on the shape of the estimated model instead of the beam shape. Solution C uses the equation 14-5 in Fomalont (1999) which is also based on the model shape. Two conclusions are drawn from the figure. First, our January 2020 observations include radio stars which were observed with a very large elongated beam shape in the declination direction. This is visible from the group of larger σ_{random} values for B compared to A and C for DR between 7 and 13. Second, the solutions based on the model shape, A and C, provide unrealistically small σ_{random} values for some stars. This is visible from any data points lying below the horizontal black line at σ_{random}=10 µas.

In addition, the positions from the task UVFIT in AIPS, which operates also in the visibility plane just like the Difmap modelfit functionality, were compared. A starting model was given to the task by using the results from JMFIT. This method did not provide robust results for the data in this work, which is why its usage was discarded.

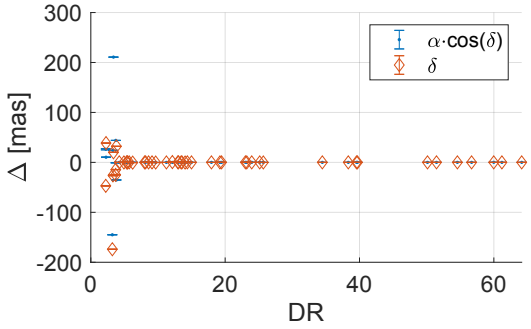

Figure B.3 Differences between the positions from the AIPS task JMFIT and the modelfit functionality from Difmap for all observed stars, sorted by the dynamic range DR from AIPS.

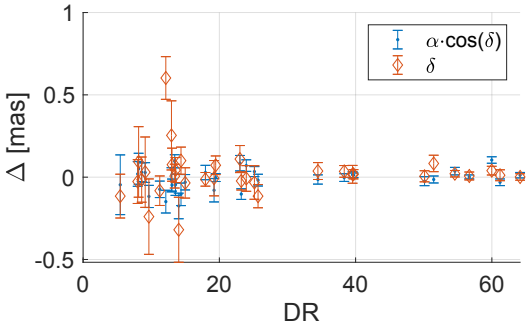

Figure B.4 Differences between the positions from the AIPS task JMFIT and the modelfit functionality from Difmap for the detected stars, sorted by the dynamic range DR from AIPS.

The differences of the DR between AIPS and Difmap solutions are shown in Fig. B.2. It is likely that the manual imaging in AIPS resulted in a slightly deeper cleaning of the data, and therefore in a higher DR. The position differences between the solutions from imaging in AIPS and Difmap for all stars where the data were corrected from a fringe fit with a point source model of the respective primary calibrator are shown in Fig. B.3. The use of a suitable DR as a cutoff criterion for a valid detection of a faint star is clearly verified by the position differences, because position differences from images with a higher DR than about 5.5 in AIPS are small, whereas position differences with smaller DR are large. The same information is given in Fig. B.4 for only the valid detections. Considering these position differences from the analysis in both software packages when detecting faint stars improved the reliability of the detection. Repeating the same analysis several times, it was found that modelfit gave more robust results for the weak objects. The position differences

between solutions from JMFIT and modelfit also provided information about the absolute position uncertainties of VLBI observations at individual epochs due to different analysis software.

ISSN 2190-7110